

Wolfgang Demtröder
Molecular Physics

Related Titles

Bethge, K., Gruber, G., Stöhlker, T.

Physik der Atome und Moleküle

Eine Einführung

437 pages with 192 figures

2004, Hardcover

ISBN 3-527-40463-5

Hollas, J. M.

Modern Spectroscopy

480 pages

2003, Hardcover

ISBN 0-470-84415-9

2003, Softcover

ISBN 0-470-84416-7

May, V., Kühn, O.

Charge and Energy Transfer Dynamics in Molecular Systems

490 pages with approx. 134 figures

2004, Hardcover

ISBN 3-527-40396-5

Brumer, P. W., Shapiro, M.

Principles of the Quantum Control of Molecular Processes

approx. 250 pages

2003, Hardcover

ISBN 0-471-24184-9

Cohen-Tannoudji, C., Dupont-Roc, J., Grynberg, G.

Atom-Photon Interactions

Basic Processes and Applications

678 pages with 108 figures

1998, Softcover

ISBN 0-471-29336-9

Wolfgang Demtröder

Molecular Physics

Theoretical Principles and Experimental Methods



WILEY-VCH Verlag GmbH & Co. KGaA

The Author

Prof. Dr. Wolfgang Demtröder
Department of Physics
University of Kaiserslautern
Germany
demtroed@rhrk.uni-kl.de

Translation

Dr. Michael Bär

Original title:

Molekülphysik. Theoretische Grundlagen und experimentelle Methoden.

© 2003 Oldenbourg Wissenschaftsverlag GmbH

All rights reserved

Authorized translation from German language edition published by Oldenbourg Wissenschaftsverlag GmbH

All books published by Wiley-VCH are carefully produced. Nevertheless, authors, editors, and publisher do not warrant the information contained in these books, including this book, to be free of errors. Readers are advised to keep in mind that statements, data, illustrations, procedural details or other items may inadvertently be inaccurate.

Library of Congress Card No.:

applied for

British Library Cataloguing-in-Publication Data

A catalogue record for this book is available from the British Library.

Bibliographic information published by**Die Deutsche Bibliothek**

Die Deutsche Bibliothek lists this publication in the Deutsche Nationalbibliografie; detailed bibliographic data is available in the Internet at <<http://dnb.ddb.de>>.

© 2005 WILEY-VCH Verlag GmbH & Co. KGaA, Weinheim

All rights reserved (including those of translation into other languages). No part of this book may be reproduced in any form – by photoprinting, microfilm, or any other means – nor transmitted or translated into a machine language without written permission from the publishers. Registered names, trademarks, etc. used in this book, even when not specifically marked as such, are not to be considered unprotected by law.

Typesetting Dr. Michael Bär, Wiesloch

Printing Strauss GmbH, Moerlenbach

Binding Litges & Dopf Buchbinderei GmbH, Heppenheim

Printed in the Federal Republic of Germany

Printed on acid-free paper

ISBN-13: 978-3-527-40566-4

ISBN-10: 3-527-40566-6

Contents

Contents	v
Preface	xiii
1	Introduction 1
1.1	Short Historical Overview 2
1.2	Molecular Spectra 4
1.3	Recent Developments 8
1.4	The Concept of This Book 10
2	Molecular Electronic States 15
2.1	Adiabatic Approximation and the Concept of Molecular Potentials 15
2.1.1	Quantum-Mechanical Description of Free Molecules 15
2.1.2	Separation of Electronic and Nuclear Wavefunctions 18
2.1.3	Born–Oppenheimer Approximation 20
2.1.4	Adiabatic Approximation 22
2.2	Deviations From the Adiabatic Approximation 23
2.3	Potentials, Curves and Surfaces, Molecular Term Diagrams and Spectra 25
2.4	Electronic States of Diatomic Molecules 28
2.4.1	Exact Treatment of the Rigid H_2^+ Molecule 29
2.4.2	Classification of Electronic Molecular States 34
2.4.2.1	Energetic Ordering of Electronic States 35
2.4.2.2	Symmetries of Electronic Wavefunctions 36
2.4.2.3	Electronic Angular Momenta 38
2.4.3	Electron Configurations and Electronic States 42
2.4.3.1	The Approximation of Separated Atoms 42
2.4.3.2	The “United Atom” Approximation 45
2.4.4	Molecular Orbitals and the Aufbau Principle 45

2.4.5	Correlation Diagrams	48
2.5	Approximation Methods for the Calculation of Electronic Wavefunctions	51
2.5.1	The Variational Method	52
2.5.2	The LCAO Approximation	53
2.6	Application of Approximation Methods to One-electron Systems	56
2.6.1	A Simple LCAO Approximation for the H_2^+ Molecule	56
2.6.2	Deficiencies of the Simple LCAO Method	58
2.6.3	Improved LCAO Approximations	60
2.7	Many-electron Molecules	63
2.7.1	Molecular Orbitals and the Single-particle Approximation	63
2.7.2	The H_2 Molecule	66
2.7.2.1	The Molecular Orbital Approximation for H_2	66
2.7.3	The Heitler–London Approximation	69
2.7.4	Improvements of Both Methods	70
2.7.5	Equivalence of Heitler–London and MO Approximation	71
2.7.6	Generalized MO Ansatz	71
2.8	Modern <i>Ab Initio</i> Methods	72
2.8.1	The Hartree–Fock Approximation	73
2.8.2	Configuration Interaction	75
2.8.3	<i>Ab Initio</i> Calculations and Quantum Chemistry	76
3	Rotation, Vibration, and Potential Curves of Diatomic Molecules	79
3.1	Quantum-mechanical Treatment	79
3.2	Rotation of Diatomic Molecules	81
3.2.1	The Rigid Rotor	81
3.2.2	Centrifugal Distortion	82
3.2.3	The Influence of Electron Rotation	84
3.3	Molecular Vibrations	86
3.3.1	The Harmonic Oscillator	87
3.3.2	The Anharmonic Oscillator	91
3.3.2.1	Morse Potential	92
3.3.2.2	Taylor Expansion of Potentials	92
3.3.2.3	Quartic Potential	93
3.3.2.4	Generalized Potential	95
3.4	Vibration–Rotation Interaction	95
3.5	Term Values of the Vibrating Rotor; Dunham Expansion	97
3.5.1	Term Values for the Morse Potential	97
3.5.2	Term Values for a Generalized Potential	98
3.5.3	Dunham Expansion	99
3.5.4	Isotopic Shifts	100

3.6	Determination of Potential Curves from Measured Term Values	100
3.6.1	The WKB Approximation	101
3.6.2	WKB Approximation and Dunham Expansion	104
3.6.3	Other Potential Expansions	105
3.6.4	The RKR Method	105
3.6.5	The Inverted Perturbation Approach	109
3.7	Potential Curves at Large Internuclear Distances	112
3.7.1	Multipole Expansion	113
3.7.2	Induction Contributions to the Interaction Potential	114
3.7.2.1	Point-charge-induced Dipole (Ion–Atom Interaction)	115
3.7.2.2	Interaction Between Two Neutral Atoms	116
3.7.3	Lennard-Jones Potential	118
4	Spectra of Diatomic Molecules	121
4.1	Transition Probabilities	122
4.1.1	Einstein Coefficients	122
4.1.2	Transition Probabilities and Matrix Elements	125
4.1.3	Matrix Elements in the Born–Oppenheimer Approximation	128
4.2	Structure of the Spectra of Diatomic Molecules	129
4.2.1	Vibration–Rotation Spectra	129
4.2.2	Pure Vibrational Transitions Within an Electronic State	131
4.2.3	Pure Rotational Transitions	133
4.2.4	Vibration–Rotation Transitions	136
4.2.5	Electronic Transitions	138
4.2.6	<i>R</i> Centroid Approximation; the Franck–Condon Principle	139
4.2.7	The Rotational Structure of Electronic Transitions	145
4.2.8	Continuous Spectra	148
4.3	Line Profiles of Spectral Lines	151
4.3.1	Natural Linewidth	152
4.3.2	Doppler Broadening	154
4.3.3	Voigt Profiles	157
4.3.4	Collisional Broadening of Spectral Lines	158
4.4	Multi-photon Transitions	161
4.4.1	Two-Photon Absorption	161
4.4.2	Raman Transitions	165
4.4.3	Raman Spectra	167
4.5	Thermal Population of Molecular Levels	170
4.5.1	Thermal Population of Rotational Levels	170
4.5.2	Population of Vibration–Rotation Levels	171
4.5.3	Nuclear Spin Statistics	171

5	Molecular Symmetry and Group Theory	175
5.1	Symmetry Operations and Symmetry Elements	175
5.2	Foundations of Group Theory	179
5.3	Molecular Point Groups	181
5.4	Classification of Molecular Point Groups	184
5.4.1	The Point Groups C_n , C_{nv} , and C_{nh}	185
5.4.2	The Point Groups D_n , D_{nd} , and D_{nh}	187
5.4.3	The groups S_n	189
5.4.4	The Point Groups T_d and O_h	190
5.4.5	How to Find the Point Group of a Molecule	191
5.5	Symmetry Types and Representations of Groups	192
5.5.1	The Representation of the Group C_{2v}	193
5.5.2	The Representation of the Group C_{3v}	195
5.5.3	Characters and Character Tables	197
5.5.4	Sums, Products, and Reduction of Representations	198
6	Rotations and Vibrations of Polyatomic Molecules	203
6.1	Transformation From the Laboratory System to the Molecule-fixed System	204
6.2	Molecular Rotation	207
6.2.1	The Rigid Rotor	207
6.2.2	The Symmetric Top	211
6.2.3	Quantum-mechanical Treatment of Rotation	212
6.2.4	Centrifugal Distortion of the Symmetric Top	214
6.2.5	The Asymmetric Top	215
6.3	Vibrations of Polyatomic Molecules	221
6.3.1	Normal Modes	222
6.3.2	Example: Calculation of the Stretching Vibrations of a Linear Molecule AB_2	225
6.3.3	Degenerate Vibrations	226
6.3.4	Quantum-mechanical Treatment	228
6.3.5	Anharmonic Vibrations	230
6.3.6	Vibration–Rotation Coupling	232
7	Electronic States of Polyatomic Molecules	237
7.1	Molecular Orbitals	237
7.2	Hybridization	240
7.3	Triatomic Molecules	245
7.3.1	The BeH_2 Molecule	245
7.3.2	The H_2O Molecule	247

- 7.3.3 The CO₂ Molecule 250
- 7.4 AB₂ Molecules and Walsh Diagrams 252
- 7.5 Molecules With More Than Three Atoms 254
- 7.5.1 The NH₃ Molecule 254
- 7.5.2 Formaldehyde 256
- 7.6 π -Electron Systems 257
- 7.6.1 Butadiene 257
- 7.6.2 Benzene 259

8 Spectra of Polyatomic Molecules 263

- 8.1 Pure Rotational Spectra 263
- 8.1.1 Linear Molecules 264
- 8.1.2 Symmetric Top Molecules 266
- 8.1.3 Asymmetric Top Molecules 267
- 8.1.4 Intensities of Rotational Transitions 269
- 8.1.5 Symmetry Properties of Rotational Levels 270
- 8.1.6 Statistical Weights and Nuclear Spin Statistics 272
- 8.1.7 Line Profiles of Absorption Lines 274
- 8.2 Vibration–Rotation Transitions 274
- 8.2.1 Selection Rules and Intensities of Vibrational Transitions 275
- 8.2.2 Fundamental Transitions 278
- 8.2.3 Overtone and Combination Bands 279
- 8.2.4 Rotational Structure of Vibrational Bands 283
- 8.3 Electronic Transitions 286
- 8.4 Fluorescence and Raman Spectra 288

9 Breakdown of the Born–Oppenheimer Approximation, Perturbations in Molecular Spectra 293

- 9.1 What is a Perturbation? 293
- 9.1.1 Quantitative Treatment of Perturbations 295
- 9.1.2 Adiabatic and Diabatic Basis 297
- 9.1.3 Perturbations Between Two Levels 299
- 9.2 Hund’s Coupling Cases 300
- 9.3 Discussion of Different Types of Perturbations 302
- 9.3.1 Electrostatic Interaction 302
- 9.3.2 Spin–Orbit Coupling 305
- 9.3.3 Rotational Perturbations 307
- 9.3.4 Vibronic Coupling 309
- 9.3.5 Renner–Teller Coupling 311
- 9.3.6 Jahn–Teller Effect 313

9.3.7	Predissociation	316
9.3.8	Autoionization	317
9.4	Radiationless Transitions	320
10	Molecules in External Fields	325
10.1	Diamagnetic and Paramagnetic Molecules	326
10.2	Zeeman Effect in Linear Molecules	327
10.3	Spin–Orbit Coupling and External Magnetic Fields	336
10.4	Molecules in Electric Fields: The Stark Effect	339
11	Van der Waals Molecules and Clusters	343
11.1	Van der Waals Molecules	345
11.2	Clusters	350
11.2.1	Alkali Metal Clusters	352
11.2.2	Rare-gas Clusters	355
11.2.3	Water Clusters	357
11.2.4	Covalently Bonded Clusters	358
11.3	Generation of Clusters	359
12	Experimental Techniques in Molecular Physics	361
12.1	Microwave Spectroscopy	362
12.2	Infrared and Fourier Spectroscopy	366
12.3	Classical Spectroscopy in the Visible and Ultraviolet	372
12.4	Laser Spectroscopy	381
12.4.1	Laser Absorption Spectroscopy	381
12.4.2	Intracavity Laser Spectroscopy	385
12.4.3	Absorption Measurements Using the Resonator Decay Time	386
12.4.4	Photoacoustic Spectroscopy	387
12.4.5	Laser-magnetic Resonance Spectroscopy	388
12.4.6	Laser-induced Fluorescence	389
12.4.7	Laser Spectroscopy in Molecular Beams	391
12.4.8	Doppler-free Nonlinear Laser Spectroscopy	395
12.4.9	Multi-photon Spectroscopy	401
12.4.10	Double Resonance Techniques	402
12.4.11	Coherent Anti-Stokes Raman Spectroscopy	406
12.4.12	Time-resolved Laser Spectroscopy	407
12.4.13	Femtochemistry	411
12.4.14	Coherent Control	412

12.5	Photoelectron Spectroscopy	415
12.5.1	Experimental Setups	416
12.5.2	Photoionization Processes	417
12.5.3	ZEKE Spectroscopy	418
12.5.4	Angular Distribution of Photoelectrons	420
12.5.5	X-ray Photoelectron Spectroscopy (XPS)	421
12.6	Mass Spectroscopy	422
12.6.1	Magnetic Mass Spectrometers	423
12.6.2	Quadrupole Mass Spectrometers	424
12.6.3	Time-of-flight Mass Spectrometers	426
12.7	Radiofrequency Spectroscopy	427
12.8	Nuclear Magnetic Resonance Spectroscopy	429
12.9	Electron Spin Resonance	432
12.10	Conclusion	434

Appendix: Character Tables of Some Point Groups 437

Bibliography 441

Index 461

Preface

During the last few decades, molecular physics has gained increasing importance in physics, chemistry and biology. There are several reasons for this progress. The development of new experimental techniques with vastly improved sensitivity and spectral resolution has allowed detailed measurements of structure and dynamics even for large molecules in minute concentrations. This opens the way for studying chemical reactions and biological processes on a molecular level. Using ultrashort laser pulses, very fast dynamical processes in excited molecular states can be measured with a time resolution of a few femtoseconds. Examples are the dissociation of excited molecules, or the redistribution of the energy pumped into a selectively excited molecular state by photon absorption. This energy redistribution onto many vibronic states can be caused by collisions or by couplings between different molecular states, and it often results in a permanent change of molecular structure (isomerization). For the first time in the development of molecular physics, such ultrashort phenomena can be measured in realtime.

Another important reason for the progress in molecular physics is the development of fast computers and sophisticated software, which allow the calculation of molecular structures and potential energy surfaces in molecular ground states and even in excited states with an astonishing accuracy. Also, the dynamics of excited molecular states can be today visualized on a computer screen in slow motion to give a vivid and detailed picture of the way molecular processes occur on a femtosecond scale. This allows a much better understanding of chemical and biological reaction paths. Quantum chemistry, working in this field, has therefore received more attention in chemistry and biology. The success of molecular biology is partly based both on the new experimental techniques and on such computer simulations.

In order to gain a more profound understanding of these developments, one has to acquire sufficient knowledge about the basic physics of molecules. This volume tries to make the fundamentals of molecular physics accessible, starting with diatomic molecules as the simplest molecular species. The different approximation methods used for the calculation of molecular structure, their physical meaning and their limitations are presented. The principles that are valid for diatomics are then transferred

to and extended to polyatomic molecules, where additional phenomena occur, such as vibronic couplings or Coriolis effects in rotating molecules. The last chapter discusses classical and modern experimental techniques used in molecular physics, giving the reader a better understanding of the possibilities, advantages, and drawbacks of the different experimental approaches to the investigation of molecules. It is in particular laser spectroscopy that has contributed in an outstanding way to the progress in molecular spectroscopy.

This book is a thoroughly revised edition of a German edition published two years ago. The author would like to thank Michael Bär who translated the German book and took care of the typesetting for his careful work and for many valuable suggestions. The author hopes that this textbook will foster the interest in molecular physics in the communities of physicists, chemists and biologists.

Since no book is perfect, the author appreciates any comments, hints to possible errors, or suggestions for improvements.

*Wolfgang Demtröder
Kaiserslautern, August 2005*

1

Introduction

Molecular physics is at the heart of chemistry and physics. A thorough understanding of chemical and biological processes has been rendered possible only by detailed investigations of the structure and dynamics of the molecules involved. A striking example is the question of chemical bond strength, which is of crucial importance for the course of chemical reactions. Molecular physics traces bond strengths back to the geometrical structure of the molecule's nuclear framework and the spatial distribution of the molecular electron density. The reason for the chemical inertness of the rare gases or the high chemical activity of the alkali metals could only be explained after the structure of the electron shell was understood.

The electron distribution in a molecule can be calculated quantitatively with the aid of quantum theory. Hence, only the application of quantum theory to molecular physics has been able to create a consistent model of molecules and has made theoretical chemistry (quantum chemistry) so successful.

Today's knowledge on the structure of molecules with electrons and nuclei as their building blocks, on the geometric arrangement of nuclei in molecules and on the spatial and energetic properties of the electron shell is based on more than 200 years of research in the field. The origin of this research was characterized by the application of a rational scientific method aiming at quantitative reproducible experimental results. This constitutes the fundamental difference between "modern chemistry" and "alchemy", which contained many mystic elements. The results obtained in these two centuries have not only revolutionized our image of molecules but have also shaped our way of thinking. A similar process can be observed at present, related to the application of physical and chemical methods to biology, where the molecular structures under investigation are particularly complex and the experimental methods employed must therefore be particularly subtle.

It is interesting to take a brief look at the historical development of molecular physics. For more detailed historical accounts we refer to the corresponding literature [1.1–1.4]. It is in many cases highly instructive to read the original research papers which proposed new ideas, models, and concepts for the first time – often in an unprecise form, sometimes still erroneous. This can fill us with more esteem for the

achievements of previous generations, who had to work with much less perfect equipment than we are used to today, yet obtained results which are often re-discovered even today and are sometimes considered new. For this reason we will often cite the original literature in this book, even though the corresponding results may already be found in textbooks of molecular physics, perhaps even presented with more didactic skill.

1.1

Short Historical Overview

The concept of a *molecule* as a combination of atoms emerged relatively late in scientific literature, at some time during the first half of the 19th century. One reason for this is that a large number of experimental investigations was necessary to replace the historical ideas of the “four elements”, water, air, earth, and fire, and the later alchemistic concepts of *elements* such as sulfur, mercury, and salt (Paracelsus, 1493–1541) with an atomistic model of matter. A major breakthrough for this model were the first critically evaluated quantitative experiments investigating the mass changes involved in combustion processes, published in 1772 by Lavoisier (1743–1794), who might be called the first modern chemist.

After Scheele (1724–1786) recognized that air is a mixture of oxygen and nitrogen, Lavoisier created the hypothesis that during combustion, substances form a compound with oxygen. From the results of British physicists from the Cavendish circle, who succeeded in producing water from hydrogen and oxygen, Lavoisier was able to deduce that water could not be an element as had long been thought, but that it had to be a compound. He defined a chemical element to be “the factual limit which can be reached by chemical analysis”. The publication of Lavoisier’s textbook *Traité élémentaire de Chimie* in 1772, which marked a breakthrough for the ideas of modern chemistry, finally surpassed the ideas of alchemy.

Lavoisier’s quantitative concept of chemical reactions furnished a number of empirical laws such as Proust’s law of constant proportions of 1797, which states that the mass proportions of elements in a chemical compound are constant and independent of the way in which the compound was prepared. The British chemist Dalton (1766–1844) was able to explain this law in 1808 on the basis of his atomic hypothesis, which postulated that all substances consist of atoms, and that upon formation of a compound from two elements one or a few atoms of one element combine with one or a few atoms of the second element (as, e.g., in NaCl, H₂O, CO₂, CH₄, Al₂O₃). Sometimes, different numbers of like atoms can combine to form different molecules. Examples are the nitrogen–oxygen compounds N₂O (dinitrogen oxide, laughing gas), NO (nitrogen monoxide), N₂O₃ (nitrogen trioxide), and NO₂ (nitrogen dioxide), where the atomic ratio N:O is 2:1, 1:1, 2:3, and 1:2, respectively. This established the concept of molecules.

Dalton also recognized that the relative atomic weights constitute a characteristic property of chemical elements. This idea was supported by Avogadro, who proposed, in 1811, the hypothesis that equal volumes of different gases at equal temperature and pressure contain an equal number of elementary particles. From the experimental finding that reaction of *one* unit volume of hydrogen with *one* unit volume of chlorine produces *two* unit volumes of hydrogen chloride, Avogadro deduced correctly that the elementary particles in chlorine and hydrogen gas are not atoms but diatomic molecules, that is, H_2 and Cl_2 , and that the reaction is therefore $\text{H}_2 + \text{Cl}_2 \rightarrow 2\text{HCl}$. More detailed accounts on this early stage of molecular science can be found in [1.1–1.4]

Although the atomic hypothesis scored undisputable successes and was accepted as a working hypothesis by most chemists, the existence of atoms as real entities was a matter of discussion among many serious scientists until the end of the 19th century. One reason for that was the fact that there were only indirect clues for the existence of atoms derived from the macroscopic behavior of matter in chemical reactions (for example equilibrium properties) while they were not directly observable.

Until the mid-19th century the size of atoms had not been the subject of scientific investigation. This was changed by the development of the kinetic theory of gases by Clausius (1822–1888), who found that the total volume of all molecules in a gas must be much smaller than the volume of the gas at standard temperature and pressure. He arrived at this conclusion by comparing the densities of gases to that of condensed matter (which is about three orders of magnitude smaller in the former) and from the fact that the molecules in a gas can move essentially free, that is, the duration of collisions is small compared to the time between collisions; otherwise the gas could not be treated as an ideal gas with negligible interaction between collision partners (billiard ball model) [1.5].

The investigation of the specific heats of gases puzzled scientists for a long time, because it showed that molecular gases possessed larger specific heats than atomic gases. After Boltzmann, Maxwell, and Rayleigh could show that the energy of a gas in thermal equilibrium is distributed evenly between all degrees of freedom of the particles, and that the energy is $kT/2$ per degree of freedom and particle, it became clear that molecules had to have more degrees of freedom than atoms, that is, the molecules could not be rigid but had to possess internal degrees of freedom. This was the first hint on the internal dynamics of molecules, an idea which established itself only towards the end of the 19th century.

Spectroscopy contributed significantly to the solution of this puzzle [1.6], in spite of the erroneous interpretation that spectra originated from the vibrations of the atoms or molecules against the “ether”, and that the wavelengths indicated the frequencies of these vibrations.

Molecular spectroscopy originated during the first half of the 19th century. For example, in 1834 D. Brewster (1781–1868) observed, after spectral dispersion with the aid of a prism, hundreds of absorption lines, extending over the complete visible

spectrum like Fraunhofer lines, when he transmitted sunlight through dense NO_2 gas over a vessel with nitric acid [1.7]. This was astonishing to Brewster, because he did not understand why the yellowish-brown NO_2 gas should feature absorption lines in the blue. He predicted that a complete explanation of this phenomenon would provide work for many generations of researchers, and – as we know today – his prediction turned out to be correct.

The importance of a quantitative interpretation of spectra for the identification of chemical compounds was only recognized after the development of spectral analysis in 1859 by Kirchhoff (1824–1887) and Bunsen (1811–1899) [1.8]. After Rowland had succeeded, in 1887, in producing optical diffraction gratings with sufficient precision [1.9], large grating spectrographs could be built, which allowed higher spectral resolutions and which could resolve individual lines at least for small molecules. They allowed the identification of a number of simple molecules by their characteristic spectra. After 1960, the introduction of narrow-band tunable lasers to molecular spectroscopy opened the way for new techniques with a spectral resolution below the Doppler width of absorption lines (see Ch. 12).

1.2

Molecular Spectra

When an atom or a molecule absorbs or emits a photon of energy $h\nu$ it makes a transition from a state with energy E_1 to another state with energy E_2 . Energy conservation requires that

$$h\nu = E_1 - E_2 .$$

The states involved can be discrete, bound states with sharply defined energies; in this case the transition takes place at an equally sharply defined frequency ν . In a spectrum such a transition shows up as a sharp line at the wavelength $\lambda = c/\nu$. Frequently, wavenumbers $\tilde{\nu} = 1/\lambda$ are used instead of wavelengths λ or frequencies $\nu = c/\lambda$. On the other hand, unstable, repulsive states, which can lead to a dissociation of the molecule, or states above the molecule's ionization threshold are usually characterized by a more or less broad-ranged frequency continuum, and transitions into or from such states produce a correspondingly broad absorption/emission spectrum.

For atoms, the possible energy states are essentially determined by different arrangements of the electron cloud (electronic states), and each line in the spectrum thus corresponds to an electronic transition. Molecules, however, have additional internal degrees of freedom, and their states are not only determined by the electron cloud but also by the geometrical arrangement of the nuclei and their movements. This makes the spectra more complicated.

First, molecules possess more electronic states than atoms. Second, the nuclei in the molecule can vibrate around their equilibrium positions. Finally, the molecule as

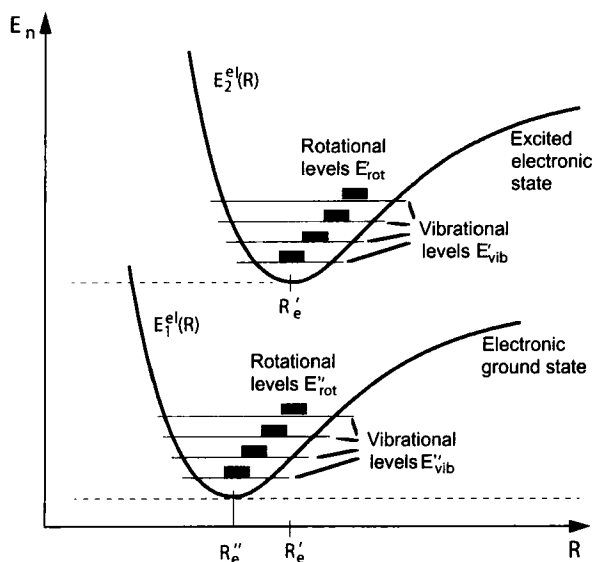


Fig. 1.1 Schematic visualization of the energy levels of a diatomic molecule.

a whole may rotate around axes through its center of mass. Therefore, for each electronic molecular state there exist a large number of vibrational and rotational energy levels (Fig. 1.1).

Molecular spectra can be categorized as follows (Fig. 1.2).

- Transitions between different rotational levels for the same vibrational (and electronic) state lead to pure rotational spectra with wavelengths in the microwave region ($\lambda \approx 1 \text{ mm to } 1 \text{ m}$).
- Transitions between rotational levels in different vibrational levels of the same electronic state lead to vibration–rotation spectra in the mid-infrared with wavelengths of $\lambda \approx 2\text{--}20 \mu\text{m}$ (Fig. 1.3).
- Transitions between two different electronic states have wavelengths from the UV to the near infrared ($\lambda = 0.1\text{--}2 \mu\text{m}$). Each electronic transition comprises many *vibrational bands* corresponding to transitions between the different vibrational levels of the two electronic states involved. Each of these bands contains many rotational lines with wavelengths λ or frequencies $\nu = c/\lambda$ given by

$$h\nu = \left(E_2^{\text{el}} + E_2^{\text{vib}} + E_2^{\text{rot}} \right) - \left(E_1^{\text{el}} + E_1^{\text{vib}} + E_1^{\text{rot}} \right),$$

as required by energy conservation (Fig. 1.2). As an example, Fig. 1.4 shows a section from the band system of the Na_2 molecule with two bands from an electronic transition in the visible spectral range.

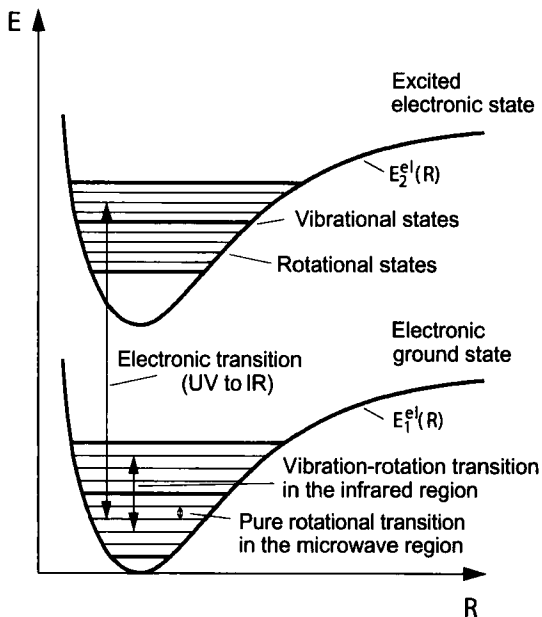


Fig. 1.2 Schematic representation of the possible transitions in diatomic molecules in the different regions of the electromagnetic spectrum.

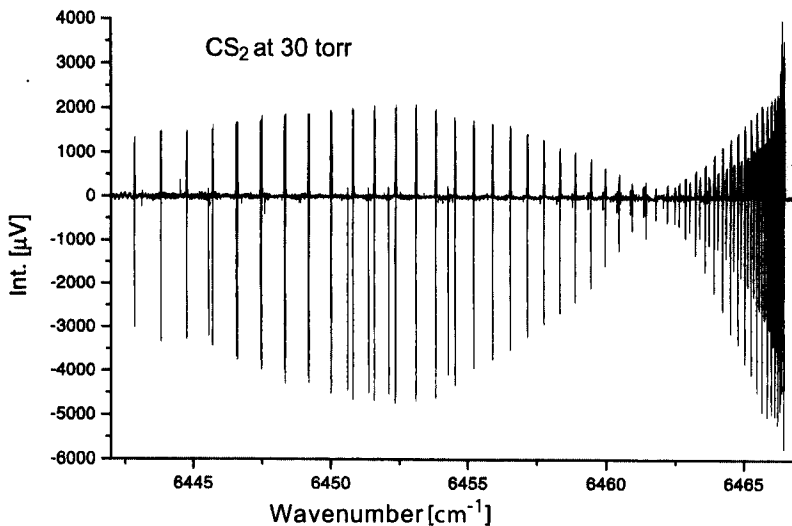


Fig. 1.3 Rotational lines of an overtone vibrational transition of the CS_2 molecule with $\Delta v_1 = 2$. (Courtesy H. Wenz, Kaiser-slautern)

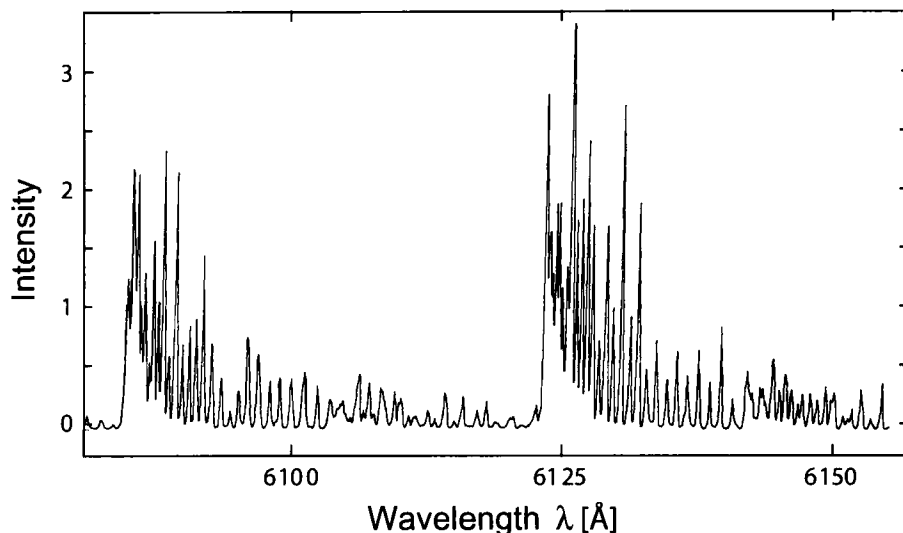


Fig. 1.4 Two vibrational bands from an electronic transition in the Na_2 molecule.

The analysis of a molecular spectrum is usually difficult. It provides a wealth of information, however. The rotational spectra yield the geometrical structure of the molecule, the vibrational spectra give information on the forces between the vibrating atoms in the molecule, and the electronic spectra tell us about the electronic states, their stabilities, and their electron distributions. Linewidths can, under suitable experimental conditions, give information on the lifetimes of excited states or on dissociation energies. The complete analysis of a spectrum of sufficient spectral resolution provides a great deal of information on a molecule. It is therefore worthwhile to put some effort into the complete interpretation of a molecular spectrum.

A deeper understanding of molecular spectra and their connections with molecular structure was achieved only in the 1920s and 1930s with the advent of quantum theory. Soon after the mathematical formulation of the theory by Schrödinger and Heisenberg [1.10, 1.11], a large number of theoreticians applied quantum mechanical calculations to the quantitative explanation of molecular spectra, and even before 1930 numerous publications on problems in molecular physics appeared. In these early publications in molecular physics, it is astonishing to observe how intuition and physical insight enabled great physicists to solve a number of important problems in molecular physics without computers and with very limited experimental equipment (see, for example, [1.12, 1.13]). It is very rewarding to read these early publications, which are therefore frequently cited in the respective sections of this book. Modern textbooks on Molecular Quantum Mechanics are, for example, [1.14, 1.15].

1.3 Recent Developments

It soon became clear that the experimental methods available at the time, that is, “classical” absorption or emission spectroscopy with spectrographs and incoherent light sources, were not able to resolve the individual lines in the spectra of many molecules. At the same time, theoretical efforts to determine the structures of small molecules reliably through *ab initio* calculations, showed some success only for the smallest systems H_2^+ and H_2 . Approximations had to be developed and lengthy numerical calculations had to be performed, which were beyond the capacities of the early computers. The focus of theoreticians thus shifted to atomic physics, where many experimental data were available and waiting to be compared to the results of theoretical methods.

During the last 50 years, however, molecular physics has experienced a very active revival. On the side of experimental techniques, the reason is the emergence of many new methods such as microwave spectroscopy, Fourier spectroscopy, photoelectron spectroscopy, the application of synchrotron radiation, and laser spectroscopy. On the theoretical side, high-speed computers with huge memories have enabled quantitative calculations that compete with experimental accuracy in many cases. The mutual stimulation of theoretical prediction and experimental verification (or refutation), or the theoretical explanation of yet unexplained experimental phenomena has produced a great progress in molecular physics. Today it is fair to say that bond energies, molecular structures, and electron distributions of ground-state molecules are essentially understood, at least for small molecules.

The situation is much more difficult for electronically excited molecular states. They are less well investigated than ground states, because only in recent years have experimental techniques been developed that allow the investigation of excited states with the same accuracy and sensitivity as for ground states. Also, they are much more difficult to treat theoretically, which is the reason why there is far less theoretical work on the structures of excited states than of ground states. However, excited states are especially interesting because many chemical reactions occur only after a certain amount of activation energy has been provided, that is, after excited states have been created. For example, this is the case for all photochemical processes, which are initiated by the absorption of light. Also, a detailed understanding of photobiological processes such as the primary visual process or photosynthesis, requires the detailed study of electronically excited states and their dynamics.

Such studies of molecular dynamics are based on the fact that molecules are not geometrically rigid entities but can change their shape. Energy that is “pumped” into a molecule selectively by the absorption of light can alter the electron distribution and can thus bring about a change in the geometrical shape of the molecule (isomerization). The energy can also be distributed evenly between the different degrees of freedom of the molecule, provided they are coupled. This process corresponds to a

heating of the whole molecule and leads to different results from the selective excitation of specific energy levels.

Interactions between different molecular states, leading to *perturbations* of molecular spectra, are much more common in excited states than in ground states. They can greatly enhance our understanding of the structures of excited states, which can in general not be described by a geometrically well-defined *static* molecular model, because the arrangement of the nuclear framework is constantly changing to adapt to changes in the electron cloud, which can take place at constant total energy (so-called *radiationless transitions*). Especially in large biomolecules, this variable geometric shape is of crucial importance for their biological function [1.16, 1.17].

Recently, the question has been discussed intensively as to whether it is possible to make predictions of the properties of chemical compounds based on the topology of the corresponding molecules. There are indications that for such a topologic analysis the real accurate three-dimensional shape as defined by bond lengths and angles of the molecules is less important than had been thought. It seems more important how many atoms a molecule contains, with how many other atoms each atom is connected, and if the connections form linear chains, rings, crosslinks or combinations of them. If the number of atoms and the number and types of their connections are characterized by index numbers, the topological structure of the molecule can also be characterized by a suitably chosen index number. It is in many cases possible to make correct and useful predictions of the properties of new molecules based on such a topological analysis before an attempt is made to synthesize them [1.18, 1.19].

The development of sensitive detection techniques has enabled the study of unstable molecular radicals, which occur as intermediates in many chemical reactions. They exist usually at very low concentration in the presence of large concentrations of other species, which makes the recording of their spectra a demanding task, especially if nothing is known about the frequencies at which they should occur. Support from theoretical predictions is very important in these cases, and many spectra of such radicals, often also of astrophysical interest, have been recorded successfully primarily on account of a close collaboration between spectroscopists and quantum chemists.

Recently, the study of molecular ions [1.20], of weakly bonded molecules M_n (van der Waals molecules) [1.21] and of larger systems consisting of n equal atoms or molecules (so-called *clusters*) [1.22] has attracted increased attention. Such clusters constitute interesting intermediates between free molecules and liquid drops, and their investigation promises detailed information about the condensation and evaporation processes and the dynamics of larger, loosely bound molecular complexes, which could, under certain conditions, make a transition to an ordered solid (crystal) for large n .

Our detailed knowledge of molecular structure has fostered the overwhelming and exciting progress in biophysics and genetic engineering. These new areas of research will revolutionize our daily life, and may have much more profound consequences than even the development of integrated circuits as a consequence of solid-state re-

search. This alone makes molecular physics a highly topical and important field. In addition, there are many open questions in such boundary areas of molecular physics, which renders the work in molecular physics truly exciting. Before progressing to the forefront of research, however, one must get acquainted with the basic foundations of molecular physics. This book will help in that process by discussing the conceptual and theoretical foundations of molecular physics and by presenting modern experimental methods used in the investigation of molecular structure.

1.4

The Concept of This Book

As the title indicates, this book aims at presenting both the theoretical foundations of molecular physics, the knowledge of which is necessary for a quantitative description of molecules, and modern experimental techniques, which enable the detailed investigation of many molecules. Theoretical and experimental parts are intentionally separated, because this arrangement allows a more consistent presentation especially in the theoretical part, and the common features of experimental methods, such as microwave and laser spectroscopy, can be worked out more clearly.

The theoretical part assumes a basic knowledge in atomic physics and quantum mechanics. The theoretical presentation starts with the introduction of the Born–Oppenheimer approximation, a fundamental concept allowing the separation of nuclear and electronic motion, which is at the heart of each molecular model based on a *nuclear framework* surrounded by an electron cloud. Within the Born–Oppenheimer approximation, the total energy of a molecule can be separated into electronic, vibrational and rotational energies. This is confirmed by spectroscopic results and will be further elucidated in a concise tabulation of the wavelength regions of the different molecular spectra and their classification as rotational, vibrational, and electronic transitions.

The major part of Ch. 2 deals with electronic states of *rigid* molecules, which neither rotate nor vibrate. The basic concepts such as angular momenta and their couplings, symmetries, and molecular orbitals are introduced phenomenologically for electronic states of diatomic molecules. Next, approximation techniques for the calculation of electronic wavefunctions, energies and potentials are presented. The chapter starts with one-electron systems and continues to discuss the problems and techniques for systems with more than one electron. Section 2.8 shows the power of modern quantum-chemical *ab initio* methods for some illustrative examples.

Chapter 3 discusses vibrations and rotations of diatomic molecules. There are in the meanwhile several methods for calculating molecular potentials from *experimentally measured term values* of vibration–rotation levels and for the determination of dissociation energies, which are discussed in detail in the second part of this chapter. The chapter closes with an overview of classical and quantum-mechanical tech-

niques for the treatment of the long-range part of the interaction potential of diatomic molecules for large internuclear separations, which is important especially in scattering experiments.

Chapter 4 deals with the central topic of molecular physics: molecular spectra. All the principal aspects can be discussed and understood for the case of diatomic molecules, where the spectra are easier to analyze. Therefore the chapter is restricted to those, while the spectra of polyatomic molecules are discussed in Ch. 8. Three questions are central:

- Between which states can transitions take place, producing absorption or emission of electromagnetic radiation?
- What is the probability of these transitions?
- What can be learned about molecular structure from the intensities, line profiles, and polarizations of the molecular spectral lines?

In polyatomic molecules, symmetry properties play a crucial role for the simplification and generalization of their representation. Therefore, we discuss molecular symmetry and its representation using group theory in Ch. 5, before we turn to a discussion of vibrations and rotations of polyatomic molecules in Ch. 6, where rotation is presented for the symmetric and asymmetric top. Next, the concept of normal modes of molecular vibration is discussed in detail and is compared with the localized-vibration model, which gives often a better description especially for higher vibrational excitations. The influence of nonlinear coupling on vibrational spectra and the question of chaotic motions is briefly outlined.

The electronic states of polyatomic molecules are discussed with the aim of conveying the most important concepts without going into too much detail. Chapter 7 presents applications of many of the ideas of molecular wavefunctions presented in Ch. 2. The construction of electronic states from molecular orbitals is discussed for some illustrative examples, and the resulting regularities for structure and symmetry of molecules in electronically excited states are emphasized. Chapter 8, dealing with spectra of polyatomic molecules, also uses many of the basics from Ch. 4.

Molecules that can *not* be described within the Born–Oppenheimer approximation are gaining increasing importance in molecular physics. Especially in electronically excited states, molecules often do not possess a fixed geometrical shape but fluctuate spontaneously from one nuclear configuration to another. Such deviations from the Born–Oppenheimer approximation show up in the molecule’s spectrum as *perturbations*, where the positions of lines are shifted from their expected values, intensities and linewidths are modified, lines are missing from the spectrum, or completely new and unexpected lines appear. These perturbations make the analysis of spectra more difficult, but they also yield important clues regarding the couplings between different Born–Oppenheimer states. For electronically excited states, they are quite common, and their treatment, described in Ch. 9, is of great importance for a complete and con-

sistent model of excited molecules. As the function of many biologically important molecules depends on such fluctuations of shape, an extension of our static molecular model is essential for applications in biology.

In Ch. 10, we touch briefly on the topic of molecules in external fields. As molecules may possess permanent or induced electric or magnetic moments (dipole, quadrupole, etc.), external electric or magnetic fields can effect shifts or mixing of molecular energy levels. Modern experimental techniques can investigate these effects in detail and have created fascinating applications such as magnetic resonance spectroscopy or magnetic resonance tomography.

A discussion of the interesting topic of van der Waals molecules and molecular clusters, which has been the subject of intensive work in recent years, closes the theoretical part of the book.

Modern experimental techniques, most notably the different methods of spectroscopy, have exerted a strong influence on modern molecular physics. Chapter 12 is therefore devoted to modern methods in molecular spectroscopy.

After an overview of the techniques of microwave spectroscopy for the measurement of rotational spectra, electric and magnetic moments, and hyperfine structures, we present recent methods in infrared spectroscopy such as Fourier spectroscopy, which has largely replaced classical absorption spectroscopy. Infrared laser spectroscopy is also finding new applications continuously as it is in many cases superior to Fourier spectroscopy in terms of spectral resolution and signal-to-noise ratio.

The investigation of radicals and unstable molecules has been made possible by *matrix isolation spectroscopy*, which uses a rare-gas matrix to confine the molecules at temperatures of a few kelvin. This method can thus produce rotation-free spectra of molecules in their lowest vibrational states.

Section 12.3 presents classical techniques of Doppler-limited laser spectroscopy in the visible and ultraviolet and Sect. 12.4 a number of Doppler-free laser-spectroscopic techniques, which allow a selective excitation of specific vibration-rotation levels even in large molecules and thus give new and detailed insight into the structures of excited molecules.

The combination of different spectroscopic techniques has led to the development of double-resonance methods, which offer huge advantages when it comes to the identification of unknown molecular spectra and which allow the application of spectroscopic methods to excited states, which could until now only be applied to ground states. For example, using infrared-microwave double resonance, one can perform microwave spectroscopy in vibrationally excited states, and optical-optical double resonance allows the investigation of high Rydberg states of molecules.

The dynamics of excited states is currently of great interest; it can be monitored using time-resolved spectroscopy. It aims at answering the question, among others, of how and how quickly the excitation energy in a molecule is distributed among the different degrees of freedom, either spontaneously or collision-induced. Such processes

can be studied with a time resolution in the femtosecond range ($1 \text{ fs} = 10^{-15} \text{ s}$). All questions relating to these studies are discussed in Sect. 12.4.12.

Besides laser spectroscopy, there are a large number of spectroscopic techniques, often complementing each other nicely. Of special importance for the study of electronic molecular states is photoelectron spectroscopy, which is therefore discussed in some detail in Sect. 12.5.

The combination of laser spectroscopy and mass spectrometry has proved especially valuable in isotope-specific spectroscopy. The most frequently used types of mass spectrometers are presented in Sect. 12.6.

A notably precise method to measure molecular moments and/or hyperfine structures is radiofrequency spectroscopy, developed by I. Rabi many years ago, which reaches today, employed in combination with laser-spectroscopic techniques, remarkable sensitivity and spectral resolution (Sect. 12.7). Electron spin resonance (ESR) and nuclear magnetic resonance have established themselves as standard tools, and they have reached an enormous importance not only in chemistry and physics but also, in the form of nuclear-resonance tomography, in medicine. They are described in Sections 12.8 and 12.9.

The spectroscopy of radicals using laser-magnetic resonance has helped, among the contributions of microwave spectroscopy, to extend significantly our knowledge of molecules in interstellar space (Sect. 12.4.5).

Although a quantitative description of molecular physics requires a certain mathematical formalism, and although molecular structure cannot be really understood without a firm grounding in quantum mechanics, the author has tried to present all topics as accessible as possible in order to convey physical insight and assist the reader in classifying the multitude of individual phenomena.

There are a large number of good books on molecular physics, some of which are listed in the bibliography. Several aspects and fields are treated in more detail in some of them, while other questions that are important today are missing. In many places throughout this book we cite not only the relevant original literature but also those textbooks which treat the corresponding topic, in the author's opinion, especially clearly. It is my hope that, by its homogeneous coverage of both theoretical and experimental aspects and by its many references to the literature, this book might prove valuable for many chemists and physicists and might thus contribute to a further flourishing of the exciting and important field of molecular physics.

2 Molecular Electronic States

2.1 Adiabatic Approximation and the Concept of Molecular Potentials

In simple mechanistic models of molecular structure, molecules are usually represented by a rigid framework of atoms in space with well-defined geometric shape and symmetry properties. The precise arrangement of the atomic nuclei in space (the *nuclear framework*) is determined by the averaged spatial distributions of all electrons, which act as a kind of “glue”, bonding the nuclei together against the repulsive forces of the positively charged nuclei. This static *equilibrium structure* of the nuclei corresponds to a minimum of the total energy of the molecule. Each motion of such a *rigid* molecule can be described as a superposition of a translational motion of the molecule’s center of mass and a rotation around this same point. More refined models allow for additional vibrational motions of the nuclei around their minimum-energy equilibrium positions.

In this chapter we will focus on the conditions under which this model can be considered “correct”, on its limits and its possible improvements. For a quantitative discussion, we will have to use quantum mechanics, because the building blocks of molecules are electrons and atomic nuclei. We assume that the foundations of quantum mechanics are already known (see, e.g., [1.14,2.1–2.4]).

2.1.1 Quantum-Mechanical Description of Free Molecules

A molecule consisting of K nuclei (with masses M_k and charges $Z_k e$) and N electrons (mass m , charge $-e$) in a state with total energy E is described by the Schrödinger equation

$$\hat{H}\Psi = E\Psi, \quad (2.1)$$

where the Hamiltonian

$$\hat{H} = \hat{T} + \hat{V} = -\frac{\hbar^2}{2m} \sum_{i=1}^N \nabla_i^2 - \frac{\hbar^2}{2} \sum_{k=1}^K \frac{1}{M_k} \nabla_k^2 + V(\mathbf{r}, \mathbf{R}) \quad (2.2)$$

can be written as the sum of the operator \hat{T} of the kinetic energy of all electrons and nuclei and the potential energy $V(\mathbf{r}, \mathbf{R})$. In this equation (and in general), lower-case letters denote electronic coordinates, \mathbf{r}_i , and upper-case letters denote nuclear coordinates, \mathbf{R}_k .

The potential energy is a sum of three terms,

$$\begin{aligned} V(\mathbf{r}, \mathbf{R}) &= V_{\text{nuc,nuc}} + V_{\text{nuc,el}} + V_{\text{el,el}} \\ &= \frac{e^2}{4\pi\epsilon_0} \left[\sum_{k>k'}^K \sum_{k=1}^K \frac{Z_k Z_{k'}}{R_{k,k'}} - \sum_{k=1}^K \sum_{i=1}^N \frac{Z_k}{r_{i,k}} + \sum_{i>i'}^N \sum_{i'=1}^N \frac{1}{r_{i,i'}} \right]. \end{aligned} \quad (2.3)$$

The first term describes the Coulomb repulsion between nuclei, the second the attraction between electrons and nuclei, and the third the mutual repulsion between the electrons, and we have used the abbreviations

$$R_{k,k'} = |\mathbf{R}_k - \mathbf{R}_{k'}|, \quad r_{i,k} = |\mathbf{r}_i - \mathbf{R}_k|, \quad r_{i,i'} = |\mathbf{r}_i - \mathbf{r}_{i'}|,$$

which are further explained in Fig. 2.1.

Here we have ignored all interactions relating to electronic or nuclear spins. Their exact description would require a relativistic treatment based on Dirac's equation [2.5]. The shifts of molecular energy levels caused by spin interactions are small, however, compared with total kinetic and potential energies. They can therefore be treated as perturbations of the Schrödinger equation (2.1), resulting in small additive corrections to the energies obtained from Eq. (2.2).

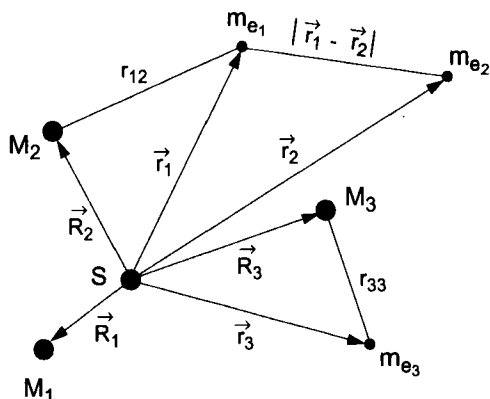


Fig. 2.1 Space-vector representation of a molecule in its center-of-mass frame.

The potential energy of a molecule depends only on the relative distances of the particles and not on the choice of a specific frame of reference. In contrast, the kinetic energy *does* depend on the chosen reference frame. Any investigation of a molecule (e.g., observation of its absorption or emission spectrum) takes place in the *laboratory frame LF*. The theoretical description is usually simplified in a frame *M* which is attached to the molecule. For moving or rotating molecules, these frames are different.

To avoid all complications arising in discussions that employ moving reference frames, we will start with a molecule *at rest*, whose center of mass is stationary in the laboratory frame and which we will describe in the laboratory frame. Thus, we start from the Schrödinger equation (2.1)

$$\left(\frac{-\hbar^2}{2m} \sum_{i=1}^N \nabla_i^2 - \frac{\hbar^2}{2} \sum_{k=1}^K \frac{1}{M_k} \nabla_k^2 + V(\mathbf{r}, \mathbf{R}) \right) \Psi = E\Psi(\mathbf{r}, \mathbf{R}) \quad (2.4)$$

of a free molecule at rest consisting of N electrons and K nuclei. The corresponding Hamiltonian is $\hat{H} = \hat{T}_{\text{el}} + \hat{T}_{\text{nuc}} + V$, where the interaction potential $V(\mathbf{r}, \mathbf{R})$ is given by Eq. (2.3). For a nonrotating molecule at rest, this equation is exact as long as we neglect all interactions due to electronic and nuclear spins.

Even for the simplest molecule, the H_2^+ molecular ion consisting of two protons and one electron, the Schrödinger equation (2.4) cannot be solved exactly. There are two general approaches that may lead to solutions of Eq. (2.4) for real molecules:

1. We can solve Eq. (2.4) *numerically* for a specific case. The accuracy that can be obtained by this procedure depends on the software used and the size and speed of the available computers. The disadvantage of this method is that the numerical errors involved are difficult to estimate, and that results obtained for one molecule are not easily transferable to other molecules.
2. We can introduce physically motivated approximations that are based on a simplified molecular model, leading to a simplified Schrödinger equation. This simplified model can then be extended step by step, and can thus be made to resemble reality as closely as desired. This procedure has the advantage that we can gain a much deeper understanding of the single steps and their physical implications.

In the following, we will use the second approach, and we will start in the next section by introducing the fundamental approximation of molecular physics, the so-called *adiabatic approximation*.

Remark: *To avoid dealing with constant factors in the lengthy calculations and to make equations and integrals more clearly legible, it is common in theoretical atomic and molecular physics and quantum chemistry to use so-called atomic units. They are obtained by defining*

$$m_e = 1, \quad \hbar = 1, \quad e = 1, \quad c = 1.$$

Note that in equating $m_e = \hbar = e = 1$ the dimensions of these quantities are ignored. Hence, equations written in atomic units are not dimensionally correct in the usual sense.

The atomic unit of length, 1 bohr, equals the radius a_0 of the lowest Bohr orbit in the hydrogen atom. In SI units,

$$a_0 = \frac{4\pi\epsilon_0\hbar^2}{me^2} \approx 0.05 \text{ nm} .$$

The atomic unit of energy, 1 hartree, is defined to be twice the ionization energy of the hydrogen atom ($= -E_{\text{pot}}$ for the electron in the lowest Bohr orbit with $n = 1$). In SI units,

$$E_{\text{pot}} = -\frac{me^4}{(4\pi\epsilon_0)\hbar^2n^2} \approx 27 \text{ eV} \quad \text{for } n = 1 .$$

In this book, we will use SI units throughout.

2.1.2

Separation of Electronic and Nuclear Wavefunctions

Because of their smaller masses, the electrons in a molecule move much faster than the vibrating nuclei. The electron cloud can therefore adjust more or less *instantaneously* to the changing nuclear frame described by a set of nuclear coordinates \mathbf{R} . In other words, for each \mathbf{R} there exists a well-defined electron distribution as specified by the wavefunction $\phi_n^{\text{el}}(\mathbf{r}, \mathbf{R})$ for the electronic state $\langle n|$, which depends on the positions of all nuclei but not (to first approximation) on their velocities. The electron cloud follows the periodically changing nuclear framework *adiabatically* during the vibrations. The corresponding molecular model is therefore called the *adiabatic approximation*.

To express this idea in mathematical language we use perturbation theory. As long as the kinetic energy of the nuclei [second term in Eq. (2.4)] is small compared to the electronic energy, we can consider it as a perturbation of the molecule with *rigid* nuclear framework ($\mathbf{R} = \text{const.}$) and zero nuclear kinetic energy. This means that we use the Hamiltonian

$$\hat{H} = \hat{H}_0 + \hat{H}' \quad \text{with } \hat{H}_0 = \hat{T}_{\text{el}} + V \quad \text{and } \hat{H}' = \hat{T}_{\text{nuc}} . \quad (2.5)$$

The unperturbed Schrödinger equation,

$$\hat{H}_0\phi^{\text{el}}(\mathbf{r}, \mathbf{R}) = E^{(0)}(\mathbf{R})\phi^{\text{el}}(\mathbf{r}, \mathbf{R}) , \quad (2.6)$$

describes a molecule in which the nuclear framework is fixed at a configuration \mathbf{R} . The square of a solution wavefunction $\phi_n^{\text{el}}(\mathbf{r}, \mathbf{R})$ of Eq. (2.6) for an arbitrary fixed nuclear framework \mathbf{R} yields the charge distribution of the electrons in an electronic state

$|n\rangle$ with the energy $E_n^{(0)}(\mathbf{R})$, where the subscript n designates the different electronic states of the rigid molecule (see Ch. 3).

Note that the functions ϕ_n^{el} depend *only* on the electronic coordinates \mathbf{r} . Nuclear coordinates \mathbf{R} do not enter as variables but only as parameters, because Eq. (2.6) contains neither differentiation nor integration with respect to \mathbf{R} .

We can choose the solutions $\phi_n^{\text{el}}(\mathbf{r}, \mathbf{R})$ of Eq. (2.6) such that they form a complete orthonormal set of functions. In this case, every solution $\Psi(\mathbf{r}, \mathbf{R})$ of the complete Schrödinger equation (2.4) can be expanded in a (generally infinite) series of these functions. To solve Eq. (2.4), we choose the ansatz

$$\Psi(\mathbf{r}, \mathbf{R}) = \sum_m \chi_m(\mathbf{R}) \phi_m^{\text{el}}(\mathbf{r}, \mathbf{R}), \quad (2.7)$$

where the expansion coefficients $\chi_m(\mathbf{R})$ depend on nuclear coordinates \mathbf{R} but not on electronic coordinates \mathbf{r} .

After substituting into Eq. (2.4), multiplication with $\phi_n^{\text{el}*}$ and integration over electronic coordinates \mathbf{r} we obtain

$$\int \left[\phi_n^{\text{el}*}(\mathbf{r}, \mathbf{R}) (\hat{H} - E) \sum_m \chi_m(\mathbf{R}) \phi_m^{\text{el}}(\mathbf{r}, \mathbf{R}) \right] d\mathbf{r} = 0. \quad (2.8)$$

If we substitute $\hat{H} = \hat{H}_0 + \hat{H}'$ in Eq. (2.8) and use Eq. (2.6) and $\int \phi_n^{\text{el}*} \phi_m^{\text{el}} d\mathbf{r} = \delta_{nm}$, we obtain for the functions $\chi_m(\mathbf{R})$

$$\left(E_n^{(0)}(\mathbf{R}) - E \right) \chi_n(\mathbf{R}) + \int \left[\phi_n^{\text{el}*} \hat{H}' \sum_m \chi_m(\mathbf{R}) \phi_m^{\text{el}}(\mathbf{r}, \mathbf{R}) \right] d\mathbf{r} = 0. \quad (2.9)$$

The last term in Eq. (2.9) can be calculated as follows, where the parentheses (...) designate the function on which H' operates:

$$\begin{aligned} \int \phi_n^{\text{el}*} \left(\hat{H}' \sum_m \chi_m \phi_m^{\text{el}} \right) d\mathbf{r} &= \int \left[\phi_n^* \sum_m (\hat{H}' \chi_m) \phi_m \right] d\mathbf{r} \\ &+ \int \left[\phi_n^* \sum_m (\hat{H}' \phi_m) \chi_m \right] d\mathbf{r} \\ &- \hbar^2 \int \phi_n^* \left[\sum_k \frac{1}{M_k} \sum \frac{\partial}{\partial R_k} \phi_m \frac{\partial}{\partial R_k} \chi_m \right] d\mathbf{r}. \end{aligned} \quad (2.10)$$

In the first term on the right-hand side we can exchange differentiation and integration, because \hat{H}' depends only on \mathbf{R} , but integration is over electronic coordinates \mathbf{r} . If we use $\int \phi_m^* \phi_n d\mathbf{r} = \delta_{mn}$, this term reduces to $\hat{H}' \chi_n$. The second and third terms on the right-hand side of Eq. (2.10) can be combined to $\sum_m c_{nm} \chi_m$, where we have introduced the abbreviation

$$c_{nm} = \int \phi_n^* \hat{H}' \phi_m d\mathbf{r} - \frac{\hbar^2}{2} \left[\int \phi_n^* \sum_k \frac{1}{M_k} \frac{\partial}{\partial R_k} \phi_m d\mathbf{r} \right] \frac{\partial}{\partial R_k}. \quad (2.11)$$

This yields for Eq. (2.9)

$$\left(E_n^{(0)}(\mathbf{R}) + \hat{H}'\right)\chi_n(\mathbf{R}) + \sum_m c_{nm}\chi_m(\mathbf{R}) = E\chi_n. \quad (2.12)$$

Equations (2.6) and (2.12),

$$\hat{H}_0\phi(\mathbf{r}, \mathbf{R}) = E^0(\mathbf{R})\phi(\mathbf{r}, \mathbf{R}), \quad (2.13a)$$

$$\hat{H}'\chi_n(\mathbf{R}) + \sum_m (c_{nm}\chi_m(\mathbf{R})) = (E - E_n^0(\mathbf{R}))\chi_n \quad (2.13b)$$

form a coupled set of equations for the electronic wavefunctions ϕ and the nuclear wavefunctions χ_n where the coupling is mediated by the coefficients $c_{nm}(\phi)$ that depend on the functions ϕ through Eq. (2.11).

The combined equations (2.13) are completely equivalent to the Schrödinger equation (2.4). Without the sum term, Eq. (2.13b) describes the motion of the nuclei with kinetic energy \hat{H}' in the potential $E_n^{(0)}(\mathbf{R})$. The potential is a solution of Eq. (2.13a) and is determined by the averaged electron distribution, because each stationary electron distribution $\phi_n(\mathbf{r})$ corresponds, for fixed \mathbf{R} , to a well-defined energy $E_n^0(\mathbf{R})$. The coefficients c_{nm} are coupling matrix elements; they describe how different electronic states ϕ_n and ϕ_m are coupled through the nuclear motion. These coefficients, which in general are small compared to $E_n^0 + H'$, will be discussed below.

2.1.3

Born–Oppenheimer Approximation

In the so-called *Born–Oppenheimer* (BO) approximation [2.6] all the c_{nm} are taken to be zero, i.e., the coupling between nuclear motion and electron distribution is completely neglected. Equation (2.13b) then reduces to

$$[\hat{H}' + E_n^{(0)}(\mathbf{R})]\chi_n(\mathbf{R}) = E\chi_n(\mathbf{R}). \quad (2.14)$$

Within the BO approximation, the Schrödinger equation for the nuclear wavefunction $\chi_n(\mathbf{R})$ in the electronic state $|n\rangle$, which determines the probability amplitudes for the nuclei at their positions \mathbf{R} , is

$$\hat{H}_{\text{nuc}}\chi_n = E\chi_n. \quad (2.14a)$$

Here the Hamiltonian,

$$\hat{H}_{\text{nuc}} = \hat{H}' + E_n^{(0)}(\mathbf{R}) = \hat{T}_{\text{nuc}} + U_n(\mathbf{R}), \quad (2.14b)$$

is the sum of the kinetic energy of the nuclei and a potential energy $U_n(\mathbf{R})$, which equals the total energy $E_n^0(\mathbf{R})$ of the rigid molecule [see Eq. (2.6)]. In other words, $E_n^{(0)}(\mathbf{R})$ contains the total potential energy, Eq. (2.3), plus the *kinetic* electron energy

averaged over the motion of the electrons. Equation (2.14) shows that $E_n^0(\mathbf{R})$ can be considered as a potential $U_n(\mathbf{R})$ in which the nuclei move. $U(\mathbf{R})$ does not depend on the electronic coordinates \mathbf{r} , because we integrated over all electronic coordinates in the calculation of $E_n^0(\mathbf{R})$. For each electronic state ϕ_n^{el} with an energy $E_n^0(\mathbf{R})$ there exists a set of solution functions χ_{nv} , which can be viewed as the nuclear wavefunctions in the electronic state ϕ_n^{el} and which describe the different vibrational states as indicated by the subscript v .

Hence, the BO approximation separates the Schrödinger equation (2.4) into two *decoupled* equations

$$\widehat{H}_0 \phi_n^{\text{el}}(\mathbf{r}) = E_n^{(0)} \phi_n^{\text{el}}(\mathbf{r}), \quad (2.15a)$$

$$(\widehat{T}_{\text{nuc}} + E_n^{(0)}) \chi_n(\mathbf{R}) = E_{n,i} \chi_{n,i}(\mathbf{R}). \quad (2.15b)$$

The solutions ϕ_n^{el} refer parametrically to the nuclear framework \mathbf{R} and the nuclear wavefunctions $\chi_{n,i}(\mathbf{R})$ for the state i of the nuclear kinetic energy in the electronic state n .

Note: *Strictly speaking, only the BO approximation enables us to speak of electronic states $|n\rangle$ and nuclear states $|i\rangle$. As the Hamiltonian $\widehat{H} = \widehat{H}_0 + \widehat{H}'$ is the sum of an electronic contribution and the nuclear kinetic energy, the total wavefunction $|n,i\rangle$ of a molecular state can be written, in the BO approximation, as a product*

$$\Psi_{n,i}(\mathbf{r}, \mathbf{R}) = \phi_n^{\text{el}}(\mathbf{r}) \times \chi_{n,i}(\mathbf{R}) \quad (2.16)$$

of an electronic wavefunction ϕ_n^{el} and a nuclear wavefunction $\chi_{n,i}$. The sum in the expansion Eq. (2.7) then reduces to a single term! This product wavefunction is possible because we neglected all interactions between nuclear and electronic motions. From Eqns. (2.16) and (2.15), it follows that the total energy is the sum of the kinetic energy of the nuclei and the electronic energy averaged over the nuclear motion, including the potential energy of the repulsion between nuclei,

$$E_{n,i} = T_{\text{nuc}}(\mathbf{R}) + E_n^0(\mathbf{R}) = \text{const.}, \quad (2.17)$$

independent of \mathbf{r} and \mathbf{R} .

The total function Ψ can be normalized by normalizing each of the two factors independently, that is,

$$\int \phi_n^{\text{el}*} \phi_n^{\text{el}} d\tau_{\text{el}} = 1 \quad \text{and} \quad \int \chi_{n,i}^* \chi_{n,i} d\tau_{\text{nuc}} = 1$$

with $d\tau_{\text{el}} = r^2 dr \sin\theta d\theta d\varphi$ and $d\tau_{\text{nuc}} = R^2 dR \sin\theta d\theta d\varphi$.

Equation (2.15a) is the foundation of quantum chemistry, which deals with the calculation of molecular electronic states as potential energy hypersurfaces $E_n^0(\mathbf{R})$ (see Sect. 2.8). Equation (2.15b) describes vibrations and rotations of the nuclear framework, which will be discussed in Ch. 3 for diatomic molecules and in Ch. 6 for polyatomic molecules.

2.1.4

Adiabatic Approximation

The matrix elements of Eq. (2.11), which have been completely neglected in the BO approximation, can be grouped into diagonal terms c_{nn} and off-diagonal terms c_{nm} ($n \neq m$). Let us first consider the diagonal terms

$$c_{nn} = \int \phi_n^{\text{el}*} \hat{H}' \phi_n^{\text{el}} d\mathbf{r} - \frac{\hbar^2}{2} \left[\int \phi_n^{\text{el}*} \sum_N \frac{1}{M_N} \frac{\partial}{\partial \mathbf{R}_N} \phi_n^{\text{el}} d\mathbf{r} \right] \frac{\partial}{\partial \mathbf{R}_N}. \quad (2.18)$$

If we exchange differentiation with respect to nuclear coordinates and integration over electronic coordinates in the second term, we see that it vanishes because $\int \phi_n^{\text{el}*} \phi_n^{\text{el}} d\mathbf{r} = 1 = \text{const.}$ and $\partial/\partial \mathbf{R}_N(\text{const.}) = 0$. This is because we can normalize the real functions ϕ_n^{el} so that $\int \phi_n^{\text{el}*} \phi_n^{\text{el}} d\mathbf{r} \equiv 1$ for *all* nuclear frameworks \mathbf{R} .

Using

$$0 = \frac{\partial^2}{\partial \mathbf{R}^2} \int \phi_n^{\text{el}*} \phi_n^{\text{el}} d\mathbf{r} = 2 \int \phi_n^{\text{el}*} \frac{\partial}{\partial \mathbf{R}^2} \phi_n^{\text{el}} d\mathbf{r} + 2 \int \left(\frac{\partial \phi_n^{\text{el}}}{\partial \mathbf{R}} \right)^2 d\mathbf{r},$$

the first term can be written as

$$c_{nn} = \int \phi_n^{\text{el}*} \hat{H}' \phi_n^{\text{el}} d\mathbf{r} = \sum_N \frac{\hbar^2}{2M_N} \int \left(\frac{\partial \phi_n^{\text{el}}}{\partial \mathbf{R}_N} \right)^2 d\mathbf{r}. \quad (2.19)$$

Thus the diagonal terms depend quadratically on changes in the electronic wavefunction ϕ_n^{el} upon variations of nuclear coordinates. These terms are small, however, because the nuclear masses M_N in the denominator are large.

If we substitute c_{nn} for the diagonal terms from Eq. (2.19) into Eq. (2.13b) while still neglecting the off-diagonal terms c_{nm} , we arrive at the so-called *adiabatic approximation* instead of Eq. (2.15b),

$$[\hat{H}' + U'_n(\mathbf{R})]\chi_n = E\chi_n, \quad (2.20)$$

where the “potential”

$$U'_n(\mathbf{R}) = E_n^{(0)}(\mathbf{R}) + \sum_N \frac{\hbar^2}{2M_N} \int \left(\frac{\partial \phi_n^{\text{el}}}{\partial \mathbf{R}_N} \right)^2 d\mathbf{r} \quad (2.21)$$

differs from the BO potential $E_n^0(\mathbf{R})$ in that it contains a corrective term depending on the masses of the nuclei, which means that it is different for different isotopes.

The effective potential $U'_n(\mathbf{R})$, in which the nuclei move, is therefore different for different isotopes, leading to small shifts in the electronic energies for the different molecular isotopomers. These shifts are small, however, compared to isotopic effects on vibrational and rotational energy levels (see Sect. 3.2) [2.7].

We can visualize the adiabatic correction as follows: if we look close enough, it turns out that the electron cloud does not follow nuclear motion *instantaneously*, but that there exists a small delay depending on the kinetic energy of the nuclei. At time t the nuclei in their configuration $\mathbf{R}(t)$ experience a potential due to an electronic configuration which would belong to a slightly earlier nuclear configuration $\mathbf{R}(t - \Delta t)$.

However, nuclear motion does *not* modify the electronic state ϕ_n^{el} in this approximation, that is, it *does not mix* wavefunctions ϕ_n^{el} , ϕ_m^{el} of different electronic states. The electronic wavefunctions follow the nuclear motion adiabatically and reversibly; *the molecule remains on the same potential surface all the time*.

Thus the adiabatic approximation goes one step further than the BO approximation. Because of the large nuclear masses in the denominator, the correction is small, however, as can easily be shown. The Hamiltonian \hat{H}_0 of the electronic wavefunctions ϕ^{el} depends on the nuclear coordinates \mathbf{R}_{nuc} only through the term $V_{\text{nuc,el}}$ in Eq. (2.3). The differentials $\partial\phi^{\text{el}}/\partial\mathbf{R}_{\text{nuc}}$ are therefore usually smaller than $\partial\phi^{\text{el}}/\partial\mathbf{r}$ as these depend also on T_{el} and $V_{\text{el,el}}$. The expression $(\hbar^2/2m)(\partial\phi^{\text{el}}/\partial\mathbf{r})^2$ represents the electronic kinetic energy. The perturbation term in Eq. (2.21) is therefore smaller than $\sum_N(m/M_N) \times E_{\text{kin}}^{\text{el}}$ and constitutes only a small correction even in the case of the light hydrogen molecule ($m_e/2m_p < 3 \times 10^{-4}$).

2.2 Deviations From the Adiabatic Approximation

If the off-diagonal elements c_{nm} are not negligible, the adiabatic approximation ceases to be valid, and we cannot separate electronic and nuclear motions. Stated differently, the nuclear motion mixes different electronic BO states. To elucidate under which circumstances this breakdown of the adiabatic approximation occurs, we use again a perturbation expansion. We write Eq. (2.5) as

$$\hat{H} = \hat{H}_0 + \hat{T}_{\text{nuc}} = \hat{H}_0 + \lambda W, \quad (2.22)$$

where H_0 is the Hamiltonian of the unperturbed rigid molecule and the perturbation operator $\hat{T}_{\text{nuc}} \hat{=} \lambda W$ describes the kinetic energy of the nuclei. The parameter $\lambda < 1$ determines the size of the perturbation, which depends on the ratio m/M of electron mass m and nuclear mass M . Born and Oppenheimer showed [2.6] that a useful choice of the perturbation parameter is $\lambda = (m/M)^{1/4}$, because in this case the nuclear vibrational energy and the nuclear rotational energy appear as perturbation terms of order λ^2 and λ^4 , respectively. In the expansion of the eigenfunction Ψ with respect to the complete orthonormal set of eigenfunctions ϕ_n^{el} of the unperturbed system from

Eq. (2.7), we use also an expansion in orders of λ for the nuclear wavefunctions χ_n :

$$\chi_n = \chi_n^{(0)} + \lambda\chi_n^{(1)} + \lambda^2\chi_n^{(2)} + \dots \quad (2.23)$$

For the respective energy eigenvalues this yields

$$E_n = E_n^{(0)} + \lambda E_n^{(1)} + \lambda^2 E_n^{(2)} + \dots \quad (2.24)$$

Now we substitute Eqns. (2.22)–(2.24) and (2.7) into the Schrödinger equation (2.4), multiply by $\phi_k^{\text{el}*}$, integrate, and compare terms of equal powers of λ , using perturbation expansions up to first order for the wavefunctions and up to second order for the energies. This procedure gives

$$E_n = E_n^{(0)} + W_{nn} + \sum_{k \neq n} \frac{W_{nk}W_{kn}}{E_n^{(0)} - E_k^{(0)}} + O(\lambda^3) + \dots \quad (2.25)$$

Here $O(\lambda^3)$ represents terms in λ^3 and higher powers that are neglected in second-order perturbation calculations.

$$W_{nk} = \int \phi_n^{\text{el}(0)*} \hat{T}_{\text{nuc}} \phi_k^{\text{el}(0)} \, d\mathbf{r} \quad (2.26)$$

is the matrix element of the perturbation operator \hat{T}_{nuc} calculated with the unperturbed solutions of Eq. (2.13a) and $W_{nn} = c_{nn}$ is the adiabatic correction of the BO energy $E_n^{(0)}$. The third term in Eq. (2.25), which is a second-order correction and which describes the coupling between electronic states $\langle \phi_n^{\text{el}} |$ and $\langle \phi_k^{\text{el}} |$, is small *provided* the energy difference $E_n^0(\mathbf{R}) - E_k^0(\mathbf{R})$ of the unperturbed states $\langle \phi_n^0 |$ and $\langle \phi_k^0 |$ at a given nuclear configuration \mathbf{R} is large compared to the matrix element $W_{nk} = \int \phi_n^{\text{el}*} \hat{T}_{\text{nuc}} \phi_k^{\text{el}} \, d\mathbf{r}$.

W_{nk} indicates the strength of the nuclear-motion-induced coupling between different electronic states, that is, it is a measure of the probability that nuclear motion induces an electronic transition from state ϕ_n^{el} to ϕ_k^{el} .

If $E_n^0 - E_k^0$ is small [e.g., when potential energy surfaces cross (Fig. 2.2)], the expansion Eq. (2.25) diverges, which means that the adiabatic approximation breaks down. This situation is frequently encountered for *excited* molecular states, but only rarely for ground states [2.8, 2.9]. In these cases the molecule can *not* be described as a nuclear framework oscillating in a potential given by the nuclear repulsion and the time-averaged spatial distribution of the electrons.

We see from the perturbation expansion that the BO approximation corresponds to the unperturbed term in the expansion with \hat{T}_{nuc} as perturbation operator, and that the adiabatic approximation includes the first-order perturbation term. The nonadiabatic terms can be included by second-order perturbation calculations [2.10], described by the third term in Eq. (2.25), while the fourth term contributes to higher-order perturbation terms, including, for example, rotational coupling of the different electronic states of the molecule (see Ch. 9).

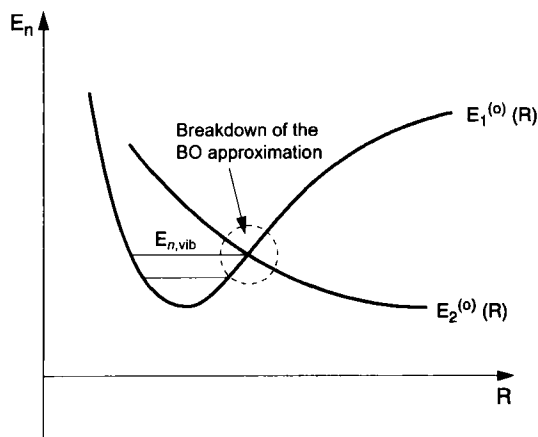


Fig. 2.2 An example for the breakdown of the Born–Oppenheimer approximation.

2.3

Potentials, Curves and Surfaces, Molecular Term Diagrams and Spectra

We have seen in the preceding section that the electronic energy $E_n^{\text{el}}(\mathbf{R})$ can be described, in the adiabatic approximation, as a potential energy surface in the space of nuclear coordinates $\mathbf{R} = \{\mathbf{R}_1, \mathbf{R}_2, \dots, \mathbf{R}_N\}$, and that this energy can be viewed as a potential in which the nuclei move.

For *diatomic* molecules, this potential energy $E_n^{\text{el}}(\mathbf{R}_1, \mathbf{R}_2)$ can be reduced, in a molecule-fixed reference frame, to a function $E_n^{\text{el}}(R)$ of just one variable R , where $R = |\mathbf{R}_1 - \mathbf{R}_2|$ is the internuclear distance. This *potential energy curve* $E_n^{\text{el}}(R) = V(R)$ is displayed schematically in Fig. 2.3 for a bound molecule, i.e., for the case

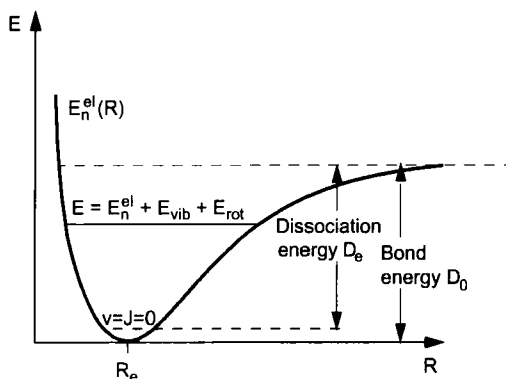


Fig. 2.3 Potential energy curve of a diatomic molecule and vibrational–rotational state with constant total energy, independent of internuclear distance R .

that the curve possesses a minimum. The internuclear distance R_e at this minimum is called *equilibrium distance* and the depth of the minimum represents the *bond energy*

$$E_b = E_n^{\text{el}}(R = \infty) - E_n^{\text{el}}(R_e) \quad (2.27)$$

of the electronic state $|n\rangle$. The dissociation energy E_d is usually defined as the energy necessary to dissociate the molecule in its lowest vibrational level $v = 0$. The difference $E_b - E_d = E_{\text{zp}} = \frac{1}{2}\hbar\omega$ equals the zero-point energy, which is by an amount $\Delta E = \frac{1}{2}\hbar\omega$ above the minimum of the potential curve. In spectroscopic discussions, the minimum $E_0^{\text{el}}(R_e)$ of the electronic ground state E_0 is usually defined to correspond to zero energy.

The total energy of the molecule in the state $|n\rangle$ is given by the sum

$$E_n = E_n^{\text{el}}(R) + E_{\text{vib}}(R) + E_{\text{rot}}(R) = \text{const.}; \quad (2.28)$$

it is constant, that is, it does not depend on the internuclear distance R . In spectroscopy, *term values* $T_n = E_n/hc$ are frequently employed instead of energies E_n . Because of $E/hc = h\nu/hc = 1/\lambda$ they are also called *wavenumbers* and are given in units of cm^{-1} .

For each electronic state E_n^{el} there exists a set of vibrational states characterized by the vibrational quantum number v , and for each vibrational state there exist a (usually large) number of rotational states characterized by the rotational quantum number J (see Fig. 2.4 and Ch. 3).

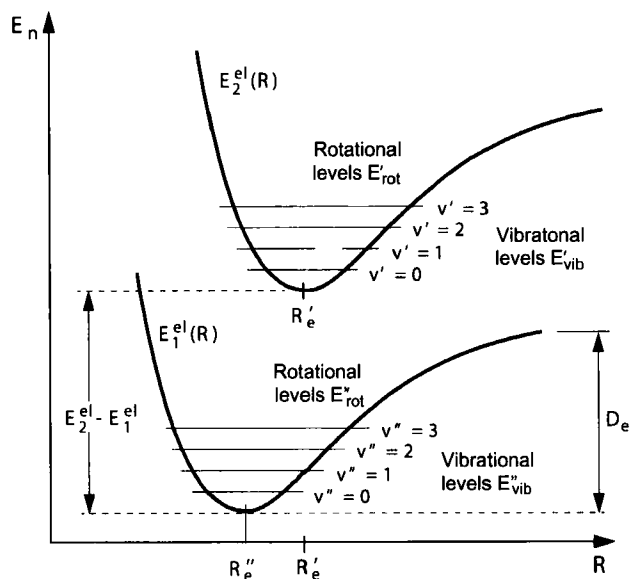


Fig. 2.4 Schematic illustration of two electronic states with their equilibrium nuclear distances R_e , vibrational-rotational levels, bond energies and electronic energies.

Transitions $(n, v_i, J_j) \leftrightarrow (m, v_k, J_l)$ between two states $E_n = E_{n, v_i, J_j} = (E_n^{\text{el}}, E''_{\text{vib}}, E''_{\text{rot}})$ and $E_m = E_{m, v_k, J_l} = (E_m^{\text{el}}, E'_{\text{vib}}, E'_{\text{rot}})$ can take place through absorption or emission of electromagnetic radiation of frequency $\nu_{nm} = (E_m - E_n)/h$ or wavenumber $1/\lambda_{nm} = T_m - T_n$, respectively. Whether such a transition actually occurs depends on several factors, for example on details of the wavefunctions and the population numbers of both states. These questions will be discussed in more detail in Ch. 4.

Figure 1.2 schematically showed such transitions between different molecular states. If a transition takes place between two adjacent rotational levels of the same vibrational state it is called a *pure rotational spectrum*. The wavelength of these transitions is usually located in the *microwave region* of the electromagnetic spectrum. Transitions $(n, v_i, J_j) \leftrightarrow (n, v_k, J_l)$ between different vibrational levels of the same electronic state constitute an *infrared spectrum*, in which all the rotational lines within a vibrational transition $v_i \leftrightarrow v_k$ are called a *vibrational band*. So-called electronic transitions between vibration-rotation levels of different electronic states can yield spectra which extend from the near infrared to the vacuum UV regions of the electromagnetic spectrum. They are usually accompanied by many vibrational bands $(n, v_i \leftrightarrow m, v_k)$, constituting a *band system* for each electronic transition $n \leftrightarrow m$.

For nonlinear triatomic molecules, the adiabatic approximation enables us to write the potential energy $E_n^{\text{el}}(\mathbf{R})$ as a function of three variables, that is, of two bond lengths R_1 and R_2 and the bending angle α . As we cannot display this surface graphically, we need to draw cuts through this surface where two of the three variables are kept constant. This results in a potential energy curve depending on only one variable as in the case of the diatomic molecule (Fig. 2.5). Alternatively, we could display the surface as contour lines of equal potential, where only one variable is kept constant, that is, the bending angle, while isopotential contour lines are plotted for $E_n^{\text{el}}(R_1, R_2)$.

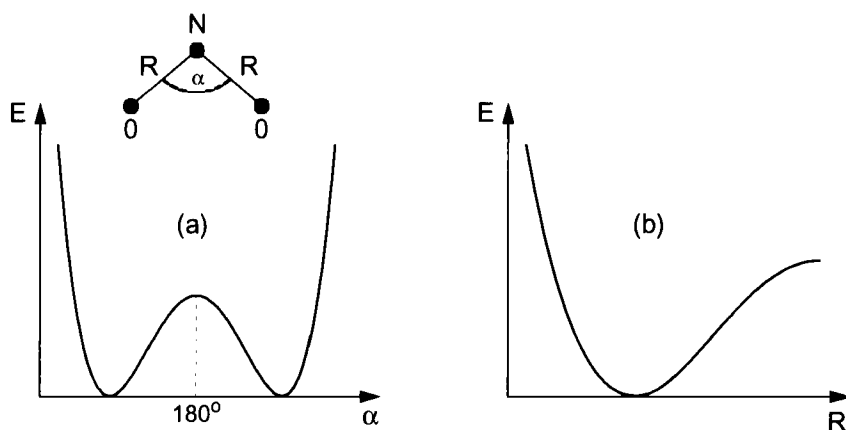


Fig. 2.5 Two cuts through the potential energy surface of a triatomic molecule; here for the NO₂ ground state. a) $E(\alpha)$; b) $E(R)$.

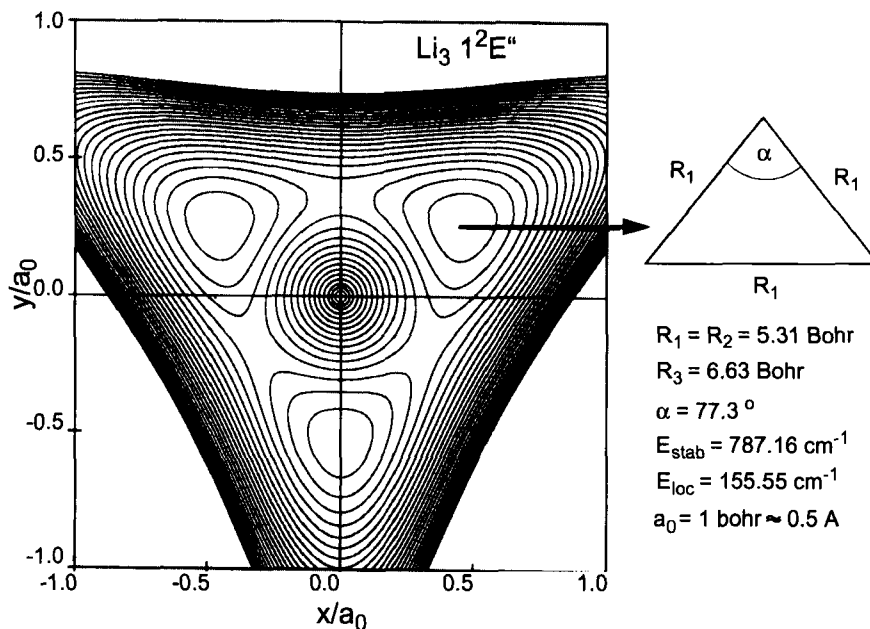


Fig. 2.6 Contour-line representation of the potential energy surface of a triatomic molecule; here for Li_3 . (Courtesy W. Meyer, Kaiserslautern)

Figure 2.6 shows the potential surface for the equilateral triangle of Li_3 , where the axes display the x and y coordinates of the nuclear displacements from the equilibrium structure.

A polyatomic molecule possesses more internal degrees of freedom, and consequently there exist more vibrations and rotations than in the diatomic case. This results in a large number of vibrational–rotational levels, and the observed spectra obtained are therefore much more complicated (see Chapters 6–8).

In the next section we will start with the discussion of the classification of electronic states before turning to their calculation. In most cases we will focus on diatomic molecules, because this allows a clearer presentation of the methods used. However, towards the end of the chapter, and also in Ch. 7, we will also give some examples for polyatomic molecules.

2.4

Electronic States of Diatomic Molecules

Many phenomena related to electronic molecular states can be introduced most easily with simple models in discussing *diatomic* molecules. Among them are, for example, the vector model of angular momentum coupling or the symmetry properties of

molecular states. Most helpful is also the *molecular orbital* concept, which reduces the treatment of many-electron molecules to a suitable combination of one-electron states.

In this chapter, we will start with the simplest molecule, the H_2^+ molecular ion, which consists of two protons and one electron. It is the only system which can be solved *exactly* within the BO approximation, that is, as a rigid nuclear framework. For this simple example we will introduce and define the characteristic properties and quantum numbers of all *one-electron systems* (Sect. 2.4.2). One-electron systems are molecules with only one unpaired electron in the highest (otherwise unoccupied) energy level. This *optical electron* is responsible for many important molecular properties. Examples of such systems are the ions H_2^+ , Li_2^+ , and Na_2^+ or the radicals CH and OH.

Starting from quantum numbers, angular momenta, and symmetries of these one-electron systems, we will generalize these quantities and their definitions to molecules with many electrons. This is the subject of Sect. 2.4.3, where we will also introduce the classification of electronic states of diatomic molecules.

Finally, the last section will discuss the two limiting cases of electronic molecular states for $R \rightarrow \infty$ (separated atoms) and $R \rightarrow 0$ (united atom). With their help, we will learn about the correlations between molecular and atomic states.

Throughout Ch. 2, we will assume that the nuclear framework is rigid and nonrotating so that the BO approximation is strictly valid. This means that to each electronic state there corresponds a *potential energy curve* $E_n(R)$, which is defined by the average (over electronic coordinates) of the total electronic and nuclear potential energy plus the averaged electronic kinetic energy (see Sect. 2.1).

2.4.1

Exact Treatment of the Rigid H_2^+ Molecule

The simplest conceivable molecules consist of two nuclei A and B with nuclear charges Z_1e and Z_2e and one electron, i.e., H_2^+ , HeH^{2+} , LiH^{3+} etc. It turns out, however, that the resulting one-electron molecular ion is stable only for $Z_1 = Z_2 = 1$, that is, the hydrogen molecular ion H_2^+ and its isotopomers HD^+ and D_2^+ . For fixed nuclei, that is, ignoring vibrations and rotations, this corresponds to an electron in a two-center potential, the Schrödinger equation of which is separable and thus exactly solvable in elliptic coordinates.

We identify the z coordinate with the internuclear axis and introduce elliptic coordinates (Fig. 2.7):

$$\varphi = \arctan(y/x), \quad \mu = \frac{r_A + r_B}{R}, \quad \nu = \frac{r_A - r_B}{R}. \quad (2.29)$$

The condition $\varphi = \text{const.}$ describes all planes which contain the internuclear axis; $\mu = \text{const.}$ are confocal rotational ellipsoids with the nuclei as focal points; $\nu = \text{const.}$

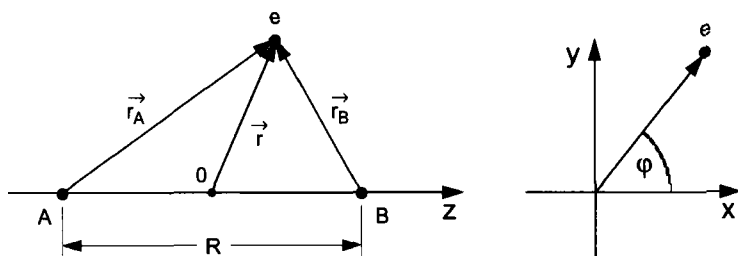


Fig. 2.7 Elliptic coordinates of the H_2^+ molecular ion.

are two-shell rotational hyperboloids, $\mu = 1$ describes the z axis between the nuclei, and $\nu = 0$ is the horizontal plane halfway between the nuclei (Fig. 2.8).

We insert the separation ansatz

$$\phi^{\text{el}} = \psi = M(\mu) \times N(\nu) \times \phi(\varphi) \quad (2.30)$$

into the electronic Schrödinger equation (2.15a) for the H_2^+ molecular ion,

$$\left[-\frac{\hbar^2}{2m} \nabla^2 + \frac{e^2}{4\pi\epsilon_0} \left(\frac{1}{R} - \frac{1}{r_A} - \frac{1}{r_B} \right) \right] \psi = E\psi, \quad (2.31)$$

where the solution ψ corresponds to the functions $\phi^{\text{el}}(\mathbf{r}, R)$ from Eq. (2.13a). This yields, in complete analogy to the solution of the Schrödinger equation for the H atom [2.1–2.4],

$$\frac{1}{\phi} \frac{d^2\phi}{d\varphi^2} + \alpha = 0, \quad (2.32a)$$

$$\frac{1}{M} \frac{d}{d\mu} (\mu^2 - 1) \frac{dM}{d\mu} - \frac{\alpha}{\mu^2 - 1} + \frac{mR^2}{\hbar^2} \left(\frac{e^2\mu}{4\pi\epsilon_0 R} + \frac{E}{2} \mu^2 \right) = \beta, \quad (2.32b)$$

$$\frac{1}{N} \frac{d}{d\nu} (1 - \nu^2) \frac{dN}{d\nu} - \frac{\alpha}{1 - \nu^2} - \frac{mR^2}{2\hbar^2} E\nu^2 = -\beta, \quad (2.32c)$$

where α and β are separation constants.

The solutions of these three equations are the functions $M(\mu)$, $N(\nu)$, and $\phi(\varphi)$, which depend not only on the separation constants α and β but also on the boundary

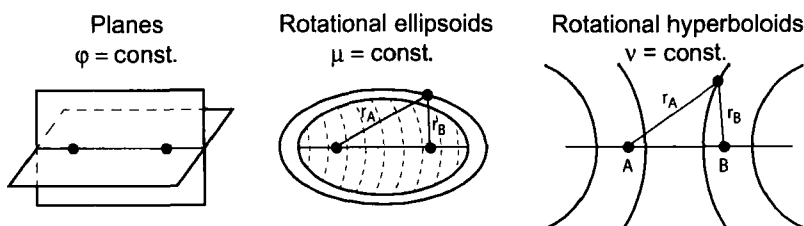


Fig. 2.8 The surfaces $\varphi = \text{const.}$, $\mu = \text{const.}$, and $\nu = \text{const.}$.

conditions (ψ must be normalizable, continuous and single-valued for all values of $\mu \geq 0$, $-\infty < \nu < +\infty$, and $0 \leq \varphi < 2\pi$).

The solutions of Eq. (2.32a) are

$$\phi = c_1 e^{i\varphi\sqrt{\alpha}} + c_2 e^{-i\varphi\sqrt{\alpha}}. \quad (2.33a)$$

The single-valuedness of ϕ requires that $\phi(\varphi + 2\pi n) = \phi(\varphi)$; $n = 1, 2, 3, \dots$, therefore $e^{\pm 2\pi i\sqrt{\alpha}} = 1 \Rightarrow \sqrt{\alpha} = \lambda$ must be integer, that is, λ must be integer, and we obtain the solutions of Eq. (2.32a),

$$\phi = c_1 e^{i\lambda\varphi} + c_2 e^{-i\lambda\varphi}. \quad (2.33b)$$

To elucidate the physical meaning of λ , we concentrate on the angular momentum ℓ of the electron. As the electric field of the nuclei, in which the electron moves, is no central force field, ℓ is not constant. However, for fixed internuclear distance R both the magnitude $|\ell|$ and the projection ℓ_z onto the internuclear axis are constant and have well-defined quantized values.

The component of the electron angular momentum along the internuclear axis is

$$\ell_z = (\mathbf{r} \times \mathbf{p})_z = xp_y - yp_x \quad (2.34a)$$

and its expectation value is

$$\langle \ell_z \rangle = \frac{\hbar}{i} \int \psi^* \left(x \frac{\partial}{\partial y} - y \frac{\partial}{\partial x} \right) \psi \, d\tau = \frac{\hbar}{i} \int \psi^* \frac{\partial}{\partial \varphi} \psi \, d\tau = \frac{\hbar}{i} \int_0^{2\pi} \phi^* \frac{\partial \phi}{\partial \varphi} \, d\varphi, \quad (2.34b)$$

because M and N do not depend on φ and are each normalized. For ϕ we substitute the solutions of Eq. (2.33b) to obtain

$$\langle \ell_z \rangle = \pm \lambda \hbar. \quad (2.35)$$

The absolute value of the quantum number λ indicates the projection of the electronic orbital angular momentum onto the molecular axis in units of \hbar (Fig. 2.9).

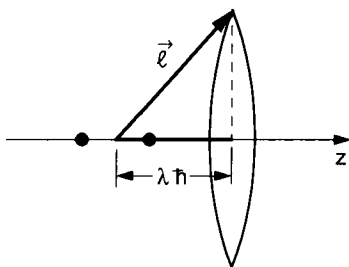


Fig. 2.9 Precessing orbital angular momentum ℓ of an electron in the cylindrically symmetric electric field of a diatomic molecule.

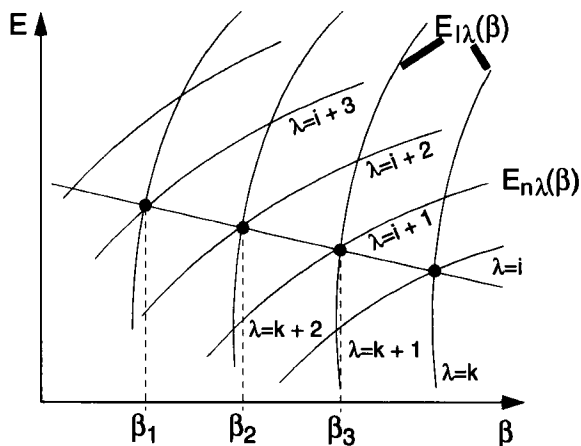


Fig. 2.10 Energy curves $E_{\ell\lambda}(\beta)$ and $E_{n\lambda}(\beta)$.

If we substitute $\alpha = \lambda^2$ in Eqns. (2.32b) and (2.32c), each of the resulting equations contains two parameters λ^2 and β . They can be solved by series expansions of the functions M and N [2.11]. It turns out that for each value of λ^2 , and obeying the boundary conditions for the wavefunctions, there exists a discrete infinite sequence of curves corresponding to energy eigenvalues $E_{n\lambda}(\beta)$ leading to meaningful solutions of Eq. (2.32b). Also, there are solutions to Eq. (2.32c) with, in general, different energy eigenvalues $E_{\ell\lambda}(\beta)$, ($\ell = 1, 2, 3, \dots$). This is displayed schematically in Fig. 2.10.

The solutions E must solve both equations simultaneously. Therefore only values of β are allowed for which $E_n(\lambda, \beta) = E_\ell(\lambda, \beta)$. These correspond to the intersections of the sets of curves $E_n(\lambda, \beta)$ and $E_\ell(\lambda, \beta)$ in Fig. 2.10. The admissible energies $E_{n,\lambda}$ therefore depend on three quantum numbers n , ℓ and λ , and they form a discrete sequence for $E < 0$.

Note:

- Equations (2.32b)–(2.32c) do not depend on λ but only on λ^2 . This means that the energy does not depend on the sign of λ . In non-rotating molecules, the two functions $\exp(\pm i\lambda\varphi)$ are energetically degenerate.
- The eigenfunctions ψ are characterized by a set of three quantum numbers (n, ℓ, λ) . They can be visualized as follows. The condition $\psi(x, y, z) = 0$ defines a surface with zero probability of finding the electron. This so-called nodal surface separates regions with $\psi > 0$ from regions with $\psi < 0$. Because of $\psi = M(\mu)N(\nu)\phi(\varphi)$, ψ can only vanish if at least one of the factors M , N or ϕ vanishes. Each of these functions depends only on one coordinate; therefore they vanish for specific values of μ , ν and φ . The nodal surfaces $\mu_k = 0$

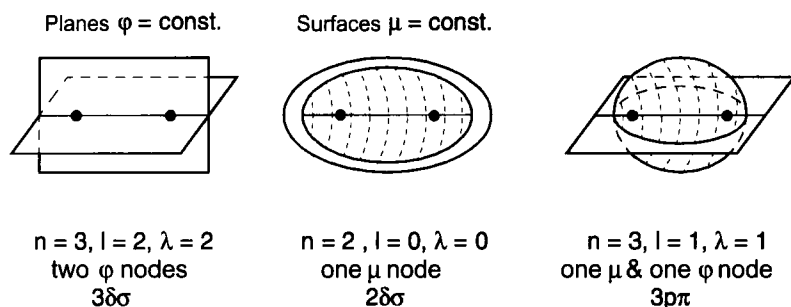


Fig. 2.11 Nodal planes $\varphi = 0$ and nodal surfaces $\mu = 0$ for some electronic states.

are rotational ellipsoids, the surfaces $\nu = \nu_i = 0$ hyperboloids and the planes $\varphi = 0$ planes through the z axis (Fig. 2.8).

- As can be seen from Eq. (2.33b), the absolute value of the quantum number λ indicates the number of nodal planes of φ . It can be shown that the quantum number ℓ is the total number of nodal planes of φ and ν . We can define the principal quantum number n to be the total number of μ , ν and φ nodal planes plus one; then we arrive at a relation very similar to that for atoms,

$$\lambda \leq \ell \leq n - 1. \quad (2.36)$$

- Each set of quantum numbers (n, ℓ, λ) corresponds to a spatial probability distribution for the electron given by the square modulus of the wavefunction,

$$W_{n,\ell,\lambda} = \psi_{n,\ell,\lambda}^* \psi_{n,\ell,\lambda} = |\psi_{n,\ell,\lambda}|^2. \quad (2.37)$$

The electron state with $\ell = 0$ is called an s state, the $\ell = 1$ state a p state, etc., in analogy to the designations of electron states in the hydrogen atom. States with the same ℓ can differ in their projection quantum numbers λ . They are labeled with lower-case Greek letters, that is, $\lambda = 0$ is called a σ state, $\lambda = 1$ a π state, $\lambda = 2$ a δ state. An electron state with the quantum numbers $(n = 3, \ell = 2, \lambda = 2)$ is therefore called a $3\delta\delta$ state (see Fig. 2.11 and Table 2.1).

Figure 2.12 illustrates the electronic wavefunctions of some states of H_2^+ ; regions with positive values of the wavefunction are displayed in dark gray, regions with negative values in light gray.

The solutions of the separated Schrödinger equations (2.32b), (2.32c) yield the potential curves $E_n(R)$ displayed in Fig. 2.13 for the H_2^+ molecular ion. Note that only the lowest electronic state, $1\sigma_g$, corresponds to a stable molecule; all higher electronic states possess repulsive potential curves (except for a shallow minimum of the $3\sigma_g$ state at large internuclear distances).

Tab. 2.1 Quantum numbers and term designations of an electron in a linear molecule with orbital angular momentum quantum number ℓ and projection quantum number $\lambda = |m_\ell|$.

Quantum numbers			Term designation
n	ℓ	λ	
1	0	0	1s σ
2	0	0	2s σ
2	1	0	2p σ
2	1	1	2p π
3	2	0	3d σ
3	2	2	3d δ

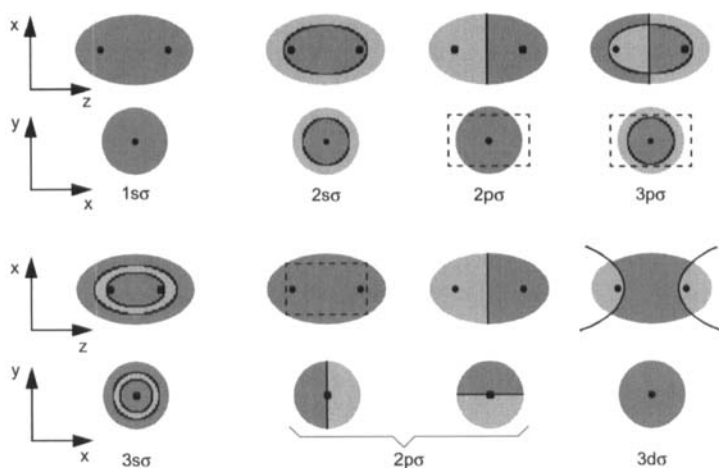


Fig. 2.12 Electronic wavefunctions for some states of H_2^+ (dark gray = positive; light gray = negative values). If the plane of the paper is a nodal plane, the sign of the wavefunction above the plane is indicated [2.11].

2.4.2

Classification of Electronic Molecular States

Electronic states of molecules with more than one electron cannot be calculated exactly. Even without explicit calculation it is possible, however, to give criteria that enable us to group all possible states into certain classes and to gain an overview and some physical insight into their electron distributions.

The different electronic states of diatomic molecules can be classified according to

1. their energy $E_i(R)$,
2. the symmetry properties of their electronic wavefunctions, and
3. the angular momenta and spins of all their electrons and their respective couplings.

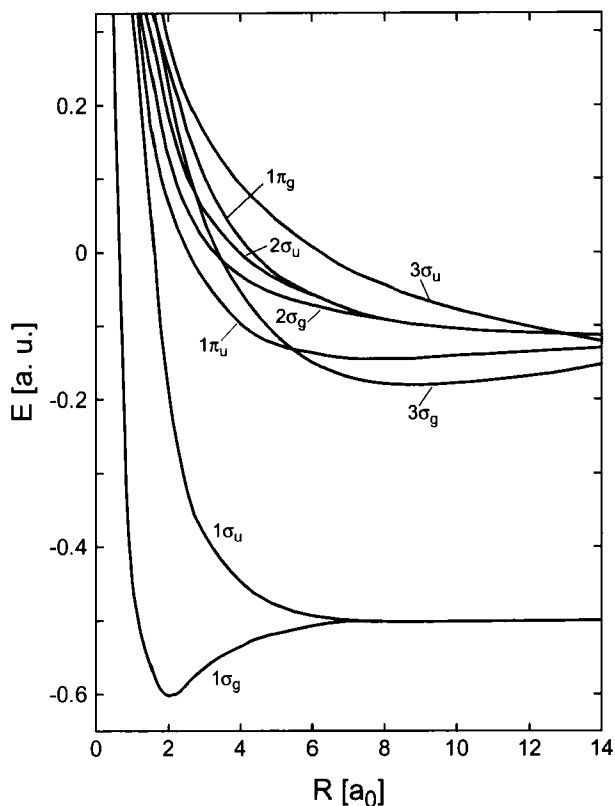


Fig. 2.13 Potential curves of H_2^+ [2.12].

2.4.2.1 Energetic Ordering of Electronic States

The subscript i in $E_i(R)$ is merely a shorthand notation for the set (n, l, λ) of principal quantum number n , angular momentum quantum numbers ℓ , and projection quantum number λ . In atoms, the principal quantum number n defines the order of all states according to energy. In molecules, this simple relation holds only for Rydberg states, in which one electron is highly excited and is located predominantly outside the *molecular core*, so that its coupling with the other electrons is small. For $R \rightarrow \infty$, the potential curves $E_n(R)$ of a Rydberg molecule AB^* merge asymptotically into the atomic ground state of atom A plus the n th Rydberg state of atom B^* (Fig. 2.14). At the equilibrium distance $R = R_e$ a simple relation holds for molecular Rydberg states:

$$E_{n+1}(R'_e) > E_n(R''_e). \quad (2.38)$$

For low-lying molecular electronic states the energy differences between states with different angular momentum can be so large that it is not possible to define a principal quantum number n with the property that it approaches the atomic states $A(n) + B$ or $A + B(n)$ for $R \rightarrow \infty$. This is especially true because there are in general sev-

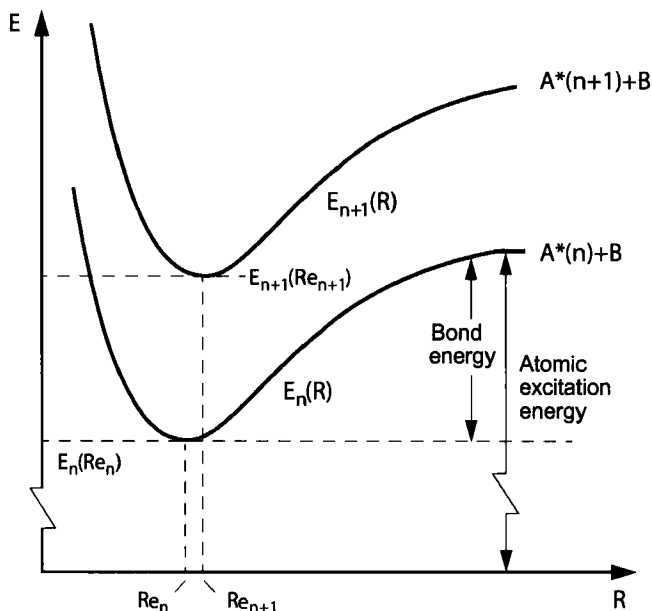


Fig. 2.14 Potential curves of Rydberg states of a diatomic molecule with dissociation channels.

eral molecular states which can dissociate to the same states of separated atoms (see Fig. 2.13 and Sect. 2.4.5). In molecular spectroscopy, a special letter notation for molecular states is commonly employed, which designates the ground state of a system with the letter X . The next state which is accessible through an optically allowed transition from the ground state is designated A , the next B and so on. States which are inaccessible via optical transitions (e.g., triplet states, for singlet ground states), are designated with lower-case letters a , b , c , etc., ordered by energy. Unfortunately, this notation is not followed consistently throughout, because there are many cases where new states have been discovered below others which had already been labeled. Therefore many authors use a different, nonsystematic, notation.

2.4.2.2 Symmetries of Electronic Wavefunctions

The symmetry of a wavefunction is of great importance for the classification of electronic states. *Symmetry operations* are actions such as a rotation of the whole molecule or the reflection of nuclear coordinates at a plane or a point (*inversion*), which leave the nuclear framework unchanged (see Ch. 5). The electron distribution does not change during a symmetry operation, that is, $|\psi_{el}|^2$ is invariant with respect to these operations.

For diatomic molecules, each plane containing the internuclear axis is a valid mirror plane, which is described by an operator σ (Fig. 2.15a). Executing this symmetry

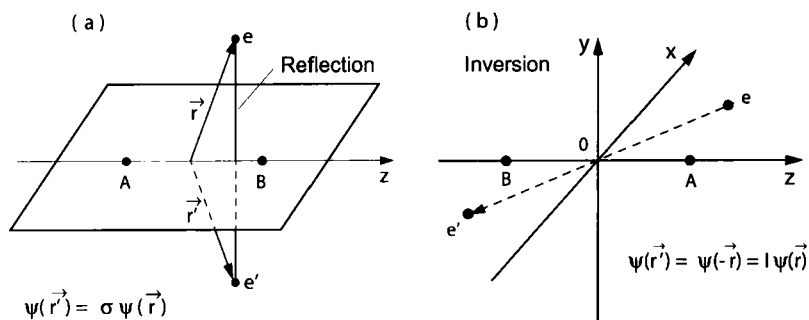


Fig. 2.15 Symmetry operations. a) Reflection; b) inversion.

operation twice returns the molecule to its original state, therefore

$$\sigma(\sigma\psi) = \sigma^2\psi = +\psi \quad \Rightarrow \quad \sigma\psi = \pm\psi. \quad (2.39)$$

Each molecular state of a diatomic molecule must therefore be described either by a wavefunction ψ^+ (even parity), for which

$$\sigma\psi^+ = +\psi^+, \quad (2.39a)$$

or by a wavefunction ψ^- (odd parity), for which

$$\sigma\psi^- = -\psi^-. \quad (2.39b)$$

For diatomic molecules with $Z_A = Z_B$, that is, for homonuclear molecules, the *inversion* I of all nuclear coordinates at the center of the molecule is another symmetry operation (Fig. 2.15b). Again, the electron distribution must not change during the symmetry operation, that is,

$$I|\psi(r)|^2 = |\psi(-r)|^2 = |\psi(+r)|^2. \quad (2.40)$$

If we look at ourselves in a mirror, we recognize that the mirror image interchanges left and right; the image possesses opposite parity with respect to left–right symmetry as compared to the original. (*Question:* Why don't you appear upside-down in a mirror?)

In analogy to our previous considerations we can define two symmetry types of wavefunctions ψ_g and ψ_u ,

$$I^2\psi = \psi \quad \Rightarrow \quad I\psi_g = +\psi_g \quad \text{and} \quad I\psi_u = -\psi_u. \quad (2.40a)$$

Molecular states with “even” wavefunctions ψ_g have *even* parity, wavefunctions with “odd” wavefunctions ψ_u have *odd* parity. The parity of a molecular state can be derived from the parities of the atomic states of the separate atoms which combine to form the molecular state (see Sect. 2.4.5).

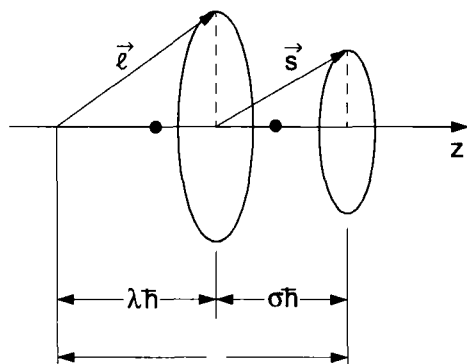


Fig. 2.16 Independent precession of electronic angular momentum ℓ and spin s .

2.4.2.3 Electronic Angular Momenta

Besides its orbital angular momentum ℓ , an electron possesses also a spin s . The orbital angular momentum ℓ precesses around the internuclear axis (z axis), thereby creating an electric current around the z axis, which in turn creates a cylindrically symmetric magnetic field B directed along the z axis. The electron experiences this magnetic field and aligns its spin magnetic moment either parallel or antiparallel to it. For nuclei with small nuclear charges the coupling between ℓ and s (*spin-orbit coupling*) is usually weaker than the coupling of ℓ to the molecular axis. In these cases ℓ and s precess independently around the internuclear axis, and their projections are $\lambda\hbar$ and $\sigma\hbar$, respectively (Fig. 2.16).

As the magnetic field B is proportional to the expectation value $\lambda\hbar$ of the orbital angular momentum projection ℓ , and the expectation value of the magnetic spin moment μ_s is proportional to the electron spin projection $\sigma\hbar$, the interaction energy between ℓ and s is

$$W = A\lambda\sigma, \quad (2.41)$$

where the constant A , the *molecular fine-structure constant*, depends on the molecular state. This interaction energy, depending on the angular momentum projections, creates a *fine-structure splitting* of molecular terms. For molecules with a single electron, $\sigma = \pm\frac{1}{2}$. This means that each energy level in electronic states with $\lambda > 0$ splits into a doublet, the components of which are separated by

$$W = A\lambda. \quad (2.41a)$$

In molecules with more than one electron, the angular momenta of the individual electrons add. The sequence in which the momenta are added depends on the relative coupling strengths. We elucidate this fact for the analogous atomic case.

We imagine the two nuclei with charges Z_Ae and Z_Be to be united into a single nucleus with charge $(Z_A + Z_B)e$. The electrons then move in the spherical symmetric

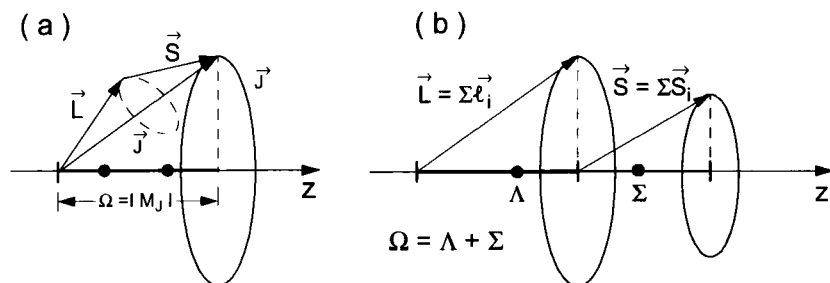


Fig. 2.17 Angular momentum coupling. a) L - S coupling; b) In-dependent coupling of L and S to the molecular axis.

potential of this nucleus, and their total angular momentum \mathbf{J} must be constant. For light atoms we can assume L - S coupling, that is, the total orbital angular momentum $\mathbf{L} = \sum_i \ell_i$ of all electrons and the total spin $\mathbf{S} = \sum_i s_i$ are vectorially combined from the orbital angular momenta ℓ_i and the spins s_i of the individual electrons. The total angular momentum of the electrons is then $\mathbf{J}_{\text{el}} = \mathbf{L} + \mathbf{S}$ and its absolute value is $|\mathbf{J}_{\text{el}}| = \sqrt{J_{\text{el}}(J_{\text{el}} + 1)}\hbar$.

If we now increase the internuclear distance until it reaches the molecule's equilibrium distance R_e , the electrons move in the cylindrically symmetric field of the two nuclei. The total angular momentum \mathbf{J}_{el} is now not constant because the field creates a torque $\mathbf{D} = d\mathbf{J}_{\text{el}}/dt$, which leads to a precession of \mathbf{J}_{el} around the internuclear axis (Fig. 2.17a). We can therefore observe only the time-average of \mathbf{J}_{el} , i.e., the projection $M_{J_{\text{el}}}\hbar$ of \mathbf{J}_{el} onto the internuclear axis. We can express this fact also by saying that J_{el} is no 'good' quantum number. The quantum number Ω of this projection is

$$\Omega = |M_{J_{\text{el}}}|, \quad \Omega = J_{\text{el}}, J_{\text{el}} - 1, \dots, \frac{1}{2} \text{ or } 0. \quad (2.42)$$

If the spin-orbit coupling energy $W = A\mathbf{L} \cdot \mathbf{S}$ in the united atom is smaller than the coupling of \mathbf{L} to the internuclear axis (which is in general true for light atoms), then \mathbf{L} and \mathbf{S} will be decoupled by the axial electric field and precess independently around the internuclear axis (Fig. 2.17b). In these cases the orbital angular momentum projection $M_L\hbar$ and the spin angular momentum projection $M_S\hbar$ are well defined, and they are best expressed in terms of the quantum numbers Λ and Σ defined by

$$\begin{aligned} \Lambda &= |M_L|, \quad \Lambda = 0, 1, 2, \dots, L \\ \Sigma &= M_S = s, s - 2, \dots, -s. \end{aligned} \quad (2.43)$$

For the projection quantum number Ω of the total angular momentum we obtain

$$\Omega = |\Lambda + \Sigma|. \quad (2.44)$$

States with $\Lambda = 0$ are called Σ states, and states with $\Lambda = 1, 2, 3$ are Π , Δ , and Φ states. The notation is analogous to the atomic case, with the Latin letters of the atomic notation replaced by the corresponding Greek symbols.

Note:

1. We denote the quantum numbers of a single electron by lowercase Greek letters, those of a many-electron system by uppercase Greek letters.
2. The symbol Σ is used with two different meanings:
 - a) To designate a state with $\Lambda = 0$ (upright Σ).
 - b) As quantum number $\Sigma = M_S$ of the total spin projection $M_S \hbar$ onto the internuclear axis (italic Σ).
3. Each state with $\Lambda > 0$ is twofold degenerate in nonrotating molecules because the two projections $\pm M_L \hbar$ of the orbital angular momenta \mathbf{L} lead to the same energy in the axial electric field of the nuclei. In other words, the energy of nonrotating molecules does not depend on the sense of rotation of the electrons around the internuclear axis! This degeneracy is removed in rotating molecules (see Sect. 3.2.3).

The energy of a molecular state depends not only on the principal quantum number n , the quantum number Λ and the spin S , but also on the quantum number $\Omega = |\Lambda + \Sigma|$. As Σ can assume $2S + 1$ values from $\Sigma = -S$ to $\Sigma = +S$, an electron configuration with given values of S and Λ results in $2S + 1$ different molecular states, which are called *fine-structure terms*, in analogy to the atomic case (Fig. 2.18).

As in one-electron molecules, the fine-structure splitting of light many-electron molecules is given by

$$W_{fs} = A\Lambda\Sigma. \quad (2.45a)$$

The term values of an electronic state with quantum numbers Λ and Σ are then

$$T_{el}^{\Lambda, \Sigma} = T_0 + A\Lambda\Sigma, \quad (2.45b)$$

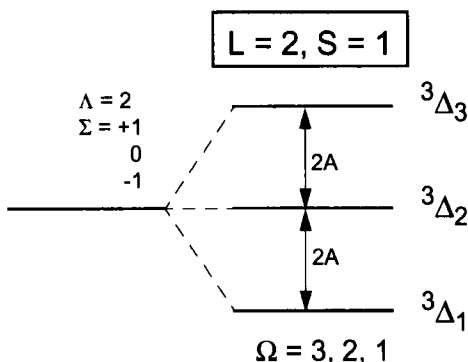


Fig. 2.18 Fine-structure splitting of a ${}^3\Delta$ state with $\Lambda = 2$, $\Sigma = 0, \pm 1$, i.e., $\Omega = 1, 2, 3$.

Tab. 2.2 Ground states of some diatomic molecules.

Molecule	H_2^+	H_2	He_2^+	B_2	C_2	O_2	NO
Ground state	$X^2\Sigma_g^+$	$X^1\Sigma_g^+$	$X^2\Sigma_u^+$	$X^3\Sigma_g^-$	$X^3\Pi_u$	$X^3\Sigma_g^-$	$X^2\Pi_{1/2}$

where T_0 is the term value for $\Sigma = 0$. The magnitude of the spin-orbit coupling constant A and its sign are determined by

1. the sum $\sum_i a_i \ell_i \times s_i$ of the interactions between spin and orbital angular momentum of the same electron, and
2. a suitable average of the sums $\sum_i b_{ij}, l_i \times s_j$ for $j = 1, \dots, N$ over interactions of the spin of the j th electron with the orbital angular momenta of all other electrons [2.13].

Which of these two effects dominates depends on the angular momentum coupling scheme employed for the angular momenta L and S of both atoms.

The complete characterization of an electronic state of a diatomic molecule with total spin quantum number S , projection quantum number $\Lambda = |M_L|$ and projection quantum number $\Omega = |\Lambda + \Sigma|$ is written, similar to the atomic case, as

$$^{2S+1} \Lambda_{\Omega} \quad (2.46)$$

with the appropriate letter (X, A, B, C , etc.), indicating energetic ordering, in front of this symbol. For example, the ground state of the NO molecule is $X^2\Pi_{1/2}$. For homonuclear molecules, the parity (“odd” or “even”) of the wavefunction is also indicated. For example, the second excited state of the Na_2 molecule is $B^1\Pi_u$, and the corresponding triplet state is $b^3\Pi_{\Omega u}$ with three fine-structure components $\Omega = 0, 1, 2$. Table 2.2 lists the ground states of some common diatomic molecules.

If the coupling between $L = \sum \ell_i$ and $S = \sum s_i$ in both atoms is so strong that the nuclear electric field along the z axis cannot break it, Λ and Σ cease to be good quantum numbers. Their sum $\Omega = |\Lambda + \Sigma|$ is still well defined, however (Fig. 2.17a). In place of the Σ, Π, Δ notation we call these states simply 0, 1/2, 1, etc., states according to their quantum number Ω .

Note:

1. In contrast to the atomic case the fine-structure terms of diatomic molecules are, in the context of this simple model, equidistant within their multiplets, and according to Eq. (2.45) their distance is $\Delta E = A\Lambda$.
2. For $\Lambda \neq 0$, the number of fine-structure components equals $2S + 1$, even for $\Lambda < \Sigma$.
3. The fine-structure splitting does not remove the Λ degeneracy for $\Lambda \neq 0$ in nonrotating molecules, that is, each fine-structure component is still twofold degenerate because of $\Lambda = |M_L|$.

2.4.3

Electron Configurations and Electronic States

To gain an overview of all possible electronic states of diatomic molecules and their symmetries and energetic ordering, we consider the two limiting cases for $R \rightarrow 0$ and $R \rightarrow \infty$. If the internuclear distance R between the nuclei with charges Z_A and Z_B approaches zero, we arrive at the limiting case of the *united atom* with charge $Z_A + Z_B$ containing the same number of electrons as the original molecule. For $R \rightarrow \infty$ we arrive at the limiting case of two completely separated, noninteracting atoms.

For $R \rightarrow \infty$, each molecular state yields a combination of known states of the two separated atoms, for $R \rightarrow 0$ a well-defined state of the united atom. The potential curves $E_i(R)$ are defined by their respective asymptotic limits $E_i(R = 0)$ and $E_i(R = \infty)$; they can be combined into a *correlation diagram*, which displays the corresponding molecular states for $R = R_c$.

2.4.3.1 The Approximation of Separated Atoms

As a start, we discuss which states of a molecule AB can be realized by coupling the given atomic angular momenta in all possible ways.

The atomic states have the orbital angular momentum quantum numbers L_A and L_B . When the two atoms approach each other, L_A and L_B precess around the z axis and their projections are $(M_L)_A \hbar$ and $(M_L)_B \hbar$, respectively. The resulting quantum number Λ is then

$$\Lambda = |(M_L)_A + (M_L)_B| . \quad (2.47)$$

As the values of M_L can assume all values from $-L$ to L , a given combination of L_A and L_B can result in a large number of values for Λ , which increases with increasing L_A and L_B . The number of possible molecular electronic states is therefore much larger than the corresponding number for the participating atoms! Table 2.3 lists, as an example, all possible molecular states that can emerge from the combination of an atomic D state with $L_A = 2$ and a P state with $L_B = 1$.

Tab. 2.3 Quantum numbers of all molecular states which can be formed from D + P atomic states.

$(M_L)_A$	$(M_L)_B$	Λ	State(s)
0	0	0	Σ
± 1	∓ 1	0	Σ^+, Σ
0	± 1	1	Π
± 1	0	1	Π
± 2	∓ 1	1	Π
± 1	± 1	2	Δ
± 2	0	2	Δ
± 2	± 1	3	Φ

Tab. 2.4 Combination of atomic states with odd or even parity to molecular states.

Atomic states	Molecular states
$S_g + S_g$ or $S_u + S_u$	Σ^+
$S_g + S_u$	Σ^-
$S_g + P_g$ or $S_u + P_u$	Σ^-, Π
$S_g + P_u$ or $S_u + P_g$	Σ^+, Π
$S_g + D_g$ or $S_u + D_u$	Σ^+, Π, Δ
$P_g + P_g$ or $P_u + P_u$	$\Sigma^+(2), \Sigma^-, \Pi(2), \Delta$
$P_g + P_u$	$\Sigma^+, \Sigma^-(2), \Pi(2), \Delta$
$P_g + D_g$ or $P_u + D_u$	$\Sigma^+, \Sigma^-(2), \Pi(3), \Delta(2), \Phi$

For $(M_L)_A = (M_L)_B$ there are three Σ states with $\Lambda = 0$. These are the combinations $|(M_L)_A + (M_L)_B| = 0$, $|(M_L)_A - (M_L)_B| = 0$ and $(M_L)_A = (M_L)_B = 0$, respectively. It can be shown that there exists always an *odd* number of Σ states [2.14]. There are six combinations which lead to $|(M_L)_A + (M_L)_B| = 1$ and thus to Π states, four combination leading to Δ states, and two combinations leading to Φ states.

The symmetry properties of molecular states are derived from those of the atomic states of the atoms A and B. An atomic state has even parity if the sum $\sum \ell_i$ over orbital angular momentum numbers ℓ_i of all electrons is even; it has odd parity if $\sum \ell_i$ is odd [2.14]. This follows from the fact that the total wavefunction of the atomic state (L, M_L) is a linear combination of products of Legendre polynomials, $\sum c_i \prod_i Y_{\ell_i}^m$. These products have even parity if $\sum \ell_i = \text{even}$. To derive the angular momenta and parities of atomic and molecular states, we need to consider only partially filled shells because for completely filled shells the orbital angular momentum $L = \sum \ell_i$ is always zero. Table 2.4 lists the parities of molecular states derived from a number of atomic states; numbers in parentheses indicate the number of possible molecular states.

Example

Three atomic p electrons can produce the atomic configurations 2P , 2D and 4S . For all these states, $\sum \ell_i = 3 = \text{odd}$ and therefore they all have *odd* parity. Four p electrons lead to 1S , 1D and 3P states. In each case, $\sum \ell_i = 4 = \text{even}$, that is, all these states have *even* parity, although the total angular momentum quantum number can assume even as well as odd values. This shows that we can *not* derive the parity from total angular momentum L .

Now we include also the spins S_A and S_B of the atomic states in our discussion. The resulting molecular spin is $S = S_A + S_B$, and its magnitude is

$$|S| = \sqrt{S(S+1)}\hbar,$$

where S is the spin quantum number. For $S_B < S_A$, the spin quantum number S can assume the $(2S_B + 1)$ values

$$S = S_A + S_B; \quad S_A + S_B - 1; \quad \dots; \quad S_A - S_B, \quad (2.48)$$

Tab. 2.5 Possible multiplicities of molecular states for given multiplicities of the atomic states.

Atom A	Atom B	Molecule AB
singlet	singlet	singlet
singlet	doublet	doublet
doublet	doublet	singlet + triplet
doublet	triplet	doublet + quadruplet
triplet	triplet	singlet, triplet, quintuplet
triplet	quadruplet	doublet + quadruplet + sextuplet

which correspond to all possible orientations of S_B relative to S_A . For $S_B \geq S_A$ we obtain correspondingly $(2S_A + 1)$ values for S (Table 2.5).

Two atomic states with spins S_A and S_B can therefore lead to $(2S_B + 1)$ or $(2S_A + 1)$ different molecular spin states characterized by the spin quantum number S . Spin-orbit coupling splits each of these states into fine-structure components with quantum number Ω (see Sect. 2.4.2.3). Table 2.6 lists some examples.

For homonuclear diatomic molecules, the number of possible molecular states is further increased by the additional property of parity, that is, each state can be classified as *even* or *odd* according to the parity of its wavefunction. If both atoms have different parity, we obtain two states for each of the molecular states shown in Table 2.4, one with even and one with odd parity. Table 2.7 lists all molecular states which can be formed from two identical atoms in identical atomic states.

Tab. 2.6 States of diatomic molecules with their quantum numbers $\Lambda = |M_L|$; S (spin quantum number), Σ (spin projection) and $\Omega = \Lambda + \Sigma$.

Λ	S	Σ	Ω	State
0	0	0	0	$^1\Sigma$
1	1	0	1	$^3\Pi_1$
1	1	1	2	$^3\Pi_2$
1	1	-1	0	$^3\Pi_0$
2	$\frac{1}{2}$	$\frac{1}{2}$	$\frac{1}{2}$	$^2\Delta_{5/2}$
3	2	1	4	$^3\Phi_4$

Tab. 2.7 Electronic states of homonuclear diatomic molecules which can be formed from two atoms in identical states.

Atomic states	Molecular states
$^1S + ^1S$	$^1\Sigma_g^+$
$^2S + ^2S$	$^1\Sigma_g^+, ^3\Sigma_u^+$
$^3S + ^3S$	$^1\Sigma_g^+, ^3\Sigma_u^+, ^5\Sigma_g^+$
$^4S + ^4S$	$^1\Sigma_g^+, ^3\Sigma_u^+, ^5\Sigma_g^+, ^7\Sigma_u^+$
$^1P + ^1P$	$^1\Sigma_g^+, ^1\Sigma_u^-, ^1\Pi_g^-, ^1\Pi_u, ^1\Delta_g$
$^2P + ^2P$	$^1\Sigma_g^+, ^1\Sigma_u^-, ^1\Pi_g^-, ^1\Pi_u, ^1\Delta_g, ^3\Sigma_u^+(2), ^3\Sigma_g^-, ^3\Pi_g^-, ^3\Pi_u, ^3\Delta_u$

2.4.3.2 The “United Atom” Approximation

If we imagine both nuclei with charges $Z_A e$ and $Z_B e$ combined in a single nucleus with charge $(Z_A + Z_B)e$, we obtain an atom with a well-known configuration of the $(Z_A + Z_B)$ electrons. For example, from ${}^7_3\text{Li } {}^1_1\text{H}$ we create the “united” atom beryllium atom ${}^8_4\text{Be}$ in its ground-state configuration $(1s)^2(2s)^2$, and from the ${}^{10}_5\text{B } {}^2_1\text{H}$ radical containing a deuterium nucleus ${}^2_1\text{H}$, the “united” carbon atom ${}^{12}_6\text{C}$ with an electron configuration $(1s)^2(2s)^2(2p)^2$ emerges, where we indicate the occupation of an atomic state by the exponent. The states $1s$, $2s$, $2p$, etc., with their respective wavefunctions are called *atomic orbitals*.

If we now separate the two nuclei from each other, the electrons with $\ell > 0$ start to precess in the axial electric field. A p electron with $\ell = 1$ can then assume the projections $m_\ell \hbar = 0$ or $m_\ell \hbar = \pm 1 \hbar$ of the electronic orbital angular momentum. Table 2.8 lists the possible molecular states and their maximum electron occupation, which can be created from the different electron configurations of the united atom. For example, from the $(1s)^2(2s)^2(2p)^2$ electron configuration of the united C atom, the following three electron configurations of the BH molecule can emerge upon separation in separate nuclei B + H through the different projections $\lambda = 0, \pm 1$ of the two p electrons

$$(1s\sigma)^2(2s\sigma)^2(2p\sigma)^2, \quad (1s\sigma)^2(2s\sigma)^2(2p\sigma)(2p\pi), \quad \text{and} \quad (1s\sigma)^2(2s\sigma)^2(2p\pi)^2.$$

Next we must decide which molecular states can be derived from these electron configurations, how they correlate with the states of the separated atoms, and what their energetic ordering will be.

2.4.4

Molecular Orbitals and the Aufbau Principle

The so-called *one-electron approximation* considers a *single* electron e_i , which moves in the electrostatic potential of the two nuclei and of the *averaged* charge distribution of all other electrons. The electronic wavefunction $\phi_i(\mathbf{r}_i)$ that describes the state of this electron and that depends only on the coordinates of this electron is called a *molecular orbital*. Its square modulus $|\phi_i(\mathbf{r}_i)|^2$ determines the spatial probability distribution for this electron. The Pauli principle allows this molecular orbital to be

Tab. 2.8 Molecular one-electron states created from the orbitals of a united atom.

State	United atom ℓ	λ	Molecule	Maximum occupation
ns	0	0	$ns\sigma$	2
np_z	1	0	$np\sigma$	2
np_x, np_y	1	1	$np\pi$	4
nd_{z^2}	2	0	$nd\sigma$	2
nd_{xz}, nd_{yz}	2	1	$nd\pi$	4
		2	$nd\delta$	4

occupied by a maximum of two electrons with antiparallel spins. The spatial distribution $\phi_i(r_i)$ of these two electrons is then identical. (Table 2.8 lists the maximum allowed occupation number for orbitals with $\lambda \geq 1$ as being four since these orbitals are twofold degenerate because of $\lambda = |\pm m_\ell|$.)

Within the one-electron approximation, we can now build the molecular electron configuration as follows. First, we decide which molecular orbitals can be created from the available atomic orbitals. The molecular orbitals can either be constructed as linear combinations of atomic orbitals of the separated atoms or taken from those of the united atom (see preceding section).

Next, the molecular orbitals are arranged in order of increasing energy, which in general is the following:

$$1s\sigma; 2s\sigma; 2p\pi; 3s\sigma; 3p\sigma; 3p\pi; 3d\sigma; 3d\pi; 3d\delta; \dots$$

These orbitals are now filled with the maximum number of electrons which is allowed by the Pauli principle (see Table 2.8). The electronic ground state wavefunction of the molecule in the one-electron approximation is then the product of all occupied molecular orbitals. This product of occupied molecular orbitals is also called the *electron configuration*. Table 2.9 lists the ground-state configurations of some common molecules.

The *singly excited* molecular states are obtained by moving one electron from an occupied into an energetically higher unoccupied orbital. Table 2.10 lists the low-

Tab. 2.9 Ground-state electron configurations of some common light molecules.

Molecule	Electron configuration	Ground state	Bond energy (eV)	
H_2^+	$\sigma_g 1s$	$2\Sigma_g^+$	2.648	
H_2	$(\sigma_g 1s)^2$	$1\Sigma_g^+$	4.476	
He_2^+	$(\sigma_g 1s)^2(\sigma_u 1s)$	$2\Sigma_u^+$	2.6	
He_2	$(\sigma_g 1s)^2(\sigma_u 1s)^2$	$1\Sigma_g^+$	0.001	
Li_2	$(\sigma_g 1s)^2(\sigma_u 1s)^2(\sigma_g 2s)^2$	$1\Sigma_g^+$	1.02	
B_2	$(\sigma_g 1s)^2(\sigma_u 1s)^2(\sigma_g 2s)^2(\sigma_u 2s)^2(\pi_u 2p)^2$	$3\Sigma_g^-$	3.6	
C_2	$(\sigma_g 1s)^2(\sigma_u 1s)^2(\sigma_g 2s)^2(\sigma_u 2s)^2(\pi_u 2p)^4$	$3\Pi_u^-$	3.6	
	or	$(\pi_u 2p)^3(\sigma_g 2p)$	$3\Sigma_u^-$	3.6

Tab. 2.10 Electron configurations in the ground and first excited states of the Li_2 molecule. KK designates the 1s orbitals in the two atomic K shells which are located around the respective nuclei.

$KK(\sigma_g 2s)^2$	$1\Sigma_g^+, 3\Sigma_u^+$
$KK(\sigma_g 2s), (\sigma_g 2p)$	$1\Sigma_u^+, 3\Sigma_g^-$
$KK(\sigma_g 2s, \pi 2p)$	$3\Pi_u, 1\Pi_g, 1\Pi_u, 3\Pi_g$
$KK(\sigma_g 2s), (\sigma_g 3s)$	$1\Sigma_g^+, 3\Sigma_u^+$

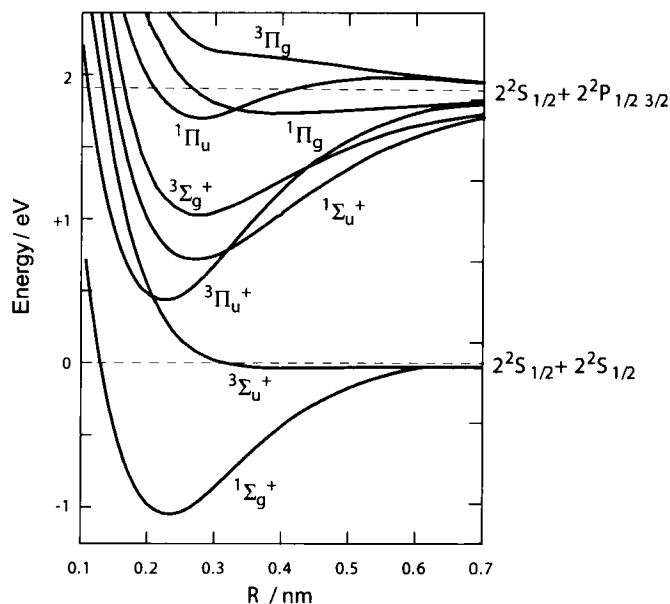


Fig. 2.19 Potential curves of the Li_2 molecule derived from two different combinations of atomic states [2.15].

est three excited electron configurations and their corresponding states for the Li_2 molecule with six electrons. Figure 2.19 displays the potential curves of the Li_2 molecule that result from the states $(2^2S_{1/2} + 2^2S_{1/2})$ and $(2^2S_{1/2} + 2^2P_{1/2,3/2})$ of the separated atoms.

Figure 2.20 illustrates once more how the atomic states 3P , 1D and 1S of the united carbon atom are constructed from the electron configuration $(1s)^2(2s)^2(2p)^2$, following the energetic ordering discussed above. The energetic ordering of the orbitals with different electron spin is determined by *Hund's rule*, which states that, for a given

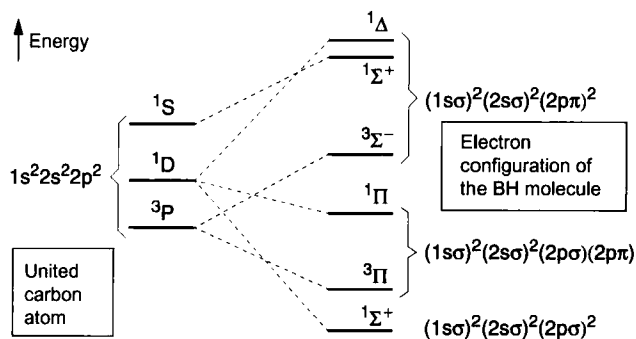


Fig. 2.20 Correlation between the electron configuration of the united carbon atom and the resulting molecular states of the BH molecule.

value of the quantum numbers l and $\lambda = |m_\ell|$, the state with maximum multiplicity is lowest in energy. This rule follows from Pauli's principle, because electrons with parallel spin have the smallest overlap between their spatial wavefunctions. Thus, they are on average farther apart from each other and their mutual Coulomb repulsion is minimized.

The atomic configuration $(1s)^2(2s)^2(2p)^2$ of the united carbon atom corresponds to the following molecular configurations and states of the BH molecule:

$$\begin{aligned}(1s\sigma)^2(2s\sigma)^2(2p\sigma)^2 &\leftrightarrow {}^1\Sigma^+ , \\ (1s\sigma)^2(2s\sigma)^2(2p\sigma)(2p\pi) &\leftrightarrow {}^1\Pi, {}^3\Pi , \\ (1s\sigma)^2(2s\sigma)^2(2p\pi)^2 &\leftrightarrow {}^3\Sigma^-, {}^1\Sigma^+, {}^1\Delta .\end{aligned}$$

From Tables 2.3–2.8 we can see which of the molecular states ${}^1\Sigma$, ${}^3\Pi$, ${}^1\Pi$, ${}^3\Sigma$ and ${}^1\Delta$ correspond to which atomic states 3P , 1D , 1S of the united atom; the resulting state diagram is shown in Fig. 2.20.

Although we can gain a lot of information on the numbers, types and energetics of molecular states from the above considerations, we still need – usually quite lengthy – calculations to determine the energies (i.e., term values) quantitatively (see Sect. 2.5). However, from a correlation diagram we can already get a qualitative picture of the different molecular states during the transition from the united atom ($R = 0$) to the separated atoms ($R = \infty$). This will be discussed next.

2.4.5

Correlation Diagrams

In this section we will discuss how the electron configuration of the “united” atom makes the transition to the electron configurations of the separated atoms when the distance R is increased from 0 to ∞ . Molecular orbital theory answers this question by providing molecular orbitals $\phi_i(R)$ for each electron i as a function of the internuclear distance R . The energy $E_n(R)$ can then be calculated as the expectation value of the Hamiltonian,

$$E_n(R) = \int \phi_n^* H \phi_n \, d\tau . \quad (2.49)$$

This will be done in Sections 2.5 and 2.6 for the H_2^+ molecular ion and the H_2 molecule. However, from conservation laws and symmetry considerations we can get a qualitative impression of such a correlation $\phi_i(R)$ between $\phi_i(0)$ and $\phi_i(\infty)$. This is achieved as follows.

First, we determine all possible molecular electron configurations at small internuclear separations R from the configuration of the united atom. This procedure yields the corresponding molecular orbitals (see Fig. 2.20) as defined through the quantum numbers (n, ℓ, m_ℓ) . If the internuclear separation increases, the molecular orbitals be-

come linear combinations of the atomic orbitals of the separated atoms. The following conservation laws apply:

1. The quantum number $\lambda = |m_\ell|$ is independent of R , because the component $m_\ell \hbar$ of the angular momentum ℓ is conserved for all internuclear distances R . The principal quantum number n and the angular momentum quantum number ℓ can change, however; that is, for the separated atoms $n = n_A + n_B$ or $\ell = \ell_A + \ell_B$ do *not* hold.
2. Wavefunction parity does not depend on the internuclear separation R ; therefore even or odd states of the united atoms yield even and odd molecular states, respectively.
3. If two different states in the united atom have the same symmetry, quantum number A , and multiplicity $2S + 1$, they can *not* become degenerate for any internuclear separation R . Stated differently: The potential curves $E(R)$ of such states can *never* cross!

This *noncrossing rule* was proven for exact wavefunctions with the aid of group theory by Neumann and Wigner [2.16, 2.17]; it is, however, still applicable for approximated wavefunctions. Figure 2.21 shows a correlation diagram for the lowest states

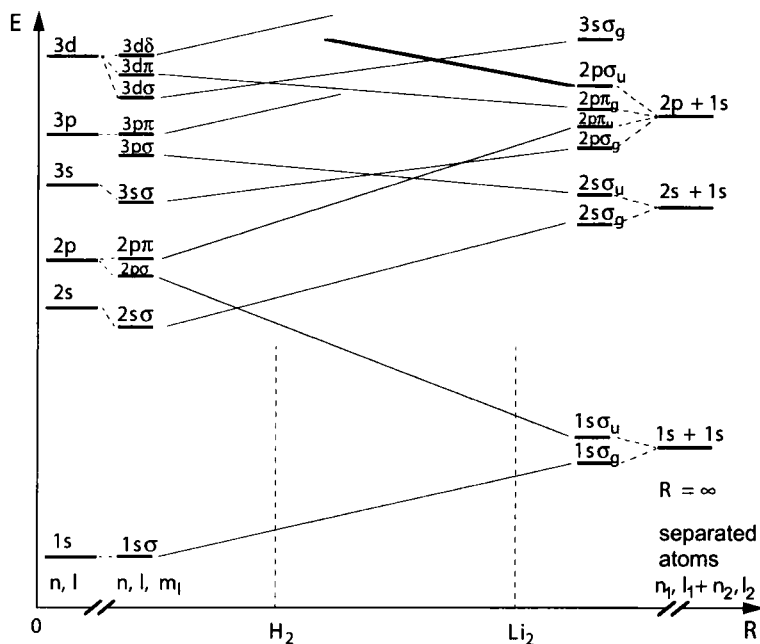


Fig. 2.21 Correlation diagram showing the energies of electronic states during the transition from the united atom ($R = 0$) to separated atoms ($R = \infty$).

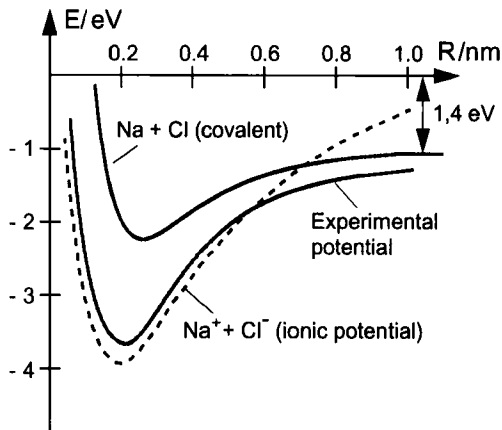


Fig. 2.22 Potential curves of the NaCl molecule, which shows a transition from neutral NaCl for small internuclear distances to ionic states Na^+Cl^- for large internuclear separations.

of a homonuclear molecule. It can be constructed as follows. We start with the lowest state of the united atom, construct from it the appropriate molecular orbitals for $R = 0$, and connect these to the lowest pair of atomic states of the same symmetry for $R \rightarrow \infty$. Usually, these are the ground states of the two atoms. The second-lowest molecular state must then dissociate into the lowest yet unused atomic states of proper symmetry, etc. Applying the noncrossing rule, we can in most cases arrive at the correct ordering of molecular states, provided we know the atomic terms for $R = 0$ and $R = \infty$. It might appear that this procedure yields always unambiguous results. Unfortunately this is not the case, because some complications arise especially for heteronuclear molecules.

1. A molecule AB can dissociate not only into neutral atoms $A + B$ but also into the ions $A^+ + B^-$. This situation occurs, for example, in the alkali halides (Fig. 2.22). These *ionic* potential curves often cross the corresponding neutral curves, leading to significant shifts in the potentials $E_n(R)$.
2. Spin-orbit coupling varies markedly with internuclear distance so that the coupling of the angular momenta L and S can be completely different in the united atom from that in the separated atoms. It is thus in many cases not possible to decide on the basis of a correlation diagram alone into which fine-structure components of the separated atoms a given molecular state (Λ, Σ, Ω) will dissociate (Fig. 2.23).
3. For repulsive potential curves, the energy $E_n(R)$ depends strongly on R . This makes an unambiguous assignment difficult.

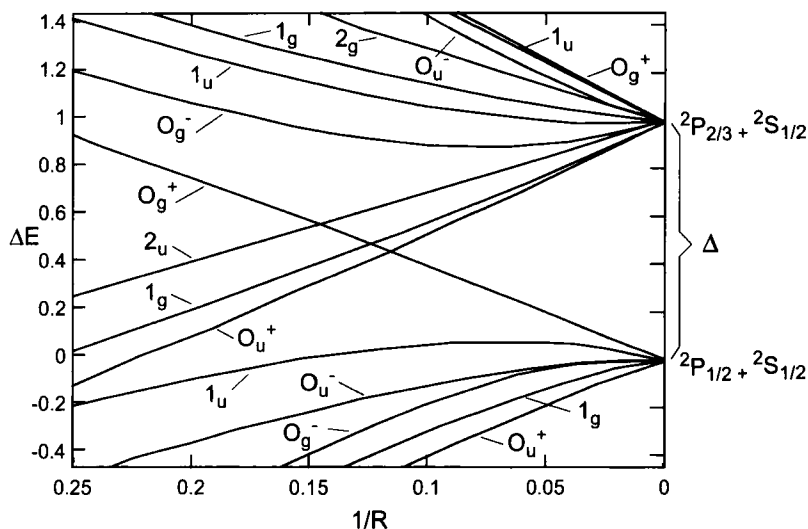


Fig. 2.23 Dependence of spin-orbit coupling on the internuclear distance for the Cs_2 molecule.

A correlation diagram is an important tool in assigning molecular states, yet it cannot replace numerical calculations of absolute energies $E_n(R)$ when it comes to quantitative discussions. Such calculations are based on approximation methods for the solution of the electronic Schrödinger equation (2.15a) which we will now discuss.

2.5

Approximation Methods for the Calculation of Electronic Wavefunctions

The electronic part, Eq. (2.13a), of the Schrödinger equation (2.4) for fixed nuclei,

$$H_0\phi_n(\mathbf{r}, \mathbf{R}) = E_n^0\phi_n(\mathbf{r}, \mathbf{R}), \quad \mathbf{R} = \text{const.},$$

cannot be solved exactly for any chemically relevant system. We must therefore employ approximative methods which yield wavefunctions that describe the potential surfaces $E_n(\mathbf{R})$ “as good as possible”.

All such methods rely on a proper choice of approximate wavefunctions (basis functions) containing adjustable parameters. These parameters are then varied so that the calculated energies $E_n(\mathbf{R})$ of molecular states match the unknown *true* energies as exactly as possible on the whole range of nuclear configurations \mathbf{R} . An important criterion for this match is provided by the *Ritz principle*, which states that the energies calculated with approximate wavefunctions are always *above* those calculated with the exact (true) wavefunctions [2.18]. This will be shown in the following section.

2.5.1

The Variational Method

Almost all approximation methods for the calculation of wavefunctions rely on the variational method to determine the values of the free parameters in the chosen basis functions. The quality of an approximated wavefunction can be judged on the basis of a simple argument.

The *exact* eigenfunctions ϕ_{el} are solutions of the Schrödinger equation $H\phi_{\text{el}} = E_{\text{el}}\phi_{\text{el}}$ with exact energies $E_{\text{el}}(R)$. An *approximate* solution function ϕ yields the expectation value

$$E = \frac{\langle \phi | H | \phi \rangle}{\langle \phi | \phi \rangle} \quad (2.50)$$

for the energy, where we have used Dirac's notation $\langle \phi | H | \phi \rangle = \int \phi^* H \phi \, d\tau_{\text{el}}$. The difference between this approximate energy E and the exact energy E_{el} is therefore

$$E - E_{\text{el}} = \frac{\langle \phi | H | \phi \rangle}{\langle \phi | \phi \rangle} - E_{\text{el}} = \frac{\langle \phi | H - E_{\text{el}} | \phi \rangle}{\langle \phi | \phi \rangle}. \quad (2.51)$$

Now we substitute $\phi = \phi_{\text{el}} + \delta\phi$ for the approximate function in Eq. (2.51), and with $H\phi_{\text{el}} = E_{\text{el}}\phi_{\text{el}}$ and due to the hermiticity of the Hamiltonian we obtain

$$E - E_{\text{el}} = \frac{\langle \delta\phi | H - E_{\text{el}} | \delta\phi \rangle}{\langle \phi | \phi \rangle}. \quad (2.52)$$

Thus, the difference $E - E_{\text{el}}$ depends quadratically on the difference $\delta\phi$ and must assume a minimum for $\delta\phi = 0$. Therefore,

$$E - E_{\text{el}} \geq 0 \Rightarrow E \geq E_{\text{el}}.$$

The energies calculated with approximate wavefunctions ϕ are always larger than the true energy E_{el} .

This means that *the expectation value of the energy assumes a minimum for the correct wavefunctions, that is, for the exact solutions of the Schrödinger equation!*

This fact is the basis for a general method to optimize approximate solutions. We write our *trial function* as a linear combination

$$\phi = \sum_i^m c_i \varphi_i \quad (2.53)$$

of known functions φ_i (which need *not* be solutions of the Schrödinger equation) and unknown coefficients c_i . Next, we optimize ϕ using the conditions

$$\frac{\partial}{\partial c_i} \left(\int \phi^* H \phi \, d\tau \right) = 0; \quad i = 1, 2, \dots, m \quad (2.54)$$

in order to obtain the minimum energy. Substitution of Eq. (2.53) leads to a linear system of m equations for the m unknown coefficients c_i

$$\begin{aligned} c_1(H_{11} - ES_{11}) + c_2(H_{12} - ES_{12}) + \cdots + c_m(H_{1m} - ES_{1m}) &= 0, \\ c_1(H_{21} - ES_{21}) + c_2(H_{22} - ES_{22}) + \cdots + c_m(H_{2m} - ES_{2m}) &= 0, \\ \vdots & \\ c_1(H_{m1} - ES_{m1}) + c_2(H_{m2} - ES_{m2}) + \cdots + c_m(H_{mm} - ES_{mm}) &= 0, \end{aligned} \quad (2.55)$$

where we have introduced the abbreviations

$$H_{ik} = \int \varphi_i^* H \varphi_k \, d\tau \quad \text{and} \quad S_{ik} = \int \varphi_i^* \varphi_k \, d\tau. \quad (2.56)$$

This system of equations has nonzero solutions c_i if and only if its determinant fulfills

$$|H_{ik} - ES_{ik}| = 0. \quad (2.57)$$

From this *secular equation* we obtain the m energies $E_1(\mathbf{R}), E_2(\mathbf{R}), \dots, E_m(\mathbf{R})$ and from Eq. (2.55) the unknown coefficients c_i for all nuclear configurations \mathbf{R} . This means that we have to calculate all the integrals H_{ik} and S_{ik} , which is possible because the φ_i are known (see Sect. 2.6).

2.5.2

The LCAO Approximation

As the electronic state of a diatomic molecule is determined by the states of the separate atoms resulting for $R \rightarrow \infty$, an obvious choice for the trial function ϕ in Eq. (2.53) is a linear combination of the eigenfunctions ϕ_A and ϕ_B of these atomic states.

That means that we approximate the molecular wavefunction ϕ by a linear combination of the corresponding atomic orbitals; the method is therefore called *linear combination of atomic orbitals* (LCAO). By *atomic orbital* we mean the atomic wavefunctions ϕ_A and ϕ_B , whose square moduli determine the electronic densities in atoms A and B, respectively, in the appropriate states. The molecular function ϕ is also called a *molecular orbital*.

Remark: For polyatomic molecules with n atoms ϕ is taken as a linear combination $\phi = \sum_i^n c_i \phi_i$. However, we will see later (in Sect. 2.8) that the number of basis functions ϕ_i does not necessarily equal the number of atoms in the molecule.

If we choose, for a diatomic molecule AB, the LCAO function $\phi = c_1 \phi_A + c_2 \phi_B$ with normalized atomic orbitals ϕ_A and ϕ_B so that $\langle \phi_A | \phi_A \rangle = \langle \phi_B | \phi_B \rangle = 1$, the molecular wavefunction ϕ can be normalized as

$$\phi = \frac{c_1 \phi_A + c_2 \phi_B}{\sqrt{c_1^2 + c_2^2 + 2c_1 c_2 S_{AB}}} \quad \text{with} \quad S_{AB} = \int \phi_A^* \phi_B \, d\tau. \quad (2.58)$$

The “best” functions ϕ in the sense of energy minimization are obtained, according to the variational principle, by differentiating the energy expectation value

$$\langle E \rangle = \int \langle \phi | H | \phi \rangle \quad (2.59)$$

with respect to the coefficients c_i and equating the result to zero. As shown before, this yields the system of equations

$$\begin{aligned} (H_{AA} - E)c_1 + (H_{AB} - ES_{AB})c_2 &= 0, \\ (H_{BA} - ES_{BA})c_1 + (H_{BB} - E)c_2 &= 0, \end{aligned} \quad (2.60)$$

from which the secular equation

$$(H_{AA} - E)(H_{BB} - E) - (H_{AB} - ES_{AB})^2 = 0 \quad (2.61)$$

results as a quadratic equation for E , where we have again used the abbreviations $H_{ik} = \int \phi_i^* H \phi_k d\tau$ and $S_{ik} = \int \phi_i^* \phi_k d\tau$ and the relations $H_{ik} = H_{ki}$ and $S_{ik} = S_{ki}$.

Note: The atomic wavefunctions $\phi_A(\mathbf{r}_A)$ and $\phi_B(\mathbf{r}_B)$ are in general one-electron functions, and the electronic coordinates \mathbf{r}_A and \mathbf{r}_B do not normally refer to the center of mass of the molecule (or another common origin) but use different reference frames with, for example, the centers of the individual atoms as origins. The integrals H_{ik} and S_{ik} are then two-center integrals and are explicitly written as

$$\begin{aligned} S_{ik} &= \int \phi_i(\mathbf{r}_A) \phi_k(\mathbf{r}_B) d\mathbf{r}; \\ H_{ik} &= \int \phi_i(\mathbf{r}_A) \hat{H}(\mathbf{r}, R) \phi_k(\mathbf{r}_B) d\mathbf{r}, \end{aligned} \quad (2.62)$$

where the coordinates \mathbf{r}_A refer to nucleus A and \mathbf{r}_B refer to nucleus B (Fig. 2.7). We can compute these integrals as a function of the internuclear distance R by introducing elliptic coordinates $r_A = R(\mu + \nu)/2$ and $r_B = R(\mu - \nu)/2$ [2.19].

From Eq. (2.61) we obtain two solutions $E_1(R)$ and $E_2(R)$ for the energy, which for the special case of two identical atoms in identical states ($\phi_A = \phi_B$, $H_{AA} = H_{BB}$) yield the simple expression

$$E_1(R) = \frac{H_{AA} + H_{AB}}{1 + S_{AB}}, \quad E_2(R) = \frac{H_{AA} - H_{AB}}{1 - S_{AB}}. \quad (2.63)$$

In this case, the coefficients c_1 and c_2 are obtained by substitution of Eq. (2.63) into Eq. (2.60),

$$|c_1|^2 = |c_2|^2, \quad c_1 = \pm c_2. \quad (2.64)$$

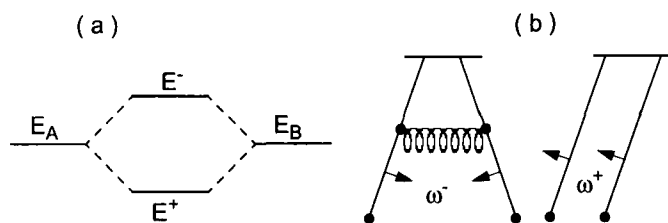


Fig. 2.24 a) Splitting of the atomic energies $E_A = E_B$ into two molecular states $E_1 = E^+$ and $E_2 = E^-$ for identical atomic states. b) Two coupled pendulums as a mechanical analogy.

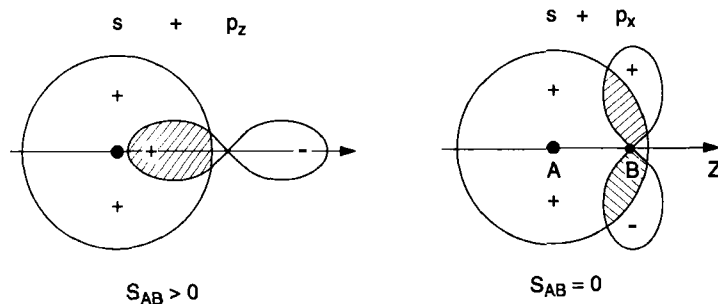


Fig. 2.25 Overlap integral of two functions of the same and different symmetry.

We see that the linear combination of two identical atomic orbitals splits the energy into two levels E_1 and E_2 (Fig. 2.24a). The magnitude of the splitting for $\phi_A = \phi_B$ is

$$\Delta E(R) = E_2 - E_1 = \frac{2H_{AA}S_{AB} - 2H_{AB}}{1 - S_{AB}^2}; \quad (2.65)$$

it depends on the *overlap integral* S_{AB} , the *Coulomb integral* H_{AA} , and the *resonance integral* H_{AB} (also called *exchange integral*).

A mechanical analog to this energy splitting consists of two coupled pendulums with resonance frequency ω_0 . Depending on the relative phase of the two oscillations $x_i(t)$, the coupling creates two *normal modes* of vibration, $x_+(t) = x_1(t) + x_2(t)$ with frequency ω_+ and $x_-(t) = x_1(t) - x_2(t)$ with frequency $\omega_- > \omega_+$ (Fig. 2.24b).

Note: Both the overlap integral S_{AB} and the resonance integral H_{AB} are zero if the functions belong to different symmetry types, that is, if they behave differently under any of the symmetry operations of the molecule. If, for example, ϕ_A is symmetric with respect to such a symmetry operation and ϕ_B is antisymmetric, the integrand $\phi_A\phi_B$ is an odd function of the relevant coordinates, and the integral $\int \phi_A\phi_B d\tau$ from $-\infty$ to $+\infty$ vanishes. Figure 2.25 exemplifies this for the overlap of a $1s$ with a p_z and a p_x function. In the first case, the two functions have the same symmetry with respect to reflection at a plane through the z axis and perpendicular

to the paper plane; in the second case their symmetries differ. Therefore, the first overlap integral is nonzero, the second vanishes. As the Hamiltonian H of a molecule must be symmetric with respect to all its symmetry operations, the above argument holds also for H_{AB} .

2.6

Application of Approximation Methods to One-electron Systems

Although we have already seen in Sect. 2.4.1 how the H_2^+ molecule can be described for fixed nuclei, it is still highly instructive to apply the LCAO method and the variational principle to this system, because by comparing the results to those of the exact treatment we can gain insight into the merits and limitations of simple approximations.

Specifically, we will see that we need to be careful with the physical interpretation of theoretical results based on approximate wavefunctions, but that we can also arrive at very reliable results if we improve, with the aid of physical insight, the basis functions employed.

2.6.1

A Simple LCAO Approximation for the H_2^+ Molecule

If we apply the LCAO approximation as outlined in Sect. 2.5.2 to the H_2^+ molecule, we obtain for the energetically lowest molecular orbital

$$\phi = c_1 \phi_A(1s) + c_2 \phi_B(1s), \quad (2.66)$$

where ϕ_A and ϕ_B are the normalized wavefunctions of the atomic hydrogen 1s ground state,

$$\phi_A = \sqrt{\frac{1}{a_0^3 \pi}} e^{-r_A/a_0}, \quad \phi_B = \sqrt{\frac{1}{a_0^3 \pi}} e^{-r_B/a_0}, \quad (2.67)$$

where $a_0 = 4\pi\epsilon_0\hbar^2/(me^2)$ is the Bohr radius in the hydrogen atom [2.18]. The ansatz Eq. (2.66) can be visualized as follows. $|\phi_A|^2$ and $|\phi_B|^2$ describe the probability density of finding the electron in the vicinity of nucleus A and B, respectively, if the other nucleus is infinitely far away. For finite internuclear distances R , $c_1\phi_A$ describes the probability amplitude that the electron is near nucleus A, and $c_2\phi_B$ gives the probability amplitude for the electron in the vicinity of nucleus B. As both possibilities are indistinguishable, both must be included, and we must use the total probability amplitude ϕ for “electron at A as well as at B”, which equals the sum of the individual amplitudes.

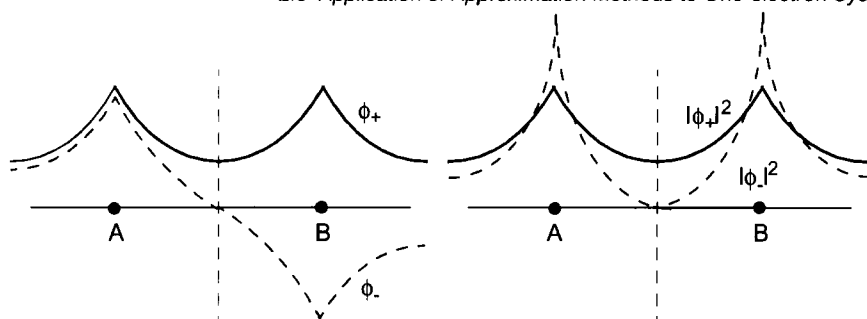


Fig. 2.26 Wavefunctions and their square moduli for the two lowest states of H_2^+ .

With the normalization condition Eq. (2.58) and with $c_1 = \pm c_2$ [see Eq. (2.64)] we obtain from Eq. (2.66) the two normalized functions

$$\phi_+ = \frac{\phi_A + \phi_B}{\sqrt{2 + 2S_{AB}}}, \quad \phi_- = \frac{\phi_A - \phi_B}{\sqrt{2 - 2S_{AB}}}. \quad (2.68)$$

From these, we can calculate the probability densities for the electron in the states ϕ_+ and ϕ_- by squaring,

$$|\phi_+|^2 = \frac{\phi_A^2 + \phi_B^2 + 2\phi_A\phi_B}{2 + 2S_{AB}}, \quad |\phi_-|^2 = \frac{\phi_A^2 + \phi_B^2 - 2\phi_A\phi_B}{2 - 2S_{AB}}. \quad (2.69)$$

Using the known functions ϕ_A , ϕ_B [Eq. (2.67)] and the overlap integral S [Eq. (2.62)] we can now compute $|\phi_+|^2$ and $|\phi_-|^2$ for any given internuclear distance R (Fig. 2.26).

From Eq. (2.63) we obtain the corresponding energies

$$E_+(R) = \frac{H_{AA} + H_{AB}}{1 + S_{AB}}, \quad E_-(R) = \frac{H_{AA} - H_{AB}}{1 - S_{AB}}. \quad (2.70)$$

The integrals S_{AB} , H_{AA} , and H_{AB} over electronic coordinates depend on the internuclear distance; they can be solved exactly. For more detailed calculations, see [2.18–2.21].

Figure 2.27 displays the functions $S_{AB}(R)$, $H_{AB}(R)$, $H_{AA}(R)$, $E_+(R)$ and $E_-(R)$ graphically so that we can gain an impression of the meaning of the different terms. We see that the overlap integral tends to 1 for $R \rightarrow 0$, and is negligible only for $R > 7a_0$. For $R \rightarrow \infty$ both $E_+(R)$ and $E_-(R)$ converge towards $H_{AA}(\infty) = E_{\text{at}} = -13.6\text{eV}$, the binding energy of the electron in the hydrogen atom.

The potential curve $E_+(R)$ describes a bonding state with a minimum of $E(R_e) = -0.13E_{\text{at}} \approx 1.76\text{eV}$ below the binding energy $-E_b$ of the electron in the hydrogen atom. The corresponding wavefunction ϕ_+ from Eq. (2.68) is symmetric with respect to inversion (reflection at the center of mass) of electronic coordinates. Thus, it describes a σ_g state, while the repulsive curve $E_-(R)$ describes a σ_u state.

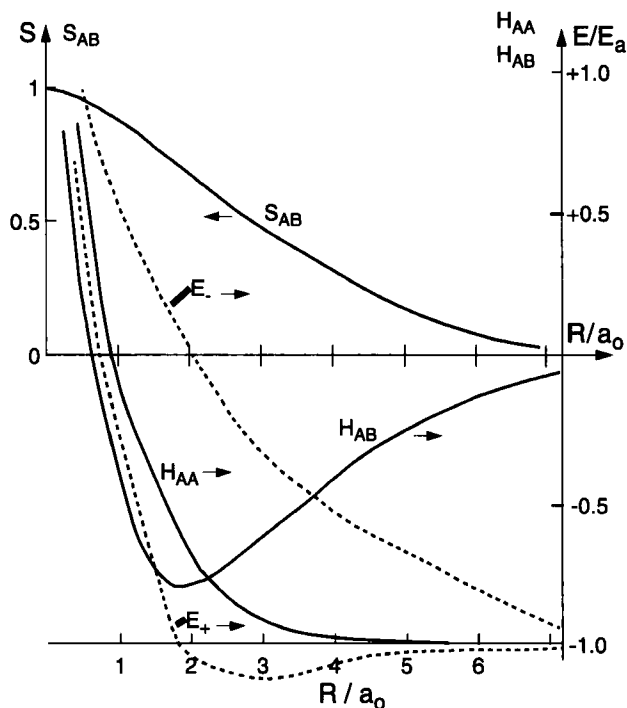


Fig. 2.27 Overlap integral S_{AB} , Coulomb integral H_{AA} , exchange integral H_{AB} and energies E_- and E_+ (broken curves) as functions of the internuclear distance R for H_2^+ [2.19].

From Fig. 2.27, we see that the LCAO approximation is correct in that it yields a bonding ground state for H_2^+ and a repulsive σ_u excited state, but that the calculated bonding energies are much too small. The reasons for this deviation will be discussed in the next section.

2.6.2

Deficiencies of the Simple LCAO Method

If we use the normalized wavefunction ϕ_+ from Eq. (2.68) to calculate the expectation values

$$\begin{aligned}
 \langle T \rangle &= - \int \phi_+^* \frac{\hbar^2}{2m} \nabla^2 \phi_+ \, dr, \\
 \langle V \rangle &= \int \phi_+^* \frac{e^2}{4\pi\epsilon_0} \left(\frac{1}{R} - \frac{1}{r_A} - \frac{1}{r_B} \right) \phi_+ \, dr, \\
 \langle E \rangle &= \int \phi_+^* \hat{H} \phi_+ \, d\tau
 \end{aligned}
 \tag{2.71}$$

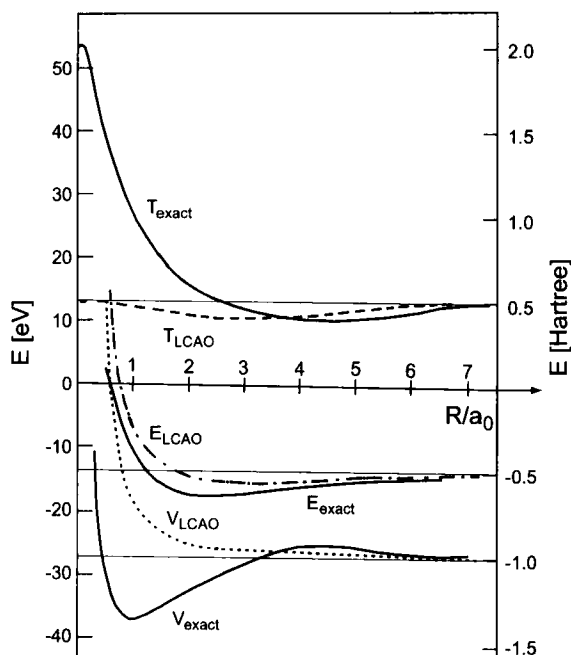


Fig. 2.28 Kinetic energy $T(R)$, potential energy $V(R)$ and total energy $E(R)$ from a simple LCAO calculation compared with the exact treatment (solid curves).

of the kinetic energy $T(R)$, the potential energy $V(R)$ and the total energy $E(R)$ of the electron in the H_2^+ molecular ion, we obtain the curves shown in Fig. 2.28. This demonstrates that in the LCAO approximation the bonding is due to a decrease in kinetic energy T while the potential energy is steadily increasing with decreasing internuclear distance R .

This is not true for the real H_2^+ molecule, however, as the exact calculation shows that the kinetic energy $T(R_e)$ in the equilibrium configuration is in fact *larger* than for $R \rightarrow \infty$. This fact can easily be rationalized: for a diatomic molecule at its equilibrium bond distance the virial theorem holds, that is, the expectation values of the kinetic and potential energy of the electron in the Coulomb potential of each nucleus are related by $\langle T \rangle + \langle V \rangle = E$ and

$$\langle T \rangle = -\frac{1}{2} \langle V \rangle = -E. \quad (2.72)$$

As the total energy E of a stable molecule must be smaller than that of the unbound atoms (otherwise no bonding would occur), $\langle T(R) \rangle$ must be larger than in the free atom.

It is highly instructive to look at the dependence of the electronic kinetic energy $T(R)$ and potential energy $V(R)$ on the internuclear distance R in some detail.

If we calculate the expectation values

$$\langle T_x \rangle = -\hbar^2 \int \phi_1 \frac{1}{2} \frac{\partial^2}{\partial x^2} \phi_1 \, d\tau = \langle T_y \rangle, \quad (2.73a)$$

$$\langle T_z \rangle = -\hbar^2 \int \phi_1 \frac{1}{2} \frac{\partial^2}{\partial z^2} \phi_1 \, d\tau \quad (2.73b)$$

for the components T_x and T_y perpendicular to the molecular axis and T_z along the molecular axis, we obtain for $R = \infty$ an isotropic electronic velocity distribution with $\langle T_x \rangle = \langle T_y \rangle = \langle T_z \rangle$. At the equilibrium bond length R_e , the expectation value $\langle T_z \rangle$ decreases, while $\langle T_x \rangle = \langle T_y \rangle$ increase.

There is a simple physical explanation for this behavior. When the two nuclei approach each other along the z direction, the electron can move *more freely* along z than in an isolated hydrogen atom. Hence, its accessible space Δz increases, and according to Heisenberg's uncertainty principle its momentum uncertainty

$$\langle \Delta p_z \rangle \geq \frac{\hbar}{\langle \Delta z \rangle} \Rightarrow \langle T_z \rangle = \left\langle \frac{\Delta p_z^2}{2m} \right\rangle \geq \frac{\hbar^2}{2m \langle \Delta z \rangle^2} \quad (2.74)$$

and thus also its kinetic energy in the z direction decrease.

In the directions perpendicular to the molecular axis the charge distribution shrinks, because the combined attraction of both nuclei increases, that is, the electron's accessible space in these directions decreases. Consequently, $\langle T_x \rangle$ and $\langle T_y \rangle$ increase.

The LCAO approximation fails to reflect the increase of $\langle T_x \rangle$ and $\langle T_y \rangle$ because the shrinkage of the wavefunction cannot be modeled by the simple ansatz of Eq. (2.68).

A further deficiency of the simple LCAO approximation is that the electronic total energy $E(R)$ approaches $E(0) = -3E_A$ for $R \rightarrow 0$, that is, for the He^+ ion, as can be seen from Eqns. (2.69) and (2.70) with $S_{AB}(R \rightarrow 0) = 1$, while the correct value is $E(\text{He}^+) = -4E_A$.

2.6.3

Improved LCAO Approximations

The simple LCAO approximation of Eq. (2.68) for the H_2^+ ground state,

$$\phi_+ = \frac{1}{\sqrt{2+2S}}(\phi_A + \phi_B) = \frac{2}{\sqrt{2+2S}} \sqrt{\frac{1}{\pi a_0^3}} e^{-r/a_0}$$

obviously approaches the hydrogen 1s orbital ϕ_A from Eq. (2.67) for $R \rightarrow 0$, because $\lim_{R \rightarrow 0} S(R) = 1$ and $\phi_B = \phi_A$.

On the other hand, the limit $R \rightarrow 0$ yields a ground-state He^+ ion (the two missing neutrons have almost no influence on the electronic energy), and the corresponding wavefunction should thus read

$$\phi(\text{He}, 1s) = \sqrt{\frac{1}{a_0^3 \pi}} e^{-2r/a_0}, \quad (2.75a)$$

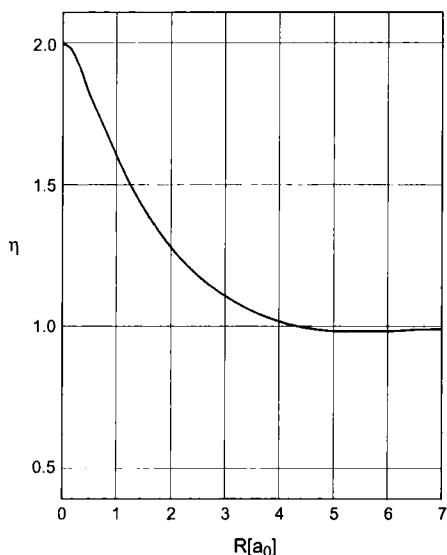


Fig. 2.29 Optimization of the contraction parameter $\eta(R)$.

because $Z = 2$ for the united atom and the electron is on average closer to the nucleus than in the case of hydrogen (this is described by the factor 2 in the exponent).

To describe this *contraction* of the electron distribution properly, we replace the functions ϕ_A and ϕ_B by modified 1s functions

$$\phi_A = Ne^{-\eta r_A/a_0}, \quad \phi_B = Ne^{-\eta r_B/a_0}, \quad (2.75b)$$

in which the parameter $\eta = \eta(R)$ depends on R and must obey the boundary conditions $\eta(0) = 2$ and $\eta(\infty) = 1$. The normalization constant N now depends on η and therefore also on R . We determine $\eta(R)$ for all internuclear distances R so that the corresponding expectation value $\langle E \rangle$ of the energy is a minimum, that is, the condition

$$\frac{\partial \langle E \rangle}{\partial \eta} = 0, \quad \text{i.e.,} \quad \frac{\partial}{\partial \eta} \int \phi_+ H \phi_+ d\tau = 0, \quad (2.76)$$

must hold for arbitrary but fixed R . This yields for $\eta(R)$ the curve shown in Fig. 2.29.

If we use these optimized functions ϕ_+ to calculate the expectation values $\langle T(R) \rangle$, $\langle V(R) \rangle$, and $\langle E(R) \rangle$, we obtain a much closer agreement with the exact curves in Fig. 2.28. From a comparison of the $E(R)$ curves in Fig. 2.30, we see that introduction of the parameter η has significantly improved our results. The calculated equilibrium distance R_e is correct; the bond dissociation energy, however, is still too small by about 20%.

Whereas this first improvement of the simple LCAO approximation by the parameter η to describe the effect of the contracting electron distribution still uses spherically symmetric basis functions ϕ_A and ϕ_B , in reality the charge distribution around nucleus

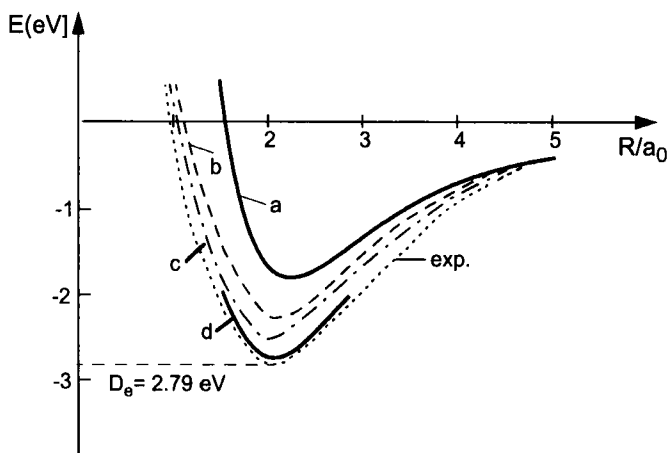


Fig. 2.30 Potential curve of the H_2^+ ground state as computed with a) simple LCAO, b) optimized parameter η , c) polarization term, and d) exact treatment.

A will be polarized in z direction by the existence of nucleus B. We can describe this polarization by introducing a polarization term into the basis functions ϕ_A and ϕ_B , that is,

$$\phi_A = e^{-\eta r_A/a_0} (1 + \lambda z), \quad (2.77)$$

and similarly for ϕ_B . Now we can optimize the parameters $\eta(R)$ and $\lambda(R)$ for each internuclear distance R , according to

$$\frac{\partial \langle H \rangle}{\partial \eta} = 0 \quad \text{and} \quad \frac{\partial \langle H \rangle}{\partial \lambda} = 0.$$

The potential curve $E(R)$ resulting from these improved basis functions resembles the exact curve very closely.

Figure 2.30 compares the potential curves $E(R)$ and Table 2.11 the values obtained for the equilibrium distances R_e and depth D_e of the potential minimum $E(R_e)$ that are computed using the different approximation levels.

When using a basis consisting of 50 functions, the experimental curve can be reproduced within experimental errors [2.22].

Tab. 2.11 Comparison of equilibrium distances and bond dissociation energies of H_2^+ as computed at different approximation levels with exact values.

Wavefunction	R_e / a_0	D_e / eV
simple LCAO	2.5	1.76
LCAO with optimum η	2.0	2.25
LCAO with additional polarization	2.0	2.65
exact calculation	2.0	2.79

We have discussed the LCAO approximation for the H_2^+ molecule in such detail because this simple example shows the merits and limitations of the approximation very clearly, and this discussion should always remind us to be careful with the interpretation of results (for example with respect to the roles of kinetic and potential energy in chemical bonding) [2.23]. Also, the often-quoted argument that exchange energy is the most prominent factor in chemical bonding is not true in the case of H_2^+ !

2.7

Many-electron Molecules

In molecules with $N \geq 2$ electrons the interaction between the electrons appears as a new term in the Hamiltonian Eq. (2.3), rendering the separation of the many-electron wavefunction $\phi(\mathbf{r}_1 \dots \mathbf{r}_N)$ in Eq. (2.7) into products of one-electron functions impossible (at least not directly). Also, the Pauli principle (which states that a state described by a spatial and a spin wavefunction may be occupied by only one electron) acts as an additional boundary condition for the distribution of electrons into orbitals. There are several approximation levels to solve this problem.

2.7.1

Molecular Orbitals and the Single-particle Approximation

In a first, rather crude, approximation, we neglect this “electron correlation” completely, i.e., we set the third term in Eq. (2.3) equal to zero. Now the electronic part of H can be written, within the BO approximation, as a sum of one-electron operators H_i ,

$$H(\mathbf{r}_1 \dots \mathbf{r}_N) = \sum_{i=1}^N H_i(\mathbf{r}_i) \quad \text{with} \quad H_i = -\frac{1}{2m} \nabla_i^2 - \frac{e^2}{4\pi\epsilon_0} \sum_i \sum_k \frac{Z_k}{r_{ik}}. \quad (2.78)$$

If we write the total electronic wavefunction as a product of one-electron wavefunctions for the electrons $1, 2, 3, \dots, N$,

$$\Phi(1 \dots N) = \phi_1(1) \times \phi_2(2) \times \dots \times \phi_n(N), \quad (2.79)$$

the Schrödinger equation can be separated into N one-electron equations

$$H_i(i)\phi_i(i) = \epsilon_i\phi_i, \quad i = 1 \dots N, \quad (2.80a)$$

and the total energy E is

$$E = \sum_{i=1}^N \epsilon_i. \quad (2.80b)$$

The one-electron wavefunctions $\phi_i(i)$ are the *molecular orbitals* of Eq. (2.53). As in Eq. (2.53), they can be written as linear combinations of atomic orbitals. It is

not possible, however, to distinguish the individual electrons, that is, we cannot tell $\phi_i(1)$ from $\phi_i(2)$, etc. In other words, the state that is described by the wavefunction of Eq. (2.79) could as well be described by any wavefunction Φ which is created by permuting the electrons in Eq. (2.79). The total wavefunction should therefore be a linear combination of all possible wavefunctions according to Eq. (2.79) with permuted electrons. The most general function of this kind is a linear combination of all $N!$ possible permutations.

If we consider also the spin of the electrons, then each of the functions ϕ can be written as a product of a spatial function $\phi(\mathbf{r})$ and a spin function $\chi(\mathbf{s})$. As the electrons are fermions with half-integer spin, the Pauli principle requires that the total wavefunction Φ (including the spin part χ) be antisymmetric with respect to a permutation of any two electrons, that is, it must change sign if we exchange electrons i and j . We can easily check for the case of three particles that the most general antisymmetric linear combination of all $N!$ permutations of the product functions Eq. (2.79) can be written in the form of a determinant

$$\Phi(1,2,\dots,N) = \begin{vmatrix} \phi_1(1)\chi_1(1) & \phi_1(2)\chi_1(2) & \dots & \phi_1(N)\chi_1(N) \\ \phi_2(1)\chi_2(1) & \phi_2(2)\chi_2(2) & \dots & \phi_2(N)\chi_2(N) \\ \vdots & \vdots & \ddots & \vdots \\ \phi_N(1)\chi_N(1) & \phi_N(2)\chi_N(2) & \dots & \phi_N(N)\chi_N(N) \end{vmatrix}, \quad (2.81)$$

where the one-electron functions are products of spatial wavefunctions ϕ and spin functions χ . The wavefunction Eq. (2.81) is called a *Slater determinant*.

A determinant vanishes if two rows or two columns are identical. A Slater determinant thus obeys the Pauli principle automatically: if two functions $\phi_i(1)$ and $\phi_k(2)$ have identical spatial parts, they *must* be combined with different spin functions or $\Phi(1\dots N)$ will vanish. This means that each molecular orbital (= spatial part of the one-electron function ϕ_i) can accommodate a maximum of two electrons with opposite spins.

If we choose the one-electron functions $\phi_i(i)$ so that

$$\int \phi_i^*(k) \times \phi_j(k) \, d\tau_k = \delta_{ij} \quad \text{for } k = 1, 2, \dots, N, \quad (2.82)$$

the square modulus of the Slater determinant is $\Phi^*\Phi = N!$. The normalized Slater determinant is therefore

$$\Phi(1,2,\dots,N) = \frac{1}{\sqrt{N!}} \begin{vmatrix} \phi_1(1) & \dots & \phi_1(N) \\ \vdots & & \vdots \\ \phi_N(1) & \dots & \phi_N(N) \end{vmatrix}, \quad (2.83)$$

where we have not written the spin part explicitly. Choosing orthonormalized basis functions offers the big computational advantage that in computing the energy integral

$$E = \frac{\int \phi^* H \phi \, d\tau}{\int \phi^* \phi \, d\tau} = \int \phi^* H \phi \, d\tau = \langle \phi | H | \phi \rangle, \quad (2.84)$$

the number of individual integrals $\langle \phi_i | \phi_k \rangle$ is reduced from $(N!)^2$ to $N!$. Nevertheless, for the H_2O molecule with $N = 10$ electrons, there are already $N! = 3\,628\,800$ of them!

At first sight, the single-particle approximation seems to be very crude, because we neglect the interaction between the electrons completely in the wavefunction. However, we can re-introduce this interaction *indirectly* by choosing a proper potential in which the particles move, that is, we do not simply use the potential of the nuclei but consider the shielding of this potential caused by the other electrons. Hence, each electron experiences a potential which is determined by the nuclei and the time-averaged motion of all other electrons (see Sect. 2.8). This is the so-called *Hartree approximation*; it includes the electron–electron interaction at least partially, but still neglects the fact that the charge distribution of the other electrons is instantaneously modified by the existence of the electron under consideration (electron correlation).

Summarizing, we can describe the important concept of molecular orbitals as follows:

1. The concept of molecular orbitals is based, similarly to the Hartree–Fock method for atoms [2.24], on the assumption that each electron moves independently of the others in an effective potential which is given by the averaged charge distribution of all other electrons and that of the nuclei.
2. Each electron i in a molecule is described by a one-electron wavefunction $\phi_i^{\text{el}}(\mathbf{r}_i, \mathbf{R})$, which is called a *molecular orbital* and which depends, for fixed nuclear configuration \mathbf{R} , only on the coordinates \mathbf{r}_i of this individual electron. The probability of finding the electron at point \mathbf{r} is given by $|\phi_i(\mathbf{r})|^2$.
3. If we consider the spin of the electron and describe the spin state by a function $\chi(\mathbf{s})$, the total wavefunction of the electron is the product of spatial and spin parts, $\Psi(\mathbf{r}, \mathbf{s}) = \phi(\mathbf{r}) \times \chi(\mathbf{s})$. Each of the functions Ψ is characterized by a set of quantum numbers (e.g., for a diatomic molecule, $n, \Lambda, \Sigma, \Omega, s$) that determine energy, angular momenta, angular momentum projections on the molecular axis and charge distribution of the orbital uniquely.
4. Due to the Pauli principle, each orbital can accommodate a maximum of two electrons with opposite spins.
5. For each molecular orbital, the expectation value of the energy is

$$E = \int \Psi^* H \Psi \, d\tau \bigg/ \int \Psi^* \Psi \, d\tau = \frac{\langle \Psi | H | \Psi \rangle}{\langle \Psi | \Psi \rangle},$$

where the right-hand side exemplifies the so-called *bracket notation* for the integral. Molecular orbitals can be written as linear combinations of atomic orbitals. While the atomic orbitals are centered at *one* atom, molecular orbitals are typically multi-centered, because each of the contributing atomic orbitals is centered at its own atom. The atomic orbitals can be classified according to

their transformation properties under the symmetry operations of the molecular symmetry group (see Sect. 5.5). The symmetry of the molecular wavefunctions constructed as linear combination of the atomic orbitals then depends on the symmetry behavior of the atomic orbitals.

To construct the electron configuration of a molecule, we start by determining the lowest-energy orbitals and their symmetries (see Sect. 2.4) from the correlation diagram. Using the Aufbau principle, we add the electrons pairwise into the orbitals in order of increasing energy.

2.7.2

The H₂ Molecule

The two-electron system H₂ (Fig. 2.31) offers, for fixed nuclei, the simplest example for an application of the single-particle approximation. Historically, another approximation was first applied to this system, the so-called *valence bond method* of Heitler and London, which starts from the separated hydrogen atoms and treats the bonding in H₂ within a perturbational approach. We will discuss both the molecular orbital and the Heitler–London method and show that the results of both are equivalent for suitably chosen wavefunctions.

2.7.2.1 The Molecular Orbital Approximation for H₂

As the ground state of the H₂ molecule dissociates into two hydrogen atoms in their 1s ground states, we choose as basis function the normalized linear combination

$$\phi_1 = \frac{1}{\sqrt{2 + 2S}}(\phi_A + \phi_B) \quad (2.85)$$

of hydrogen 1s functions, Eq. (2.67), just as in the case of H₂⁺, Eq. (2.68). We can fill this orbital with two electrons of opposite spin so that the Slater determinant of

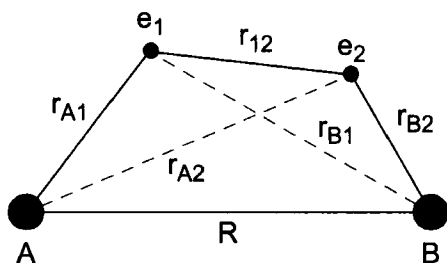


Fig. 2.31 Coordinate designations in the H₂ molecule.

Eq. (2.83), including spin, is

$$\begin{aligned}\phi(1,2) &= \begin{vmatrix} \phi_1(1)\alpha(1)\phi_1(2)\alpha(2) \\ \phi_1(1)\beta(1)\phi_1(2)\beta(2) \end{vmatrix} \\ &= \phi_1(1)\phi_1(2) [\alpha(1)\beta(2) - \alpha(2)\beta(1)],\end{aligned}\quad (2.86)$$

where $\alpha(i)$ represents the spin function with $s_z = +\frac{1}{2}\hbar$ for the electron i and β the corresponding function with $s_z = -\frac{1}{2}\hbar$. If we substitute Eq. (2.85), we obtain for the spatial part of $\phi(1,2)$

$$\begin{aligned}\phi &= \phi_1(1)\phi_1(2) = \frac{1}{2+2S} [\phi_A(1)\phi_A(2) + \phi_B(1)\phi_B(2) + \phi_A(1)\phi_B(2) \\ &\quad + \phi_A(2)\phi_B(1)].\end{aligned}\quad (2.87)$$

The Hamiltonian of the H_2 molecule (Fig. 2.31),

$$H = -\frac{\hbar^2}{2m} (\nabla_1^2 + \nabla_2^2) + \frac{e^2}{4\pi\epsilon_0} \left(-\frac{1}{r_{A_1}} - \frac{1}{r_{B_1}} - \frac{1}{r_{A_2}} - \frac{1}{r_{B_2}} + \frac{1}{r_{12}} + \frac{1}{R} \right) \quad (2.88)$$

can be separated in a sum of three terms using $H_i = \frac{\hbar^2}{2m} \nabla_i^2 - \frac{e^2}{4\pi\epsilon_0} \left(\frac{1}{r_{A_i}} + \frac{1}{r_{B_i}} - \frac{1}{R} \right)$,

$$H = H_1 + H_2 + \frac{e^2}{4\pi\epsilon_0} \left(\frac{1}{r_{12}} - \frac{1}{R} \right), \quad (2.89)$$

where H_1 and H_2 are the Hamiltonians of the first and second electron, respectively, in the field of both nuclei. These terms thus correspond to the H_2^+ problem discussed in Sect. 2.6. The third term describes the mutual repulsion of the electrons. The internuclear repulsion must be subtracted, because it was taken into account both in H_1 and H_2 , that is, it has been counted twice.

The expectation value of the total energy is then

$$\langle E \rangle = \langle \phi | H | \phi \rangle = \langle \phi | H_1 | \phi \rangle + \langle \phi | H_2 | \phi \rangle + \frac{e^2}{4\pi\epsilon_0} \left\langle \phi \left| \frac{1}{r_{12}} - \frac{1}{R} \right| \phi \right\rangle. \quad (2.90)$$

We substitute Eq. (2.87) for ϕ and obtain, in addition to the integrals which we already know from our discussion of H_2^+ , a term

$$\left\langle \frac{1}{r_{12}} \right\rangle = \int \phi^* \frac{1}{r_{12}} \phi \, d\tau_1 \, d\tau_2 \quad (2.91)$$

describing the average repulsion between the electrons.

All two-center integrals in Eq. (2.90) can be solved and written as a function of the internuclear distance R (see, e.g., [2.19]). This yields

$$E(R)_{H_2} = 2E(R)_{H_2^+} + \frac{e^2}{4\pi\epsilon_0 a_0} \left[\frac{5}{16} - \frac{a_0}{2R} - \frac{a_0}{2R} \left(1 + \frac{11R}{8a_0} + \frac{3R^2}{4a_0^2} + \frac{1R^3}{6a_0^3} \right)^{2R/a_0} \right]. \quad (2.92)$$

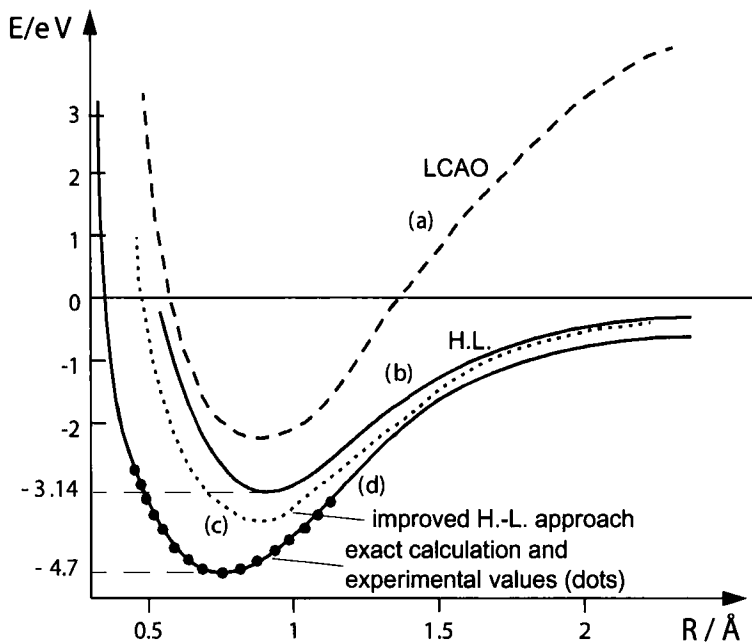


Fig. 2.32 Comparison of different approximation levels for the computed potential curves of the H_2 molecule. a) LCAO, b) LCAO with variable parameter λ , c) Heitler–London, d) experimental potential. Here, the energy of the separated atoms is taken as the zero point; the bond energies are therefore negative.

As we can see from Fig. 2.32, this simple LCAO approximation for H_2 yields about twice the bond energy of H_2^+ . This result is a consequence of the fact that in the vicinity of the minimum of $E(R)$ at $R = R_e \approx 1.5a_0$, the whole bracketed term in Eq. (2.92) is very small.

As in the case of the H_2^+ ion, the calculated values for the bond energy $D_e = E(R_e) - 2E(\text{H}_{1s})$ and equilibrium distance R_e of H_2 obtained with the simple LCAO approximation do not agree very well with the real values. There are several reasons for this, as will be discussed in the following.

The wavefunction Eq. (2.87) contains the *ionic* contributions $\phi_A(1)\phi_A(2)$ and $\phi_B(1)\phi_B(2)$, which describe a situation in which both electrons are at the same nucleus A or B, with the same weight as the covalent contribution $\phi_A(1)\phi_B(2)$. The probability of finding both electrons at the same nucleus is obviously much smaller in the real H_2 molecule. This deficiency of the approximation is connected with the neglect of electron correlation in the choice of the one-electron wavefunction Eq. (2.87). In fact, we have included the interaction between the electrons only in the Hamiltonian, but not in the wavefunction. This overestimation of the ionic character (H^-H^+) leads to a wrong asymptotic behavior of the potential curve $E(R)$ for $R \rightarrow \infty$ (see Fig. 2.32). Another factor stems from the fact that the bond energy E_b is the small

difference of several large energy contributions. From Eq. (2.90), we have

$$\begin{aligned}
 E_b &= E(R_e) - E(R = \infty) = E(R_e) - 2E_{H(1s)} \\
 &= 2E(H_2^+) - E(\text{nuclear repulsion}) + E(\text{electronic repulsion}) \\
 &\quad - 2E(\text{atomic hydrogen}) \\
 &= 2 \times 16.2 \text{ eV} - 19.3 \text{ eV} + 17.8 \text{ eV} - 2 \times 13.6 \text{ eV} \\
 &= 3.6 \text{ eV}
 \end{aligned} \tag{2.93}$$

The problem is that relatively minor discrepancies between the calculated values of the terms in Eq. (2.93) and their real values can lead to large relative errors in E_b . Before discussing improvements to our wavefunction Eq. (2.85), as we did in the case of H_2^+ , we will now look at a different approach to the H_2 problem, the *valence bond approximation* of Heitler and London [2.25].

2.7.3

The Heitler–London Approximation

The Heitler–London approximation for the H_2 molecule starts from two infinitely separated hydrogen atoms described by their atomic wavefunctions, Eq. (2.67). The Hamiltonian Eq. (2.88) is now separated differently from before in Eq. (2.89),

$$\begin{aligned}
 H &= \left(-\frac{\hbar^2}{2m} \nabla_1^2 - \frac{e^2}{4\pi\epsilon_0 r_{A1}} \right) + \left(-\frac{\hbar^2}{2m} \nabla_2^2 - \frac{e^2}{4\pi\epsilon_0 r_{A2}} \right) \\
 &\quad + \frac{e^2}{4\pi\epsilon_0} \left[-\left(\frac{1}{r_{A2}} + \frac{1}{r_{B1}} \right) + \frac{1}{r_{12}} + \frac{1}{R} \right] \\
 &= H_A + H_B - H_{AB} = 2H_A - H_{AB} .
 \end{aligned} \tag{2.94}$$

The first two brackets represent the energies of the separated hydrogen atoms and the last one the bonding energy of the molecule. A bonding state exists only if the last bracket yields a contribution $\Delta E < 0$; for $\Delta E > 0$ a repulsive potential curve $E(R)$ results. If the interaction between the hydrogen atoms is small compared with the binding energies of the electrons to their respective nuclei (i.e., $H_{AB} \ll H_A + H_B$), the wavefunction ϕ can be approximated as a product

$$\phi_1 = \phi_A(1)\phi_B(2) . \tag{2.95a}$$

This is exact only for $R \rightarrow \infty$, because in this case the interaction vanishes.

As the two electrons 1 and 2 are indistinguishable, the state Eq. (2.95a) cannot be distinguished from the state

$$\phi_2 = \phi_A(2)\phi_B(1) , \tag{2.95b}$$

in which both electrons have been exchanged. Taking this into account, it seems straightforward to describe the state by a linear combination

$$\phi = c_1\phi_1 + c_2\phi_2 . \tag{2.95c}$$

As shown in Sect. 2.6.1, optimization of the coefficients c_1 and c_2 with respect to the energy yields the condition $|c_1^2| = |c_2|^2$ and the optimized normalized wavefunctions

$$\phi_+ = \frac{1}{\sqrt{2(1+S^2)}} [\phi_A(1)\phi_B(2) + \phi_A(2)\phi_B(1)] , \quad (2.96a)$$

$$\phi_- = \frac{1}{\sqrt{2(1+S^2)}} [\phi_A(1)\phi_B(2) - \phi_A(2)\phi_B(1)] . \quad (2.96b)$$

If we substitute these functions together with the Hamiltonian Eq. (2.94) into the Schrödinger equation (2.15a), we obtain the two potential curves

$$E^+(R) = \frac{H_{11} + H_{12}}{1 + S^2} ; \quad E^-(R) = \frac{H_{11} - H_{12}}{1 - S^2} , \quad (2.97)$$

where we have used the following abbreviations for the two-center integrals:

$$H_{11} = \int a(1)b(2)H a(1)b(2) d\tau_1 d\tau_2 \quad \text{with} \quad a(1) = \phi_A(1) \text{ etc.} , \quad (2.98a)$$

$$H_{12} = \int a(1)b(2)H a(2)b(1) d\tau_1 d\tau_2 , \quad (2.98b)$$

$$\begin{aligned} S^2 &= \int a(1)b(1)a(2)b(2) d\tau_1 d\tau_2 \\ &= \int a(1)b(1) d\tau_1 \times \int a(2)b(2) d\tau_2 . \end{aligned} \quad (2.98c)$$

Computation of the integrals yields a bond energy $E_b(\text{H}_2) = -3.14\text{eV}$ for the H_2 molecule, much closer to the experimental value of 4.7eV than by using simple MO theory, but still not satisfying.

The reason is that Heitler–London theory with the wavefunctions Eq. (2.96) neglects the ionic contribution to bonding completely, while the MO wavefunction, Eq. (2.87), overestimates it.

2.7.4

Improvements of Both Methods

We can correct for the overestimation of the ionic contribution $a(1)b(1) + a(2)b(2)$ in the wavefunction Eq. (2.87), if we introduce a new parameter $\lambda_i(R)$ and write the wavefunction as

$$\phi = \frac{1}{\sqrt{2+2S^2}} \{ \lambda_1 [a(1)a(2) + b(1)b(2)] + a(1)b(2) + a(2)b(1) \} . \quad (2.99)$$

We can now optimize $\lambda_1(R)$ using a variational calculation to obtain the curve displayed in Fig. 2.32(c). The calculated bond energy is then $E_b = -4.02\text{eV}$, in much better agreement with experiment than before.

A further improvement can be achieved, as in the case of the H_2^+ molecular ion, by allowing for shrinkage and polarization of the atomic orbitals with decreasing distance

between the two hydrogen atoms. Thus we choose an improved ansatz for the atomic orbital of Eq. (2.67),

$$\phi_A = N_A(1 + \lambda_2 z)e^{-\lambda_3 r_A/a_0}, \quad (2.100)$$

which yields, for optimized parameters λ_2 and λ_3 , almost the experimental values for the potential curve in Fig. 2.32.

2.7.5

Equivalence of Heitler–London and MO Approximation

The ansatz Eq. (2.99) renders the Heitler–London approximation and the MO method equivalent, as can easily be shown.

The extended Heitler–London approximation

$$\phi^{\text{HL}} = [a(1)b(2) + b(1)a(2)] + \lambda_1 [a(1)a(2) + b(1)b(2)], \quad (2.101a)$$

which improves the weight of the ionic contributions to the wavefunction by using an optimized weight factor λ_1 , equals the improved MO approximation

$$\phi^{\text{MO}} = [a(1) + b(1)] \times [a(2) + b(2)] + k[a(1) - b(1)] \times [a(2) - b(2)], \quad (2.101b)$$

which employs a linear combination of the symmetric product ansatz Eq. (2.85) and the antisymmetric function $(\phi_A - \phi_B)$, provided that

$$\lambda_1 = \frac{1+k}{1-k}.$$

Taking normalization into account, Eqns. (2.101a) and (2.101b) give

$$\phi = \frac{(a+b)(a+b)}{2(1+S)} - \kappa \frac{(a-b)(a-b)}{2(1-S)} \quad (2.101c)$$

with $\kappa = \frac{1-S}{1+S}k$.

From the improved equivalent expressions Eqns. (2.101a) and (2.101b) for the wavefunction ϕ , we see that the simple MO approximation underestimates electron correlation (because it neglects electron exchange) while the Heitler–London approximation overestimates correlation (because it neglects the ionic contribution completely).

2.7.6

Generalized MO Ansatz

The generalized expression for a molecular orbital $\phi(1,2)$ from Eq. (2.86) for the H_2 molecule employs a linear combination

$$\phi(1,2) = \sum_{i=1}^k c_i \phi_i(1) \phi_i(2). \quad (2.102)$$

Tab. 2.12 Results of different approximate calculations for the H₂ molecule.

Approximation used	E_b /eV	R_e /Å
simple molecular orbitals	-2.70	0.85
Heitler–London	-3.14	0.87
H–L + ionic contribution, Eq. (2.101a)	-4.02	0.75
H–L + ionic contribution + polarization, Eq. (2.99)	-4.12	0.75
MO + correlation, Eq. (2.101b)	-4.11	0.71
Coolidge–James	-4.72	0.74
Kolos–Roothan	-4.746	0.741
experimental	-4.747	0.741

The sum runs over all functions ϕ_i that have the appropriate symmetry and describe the deformed (contracted and polarized) orbital upon the approach of the two hydrogen atoms as well as possible. The number k of sum terms can be very large (e.g., $k = 30$ – 50). The coefficients c_i are again determined using the variational principle,

$$\frac{\partial}{\partial c_i} \left(\int \phi^* H \phi \, d\tau \right) = 0. \quad (2.103)$$

This yields a system of equations such as Eq. (2.55), the solution of which gives the energies $E_i(R)$ and thus the potential curves of the desired molecular states.

Calculations of James and Coolidge using 13 functions [2.26] gave $E_b(\text{H}_2) = -4.69$ eV, already quite close to the experimental value (Fig. 2.32). The best calculation yet, of Kolos und Roothaan [2.27, 2.28], used 50 functions ϕ_i in the expansion Eq. (2.102) and yielded $E_b = -4.7467$ eV. Table 2.12 summarizes the results of different approximate calculations for H₂.

2.8

Modern *Ab Initio* Methods

To be able to perform *ab initio* calculations for large molecules in acceptable time, we must accept further approximations [2.29, 2.30] either in the wavefunctions or in the Hamiltonian. The wavefunctions are expanded as linear combinations of suitably chosen basis functions as shown in Sect. 2.7.6. Basis functions can be selected on the basis of physical considerations (e.g., the eigenfunctions of the atomic states involved in bonding could be used, allowing for polarization effects), or of computational efficiency (which favors the use of Gaussian functions because they allow an easy computation of overlap and exchange integrals).

In the Hamiltonian, the electron–electron interaction terms provide the most difficult part, because they act between all pairs of electrons in the molecule so that a change in one electron coordinate affects all other electrons. In all single-particle approximations, these interactions (correlations) are either neglected completely or included in an averaged manner (e.g., in the Hartree–Fock method).

2.8.1

The Hartree–Fock Approximation

In the preceding section we saw that neglecting the electron–electron interaction in the choice of one-electron wavefunctions (orbitals) leads to relatively large errors in the energies $E(\mathbf{R})$. On the other hand, using $3N$ -dimensional n -electron functions for a molecule with N electrons would lead to enormous computational problems. Hence, we need to find a compromise that allows us to continue using one-electron functions but includes electron interactions at least in an *averaged* manner.

This can be achieved by optimizing one-electron functions $\phi_i(i)$ as solutions of the Schrödinger equation

$$H\phi_i = E\phi_i \quad \text{with} \quad H = -\frac{\hbar^2}{2m}\nabla_i^2 + V_{\text{eff}}(\mathbf{r}_i), \quad (2.104)$$

where the effective potential for an electron i ($1 \leq i \leq N$) contains the Coulomb potential of the nuclei plus the potential from the time-averaged charge distribution of the $(N - 1)$ other electrons.

The difficulty is that we need the wavefunctions of these $(N - 1)$ electrons to compute their charge distributions and the potential derived from it. Fortunately, the problem can be solved iteratively: we start from a first guess of one-electron functions $\phi_i^0(i)$ ($i = 1 \dots N$) built, for example, from linear combinations of atomic orbitals. Using these $\phi_i^0(i)$, we compute the charge distribution of the $N - 1$ electrons and the effective potential in which the N th electron moves. We obtain a further improved one-electron function $\phi_N^{(1)}(N)$ for this N th electron, and the process is repeated for all N electrons.

The $\phi_i^{(1)}(i)$ thus obtained are then again used to calculate the charge distribution of $N - 1$ electrons and to obtain an improved $\phi_N^{(2)}(N)$ for the N th electron. This procedure is repeated until, after k iterations, the $\phi_N^{(k)}(N)$ do not differ from the $\phi_N^{(k-1)}(N)$ of the previous iteration by more than certain predefined limits. The optimized one-electron functions are then called *self-consistent field (SCF) functions*, because the functions are consistent with the electric field they produce. Figure 2.33 visualizes the SCF procedure in a flow diagram.

If the total wavefunction is written as a nonsymmetrized (with respect to electron exchange) product

$$\phi(1 \dots N) = \prod_{i=1}^N \phi_i(i) \quad (2.105)$$

of these optimized one-electron functions (molecular orbitals), the resulting procedure is called the *Hartree method* [2.31].

Until now we have ignored electron spin. Fock suggested the use of products of spatial and spin functions as optimized one-electron functions, the so-called *spin orbitals*, and to write the total wavefunction $\Phi(1 \dots N)$ as a Slater determinant, Eq. (2.81),

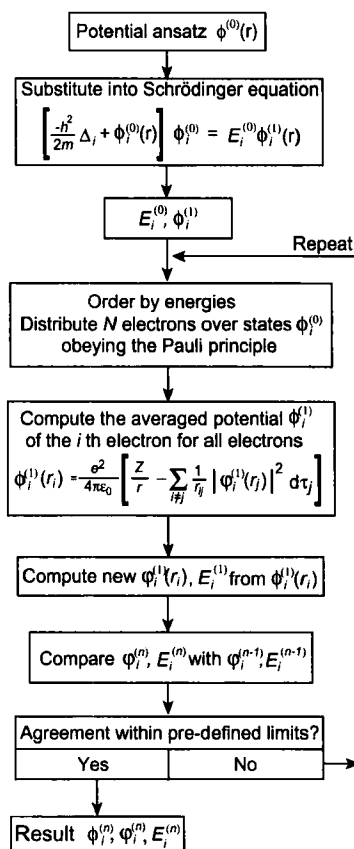


Fig. 2.33 Flow diagram for the computational procedure in the Hartree approximation.

built from these spin orbitals. As discussed in Sect. 2.7.1, such a wavefunction satisfies the Pauli principle automatically. These antisymmetric (with respect to electron exchange) total wavefunctions $\Phi(1 \dots N)$ are called *SCF-HF functions* (short for self-consistent field Hartree–Fock) [2.32].

These improvements increase the computational effort – which is already large for the Hartree method – significantly, but the improved results make the additional effort worthwhile. Nowadays, for the computation of electronic molecular states and their properties, HF functions are used almost exclusively.

Even in this most sophisticated of all one-electron models the *instantaneous* interaction e^2/r_{ij} of the electrons is not properly included. The error in the total energy induced by this effect (deviation of the calculated HF energy from the “true” total energy) is called *correlation energy* [2.33–2.35].

Typically, the correlation energy amounts to about 1% of the calculated HF total energy. As the total energy is the total binding energy of all electrons (the sum of all

ionization energies), 1% of this large energy can be larger than the dissociation energy of the molecule. Thus, in unfavorable cases HF calculations can yield a completely wrong picture of the bonding in a molecule (e.g., bond dissociation energies are notoriously overestimated by HF calculations due to the completely different electronic situation in open-shell fragments as compared to the – closed-shell – intact molecule).

2.8.2

Configuration Interaction

The most important and most frequently used method to account for electron correlation is the *configuration interaction* (CI) method. In combination with the Hartree–Fock method it is the most accurate approximation for the calculation of molecular wavefunctions and states. In the CI method, the wavefunction of a state is represented by a linear combination

$$\Psi = \sum c_k \Phi_k \quad (2.106)$$

of Slater determinants. The different Slater determinants are called *configurations*, because they describe the electron occupation of the molecular orbitals. The sum Eq. (2.106) contains only determinants with the same symmetry and the same spin, because only for such functions

$$H_{ki} = \langle \Phi_k | H | \Phi_i \rangle \neq 0 .$$

The Slater determinants ϕ_k in the sum Eq. (2.106) are usually obtained by the Hartree–Fock method, but include orbitals which are unoccupied in the HF ground-state wavefunction (so-called virtual orbitals). A suitable choice of the basis, guided by physical intuition, results in a better convergence of the computed energies towards the “true” energies.

Finally, we summarize the structure of the complete procedure used to obtain SCF-CI wavefunctions:

1. One-electron atomic orbitals or other, computationally more efficient functions such as Gaussian or Slater functions, which approximate the atomic electron distributions, are chosen as basis functions (see next section).
2. Molecular one-electron functions, the molecular orbitals, are built from linear combinations of these basis functions.
3. Each molecular orbital is written as a product of spatial and spin function. It can therefore accommodate a maximum of two electrons with opposite spins.
4. The molecular orbitals of all electrons are then combined into Slater determinants, which are antisymmetrized linear combinations of products of molecular

orbitals with permuted electrons. Each Slater determinant describes a molecular configuration. The free parameters in a Slater determinant are the LCAO coefficients. They are optimized iteratively in the Hartree–Fock procedure.

5. The total many-electron wavefunction is written as a linear combination of Slater determinants, and the selection of contributing configurations is based on symmetry arguments and physical considerations. The coefficients c_k are determined according to the variational principle by minimizing the energy.

2.8.3

Ab Initio Calculations and Quantum Chemistry

The HF-CI method is the basis for the most accurate calculations which can be performed today on fast computers for small- to medium-sized molecules.

Such calculations are performed with the exact nonrelativistic Hamiltonian, Eq. (2.2), without further approximations, that is, ‘from the beginning’. All such calculations, which are not based on assumed models but use numerical solutions of the Schrödinger equation, are generally called *ab initio* calculations (*ab initio* is Latin for “from the beginning”). There is also an increasing number of software packages which solve the Dirac equation numerically using Hartree–Fock Slater determinants, that is, which use the relativistic Hamiltonian and which are therefore called relativistic *ab initio* calculations.

We have seen in the preceding sections that a suitable choice of the basis functions is crucial for the quality of the results obtained. For larger molecules, where the atomic ground states involve higher principal quantum numbers n , the atomic orbitals get quite complicated and the numerical computation of the overlap and exchange integrals is tedious. As a compromise between quality and computational effort, a number of types of basis functions have established themselves as a kind of standard:

1. Slater functions

$$\Psi = N r^n e^{-\alpha r} Y_l^m(\theta, \varphi), \quad (2.107)$$

where the Y_l^m are the Legendre polynomials.

2. Pure Gaussian functions

$$\Psi = N e^{-\beta(r-r_0)^2}, \quad (2.108)$$

3. Cartesian Gaussian functions

$$\Psi = N x^l y^n z^m e^{-\beta(r-r_0)^2}. \quad (2.109)$$

The linear combinations of these basis functions form the molecular orbitals.

Gaussian functions offer a huge computational advantage, because the necessary integrals are much easier to calculate than for Slater functions.

Instead of keeping the origin of these functions fixed at the respective nuclei as described for the LCAO method in Sect. 2.5.2, it is often advantageous to use the origin as an additional variable parameter. Such *floating* atomic orbitals can in many cases provide a quicker convergence of the calculations.

Further details can be found in the quantum-chemical literature [2.24, 2.29, 2.30, 2.36].

3 Rotation, Vibration, and Potential Curves of Diatomic Molecules

After having discussed, in the previous chapter, general approximation methods for the calculation of electronic wavefunctions, we will now turn to a more detailed treatment of *nonrigid* diatomic molecules. We start with rotation and vibration, and will later present semiempirical methods for the numerical high-precision determination of potential energy curves from measured rotation–vibration term values. The results of these procedures will then be compared to theoretical treatments and their results. The interatomic potential for large internuclear separations and the determination of the dissociation energy, which is of great importance in chemistry, will be discussed.

3.1 Quantum-mechanical Treatment

Within the BO approximation we had obtained, in Ch. 2, Eq. (2.15b),

$$(\hat{H}' + E_n^0) \chi_{nm} = E_{nm} \chi_{nm} \quad (3.1)$$

for the movement of the nuclei in the potential $E_n^0(\mathbf{R})$ of the electronic state $|n\rangle$. For diatomic molecules, Eq. (3.1) reduces to

$$\left[\frac{-\hbar^2}{2M_1} \nabla_1^2 - \frac{\hbar^2}{2M_2} \nabla_2^2 + E_n^{(0)}(R) \right] \chi_{nm}(\mathbf{R}) = E_{nm} \chi_{nm}(\mathbf{R}), \quad (3.2)$$

where $\mathbf{R} = (\mathbf{R}_a, \mathbf{R}_b)$ represents the nuclear coordinates and $R = |\mathbf{R}_a - \mathbf{R}_b|$ the internuclear distance. The wavefunction χ_{nm} of nuclear motion characterizes the m th vibration–rotation level of the electronic state $|n\rangle$.

If we make a coordinate transformation to the molecule's center-of-mass frame (separation of translation) and introduce the reduced nuclear mass,

$$\mu = \frac{M_1 M_2}{M_1 + M_2},$$

Eq. (3.2) reduces to

$$\left[\frac{-\hbar^2}{2\mu} \nabla^2 + E_n^{(0)}(R) \right] \chi_{nm}(\mathbf{R}) = E_n \chi(\mathbf{R}). \quad (3.3)$$

The potential energy $E_n^{(0)}(R)$ in the n th electronic state depends now only on the internuclear distance $R = |\mathbf{R}_1 - \mathbf{R}_2|$, and therefore is *spherical symmetric!* Equation (3.3) formally corresponds to the Schrödinger equation for the hydrogen atom and can, in spherical coordinates, be separated into a radial and an angular part [3.1]. In analogy to the treatment of the hydrogen atom we make the separation ansatz

$$\chi(R, \theta, \phi) = S(R) \times Y(\theta, \phi) \quad (3.4)$$

with the spherical harmonics $Y(\theta, \phi)$. The radial function $S(R)$ will of course be different from the Laguerre function of the hydrogen atom, because $E_n^{(0)}(R)$ is not a Coulomb potential. The Laplacian $\Delta = \nabla^2$ is in spherical coordinates

$$\Delta = \frac{1}{R^2} \frac{\partial}{\partial R} \left(R^2 \frac{\partial}{\partial R} \right) + \frac{1}{R^2 \sin \theta} \frac{\partial}{\partial \theta} \left(\sin \theta \frac{\partial}{\partial \theta} \right) + \frac{1}{R^2 \sin^2 \theta} \frac{\partial^2}{\partial \phi^2}. \quad (3.5)$$

If we substitute the ansatz Eq. (3.4) into Eq. (3.3) and use Eq. (3.5), we obtain, after multiplication with R^2/χ and rearranging terms,

$$\begin{aligned} \frac{1}{S} \frac{\partial}{\partial R} R^2 \frac{\partial S}{\partial R} + \frac{2\mu R^2}{\hbar^2} [E - E_n^{(0)}(R)] = \\ \frac{1}{Y} \left[\frac{1}{\sin \theta} \frac{\partial}{\partial \theta} \left(\sin \theta \frac{\partial Y}{\partial \theta} \right) + \frac{1}{\sin^2 \theta} \frac{\partial^2 Y}{\partial \phi^2} \right]. \end{aligned} \quad (3.6)$$

As the left-hand side of this equation does not depend on θ and ϕ , and the right-hand side does not depend on R , both sides must equal a constant C , and we obtain the two equations separated in R and θ, ϕ ,

$$\frac{1}{R^2} \frac{d}{dR} \left(R^2 \frac{dS}{dR} \right) + \frac{2\mu}{\hbar^2} \left[E - E_n^{(0)}(R) - \frac{C\hbar^2}{2\mu R^2} \right] S = 0, \quad (3.7)$$

$$\frac{1}{\sin \theta} \frac{\partial}{\partial \theta} \left(\sin \theta \frac{\partial Y}{\partial \theta} \right) + \frac{1}{\sin^2 \theta} \frac{\partial^2 Y}{\partial \phi^2} + CY = 0. \quad (3.8)$$

These two equations are the basis for the exact treatment of rotation and vibration of diatomic molecules! As soon as the potential curve $E_n^{(0)}(R)$ for the n th electronic state is known, the functions S are completely determined. The spherical harmonics Y are of course known, and they describe the angular distribution of the functions χ_{nm} .

The first equation describes the radial motion of the nuclei, i.e., the vibration of the molecule, while the second describes the azimuthal motion, i.e., its rotation. We will start discussing molecular rotation in the next section. The separation constant C turns out to be, in complete analogy to the separation treatment of the hydrogen atom [3.1],

$C = J(J + 1)$, where J is the quantum number of total angular momentum. The term $J(J + 1)\hbar^2 / (2\mu R^2)$ in Eq. (3.7) gives then the centrifugal energy.

3.2

Rotation of Diatomic Molecules

The simplest model of a rotating molecule is obtained if we assume that the internuclear distance R does not change during rotation. In this *rigid rotor* model, in which the nuclei are connected by a massless rod and rotate around their center of mass, the constant moment of inertia is $I = \mu R^2$. The angular momentum

$$\mathbf{J} = \sqrt{J(J + 1)}\hbar\hat{e}_\perp$$

is perpendicular to the internuclear axis (which we choose to be the z axis) as indicated by the unit vector \hat{e}_\perp .

In real molecules, the nuclei vibrate around their equilibrium distance R_e so that R varies periodically during molecular rotation. Furthermore, the equilibrium distance increases with increasing rotational excitation due to centrifugal forces. The electronic moment of inertia, depending on the density distribution in the electron cloud, also contributes to the rotational energy. If the electrons possess an orbital angular momentum \mathbf{L} with the projection $\Lambda \neq 0$, the total angular momentum does not remain perpendicular to the intermolecular axis.

We first discuss the rigid rotor and then centrifugal distortion, before we elucidate the influence of the electrons in Sect. 3.2.3. Finally, in Sect. 3.4 after discussing vibrations, we will turn to the interaction between vibrations and rotations.

3.2.1

The Rigid Rotor

For the rigid rotor, the internuclear distance is $R = R_e = \text{const}$. It follows that the function $S(R)$ in Eq. (3.7) is constant and its derivative is zero. Also, the value of the potential $E_{\text{pot}}(R_e)$ at the equilibrium distance R_e is constant and assumes a minimum. We choose the energy scale so that $E_{\text{pot}}(R_e) = 0$. With $C = J(J + 1)$, we obtain from Eq. (3.7) the energies of the rigid rotor,

$$E(J) = \frac{J(J + 1)\hbar^2}{2\mu R_e^2}. \quad (3.9)$$

We see that the rotational energy increases quadratically with the rotational quantum number J (Fig. 3.1). The difference between neighboring rotational levels,

$$\Delta E(J) = E(J + 1) - E(J) = \frac{(J + 1)\hbar^2}{\mu R_e^2}, \quad (3.10a)$$

increases linearly with J .

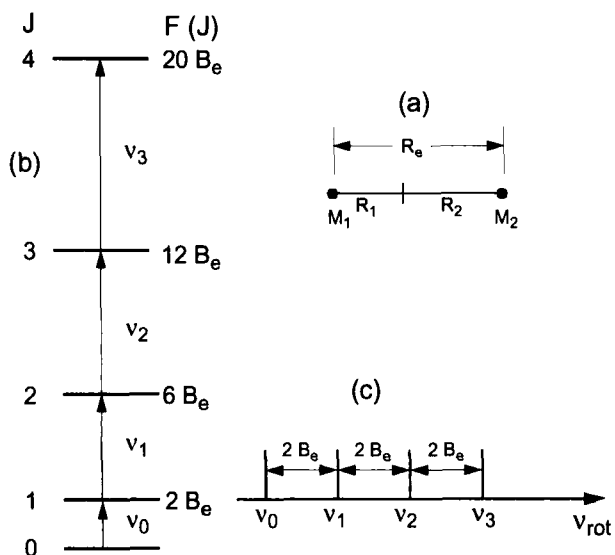


Fig. 3.1 Rigid rotor. a) Schematic representation; b) term diagram; c) rotational spectrum.

In spectroscopy, term values $F = E/(hc)$ are generally used rather than energies, and they are given in wavenumbers, cm^{-1} , because then also the term differences $\Delta F = \Delta E/(hc)$ measured during absorption or emission of radiation of energy $h\nu$ appear in reciprocal wavelengths, $h\nu/(hc) = 1/\lambda$.

The rotational term values $F(J)$ then become

$$F(J) = B_e J(J+1), \quad (3.11)$$

where the *rotational constant*

$$B_e = \frac{\hbar}{4\pi c \mu R_e^2} \quad (3.12)$$

(in units of cm^{-1}) is a measure for the inverse moment of inertia and thus also for the equilibrium distance R_e . The wavenumbers $\tilde{\nu}(J) = \Delta E(J)/hc$ of transitions between neighboring rotational levels are then

$$\tilde{\nu}_{\text{rot}} = F(J+1) - F(J) = 2B_e(J+1). \quad (3.10b)$$

A pure rotational spectrum of a diatomic molecule appears in the rigid-rotor approximation as a number of equidistant lines (Fig. 3.2).

3.2.2

Centrifugal Distortion

In a nonrotating molecule, the equilibrium distance R_e in the electronic state $|n\rangle$ assumes a value such that the potential $E_n^{(0)}(R_e)$ is a minimum and therefore the re-

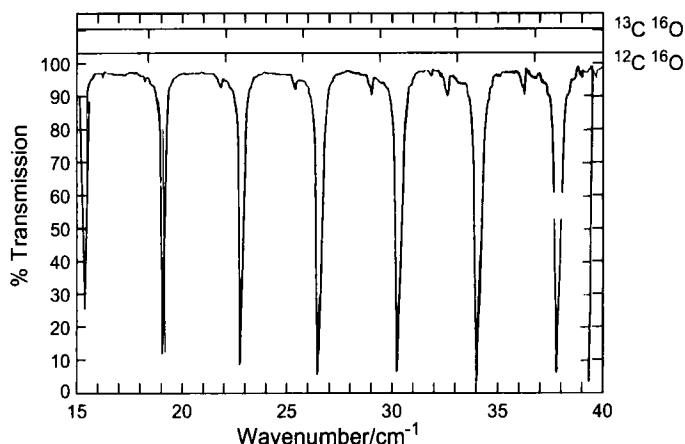


Fig. 3.2 Section from the far-infrared rotational spectrum of CO between 15 cm^{-1} and 40 cm^{-1} for $^{12}\text{C}^{16}\text{O}$ and $^{13}\text{C}^{16}\text{O}$ (weak lines), measured as an absorption spectrum [3.2].

sulting force on the nuclei vanishes. In a rotating molecule with angular momentum $\mathbf{J} = \sqrt{J(J+1)}\hbar$ an additional centrifugal force

$$F_c = \mu\omega_{\text{rot}}^2 R = \frac{|\mathbf{J}|^2}{\mu R^3} \quad \text{because} \quad |\mathbf{J}| = \mu R^2 \omega \quad (3.13a)$$

appears which leads, in the nonrigid rotor, to an increase in the internuclear distance from R_e to R . This creates an electrostatic restoring force

$$F_r = -\frac{\partial}{\partial R} \left(E_n^{(0)}(R) \right), \quad (3.13b)$$

which for sufficiently small displacements ($R - R_e$) is proportional to the displacement, because the potential $E_n^{(0)}(R)$ can be described, in the vicinity of the minimum, to good approximation by a parabolic potential (see Sect. 3.3). We can therefore write

$$F_r = k(R - R_e). \quad (3.13c)$$

At equilibrium, both forces must be equal and opposite. For $|R - R_e| \ll R_e$, this results in

$$(R - R_e) = \frac{|\mathbf{J}|^2}{\mu R^3 k} \cong \frac{|\mathbf{J}|^2}{\mu R_e^3 k}. \quad (3.14)$$

In addition to the kinetic energy of rotation $|\mathbf{J}|^2 / (2\mu R^2)$ of the rigid rotor, the centrifugal distortion now creates an additional potential energy $E_n^0(R) \cong \frac{1}{2}k(R - R_e)^2$, so that the total energy becomes

$$E_{\text{rot}} = \frac{|\mathbf{J}|^2}{2\mu R^2} + \frac{1}{2}k(R - R_e)^2. \quad (3.15)$$

The second term in Eq. (3.15) can be rearranged with the aid of Eq. (3.14) to yield

$$E_n^{(0)}(R) = \frac{1}{2} \frac{|J|^4}{\mu^2 R_e^6 k} \quad (3.16)$$

If we express R in terms of R_e using Eq. (3.14), we obtain

$$R = R_e \left(1 + \frac{J^2}{\mu k R_e^4} \right) = R_e (1 + x) \quad \text{with } x \ll 1,$$

and from this the Taylor expansion

$$\frac{1}{R^2} = \frac{1}{R_e^2} \left[1 - \frac{2|J|^2}{\mu k R_e^4} + \left(\frac{3|J|^2}{\mu k R_e^4} \right)^2 - \dots + \right]. \quad (3.17)$$

The rotational energy Eq. (3.15) is then

$$E_{\text{rot}} = \frac{|J|^2}{2\mu R_e^2} - \frac{|J|^4}{2k\mu^2 R_e^6} + \frac{3|J|^6}{2\mu^3 k^2 R_e^{10}} + \dots \quad (3.18a)$$

The term values $F_{\text{rot}} = E_{\text{rot}}/hc$ are then, using $|J|^2 = J(J+1)\hbar^2$,

$$F_{\text{rot}} = B_e J(J+1) - D_e J^2(J+1)^2 + H_e J^3(J+1)^3 + \dots, \quad (3.18b)$$

where the centrifugal constants are defined as

$$D_e = \frac{\hbar^3}{4\pi k c \mu^2 R_e^6}, \quad (3.19a)$$

$$H_e = \frac{3\hbar^5}{4\pi k^2 c \mu^3 R_e^{10}}. \quad (3.19b)$$

Today we can achieve such a high precision in our measurements that we need to include the third term in Eq. (3.18b) for larger values of J . Figure 3.3 displays the shifts, Eq. (3.18), of the energy levels from those of the rigid rotor, and Table 3.1 lists some values for the constants B_e , D_e and H_e for a selection of molecules.

3.2.3

The Influence of Electron Rotation

In the axially symmetric electrostatic field of the nuclei, the angular momentum L of the electron shell is not constant as in the spherically symmetric Coulomb field of a nucleus, but it precesses around the internuclear axis (z axis). The projection of L onto the axis (Fig. 2.9) is designated with lower-case λ for one-electron systems, and with upper-case Λ for many-electron systems, and is a characteristic constant for each electronic state (see Sect. 2.4).

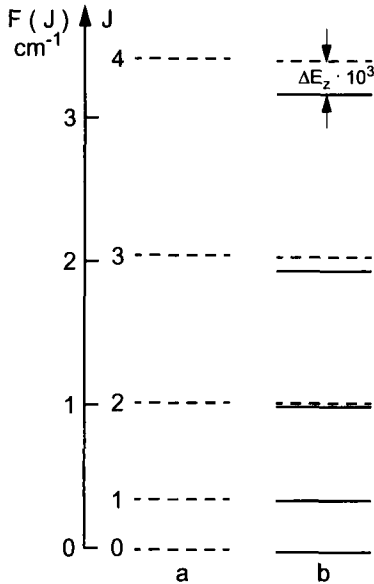


Fig. 3.3 Deviations ΔE of rotational term values of a nonrigid molecule (b) from those of a rigid rotor (a).

The total angular momentum J is a combination of Λ and the angular momentum N of the rotating nuclear frame, and for $\Lambda \neq 0$ it is not perpendicular to the internuclear axis (Fig. 3.4). As the total angular momentum for the free molecule must be constant, the molecule rotates around the direction of J , i.e., for $\Lambda \neq 0$ not around an axis perpendicular to the z axis! If the electron cloud is viewed as a rigid entity rotating around the z axis, the rotating molecule can be described as a symmetric top rotor with two different moments of inertia: the moment of inertia I_A of the electron cloud around the z axis, and the moment of inertia I_B of the nuclei around an axis perpendicular to the z axis. Because of the small electron mass, $I_A \ll I_B$.

Tab. 3.1 Molecular constants for the ground states of some diatomic molecules, in cm^{-1} .

Molecule	B_e	α_e	ω_e	$\omega_e x_e$	D_e	H_e
H ₂	60.85	3.06	4401	121.3	1.6×10^{-2}	–
D ₂	30.44	1.08	3116	61.8	1.1×10^{-2}	6.7×10^{-6}
H ³⁵ Cl	10.59	0.31	2990	52.8	5.3×10^{-4}	1.7×10^{-8}
D ³⁵ Cl	5.45	0.11	2145	27.2	1.4×10^{-4}	1.5×10^{-9}
H ³⁷ Cl	10.57	0.309	2988	52.7	5.3×10^{-4}	1.6×10^{-8}
Li ₂	0.67	0.007	351.4	2.6	9.9×10^{-6}	1.5×10^{-10}
Cs ₂	0.013	2.6×10^{-5}	42.0	0.08	4.6×10^{-9}	2×10^{-14}
CO	1.931	0.017	2170	13.29	6.1×10^{-6}	1.8×10^{-9}

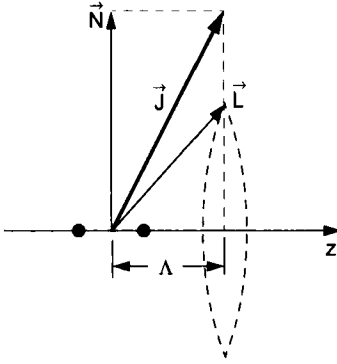


Fig. 3.4 Addition of rotational angular momentum N and the projection of the electronic angular momentum L to yield the total angular momentum J .

The rotational energy of this symmetric top is

$$E_{\text{rot}} = \frac{J_x^2}{2I_x} + \frac{J_y^2}{2I_y} + \frac{J_z^2}{2I_z}.$$

From Fig. 3.4 we see that $J_z^2 = \Lambda^2 \hbar^2$ and $J_x^2 + J_y^2 = N^2 \hbar^2 = (J(J+1) - \Lambda^2) \hbar^2$.

Thus, with the rotational constant $A = \hbar / (4\pi c I_A)$, we obtain for the term values,

$$F(J, \Lambda) = B_e J(J+1) + (A - B_e) \Lambda^2 - D_e J^2 (J+1)^2 + \dots, \quad (3.20)$$

where $A \gg B$ because $I_A \ll I_B$. The term $A \Lambda^2$ is usually added to the electronic energy T_{el} because it is constant for a given electronic state, i.e., independent of J . Thus we obtain for the rotational term value

$$F(J, \Lambda) = B_e [J(J+1) - \Lambda^2] - D_e J^2 (J+1)^2 + H_e J^3 (J+1)^3. \quad (3.21)$$

3.3

Molecular Vibrations

To solve Eq. (3.7) for the vibration of a diatomic molecule, we consider first the case of a nonrotating molecule for which $C = J(J+1) = 0$. Substituting

$$U(R) = R \times S(R),$$

Eq. (3.7) becomes

$$\frac{d^2 U}{dR^2} + \frac{2\mu}{\hbar^2} [E - E_n^{(0)}(R)] U = 0. \quad (3.22)$$

The subsequent procedure depends on the choice of the potential $E_n^{(0)}(R)$ in the electronic state $|n\rangle$.

3.3.1

The Harmonic Oscillator

Close to the equilibrium distance R_e , i.e., for small displacements $r = R - R_e$, the potential can to good approximation be described by a parabolic potential

$$E_{\text{pot}}(R) = \frac{1}{2}k_r(R - R_e)^2 = \frac{1}{2}k_r r^2, \quad (3.23)$$

where the constant k_r describes the magnitude of the restoring force $F = -k_r r$. We choose the origin of our reference frame so that $R_e = 0$ and $R = r$. For a harmonic oscillator with frequency ω_0 and reduced mass μ , we have $k_r = \mu\omega_0^2$. With the abbreviations

$$\alpha = \frac{2\mu E}{\hbar^2} \quad \text{and} \quad \beta = \frac{\sqrt{\mu k_r}}{\hbar} \quad \Rightarrow \quad \frac{\alpha}{\beta} = \frac{2E}{\hbar\omega_0},$$

and with the variable transformation $\xi = r\sqrt{\beta}$, Eq. (3.22) becomes

$$\frac{d^2 U}{d\xi^2} + \left(\frac{\alpha}{\beta} - \xi^2 \right) U = 0. \quad (3.24)$$

In the limiting case $\xi^2 \gg \alpha/\beta$, i.e., $r \rightarrow \infty$, we can neglect α/β . In this case we can write the asymptotic solutions immediately as

$$U = C e^{\pm \xi^2/2},$$

as can easily be verified.

As the wavefunction $U(\xi)$ must remain finite for $\xi \rightarrow \infty$, i.e., for $r \rightarrow \infty$, the solution with positive exponent is physically not plausible.

For the general solution of Eq. (3.24) we apply now the ansatz

$$\psi_{\text{vib}} = C \times H(\xi) e^{-\xi^2/2}. \quad (3.25)$$

If we substitute Eq. (3.25) into Eq. (3.24), we obtain for the function $H(\xi)$ the differential equation

$$\frac{d^2 H}{d\xi^2} - 2 \frac{dH}{d\xi} + \left(\frac{\alpha}{\beta} - 1 \right) H = 0. \quad (3.26)$$

If we use for the solution a power series in ξ ,

$$H(\xi) = \sum_k a_k \xi^k, \quad (3.27)$$

we obtain, by substitution of Eq. (3.27) into Eq. (3.26), a recursion formula for the coefficients a_k ,

$$(k+2)(k+1)a_{k+2} = (2k+1 - \alpha/\beta)a_k. \quad (3.28)$$

The function ψ_{vib} can only be finite if the series Eq. (3.27) consists of a finite number of terms; otherwise it would diverge for $\xi > 1$. This means that the series has to terminate after the term ξ^v , all terms in Eq. (3.27) with $k > v$ need to be zero. This requires that in Eq. (3.28), $(2v + 1) - \alpha/\beta = 0$, because then $a_{v+2} = 0$. With the definitions for α and β we obtain for the possible energies

$$E_v = \hbar\omega_0 \left(v + \frac{1}{2} \right) \quad \text{with} \quad \omega_0 = \sqrt{k_r/\mu}. \quad (3.29)$$

The energy eigenvalues E_v of the harmonic oscillator are equidistant. The lowest vibrational state with vibrational quantum number $v = 0$ possesses a zero-point energy $E_0 = \hbar\omega_0/2$.

In spectroscopy, term values $G(v) = E_v/(hc)$ are employed rather than the energy eigenvalues of Eq. (3.29). They are written as

$$G(v) = \omega_e \left(v + \frac{1}{2} \right) \quad (3.29a)$$

with the vibrational constant $\omega_e = \omega_0/(2\pi c)$, measured in cm^{-1} .

Note that the quantization of the energy is a result of the requirement that the function $H(\xi)$ be *finite* in the whole range ξ , i.e., that it must be possible to represent it by a power series with a finite number of terms.

The choice $(\alpha/\beta - 1) = 2v$ makes Eq. (3.26) a Hermite differential equation, the solutions of which are the Hermite polynomials $H(\xi)$. A number of these functions are listed in Table 3.2. The normalization factor C in Eq. (3.25) is chosen so that $\int U^*U \, dr = 1$. The vibrational wavefunctions $\psi_{\text{vib}} = U(\xi) = H(\xi) \times \exp[-\xi^2/2]$ are displayed in Fig. 3.5 for a number of vibrational quantum numbers v .

For large v , $|\psi_{\text{vib}}|^2$ assumes large values in the vicinity of the classical turning points, where the classical oscillator also has the largest probability of being found. This situation is nicely described by the *correspondence principle*, which states that for large quantum numbers v , the quantum-mechanical description converges towards the classical description. Figure 3.6 compares the quantum-mechanical probability distribution $|U(\xi)|^2 \, dr$ (solid curves) with the classical value for two vibrational levels, $v = 0$ and $v = 20$. For large v , the classical curve resembles the spatial average of the quantum-mechanical distribution, while for $v = 0$ both descriptions yield completely different results.

Tab. 3.2 Hermite polynomials for the six lowest vibrational levels of the harmonic oscillator.

v	$H_v(\xi)$
0	1
1	2ξ
2	$4\xi^2 - 2$
3	$8\xi^3 - 12\xi$
4	$16\xi^4 - 48\xi^2 + 12$
5	$32\xi^5 - 160\xi^3 + 120\xi$

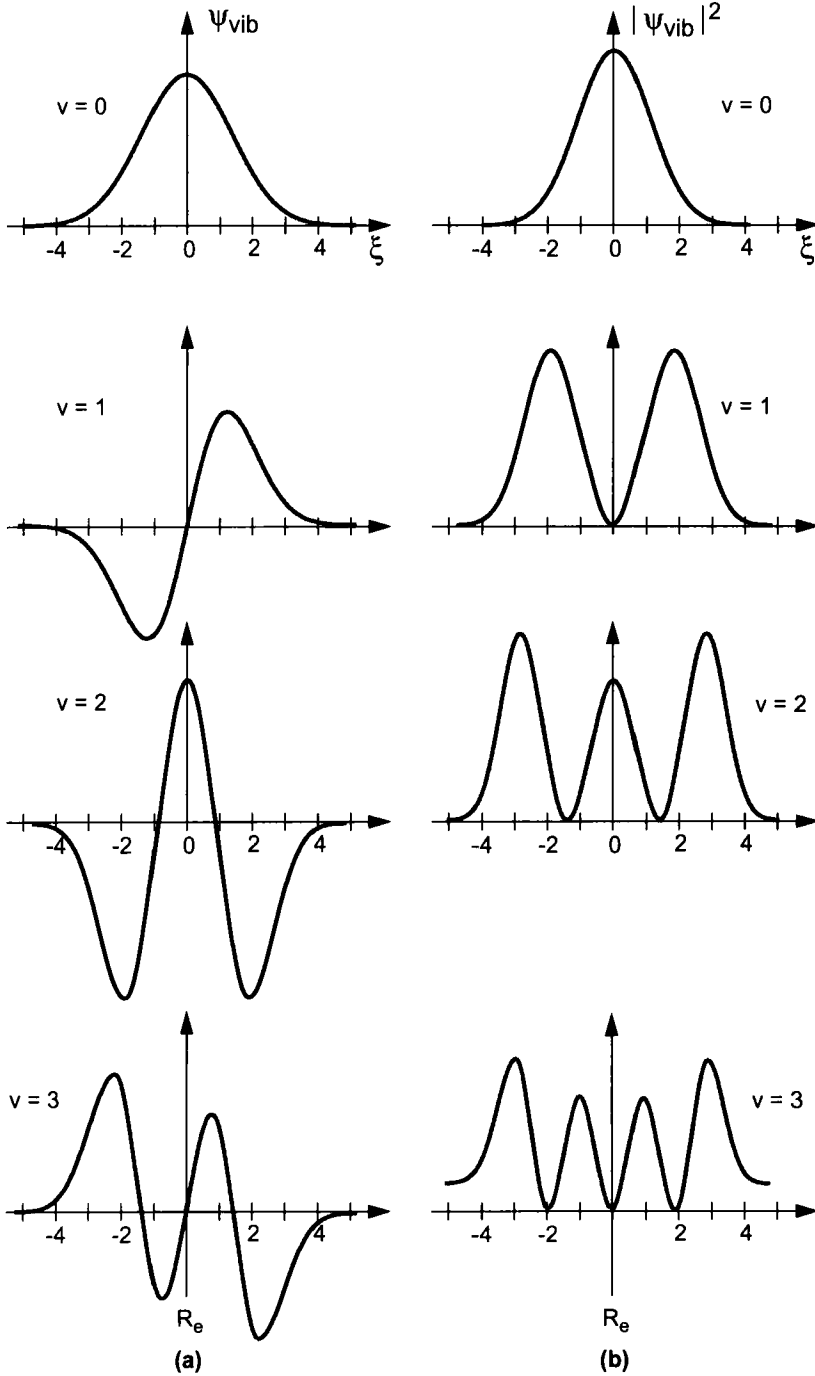


Fig. 3.5 a) Vibrational wavefunctions ψ_{vib} and b) their square moduli for some vibrational levels of the harmonic oscillator.

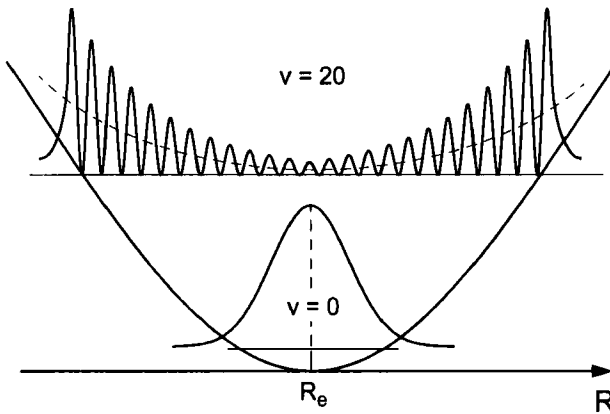


Fig. 3.6 Comparison between classical probability density (dotted lines) and the square moduli of the vibrational wavefunctions for $v = 0$ and $v = 20$.

Table 3.3 lists measured values of the vibrational constants ω_e and the rotational constants B_e for some molecules. It is useful to memorize the *magnitude of the vibrational period* $T = (\omega_e c)^{-1}$, which is $T = 8 \times 10^{-15}$ s for the lightweight H_2 molecule and 8×10^{-13} s for the heavy Cs_2 molecule, i.e., it generally falls in the range 10^{-12} – 10^{-14} s. In contrast, the rotational periods for the lowest rotational level, $T_{\text{rot}} = (2B_e c)^{-1}$, are $T_{\text{rot}}(\text{H}_2) \approx 2.5 \times 10^{-13}$ s and $T_{\text{rot}}(\text{Cs}_2) = 1.5 \times 10^{-9}$ s, i.e., they are larger by two to three orders of magnitude.

The square moduli of the time-independent vibrational wavefunctions give the time-average of the probability density of the vibrating nuclei. If we want to transfer the classical picture of oscillating nuclei into a quantum-mechanical description, we need to take into account that by specifying the position of a nucleus we introduce an uncertainty in its momentum and hence its vibrational energy $E = p^2/2m$. For example, for a spatial resolution of 0.01 nm and a velocity of 10^4 m/s of the vibrating nucleus, the maximum possible energy resolution is only about 10^{-19} J = 1 eV. This means that individual vibrational levels cannot be resolved if we want to determine

Tab. 3.3 Vibrational constants ω_e and rotational constants B_e for some diatomic molecules.

Molecule	ω_e/cm^{-1}	B_e/cm^{-1}
H_2	4395	60.80
N_2	2360	2.01
O_2	1580	1.45
Li_2	351	0.67
Na_2	159	0.15
Cs_2	42	0.01
HCl	2990	10.59

the position of a nucleus at the same time. A superposition of the time-dependent vibrational wavefunctions of neighboring vibrational levels yields a wavepacket which oscillates between the classical turning points of the vibration, and which resembles the classical picture of vibrating nuclei much better than the time-averaged model of stationary wavefunctions.

3.3.2

The Anharmonic Oscillator

For larger vibrational amplitudes, i.e., larger vibrational quantum numbers v , the observed vibrational frequencies ω_{vib} differ significantly from the constant ω_0 of the harmonic oscillator. Usually, they decrease for increasing quantum number v . The reason for this behavior is that the real molecular potential $E_n^{(0)}(R)$ does not approach ∞ for large internuclear distance $R \rightarrow \infty$ but converges towards the dissociation energy E_d of the molecule (see Fig. 3.7). The *dissociation energy* E_d is the bond energy E_b in the electronic state under consideration minus the zero-point energy $E_{\text{vib}}^{(0)} = \frac{1}{2}\hbar\omega_0$. E_b corresponds to the difference $E(A) + E(B) - E(AB)$ between the electronic energies $E(A) + E(B)$ of the separated atoms A and B and the electronic energy $E(AB)$ of the molecule at the minimum of the potential curve.

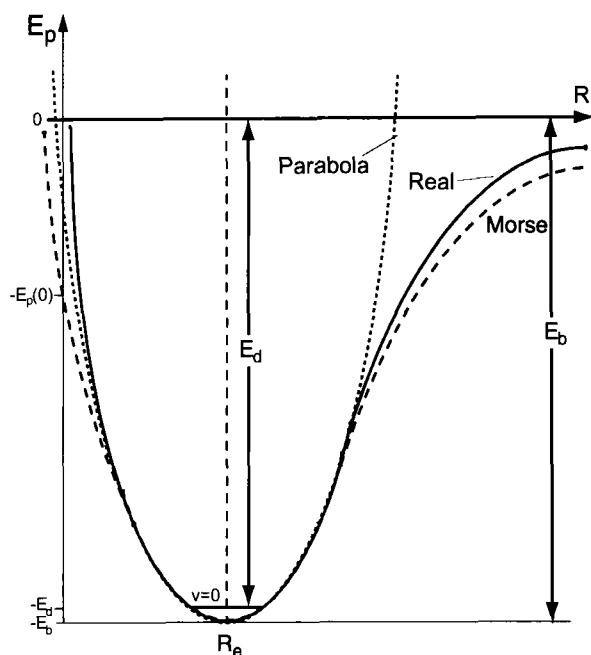


Fig. 3.7 Comparison between the harmonic oscillator potential, the Morse potential, and a real molecular potential.

3.3.2.1 Morse Potential

Morse [3.3] suggested a potential

$$E_p(R) = E_b \left[1 - e^{-a(R-R_e)} \right]^2, \quad (3.30)$$

which provides a good approximation for the attractive part of the potential because it converges towards the energy $E_p(R) = 0$ for $R \rightarrow \infty$. The repulsive part of the potential, ($R < R_e$), which converges towards $\lim_{R \rightarrow 0} E_p(R) = -E_b [1 - \exp(+aR_e)]^2$, shows in many cases larger deviations from measured values (see Fig. 3.7).

The Morse potential has the big advantage that it allows an exact solution of the Schrödinger equation (3.22) [3.4].

By inserting Eq. (3.30) into Eq. (3.22), we obtain for the energies $E(v)$ of the vibrational levels v

$$E_v = \hbar\omega_0 \left(v + \frac{1}{2} \right) - \frac{\hbar^2\omega_0^2}{4E_b} \left(v + \frac{1}{2} \right)^2, \quad (3.31a)$$

and for the term values $T_v = E_v/hc$,

$$T_v = \omega_e \left(v + \frac{1}{2} \right) - \omega_e x_e \left(v + \frac{1}{2} \right)^2 \quad (3.31b)$$

with $\omega_e = \omega_0/2\pi c$ and $\omega_e x_e = \hbar\omega_0^2/(8\pi c E_b) = hc\omega_e^2/4E_b$.

The frequency

$$\omega_0 = a\sqrt{2E_b/\mu}$$

corresponds to the frequency of a classical oscillator with force constant $k_r = 2a^2 E_b$. The constant a in the Morse potential Eq. (3.30) can be determined from a measurement of ω_0 and E_b .

The *term differences* between neighboring vibrational levels,

$$\Delta T_v = T_{v+1} - T_v = \omega_e - \omega_e x_e (v+2) \quad (3.32)$$

decrease linearly with the vibrational quantum number v (Fig. 3.8) – in contrast to the harmonic oscillator, where they are constant.

3.3.2.2 Taylor Expansion of Potentials

Better approximations to the real molecular potential $E_p(R)$ are obtained if we expand the molecular potential in a Taylor series around the equilibrium distance R_e . With $r = R - R_e$ this yields

$$E_p(r) = E_p(0) + E_p'(0)r + \frac{r^2}{2}E_p''(0) + \frac{r^3}{3}E_p'''(0) + \dots \quad (3.33)$$

Usually the origin of the energy scale is chosen to be the minimum of the potential, i.e., $E_p(0) = 0$. As $E_p(r)$ assumes a minimum for $r = 0$, its first derivative is also

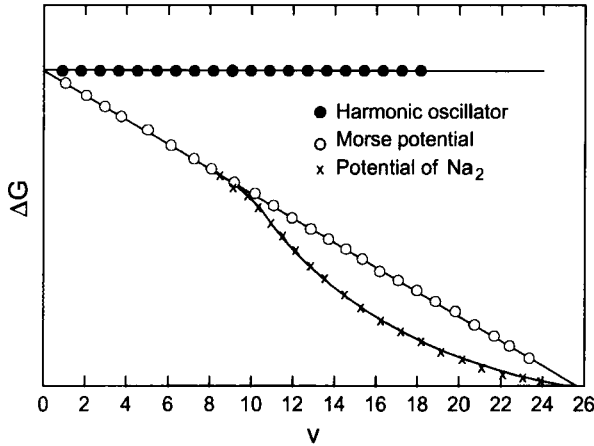


Fig. 3.8 Term difference $\Delta G_v = G(v+1) - G(v)$ as a function of the vibrational quantum number v for the harmonic potential, the Morse potential, and the measured potential of the Na_2 molecule [3.5].

zero, $E'_p(0) = 0$. The first nonvanishing term in the Taylor expansion is therefore the harmonic potential

$$E_p(r) = \frac{r^2}{2} E''_p(0) .$$

A comparison with Eq. (3.23) shows that $E''_p(0)$ equals the force constant k_r . Using the general ansatz Eq. (3.33) for the potential, the Schrödinger equation (3.22) can be solved only numerically.

3.3.2.3 Quartic Potential

We will demonstrate the approximate computation of energy eigenvalues for the example of a quartic potential,

$$E_p(r) = \frac{1}{2} k_r r^2 + ar^3 + br^4 , \quad (3.34)$$

which plays a role in the description of double-minimum potentials (Fig. 3.9). We write the Hamiltonian H as

$$H = H_0 + H_1 + H_2 \quad \text{with} \quad H_0 = -(\hbar^2/2\mu) \Delta + \frac{1}{2} k_r r^2 \quad (3.35a)$$

$$H_1 = ar^3 \quad \text{and} \quad H_2 = br^4 .$$

Next, we write the energy eigenvalues as

$$E(v) = E_0(v) + E_1(v) + E_2(v) , \quad (3.35b)$$

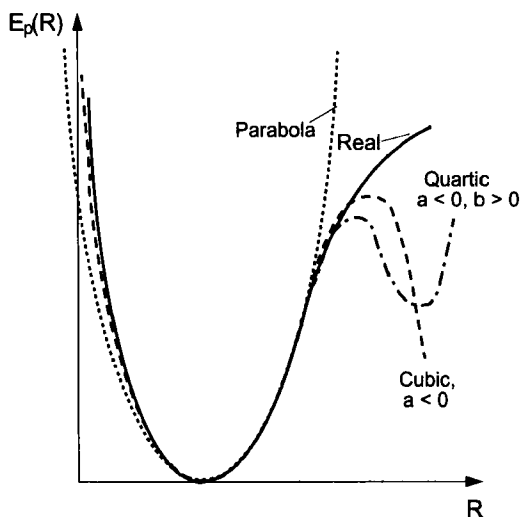


Fig. 3.9 Comparison of parabolic, cubic, and quartic potentials with a real molecular potential.

where the $E_0(v)$ are the eigenvalues of the harmonic oscillator. In first-order perturbation theory, this yields

$$E_1 = \int \Psi_0^* a r^3 \Psi_0 \, dr \quad \text{and} \quad E_2 = \int \Psi_0^* b r^4 \Psi_0 \, dr ,$$

where Ψ_0 are the eigenfunctions $H(\xi) \times \exp(-\xi^2/2)$ of the harmonic oscillator. Being Hermite polynomials, the functions Ψ_0 are real, and $\Psi_0 \times \Psi_0$ is a quadratic function of r ; therefore the first integral vanishes because the integrand is an odd function of r , that is, the cubic term in the potential does not, to first approximation, contribute to the energy.

To compute the second integral as a function of the vibrational quantum number v , the following relation for Hermite polynomials $H(\xi)$,

$$H_v(\xi) = (-1)^v e^{\xi^2} \frac{d^v}{d\xi^v} (e^{-\xi^2}) ,$$

is useful. By stepwise partial integration we obtain [3.6]

$$E_2 = \frac{3b}{2\beta^2} \left[\left(v + \frac{1}{2}\right)^2 + \frac{1}{4} \right] . \quad (3.36)$$

The energies are shifted upwards from the harmonic-oscillator levels. In second-order perturbation theory, the cubic term also contributes to the energy; a detailed calculation can be found in [3.6]. Modern procedures do not start from the harmonic oscillator as the unperturbed system but from a Morse potential or even from approximated functions for the quartic oscillator. Perturbational calculations then converge more rapidly. A detailed account can be found in [3.7].

3.3.2.4 Generalized Potential

The most frequently employed form for a molecular potential is semiempirical. Here, the term values $G(v) = E_v / (hc)$ are described by a power series in $(v + \frac{1}{2})$,

$$G(v) = \omega_e \left(v + \frac{1}{2}\right) + \omega_e x_e \left(v + \frac{1}{2}\right)^2 + \omega_e y_e \left(v + \frac{1}{2}\right)^3 + \omega_e z_e \left(v + \frac{1}{2}\right)^4 + \dots, \quad (3.37)$$

and the coefficients $\omega_e, \omega_e x_e, \omega_e y_e, \dots$ are determined from a least-squares fit of this expression to the experimentally determined term values. Section 3.6 will describe how the potential is calculated from these coefficients.

3.4

Vibration–Rotation Interaction

To describe vibration *and* rotation of a diatomic molecule, we must include the centrifugal term $J(J+1)\hbar^2 / (2\mu R^2)$ in Eq. (3.7), which can be combined with the potential $E_p(R)$ to form an effective potential

$$E_{p,\text{eff}}(R, J) = E_p(R, J=0) + \frac{J(J+1)\hbar^2}{2\mu R^2}. \quad (3.38)$$

The energies $E(v, J)$ and the averaged internuclear distance depend now not only on $E_p(R)$ but also on the vibrational quantum number v and the rotational quantum number J . Before developing the mathematical treatment of the vibrating rotor, we will first concentrate on the physical foundations.

During one full rotation, a molecule completes usually many vibrational periods (typically 10–100). This means that the internuclear distance is periodically changing during rotation (Fig. 3.10). As the angular momentum $J = I\omega$ of a free molecule is constant in time but the moment of inertia $I \cong \mu R^2$ is periodically changing, the

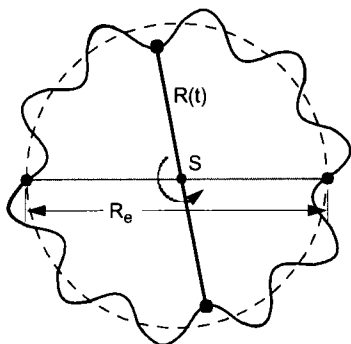


Fig. 3.10 Vibrating rotor.

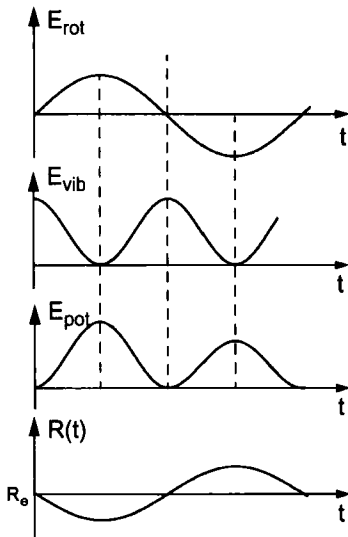


Fig. 3.11 Exchange of vibrational, rotational, and potential energy in the vibrating rotor.

frequency ω of rotation must also change periodically, in phase with the molecular vibration. Thus, the rotational energy $E_{\text{rot}} = J(J+1)\hbar^2/(2\mu R^2)$ varies also with R . As the total energy $E = E_{\text{rot}} + E_{\text{vib}} + E_{\text{p}}$ must of course remain constant, the energy in the vibrating rotor flows constantly between vibrational, rotational, and potential energy (Fig. 3.11). When talking of the rotational energy of a vibrating molecule, we mean the time-average, averaged over many vibrational periods.

As $|\psi_{\text{vib}}(R)|^2 dR$ is the probability of finding the nuclei at an internuclear distance between R and $R + dR$, the mean value (quantum-mechanical expectation value) of the internuclear distance is

$$\langle R \rangle = \int \psi_{\text{vib}}^*(R, v) R \psi_{\text{vib}}(R, v) dR. \quad (3.39)$$

Analogously we can define a mean rotational energy

$$\langle E_{\text{rot}} \rangle = \frac{J(J+1)\hbar^2}{2\mu} \int \psi_{\text{vib}}^*(v, R) \frac{1}{R^2} \psi_{\text{vib}}(v, R) dR, \quad (3.40)$$

which is proportional to the expectation value $\langle 1/R^2 \rangle$.

To be able to express the rotational term values $F = E_{\text{rot}}/\hbar c$ in terms of a rotational constant as in Eq. (3.11), we define a vibration-dependent mean rotational constant in analogy to Eq. (3.12),

$$B_v = \frac{\hbar}{4\pi\mu c} \int \psi_{\text{vib}}^* \frac{1}{R^2} \psi_{\text{vib}} dR. \quad (3.41)$$

The vibrational functions ψ_{vib} and thus also B_v depend on the choice of the potential $E_{\text{p}} = E_{\text{pot}}(R)$.

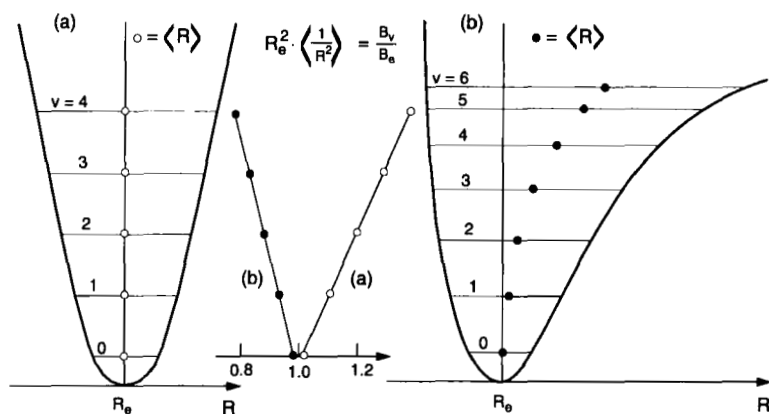


Fig. 3.12 Mean values $\langle R \rangle$ and $\langle 1/R^2 \rangle$ as functions of the vibrational quantum number v , a) in a harmonic, and b) in an anharmonic potential.

Note: While for a harmonic potential, $\langle R \rangle$ is independent of the vibrational quantum number v , this is not true for asymmetric potentials such as the Morse potential. The mean $\langle 1/R^2 \rangle$ depends on v even in the harmonic case, where it increases with increasing v , while it decreases in real potentials (Fig. 3.12).

3.5

Term Values of the Vibrating Rotor; Dunham Expansion

The most precise determination of the effective potential Eq. (3.38) of a vibrating and rotating molecule is based on a measurement of energies or term values of vibration-rotation levels. The potential can then be calculated numerically from the term values, independent of model potentials. As this is today's standard procedure for the determination of potentials in diatomic molecules, we will discuss it in more detail in the following, and we will also give some examples.

3.5.1

Term Values for the Morse Potential

For a nonrotating molecule with an assumed Morse potential, the term values Eq. (3.31) can be obtained analytically by solving the Schrödinger equation (3.22). For the rotating molecule, we must employ the effective Morse potential

$$V_{\text{eff}}(R) = E_{p,\text{eff}}(R, J) = E_b \left[1 - e^{-a(R-R_e)} \right]^2 + \frac{J(J+1)\hbar^2}{2\mu R^2} \quad (3.42)$$

which includes the additional centrifugal term $J(J+1)\hbar^2/(2\mu R^2)$. For this potential, approximate solutions to the Schrödinger equation have been found by Pekeris [3.8]. The corresponding term values are

$$T(v, J) = G(v) + F(v, J) = \omega_e \left(v + \frac{1}{2}\right) - \omega_e x_e \left(v + \frac{1}{2}\right)^2 + B_v J(J+1) - D_v J^2(J+1)^2. \quad (3.43)$$

The rotational and vibrational constants can be written as

$$B_v = B_e - \alpha_e \left(v + \frac{1}{2}\right), \quad (3.44a)$$

with

$$B_e = \frac{\hbar}{4\pi c \mu R_e^2} \quad \text{and} \quad \alpha_e = \frac{3\hbar^2 \omega_e}{4\mu R_e^2 E_b} \left(\frac{1}{aR_e} - \frac{1}{a^2 R_e^2} \right),$$

and

$$D_v = D_e + \beta_e \left(v + \frac{1}{2}\right) \quad \text{with} \quad \beta_e = D_e \left(\frac{8\omega_e x_e}{\omega_e} - \frac{5\alpha_e}{\omega_e} - \frac{\alpha_e^2 \omega_e}{24B_e^3} \right). \quad (3.44b)$$

For the vibrational constants, we obtain

$$\omega_e = \frac{a}{2\pi c} \sqrt{\frac{2E_b}{\mu}}; \quad \omega_e x_e = \frac{hc\omega_e^2}{4E_d} = \frac{ha^2}{8\pi^2 \mu c}, \quad (3.45)$$

where E_b is given in joule, and μ in kilogram.

The centrifugal constant can be calculated from the *Kratzer relation*

$$D_e = \frac{4B_e^3}{\omega_e^2}, \quad (3.46)$$

which follows, for a Morse potential, from Eqns. (3.12), (3.19a) and (3.45). While Eq. (3.46) is exact only for a Morse potential, it is still a good approximation for real molecular potentials.

3.5.2

Term Values for a Generalized Potential

As the vibrational functions in Eq. (3.41) for an *arbitrary potential* are in general not known, B_v is frequently expanded in a power series in $(v + \frac{1}{2})$,

$$B_v = B_e - \alpha_e \left(v + \frac{1}{2}\right) + \gamma_e \left(v + \frac{1}{2}\right)^2 + \dots, \quad (3.47)$$

and analogously for the centrifugal constant,

$$D_v = D_e + \beta_e \left(v + \frac{1}{2}\right) + \delta_e \left(v + \frac{1}{2}\right)^2 + \dots, \quad (3.48)$$

and the coefficients B_e , α_e , γ_e , D_e , β_e , and δ_e are determined by fitting the calculated term values, Eq. (3.43),

$$T(v, J) = \omega_e \left(v + \frac{1}{2}\right) - \omega_e x_e \left(v + \frac{1}{2}\right)^2 + \omega_e y_e \left(v + \frac{1}{2}\right)^3 + \omega_e z_e \left(v + \frac{1}{2}\right)^4 \dots + B_v J(J+1) - D_v J^2(J+1)^2 + H_v J^3(J+1)^3 \dots \quad (3.49)$$

to the experimentally determined term values. The coefficients characterize the internuclear distance R_e and the potential in which the nuclei oscillate. They are thus called *molecular constants*. Table 3.1 lists some values of the most important constants for a number of molecules.

3.5.3

Dunham Expansion

As a realization of a generalized potential of a rotating molecule,

$$E_{\text{pot}}(R, J) = E_{\text{pot}}(R, J=0) + \frac{J(J+1)\hbar^2}{2\mu R^2},$$

Dunham [3.9] suggested a power-series expansion

$$\frac{E_{\text{pot}}(R, J)}{hc} = a_0 \xi^2 (1 + a_1 \xi + a_2 \xi^2 + \dots) + B_e J(J+1) [1 - 2\xi + 3\xi^2 - 4\xi^3 + \dots] \quad (3.50)$$

with $\xi = (R - R_e)/R_e$, and expressed the term values of the vibration–rotation levels by a power series analogous to Eq. (3.49),

$$T(v, J) = \sum_i \sum_k Y_{ik} \left(v + \frac{1}{2}\right)^i [J(J+1)]^k. \quad (\text{Dunham expansion}) \quad (3.51)$$

This gives a relation between the Dunham coefficients Y_{ik} and the coefficients a_i of the potential expansion which was determined by Dunham [3.9].

The Dunham coefficients Y_{ik} essentially correspond to the coefficients ω_e , $\omega_e x_e$, etc., in the expansion Eq. (3.49) if the latter are simply considered as expansion coefficients that are fitted to measured values. If the physical meaning of the coefficients in Eq. (3.49) and the definitions from Eqns. (3.12), (3.19a), and (3.43)–(3.46), which are strictly valid only for a Morse potential, need to be retained, then small deviations of order $(B_e/\omega_e)^2$ occur [3.9] (see Sect. 3.6.2). If $(B_e/\omega_e)^2$ is sufficiently small, they can be neglected, and we obtain

$$\begin{aligned} Y_{10} &\approx \omega_e; & Y_{01} &\approx B_e; & Y_{11} &= -\alpha_e \\ Y_{20} &\approx -\omega_e x_e; & Y_{02} &\approx D_e; & Y_{12} &\approx \beta_e \\ Y_{30} &\approx \omega_e y_e; & Y_{03} &\approx H_e; & Y_{21} &\approx \gamma_e. \end{aligned} \quad (3.52)$$

An exact comparison for the coefficient Y_{00} yields not zero but

$$Y_{00} = \frac{B_e - \omega_e x_e}{4} + \frac{\alpha_e \omega_e}{12B_e} + \frac{\alpha_e^2 \omega_e^2}{144B_e^2}. \quad (3.53)$$

For a Morse potential, the only nonvanishing coefficients are Y_{10} , Y_{20} , Y_{01} , Y_{02} , Y_{11} , and Y_{12} , so that the Dunham expansion reduces to only a few terms.

The Dunham expansion is the most frequently used method to determine molecular constants from a least-squares fit of the measured term values to Eq. (3.51).

Equation (3.52) creates a relation between the Dunham coefficients Y_{ik} , which may be considered pure fit parameters, and the molecular constants ω_e , β_e , etc., which have a real physical meaning.

3.5.4

Isotopic Shifts

Both vibrational and rotational energies depend on the masses of the atoms involved. Therefore, different isotopomers of a molecule have different term values $T(v, J)$. Recording spectra of different isotopomers is often helpful to identify specific lines, i.e., to determine the quantum numbers v and J of a transition, because the isotopic shifts, which depend on v and J , can be calculated precisely.

From Eq. (3.12) we see that the rotational constant B_e is inversely proportional to the reduced mass $\mu = M_1 M_2 / (M_1 + M_2)$ of the molecule. The centrifugal constant D_e is, according to Eq. (3.19a), $D_e \propto 1/\mu^2$, and the vibrational constants are, according to Eq. (3.44), $\omega_e \propto \sqrt{\mu}$ and $\omega_e x_e \propto \mu$.

In the approximation Eq. (3.52), the mass dependence of the Dunham coefficients Y_{ik} in Eq. (3.51) can be expressed through $Y_{ik}^{(\mu_1)} / Y_{ik}^{(\mu_2)} = (\mu_2 / \mu_1)^{(i+2k)/2}$. For the more exact relation Eq. (3.51) including higher terms, the corresponding expression is [3.10]:

$$\frac{Y_{ik}^{(\mu_1)}}{Y_{ik}^{(\mu_2)}} = \left(\frac{\mu_2}{\mu_1} \right)^{(i+2k)/2} \left[1 + (\beta_{ik} B_e^2 / \omega_e^2) \frac{\mu_2 - \mu_1}{\mu_2} \right], \quad (3.54)$$

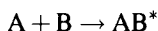
and the β_{ik} are tabulated as functions of the coefficients Y_{ik} in [3.9] and [3.10]. For comparison with more accurate measurements, the correction term in Eq. (3.54) must be taken into account.

3.6

Determination of Potential Curves from Measured Term Values

The accurate determination of potential curves $E_{\text{pot}}^{(i)}(R)$ for the different electronic states i of a molecule is among the major objectives of the spectroscopy of diatomic

molecules. For a known potential $E_{\text{pot}}(R)$ we know the bond energy E_{b} and the equilibrium bond distance R_{e} and we can, at least numerically, calculate all relevant vibrational and rotational levels from the Schrödinger equation. Knowledge of the potential curves $E_{\text{p}}(R)$ is also crucial for the calculation of reaction rates for collisions of two atoms



and their dependence on the internal energy of the collision partners A or B. The form of the potential curve ($E_{\text{pot}}(R_{\text{AB}})$) decides whether a reaction is endothermic or exothermic.

For small diatomic molecules (e.g., H_2 , Li_2 , LiH , etc.) the ground-state potentials can be computed, without any information on experimental data, with an accuracy of a few cm^{-1} by modern *ab initio* methods (see Sect. 2.8). Although there are computed high-quality potential curves for heavier diatomic molecules [3.11, 3.12], the results can not in general compete with the accuracy achievable by spectroscopic methods. They still provide useful information as to which electronic states of a molecule occur (see Sections 2.4 and 2.8), whether they are binding or repulsive, and on their approximate energies. Such calculations can therefore greatly facilitate the interpretation of measured spectra.

All presently known precise potential curves have been derived from experimental data with the aid of different computational schemes. They are thus relying on semiempirical methods that do not require a knowledge of the electronic wavefunctions ϕ in Eq. (2.7). Some of these methods are based on the WKB procedure, an approximation method for the solution of the one-dimensional Schrödinger equation (3.7), named after the initials of the inventors *Wentzel*, *Kramers*, and *Brillouin* [3.13]. We will therefore start by discussing the WKB approximation [3.14], before we continue by presenting today's most frequently used methods for the determination of molecular potential curves.

3.6.1

The WKB Approximation

We start from the radial Schrödinger equation (3.7), from which we obtain, by substituting $\Psi = R \times S(R)$, the equation

$$\frac{d^2\Psi}{dR^2} + \frac{2\mu}{\hbar^2} (E - V_{\text{eff}}) \Psi = 0 \quad (3.55)$$

with

$$V_{\text{eff}} = E_{\text{pot}}(R) - \frac{J(J+1)\hbar^2}{2\mu R^2} \quad (3.55a)$$

for the vibrating and rotating molecule.

The kinetic energy of the radial motion,

$$E_{\text{kin}} = E - V_{\text{eff}} = \frac{p^2}{2\mu}, \quad (3.56)$$

can be expressed through the radial momentum $p(R) = \sqrt{2\mu(E - V_{\text{eff}})}$.

With $k = p/\hbar$, we obtain from Eq. (3.55)

$$\frac{d^2\psi}{dR^2} + k^2\psi = 0. \quad (3.57)$$

For constant potential, $V_{\text{eff}} = \text{const.}$, independent of R , $k = k_0 = \text{const.}$, and Eq. (3.57) describes a free particle. The solution of Eq. (3.57) is in this case

$$\psi = A e^{\pm ik_0 R}.$$

If $V(R)$ varies only slowly with R , an obvious idea is to try a solution of the form

$$\psi = A e^{iu(R)}. \quad (3.58)$$

If we substitute Eq. (3.58) into Eq. (3.57), we obtain an equation for the unknown function $u(R)$

$$i \frac{d^2 u}{dR^2} - \left(\frac{du}{dR} \right)^2 + k^2(R) = 0. \quad (3.59)$$

If the potential does not vary quickly with R , the second derivative $d^2 u/dR^2$ will be negligible in a crude approximation, and we obtain the “zeroth-approximation $u_0(R)$ ” from Eq. (3.59) with $u'_0 = du_0/dR$

$$u'^2_0 = [k(R)]^2 \Rightarrow u_0 = \int k(R) dR + C. \quad (3.60)$$

If we substitute this result into Eq. (3.59), we obtain the first approximation:

$$\left(\frac{du_1}{dR} \right)^2 = k^2(R) + i \frac{d^2 u_0}{dR^2} \Rightarrow u_1 = \pm \int [k^2(R) + i u''_0(R)]^{1/2}. \quad (3.61)$$

This can be used as a basis for an iterative approximation method, where we insert the $(n-1)$ th approximation on the right-hand side of Eq. (3.61) and obtain the n th approximation for $u(R)$ on the left-hand side. The solutions are then

$$u_n(R) = \pm \int \sqrt{k^2(R) + i u''_{n-1}(R)} dR + C_n, \quad (3.62)$$

where C_n is an integration constant determined by boundary conditions.

For the first approximation, we obtain

$$\begin{aligned} u_1(R) &= \pm \int \sqrt{k^2(R) + i u''_0(R)} dR + C_1 \\ &= \pm \int \sqrt{k^2(R) + ik'(R)} dR. \end{aligned} \quad (3.63)$$

The procedure converges if $|k'(R)| \ll |k^2(R)|$. Expansion of the integrand yields

$$\begin{aligned} u_1(R) &= \pm \int k(R) \left[1 + \frac{i}{2} \left(\frac{k'(R)}{k^2(R)} \right) \right] dR + C_1 \\ &= \pm \int k(R) dR + \frac{i}{2} \ln k(R) + C_1 . \end{aligned}$$

For the wavefunction $\Psi(R)$ we obtain thus the approximate solution

$$\Psi(R) = \frac{1}{\sqrt{k(R)}} \exp \left[\pm \frac{i}{h} \int p(R) dR \right] , \quad (3.64)$$

which is known as the *WKB approximation*. Introduction of the de Broglie wavelength

$$\lambda = \frac{h}{p} = \frac{2\pi}{k(R)} ,$$

allows the convergence criterion $k' \ll k^2$ to be written as

$$\frac{\lambda}{2\pi} \frac{dp}{dR} \ll p(R) , \quad (3.65)$$

that is, the approximation is valid if *the variation of the momentum within one de Broglie wavelength is small with respect to the momentum itself*.

This condition is *not* met at the classical turning points of an oscillator, because there $p(R) = 0$. The resulting difficulty for the application of the WKB approximation can be circumvented, however, by using special solutions of the Schrödinger equation (3.55) in the vicinity of the turning points, which can be obtained by linearizing the potential $E_{\text{pot}}(R)$ in a small interval around the turning points R_1, R_2 , i.e., if we write $E_{\text{pot}}(R) = a(R - R_i)$. For a detailed justification we refer the reader to [3.6].

For a periodic motion of the vibrating nuclei between the positions R_1 and R_2 , we obtain by integrating over a full vibrational period, i.e., over the path from R_1 through R_2 and back to R_1 , the so-called *action integral*

$$I = \oint p(R) dR . \quad (3.66)$$

The condition that the solution function be single-valued, Eq. (3.64), requires that the function must return to its original value after one revolution. Therefore, it follows for the exponent in Eq. (3.64) after v vibrational periods,

$$\frac{i}{h} \oint p(R) dR = iv(2\pi + 1) ,$$

where we have accounted for the fact that upon reflection a phase shift of π is introduced in the wavefunction. This yields the condition

$$I = \left(v + \frac{1}{2} \right) h , \quad (3.67)$$

for the action integral that determines that phase factor of the wavefunctions Eq. (3.64), where $v = 0, 1, 2, \dots$ is the integer vibrational quantum number.

With $p = \sqrt{2\mu(E - V_{\text{eff}})}$, this gives a quantization condition for the allowed energies E ,

$$\oint \sqrt{2\mu(E - V_{\text{eff}}(R))} \, dR = (v + \frac{1}{2})h, \quad (3.68)$$

which contains the dependence of the energy levels $E(v, J)$ of the vibrating rotor on the effective potential $V_{\text{eff}} = E_{\text{pot}}(R) + J(J+1)\hbar^2/(2\mu R^2)$.

If we treat E as a continuous variable, differentiation yields

$$\frac{dI}{dE} = \sqrt{\frac{\mu}{2}} \oint \frac{dR}{\sqrt{E - V_{\text{eff}}(R)}}. \quad (3.69)$$

This is equal to the classical vibrational period T_{vib} , as can be seen from the following relation:

$$E = \frac{1}{2}\mu\dot{R}^2 + V_{\text{eff}}(R) \quad \Rightarrow \quad \frac{dR}{dt} = \sqrt{\frac{2}{\mu}(E - V_{\text{eff}})}. \quad (3.70)$$

Integration gives

$$T_{\text{vib}} = \oint dt = \sqrt{\frac{\mu}{2}} \oint \frac{dR}{\sqrt{E - V_{\text{eff}}(R)}} = \frac{dI}{dE}. \quad (3.71)$$

3.6.2

WKB Approximation and Dunham Expansion

As mentioned in Sect. 3.5.3, Dunham [3.9] used a power-series expansion for the effective potential V_{eff} with the normalized expansion parameter $\xi = (R - R_e)/R_e$,

$$V_{\text{eff}} = hca_0\xi^2 [1 + a_1\xi + a_2\xi^2 + a_3\xi^3 + \dots] + hcB_eJ(J+1) [1 - 2\xi + 3\xi^2 - 4\xi^3 + \dots]. \quad (3.72)$$

The parameter $a_0 = \omega_e^2/4B_e$ is determined by the classical oscillation frequency ω_e for small displacements (i.e., the frequency of the harmonic oscillator) and by the rotational constant $B_e = \hbar/(4\pi\mu cR_e^2)$ at the equilibrium distance R_e .

If we substitute this potential ansatz into the Schrödinger equation, we can solve it within the WKB approximation. The relation between V_{eff} and the action integral can be written, using Eqns. (3.66) and (3.67), as

$$\oint \sqrt{E - V_{\text{eff}}} \, dR = \frac{(v + \frac{1}{2})h}{\sqrt{2\mu}} \quad (3.72a)$$

Inserting Eq. (3.72) into Eq. (3.72a) and expanding the square root. The result is the term values $T(v, J) = E(v, J)/hc$ in the form of the Dunham expansion

$$T(v, J) = \sum_i \sum_k Y_{ik} \left(v + \frac{1}{2}\right)^i [J(J+1)]^k, \quad (3.73)$$

where the Dunham coefficients Y_{ik} are connected with the coefficients a_i in the expansion of the potential.

A list of the relations for the first 15 Dunham coefficients can be found in [3.9, 3.15].

Note: As the expansion of the potential Eq. (3.72) converges only for $\xi < 1$, its validity is limited to internuclear distances $0 \leq R \leq 2R_e$. Nevertheless, Eq. (3.73) can be used to fit measured term values also for $R \geq 2R_e$. However, the Dunham coefficients Y_{ik} derived from that fit bear no direct physical meaning, but can still be viewed as numerical data for the determination of term values and they are useful for the calculation of line positions in the spectra of transitions $(v', J') \leftarrow (v'', J'')$.

3.6.3

Other Potential Expansions

Finlan and Simons [3.16] suggested a potential expansion with arbitrary convergence limit, using not $\xi = (R - R_e)/R_e$ as expansion parameter but $z = (R - R_e)/R$. This means that $z < 1$ for all values of R . The potential $V(R)$ is similar to Eq. (3.72),

$$V(R) = A_0 z^2 (1 + b_1 z + b_2 z^2 + \dots). \quad (3.74)$$

The authors showed that the coefficients b_i are related to the coefficients a_i of the Dunham potential by

$$a_n = b_n + \sum_{i=1}^{n-1} (-1)^i b_{n-i} \binom{n+1}{i} + (-1)^n (n+1). \quad (3.75)$$

Because for $R \rightarrow \infty$, that is for $z \rightarrow 1$, the potential $E_{\text{pot}}(R)$ converges towards the dissociation energy E_d , we arrive at an additional boundary condition,

$$E_d = A_0 \left(1 + \sum_n b_n\right). \quad (3.76)$$

A generalized potential that contains many approximations as special cases has been developed by Thakkar [3.17].

3.6.4

The RKR Method

Today's most frequently used method for the exact calculation of molecular potential curves is based on work by Rydberg [3.18], Klein [3.19] and Rees [3.20]. It uses the

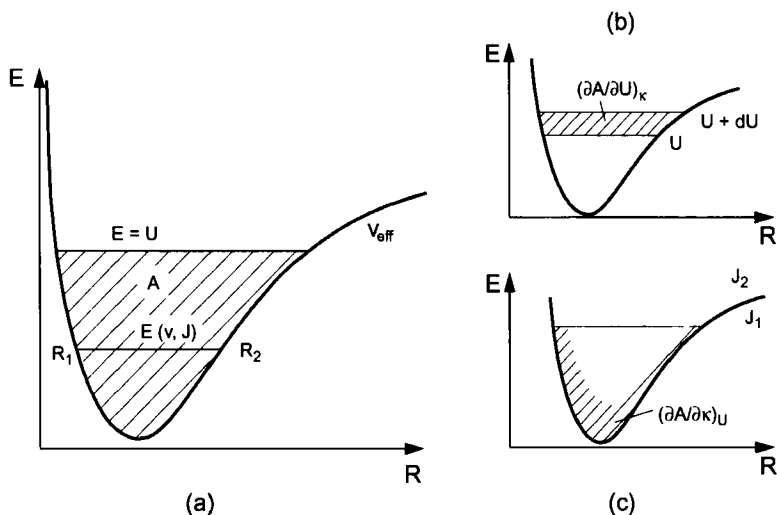


Fig. 3.13 Explanation of the RKR procedure. a) Integral A as area between $E = 0$ and $E = U$ inside the potential curve; b) and c) variation of A with U and κ .

WKB approximation to derive the classical turning points R_1 and R_2 of the vibrating molecule from the measured energy levels $E(v, J)$. At these points the total energy $E(v, J)$ equals the potential energy. With the aid of these turning points R_i , the whole potential curve $E_{\text{pot}}(R)$ is then constructed point by point. This means that the potential $E_{\text{pot}}(R)$ is not provided in analytical form, but is only tabulated at discrete points $E_{\text{pot}}(R_i)$, where the number of turning points employed corresponds to the number of measured energy levels. The RKR procedure yields more exact potential curves than all other methods discussed up to now, and it is therefore the standard procedure in molecular spectroscopy. Its precision is only surpassed by that of the yet less well-known IPA procedure (see next section).

The RKR procedure will be investigated more closely with the aid of Fig. 3.13. The energy E is taken to be that of a measured vibration–rotation level $E(v, J)$. The shaded area A in Fig. 3.13 between the total energy

$$U = E_{\text{pot}}(R) + \frac{J(J+1)\hbar^2}{2\mu R^2} + \frac{p_R^2}{2\mu} = E_{\text{pot}} + E_{\text{rot}} + E_{\text{vib}} \quad (3.77)$$

and the potential curve

$$V_{\text{eff}}(R) = E_{\text{pot}}(R) + \frac{\kappa}{R^2} \quad \text{with} \quad \kappa = \frac{J(J+1)\hbar^2}{2\mu} \quad (3.78)$$

is given by the integral

$$A = \int_{R_1}^{R_2} \left(U - E_{\text{pot}}(R) - \frac{\kappa}{R^2} \right) dR. \quad (3.79)$$

We treat U as a continuous variable and differentiate A with respect to U for constant κ .

The partial derivative

$$\left(\frac{\partial A}{\partial U}\right)_{\kappa} = \int_{R_1}^{R_2} dR = R_2 - R_1 \quad (3.80)$$

gives the change in area A upon changing the total energy U for constant rotational energy (Fig. 3.13b). Differentiation with respect to κ at constant U gives

$$\left(\frac{\partial A}{\partial \kappa}\right)_U = \int_{R_1}^{R_2} \frac{dR}{R^2} = \frac{1}{R_2} - \frac{1}{R_1}. \quad (3.81)$$

This describes the change of the area A at constant total energy U , but changing rotational energy, which implies a change of $E_{\text{pot}}^{\text{eff}}(R)$ (Fig. 3.13c). With the abbreviations

$$f = \frac{1}{2} \left(\frac{\partial A}{\partial U}\right)_{\kappa} = \frac{1}{2}(R_2 - R_1), \quad (3.82a)$$

$$g = \frac{1}{2} \left(\frac{\partial A}{\partial \kappa}\right)_U = \frac{1}{2} \left(\frac{1}{R_2} - \frac{1}{R_1}\right), \quad (3.82b)$$

we obtain from Eq. (3.82) for the classical turning points in the potential $E_{\text{pot}}^{\text{eff}}$ at the term energy $U = E(v, J)$

$$R_1 = \left(\frac{f}{g} + f^2\right)^{1/2} - f; \quad R_2 = \left(\frac{f}{g} + f^2\right)^{1/2} + f. \quad (3.83)$$

If we can determine the quantities f and g from measured energy levels $E(v, J)$, the turning points at these energies can be obtained from Eq. (3.83). The connection between f , g and $E(v, J)$ is given within the WKB approximation by the action integral Eq. (3.68),

$$I = \int p(R) dR = \int \sqrt{2\mu \left(E - E_{\text{pot}}(R) - \frac{\kappa^2}{R^2}\right)} dR = h\left(v + \frac{1}{2}\right),$$

because with the aid of the Euler relation [3.21],

$$U - E_{\text{pot}}^{\text{eff}} = \frac{2}{\pi} \int_{V_{\text{eff}}}^U \left(\frac{U - E}{E - E_{\text{pot}}^{\text{eff}}}\right)^{1/2} dE, \quad (3.84)$$

we can express the area A in terms of the action integral I .

If we substitute the integral Eq. (3.84) into Eq. (3.79) for $(U - V_{\text{eff}})$, we arrive at the double integral

$$A = \frac{2}{\pi} \int_{R_1}^{R_2} \left[\int_{V_{\text{eff}}}^U \left(\frac{U - E}{E - V_{\text{eff}}}\right)^{1/2} dE \right] dR \quad (3.85)$$

for the area A . By exchanging the order of integration, this yields

$$A = \frac{1}{\pi} \int_{U_0}^U \left[(U - E)^{1/2} \int_{R_1}^{R_2} \frac{dR}{(E - E_{\text{pot}}^{\text{eff}})^{1/2}} \right] dE, \quad (3.86)$$

where U_0 is the energy at the minimum of $E_{\text{pot}}^{\text{eff}}$. The integral over R is, according to Eq. (3.69), equal to $\sqrt{2/\mu} dI/dE$. Hence, we obtain for the area

$$\begin{aligned} A &= \sqrt{\frac{2}{\mu\pi^2}} \int_{U_0}^U (U - E)^{1/2} \frac{dI}{dE} dE \\ &= \sqrt{\frac{2}{\mu\pi^2}} \int_0^{I^*} [V - E(I, \kappa)]^{1/2} dI, \end{aligned} \quad (3.87)$$

where I^* is the value of the action integral for which $E(I, \kappa) = U$. The energy $E(I, \kappa)$ of the vibration–rotation levels can be obtained from the Dunham expansion Eq. (3.25) by inserting I/h for $(v + \frac{1}{2})$ according to Eq. (3.67). This yields for the term values

$$T(v, J) = \frac{E(I, \kappa)}{hc} = \sum_i \sum_k Y_{ik} \left(\frac{I}{h}\right)^i \left(\frac{\kappa}{h^2}\right)^k. \quad (3.88)$$

Usually, the potential curve $E_{\text{pot}}(R)$ is given for the nonrotating molecule. The term values $T(v, J) = G(v) + F(v, J)$ then reduce to the pure vibrational term values $G(v)$. With $K = 0$, we obtain for f and g in Eq. (3.82),

$$\begin{aligned} f(U) &= \left(\frac{\partial A}{\partial U}\right)_\kappa = \sqrt{\frac{1}{2\mu\pi^2}} \int_0^{I^*} \frac{dI}{\sqrt{U^* - G(I)}} \\ &= \sqrt{\frac{h^3}{2\mu\pi^2 c}} \int_0^{U^*} \frac{dv}{\sqrt{U^* - G(v)}}, \end{aligned} \quad (3.89a)$$

$$\begin{aligned} g(U) &= \left(\frac{\partial A}{\partial \kappa}\right)_U = \sqrt{2\mu/m^2} \int_0^{I^*} \frac{\left(\frac{\partial E}{\partial \kappa}\right) dI}{\sqrt{U - E(I, \kappa)}} \\ &= 8\pi \sqrt{\frac{2\mu c}{h}} \int_0^{U^*} \frac{B_v dv}{\sqrt{U^* - G(v)}}. \end{aligned} \quad (3.89b)$$

One problem in the computation of these integrals is caused by the singularity of the integrand at the upper integration limit $G(v) = U^*$. Below the singularity, the numerical integration is usually carried out using the standard Simpson method, while the last part up to the zero point of the denominator, which yields large contributions to the integral, is calculated using a Gaussian quadrature [3.22, 3.23].

The quantities

$$G(v) = \sum_i Y_{i0} \left(v + \frac{1}{2}\right)^i = \sum Y_{i0} \left(\frac{I}{h}\right)^i \quad (3.90)$$

$$B_v = \sum_i Y_{i1} \left(v + \frac{1}{2}\right)^i = \sum Y_{i1} \left(\frac{I}{h}\right)^i \quad (3.91)$$

are determined from the Dunham expansion for the nonrotating molecule ($J = 0$), where the Dunham coefficients Y_{i0} and Y_{i1} are calculated from a least-squares fit of the measured term values $T(v, J)$ in Eq. (3.66).

Although the RKR method is based on a first-order WKB approximation, it turns out that it is the most accurate of all methods for the determination of molecular potential curves discussed until now. This can be rationalized as follows: In the vicinity of the potential minimum, the WKB term values are exact. Close to the dissociation limit, for large v , the motion of the vibrating nuclei resembles the classical vibrational motion (see Fig. 3.6), and the WKB approximation, being semiclassical, should also be reliable in this region. As the RKR procedure involves an integration from the potential minimum to the highest measured energy levels, the WKB approximation suits this method well [3.11]. From the RKR potentials, the molecular centrifugal constants can be obtained [3.24].

3.6.5

The Inverted Perturbation Approach

All methods for the determination of potential curves discussed up to now use a set of molecular constants (for example, the Dunham coefficients Y_{ik}) that are determined by a least-squares fit to measured term values $T(v, J)$. With the aid of this set of constants, the potential $E_{\text{pot}}(R)$ is determined, either through a power series expansion, the coefficients of which are related to the molecular constants (Dunham expansion), or through calculation of the classical turning points R_i of the vibration and point-to-point construction of the potential curve (RKR procedure).

The individual molecular constants Y_{ik} are not uniquely determined in general, because there exist correlations between them, the degree of which depends on the number of measured term values. For example, the value of the rotational constant $B_e \approx Y_{01}$ that is obtained from a fit to a set of measured term values depends on the number of centrifugal constants Y_{0k} ($k = 2, 3, \dots$) included in the fit. The same is true for the vibrational constants. As discussed in Sect. 3.5.2, the Dunham coefficients are primarily fit parameters. Their physical interpretation as vibrational or rotational constants depends on the form of the potential employed.

To ensure the uniqueness of the molecular constants and to provide them with a well-defined physical meaning, we need to find constants which do not only allow one to reproduce measured term values and predict unknown ones, but which also adhere

to the boundary conditions that are imposed by the Hamiltonian of the molecular system under consideration. The *inverted perturbation approach* (IPA) discussed in this section, first suggested by Kosman and Hinze [3.25], is based on the variational principle and obeys the above-mentioned requirements much better than all other methods discussed up to now. It was further developed by Vidal [3.26] into a numerical procedure for the accurate determination of molecular constants and potential curves. Its superiority over the RKR procedure has been demonstrated in several investigations [3.27, 3.28]. The following outline is based on the presentation in [3.26].

The IPA procedure uses an optimization method for the rotation-free potential $E_{\text{pot}}(R)$, which is determined by the Schrödinger equation (3.22) of the nonrotating molecule,

$$H_0\Psi = E\Psi \quad \text{with} \quad H_0 = \frac{-\hbar^2}{2m} \frac{d^2}{dR^2} + E_{\text{pot}}(R). \quad (3.92a)$$

The rotating molecule is described by the Schrödinger equation of the vibrating rotor,

$$(H_0 + H_{\text{rot}})\Psi_{(v,J)}(R) = E(v,J) \times \Psi_{(v,J)}(R) \\ \text{with} \quad H_{\text{rot}} = \frac{\hbar^2 J(J+1)}{2\mu} \frac{1}{R^2}. \quad (3.92b)$$

Using a variational procedure, $E_{\text{pot}}(R)$ is now optimized until the measured energies $E(v,J)$ agree with the values calculated from Eq. (3.92b), in a least-squares sense, within predefined limits.

We start from the ansatz

$$E_{\text{pot}}(R) = E_{\text{pot}_0}(R) + \Delta E_{\text{pot}}(R), \quad (3.93)$$

where $E_{\text{pot}_0}(R)$ is the *starting-point potential* (e.g., the RKR potential determined from the Dunham coefficients) and $\Delta E_{\text{pot}}(R)$ is a correction term. The correction $\Delta E_{v,J}$ of the energies is obtained from a first-order perturbation calculation through

$$\Delta E_{v,J} = \left\langle \Psi_{v,J}^{(0)} \left| \Delta E_{\text{pot}}(R) \right| \Psi_{v,J}^{(0)} \right\rangle, \quad (3.94)$$

where the *unperturbed* wavefunctions $\Psi^{(0)}$ are solutions of the starting-point equation (3.92b)

$$(H_0^{(0)} + H_{\text{rot}})\Psi_{v,J}^{(0)} = E_{v,J}^{(0)}\Psi_{v,J}^{(0)} \quad \text{with} \quad H_0^{(0)} = -\frac{\hbar^2}{2\mu} \frac{d^2}{dR^2} + E_{\text{pot}_0}(R). \quad (3.95)$$

In contrast to the usual perturbational method, where energy corrections ΔE are calculated for a given perturbation $\Delta E_{\text{pot}}(R)$, we use here the inverse procedure to calculate $\Delta E_{\text{pot}}(R)$ from the energy differences

$$\Delta E_{v,J} = E_{v,J}^{\text{exp}} - E_{v,J}^{(0)}$$

between the experimentally measured values $E_{v,J}^{\text{exp}}$ and the energies $E_{v,J}^{(0)}$ calculated from the starting-point equation (3.92). If the starting-point potential $E_{\text{pot}}(R)$ is already sufficiently good, a first-order perturbation calculation suffices to determine $\Delta E_{\text{pot}}(R)$, because in this case the higher orders contribute so little that they can be neglected within experimental accuracy. This can be developed into an iteration method by using the new potential $E_{\text{pot}}(R)$ obtained in the first approximation step as starting-point potential for the second step, etc. The functional form chosen for $\Delta E_{\text{pot}}(R)$ is crucial to achieve a rapid convergence of the iterations. A linear superposition of products of Legendre polynomials $P_i(x)$ and Gaussian functions $\exp[-\alpha(x-x_i)^{2n}]$,

$$V(R) = \sum_i c_i P_i(x) \exp[-\alpha(x-x_i)^{2n}] \quad (3.96)$$

turns out to be optimal for the numerical integration of the Schrödinger equation in the individual iterations. The exponent n is typically in the range $1 \leq n \leq 5$. The argument x of the functions P and the Gaussian functions is determined by the internuclear distance R and the inner and outer turning points $R_1 = R_{\text{min}}$ and $R_2 = R_{\text{max}}$ in the potential $E_{\text{pot}}(R)$ and it is defined as

$$x = \frac{(R - R_e)(R_{\text{max}} - R_{\text{min}})}{(R_{\text{max}} + R_{\text{min}})(R + R_e) - 2R_{\text{max}}R_{\text{min}} - 2RR_e}, \quad (3.97)$$

so that $x = 1$ for $R = R_{\text{max}}$, $x = -1$ for $R = R_{\text{min}}$ and $x = 0$ for $R = R_e$. For a harmonic potential, $R_e = (R_{\text{max}} + R_{\text{min}})/2$, so that, in this case, $x = 2(R - R_e)/(R_{\text{max}} + R_{\text{min}})$ is a linear interpolation for R_e . From the iteratively determined potential $E_{\text{pot}}(R)$, the term values $G(v)$ can be calculated as eigenvalues of the Schrödinger equation (3.92a) of the nonrotating molecule,

$$G(v) = \frac{E_{v,J=0}}{hc}.$$

The rotational constant B_v is given, according to Eq. (3.41), by the expectation value

$$B_v = \frac{\hbar}{4\pi\mu c} \left\langle \Psi_{v,J=0} \left| \frac{1}{R^2} \right| \Psi_{v,J=0} \right\rangle, \quad (3.98)$$

where the vibrational functions are determined by numerical integration of the Schrödinger equation (3.92a).

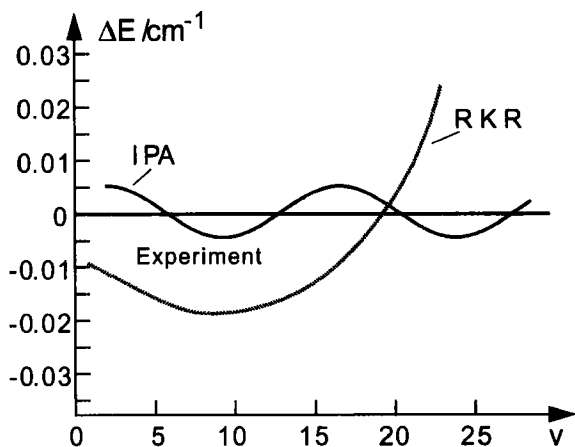


Fig. 3.14 Comparison between measured term values and those calculated with the IPA and RKR methods for the Mg_2 molecule [3.29].

Figure 3.14 displays the differences ΔE between measured and calculated term values for transitions in the $A^1\Sigma_u \leftarrow X^1\Sigma_g^+$ system of Mg_2 for different vibrational quantum numbers v [3.26]. This figure clearly demonstrates the superiority of the IPA procedure over the RKR method.

3.7

Potential Curves at Large Internuclear Distances

For sufficiently large internuclear distances R , where the overlap of the electron clouds of the two nuclei ceases to be significant, a classical view on the interaction between two atoms does not only provide a deeper insight into the physical causes of their interaction, but can also provide a quantitative description of the potential $E_{\text{pot}}(R)$. The question Under which circumstances can two neutral atoms attract each other? will be answered in the course of this discussion by the calculation of the multipole moments of the atomic charge distributions. When combined with quantum-theoretical computations of these charge distributions, such a *semiclassical* method allows an accurate determination of the potential $E_{\text{pot}}(R)$ for large R .

This procedure is especially important if the energy levels $E(v, J)$ cannot be measured up to the dissociation limit. In these cases, the RKR or IPA procedures to determine the potential work only up to the highest measured energy and hence up to a maximum internuclear distance R_{max} in the potential $V(R)$. For $R > R_{\text{max}}$, the measured part of the potential can be extrapolated accurately using such semiclassical methods.

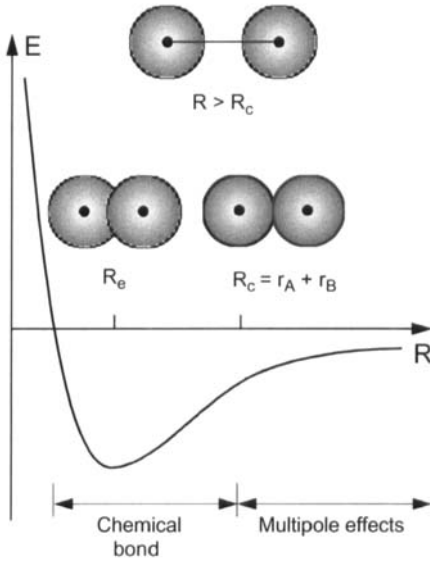


Fig. 3.15 Regions of internuclear distances with chemical bonding for $R < R_c$ and long-range multipole interactions for $R > R_c$.

The method of multipole expansion, based on classical electrodynamics, is not applicable in the region $R < R_c$ below a critical internuclear distance R_c , when the overlap of the atomic electron clouds leads to exchange effects and makes a quantum-mechanical treatment unavoidable (Fig. 3.15).

3.7.1

Multipole Expansion

We consider the potential $E_{\text{pot}}(P)$ at point P , created by a distribution of point charges $q_i(r_i)$ (Fig. 3.16). If the distance R between P and the center of charge S is large compared with all occurring r_i , we can expand $E_{\text{pot}}(R, r_i)$ in a convergent Taylor

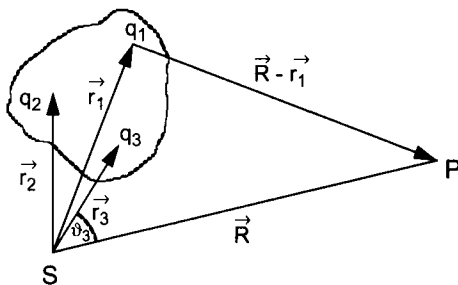


Fig. 3.16 Multipole expansion.

series with successively decreasing terms,

$$\begin{aligned}
 E_{\text{pot}}(P) &= \frac{1}{4\pi\epsilon_0} \sum_i \frac{q_i}{|\mathbf{R} - \mathbf{r}_i|} = \frac{1}{4\pi\epsilon_0} \sum_i \frac{q_i}{(R^2 + r_i^2 - 2Rr_i \cos \theta_i)^{1/2}} \\
 &\approx \frac{1}{4\pi\epsilon_0 R} \sum_i q_i \left[1 + \frac{r_i}{R} \cos \theta_i + \frac{1}{2} \frac{r_i^2}{R^2} (3 \cos^2 \theta_i - 1) + \dots \right] \\
 &= \frac{q}{4\pi\epsilon_0 R} + \frac{\mathbf{p} \times \hat{\mathbf{R}}_0}{4\pi\epsilon_0 R^2} + \frac{1}{2} \frac{\tilde{Q}}{4\pi\epsilon_0 R^3} + \dots \quad (3.99) \\
 &= \text{monopole} + \text{dipole} + \text{quadrupole} + \text{higher terms} ,
 \end{aligned}$$

where

$$q = \sum_i q_i \quad \text{is the total charge} ,$$

$$\mathbf{p} = \sum_i q_i \mathbf{r}_i \quad \text{is the total dipole moment} ,$$

$$\tilde{Q} = \sum_i q_i [3(\hat{\mathbf{R}}_0 \mathbf{r}_i)^2 - r_i^2] \quad \text{is the quadrupole moment}$$

of the complete charge distribution.

For neutral atoms, $\sum q_i = 0$, and the first term in Eq. (3.99) is zero. In the absence of external fields, atoms possess, averaged over time, no permanent electric dipole moment, and therefore the second term also vanishes. For a spherical symmetric charge distribution, the quadrupole moment is also zero. Thus, the potential

$$E_{\text{pot}}(P) = \sum \frac{C_n}{R^n}$$

created by a neutral atom can only contain terms with $n > 3$.

The interaction between two neutral atoms is due to induced moments, as will be shown in the next section.

3.7.2

Induction Contributions to the Interaction Potential

An atom in an S state possesses, averaged over time, no dipole moment, because the time-averaged charge distribution is spherically symmetric and thus the expectation value of the electric dipole moment is zero,

$$\langle \mathbf{p} \rangle = q \int \Psi^* \mathbf{r} \Psi \, d\tau = 0 .$$

There exists, however, at each time an instantaneous nonvanishing dipole moment $\mathbf{p}(t)$ that changes its direction continuously so that its time-average vanishes. For example, for the hydrogen atom in the 1S state, $\mathbf{p}(t) = -e\mathbf{r}(t)$, where $\mathbf{r}(t)$ is the vector from the nucleus to the electron (Fig. 3.17).

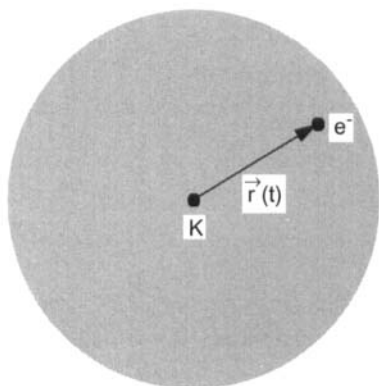


Fig. 3.17 Instantaneous and time-averaged electric dipole moment of an atom in a S state.

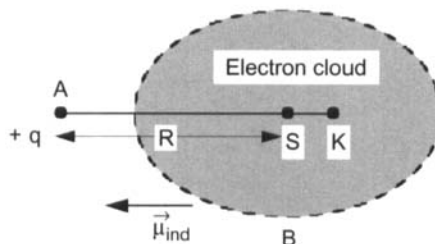


Fig. 3.18 Induced dipole moment in the electric field of a point charge.

In an external electric field \mathbf{E} , the energy $W = \mathbf{p}(t) \cdot \mathbf{E}$ will change almost randomly, because the direction of $\mathbf{p}(t)$ changes, but orientations of \mathbf{p} with lower energies are favored over those with higher energies. Therefore the time-average of $\mathbf{p}(t)$ does not vanish, and an *induced* dipole moment

$$\boldsymbol{\mu}_{\text{ind}} = \alpha \mathbf{E}, \quad (3.100)$$

occurs, with a magnitude proportional to the strength of the external field. We will elucidate this for a few examples.

3.7.2.1 Point-charge-induced Dipole (Ion-Atom Interaction)

The Coulomb field

$$\mathbf{E}_A = \frac{q}{4\pi\epsilon_0 R^2} \hat{\mathbf{R}}_0$$

of a point charge q at point A induces a polarization in a neutral atom B at a distance R from A. The center of the distribution of negative charges is shifted with respect to the positive charge in the nucleus (Fig. 3.18). This shift, which is proportional to the strength of the electric field at the location of atom B, leads to an induced dipole moment

$$\boldsymbol{\mu}_{\text{ind}} = +\alpha_B \mathbf{E}_A = +\frac{q\alpha_B}{4\pi\epsilon_0 R^2} \hat{\mathbf{R}}_0. \quad (3.101)$$

The interaction potential between an ion A with charge q and the induced dipole moment of the atom B,

$$E_{\text{pot}}(\text{AB}) = -\boldsymbol{\mu}_{\text{ind}} \cdot \mathbf{E}_A = -\alpha_B \left(\frac{q}{4\pi\epsilon_0 R^2} \right)^2 = -\frac{C}{R^4}, \quad (3.102)$$

leads to a negative energy and thus to an attraction that decreases as R^{-4} .

3.7.2.2 Interaction Between Two Neutral Atoms

Isolated neutral atoms have a total charge $q = 0$ and the time-average of a possibly occurring instantaneous electric dipole moment is also zero. However, if two atoms A and B approach each other, the instantaneous dipole moment $\mu_A(t)$ of atom A creates a field

$$E_A(B) = \frac{1}{4\pi\epsilon_0 R^3} \mu_A \cdot \hat{R}_0 \quad (3.103)$$

at the location of atom B (Fig. 3.19), which induces a dipole moment $\mu_{\text{ind}}(B) = \alpha_B E_A$ in atom B. This dipole moment in turn creates an electric field $E_B(A)$ at the location of atom A, which induces a time-averaged dipole moment $\mu_A = \alpha_A E_B(A)$ in atom A (Fig. 3.20). The interaction energy between the two induced dipoles μ_A^{ind} and μ_B^{ind} is then

$$E_{\text{pot}} = -\mu_B \cdot E_A = -\frac{\mu_B \mu_A}{4\pi\epsilon_0 R^3} = -\mu_A \cdot E_B. \quad (3.104)$$

Inserting $\mu_A = \alpha_A E_B$ and $\mu_B = \alpha_B E_A$ yields

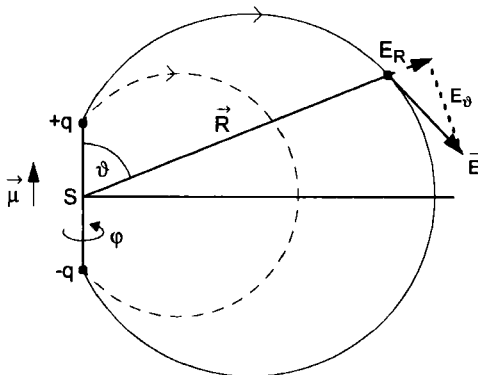
$$E_{\text{pot}} = -C \frac{\alpha_A \alpha_B}{R^6} = -\frac{C_6}{R^6} \quad \text{with} \quad C_6 = \frac{\alpha_A \alpha_B}{(4\pi\epsilon_0)^2}. \quad (3.105)$$

Hence, the interaction between two neutral atoms without permanent dipole moments (*van der Waals interaction*) decreases with $1/R^6$!

If we write the interaction potential between the atoms as a power series

$$E_{\text{pot}}(R) = -\sum_{n=0}^{\infty} \frac{C_n}{R^n},$$

the term in R^{-6} is the first nonvanishing term, describing the interaction between two induced dipoles.



$$E_R = \frac{2\mu \cdot \cos \vartheta}{4\pi\epsilon_0 \cdot R^3} \quad E_\vartheta = \frac{\mu \cdot \sin \vartheta}{4\pi\epsilon_0 \cdot R^3}; \quad E_\varphi = 0$$

Fig. 3.19 Electric field of a dipole.

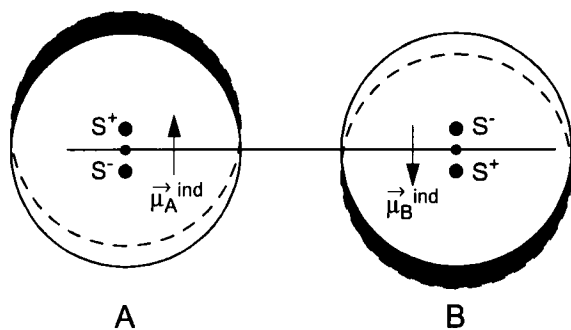


Fig. 3.20 Mutual induction of two atoms without permanent dipole moments.

If we take into account induced quadrupole moments, terms with R^{-8} and R^{-10} appear. Because of the mirror symmetry of the system, only even powers of R occur for identical atoms.

The interaction potential between neutral atoms at large distances, where the overlap of the electron clouds can be neglected, can then be written as

$$E_{\text{pot}}(R) = - \sum_{n=6}^{\infty} \frac{C_n}{R^n}. \quad (3.106)$$

The interaction is attractive, as can be seen from the negative sign in Eq. (3.106). It is a short-range interaction because it decreases at least as $1/R^6$. The atomic polarizabilities are usually determined experimentally, but high-precision *ab initio* values are also available.

Figure 3.21 compares the different contributions to the interaction between two atoms in their S states at large internuclear distances for the ground state potential of the Cs_2 molecule. Curve (a) displays the potential if only the quantum-mechanical exchange term V_{ex} is included. We see that this term plays virtually no role for distances larger than about 1 nm. For curve (b), the induced dipole–dipole interaction $-V_6 = -C_6/R^6$ is additionally included, for curve (c) also the quadrupole interaction $-V_8 = -C_8/R^8$, for curve (d) also the term C_{10}/R^{10} . If one goes even further and includes also the C_{12}/R^{12} contribution in Eq. (3.106), the calculated potential curve and the vibrational term values $G(v'', J'' = 0)$ derived from it agree perfectly with the experimental results within experimental accuracy.

Remark: *Even for the long-range interactions, the quantum-mechanical description is more accurate than the power-series-based multipole model, because the wavefunctions of the two atoms provide of course more accurate electronic charge distributions. The quantum-mechanical calculation is much more laborious, however. For example, the van der Waals interaction is computed by a second-order perturbation calculation with the unperturbed atomic wavefunctions [3.30, 3.31].*

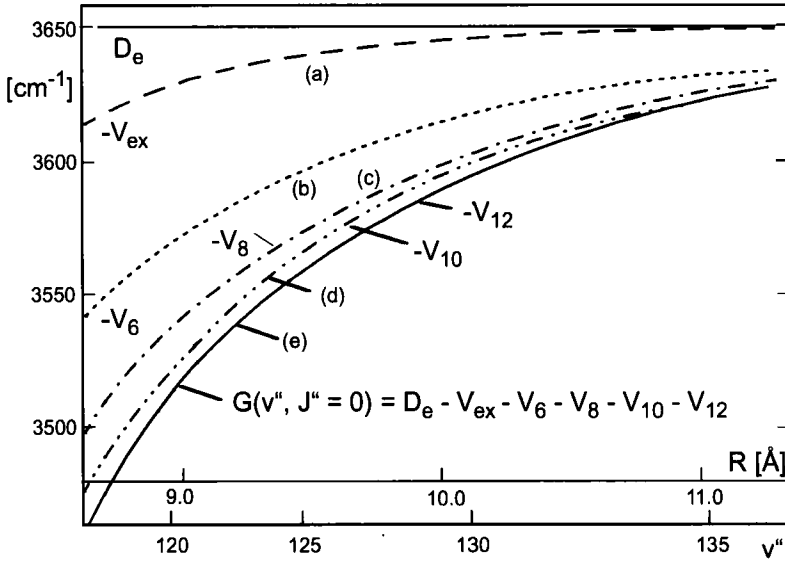


Fig. 3.21 Potential curves of the Cs_2 molecule at large internuclear distances.

3.7.3

Lennard-Jones Potential

The complete range of the interaction potential between two neutral atoms can be described by the empirical Lennard-Jones potential (Fig. 3.21)

$$E_{\text{pot}}(R) = \frac{a}{R^{12}} - \frac{b}{R^6}, \tag{3.107}$$

where the constants a and b are adjustable parameters depending on the interacting atoms.

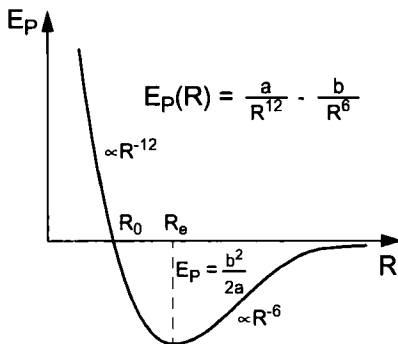


Fig. 3.22 Lennard-Jones potential.

From Eq. (3.107) we see that $E_{\text{pot}}(R) = 0$ for $R = R_0 = (a/b)^{1/6}$ (Fig. 3.22). The potential possesses a minimum for $dE_{\text{pot}}/dR = 0$, which yields for the distance R_e at the minimum

$$R_e = \left(\frac{2a}{b}\right)^{1/6} = R_0 \times 2^{1/6}. \quad (3.108)$$

The bond energy of the molecule is then (neglecting zero-point energy)

$$E_B = -E_{\text{pot}}(R_e) = \frac{b^2}{2a}. \quad (3.109)$$

The coefficients a and b are adjusted for the specific molecule so that the potential resembles the experimentally determined curve as closely as possible.

More detailed accounts on the long-range part of the potential for diatomic molecules can be found in [3.30–3.32].

4 Spectra of Diatomic Molecules

Up to now we have discussed only the possible energy levels of molecules and the symmetries of the corresponding wavefunctions. In this chapter we will now turn to the central topic in molecular spectroscopy: the explanation and interpretation of molecular spectra and their importance for the investigation of molecular structure.

The relation $h\nu_{ik} = E_i - E_k$ associates a defined frequency ν_{ik} to each possible combination of energy levels E_i and E_k of a molecule. Whether this frequency is indeed observable in the spectrum depends on a number of selection rules, which decide, based on symmetry considerations, between which combinations of energy levels E_i , E_k radiating transitions may occur, the so-called *allowed* transitions. The *intensity* of an allowed spectral line depends on the occupation numbers N_i of the absorbing and N_k of the emitting molecular level, on the probability for a transition $|k\rangle \rightarrow |i\rangle$ and, in the case of stimulated transitions, on the intensity and polarization of the incident light.

In this chapter, we will provide answers to the following questions:

1. Between which pairs of molecular states can transitions take place by absorption or emission of electromagnetic radiation?
2. What is the *transition probability* and what are the factors by which it is determined?
3. What are the spectral profiles of emission or absorption lines for such a transition?

Although we will answer these questions for diatomic molecules in this chapter, the results can be transferred with only minor modifications to polyatomic molecules (see Ch. 8).

First, we will discuss the concept of *transition probability* and elucidate its connection with the wavefunctions of the molecular states involved in the transition. This will lead us to *dipole matrix elements* and symmetry selection rules. Section 4.3 discusses the spectral profiles of molecular transitions and explains the different reasons for linewidths. Finally, we will discuss *two-photon transitions*, Raman spectra and two-photon absorption as illustrative examples.

4.1

Transition Probabilities

We will start with a basic definition of transition probabilities, first introduced by Einstein, and then elucidate the connection between transition probabilities and the molecular wavefunctions. For more detailed derivations of this approach in the *semi-classical approximation*, we refer the reader to [2.2, 2.3, 4.1, 4.2].

4.1.1

Einstein Coefficients

We consider a molecule with the energy levels E_i and E_k in an electromagnetic radiation field with spectral energy density $\rho(\nu)$ (energy per unit volume and frequency interval). The probability $(dW_{ik}/dt)_{\text{abs}}$ that this molecule absorbs a photon $h\nu = (E_k - E_i)$ and undergoes a transition from its state $|i\rangle$ to the energetically higher state $|k\rangle$ (Fig. 4.1) is proportional to the number of photons with frequency ν incident on the molecule per unit time, which in turn is proportional to the spectral radiation density $\rho(\nu)$,

$$\left(\frac{dW_{ik}}{dt}\right)_{\text{abs}} = B_{ik}\rho(\nu). \quad (4.1)$$

The constant B_{ik} is the so-called *Einstein coefficient of absorption*; it depends on the specific transition $|i\rangle \rightarrow |k\rangle$ of the corresponding molecule.

Analogously, the probability for a molecule in the excited state $|k\rangle$ undergoing a transition into the lower state $|i\rangle$ by *stimulated emission* is

$$\left(\frac{dW_{ki}}{dt}\right)_{\text{stim}} = B_{ki}\rho(\nu). \quad (4.2)$$

In this process, the incident photon stimulates emission of another photon from the molecule. The constant B_{ki} is the Einstein coefficient of stimulated emission. A molecule in the excited state $|k\rangle$ can also relax to a lower state *spontaneously*, that

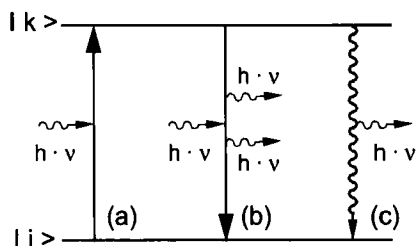


Fig. 4.1 Stimulated and spontaneous transitions. a) Absorption, b) stimulated emission, c) spontaneous emission.

is, without interacting with an external radiation field, by emitting a fluorescence photon $h\nu = (E_k - E_i)$. The probability for such a spontaneous emission is independent of the radiation field,

$$\left(\frac{dW_{ki}}{dt}\right)_{\text{spont}} = A_{ki}, \quad (4.3)$$

where A_{ki} is the *Einstein coefficient of spontaneous emission*.

If molecule and radiation field are in thermal equilibrium, the rate of absorption processes must be equal to the rate of emission processes per unit time, because otherwise no stationary population densities N_i and N_k would exist. It therefore follows that

$$N_i B_{ik} \rho(\nu) = N_k (A_{ki} + B_{ki} \rho(\nu)). \quad (4.4)$$

The ratio of the population densities is given by the Boltzmann distribution,

$$\frac{N_k}{N_i} = \frac{g_k}{g_i} e^{-(E_k - E_i)/k_B T}, \quad (4.5)$$

where $g = (2J + 1)$ is the statistical weight of a molecular state with the total angular momentum J and $k_B = 1.38 \times 10^{-23} \text{ J K}^{-1}$ is the Boltzmann constant.

If we substitute Eq. (4.5) with $(E_k - E_i) = h\nu$ into Eq. (4.4) and solve for $\rho(\nu)$, we obtain

$$\rho(\nu) = \frac{A_{ki}/B_{ki}}{\frac{g_i}{g_k} \frac{B_{ik}}{B_{ki}} e^{h\nu/k_B T} - 1}. \quad (4.6a)$$

Also, a thermal radiation field obeys the Planck law,

$$\rho(\nu) = \frac{8\pi h\nu^3}{c^3} \times \frac{1}{e^{h\nu/k_B T} - 1}. \quad (4.6b)$$

Equations (4.6a) and (4.6b) must hold for arbitrary temperatures T and for all frequencies ν . We can therefore compare coefficients and obtain the important relations between the Einstein coefficients,

$$\begin{aligned} B_{ik} &= \frac{g_k}{g_i} B_{ki}, \\ A_{ki} &= \frac{8\pi h\nu^3}{c^3} B_{ki}. \end{aligned} \quad (4.7)$$

Note:

1. The quantities (dW_{ik}/dt) indicate probabilities per unit time; they can be larger than one! For example, $A_{ik} \approx 10^8 \text{ s}^{-1}$ for the sodium $3p \rightarrow 3s$ transition.

2. If the spectral energy density $\rho(\nu)$ is given in angular frequencies $\omega = 2\pi\nu$, $\rho(\omega)$ decreases by a factor of 2π , because the interval $d\omega = 1$ corresponds to the interval $d\nu = 2\pi$ and $\rho(\omega) d\omega = \rho(\nu) d\nu$ must hold. As the probability of stimulated emission $B_{ki}^{(\omega)} \rho(\omega) = B_{ki}^{(\nu)} \rho(\nu)$ does not depend on the choice of a specific unit for the frequency, the relation $B_{ki}^{(\omega)} = 2\pi B_{ki}^{(\nu)}$ must hold and Eq. (4.7) becomes

$$A_{ki} = \frac{\hbar\omega^3}{\pi^2 c^3} B_{ki}^{(\omega)}. \quad (4.7a)$$

The fluorescence radiant power emitted by N_K molecules per unit volume into the solid angle 4π by a transition $|k\rangle \rightarrow |i\rangle$ is

$$P_{ki}^{\text{spont}} = N_K h\nu A_{ki} \propto \nu^4 B_{ki}. \quad (4.8)$$

Although the fluorescence intensity of a single molecular dipole has an angular distribution $I_{\text{fl}}(\theta) \propto \sin^2 \theta$, where θ is the angle between the dipole axis and the direction of observation, the total emission from N molecules with random orientations in space is isotropic.

The absorption of an electromagnetic wave with intensity $I = c\rho$, where $\rho(\nu)$ is the spectral energy density, can be obtained as follows. If an electromagnetic wave of beam cross-section Q and spectral density $\rho(\nu)$ is incident on a sample of molecules in the z direction, the net absorbed power (absorption minus stimulated emission) per unit volume $dV = Q dz$ is

$$P_{ik}^{\text{abs}} = (N_i B_{ik} - N_k B_{ki}) \rho(\nu) h\nu. \quad (4.9)$$

This can be written, using relation Eq. (4.7), $B_{ik} = (g_k/g_i) B_{ki}$, as

$$P_{ik}^{\text{abs}} = \left(N_i - \frac{g_i}{g_K} N_K \right) B_{ik} \rho(\nu) h\nu. \quad (4.9a)$$

For energies $E_K \gg k_B T$, the populations satisfy $N_k \ll N_i$ and the second term in parentheses can be neglected.

Usually, the absorption of a plane wave of intensity $I = c\rho$ (spectral power density per frequency interval $d\nu$ and per unit area) traversing an absorbing medium in the z direction is described by the decrease

$$dI = -\alpha(\nu) I dz \Rightarrow I = I_0 e^{-\alpha z} \quad (4.10)$$

of the intensity $I(z)$ with increasing absorption path length z , where $\alpha(\nu)$ is the frequency-dependent absorption coefficient. The power absorbed on the transition $|i\rangle \rightarrow |k\rangle$ per unit volume $dV = Q dz$ for a cross-section Q of the plane wave is

$$P_{ik}^{\text{abs}} = Q \int \left(\frac{dI}{dz} \right) d\nu = Q \int \alpha(\nu) I d\nu, \quad (4.11)$$

where the integration is over the spectral profile of the absorption line (see Sect. 4.3). If the intensity I of the incident radiation is constant over the frequency range of the spectral line of an absorbing transition, I can be moved outside the integral, and by comparing Eq. (4.9a) and Eq. (4.11) we obtain the relation

$$\int \alpha(\nu) d\nu = \left(N_i - \frac{g_i}{g_k} N_k \right) B_{ik} \rho(\nu) h\nu \tag{4.12}$$

between absorption coefficient and Einstein coefficient. For monochromatic radiation $I(\nu)$, the absorbed power depends on the frequency detuning $(\nu - \nu_{ik})$ if ν_{ik} is the central frequency of the absorption line (see Sect. 4.3).

4.1.2

Transition Probabilities and Matrix Elements

Electrodynamics shows [4.3] that a classical oscillating dipole with an electric dipole moment

$$\mathbf{d} = q\mathbf{r} = d_0 \sin \omega t \tag{4.13}$$

radiates an average power of

$$\bar{P} = \frac{2}{3} \frac{\bar{d}^2 \omega^4}{4\pi\epsilon_0 c^3} \quad \text{with} \quad \bar{d}^2 = \frac{1}{2} d_0^2, \tag{4.14}$$

integrated over all angles ϑ (Fig. 4.2a).

In the quantum-mechanical treatment, the mean value \bar{d} of the electric dipole moment of an atom with an optical electron in a stationary state $(n, l, m_l, m_s) = i$ is described by the expectation value

$$\langle d \rangle = e \langle r \rangle = e \int \psi_i^* \mathbf{r} \psi_i d\tau \tag{4.15}$$

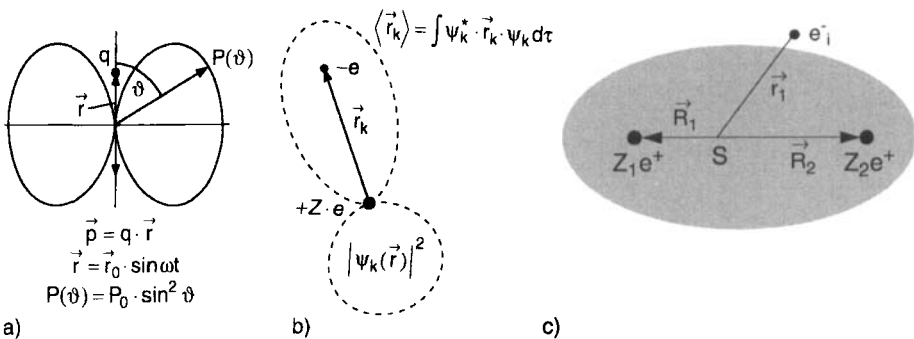


Fig. 4.2 a) Radiation characteristic of a classical dipole. b) Expectation value of d for an atomic p state. c) Electric dipole moment of a diatomic molecule.

(Fig. 4.2b), where the vector \mathbf{r} is the position vector of the electron. The integration is over the spatial coordinates of the electron, that is, $d\tau = dx dy dz$ or, in spherical coordinates, $r^2 dr \sin \vartheta d\vartheta d\varphi$.

For a transition $E_i \rightarrow E_k$, the wavefunctions of both states must contribute to the expectation value $\langle \mathbf{r} \rangle$. We therefore define the expectation value $\mathbf{D}_{ik} = \langle \mathbf{d}_{ik} \rangle$ of the so-called *transition dipole moment* \mathbf{d}_{ik} to be

$$\mathbf{D}_{ik} = e \int \psi_i^* \mathbf{r} \psi_k d\tau, \quad (4.16)$$

where the subscripts i and k are merely shorthand notations for all quantum numbers of the states involved in the transition. Of course, we might as well have used the quantity \mathbf{D}_{ki} , because $|\mathbf{D}_{ik}| = |\mathbf{D}_{ki}|$.

If we replace in Eq. (4.14) the classical average $\overline{d^2}$ by the quantum-mechanical expression

$$\frac{1}{2} (|\mathbf{D}_{ik}| + |\mathbf{D}_{ki}|)^2 = 2 |\mathbf{D}_{ik}|^2, \quad (4.17)$$

we obtain for the average power emitted in the transition $E_i \rightarrow E_k$ by an atom in state E_i

$$\langle P_{ik} \rangle = \frac{4}{3} \frac{\omega_{ik}^4}{4\pi\epsilon_0 c^3} |\mathbf{D}_{ik}|^2, \quad (4.18)$$

which is completely analogous to the classical emitting power of an oscillating dipole if $\langle d^2 \rangle$ is replaced by $2 |\mathbf{D}_{ik}|^2$.

N_i atoms in the state E_i radiate an average power $P = N_i \langle P_{ik} \rangle$ at frequency ω_{ik} .

With the *probability per unit time* A_{ik} that an atom in state E_i undergoes a spontaneous transition to state E_k and emits a photon $h\nu$, the mean power emitted by N_i atoms in the state E_i is

$$\langle P \rangle = N_i A_{ik} h\nu_{ik}. \quad (4.19)$$

The factor A_{ik} is the *Einstein coefficient* of spontaneous emission introduced in the preceding section. Comparison of Eqns. (4.19) and (4.18) yields, together with Eq. (4.16), the relation

$$A_{ik} = \frac{2}{3} \frac{e^2 \omega_{ik}^3}{\epsilon_0 c^3 h} \left| \int \psi_i^* \mathbf{r} \psi_k d\tau \right|^2. \quad (4.20)$$

The probability of spontaneous transitions is thus directly proportional to the squared matrix element. If we know the wavefunctions ψ_i and ψ_k of the states involved in the transition, we can calculate the transition probability A_{ik} from Eq. (4.20), and, using Eq. (4.19), the power emitted by N_i atoms in the state E_i at a frequency ν_{ik} .

The expectation values \mathbf{D}_{ik} for all transitions $|i\rangle \rightarrow |k\rangle$ of an atom can be arranged in a matrix so that its nonzero elements indicate all allowed transitions and their intensities. The \mathbf{D}_{ik} are therefore called *matrix elements*.

Remark: As its classical analog Eq. (4.14), Eq. (4.20) is valid if the wavelength λ is large compared to the diameter of the dipole (dipole approximation). For visible light, this condition is always fulfilled, but not necessarily for X rays, when $\lambda < 1$ nm.

Example

$$\lambda = 500 \text{ nm}, |\mathbf{r}| = 0.5 \text{ nm} \quad \Rightarrow \quad \frac{|\mathbf{r}|}{\lambda} \approx 10^{-3}.$$

As Eqns. (4.7) relate the Einstein coefficients of spontaneous emission A to those of stimulated absorption or emission B , the probabilities of the latter must also be proportional to the square of the matrix element. They must, however, also depend on the intensity of the incident light wave, because the corresponding transition probabilities W_{ik} depend on the spectral energy density $\rho(\nu)$ of the radiation field.

The quantum-mechanical treatment (a time-dependent perturbation calculation, in which the electromagnetic field is treated as a perturbation of the molecule's Hamiltonian) yields, in the dipole approximation, a result for the transition probability of absorption that is completely analogous to the corresponding result of the classical treatment,

$$\left(\frac{dW_{mk}}{dt} \right)_{\text{abs}} = \frac{2\pi e^2}{\hbar^2} |\mathbf{E}_0 \cdot \mathbf{D}_{mk}|^2, \quad (4.21)$$

where \mathbf{E}_0 is the electric field vector of the wave and \mathbf{D}_{mk} is the dipole matrix element for the transition from state $|m\rangle$ to state $|k\rangle$. While for atoms, the matrix element Eq. (4.16) depends only on the position vector \mathbf{r} of the optical electron, in molecules the nuclei with charges Ze can also contribute to the dipole moment. We will now take a closer look at the dipole matrix elements for diatomic molecules.

If we choose a reference frame with the origin at the charge center S of the molecule (Fig. 4.2c), the dipole operator for a diatomic molecule,

$$\begin{aligned} \mathbf{d} &= -e \sum_i \mathbf{r}_i + Z_1 e \mathbf{R}_1 + Z_2 e \mathbf{R}_2 \\ &= \mathbf{d}_{\text{el}} + \mathbf{d}_{\text{nuc}}, \end{aligned} \quad (4.22)$$

is determined by the contributions \mathbf{d}_{el} of the electrons and \mathbf{d}_{nuc} of the nuclei to the dipole moment. The dipole matrix element for a transition from state m to a state k is then

$$\mathbf{D}_{mk} = \int \psi_m^* \mathbf{d} \psi_k \, d\tau_{\text{el}} \, d\tau_{\text{nuc}}, \quad (4.23)$$

where the integration $d\tau_{\text{nuc}}$ is over the configuration space of the two nuclei and $d\tau_{\text{el}}$ over the configuration space of the electrons.

Note: The vector E_0 is defined in the laboratory frame (X, Y, Z) , whereas D_{mk} is defined in the molecule-fixed frame (x, y, z) . For the explicit calculation of Eq. (4.21) we must therefore introduce a relation between the two reference frames with the aid of the Euler angles (see Sect. 4.2.1).

4.1.3

Matrix Elements in the Born–Oppenheimer Approximation

Within the BO approximation (Sect. 2.1.3), we can separate the total wavefunction into a product

$$\Psi = \psi_{\text{el}} \psi_{\text{nuc}} = \phi \times \chi \quad (4.24)$$

of an electronic wavefunction $\psi_{\text{el}} = \phi(\mathbf{r}, \mathbf{R})$ and a nuclear wavefunction $\psi_{\text{nuc}} = \chi(\mathbf{R})$. Now Eq. (4.23) can be written as

$$\begin{aligned} D_{mk} &= \int \phi_m^* \chi_m^* (\mathbf{d}_{\text{el}} + \mathbf{d}_{\text{nuc}}) \phi_k \chi_k \, d\tau_{\text{el}} \, d\tau_{\text{nuc}} \\ &= \int \chi_m^* \left[\int \phi_m^* \mathbf{d}_{\text{el}} \phi_k \, d\tau_{\text{el}} \right] \chi_k \, d\tau_{\text{nuc}} + \int \chi_m^* \mathbf{d}_{\text{nuc}} \left[\int \phi_m^* \phi_k \, d\tau_{\text{el}} \right] \chi_k \, d\tau_{\text{nuc}} . \end{aligned} \quad (4.25)$$

Now we must distinguish two cases:

- (a) The levels m and k belong to the same electronic state, that is, the dipole transition occurs between two vibration–rotation levels within one electronic state. Then $\phi_m = \phi_k$, and the first term in Eq. (4.25) vanishes, because the integrand in the integral over $d\tau_{\text{el}}$, i.e., $\phi_m^* \mathbf{d}_{\text{el}} \phi_m = e \phi_m^* \mathbf{r} \phi_m = e r |\phi_m|^2$, is an odd function of the integration variables so that the integral over the whole electronic configuration space vanishes. As the electronic wavefunctions ϕ_i are orthonormal the integral in the second term is $\int \phi_m^* \phi_m \, d\tau_{\text{el}} = 1$. Hence, the matrix element is, in this case

$$D_{mk} = \int \chi_m^* \mathbf{d}_{\text{nuc}} \chi_k \, d\tau_{\text{nuc}} . \quad (4.26)$$

The matrix element for vibrational–rotational transitions within the same electronic state is determined by the dipole moment \mathbf{d}_{nuc} and the wavefunctions χ of the nuclear framework.

- (b) For transitions between different electronic states ($\phi_m \neq \phi_k$), the integral in the second term in Eq. (4.25) vanishes because of the orthonormality of the electronic wavefunctions,

$$\int \phi_m^* \phi_k \, d\tau_{\text{el}} = \delta_{mk} = 0 \text{ for } m \neq k .$$

The matrix element is then

$$\begin{aligned} D_{mk} &= \int \chi_m^* \left[\int \phi_m^* \mathbf{d}_{\text{el}} \phi_k \, d\tau_{\text{el}} \right] \chi_k \, d\tau_{\text{nuc}} \\ &= \int \chi_m^* \mathbf{D}_{mk}^{\text{el}} \chi_k \, d\tau_{\text{nuc}} , \end{aligned} \quad (4.27)$$

where

$$\mathbf{D}_{mk}^{\text{el}}(\mathbf{R}) = \int \phi_m^* \mathbf{d}_{\text{el}} \phi_k \, d\tau_{\text{el}} \quad (4.28)$$

is the electronic part of the matrix element, which in general depends also on the nuclear coordinates \mathbf{R} because $\phi = \phi(\mathbf{r}, \mathbf{R})$.

Matrix elements of electronic transitions depend on the dipole moment of the excited electron and both the electronic and the nuclear wavefunctions.

4.2

Structure of the Spectra of Diatomic Molecules

As mentioned at the beginning of this chapter, the frequencies ν (or the wavenumbers $\tilde{\nu} = 1/\lambda$) of the lines in a molecule's absorption or emission spectrum depend on the term values of the molecular energy levels involved in the transitions. Their intensities are determined by matrix elements. Measurements of line positions and intensities allow therefore the determination of energy levels and transition probabilities. We will now discuss the structure of the spectra of diatomic molecules based on the arguments from the preceding section.

4.2.1

Vibration–Rotation Spectra

We start with case (a) as discussed above, that is, with transitions within the same electronic state. Such transitions form the vibration–rotation spectrum located in the infrared region of the electromagnetic spectrum, or the pure rotational spectrum located in the microwave region.

If we substitute Eq. (4.22) for the dipole operator \mathbf{d}_{nuc} into the expression for the matrix element Eq. (4.26), we obtain

$$\mathbf{D}_{mk} = e \int \chi_m^* (Z_1 \mathbf{R}_1 + Z_2 \mathbf{R}_2) \chi_k \, d\tau_{\text{nuc}} . \quad (4.29)$$

For homonuclear molecules with nuclear charges $Z_1 e = Z_2 e$ and atomic masses $M_1 = M_2$, $\mathbf{R}_1 = -\mathbf{R}_2$. Hence, from Eq. (4.29) it follows that $\mathbf{D}_{mk} = \mathbf{0}$. In other words, *homonuclear molecules possess, in the dipole approximation, no allowed vibration–rotation transitions!* Hence, they show neither pure rotational nor vibration–rotation spectra.

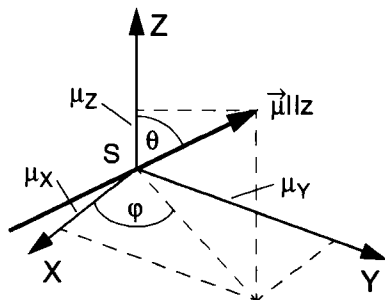


Fig. 4.3 Orientation of the molecular axis (z axis) in the laboratory frame X, Y, Z .

We will now turn to the discussion of the general case of heteronuclear diatomic molecules, when $D_{mk} \neq 0$. The dipole moment Eq. (4.29) is directed along the molecular axis. The z axis of a rotating diatomic molecule encloses the polar angle θ with the Z axis and the azimuthal angle φ with the X axis of a laboratory frame with its origin at the center of mass S . The dipole moment vector \mathbf{d}_{nuc} of the nuclear framework,

$$\begin{aligned} \mathbf{d}_{\text{nuc}} &= e(Z_1 \mathbf{R}_1 + Z_2 \mathbf{R}_2) = e(Z_1 \mathbf{R}_1 - Z_2 \mathbf{R}_2) \mathbf{R}_0 \\ &= |\mathbf{d}_{\text{nuc}}| \cdot \hat{\mathbf{R}}_0, \end{aligned} \quad (4.30)$$

is directed along the molecular axis. To express it in the coordinates of the laboratory frame (in which we observe emission or absorption) we separate \mathbf{d}_{nuc} into a product of its magnitude $|\mathbf{d}_{\text{nuc}}| = (Z_1 \mathbf{R}_1 - Z_2 \mathbf{R}_2)e$ and the unit vector

$$\hat{\mathbf{R}}_0 = \{\sin \theta \cos \varphi, \sin \theta \sin \varphi, \cos \theta\}, \quad (4.31)$$

which defines the orientation of the molecular axis relative to the laboratory frame (X, Y, Z) , in which the vector \mathbf{E}_0 of the electromagnetic wave $\mathbf{E} = \mathbf{E}_0 e^{i\omega t - \mathbf{k} \cdot \mathbf{R}}$ is defined (Fig. 4.3).

Generally, infrared spectra are observed in absorption rather than emission. This can be traced to a number experimental subtleties. For example, the spontaneous lifetime of excited vibrational levels is rather long, and hence the excited molecule could diffuse away from the observation region before emitting a photon.

The transition probability during the absorption of an electromagnetic wave with electric field strength \mathbf{E}_0 is, according to Eq. (4.21),

$$\left(\frac{dW_{mk}}{dt} \right)_{\text{abs}} = \frac{2\pi e^2}{\hbar^2} \left| \int \chi_m^* (Z_1 \mathbf{R}_1 - Z_2 \mathbf{R}_2) \mathbf{E}_0 \cdot \hat{\mathbf{R}}_0 \chi_k d\tau_{\text{nuc}} \right|^2. \quad (4.32)$$

If we neglect the interaction between vibration and rotation of the molecule, the normalized nuclear wavefunction χ_{nuc} can be separated according to Eq. (3.4) into a product

$$\chi_{\text{nuc}}(R, \theta, \varphi) = S(R)Y(\theta, \varphi) \quad (4.33)$$

of the vibrational function $\psi_{\text{vib}}(R) = RS(R)$ (see Eq. (3.25)), which depends only on the magnitude $R = |\mathbf{R}_1| + |\mathbf{R}_2|$ of the internuclear distance, and the wavefunction $\psi_{\text{rot}}(\theta, \varphi) = Y(\theta, \varphi)$ of a rigid rotor, which depends only on the angles θ and φ . Correspondingly, the volume element $d\tau_{\text{nuc}}$ can be written as

$$\begin{aligned} d\tau_{\text{nuc}} &= d\tau_{\text{vib}} d\tau_{\text{rot}} \\ &= R^2 dR \sin\theta d\theta d\varphi. \end{aligned}$$

With $R_1/R_2 = M_2/M_1$ and $R = R_1 + R_2$ we obtain furthermore

$$Z_1 R_1 - Z_2 R_2 = \frac{Z_1 M_2 - Z_2 M_1}{M_1 + M_2} R.$$

Now we can write the matrix element D_{mk} in Eq. (4.29) in the laboratory frame as a product of two integrals

$$\begin{aligned} D_{mk} &= \frac{Z_1 M_2 - Z_2 M_1}{M_1 + M_2} \left[\int (\psi_{\text{vib}})_m d_{\text{nuc}}(R) (\psi_{\text{vib}})_k dR \right] \\ &\quad \times \left[\int_{\theta, \varphi} (\psi_{\text{rot}})_m (\psi_{\text{rot}})_k \hat{\mathbf{R}}_0 \sin\theta d\theta d\varphi \right], \end{aligned} \quad (4.34)$$

where $\psi_{\text{vib}} = R \times S(R)$ and $\psi_{\text{rot}} = Y(\theta, \varphi)$. The first integral, which is independent of the molecule's orientation in the laboratory frame, describes transitions between different vibrational levels $|m\rangle$ and $|k\rangle$ in the same electronic state, while the second, describing the direction of D_{mk} , describes transitions between two rotational levels. Quantitative calculations and their results for term energies and line intensities can be found in [4.4].

4.2.2

Pure Vibrational Transitions Within an Electronic State

The contribution $d_{\text{nuc}}(R)$ of the nuclear dipole moment can be expanded in a Taylor series

$$d_{\text{nuc}}(R) = d_{\text{nuc}}(R_e) + \frac{d}{dR} (d_{\text{nuc}})|_{R_e} \times (R - R_e) + \dots \quad (4.35)$$

in the displacements $(R - R_e)$ from the equilibrium position. If we substitute this into

the vibrational part of the matrix element Eq. (4.34), we obtain with $C = (Z_1M_2 - Z_2M_1)/(M_1 + M_2)$

$$\begin{aligned} D_{mk}^{\text{vib}} &= C \int (\psi_{\text{vib}}^*)_{\text{m}} d_{\text{nuc}}(R) (\psi_{\text{vib}})_{\text{k}} dR \\ &= C \left[d_{\text{nuc}}(R_e) \int (\psi_{\text{vib}}^*)_{\text{m}} (\psi_{\text{vib}})_{\text{k}} dR \right. \\ &\quad \left. + \frac{d}{dR} (d_{\text{nuc}}) \Big|_{R_e} \int (\psi_{\text{vib}}^*)_{\text{m}} (R - R_e) (\psi_{\text{vib}})_{\text{k}} dR \right]. \end{aligned} \quad (4.36a)$$

As the wavefunctions ψ_{vib} are normalized so that

$$\int (\psi_{\text{vib}}^*)_{\text{m}} (\psi_{\text{vib}})_{\text{k}} = \delta_{mk}, \quad (4.36b)$$

the first term in Eq. (4.36a) yields the static dipole moment $d_{\text{nuc}}(R_e)$ in the state $|m\rangle$ for $m = k$. For $m \neq k$, this term vanishes!

The second term consists of two contributions. The first contribution with the integrand $(\psi_{\text{vib}}^*)_{\text{m}} R (\psi_{\text{vib}})_{\text{k}}$ vanishes for $m = k$ because the integrand is an odd function of R . The second contribution vanishes for $m \neq k$ because of Eq. (4.36b), and yields R_e for $m = k$. We therefore retain only one term in Eq. (4.36a) for transitions $|m\rangle \leftarrow |k\rangle$,

$$D_{mk}^{\text{vib}} = C \frac{d}{dR} (d_{\text{nuc}}) \int (\psi_{\text{vib}}^*)_{\text{m}} R (\psi_{\text{vib}})_{\text{k}} dR. \quad (4.36c)$$

The matrix element for pure vibrational transitions differs from zero only if the dipole moment d_{nuc} depends on the internuclear distance R , that is, if $d(d_{\text{nuc}})/dR \neq 0$.

If we substitute for ψ_{vib} the wavefunctions Eq. (3.25) of the harmonic oscillator [2.11] for $m \neq k$ into the integral Eq. (4.36c), we obtain

$$\int (\psi_{\text{vib}}^*)_{\text{m}} R (\psi_{\text{vib}})_{\text{k}} dR = 0, \quad \text{except for } m - k = \Delta v = \pm 1. \quad (4.36d)$$

Vibrational quantum numbers are generally designated by the letter v , indicating the lower state by v'' and the upper state by v' .

We therefore obtain the result that within the harmonic approximation, transitions are allowed only between adjacent vibrational levels and only if the dipole moment changes during the transition.

For anharmonic oscillators, there are also nonvanishing contributions for $\Delta v = v'' - v' = \pm 2, \pm 3, \dots$, but these are much smaller than those for $\Delta v = \pm 1$. Transitions with $\Delta v = \pm 1$ in the infrared spectrum are called *fundamental modes* or *first harmonics*, while those with $\Delta v > 1$ are called *overtone bands* or *higher (second, third, etc.) harmonics*. *Overtone bands appear in the spectrum on account of the anharmonicity of the molecule's vibrational potential* and also upon inclusion of more terms in the series expansion Eq. (4.35) or of higher moments (e.g., quadrupole moments).

4.2.3

Pure Rotational Transitions

For transitions between two rotational levels of the same vibrational state, the first integral in Eq. (4.34) with the Taylor expansion Eq. (4.35) yields the constant $d_{\text{nuc}}(R_e)$. The second integral can be evaluated by substituting for the wavefunctions ψ_{rot} of the rigid rotor the spherical harmonics

$$Y_J^M(\theta, \varphi) = P_J^{(M)}(\cos \theta) e^{iM\varphi} \quad (4.36e)$$

as products of Legendre polynomials $P_J^{(M)}$ and the factor $\exp(iM\varphi)$ (see Ch. 3). The wavefunctions depend on the two quantum numbers J and M . Here, J is the angular momentum quantum number,

$$J = \sqrt{J(J+1)}\hbar,$$

and M is the quantum number of its projection

$$J_Z = M\hbar$$

onto the Z axis in the laboratory frame.

Substituting Eq. (4.36e) into Eq. (4.34) yields, with $m = (J'', M'')$ and $k = (J', M')$, the dipole matrix element for pure rotational transitions,

$$D_{mk}^{\text{rot}}(J'', M'', J', M')_Z = d_{\text{nuc}}(R_e) \int_{\theta} P_{J''}^{(M'')} P_{J'}^{(M')} \mathbf{R}_0 \sin \theta \, d\theta \int e^{i(M''-M')\varphi} \, d\varphi. \quad (4.37)$$

The transition probability depends on the polarization of the electromagnetic wave inducing the transitions $m \leftrightarrow k$. For linearly polarized light with \mathbf{E} in the Z direction, the transition probability for rotational transitions $J'' \rightarrow J' = J'' + 1$ within a vibrational level $v' = v''$ is, according to Eqns. (4.31) and (4.37) with $\mathbf{E} \cdot \mathbf{R}_0 = E_0 \cos \theta$, where θ denotes the angle between molecular axis and \mathbf{E} ,

$$\frac{dW_{mk}}{dt} = \frac{2\pi E_0^2}{\hbar^2} d_{\text{nuc}}^2(R_e) \left| \int P_{J''}^{M''} P_{J'}^{M'} \cos \theta \sin \theta \, d\theta \int_0^{2\pi} e^{i(M''-M')\varphi} \, d\varphi \right|^2 \quad (4.38)$$

with $d_{\text{nuc}}(R_e) = e(Z_1 R_1 - Z_2 R_2) R_e$ the dipole moment of the nuclear framework at the equilibrium distance R_e . The second integral is nonvanishing only for $M'' = M' = M$ and then yields 2π .

For absorption or emission of linearly polarized radiation, the selection rule for the projection quantum number M is $\Delta M = 0$.

For the evaluation of the first integral we use the recursion relation for the Legendre polynomials,

$$\cos \theta P_J^M = \frac{J+|M|}{2J+1} P_{J-1}^{|M|} + \frac{J+1-|M|}{2J+1} P_{J+1}^{|M|}, \quad (4.39)$$

and the rotational contribution Eq. (4.37) to the dipole operator becomes

$$D_{\text{rot}}(J'', M, J', M)_Z = 2\pi \left[\frac{J'' + |M|}{2J'' + 1} \int P_{J''-1}^{|M|} P_{J'}^{|M|} \sin \theta \, d\theta \right. \\ \left. + \frac{J'' + |M| - 1}{2J'' + 1} \int P_{J''+1}^M P_{J'}^M \sin \theta \, d\theta \right]. \quad (4.40)$$

The first term is nonvanishing only for $J' = J'' - 1$ (i.e., it describes the emission process), the second for $J' = J'' + 1$ (absorption process). Inserting the explicit form of the Legendre polynomials Eq. (4.40) and performing the integration yields, for $J'' = J$,

$$\left[D_{\text{rot}}(J, M, J + 1, M) \right]_Z = \sqrt{\frac{(J + 1)^2 - M^2}{(2J + 1)(2J + 3)}}. \quad (4.41)$$

This gives for the transition probability Eq. (4.38) for the absorption of linearly polarized radiation on a pure rotational transition ($J', M \leftarrow J'', M$),

$$\left[\frac{d[W(J, M, J + 1, M)]}{dt} \right]_{\text{linear}} = \frac{2\pi E_0^2}{\hbar^2} d_{\text{nuc}}^2(R_c) \frac{(J + 1)^2 - M^2}{(2J + 1)(2J + 3)}. \quad (4.42)$$

In the absence of an external field, the $(2J'' + 1)$ different M'' levels of a rotational state are energetically degenerate. Hence, we obtain for the transition probability of the whole transition $J'' \rightarrow J'$ for linearly polarized radiation

$$\left(\frac{dW_{mk}}{dt} \right)_{\text{linear}} = \frac{\pi E_0^2}{\hbar^2} d_{\text{nuc}}^2 \sum_{M''=-J''}^{+J''} \sum_{M'} |D(J'', M'', J', M')|^2 \\ = \frac{1}{3} \frac{\pi E_0^2}{\hbar^2} d_{\text{nuc}}^2 (J'' + 1). \quad (4.43)$$

This is larger than the result in Eq. (4.42) by a factor of $\frac{1}{3}(2J + 1)$ because we summed over $(2J + 1)$ levels with different values of M'' . The factor $\frac{1}{3}$ stems from the spatial averaging over the statistically oriented molecules, because for unpolarized, isotropic radiation,

$$(D_{mk})_x^2 = (D_{mk})_y^2 = (D_{mk})_z^2 = \frac{1}{3} |D_{mk}|^2. \quad (4.44)$$

For circularly polarized light propagating in the z direction, the scalar product $\mathbf{E} \cdot \mathbf{R}_0$ is

$$\mathbf{E} \cdot \mathbf{R}_0 = \frac{1}{\sqrt{2}} (E_x \sin \theta \cos \varphi \pm i E_y \sin \theta \sin \varphi). \quad (4.45)$$

With $\cos\varphi + i\sin\varphi = \exp(i\varphi)$ we obtain for the integrand in the second factor in the matrix element Eq. (4.37) $\exp[i(M'' - M' \pm 1)\varphi]$ and hence the selection rule

$$\Delta M = M'' - M' = \pm 1. \quad (4.46)$$

In the first term, a factor $\sin\theta$ now arises instead of $\cos\theta$ as in Eq. (4.38). Evaluation of the integrals over Legendre polynomials again yields the selection rule $\Delta J = J'' - J' = \pm 1$, and for a transition $(J, M \rightarrow +J + 1, M \pm 1)$, we obtain the probability

$$\left[\frac{dW(J, M, J + 1, M \pm 1)}{dt} \right]_{\text{circular}} = \frac{\pi E_0^2}{\hbar^2} d_{\text{nuc}}^2 \frac{(J \pm M + 1)(J \pm M + 2)}{(2J + 1)(2J + 3)}. \quad (4.47)$$

We can understand these results for the selection rules $\Delta M = 0, \pm 1$, obtained from the matrix elements through mathematical analysis, in a very vivid model. If we choose the Z axis of the laboratory frame as the quantization axis for J , so that $J_Z = M\hbar$, the following pure polarized states of the electromagnetic wave occur:

- linearly polarized radiation propagating in the X direction, called π light, for which

$$\mathbf{E} = \{0, 0, E_Z\}.$$

The expectation value of the photon's angular momentum in the Z direction vanishes, which means that it cannot transfer any angular momentum in the Z direction to the absorbing molecule, so

$$\Delta M = M'' - M' = 0. \quad (4.48)$$

- σ^+ light, for which

$$\mathbf{E} = \frac{1}{\sqrt{2}} \{E_X + iE_Y\}. \quad (4.49)$$

This is a left-hand circularly polarized wave propagating in the Z direction. Its angular momentum in the Z direction is $+\hbar$, and upon absorption a transition $M'' \rightarrow M' = M'' + 1$ with $\Delta M = +1$ is induced.

- σ^- light, for which

$$\mathbf{E} = \frac{1}{\sqrt{2}} \{E_X - iE_Y\}. \quad (4.50)$$

This is a right-hand circularly polarized wave propagating in the Z direction. Its angular momentum in the Z direction is $-\hbar$, and therefore it induces transitions $M'' \rightarrow M' = M'' - 1$ with $\Delta M = -1$.

If we consider an electromagnetic wave that propagates in the Z direction and is linearly polarized in the X direction, this does not correspond to a pure polarized state in our chosen system. It can be described, however, as a superposition of σ^+ and σ^- light, because

$$\mathbf{E} = \{E_X, 0, 0\} = \frac{1}{2}\{E_X + iE_Y\} + \frac{1}{2}\{E_X - iE_Y\}. \quad (4.51)$$

The first contribution induces transitions with $\Delta M = +1$, the second part induces transitions with $\Delta M = -1$, so that the transition probabilities for this case are

$$\frac{dW_{mk}}{dt} = \frac{\pi E_0^2}{2\hbar^2} d_{\text{nuc}}^2 \left| D_{mk}^{\sigma^+} + D_{mk}^{\sigma^-} \right|^2, \quad (4.52)$$

and transitions with both $\Delta M = +1$ and $\Delta M = -1$ occur. The same is true, analogously, for $\mathbf{E} = \{0, E_Y, 0\}$.

As *unpolarized* light incident in the Z direction can be considered a statistical superposition of linearly X - and Y -polarized light, transitions with $\Delta M = +1$ and $\Delta M = -1$ have equal probabilities, averaged over time.

If the molecules are immersed in an isotropic, unpolarized radiation field, the total transition probability for a transition $(J'', M'') \rightarrow (J' = J'' + 1, M')$ becomes

$$\begin{aligned} \left(\frac{dW_{mk}}{dt} \right)_{\text{unpol}} &= \frac{\pi E_0^2}{\hbar^2} d_{\text{nuc}}^2 \sum_{M' = M'' - 1}^{M'' + 1} \left[|(D_{mk})_x|^2 + |(D_{mk})_y|^2 + |(D_{mk})_z|^2 \right] \\ &= \frac{\pi E_0^2}{\hbar^2} d_{\text{nuc}}^2 \frac{J'' + 1}{2J'' + 1}, \end{aligned} \quad (4.53)$$

independent of M'

4.2.4

Vibration–Rotation Transitions

For transitions between rotational levels $|J, M\rangle$ of two different vibrational states of the same electronic state (Fig. 4.4), the transition probability depends on both factors in Eq. (4.34). The spectrum consists of all transitions from levels $|J'', M''\rangle$ in the lower vibrational state to the corresponding rotational states $|J', M'\rangle$ in the upper vibrational state, where $M' = M''$ or $M' = M'' \pm 1$ depending on the polarization of the absorbed or emitted radiation. The selection rule for the rotational quantum number J is the same as for pure rotational spectra, $\Delta J = \pm 1$. The complete system of all rotational lines for a vibrational transition is called a *vibrational band*. All lines with $\Delta J = J' - J'' = +1$ form the R branch of the band; those with $\Delta J = -1$ the P branch.

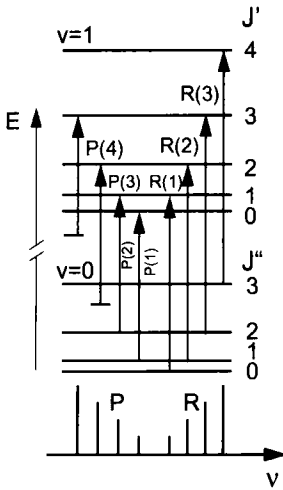


Fig. 4.4 Term diagram and allowed vibration–rotation transitions.

During a transition between different vibrational states, the internuclear distance R changes, and thus also the rotational constant $B_v = B_e - \alpha_e(v + \frac{1}{2})$ changes slightly (see Sect. 3.4). The spacings between adjacent rotational levels in the two vibrational states are therefore slightly different. The wavenumbers of the rotational lines are

$$\tilde{\nu} = \tilde{\nu}_0 + B'_v J'(J' + 1) - B''_v J''(J'' + 1), \quad (4.54)$$

where $\tilde{\nu}_0$ is the difference between the vibrational levels without rotation. For the R branch with $J' = J'' + 1 = J + 1$ this yields

$$\tilde{\nu}_R = \tilde{\nu}_0 + 2B'_v + (3B'_v - B''_v)J + (B'_v - B''_v)J^2, \quad (4.55)$$

and for the P branch with $J' = J'' - 1 = J - 1$,

$$\tilde{\nu}_P = \tilde{\nu}_0 - (B'_v + B''_v)J + (B'_v - B''_v)J^2. \quad (4.56)$$

Figure 4.5 displays the wavenumbers of the P and R branches as functions of the rotational quantum number $J'' = J$ (Fortrat diagram). As an example of such a vibration–rotation band, Fig. 4.6 shows the infrared absorption spectrum of the HCl molecule in the range between 2600 and 3100 cm^{-1} . The weaker lines, shifted towards smaller wavenumbers, belong to the H^{37}Cl isotopomer. The ratio $^{35}\text{Cl}/^{37}\text{Cl}$ is 75.5/24.5. The main contribution to the isotopic shift stems from the different vibrational energies; smaller contributions are due to the change in rotational energy because of the different moments of inertia of the two isotopomers.

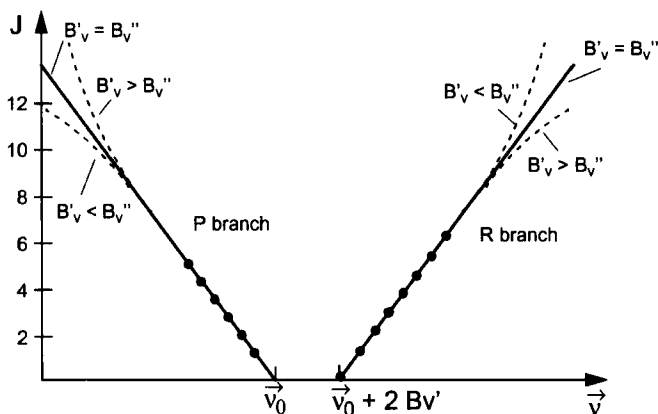


Fig. 4.5 Fortrat diagram of P and R branches in vibration-rotation transitions.

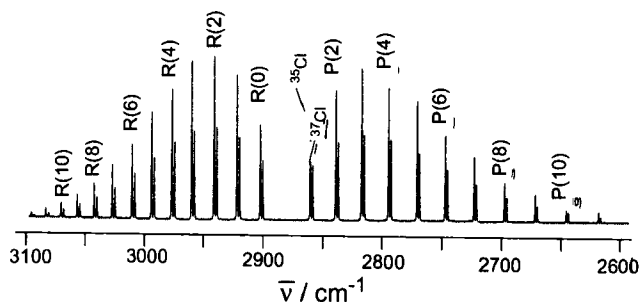


Fig. 4.6 Vibration-rotation spectrum of the ($v' = 0 \leftarrow v'' = 0$) vibrational band of the HCl molecule for the two isotopomers H^{35}Cl and H^{37}Cl [4.5].

4.2.5

Electronic Transitions

We will now turn our attention to dipole transitions between vibration-rotation levels $m = (v'', J'') \rightarrow k = (v', J')$ in *different* electronic states m and k . Such transitions cause the visible and ultraviolet spectrum of molecules. We start from the first term in the matrix element Eq. (4.25)

$$D_{mk} = \int \chi_m^* D_{mk}^{\text{el}} \chi_k d\tau_{\text{nuc}}. \quad (4.57)$$

The electronic part of the matrix element,

$$D_{mk}^{\text{el}} = \int \phi_m(r, R) \sum_i e r_i \phi_k(r, R) d\tau_{\text{el}}, \quad (4.58)$$

depends on the vector $\mathbf{r} = \sum r_i$ of the electronic dipole moment, where the summation is over all electrons contributing to the dipole moment. As in Eq. (4.33), we write the

nuclear wavefunctions χ as a product

$$\chi = S_{\text{vib}}(R)Y_J^M(\theta, \varphi)$$

of vibrational functions $S_{\text{vib}}(R)$ depending only on the internuclear distance R and rotational functions depending only on the angles θ and φ . With the normalized vibrational functions $\psi_{\text{vib}} = RS_{\text{vib}}$ and $d\tau_{\text{nuc}} = R^2 dR \sin\theta d\theta d\varphi$, Eq. (4.57) becomes

$$D_{mk} = \int \psi_{\text{vib}}(v'') D_{mk}^{\text{el}} \psi_{\text{vib}}(v') dR \iint Y_{J''}^{M''} Y_{J'}^{M'} \sin\theta d\theta d\varphi. \quad (4.59)$$

The square modulus of the first integral in Eq. (4.59) is called *band strength* $S_{v'',v'}$, because it indicates the transition probability for the complete vibrational band $v'' \leftrightarrow v'$. Often D_{mk}^{el} depends only slightly on R . We can then replace $D_{mk}^{\text{el}}(R)$ by the average value $D_{mk}^{\text{el}}(R_e)$, which can be moved outside the integral over R , yielding

$$D_{mk} = D_{mk}^{\text{el}}(R_e) \int \psi_{\text{vib}}(v'') \psi_{\text{vib}}(v') dR \iint Y_{J''}^{M''} Y_{J'}^{M'} \sin\theta d\theta d\varphi. \quad (4.59a)$$

The square modulus of the first integral,

$$q_{v'',v'} = \left| \int \psi_{\text{vib}}(v'') \psi_{\text{vib}}(v') dR \right|^2 \quad (4.59b)$$

is called the *Franck–Condon factor*.

The second integral in Eq. (4.59) depends on the quantum numbers $J''M''$ and $J'M'$ of both states (see preceding section). Summation over all M' and M'' and squaring gives the so-called *Hönl–London factor* $S_{J'',J'}$, also called the *line strength*, because it indicates the intensity of a rotational line in a band.

The transition probability for the spontaneous transition $k(v'J') \rightarrow m(v'',J'')$ is then

$$\frac{d}{dt} \left(W_{km}^{\text{(el)}} \right) \approx \left| D_{mk}^{\text{el}}(R_e) \right|^2 q_{v'',v'} S_{J'',J'}. \quad (4.60a)$$

In the field of a linearly polarized electromagnetic wave with the amplitude vector \mathbf{E}_0 , the absorption probability per molecule and unit time is

$$\frac{dW_{mk}^{\text{abs}}}{dt} \propto \left| D_{mk}^{\text{el}} \right|^2 q_{v'',v'} S_{J'',J'} \left| \mathbf{r}_0 \cdot \mathbf{E}_0 \right|^2, \quad (4.60b)$$

where \mathbf{r}_0 is the unit vector in the direction of D_{mk} .

4.2.6

***R* Centroid Approximation; the Franck–Condon Principle**

In general, D_{mk}^{el} depends on the internuclear distance R . We can then expand the R -dependent electronic part of the matrix element D_{mk} in Eq. (4.59) in a power series

$$D_{mk}^{\text{el}} = \sum_n a_n R^n \quad \text{with} \quad a_0 = D_{mk}^{\text{el}}(R_e), \quad (4.61)$$

to obtain for the band strength

$$\begin{aligned} S_{v''v'} &= \left| \int \psi_{v''} \sum a_n R^n \psi_{v'} \, dR \right|^2 \\ &= \left| \sum a_n \int \psi_{v''} R^n \psi_{v'} \, dR \right|^2. \end{aligned} \quad (4.62)$$

The mean of R^n , weighted by the vibrational functions,

$$\langle R^n \rangle_{v''v'} = \frac{\int \psi_{v''} R^n \psi_{v'} \, dR}{\int \psi_{v''} \psi_{v'} \, dR} \quad (4.63)$$

is called the n th-order R centroid. Using Eq. (4.59b), we obtain now for the band strength

$$S_{v''v'} = \left| \sum a_n \langle R^n \rangle_{v''v'} \right|^2 q_{v''v'}. \quad (4.64)$$

In the approximation

$$\langle v'' | R^n | v' \rangle = |\langle v'' | R | v' \rangle|^n = R_{v''v'}^n q_{v''v'} \quad (R \text{ centroid approximation}), \quad (4.65)$$

which is usually well obeyed [4.6, a)], we obtain from Eq. (4.62), using Eq. (4.65),

$$S_{v''v'} = \left| D_{mk}^{\text{el}}(R_{v''v'}) \right|^2 q_{v''v'}, \quad (4.66)$$

which can be visualized as follows. The band strength is given by the overlap integral $q_{v''v'}$ of Eq. (4.59b) of the vibrational wavefunctions multiplied by the electronic transition probability, which equals the square modulus of the average $\langle D_{mk}^{\text{el}} \rangle$ weighted by the vibrational functions.

The transition probability of a spontaneous electronic transition is then given by a combination of three factors:

1. the square modulus of the electronic transition dipole moment $|D_{mk}^{\text{el}}(R_{v''v'})|^2$ weighted by the vibrational wavefunctions $\psi(R)$,
2. the Franck–Condon factor

$$q_{v''v'} = \left| \int \psi_{v''} \psi_{v'} \, dR \right|^2, \quad (4.67)$$

and

3. the Hönl–London factor

$$|D_{mk}^{\text{rot}}|^2 = S_{J''J'} = \left| \sum_{M'',M'} Y_{J''}^{M''} Y_{J'}^{M'} \sin \theta \, d\theta \, d\varphi \right|^2.$$

An optical transition between two electronic states occurs so quickly that neither the positions nor the velocities of the nuclei change significantly during the transition. Hence, the nuclear kinetic energy must also remain unchanged during the transition. In other words, the electronic transition occurs *vertically* in the potential energy diagram of Fig. 4.7 (Franck–Condon principle). If a photon $h\nu$ is emitted between two states m and k with the term energies $E_m(v'')$ and $E_k(v')$, the potential energies $E''_{\text{pot}}(R)$ and $E'_{\text{pot}}(R)$ and the kinetic energies $T''(R) = T'(R)$ then follow the relation

$$\begin{aligned} h\nu &= E(v') - E(v'') = E'_{\text{pot}}(R) + T'(R) - (E''_{\text{pot}} + T''(R)) \\ &= E'_{\text{pot}}(R^*) - E''_{\text{pot}}(R^*) , \end{aligned} \quad (4.68)$$

where R^* is the internuclear distance at which the transition occurs. Using Mulliken's difference potential

$$U(R) = E''_{\text{pot}}(R) + E(v') - E'_{\text{pot}}(R) , \quad (4.69)$$

the condition $T''(R^*) = T'(R^*)$ in Eq. (4.68) can be written as

$$U(R^*) = E(v'') , \quad (4.70)$$

that is, the transition occurs at the internuclear distance R^* for which the difference potential intersects the energy $E(v'')$ (Fig. 4.7).

Within this purely classical argumentation, it follows from the Franck–Condon principle and energy conservation that *the transition occurs at a precisely defined internuclear distance $R = R^*$, the classical transition point in the $E_{\text{pot}}(R)$ diagram [4.6, b)].*

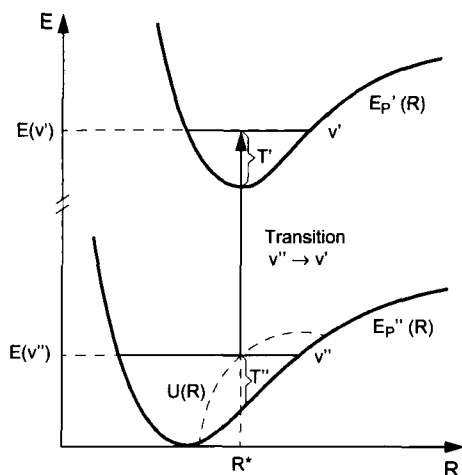


Fig. 4.7 Representation of electronic transitions as vertical lines $R = R^* = \text{const.}$ in the potential diagram $E_{\text{pot}}(R)$ and difference potential $U(R) = E''_{\text{pot}}(R) - E'_{\text{pot}}(R) + E(v')$.

For a quantum-mechanical formulation of the Franck–Condon principle, we consider the matrix element

$$\langle v' | H' - H'' | v'' \rangle = [E(v') - E(v'')] \langle v' | v'' \rangle \quad (4.71)$$

of the difference Hamiltonian $H' - H''$ for the upper and the lower state, where $H = T + E_{\text{pot}}(R)$. We can therefore write Eq. (4.71) as

$$\begin{aligned} \langle v' | H' - H'' | v'' \rangle &= \langle v' | T' + E'_{\text{pot}}(R) - T'' - E''_{\text{pot}}(R) | v'' \rangle \\ &= \langle v' | E'_{\text{pot}}(R) - E''_{\text{pot}}(R) | v'' \rangle, \end{aligned} \quad (4.72)$$

because the kinetic-energy operators T' and T'' are identical for both states.

If we now use the approximation

$$\overline{f(R)} = \frac{\langle v' | f(R) | v'' \rangle}{\langle v' | v'' \rangle} \cong f(\bar{R}), \quad (4.73)$$

which for $f(R) = R^n$ is the basis of the R centroid approximation, we obtain from Eq. (4.73) for $f(R) = E_{\text{pot}}(R)$

$$\langle v' | E'_{\text{pot}}(R) - E''_{\text{pot}}(R) | v'' \rangle = [E'_{\text{pot}}(\bar{R}) - E''_{\text{pot}}(\bar{R})] \langle v' | v'' \rangle, \quad (4.74)$$

and with Eqns. (4.71) and (4.72) we arrive at the relation

$$E(v') - E(v'') = E'_{\text{pot}}(\bar{R}) - E''_{\text{pot}}(\bar{R}). \quad (4.75)$$

Comparison with Eq. (4.68) shows that $R^* = \bar{R}$, which means that the R centroid $\langle R \rangle$ equals the classical transition point R^* as long as the R centroid approximation Eq. (4.73) is valid. The R centroid approximation therefore connects classical and quantum-mechanical formulations of the Franck–Condon principle.

The validity of the R centroid approximation can be revealed as follows. The weight function

$$W(R) dR = \frac{(\psi_{\text{vib}}(R))_{v'} (\psi_{\text{vib}}(R))_{v''} dR}{\langle v' | v'' \rangle} \quad (4.76)$$

determines the probability that the optical transition $v' \rightarrow v''$ occurs in the interval R to $R + dR$ of the internuclear distance. The uncertainty width ΔR of the R centroid $\langle R^n \rangle_{v'' v'}$ can be characterized by the variance

$$(\Delta \bar{R})^2 = \overline{R^2} - \bar{R}^2 = \int_0^{\infty} R^2 W(R) dR - \left[\int_0^{\infty} R \times W(R) dR \right]^2. \quad (4.77)$$

If the R centroid approximation is exact, $\overline{R^2} = \bar{R}^2$ and $(\Delta \bar{R})^2 = 0$, that is, the optical transition occurs exactly at the internuclear distance $\bar{R} = R^*$. The more “classical” the transition becomes, the more $(\Delta \bar{R})^2$ decreases, and the quality of the R centroid

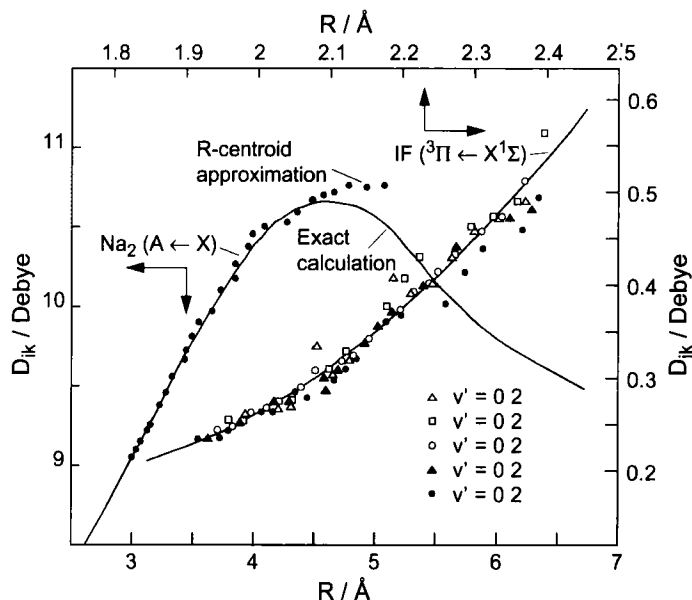


Fig. 4.8 Electronic transition dipole moment matrix element $D_{mk}(R)$ for the transitions $A^1\Sigma_u \leftarrow X^1\Sigma_g$ in the Na_2 molecule and ${}^3\Pi \leftarrow X^1\Sigma^+$ in the IF molecule; comparison of the R centroid approximation with exact values. Note the different scales for the two curves.

approximation improves (Fig. 4.8). Hence, the R centroid approximation is especially suitable

- (a) for molecules with heavy nuclei, and
- (b) for transitions between highly excited levels, that is, $v', v'' \gg 1$.

The internuclear distance $R^* = \bar{R}$ at which the optical transition takes place depends on the relative shift of the potential minima and the slopes of both potential curves $E'_{\text{pot}}(R)$ and $E''_{\text{pot}}(R)$. As Fig. 4.7 shows, this distance does not necessarily coincide with the classical transition point.

If the two potential curves have their minima at the same internuclear distance ($R'_e = R''_e$) and if their slopes $dE_{\text{pot}}(R)/dR$ are similar for corresponding values of R (Fig. 4.9a), transitions with $\Delta v = 0$ possess by far the largest Franck–Condon factors. If the potential curves are displaced, however, as in Fig. 4.9b, the spectrum comprises mainly vibrational bands with larger values of Δv . This is exemplified by the fluorescence spectrum of the selectively excited level ($v' = 23, J' = 82$) in the $D^1\Sigma_u$ state of the Cs_2 molecule, which features transitions with $\Delta v > 60$ (Fig. 4.10).

For some molecular transitions, the difference potential intersects the energy $E(v'')$ twice. In these cases, there are two classical transition points R_1^* and R_2^* (Fig. 4.11). This means that for a transition $E(v') \rightarrow E(v'')$ there are two contributions with am-

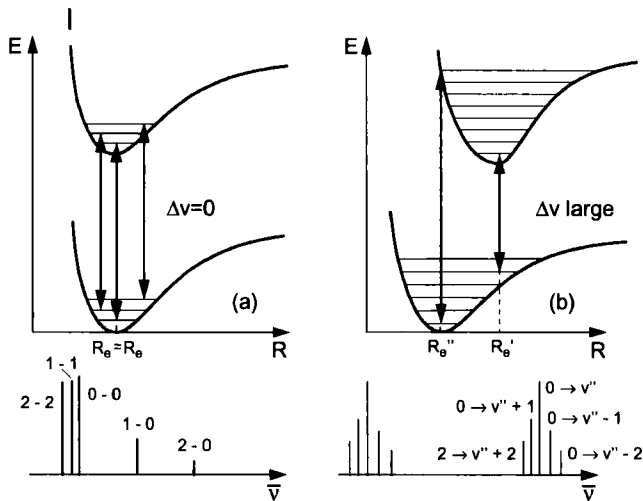


Fig. 4.9 Electronic transitions with maximum Franck–Condon factors a) for potential curves with $R'_e \approx R''_e$ and b) for displaced potential curves ($R'_e \neq R''_e$).

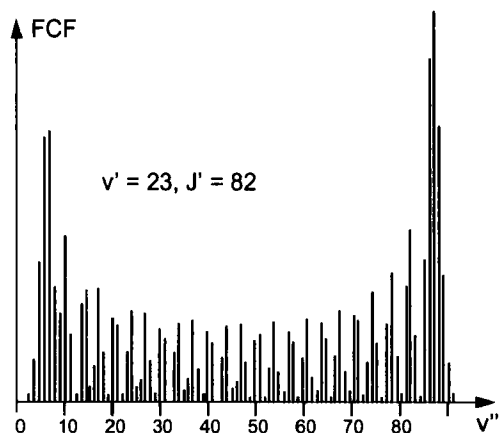


Fig. 4.10 Franck–Condon factors for the fluorescence spectrum of a selectively excited level ($v' = 23, J' = 82$) in the $D^1\Sigma_u$ state of the Cs_2 molecule for the vibrational transitions $^1\Sigma_u(v' = 23) \rightarrow ^1\Sigma_g(v'')$ [4.7].

plitudes A_1 and A_2 which add up to the total amplitude

$$A = A_1 + A_2 = \langle \psi_{v'}(R_1^*) \psi_{v''}(R_1^*) \rangle + \langle \psi_{v'}(R_2^*) \psi_{v''}(R_2^*) \rangle . \tag{4.78}$$

The transition probability $W \propto |A_1 + A_2|^2$ then contains interference contributions $A_1 A_2$ that can influence the intensity of this transition. For such cases, a generalized R centroid approximation can be developed (see [4.8]).

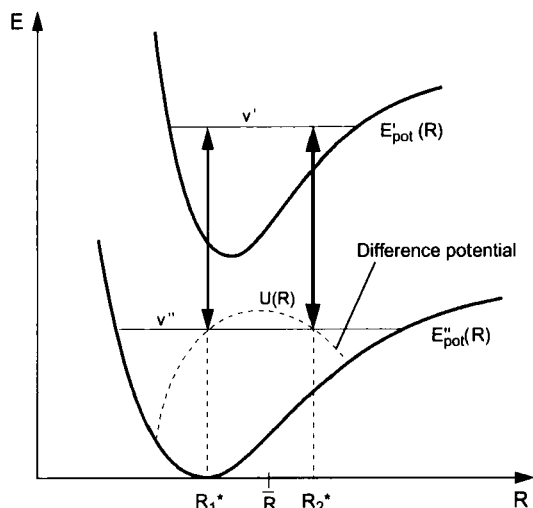


Fig. 4.11 Transition with two intersections of the difference potential with $E(v'')$.

4.2.7

The Rotational Structure of Electronic Transitions

The wavenumber of an electronic transition between the vibration–rotation levels (v'', J'') in the lower and (v', J') in the upper electronic state is given by the difference of their respective term values [see Eqns. (3.18), (3.37), and (3.42)],

$$\begin{aligned} \tilde{\nu} &= [T'_{\text{el}} - T''_{\text{el}}] + \{ [G(v') - G(v'')] + [F(J') - F(J'')] \} \\ &= \tilde{\nu}_0 + \left[B'_v J'(J' + 1) - D'_v J'^2 (J' + 1)^2 \right] \\ &\quad - \left[B''_v J''(J'' + 1) - D''_v J''^2 (J'' + 1)^2 \right]. \end{aligned} \quad (4.79)$$

Here, T'_{el} , T''_{el} are the electronic term values at the minima of the potential curves, $G(v)$ are the vibrational term values, $F(J)$ are the rotational term values, and $\tilde{\nu}_0$ is the wavenumber of the pure vibrational transition between $|v'\rangle$ and $|v''\rangle$, where $J' = J'' = 0$ (also called the *band origin*). B_v and D_v are the rotational and centrifugal constants, which depend on the vibrational level v according to Eqns. (3.43) and (3.44)). The ensemble of all possible rotational transitions between two vibrational levels v' and v'' is called a *vibrational band*.

The selection rules for the rotational quantum number J are, exactly as for vibration–rotation transitions within the same electronic state,

$$\Delta J = 0, \pm 1; \quad 0 \not\rightarrow 0,$$

only that now transitions with $\Delta J = 0$ are also allowed if the electronic angular momentum changes by $1\hbar$, because the total angular momentum must be conserved upon

absorption or emission of a photon with angular momentum $1\hbar$. This excludes transitions $J' = 0 \leftrightarrow J'' = 0$, because here the electronic angular momentum quantum number Λ would need to be zero in both states.

Hence, for Σ - Σ transitions there are only P ($\Delta J = -1$) or R ($\Delta J = +1$) lines, but for Σ - Π or Π - Π transitions, Q lines with $\Delta J = 0$ occur also.

For the R lines, we obtain from Eq. (4.79) with $J' = J'' + 1$ and $J'' = J$, neglecting the centrifugal term,

$$\tilde{\nu}_R(J) = \tilde{\nu}_0 + (B'_v - B''_v)J(J+1) + 2B'_v(J+1), \quad (4.80a)$$

and for the P lines with $J' = J'' - 1 = J - 1$

$$\tilde{\nu}_P(J) = \tilde{\nu}_0 + (B'_v - B''_v)J(J+1) - 2B'_vJ, \quad (4.80b)$$

while the wavenumbers of the Q lines are given by

$$\tilde{\nu}_Q(J) = \tilde{\nu}_0 + (B'_v - B''_v)J(J+1). \quad (4.80c)$$

The R branch starts at $J = 0$; Q and R branches start at $J = 1$.

The appearance of such a rotation-resolved spectrum depends on whether $B'_v < B''_v$ (which means that the internuclear distance is larger in the upper level), or $B'_v > B''_v$ (which means that the molecule is more strongly bound in the upper state). Figure 4.12 shows the Fortrat diagram for both cases. We see that for $B'_v < B''_v$, the lines in the R branch are first shifted to larger wavenumbers for increasing J , but their spacing decreases continuously, until, at a rotational quantum number

$$J^* = \frac{3B'_v - B''_v}{2(B''_v - B'_v)}, \quad (4.81)$$

the trend reverses and their wavenumbers decrease. The R branch shows a reversal ($d\tilde{\nu}/dJ = 0$) at J^* , which is called a *band edge*. Towards smaller wavenumbers, all three branches progress monotonically. The Q branch shows the largest density of lines for small J . The density is largest if B'_v and B''_v do not differ by much. For

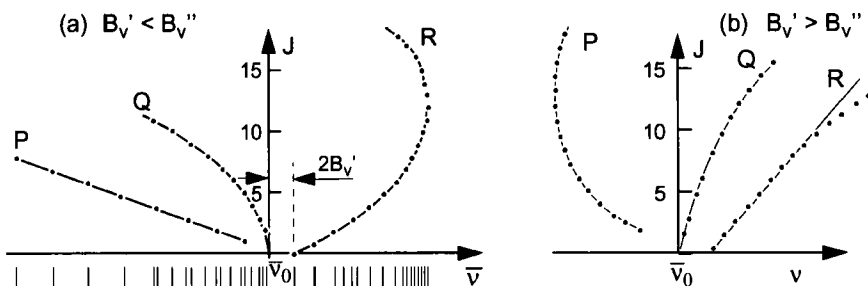


Fig. 4.12 Fortrat diagram of the rotational structure of electronic transitions with P, Q, and R branches. a) $B'_v < B''_v$; b) $B'_v > B''_v$.

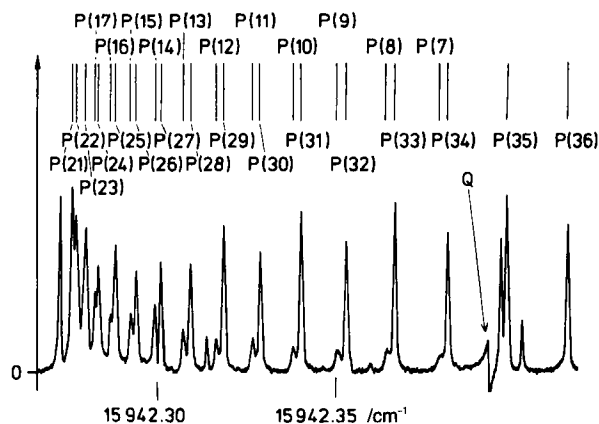


Fig. 4.13 Example of a band head with band edge: Doppler-free absorption spectrum of the 0–0 band of the electronic transition $C^1\Pi_u-X^1\Sigma_g$ of the Cs_2 molecule.

$B'_v = B''_v$, all Q lines coincide. In this case, the Q branch is a vertical straight line in the Fortrat diagram.

Such a band (that is, the ensemble of all P, Q, and R lines) features a sharp boundary towards the blue region but appears diffuse towards the red spectral region on photographic recordings. This diffuse appearance is most notable for inadequate spectral resolution. The band is therefore called “red-shaded”.

For $B'_v > B''_v$, the P branch of a band edge faces the red region, while the R and the Q branches progress monotonically to the right towards larger wavenumbers. Such a band is called “blue-shaded”. As an example, Fig. 4.13 displays the P branch of the 0–0 band of the electronic transition $C^1\Pi_u-X^1\Sigma_g$ of the Cs_2 molecule as recorded using Doppler-free laser spectroscopy.

The ensemble of all vibrational bands of an electronic transition is called a band system.

We see that we can learn simply from the appearance of a band whether the internuclear distance in the upper state is larger or smaller than in the lower state.

Also, we can easily deduce from the rotational structure of a band and its intensity distribution if the corresponding transition is $\Sigma-\Sigma$, $\Pi-\Sigma$, or $\Pi-\Pi$, because the intensity ratios of Q to P or R branch are different for the three cases. To derive this relation, the Hönl–London factor [the squared double integral over θ and φ in Eq. (4.59)] for transitions between the different electronic states must be evaluated.

For electronic states with $\Lambda \neq 0$, we must take into account that the total angular momentum consists of rotational and electronic angular momentum, so that Eq. (3.21) must be used for the term values $F(J)$. The term with Λ , which is independent of v and J , can be included in the electronic energy, however, and has already been included in the band origin $\tilde{\nu}_0$ in Eq. (4.79).

The results of the calculations for the line intensities $S_R(J)$, $S_P(J)$, $S_Q(J)$ of the rotational lines with $\Delta J = \pm 1, 0$ are the Hönl–London factors:

(a) for transitions with $\Delta A = 0$,

$$\begin{aligned} S_R(J) &= \frac{(J' + A')(J' - A')}{J'} ; \\ S_P(J) &= \frac{(J'' + A'')(J'' - A'')}{J''} ; \\ S_Q(J) &= \frac{(2J' + 1)A'^2}{J'(J' + 1)} ; \end{aligned} \quad (4.82a)$$

(b) for transitions with $\Delta A = +1$,

$$\begin{aligned} S_R(J) &= \frac{(J' + A')(J' - 1 + A')}{4J'} ; \\ S_P(J) &= \frac{(J'' - 1 - A'')(J'' - A'')}{4J''} ; \\ S_Q(J) &= \frac{(J' + A')(J' + 1 - A')(2J' + 1)}{4J'(J' + 1)} ; \end{aligned} \quad (4.82b)$$

(c) for transitions with $\Delta A = -1$,

$$\begin{aligned} S_R(J) &= \frac{(J' - A')(J' - 1 - A')}{4J'} ; \\ S_P(J) &= \frac{(J'' - 1 + A'')(J'' + A'')}{4J''} ; \\ S_Q(J) &= \frac{(J' - A')(J' + 1 + A')(2J' + 1)}{4J'(J' + 1)} . \end{aligned} \quad (4.82c)$$

4.2.8

Continuous Spectra

Up to now we have considered only transitions between two discrete levels $(v'', J'') \leftrightarrow (v', J')$ within one or between two *bound* electronic states, leading to molecular *line spectra*. Now we turn to the case that at least one of the two states possesses a repulsive potential curve, which means that the molecule is not stable in this state. Such transitions lead to continuous spectra.

Examples for continuous *absorption spectra* are transitions from the bound ground state of a molecule to unstable excited states with repulsive potential curves (see Fig. 4.14a), or to states above the dissociation limit of a bound state. Continuous *fluorescence spectra* can occur through transitions from a discrete level (v', J') of a bound electronic state to lower, unstable states with repulsive potential curves. Such spectra can be observed, for example, for excimers (= excited dimers). These are

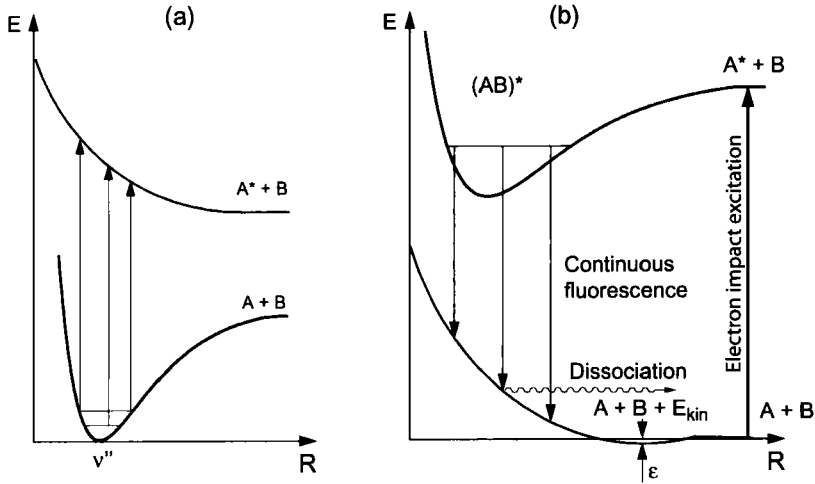


Fig. 4.14 The occurrence of continuous spectra in diatomic molecules. a) Absorption spectra; b) emission spectra of excimers.

molecules that are stable only in excited states and dissociate in their ground states, because their ground-state potential curves are largely repulsive, possessing at most a shallow van der Waals minimum (Fig. 4.14b). The rare-gas dimers He_2 , Ar_2 , Kr_2 , and Xe_2 or some rare-gas halides such as KrF or XeCl are examples of excimers.

Emission transitions into energy states above the dissociation limit of a bound lower state can also lead to continuous fluorescence spectra. Figure 4.15 shows a section from the fluorescence spectrum of the NaK molecule corresponding to the electronic transition $D^1\Pi \rightarrow a^3\Sigma$ from a bound level $(v', J') = (12, 14)$ of the $D^1\Pi$ state into the weakly bound $a^3\Sigma$ state. If the lower states of the fluorescence transition are bound states (v'', J'') below the dissociation threshold of the $a^3\Sigma$ state, a line spectrum results. If these states are above the dissociation limit, a continuous fluorescence spectrum results.

To understand the pronounced intensity modulation in the continuous part of the spectrum, we must extend the Franck–Condon principle to continuous spectra. To achieve this, we consider the transition from a level (v', J') with energy $E'(v', J')$ into states E'' above the dissociation limit D (Fig. 4.16). As the kinetic energy of the nuclei is conserved during the transition $E' \rightarrow E'' = E' - h\nu$, all transitions end on the curve of the difference potential

$$U(R) = E''_{\text{pot}}(R) + E(v') - E'_{\text{pot}}(R). \quad (4.83a)$$

If $U(R)$ is a monotonous function of R , each internuclear distance R corresponds to exactly one wavelength λ or frequency $\nu = c/\lambda$ in the fluorescence spectrum, which is given by

$$h\nu(R) = E(v') - U(R) = E'_{\text{pot}}(R) - E''_{\text{pot}}(R). \quad (4.83b)$$

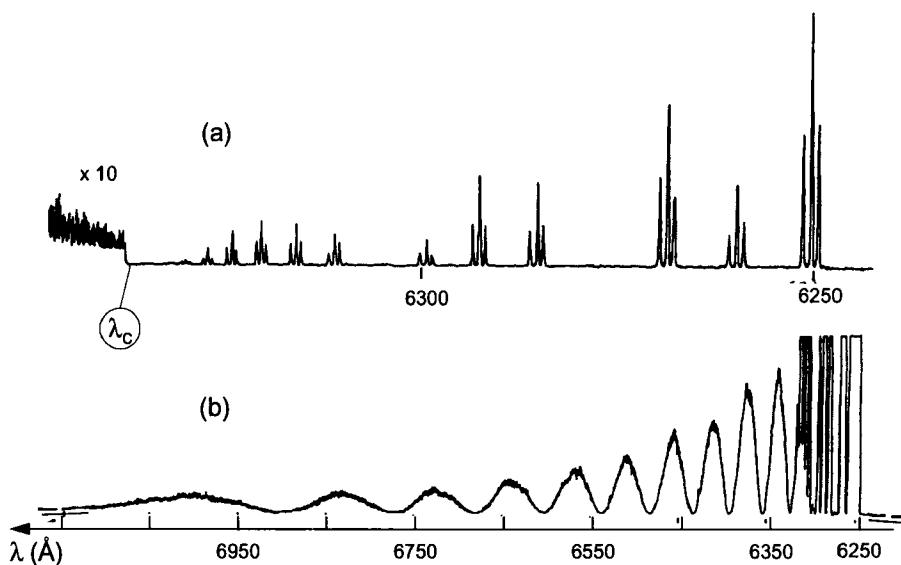


Fig. 4.15 Modulated emission continuum emitted from the vibrational level $v' = 14$ in the ${}^3\Pi$ state of the NaK molecule during the transition ${}^3\Pi \rightarrow {}^3\Sigma$ into a) bound

states of the ${}^3\Sigma$ state and b) continuum states above the ${}^3\Sigma$ dissociation limit. The spectrum in a) is an enlarged section from the right-hand part of b) [4.9].

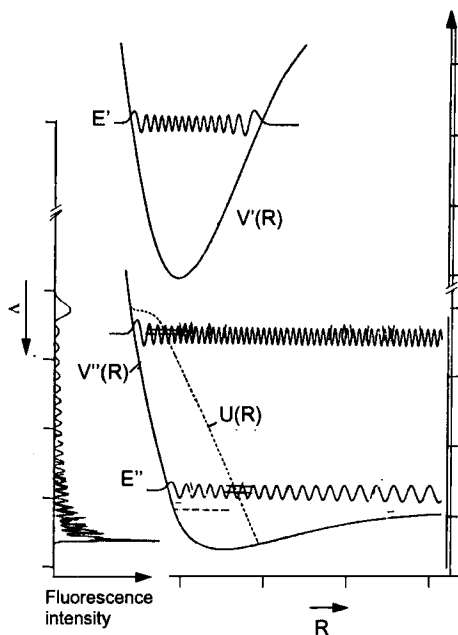


Fig. 4.16 Term diagram and vibrational wavefunctions for the NaK emission continuum of Fig. 4.15b.

The fluorescence intensity in the interval $d\tilde{\nu}$ at wavenumber $\tilde{\nu}$ is given by the Franck-Condon factor

$$I_{fl}(\tilde{\nu}) d\tilde{\nu} \propto \left| \chi(v', R) \chi(E'', R) dR \right|^2, \tag{4.84a}$$

where R is the internuclear distance at which the line $E = E''$ intersects the difference potential. The continuum wavefunction $\chi(E'' > D, R)$ can in many cases be approximated by a normalized Airy function.

If the monochromator used for measuring the spectral intensity distribution $I_{fl}(\tilde{\nu})$ of the fluorescence spectrum has the resolution $\Delta\tilde{\nu}$, it will record the intensity

$$\int_{-\Delta\tilde{\nu}/2}^{+\Delta\tilde{\nu}/2} I(\tilde{\nu}) d\tilde{\nu} \propto \left| \int_{R_1}^{R_2} \psi_{vib}(v', R) \psi_{vib}(E'', R) dR \right|^2 \tag{4.84b}$$

for each $\tilde{\nu}$, where $\Delta R = R_2 - R_1$ is the range of internuclear distances in which the difference potential $U(R)$ changes by $\Delta E = h\Delta\nu = (hc/\lambda^2)\Delta\lambda$.

If the oscillation period of the function $\psi_{vib}(E'', R)$ is small compared to ΔR , but that of the function $\psi_{vib}(v', R)$ is larger than ΔR (Fig. 4.16), the measured fluorescence intensity $I_{fl}(\tilde{\nu})$ will reflect the $(v' + 1)$ maxima of the vibrational wavefunction $\psi_{vib}(v', R)$. From the number of maxima, one can therefore directly deduce the vibrational quantum number v' of the emitting state [4.9].

4.3 Line Profiles of Spectral Lines

Spectral lines recorded during the absorption or emission of electromagnetic radiation are never strictly monochromatic. Instead, the intensity $I(\nu - \nu_0)$ of the lines around the mean frequency ν_0 obeys a distribution determined by several factors (Fig. 4.17a). The frequency interval $\Delta\nu = \nu_1 - \nu_2$ between the two frequencies ν_1 and ν_2 , for which the intensity I has decreased to $I(\nu_0)/2$, is called the *full width at half maximum* $\delta\nu$ of

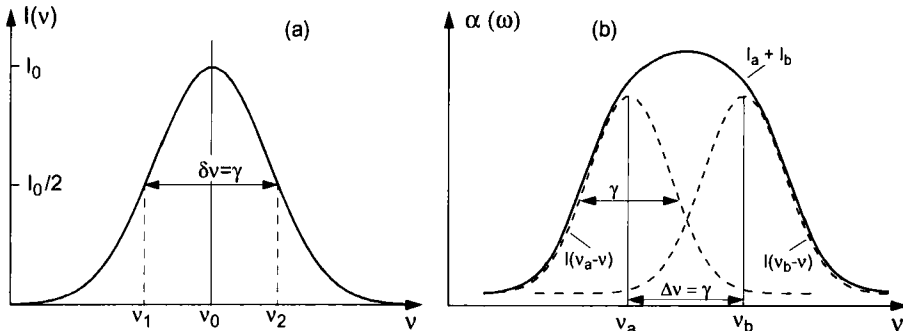


Fig. 4.17 a) Spectral line profile. b) Spectral resolution limit.

the spectral line. The finite linewidth limits spectral resolution, because two spectral lines separated by less than $\delta\nu$ cannot be resolved as separate lines (Fig. 4.17b).

Generally, the spectral resolution of the spectrograph employed provides a practical limit for the measured linewidths. Only by using interferometers can we achieve such high resolutions that we can recognize the intrinsic limits on linewidths: the natural linewidth, Doppler broadening, and collisional broadening. We will now consider these mechanisms in detail.

4.3.1

Natural Linewidth

An excited molecule at rest in a state $|k\rangle$ can dispose of its excitation energy by emitting radiation after an average time τ . To determine the spectral profile of this radiation, we start by employing a classical model, in which the excited molecule is described by a classical damped oscillator with center frequency ω_0 and damping constant γ . The time-dependency of its vibrational amplitude is given by the differential equation

$$\ddot{x} + \gamma\dot{x} + \omega_0^2 x = 0, \quad (4.85)$$

where the frequency $\omega_0 = \sqrt{D/m}$ is determined by the force constant D and the mass m of the oscillator. With the initial conditions $x(0) = x_0$ and $\dot{x}(0) = 0$, the solution of Eq. (4.85) is

$$x(t) = x_0 e^{-(\gamma/2)t} \left[\cos \omega t + \left(\frac{\gamma}{2\omega} \right) \sin \omega t \right] \quad \text{with} \quad \omega = \sqrt{\omega_0^2 - \left(\frac{\gamma}{2} \right)^2}. \quad (4.86)$$

The damping of a molecular oscillator is extremely small (for $\omega_0 = 2\pi \times 6 \times 10^{14} \text{ s}^{-1}$ and a relaxation time $\tau = 10^{-8} \text{ s}$, the ratio γ/ω_0 is 2.8×10^{-8}). The second term in Eq. (4.86) can therefore be neglected, and we obtain for the time-dependent amplitude of the damped oscillation (Fig. 4.18a)

$$x(t) \approx x_0 e^{-(\gamma/2)t} \cos \omega_0 t. \quad (4.87)$$

Because of the decreasing vibrational amplitude, the frequency of the emitted radiation is now not monochromatic as it would have been for an undamped oscillation with temporally constant amplitude, but it displays a frequency spectrum $A(\omega)$, which can be determined by a Fourier transformation of $x(t)$. If we write $x(t)$ as a superposition of the different frequency contributions with amplitudes $A(\omega)$,

$$x(t) = \frac{1}{\sqrt{2\pi}} \int_0^\infty A(\omega) e^{i\omega t} d\omega, \quad (4.88)$$

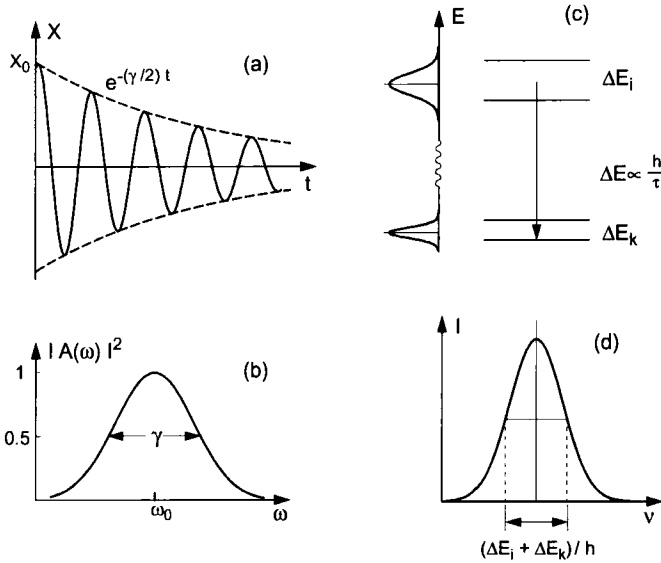


Fig. 4.18 a) Damped oscillation and b) Fourier transform of the corresponding line profile. c) Natural linewidths as a consequence of energy uncertainties due to limited lifetimes. d) Resultant linewidth $\Delta\nu$.

we can obtain $A(\omega)$ from the Fourier transform

$$\begin{aligned}
 A(\omega) &= \frac{1}{\sqrt{2\pi}} \int_{-\infty}^{+\infty} x(t) e^{-i\omega t} dt \\
 &= \frac{1}{\sqrt{2\pi}} \int_{-\infty}^{+\infty} x_0 e^{-(\gamma/2)t} \cos \omega_0 t e^{-i\omega t} dt,
 \end{aligned} \tag{4.89}$$

where we have used $x(t) = 0$ for $t < 0$.

Evaluation of the integrals is elementary and yields the complex amplitude distribution

$$A(\omega) = \frac{x_0}{\sqrt{8\pi}} \left(\frac{1}{i(\omega - \omega_0) + (\frac{\gamma}{2})} + \frac{1}{i(\omega + \omega_0) + (\frac{\gamma}{2})} \right), \tag{4.90}$$

from which the intensity distribution $I(\omega) \propto |A(\omega)|^2$,

$$I(\omega) = \frac{C}{(\omega - \omega_0)^2 + (\frac{\gamma}{2})^2} \tag{4.91}$$

follows (Fig. 4.18b). The constant C can be chosen so that the total intensity, integrated over the whole line profile, is

$$\int I(\omega) d\omega = I_0. \tag{4.92}$$

Hence, $C = I_0 \gamma / 2\pi$.

The line profile Eq. (4.91) is called a Lorentzian profile. Its full width at half maximum is

$$\delta\omega_n = \gamma; \quad \delta\nu_n = \frac{\gamma}{2\pi}; \quad (4.93)$$

it is called the *natural linewidth* of the transition.

A quantum-mechanical treatment gives a similar result. Here, the linewidth of a transition between two levels $|k\rangle$ and $|i\rangle$ with lifetimes τ_k and τ_i results from the sum of the level uncertainties $\Delta E_k = \hbar/\tau_k$ and $\Delta E_i = \hbar/\tau_i$, as a consequence of the uncertainty relation $\Delta E \times \Delta t > \hbar$ (Fig. 4.18c,d). The resulting linewidth is then

$$\Delta\nu = \frac{1}{h}(\Delta E_k + \Delta E_i) = \frac{1}{2\pi} \left(\frac{1}{\tau_k} + \frac{1}{\tau_i} \right). \quad (4.93a)$$

If the transition occurs from an excited state $|k\rangle$ into the ground state ($\tau_i = \infty$), the linewidth is determined solely by the lifetime τ_k and

$$\Delta\omega_n = A_k = \frac{1}{\tau_k}; \quad \Delta\nu_n = \frac{1}{2\pi\tau_k}, \quad (4.93b)$$

where A_k is the Einstein coefficient of spontaneous emission introduced in Sect. 4.1.1.

Examples

- (a) Consider a vibration-rotation transition $(v', J') \leftarrow (v'', J'')$ in the electronic ground state. The lifetime of the upper level is $\tau_k = 1$ ms, that of the lower level is $\tau_i = \infty$. The natural linewidth of the transition is then $\Delta\nu_n = 150$ Hz!
- (b) A typical lifetime of an electronically excited level is $\tau = 10^{-8}$ s, from which it follows that $\Delta\nu_n = 15$ MHz.

4.3.2

Doppler Broadening

If an excited molecule moves with the velocity $v = \{v_x, v_y, v_z\}$ with $|v| \ll c$ with respect to an observer at rest (Fig. 4.19), the mean frequency ν_0 of the emission with the wavevector $\mathbf{k} = (2\pi/\lambda)\hat{e}$, where \hat{e} is the unit vector in the direction of emission, is shifted for the observer to a frequency

$$\nu = \nu_0 + \frac{1}{2\pi} \mathbf{k} \cdot \mathbf{v} = \nu_0 \left(1 + \frac{\mathbf{v} \cdot \hat{e}}{c} \right) \quad (4.94a)$$

due to the nonrelativistic Doppler effect. To avoid the factor 2π in the equations, the angular frequency $\omega = 2\pi\nu$ is frequently used, for which

$$\omega = \omega_0 + \mathbf{k} \cdot \mathbf{v}. \quad (4.94b)$$

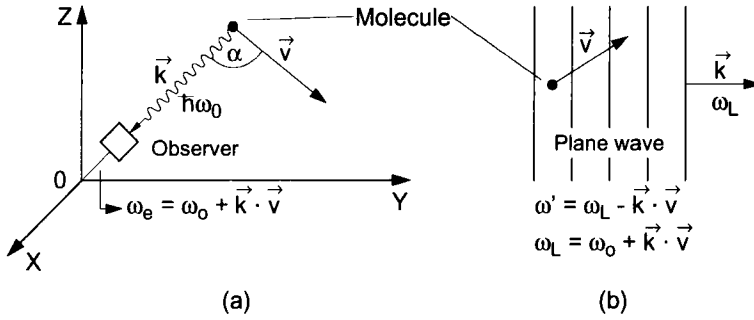


Fig. 4.19 Doppler shift of a) emission lines, b) absorption lines.

The absorption frequency ω_0 of a molecule moving with the velocity v with respect to a plane light wave of frequency ω_L and wavevector \mathbf{k} is also shifted, because the frequency of the wave appears, in the moving molecule's reference frame, as $\omega' = \omega_L - \mathbf{k} \cdot \mathbf{v}$ (Fig. 4.19b). The molecule absorbs if $\omega' = \omega_0$, that is, if the frequency of light ω_L as measured in the laboratory frame obeys the condition

$$\omega_L = \omega_0 + \mathbf{k} \cdot \mathbf{v} . \quad (4.95)$$

If the light wave propagates in the z direction ($\mathbf{k} = \{0, 0, k_z\}$), Eq. (4.95) can be written as

$$\omega_L = \omega_0 + k_z v_z = \omega_0 \left(1 + \frac{v_z}{c} \right) . \quad (4.96)$$

This shows that only the velocity component along \mathbf{k} contributes to the Doppler shift.

But how does the Doppler broadening arise? In thermal equilibrium, the molecules in a gas assume a Maxwellian velocity distribution. At a temperature T , the density $n_i(v_z)$ of light-emitting or absorbing molecules in the state $|i\rangle$ with a velocity component in the interval v_z to $v_z + dv_z$ is

$$n_i(v_z) dv_z = \frac{N_i}{v^* \sqrt{\pi}} e^{-(v_z/v^*)^2} dv_z , \quad (4.97)$$

where $v^* = (2k_B T/m)^{1/2}$ is the *most probable velocity*, N_i is the total number of molecules in the state E_i per unit volume, m is the molecular mass and k_B is the Boltzmann constant.

If we express v_z and dv_z in Eq. (4.97) by ω and $d\omega$ using Eq. (4.96), we obtain the number of molecules that absorb (or emit) in the frequency interval between ω and $\omega + d\omega$, that is

$$n_i(\omega) d\omega = N_i \frac{c}{v^* \omega_0 \sqrt{\pi}} \exp \left[- \left(c \frac{(\omega - \omega_0)}{(\omega_0 v^*)} \right)^2 \right] d\omega . \quad (4.98)$$

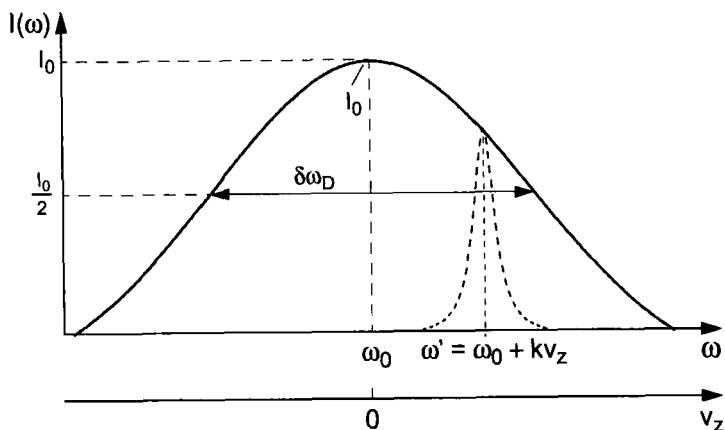


Fig. 4.20 Gaussian profile of a Doppler-broadened spectral line.

As the emitted or absorbed intensity $I(\omega)$ is proportional to $n_i(\omega)$, the intensity profile of the Doppler-broadened spectral line is

$$I(\omega) = I(\omega_0) \exp \left[- \left(c \frac{(\omega - \omega_0)}{(\omega_0 v^*)} \right)^2 \right]. \quad (4.99)$$

This is a Gaussian function (Fig. 4.20); its full width at half maximum $\delta\omega_D = |\omega_1 - \omega_2|$ can be obtained from the condition $I(\omega_1) = I(\omega_2) = I(\omega_0)/2$,

$$\delta\omega_D = 2\sqrt{\ln 2} \omega_0 \frac{v^*}{c}, \quad (4.100a)$$

or, with $v^* = \sqrt{2k_B T/m}$

$$\delta\omega_D = \left(\frac{\omega_0}{c} \right) \sqrt{\frac{8k_B T \ln 2}{m}}. \quad (4.100b)$$

We see that the Doppler width increases linearly with the frequency ω_0 , and for a given temperature T is largest for molecules with small masses.

If we expand the radicand in Eq. (4.100b) by Avogadro's constant N_A (= number of molecules per mole), the Doppler width can be expressed by the molar mass $M = mN_A$ and the gas constant $R = k_B N_A$ to obtain for the Doppler width in frequency units

$$\delta\nu_D = \frac{2\nu_0}{c} \sqrt{\frac{2RT \ln 2}{M}} = 7.16 \times 10^{-7} \nu_0 \sqrt{\frac{T}{M}} \text{ s}^{-1}. \quad (4.100c)$$

With $(4 \ln 2)^{-1/2} \approx 0.6$, we obtain for the Doppler-broadened line profile Eq. (4.99),

$$I(\omega) = I(\omega_0) \exp \left[- \left(\frac{\omega - \omega_0}{0.6 \delta\omega_D} \right)^2 \right]. \quad (4.101)$$

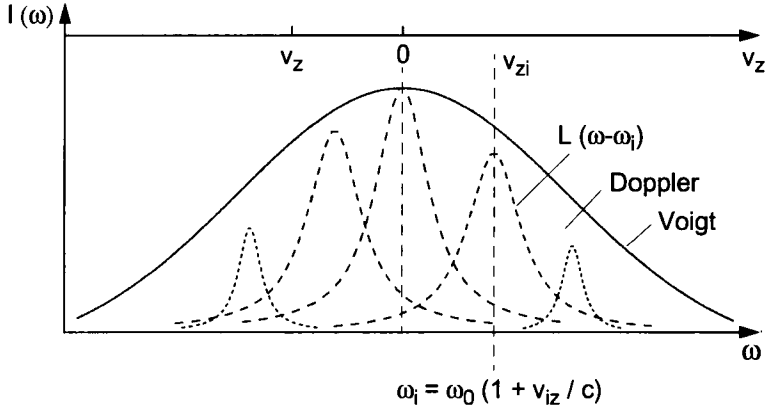


Fig. 4.21 Voigt profile as a superposition of the Doppler-shifted Lorentz profiles of molecules with different velocity components v_z .

Examples

- (a) In the infrared: vibration–rotation transition of CO_2 with $\lambda = 10\text{ mm}$; $\nu_0 = 3 \times 10^{13}\text{ s}^{-1}$, $T = 300\text{ K}$, $M = 44\text{ g/mol}$, $\Rightarrow \delta\nu_D = 5.6 \times 10^7\text{ s}^{-1} \cong 56\text{ MHz}$.
- (b) In the visible: electronic transition in the Na_2 molecule with $\lambda = 500\text{ nm}$; $\nu_0 = 6 \times 10^{14}\text{ s}^{-1}$, $T = 500\text{ K}$, $M = 46\text{ g/mol}$, $\Rightarrow \delta\nu_D = 1.4 \times 10^9\text{ s}^{-1} = 1.4\text{ GHz}$.

From these examples, we see that in the visible, Doppler broadening exceeds natural linewidths by about two orders of magnitude.

The Doppler broadening can be reduced or even eliminated experimentally by several, so-called Doppler-free, spectroscopic techniques (see Sect. 12.4). Still, there remains a finite linewidth, which is partly caused by the natural linewidth.

4.3.3

Voigt Profiles

Until now we have assumed that the molecular oscillator is at rest. If the molecule moves with a velocity v , its absorption or emission frequency is Doppler-shifted, and we obtain, according to Eq. (4.94b), for the line profile of the molecule instead of Eq. (4.91) the Lorentz profile

$$I(\omega) = \frac{C}{(\omega - \omega')^2 + (\frac{\gamma}{2})^2} \quad \text{with} \quad \omega' = \omega_0 + \mathbf{k} \cdot \mathbf{v}. \quad (4.102)$$

The total absorption profile of all molecules with the thermal velocity distribution Eq. (4.97) is obtained by the convolution

$$I(\omega) = C \int_{-\infty}^{+\infty} \frac{e^{-[c(\omega-\omega')/\omega_0 v^*]^2}}{(\omega-\omega')^2 + (\gamma/2)} d\omega', \quad (4.103)$$

of the differently Doppler-shifted Lorentz profiles of the individual molecules with the Gaussian velocity distribution of all molecules (Fig. 4.21). This convolution of Lorentzian and Gaussian profiles is called *Voigt profile*.

4.3.4

Collisional Broadening of Spectral Lines

If a molecule A with energy levels E_i and E_f approaches another atom or molecule B, its energy levels are shifted due to the interaction between A and B. The extent of the shifts depends on the structure of the electron clouds of A and B, the states E_i and E_f , which may belong to the same (rotational and vibrational transitions) or two different (electronic transitions) electronic configurations, and on the mutual distance $R(A, B)$, which we define to be the distance between the molecular centers of mass of A and B. The shifts are in general different for different levels E_j , and they can be towards higher energies (for repulsive potential between A(E_i) and B) or towards lower energies (for an attractive interaction). If we plot the energy $E_i(R)$ of the levels of A as a function of the distance R , we obtain the potential curves displayed schematically in Fig. 4.22. The system AB(R) is called *collision pair*, and the approach of two particles up to a distance R in which their mutual interaction is non-negligible is also called a *collision*. If A and B approach each other along a potential curve that possesses a minimum, a stable molecule may result if excess energy can be removed from the system during the collision by emission of radiation or by a collision with a third particle. In this case, the collision pair is said to be “stabilized”.

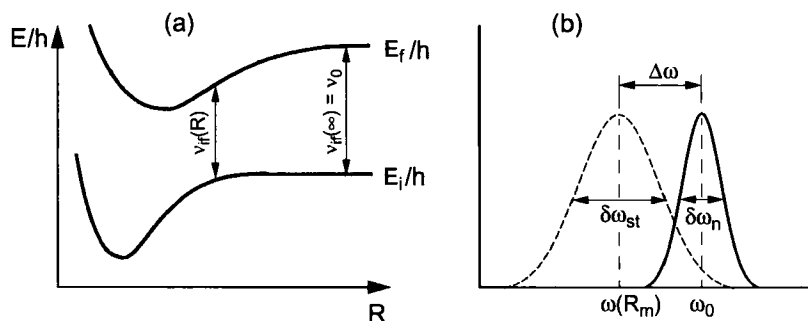


Fig. 4.22 a) Schematic potential curves of a collisional pair, and b) explanation of collisional broadening and shifts.

If an absorption or emission transition occurs between the levels E_i and E_f during the collision, the frequency $\nu_{if} = \omega_{if}/2\pi$ of the absorbed or emitted light depends, according to $h\nu_{if} = |E_f(R) - E_i(R)|$, on the distance R between A and B at the time of the transition.

In a gas containing molecules A and B, the distances R between pairs of particles are distributed statistically around a mean value \bar{R} that depends on the pressure and the temperature of the gas. Consequently, the frequencies ν_{if} are also statistically distributed around a mean value $\bar{\nu}$, which in general is shifted with respect to the frequency ν_0 of the unperturbed atom. The shift $\Delta\nu = \nu_0 - \bar{\nu}$ is a measure for the *difference* of the energy shifts of both levels E_i and E_f at a distance R_{\max} , for which the maximum light emission occurs. The profile of the collision-broadened spectral line conveys information on the R dependence of the difference potential curve $E_f(R) - E_i(R)$ and hence on the difference of the interaction potentials $V[A(E_f)B] - V[A(E_i)B]$.

In the process described above, light emission (or absorption) occurred from the initially occupied level E of atom A, which was (slightly) shifted only during the interaction, but quickly relaxed to its original energy after the interaction. We call this situation a line broadening $\delta\nu$ and line shift $\Delta\nu$ by *elastic collisions*. The small energy difference $h\Delta\nu = E_f - E_i - h\nu$ is provided, for positive $\Delta\nu$, by the kinetic energy of the collision partners and not by some kind of internal energy of one of the partners. For negative $\Delta\nu$, the excess energy is converted to kinetic energy.

Apart from such elastic collisions, *inelastic collisions* can also occur, in which the excitation energy E_i is partly or completely converted to internal energy of the collision partner B or to kinetic energy of both partners. Such collisions are also called *quenching collisions*, because they reduce the population of level E_i and hence decrease the corresponding fluorescence intensity.

The probability that the excitation energy E_i can be transferred to the collision partner B is particularly large if B is a molecule with many vibration-rotation levels in the different electronic states, which therefore possesses many allowed resonant transitions $E_l \rightarrow E_m$ with $|E_l - E_m| \cong |E_i - E_f|$. If S_{ik} is the probability that an excited state E_i undergoes a radiationless transition to a state E_k by the collision with B, the total transition probability from level E_i to other states E_k of particle A is

$$A_i = \sum_k A_{ik}(\text{spontaneous}) + \sum_k S_{ik} . \quad (4.104)$$

The probability S_{ik} for such a collision-induced transition depends on the density N_B of particles B, on the mean relative velocity \bar{v} of the collision partners, and on the collision cross-section σ_{ik} , that is

$$S_{ik} = N_B \bar{v} \sigma_{ik} . \quad (4.105)$$

In thermal equilibrium, the mean relative velocity at a temperature T is given by

$$\bar{v} = \sqrt{\frac{8k_B T}{\pi} \left(\frac{1}{M_A} + \frac{1}{M_B} \right)} , \quad (4.106)$$

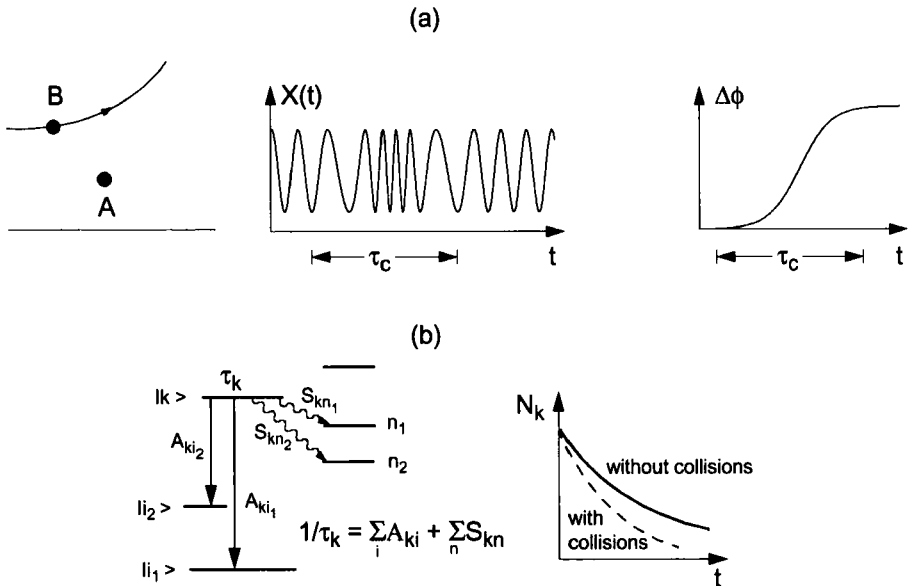


Fig. 4.23 a) Elastic collisions as phase-disturbing collisions; b) inelastic collisions as lifetime-reducing deactivation processes for an excited level.

so that the collision-induced transition probability per unit time for the transition $E_i \rightarrow E_k$ is

$$S_{ik} = N_B \sigma_{ik} \sqrt{\frac{8k_B T}{\pi \mu}}, \quad (4.107)$$

where $\mu = M_A M_B / (M_A + M_B)$ is the reduced mass of the collision pair.

The effective lifetime $\tau_{\text{eff}} = 1/A_i$ of the level E_i is decreased by the collisions. As a consequence, the linewidth of the radiation from E_i increases (Sect. 4.3.1). As the linewidth is $\delta\nu_{if} = A_i/2\pi$, Eq. (4.93b), we see from Eqns. (4.104) and (4.105) that it increases linearly with the density N , that is with the pressure of component B. Collision-induced broadening is therefore also called *pressure broadening*. If the collision partners A and B are identical molecules ($A = B$), the term *self-pressure broadening* is used (Fig. 4.23a).

We have seen that both elastic and inelastic collisions lead to a broadening of spectral lines, and that elastic collisions additionally lead to line shifts.

Both processes can be treated classically in the framework of the damped harmonic oscillator model as demonstrated by Weißkopf [4.10]. In this model, inelastic collisions change the amplitude of the oscillation. This can be described by introducing a damping constant γ_{coll} (in addition to the radiation-induced damping γ_n), and the arguments discussed in Sect. 3.1 then lead to a Lorentzian profile with a linewidth $\delta\omega = \gamma_n + \gamma_{\text{coll}}$.

Elastic collisions do not influence the amplitude of the oscillation in this model, but change its *phase* (by frequency detuning during the interaction). They are thus also called *phase-disturbing collisions* (Fig. 4.23a). If the phase shift $\Delta\phi$ during a collision is large enough, the oscillations before and after the collision are uncorrelated and two independent wavepackets result, the mean lengths of which are determined by the mean time between two collisions. A Fourier analysis of these wavepackets then yields the frequency spectrum and hence the line profile.

After lengthy calculations, one obtains for the line profile as determined by elastic and inelastic collisions the expression

$$I(\omega) = I_0 \frac{[(\gamma + \gamma_{\text{inel}})/2 + N\bar{v}\sigma_b]^2}{(\omega - \omega_0 - N\bar{v}\sigma_s)^2 + [(\gamma + \gamma_{\text{inel}})/2 + N\bar{v}\sigma_b]^2}, \quad (4.108)$$

where N is the density of the colliding molecules B, \bar{v} is the mean relative velocity, and $I_0 = I(\omega'_0)$ is the intensity at the line maximum at the shifted frequency $\omega'_0 = \omega_0 + N\bar{v}\sigma_s$. The cross-sections σ_b and σ_s determine the line broadening and shifts by the elastic phase-disturbing collisions. The condition $\sigma_b > 0$ always holds, whereas σ_s can be positive or negative.

4.4

Multi-photon Transitions

In this section, we will consider the simultaneous absorption of two or more photons by a molecule, leading to a transition $E_i \rightarrow E_f$ with $(E_f - E_i) = \sum \hbar\omega_n$.

The probability of multi-photon transitions depends on the corresponding matrix element and on the probability that m photons can interact with the molecule simultaneously. For classical light sources, this probability is extremely small. Hence, multi-photon transitions could be investigated with a sufficiently large signal-to-noise ratio only after lasers were introduced into experimental molecular physics. The absorbed photons can be from a single laser beam or, if the sample is irradiated with several lasers, from different beams.

4.4.1

Two-Photon Absorption

The first detailed theoretical treatment of two-photon absorption processes was given by Göppert-Mayer in 1931 [4.12], but the experimental realization of the effect succeeded only in 1961 using a pulsed laser [4.13].

The probability W_{if} that a molecule with velocity v in a state E_i absorbs two photons $\hbar\omega_1$ and $\hbar\omega_2$ simultaneously from two light waves with wavevectors \mathbf{k}_1 and \mathbf{k}_2 , polarization vectors $\hat{\mathbf{e}}_1$ and $\hat{\mathbf{e}}_2$, and intensities I_1 and I_2 , and is excited into a state E_f ,

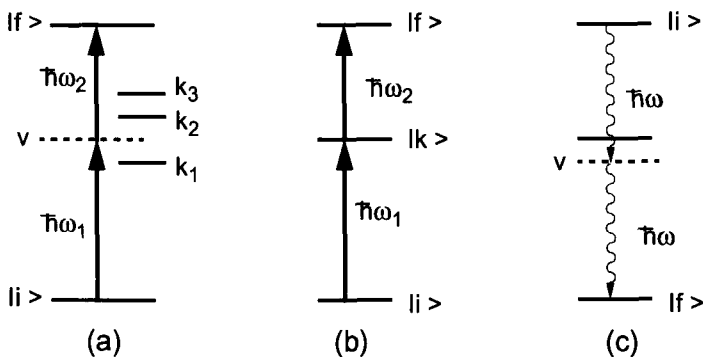


Fig. 4.24 Two-photon transitions. a) Nonresonant two-photon absorption with virtual level v ; b) resonant two-photon absorption; c) two-photon emission.

can be written as a product of two factors [4.14],

$$W_{if} \sim \frac{\gamma_{if} I_1 I_2}{\left[\omega_{if} - \omega_1 - \omega_2 - v \cdot (\mathbf{k}_1 + \mathbf{k}_2) \right]^2 + (\gamma_{if}/2)^2} \times \left| \sum_k \frac{(\mathbf{R}_{ik} \cdot \hat{\mathbf{e}}_1)(\mathbf{R}_{kf} \cdot \hat{\mathbf{e}}_2)}{(\omega_{ik} - \omega_1 - \mathbf{k}_1 \cdot v)} + \frac{(\mathbf{R}_{ik} \cdot \hat{\mathbf{e}}_2)(\mathbf{R}_{kf} \cdot \hat{\mathbf{e}}_1)}{(\omega_{ik} - \omega_2 - \mathbf{k}_2 \cdot v)} \right|^2. \quad (4.109)$$

As two photons must be absorbed simultaneously by the molecule, the transition probability per molecule is proportional to the product $I_1 I_2$ of the two intensities, provided one photon from each wave contributes to the transition. If both photons are from the same beam, $I_1 = I_2$, $\omega_1 = \omega_2$, and $\mathbf{k}_1 = \mathbf{k}_2$.

The first factor in Eq. (4.109) describes the spectral line profile of the transition $E_i \rightarrow E_f$ and corresponds exactly to the line profile of a one-photon transition with the Doppler-shifted mean frequency $\omega_{if} = \omega_1 + \omega_2 + v \cdot (\mathbf{k}_1 + \mathbf{k}_2)$ and the homogeneous linewidth γ_{if} . Integration over the molecular velocity distributions $N_i(v_z)$ yields a Voigt profile with a width depending on the relative orientation of the two wavevectors \mathbf{k}_1 and \mathbf{k}_2 . For collinear laser beams $\mathbf{k}_1 \parallel \mathbf{k}_2$, and the Doppler width assumes a maximum, whereas for anti-collinear beams with $\mathbf{k}_1 = -\mathbf{k}_2$, the Doppler broadening of the two-photon transition vanishes, and a pure homogeneously broadened signal of width γ_{if} is obtained. This so-called *Doppler-free two-photon spectroscopy* is described in Sect. 12.4.9.

The second factor in Eq. (4.109), which is obtained quantum mechanically through a second-order perturbation calculation, describes the probability of a two-photon absorption as the square of a sum over the products of one-photon matrix elements. It can be visualized as follows (Fig. 4.24). The two-photon transition can be considered as a (not necessarily resonant) two-stage process $|i\rangle \rightarrow |k\rangle \rightarrow |f\rangle$, where the sum runs over all intermediate states $|k\rangle$ accessible from the initial state $|i\rangle$ of the molecule. The

first photon can excite the off-resonance state $|k\rangle$ somewhere in the outer regions of the one-photon absorption line profile. However, the denominators of the sum terms become sufficiently small only if $\omega_1 - \mathbf{k}_1 \cdot \mathbf{v}$ is close to a one-photon resonance ω_{ik} of the molecule and $\omega_2 - \mathbf{k}_2 \cdot \mathbf{v} \approx \omega_{fk}$, so that in general only a few intermediate states $|k\rangle$ contribute significantly to the total transition probability, that is, only a few terms of Eq. (4.109) survive.

This two-stage process is often described by symbolically introducing a resonant *virtual state* $|v\rangle$ of the molecule, which is not a real eigenstate. The two sums in Eq. (4.109) then correspond to the two two-stage processes

$$E_i + \hbar\omega_1 \rightarrow E_v ; \quad E_v + \hbar\omega_2 \rightarrow E_f , \quad (4.110a)$$

$$E_i + \hbar\omega_2 \rightarrow E_v ; \quad E_v + \hbar\omega_1 \rightarrow E_f . \quad (4.110b)$$

As the two alternatives cannot be distinguished and lead to the same result – the excitation of the real final state E_f – the total probability of the two-photon transition equals the square of the sum of both amplitudes.

The second factor in Eq. (4.109) describes the general probability for two-photon transitions such as nonresonant two-photon absorption (Fig. 4.24a), resonant two-stage excitation (Fig. 4.24b), two-photon emission (Fig. 4.24c) or Raman scattering (see next section). For all these processes, the same selection rules hold.

For the two-photon process to be allowed, the matrix elements R_{ik} for the transition $|i\rangle \rightarrow |k\rangle$ and R_{kf} for the transition $|k\rangle \rightarrow |f\rangle$ must both be nonzero. One consequence of this fact is that two-photon transitions always occur between states of like parity. For example, in homonuclear diatomic molecules, $g \rightarrow g$ transitions between two even (g) states or $u \rightarrow u$ transitions between two odd (u) states can be induced, which are forbidden for one-photon absorption. In vibration–rotation transitions $(v', J') \leftarrow (v'', J'')$, transitions with $J' = J''$ or $J' = J'' \pm 2$ become possible, and for electronic transitions $\Delta\Lambda = 0, 1, 2$ is allowed.

This shows that through two-photon absorption from the thermally occupied ground state, molecular states can be reached which cannot be populated using one-photon absorption, and indeed a number of hitherto unknown states have been discovered using this technique. Frequently, states accessible through one-photon absorption are *perturbed* by other states of opposite parity due to a coupling with $\Delta L = \pm 1$ (i.e., through spin–orbit or Coriolis coupling) between perturbing and perturbed state (see Ch. 9). This perturbing state can be investigated only indirectly using one-photon absorption, but it is directly accessible for two-photon spectroscopic methods. Hence, both methods yield complementary information on excited states.

The characteristics and advantages of two-photon spectroscopy can be summarized as follows:

1. Through two-photon absorption, excited molecular states can be reached that are not accessible from the absorbing initial state through one-photon dipole processes for symmetry reasons.

2. Using laser beams in the visible, multi-photon absorption can populate highly excited molecular levels with energies

$$\hbar\omega = \sum \hbar\omega_n,$$

which would need ultraviolet photons in the one-photon case.

3. Auto-ionizing states (such as Rydberg states above the molecule's ionization energy) can often be excited using multi-photon absorption. Such excitations have, in general, cross-sections that are several orders of magnitude larger than those of direct photoionization. Measurement of the ions then provides a very sensitive detection of small concentrations of molecules. Hence, multi-photon ionization is useful as a highly sensitive method of analysis, and is already used as such in many cases.
4. Multi-photon absorption of infrared radiation (e.g., from a CO₂ laser) can be used, under suitable experimental conditions, to dissociate molecules in specific fragments. This method opens ways to selectively start laser-induced chemical reactions.
5. With a suitably chosen geometrical arrangement of laser beams, the vectorial sum of the photon momenta absorbed by a molecule can be made to vanish. In such a case, the absorption frequencies of a molecule are independent of its velocity, and Doppler-free absorption profiles are obtained.

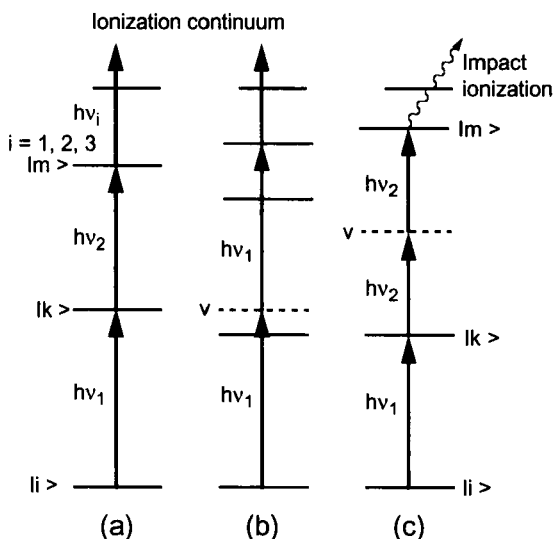


Fig. 4.25 a) and c) Doubly-resonant and b) singly-resonant three-photon ionization. In a) and b) the ionization is effected by the third photon, in c) a highly excited

Rydberg state is populated by nonresonant two-photon absorption from the excited state k , which can then be ionized by collisions.

By absorption of three photons, states of opposite parity can be reached from the ground state just as in the case of one-photon absorption. However, highly excited states with energies $3\hbar\omega$ above the ground state can be reached using laser light in the visible. The absorption probability is largely enhanced if at least one of the photons is at resonance with an allowed transition in the molecule. In the case of a two-photon resonance, it is even larger (Fig. 4.25).

If a state less than $\hbar\omega$ below the molecule's ionization threshold can be reached with two photons, the third can be used to ionize the molecule from that intermediate excited state. More detailed information can be found in the proceedings of a biannual conference series on multi-photon spectroscopy [4.15].

4.4.2

Raman Transitions

Raman transitions can be considered inelastic scattering processes of a photon $\hbar\omega_i$ at a molecule in the initial state $|i\rangle$ with the energy E_i , during which the molecule makes a transition to the higher state E_f , and the scattered photon with frequency ω_{sc} has lost the energy $\Delta E = E_f - E_i = \hbar(\omega_i - \omega_{sc})$ (Fig. 4.26a),

$$\hbar\omega_i + M(E_i) \rightarrow M^*(E_f) + \hbar\omega_{sc} . \quad (4.111)$$

The energy difference ΔE can be converted to rotational, vibrational, or electronic energy of the molecule. The intermediate state $|v\rangle$ with energy

$$E_v = E_i + \hbar\omega_i$$

of the system (molecule + photon) during the scattering process is formally called a *virtual state* (Fig. 4.26b); only in the special case of *resonant Raman scattering* does it coincide with a real state of the molecule.

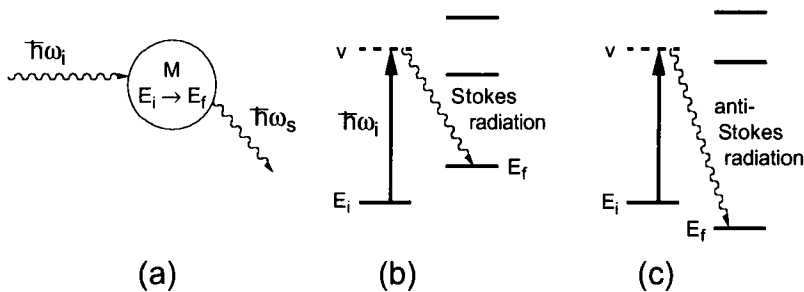


Fig. 4.26 a) Raman scattering as inelastic scattering of photons; b) nonresonant Raman–Stokes process; c) formation of anti-Stokes radiation.

The classical description of the Raman effect assumes that an incident light wave $\mathbf{E} = \mathbf{E}_0 \cos \omega t$ induces an oscillating dipole moment

$$\boldsymbol{\mu}_{\text{ind}} = \alpha \mathbf{E}$$

in the molecule, where α is the molecule's polarizability. This induced moment is superimposed upon an existing permanent dipole moment $\boldsymbol{\mu}_0$, so that the total dipole moment is

$$\boldsymbol{\mu} = \boldsymbol{\mu}_0 + \alpha \mathbf{E} . \quad (4.112)$$

Both dipole moment and polarizability depend on the internuclear distance and the electronic configuration. For small displacements of the nuclei from their equilibrium positions we can approximate both quantities by the first term of a Taylor expansion

$$\begin{aligned} \boldsymbol{\mu} &\approx \boldsymbol{\mu}(0) + \left(\frac{\partial \boldsymbol{\mu}}{\partial R} \right)_{R_e} (R - R_e) ; \\ \alpha(R) &\approx \alpha(0) + \left(\frac{\partial \alpha}{\partial R} \right)_{R_e} (R - R_e) , \end{aligned} \quad (4.113)$$

where $\boldsymbol{\mu}(0)$ and $\alpha(0)$ are the dipole moment and the polarizability at the equilibrium internuclear distance. For small vibrational amplitudes, the molecular vibrations can be considered harmonic, thus we obtain for $\Delta R = R - R_e$

$$\Delta R(t) = A_v \cos \omega_v t , \quad (4.114)$$

where A_v and ω_v are the amplitude and the frequency of the molecular vibration, respectively. If we substitute Eqns. (4.113) and (4.114) into Eq. (4.112), we obtain the time-dependent dipole moment

$$\begin{aligned} \boldsymbol{\mu}(t) &= \boldsymbol{\mu}_0 + \left(\frac{\partial \boldsymbol{\mu}}{\partial R} \right)_{R_e} A_v \cos \omega_v t + \alpha(0) \mathbf{E}_0 \cos \omega t \\ &\quad + \frac{\mathbf{E}_0}{2} \left(\frac{\partial \alpha}{\partial R} \right)_{R_e} A_v [\cos(\omega - \omega_v)t + \cos(\omega + \omega_v)t] . \end{aligned} \quad (4.115)$$

The first term describes the molecular permanent dipole moment, the second term represents contributions oscillating with the molecular vibration that are responsible for the infrared spectrum of the molecule (see Sect. 4.2.2). The further terms describe contributions to the molecular dipole moment induced by the incident electromagnetic wave. As an oscillating dipole moment creates new electromagnetic waves, we see from Eq. (4.115) that each molecule contributes microscopically to the elastic scattering at the incident frequency ω (*Rayleigh scattering*) and to the inelastic scattering (*Raman scattering*) at the frequencies $(\omega - \omega_n)$ (*Stokes waves*). If the molecule exists in an excited state before the scattering, superelastic scattering can also occur, where the scattered wave displays frequencies $(\omega + \omega_n)$, which are called *anti-Stokes components* (Fig. 4.26c).

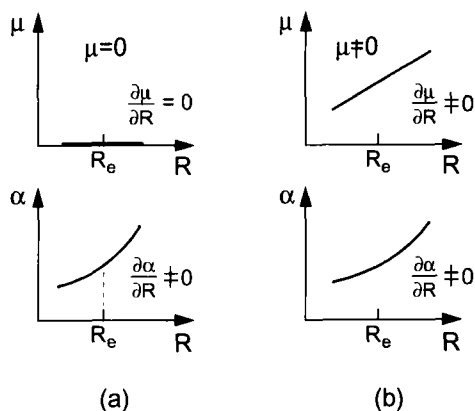


Fig. 4.27 Variations of electric dipole moment and polarizability a) for homonuclear and b) for heteronuclear diatomic molecules.

These microscopic contributions of the individual molecules to the scattered radiation combine to form macroscopic waves with intensities depending on the incident intensity I_L , the population density N_i of the scattering molecules, the phase differences of the individual scattered waves, and on the coefficients $(\partial\alpha/\partial R)$.

We see from Eq. (4.115) that the infrared absorption depends on the variation of the molecular dipole moment with nuclear coordinates, $(\partial\mu/\partial R)$, whereas the intensity of Raman scattering is determined by the variation of the molecular *polarizability*, $(\partial\alpha/\partial R)$. Hence, homonuclear diatomic molecules possess no infrared spectrum (because $\partial\mu/\partial R = 0$ for symmetry reasons) but they do show a Raman spectrum, provided $\partial\alpha/\partial R \neq 0$ (Fig. 4.27). Heteronuclear molecules can show both an infrared and a Raman spectrum.

Although the classical description of Raman scattering outlined above yields the correct frequencies for the Raman lines, their intensities can only be calculated with the aid of quantum theory. For this purpose, we need to compute the expectation value

$$\langle \alpha_{ik} \rangle = \int \psi_i^* \alpha \psi_k d\tau \quad (4.116)$$

of the polarizability α . Formally, it corresponds to the matrix element Eq. (4.23) for a dipole transition [4.16].

4.4.3

Raman Spectra

While for one-photon dipole transitions, the selection rules $\Delta J = \pm 1$ or $\Delta J = 0$ (for $\Delta l = \pm 1$) hold for the rotational quantum number J , these are modified for two photons to become

$$\Delta J = 0, \pm 2 .$$

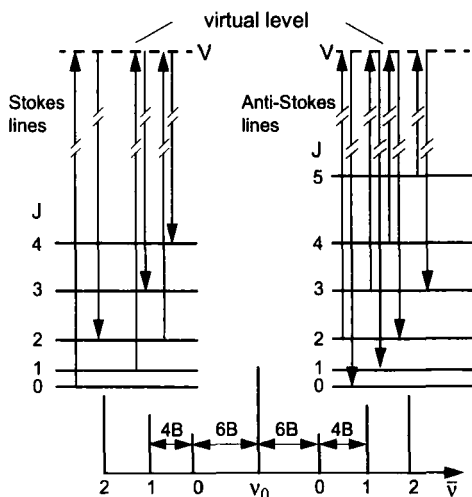


Fig. 4.28 Rotational Raman transitions. J is always the quantum number of the lower level.

For rotational Raman spectra, where E_i and E_f correspond to rotational levels in the electronic ground state and the same vibrational level, we obtain for the Stokes lines $J_f \rightarrow J_i + 2$ with $\Delta J = +2$ and for the anti-Stokes lines $J_f = J_i - 2$ with $\Delta J = -2$ (Fig. 4.28). Neglecting centrifugal distortion, the wavenumbers of the Stokes lines are shifted by an amount

$$\Delta\nu = B[J(J+1) - (J+2)(J+3)] = -2B(2J+3) \quad (4.117)$$

with respect to the incident line, which starts from a level with quantum number J , whereas the anti-Stokes lines are shifted by

$$\Delta\nu = B[(J+2)(J+3) - J(J+1)] = +2B(2J+3) \quad (4.118)$$

for an excitation from a level $(J+2)$.

Hence, the distances between rotational Raman lines are different from those of the one-photon rotational lines in Fig. 3.1.

In vibration-rotation Raman spectra, the vibrational quantum number v also changes, and the Raman transitions $(v_i, J_i \rightarrow v_f, J_f)$ consist of an S branch ($J_i \rightarrow J_f = J_i + 2$) with $\Delta J = +2$, a Q branch ($J_i = J_f$) with $\Delta J = 0$, and an O branch ($J_i \rightarrow J_f = J_i - 2$) with $\Delta J = -2$ both in the Stokes spectrum ($v_i \rightarrow v_f = v_i + 1$) and in the anti-Stokes spectrum ($v_i \rightarrow v_f = v_i - 1$) (Fig. 4.29). Transitions with $\Delta v = \pm 2, 3, \dots$ occur also, but with lower intensity.

The term values of the involved levels $v_i = 0$ and $v_f = 1$ are (neglecting anharmonicities and centrifugal effects)

$$E_{0J} = \frac{1}{2}\omega_e + B_0J_i(J_i + 1); \quad E_{1J} = \frac{3}{2}\omega_e + B_1J_f(J_f + 1). \quad (4.119)$$

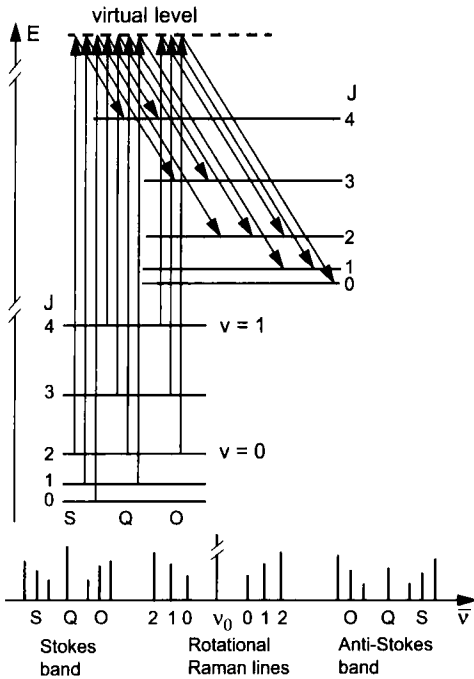


Fig. 4.29 Stokes Raman spectrum of vibration–rotation transitions. The anti Stokes transitions are obtained by reversing all arrow directions.

The Stokes transitions for the S branch ($0, J \rightarrow 1, J + 2$) occur at the wavenumbers

$$\tilde{\nu}_S^{\text{St}} = \tilde{\nu}_0 - \omega_e - 6B_1 - (5B_1 - B_0)J - (B_1 - B_0)J^2, \quad (4.120a)$$

for the Q branch ($0, J \rightarrow 1, J$) at

$$\tilde{\nu}_Q^{\text{St}} = \tilde{\nu}_0 - \omega_e - (B_1 - B_0)J - (B_1 - B_0)J^2, \quad (4.120b)$$

and for the O branch ($0, J \rightarrow 1, J - 2$) at

$$\tilde{\nu}_O^{\text{St}} = \tilde{\nu}_0 - \omega_e - 2B_1 + (B_0 + 3B_1)J - (B_1 - B_0)J^2, \quad (4.120c)$$

where ν_0 is the wavenumber of the exciting transition. For anti-Stokes lines corresponding expressions are obtained.

As vibrational frequencies are about two orders of magnitude larger than rotational frequencies, lines appear in vibration–rotation Raman spectra that are shifted from the exciting line by vibrational frequencies and that contain the respective rotational lines as fine structure (Fig. 4.29).

This may be compared to the corresponding infrared vibration–rotation transitions in Fig. 4.4.

4.5

Thermal Population of Molecular Levels

The intensity of spectral lines depends not only on the corresponding transition probabilities but also on the population density N_i (number of molecules in the state $|i\rangle$ per unit volume) of the molecular levels involved in the transition.

For emission spectra, this is the population of the upper emitting level, for absorption spectra it is the population difference between lower and upper level, for Raman spectra it is the population of the lower level from which the excitation occurs.

The population density depends on the temperature T and the statistical weight of the state. The statistical weight g indicates the number of energetically identical (degenerate) sublevels of a molecular state. For example, the statistical weight of a rotational level is $g = 2J + 1$, because the angular momentum J can assume $2J + 1$ possible orientations in space with the orientational quantum number M ($-J < M < +J$), which are energetically identical in the absence of an external field.

Additionally, the nuclear spins on the nuclei in a molecule contribute also to the statistical weight of a molecular level, as will be explained below.

4.5.1

Thermal Population of Rotational Levels

As explained in textbooks of physics, the population density N_i of a level with energy E_i is given by the Boltzmann factor

$$N_i = g_i \left(\frac{N}{Z} \right) e^{-E_i/k_B T}, \quad (4.121)$$

where $N = \sum_i N_i$ is the total density of the molecules and $Z = \sum e^{-E_i/k_B T}$ is the partition function, which acts as a normalization factor ensuring the condition $\sum N_i = N$ when Z is substituted into Eq. (4.121). The statistical weight

$$g_i = (g_{\text{rot}} g_{\text{vib}} g_{\text{nuc}})_i \quad (4.122)$$

of a vibration–rotation level contains contributions from rotation, vibration, and the nuclear spins.

If we ignore nuclear spin effects for the moment, the population of the rotational levels of a diatomic molecule is given, according to Eq. (4.121), by

$$N_i(J) = (2J + 1) \left(\frac{N_v}{Z} \right) e^{-E(J)/k_B T} \quad (4.123)$$

(Fig. 4.30b), where N_v is the total population of the vibrational level $|v\rangle$.

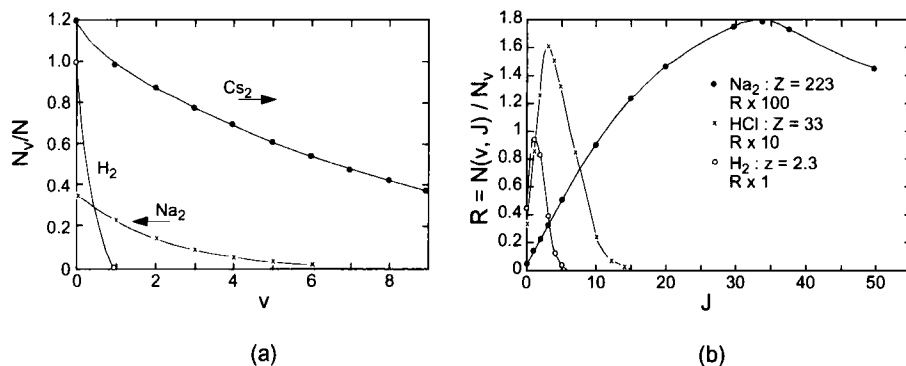


Fig. 4.30 Thermal population of a) the vibrational levels and b) rotational levels of some diatomic molecules at $T = 300$ K.

4.5.2

Population of Vibration–Rotation Levels

The rotationless vibrational levels of a diatomic molecule possess only one degree of freedom, that is, they are nondegenerate and hence their statistical weight is $g_v = 1$. The population distribution over the vibrational levels with energies $E_i = (v_i + \frac{1}{2})h\omega_v$ is then

$$N_i(v) = \left(\frac{N}{Z_{\text{vib}}} \right) e^{-E_i/k_{\text{B}}T}, \quad (4.124)$$

where $Z_{\text{vib}} = \sum_i e^{-E_i/k_{\text{B}}T}$ is the vibrational partition function and N is the total number of molecules per unit volume (Fig. 4.30a).

If we combine Eqns. (4.123) and (4.124), we obtain the population density N_i in a vibration–rotation level (v, J) ,

$$N_i(v, J) = (2J + 1) \frac{N}{Z_{\text{rot}}Z_{\text{vib}}} e^{-E_{\text{rot}}/k_{\text{B}}T} e^{-E_{\text{vib}}/k_{\text{B}}T}. \quad (4.125)$$

4.5.3

Nuclear Spin Statistics

Finally, we will turn our attention to the influence of the nuclear spins on the population distributions.

If we exchange the nuclei in a homonuclear diatomic molecule, the wavefunction of a state can be symmetric (i.e., it remains unchanged if the nuclei are exchanged) or antisymmetric (it changes sign). Within the Born–Oppenheimer approximation the total wavefunction can be written as a product

$$\Psi = \psi_{\text{el}}\psi_{\text{vib}}\psi_{\text{rot}}\psi_{\text{ns}} \quad (4.126)$$

of electronic, vibrational, rotational, and nuclear spin contributions. Nuclei with half-integer nuclear spin $I = (n + \frac{1}{2})h$ are fermions. The total wavefunction must therefore be antisymmetric with respect to the exchange of identical nuclei. Nuclei with integer nuclear spin $I = nh$ are bosons, and the total wavefunction must be symmetric with respect to the exchange of identical nuclei. As both ψ_{el} and ψ_{vib} are symmetric with respect to exchange of nuclei, the product $\psi_{\text{rot}}\psi_{\text{ns}}$ must be antisymmetric for nuclei with half-integer spin and symmetric for nuclei with integer spin.

As an example, we consider the rotational levels in a Σ_{g}^{+} state. Here, ψ_{rot} is symmetric for levels with even rotational quantum number J and antisymmetric for odd J . To make the product $\psi_{\text{rot}}\psi_{\text{ns}}$ antisymmetric, symmetric nuclear spin functions ψ_{ns} must be combined with odd values of J , and antisymmetric nuclear spin functions ψ_{ns} must be combined with even values of J . For example, if the identical nuclei possess nuclear spin $\frac{1}{2}$, their nuclear spin quantum number is $\pm\frac{1}{2}$ [i.e., the spins can be oriented up (α) or down (β)]. We can then construct three symmetric nuclear spin functions $\alpha\alpha$, $\beta\beta$, and $(\alpha\beta + \beta\alpha)/\sqrt{2}$, but only one antisymmetric combination $(\alpha\beta - \beta\alpha)/\sqrt{2}$.

This means that for a nuclear spin of $\frac{1}{2}$, the statistical weight of the symmetric nuclear spin functions is three times that of the antisymmetric functions. Hence, the population of the rotational levels in the Σ_{g}^{+} ground state of the H_2 molecule (nuclear spin of the nuclei is $\frac{1}{2}$) for odd rotational quantum numbers J is (apart from the Boltzmann factor) three times that of the states with even J .

Generally, for homonuclear diatomic molecules with nuclear spins I , there are $(2I + 1)(I + 1)$ symmetric and $(2I + 1)I$ antisymmetric nuclear spin wavefunctions. The ratio of the two statistical weights is therefore

$$\frac{g_{\text{ns}}(\text{sym})}{g_{\text{ns}}(\text{asym})} = \frac{(I + 1)}{I}. \quad (4.127a)$$

For half-integer I (nuclei are fermions) the population ratio of rotational levels in symmetric electronic states is

$$\frac{N(J = \text{odd})}{N(J = \text{even})} = \frac{I + 1}{I}. \quad (4.127b)$$

In antisymmetric electronic states (e.g., Σ_{g}^{-}),

$$\frac{N(J = \text{odd})}{N(J = \text{even})} = \frac{I}{I + 1}. \quad (4.127c)$$

Therefore the line intensities in rotation-resolved absorption spectra of H_2 alternate by a factor of three. Before arriving at the correct explanation of this phenomenon it was believed that there are two different types of hydrogen, called para hydrogen (with antiparallel nuclear spins and therefore total spin $I_1 + I_2 = 0$) and ortho hydrogen (with parallel nuclear spins and total nuclear spin $I_1 + I_2 = 1$). In para hydrogen, the

Tab. 4.1 Nuclear spin statistics: symmetries of ψ_{rot} , ψ_{nuc} , and Ψ , and statistical weights for fermionic and bosonic nuclei.

Electronic State		Fermions					Bosons				
		ψ_{rot}	ψ_{ns}	Ψ	g_{nuc}		ψ_{rot}	ψ_{ns}	Ψ	g_{nuc}	
$I = \frac{1}{2}$	$I = \frac{3}{2}$				$I = 0$	$I = 1$					
Σ_g^+	even	s	a	a	1	6	s	s	s	1	6
	odd	a	s	a	3	10	a	a	s	0	3
Σ_g^-	even	s	s	a	3	10	s	a	s	0	3
	odd	a	a	a	1	6	a	s	s	1	6

nuclear spin wavefunction is antisymmetric, and therefore only rotational levels with even J are occupied; in ortho hydrogen only those with odd J are occupied.

For bosonic nuclei with even nuclear spin quantum number I the total wavefunction must be symmetric, and therefore the rotational levels with even rotational quantum number J in an electronic Σ_g state possess the statistical weight $(2I + 1)(I + 1)$, whereas levels with odd J possess the weight $(2I + 1)I$.

For the nitrogen molecule N_2 , the nuclear spins are $I = 1$, that is, the nuclei are bosons. The product $\psi_{\text{rot}}\psi_{\text{ns}}$ must therefore be symmetric. The ratio of the population numbers of rotational levels is then $N(J = \text{even})/N(J = \text{odd}) = (I + 1)/I = 2$. The populations of the rotational levels alternate by a factor of two.

For the oxygen molecule O_2 , the nuclear spins are $I = 0$, that is, the nuclei are bosons, and there is only a symmetric nuclear spin wavefunction. Therefore the statistical weight of rotational levels with odd J vanishes, that is, these levels are not populated and no transitions from rotational levels with odd J appear in the spectrum. Hence, in the spectrum every other rotational line is missing!

Table 4.1 lists the statistical nuclear spin weights g_{nuc} , which indicate the number of possible relative orientations of the nuclear spins, for some states in homonuclear molecules.

5 Molecular Symmetry and Group Theory

The huge variety of molecules can be grouped into certain well-defined classes according to the symmetry properties of their nuclear frameworks. This fortunate fact greatly facilitates the determination of molecular states and especially the discussion of *allowed* and *forbidden* transitions between levels during absorption or emission of electromagnetic radiation. It is particularly the application of mathematical group theory to the description of molecular symmetry that has provided a very concise, clear, and elegant representation of the symmetry types of molecular states and of the spectra of polyatomic molecules.

Before turning to polyatomic molecules and their spectra, we will therefore discuss these topics in some detail, the knowledge of which is of crucial importance for each chemist or physicist who wants to do serious work in molecular physics. More detailed accounts can be found in monographs such as [5.1–5.6].

5.1 Symmetry Operations and Symmetry Elements

We start from the geometrical arrangement of the rigid nuclear framework of a molecule, in which all nuclei are fixed to their equilibrium positions. For each molecule, there are certain transformations, or mappings, of the nuclei (e.g., rotations of the nuclear framework around an axis, or reflection of all nuclei at a plane or at the molecular center of mass), for which the framework as a whole transforms into an identical configuration. Identical nuclei (with identical numbers of neutrons and protons) are considered undistinguishable, that is, identical, for this purpose.

Definition: *Transformations which map the rigid nuclear framework of a molecule onto itself are called symmetry operations of this molecule.*

As an example, Fig. 5.1 shows all symmetry operations of the H₂O molecule. Note that a symmetry operation does not necessarily map each individual nucleus onto itself. In general, it must only be mapped onto an identical nucleus, that is, a nucleus

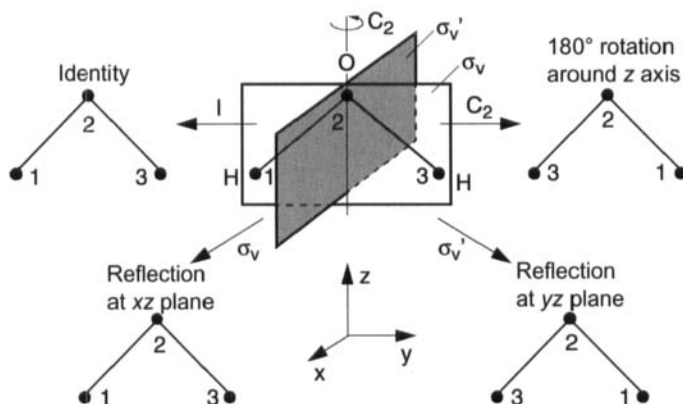


Fig. 5.1 Symmetry operations of the H_2O molecule.

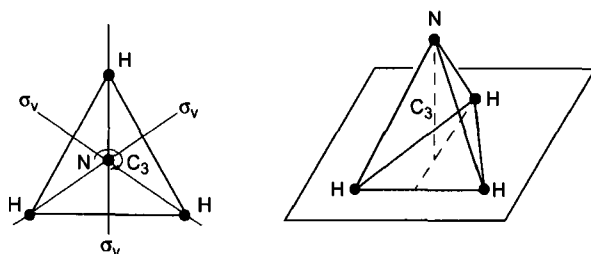


Fig. 5.2 The NH_3 molecule, exemplifying the C_{3v} symmetry group.

which cannot be distinguished from the original. To clarify this point, the nuclei in Fig. 5.1 are numbered, and the nuclei 1 and 3 are identical.

Symmetry planes, axes or points are collectively called *symmetry elements*. The symmetry of a molecule can be classified according to the number and types of symmetry elements. For this purpose, certain notations have been introduced (Schönflies notation) to designate the different symmetry elements.

1. Symmetry axes C_n

A molecule possesses an n -fold symmetry axis (axis of rotation) C_n , if its nuclear framework is mapped onto itself upon a rotation by an angle of $\alpha = 2\pi/n$ around this axis. If a molecule possesses more than one symmetry axis C_n , that with the largest n is taken to be the z direction.

Examples

The H_2O molecule from Fig. 5.1 possesses a C_2 axis, the NH_3 molecule (Fig. 5.2) a C_3 symmetry axis. Benzene (Fig. 5.3) possesses a C_6 axis in the z direction and six C_2 axes in the xy plane. Linear molecules possess a C_∞ axis, because their nuclear framework can be rotated by arbitrary angles around the molecular axis.

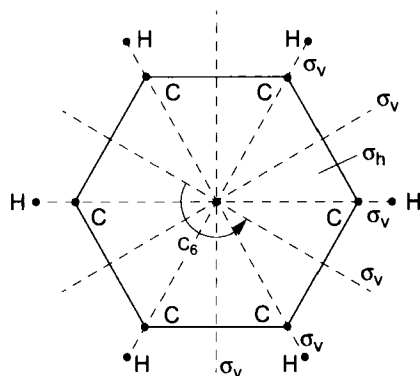


Fig. 5.3 Some symmetry elements of the benzene molecule C_6H_6 .

2. Symmetry planes (σ)

A molecule possesses a symmetry plane if its nuclear framework remains unchanged upon reflection at this plane. It is called a *vertical plane* and designated σ_v if the molecule's symmetry axis C_n with largest n lies in this plane (because the C_n with largest n is always chosen to be in the z direction, i.e., vertical). Symmetry planes perpendicular to this vertical axis, that is, in the xy plane, are designated σ_h (horizontal).

Examples

The H_2O molecule in Fig. 5.1 possesses two σ_v planes, σ_{xz} and σ_{yz} (also designated σ_v and σ'_v), the NH_3 molecule in Fig. 5.2 possesses three σ_v planes, the benzene molecule (Fig. 5.3) possesses one σ_h plane in the xy plane and six σ_v planes containing the sixfold symmetry axis C_6 in the z direction. The six C_2 symmetry axes are the intersections of the σ_v planes and the σ_h plane.

All planar molecules possess at least one symmetry plane that contains all nuclei.

3. Rotary–reflection axes (S_n)

A molecule possesses an n -fold rotary–reflection axis S_n if its nuclear framework is mapped onto itself upon rotation by an angle $\alpha = 2\pi/n$ around the axis, followed by a reflection of all nuclei at a plane perpendicular to this axis.

Examples

The allene molecule C_3H_4 , in which the two CH_2 groups are twisted by 90° with respect to each other (Fig. 5.4a), possesses one S_4 and three C_2 symmetry axes; the twisted isomer of the ethane molecule C_2H_6 (Fig. 5.4b) possesses one C_3 and one S_6 symmetry axes.

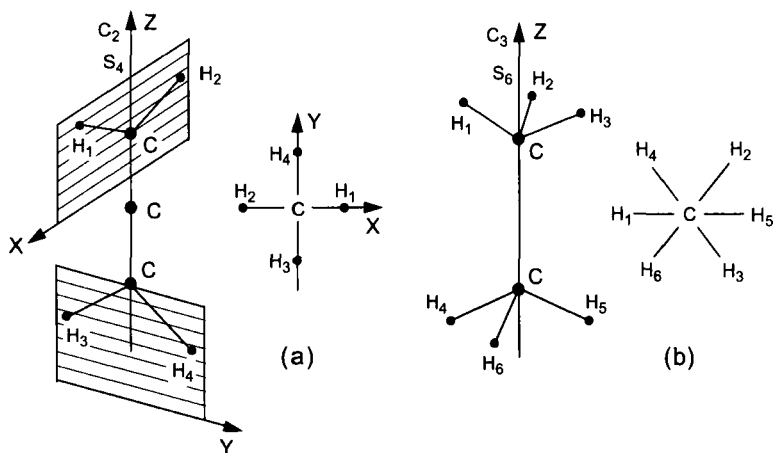


Fig. 5.4 a) The twisted allene molecule C_3H_4 belongs to the point group D_2 . b) The twisted isomer of the ethane molecule C_2H_6 possesses one C_3 symmetry axis and an S_6 rotary-reflection axis.

4. Center of inversion (i)

A molecule possesses a center of inversion i , if its nuclear framework is mapped onto itself upon reflection of all nuclei at this center (inversion). A center of inversion lies necessarily in the molecule's center of mass, which is chosen as the origin of the molecule-fixed reference frame. In this reference frame, all nuclear coordinates (x, y, z) change their sign upon inversion, that is, (x, y, z) is transformed into $(-x, -y, -z)$.

The inversion can also be described by consecutive execution of two other symmetry operations: if the nuclear framework is rotated by 180° (π) around a C axis and afterwards reflected at a σ_h plane perpendicular to this axis, the same result as for an inversion is obtained.

Examples

All homonuclear diatomic molecules, but also CO_2 , benzene C_6H_6 and ethyne C_2H_2 (acetylene) possess a center of inversion. Whereas i lies at the carbon nucleus in CO_2 , it is not located at a nucleus in C_2H_2 or C_6H_6 (Fig. 5.5).

Symmetry operations and symmetry elements can readily be visualized using simple geometrical bodies. For example, a cube (Fig. 5.6) possesses three C_4 axes pointing in the x , y and z direction and intersecting in the center of the cube. The three diagonals are C_3 axes, and the connecting lines from the center of one edge to the diagonally opposed edge are eight C_2 axes. In addition, there is a center of inversion, and for each C_4 axis, there are four σ_v planes and one σ_h plane.

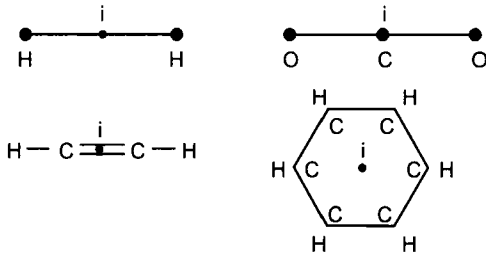


Fig. 5.5 Molecules with a center of inversion i . For CO_2 , i coincides with an atom, but not for the other examples.

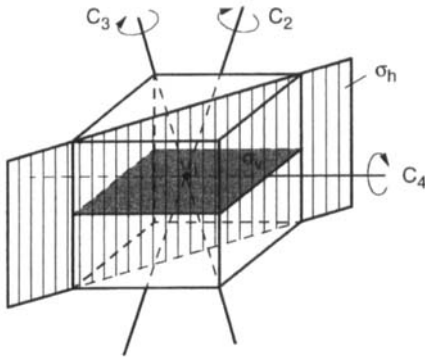


Fig. 5.6 Some symmetry elements of a cube.

We will show in the following that the set of symmetry operations of a molecule can be considered a *group* in the mathematical sense, and that this group is unique for a specific symmetry class and describes the symmetry properties of a molecule completely and unambiguously

But first, we must get acquainted with the basic foundations of mathematical group theory.

5.2

Foundations of Group Theory

We start from a set of N elements a_n ($n = 1, \dots, N$) between which an operation such as addition or multiplications is defined. These elements form a *multiplicative group* G if the following conditions hold:

1. $a_i, a_k \in G \rightarrow (a_i \times a_k) = a_n \in G$, where the symbol “ \times ” indicates multiplication. In other words, *the product of two elements of the group is again an element of the group.*
2. $a_i \times (a_k \times a_j) = (a_i \times a_k) \times a_j$ (*associative law*), that is, the product of several factors does not depend on how the factors are combined.

3. There exists a *neutral element* $e \in G$ for which $e \times a_n = a_n \times e = a_n$ for all $a_n \in G$.
4. For each element $a_n \in G$ there is an *inverse element* $a_n^{-1} \in G$ for which $a_n \times a_n^{-1} = a_n^{-1} \times a_n = e$.

For some groups, the so-called *commutative* or *Abelian groups*, the *commutative law* also holds: $a_i \times a_k = a_k \times a_i$ for all $a_i, a_k \in G$. Note, however, that there are many groups that are *not* Abelian (for examples, see Sect. 5.3).

The number N of group elements is called the *order* of the group. If the group axioms (1)–(4) hold for a subset of n elements $a_i \in G$ with $n < N$, this subset is called a *subgroup* of G .

Example

The number 1 represents the neutral element of the group of all rational numbers under multiplication, and it forms a trivial subgroup of this group.

The following rules apply (for proofs, see [5.7]):

- (a) The order n of a subgroup is a divisor of the order N of the complete group (i.e., N/n is integer). From this follows that there are no nontrivial (i.e., $1 < n < N$) subgroups if N is prime.
- (b) If in addition to an element $a_i \in G$, the element $a_i \times a_i = a_i^2$ also belongs to the finite group G , then all powers a_i, a_i^2, \dots, a_i^p must belong to the group. There must be a finite number $p < N$, so that $a_i^p = e$. The elements $a_i, a_i^2, \dots, a_i^p = e$ are a subgroup of G , which is called a *cyclic* group.

The elements of a group G can be grouped into *classes* by the following definition: two elements a and b belong to the same class if there is an element $x \in G$ for which

$$a = bx^{-1}. \quad (5.1)$$

The elements within a class are called *mutually conjugated*. The classes of a group are disjunct, that is, no element can belong to more than one class.

Proof: We consider two elements f and g from different classes, and we assume that the element h belongs to the class of f and to that of g simultaneously. Hence, $h = xf x^{-1} = ygy^{-1}$ from which follows that $f = x^{-1}ygy^{-1}x = (x^{-1}y)g(x^{-1}y)^{-1}$, that is, f and g belong to the same class, contrary to our assumption that f and g are from different classes. Therefore, h cannot belong to two different classes. We see immediately that for Abelian groups, each class consists of one element only, because from

$$a = bx^{-1} = xx^{-1}b = eb = b$$

we obtain that $a = b$. Each element of an Abelian group forms its own class. In Abelian groups, there are therefore N classes.

5.3 Molecular Point Groups

We will now demonstrate for some illustrative examples that the symmetry operations of a molecule are the elements of a multiplicative group. The operation (“multiplication”) is the *sequential application* of two symmetry operations, and the neutral element is the *identity operation* where no action takes place, that is, all nuclei remain at their respective positions.

As a first example, we consider the symmetry operations of the H_2O molecule (Fig. 5.1):

I : identity operation

C_2 : rotation by 180° (π) around the z axis

σ_v : reflection at the xz plane

σ'_v : reflection at the yz plane

The *product* ($C_2 \times \sigma_v$) means that first the reflection at the xz plane takes place (σ_v) and then the rotation around the z axis (C_2). We can see from Fig. 5.7 that the result is the same as if we had simply reflected the nuclei at the yz plane (σ'_v plane). This is expressed by the notation

$$C_2 \times \sigma_v = \sigma'_v.$$

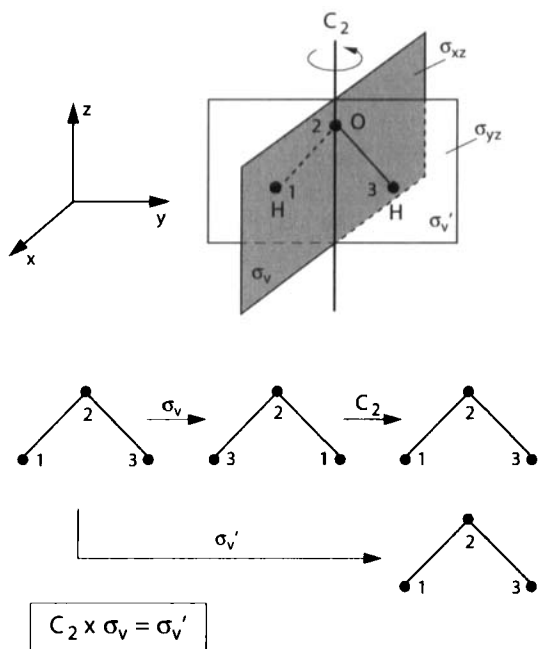


Fig. 5.7 Subsequent applications of the symmetry operations σ_v and C_2 in the group C_{2v} leads to the same result as the reflection σ'_v .

Tab. 5.1 Multiplication table of the group C_{2v} .

C_{2v}	I	C_2	$\sigma_v(xz)$	$\sigma'_v(yz)$
I	I	C_2	σ_v	σ'_v
C_2	C_2	I	σ'_v	σ_v
σ_v	σ_v	σ'_v	I	C_2
σ'_v	σ'_v	σ_v	C_2	I

All other possible products can be constructed correspondingly by using Fig. 5.7. For the C_{2v} group we obtain the result that each symmetry operation, when applied twice, yields the original nuclear configuration,

$$C_2 \times C_2 = I; \quad \sigma_v \times \sigma_v = I; \quad \sigma'_v \times \sigma'_v = I.$$

In other words, each element is its own inverse.

The products of all symmetry operations can be clearly laid out in the form of a multiplication table (Table 5.1).

We see that the symmetry operations obey conditions (1)–(4) from Sect. 5.2 for the elements of a group, that is, the symmetry operations of the H_2O molecule form a group of order $N = 4$, which is called C_{2v} because it consists of one C_2 axis and two σ_v planes. The group is Abelian, because for all elements a_i, a_j from G , $a_i \times a_j = a_j \times a_i$, as can easily be verified from the multiplication table.

Together with the neutral element, each of the elements C_2 , σ_v and σ'_v forms a subgroup of order two. Thus, there are three real subgroups in C_{2v} (in addition to the trivial subgroup of order one containing only the neutral element). As the group is commutative, each element is in its own class, that is, there are four disjoint classes.

Remark: For the nuclear framework of the H_2 molecule, the operation σ'_v equals the identity I . This is not true, however, if we take the molecule's electron cloud into account. As we will later apply group theory to the symmetry properties of electronic states, it is necessary to include σ'_v as a separate symmetry operation.

We will now continue by discussing the non-Abelian group C_{3v} , to which the molecule NH_3 (Fig. 5.2) belongs. Figure 5.8 shows the symmetry operations of this group, I , C_3 , C_3^2 , σ_v , σ'_v and σ''_v , where C_3 is a clockwise rotation by 120° , and C_3^2 is a clockwise rotation by 240° . The multiplication table (Table 5.2) shows clearly that the group is noncommutative. The six elements fall into three classes, of which the first contains only the neutral element I , the second contains the two rotations C_3 and C_3^2 , and the third contains the reflections σ_v , σ'_v and σ''_v . This is illustrated in Fig. 5.9a for the elements C_3 and C_3^2 , for which

$$C_3 = \sigma_v^{-1} \times C_3^2 \times \sigma_v. \quad (5.2)$$

Figure 5.9b and c demonstrate that the three reflections are mutually conjugate elements.

Tab. 5.2 Multiplication table of the group C_{3v} .

C_{3v}	I	C_3	C_3^2	σ_v	σ'_v	σ''_v
I	I	C_3	C_3^2	σ_v	σ'_v	σ''_v
C_3	C_3	C_3^2	I	σ''_v	σ_v	σ'_v
C_3^2	C_3^2	I	C_3	σ'_v	σ''_v	σ_v
σ_v	σ_v	σ'_v	σ''_v	I	C_3	C_3^2
σ'_v	σ'_v	σ''_v	σ_v	C_3^2	I	C_3
σ''_v	σ''_v	σ_v	σ'_v	C_3	C_3^2	I

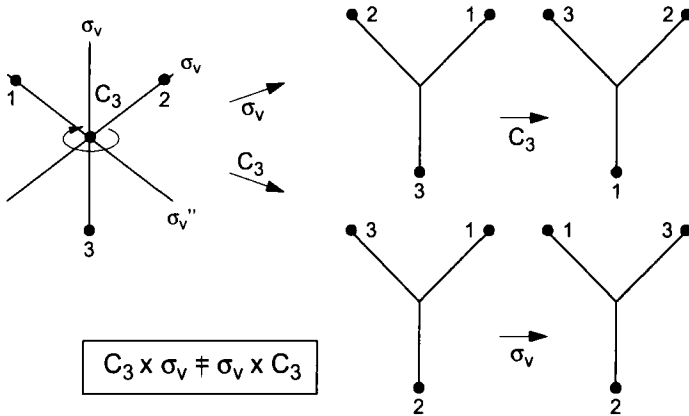


Fig. 5.8 The noncommutative group C_{3v} and its symmetry operations.

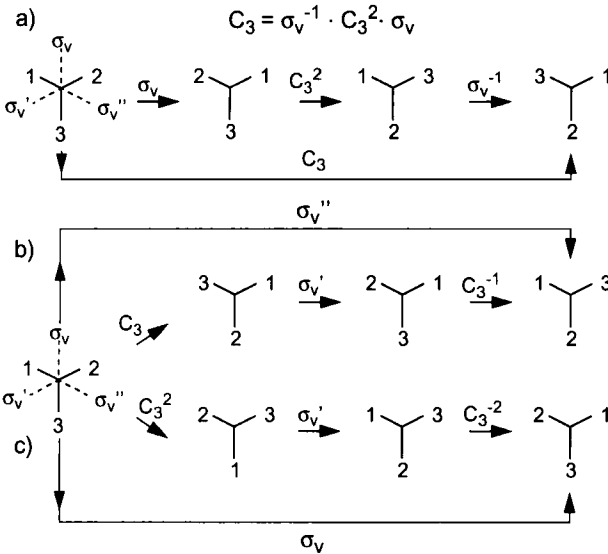


Fig. 5.9 Pairs of mutually conjugate group elements: a) C_3 and $\sigma_v C_3^2 \sigma_v^{-1}$, b) σ'_v and $C_3 \sigma'_v C_3^{-1}$, c) σ_v and $C_3^2 \sigma'_v C_3^{-2}$.

Similarly, it can be shown that all symmetry groups listed in the next section satisfy the group axioms. These groups of molecular symmetry operations are also called molecular *point groups*, because the molecule's center of mass – which is common to all symmetry elements (axes and planes) – is mapped onto itself during all symmetry transformations, that is, it is invariant.

Note: *The elements of the point groups are the symmetry operations, which must be distinguished from the symmetry elements (rotation axes, rotary–reflection axes and mirror planes) of the molecules.*

In the next section, we will give an overview of the different molecular point groups.

5.4

Classification of Molecular Point Groups

The point group of a molecule comprises all symmetry operations possible for this molecule. This means, it depends on the number and types of symmetry elements in the molecule (see Sect. 5.1). To specify a molecule's point group unambiguously, the Schönflies notation is commonly employed, which uses the symbols listed in Table 5.3 in order of *increasing* symmetry. We will now take a closer look at some examples of molecular point groups.

Tab. 5.3 Schönflies notation for molecular point groups.

Group symbol	Symmetry elements
C_n	1 C_n axis
C_{nv}	1 C_n axis + n mirror planes containing this axis
C_{nh}	1 C_n axis + 1 mirror plane perpendicular to C_n ; for even n also a center of inversion i .
D_n	1 C_n axis + n C_2 axes perpendicular to C_n
D_{nd}	as D_n , but additionally n mirror planes containing the C_n axis and one line bisecting the C_2 axes
D_{nh}	as D_n , + 1 mirror plane perpendicular to C_n
S_n	1 S_n axis
T_d	all symmetry elements of a regular tetrahedron
O_h	all symmetry elements of a regular octahedron or cube
I_h	all symmetry elements of an icosahedron
special labels	$C_5 \equiv C_{1v} \equiv C_{1h} \equiv S_1$; $C_i \equiv S_2$

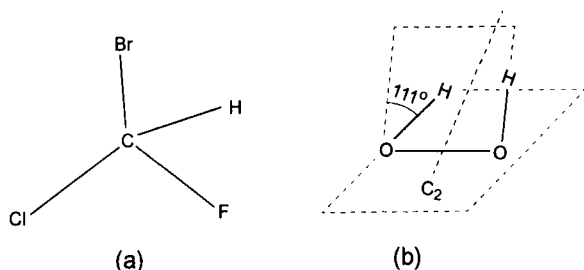


Fig. 5.10 a) The substituted methane molecule CHClFBr exemplifying the point group C_1 ; b) the molecule H2O2 exemplifying the point group C_2 .

5.4.1

The Point Groups C_n , C_{nv} , and C_{nh}

The molecules with lowest symmetry are those belonging to group C_1 . They possess no “real” symmetry element, and their point group thus consists solely of the identity I .

Example

The substituted methane molecule CHClFBr (Fig. 5.10a).

The point group C_2 (only one twofold symmetry axis) comprises, for example, the hydrogen peroxide molecule H2O2 (Fig. 5.10b). There are only very few examples of molecules belonging to point groups C_n with $n \geq 3$.

Molecules from group $C_S = C_{1v}$, C_{1h} have a mirror plane as their only symmetry element. All plane molecules without further symmetry elements belong to this group.

Examples

The water isotopomer HDO or phenol (Fig. 5.11).

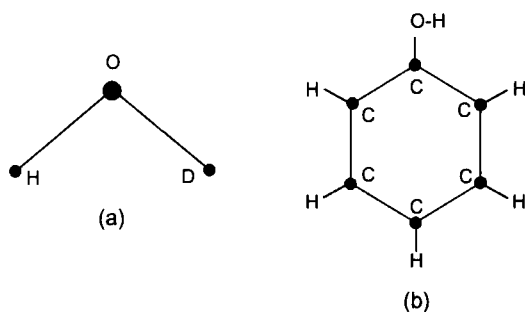


Fig. 5.11 The molecules a) HDO and b) phenol, exemplifying the point group C_S .

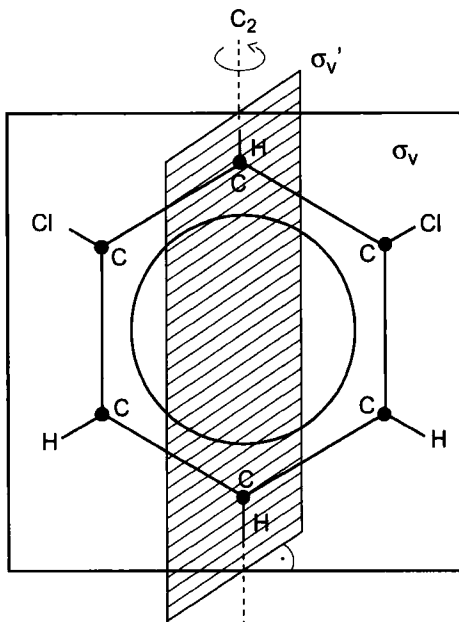


Fig. 5.12 Dichlorobenzene $C_6H_4Cl_2$, representing the C_{2v} point group.

The group C_{2v} (one C_2 axis and two vertical mirror planes) comprises a large number of triatomic and polyatomic molecules.

Examples

H₂O (Fig. 5.1), NO₂, SO₂, difluoromethane CH₂F₂, and dichlorobenzene C₆H₄Cl₂ (Fig. 5.12).

The group C_{3v} (one C_3 axis and three vertical mirror planes) is exemplified by the NH₃ molecule (Figs. 5.2 and 5.8).

Another important point group is $C_{\infty v}$, which comprises all linear unsymmetrical molecules such as HCN or OCS, and specifically all heteronuclear diatomic molecules (CO, NO, LiH, but also ⁶Li⁷Li). Each plane containing the molecular axis is a mirror plane, and each rotation by an arbitrary angle α around this axis is a symmetry operation.

The group C_{nh} (one C_n axis and a mirror plane perpendicular to it) contains the symmetry elements C_n , that is, a rotation around the symmetry axis by an angle $\alpha_n = 2\pi/n$, and the reflection σ_h . As always, all products of these elements must also be group elements. For example, the inversion i can be written as the product $i = C_2 \times \sigma_h$, and it is therefore also an element of the group C_{2h} . Analogously, the rotary-reflection $S_3 = \sigma_h \times C_3$ is an element of the group C_{3h} .

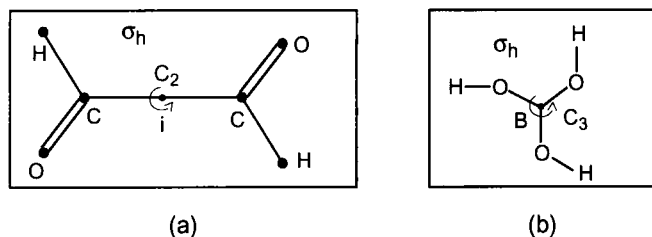


Fig. 5.13 The planar molecules a) glyoxal, OHCCHO , and b) ortho-boric acid, H_3BO_3 , exemplifying the point groups C_{2h} and C_{3h} , respectively.

Tab. 5.4 Multiplication table of the group C_{2h} .

C_{2h}	I	C_2	σ_h	i
I	I	C_2	σ_h	i
C_2	C_2	I	i	σ_h
σ_h	σ_h	i	I	C_2
i	i	σ_h	C_2	I

Examples

Examples representing the group C_{2h} are the plane molecules glyoxal OHCCHO (Fig. 5.13a) and butadiene, C_4H_6 . Table 5.4 shows the multiplication table of this group. An example for the group C_{3h} is ortho boric acid, H_3BO_3 (Fig. 5.13b).

5.4.2

The Point Groups D_n , D_{nd} , and D_{nh}

Molecules belonging to the point groups D_n (one C_n axis and n C_2 axes perpendicular to it, intersecting at angles π/n) can be constructed by combining two identical fragments of C_{nv} symmetry along the C_n axis so that both fragments are rotated by an angle $\alpha = m\pi/n$ (m, n integer) with respect to each other. For example, the molecule C_2H_4 , which is planar in the ground state, possesses an excited state in which the two CH_2 fragments with C_{2v} symmetry are twisted by 90° so that the nuclear framework of the excited ethene has D_2 symmetry (Fig. 5.14b). The two C_2 axes perpendicular to the S_4 axis lie within the planes bisecting the two σ_v planes. There are only very few examples of molecules belonging to the point groups D_n with $n \geq 3$.

Molecules belonging to the point groups D_{nd} contain additional mirror planes σ_d containing the C_n axis and one of the lines bisecting two C_2 axes. They can be constructed from two identical fragments of C_{nv} symmetry that are twisted along the C_n axis by an angle $\alpha = \pi/n$. For odd values of n , the molecules possess also a center of inversion.

Examples

Allene, C_3H_4 (Fig. 5.4a), belongs to group D_{2d} . The existence of three C_2 axes and two mirror planes requires also an S_4 axis as a symmetry element. Analogously, ethane C_2H_6 (D_{3d}) possesses, in addition to the C_3 axis and the three mirror planes, an S_6 rotary–reflection axis and a center of inversion i (Fig. 5.4b).

The groups D_{nh} contain, in addition to the symmetry elements of the groups D_n , a horizontal mirror plane σ_h and n σ_d planes containing the C_n axis. For even n , the molecules possess also a center of inversion i .

Examples

Ground-state ethene belongs to group D_{2h} (Fig. 5.14a). Its symmetry elements are three mutually perpendicular C_2 axes, three mirror planes σ , and a center of inversion.

Boron trifluoride, BF_3 , sulfur trioxide, SO_3 , and trifluorobenzene, $C_6H_3F_3$, are examples for the group D_{3h} (Fig. 5.15a,b). They possess a C_3 axis, three C_2 axes, three σ_v planes and one σ_h plane. The corresponding group elements are, in addition to the operations C_3 , C_2 , σ_v , and σ_h also C_3^2 , S_3 and S_3^2 .

All homonuclear diatomic molecules and all symmetric linear molecules such as CO_2 or ethyne C_2H_2 (acetylene) belong to the important point group $D_{\infty h}$ (Fig. 5.15c). It differs from the groups $C_{\infty v}$ by the additional σ_h mirror plane, and hence also by a center of inversion i .

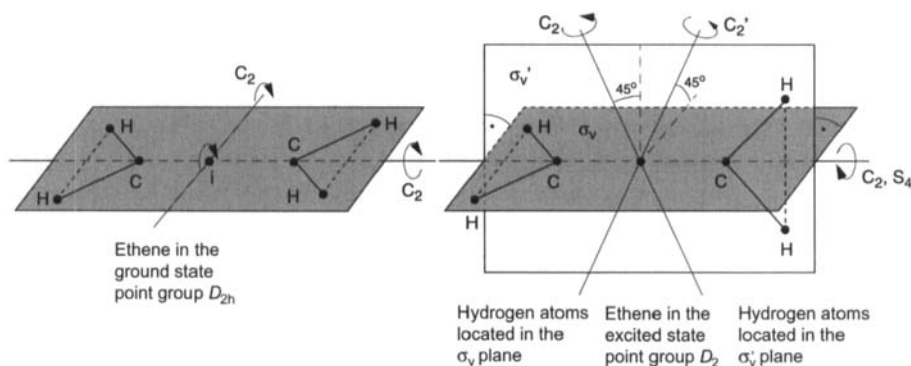


Fig. 5.14 a) The electronic ground state (C_{2v}) and b) an excited state (D_2) of the ethene molecule possess different geometries and therefore belong to different point groups.

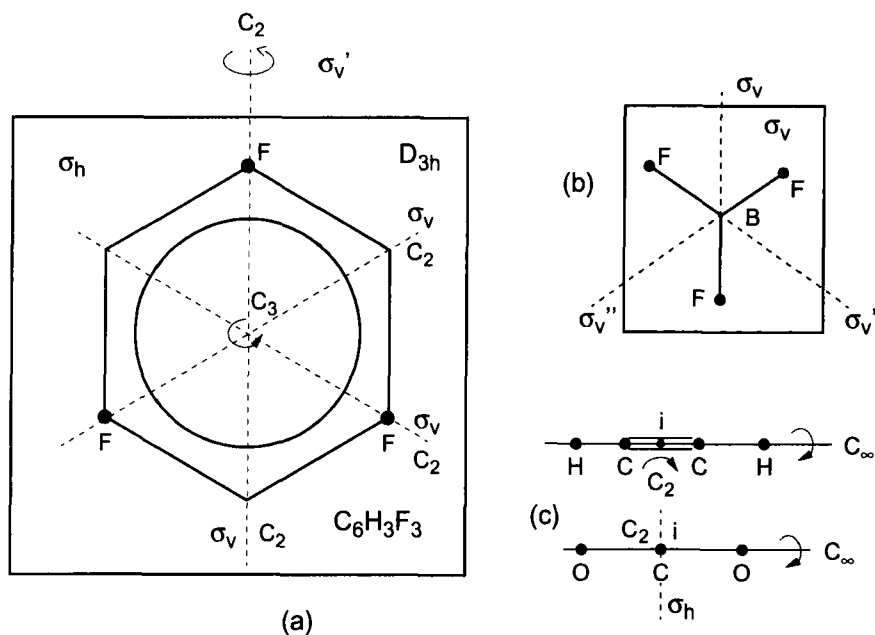


Fig. 5.15 a) Trifluorobenzene $C_6H_3F_3$ and b) boron trifluoride BF_3 as examples for the group D_{3h} , and c) the linear symmetric molecules CO_2 and C_2H_2 as examples for the group $D_{\infty h}$.

5.4.3

The groups S_n

Molecules belonging to the S_n point groups possess an S_n rotary–reflection axis as their only symmetry element. The point groups contains therefore the elements $E, S_n, S_n^2, S_n^3, \dots, S_n^{n-1}$. For example, the group S_4 consists of $E, S_4, S_4^2 = C_2$, and S_4^3 .

For $n = 2$, the symmetry axis S_2 is equivalent to a center of inversion i , and the group S_2 is therefore also called C_i ($S_2 \equiv C_i$).

Examples

The dichlorodifluoroethane isomer $(CHClF)_2$ in which the two $(CHClF)$ groups are twisted by 180° (Fig. 5.16) belongs to group C_i .

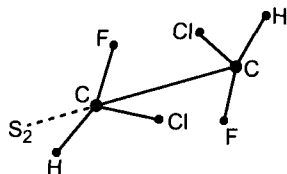


Fig. 5.16 Dichlorodifluoroethane isomer exemplifying the group C_i .

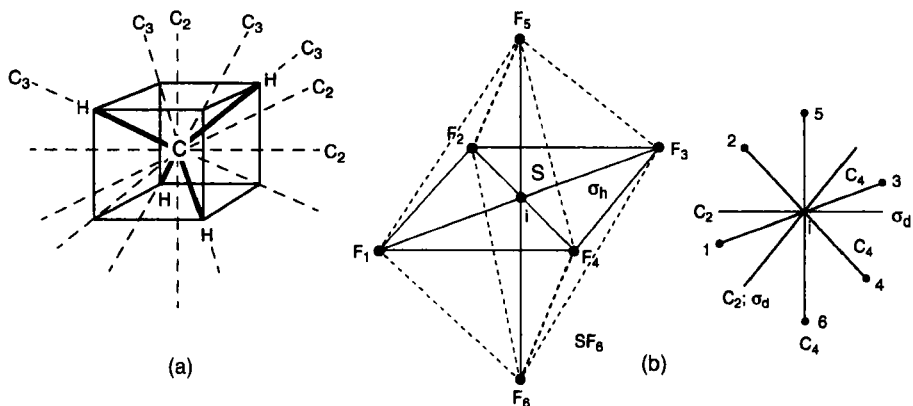


Fig. 5.17 a) Methane, representing the group T_d ; b) SF_6 as an example of the group O_h .

5.4.4

The Point Groups T_d and O_h

All molecules belonging to the point group T_d possess the symmetry of a tetrahedron (i.e., they possess four C_3 axes, three C_2 axes and six σ_d mirror planes).

Examples

Methane CH_4 (Fig. 5.17a) and carbon tetrachloride CCl_4 belong to group T_d .

We can visualize the different symmetry elements most easily if we imagine the tetrahedron to be surrounded by a cube. For CH_4 , the four hydrogen atoms lie at four corners of the cube so that each pair of them is connected through a diagonal across one face of the cube. The four C_3 axes are then the diagonals through the cube, the three C_2 axes connect the midpoints of opposite faces, and the six σ_d planes are the planes through diagonally opposed pairs of edges of the cube.

The symmetry group of a regular octahedron is called O_h ; it comprises three C_4 axes, four C_3 axes, six C_2 axes, three σ_h planes, and six σ_d planes. An example for a molecule belonging to this point group is SF_6 (Fig. 5.17b). If the octahedron is included in a cube so that the corners of the octahedron coincide with the centers of the faces of the cube, we recognize that a cube possesses the same symmetry elements as the octahedron (Fig. 5.6). The molecular point groups T_d and O_h possess the largest number of symmetry elements and have thus the highest symmetry.

5.4.5

How to Find the Point Group of a Molecule

We address now the crucial question as to how we can find out to which point group a specific molecule belongs. To facilitate a systematic approach, we provide some “recipes” that allow a quick classification [5.1].

- (a) If the molecule is *linear*, it must belong to one of the groups $C_{\infty v}$ or $D_{\infty h}$. If it possesses a center of inversion, it belongs to $D_{\infty h}$, or else to $C_{\infty v}$.
- (b) If the molecule is tetrahedral, such as CCl_4 , it belongs to T_d .
- (c) If the molecule is octahedral (such as SF_6), it has O_h symmetry.
- (d) If the molecule does not fall in any of the classes a)–c), we must check if there is a symmetry axis C_n with $n > 1$. If there is none, the molecule belongs to group C_s if there is a mirror plane σ , to group $C_i = S_2$ if there is a center of inversion i , and to group C_1 if there is no symmetry element at all.
- (e) If there is a C_n axis with $n > 1$ and if this axis is at the same time a rotary–reflection axis S_{2n} and there are no further symmetry elements (except the center of inversion i for even n), the molecule belongs to group S_n .
- (f) If there are further symmetry elements besides those listed in e), the molecule belongs to one of the groups D_n , D_{nh} , D_{nd} , C_n , C_{nv} or C_{nh} . To find the correct group, we need to check if there are n C_2 axes perpendicular to the principal C_n axis.
 - (f₁) If yes, the molecule belongs to one of the D groups. If there is a σ_h plane, the point group is D_{nh} ; if there are n σ_d planes, the correct group is D_{nd} ; if there are no σ_h or σ_d planes, the group is D_n .
 - (f₂) If there are no n C_2 axes, the molecule belongs to one of the C groups. If there is a σ_h plane, the group is C_{nh} ; if there are n σ_v planes, it is C_{nv} ; if there are neither σ_h nor σ_v planes it is C_n .

We will demonstrate the usage of this “recipe” for two examples.

1. The planar molecule BF_3 (Fig. 5.15b) possesses one C_3 axis, three C_2 axes, one σ_h plane containing all nuclei, and three σ_d planes. Consequently, it belongs to group D_{3h} .
2. The butadiene molecule C_4H_6 possesses one planar isomer (Fig. 5.18). There is a C_2 axis perpendicular to the molecular plane, which is therefore a σ_h mirror plane. There is a center of inversion, but no σ_d planes. Hence, the molecule must belong to the point group C_{2h} . It contains the symmetry operations E , C_2 , σ_h , and i ; its multiplication table is displayed in Table 5.4.

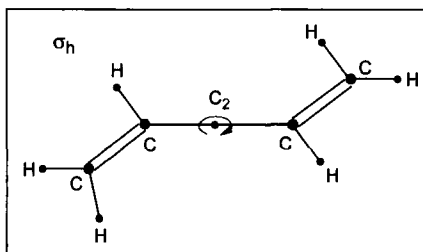


Fig. 5.18 Planar isomer of the butadiene molecule belonging to group C_{2h} .

5.5

Symmetry Types and Representations of Groups

As the nuclear framework of a molecule does not change during a symmetry transformation, the Coulomb potential of the nuclei, in which the electrons move, remains also constant, that is, the potential energy in the Hamiltonian Eq. (2.2) is invariant with respect to all symmetry operations. It is easy to understand that the mean kinetic energy of the electrons in a given electronic state is also constant, because it is determined by the equilibrium nuclear configuration.

The normal modes of a molecule (see Sect. 6.3.1) can also be classified with respect to molecular symmetry. They are designated by lower-case letters to distinguish them from the symmetry classifications of electronic states, where upper-case letters are used. Figure 5.19 visualizes the vibrational state of a molecule during its three normal modes by indicating the nuclear velocities through arrows. This shows that the nuclear kinetic energy is also invariant with respect to symmetry operations, because the lengths of the arrows, that is, the absolute values $|v_i|$ of the nuclear velocities, do not change during such an operation and hence $(m/2)v_i^2$ remains constant although

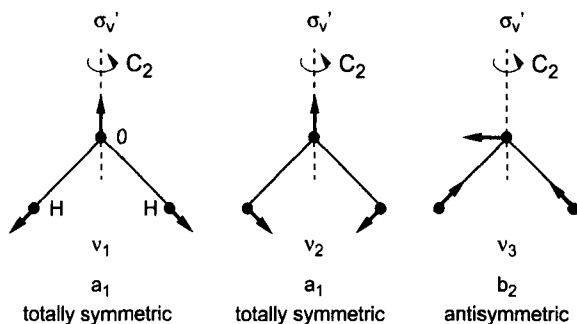


Fig. 5.19 Changes in the nuclear velocity arrows of the three vibrational normal modes of a triatomic C_{2v} molecule during symmetry operations.

the direction of the arrows, that is, the phase of the vibration, changes for ν_3 during the operations σ'_v and C_2 .

Hence, the total energy of a state and also the electron density distribution remain constant during the symmetry operations of the molecule. The wavefunctions of the states can change, however. From the requirement that $|\Psi|^2$ remain constant during a symmetry operation, we obtain for *nondegenerate* states due to the single-valuedness of $\Psi(x, y, z)$

$$|\Psi|^2 \xrightarrow{\text{s.o.}} |\Psi|^2 \Rightarrow \Psi \xrightarrow{\text{s.o.}} \pm\Psi. \quad (5.3)$$

For example, upon double reflection at the same plane ($\sigma^2 = I$), the function Ψ must return to its original value,

$$\sigma(\sigma\Psi) \equiv \Psi \Rightarrow \sigma\Psi = \pm\Psi. \quad (5.4)$$

This is not necessarily true for degenerate states, as an n -fold degenerate state is described by a linear combination of n independent functions Ψ_n . Each of these functions Ψ_n can be mapped by a symmetry operation onto any of the other functions Ψ_i ($i \neq n$) or any linear combination of them (see examples below).

Within the BO approximation, the total wavefunction can be written as a product

$$\Psi = \psi_{\text{el}}\psi_{\text{vib}}\psi_{\text{rot}}$$

of electronic, vibrational, and rotational contributions. The symmetry of Ψ is therefore determined by the symmetries of the three factors.

It is now important to decide how the molecular wavefunctions transform under the different symmetry operations in the various point groups, and how the symmetries of the three factors determine the symmetry of the product wavefunction. This will be possible by using the *representations* of groups. This will be demonstrated in the following for the example of the C_{2v} group, before the concept of a *representation* and its *characters* is defined in general.

5.5.1

The Representation of the Group C_{2v}

We will first examine how the three components of a translation vector $T = \{T_x, T_y, T_z\}$ or a position vector $r = \{x, y, z\}$ transform under the symmetry operations of the group C_{2v} . From Fig. 5.20 we see that for a rotation around the C_2 axis,

$$T_x \xrightarrow{C_2} -T_x; \quad T_y \xrightarrow{C_2} -T_y \quad \text{and} \quad T_z \xrightarrow{C_2} +T_z, \quad (5.5a)$$

while for the reflection σ_v at the xz plane,

$$T_x \xrightarrow{\sigma_v} +T_x; \quad T_y \xrightarrow{\sigma_v} -T_y \quad \text{and} \quad T_z \xrightarrow{\sigma_v} T_z, \quad (5.5b)$$

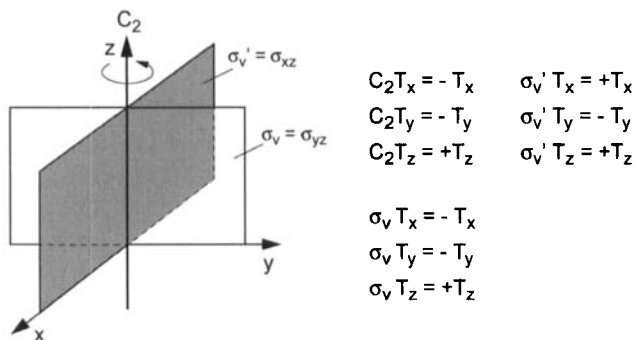


Fig. 5.20 Transformation of the components of a translation vector under the symmetry operations of the group C_{2v} .

and for the reflection σ'_v at the yz plane

$$T_x \xrightarrow{\sigma'_v} -T_x ; \quad T_y \xrightarrow{\sigma'_v} T_y \quad \text{and} \quad T_z \xrightarrow{\sigma'_v} T_z . \quad (5.5c)$$

Hence, the behavior of the component T_x under the symmetry operations I , C_2 , σ_v , and σ'_v can be represented by a suitable combination of the numbers $+1$, -1 , $+1$, -1 (Table 5.5).

The behavior of the translation vector $\mathbf{T} = \{T_x, T_y, T_z\}$, the rotation $\mathbf{R} = \{R_x, R_y, R_z\}$, and the vibrational normal coordinates Q_i is summarized in Table 5.5, where $+1$ means that the corresponding quantity remains unchanged under the respective symmetry operation, and -1 means that it changes sign.

The combinations of the numbers $+1$ and -1 listed in the i th row of Table 5.5 are called a *representation* Γ_i of the symmetry group C_{2v} , because they represent the symmetry properties of a quantity (i.e., a normal coordinate or a component of the translation vector) under the symmetry operations of the group C_{2v} .

The numbers themselves are called the *characters* of the representation. The individual representations are often designated by upper-case letters such as A , if the character for the rotation C_2 is $+1$, or B , if it is -1 . A further distinction is made regarding the behavior upon reflection σ_v : representations labeled A_1 or B_1 have the character $+1$ for σ_v , representations A_2 or B_2 correspondingly have character -1 .

Analogously, we can examine with the aid of Fig. 5.19 how the displacements of the nuclei during the three normal vibrations v_i of the molecule with frequencies

Tab. 5.5 Character table and representation of the group C_{2v} .

C_{2v}	I	C_2	σ_v	σ'_v	transl., rot., vib.	symmetry type
Γ_1	1	1	1	1	T_z, Q_1, Q_2	A_1
Γ_2	1	1	-1	-1	R_z	A_2
Γ_3	1	-1	1	-1	T_x, R_y	B_1
Γ_4	1	-1	-1	1	T_y, R_x, Q_3	B_2

ν_i (see Ch. 6) transform under the symmetry operations. We obtain for the normal coordinates Q_i that Q_1 and Q_2 remain unchanged during all symmetry operations, while for Q_3

$$Q_3 \xrightarrow{C_2} -Q_3 ; \quad Q_3 \xrightarrow{\sigma_v} -Q_3 \quad \text{and} \quad Q_3 \xrightarrow{\sigma'_v} Q_3 . \quad (5.6)$$

The representation of Q_3 is therefore $\Gamma_4 = (+1, -1, -1, +1)$.

Definition: A representation of a group G is a transformation of the group elements g_i onto other elements M_i with the condition that with each element $g_i \in G$ is uniquely associated a mathematical quantity M_i (number, square matrix, etc.) so that the product $g_i \times g_k$ is uniquely associated with the product $M_i \times M_k$.

In cases like the group C_{2v} , where each symmetry operation is uniquely associated with a number (i.e., $+1$ or -1), the representation is called *one-dimensional*. By comparing Tables 5.1 and 5.2, it can easily be verified that the definition of a representation is satisfied.

Such one-dimensional representations can always be found if each element of the point group forms its own class, that is, if the group is commutative. The states of the molecule are then *nondegenerate* (except for an accidental degeneracy, which bears no relationship to symmetry).

One-dimensional representations are not possible for groups where several group elements belong to the same class. Here, n -dimensional representations with $n \geq 2$ are employed, for example square matrices of dimension n .

We will elucidate this for the example of the group C_{3v} .

5.5.2

The Representation of the Group C_{3v}

The symmetry properties of the z component T_z of the translation vector under the symmetry operations in C_{3v} are (see Fig. 5.21)

$$\begin{aligned} IT_z &= +T_z ; \\ C_3 T_z &= C_3^2 T_z = +T_z ; \\ \sigma_v T_z &= \sigma'_v T_z = \sigma''_v T_z = +T_z . \end{aligned} \quad (5.7)$$

The transformation properties of T_z can therefore be described by the one-dimensional representation Γ_1 of type A_1 , for which all characters are $+1$.

This is not true, however, for T_x and T_y . Upon rotation by an angle φ around the z axis (Fig. 5.21), the coordinates x, y are transformed to

$$\begin{aligned} x^* &= x \cos \varphi - y \sin \varphi \\ y^* &= x \sin \varphi + y \cos \varphi \end{aligned} \quad \text{or} \quad \begin{pmatrix} x^* \\ y^* \end{pmatrix} = \begin{pmatrix} \cos \varphi & -\sin \varphi \\ \sin \varphi & \cos \varphi \end{pmatrix} \begin{pmatrix} x \\ y \end{pmatrix}, \quad (5.8)$$

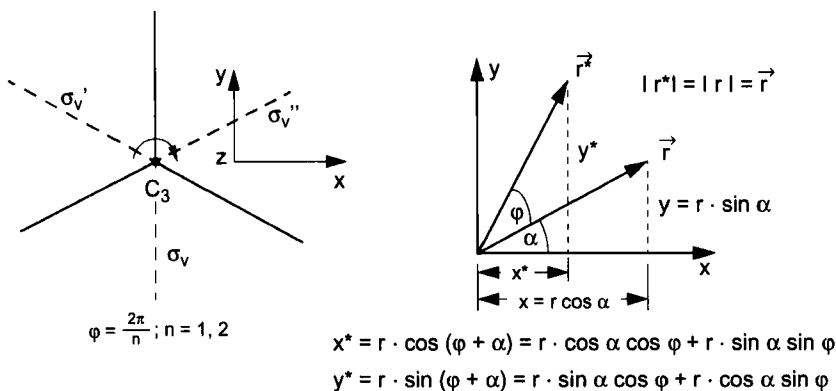


Fig. 5.21 Transformation properties of the components T_x and T_y of the translation vector upon rotation by an angle φ around the z axis.

where we have used $x = r \cos \alpha$, $y = r \sin \alpha$, and x^* , y^* are the components of the vector \mathbf{r}^* which is generated from $\mathbf{r} = \{x, y\}$ after the rotation (Fig. 5.21).

The symmetry operation C_3 effects a rotation by $\varphi = -120^\circ$, while C_3^2 results in a rotation by -240° or $+120^\circ$. The rotation matrix for C_3 is therefore

$$\begin{pmatrix} \cos(-120^\circ) & -\sin(-120^\circ) \\ \sin(-120^\circ) & \cos(-120^\circ) \end{pmatrix} = \begin{pmatrix} -\frac{1}{2} & \frac{1}{2}\sqrt{3} \\ -\frac{1}{2}\sqrt{3} & -\frac{1}{2} \end{pmatrix}. \quad (5.9)$$

The transformation properties under C_3^2 , σ_v , σ_v' , and σ_v'' can be deduced analogously. Overall, we obtain the two-dimensional representation Γ_3 from Table 5.6, which is usually denoted by E , whereas three-dimensional representations are denoted by the letter T .

In many cases, higher-dimensional representations can be reduced to representations of a lower dimension by a suitable transformation. Such representations are therefore called *reducible*. If this reduction is not possible, the representation is called *irreducible*. Table 5.6 shows, as an example, the irreducible representation of the group C_{3v} .

Tab. 5.6 Irreducible representations of the group C_{3v} .

C_{3v}		I	C_3	C_3^2	σ_v	σ_v'	σ_v''	
Γ_1	A_1	1	1	1	1	1	1	T_z
Γ_2	A_2	1	1	1	-1	-1	-1	R_z
Γ_3	E	$\begin{pmatrix} 1 & 0 \\ 0 & 1 \end{pmatrix}$	$\begin{pmatrix} -\frac{1}{2} & \frac{\sqrt{3}}{2} \\ -\frac{\sqrt{3}}{2} & -\frac{1}{2} \end{pmatrix}$	$\begin{pmatrix} -\frac{1}{2} & -\frac{\sqrt{3}}{2} \\ +\frac{\sqrt{3}}{2} & -\frac{1}{2} \end{pmatrix}$	$\begin{pmatrix} -1 & 0 \\ 0 & 1 \end{pmatrix}$	$\begin{pmatrix} \frac{1}{2} & -\frac{\sqrt{3}}{2} \\ -\frac{\sqrt{3}}{2} & -\frac{1}{2} \end{pmatrix}$	$\begin{pmatrix} \frac{1}{2} & \frac{\sqrt{3}}{2} \\ \frac{\sqrt{3}}{2} & -\frac{1}{2} \end{pmatrix}$	$\left. \begin{matrix} T_x, T_y \\ R_x, R_y \end{matrix} \right\}$

5.5.3

Characters and Character Tables

The traces of the matrices, that is, the sum of their diagonal elements, are called the *characters* χ_{ik} of the representation Γ_i . For one-dimensional representations, the character equals the number ± 1 as explained above. The subscript i labels representations Γ_i , that is, it runs from 1 to the number m of irreducible representations, whereas $k = 1, \dots, N$ labels symmetry operations, N being the order of the group.

Characters are an important tool in determining the smallest possible dimension of a representation. If, for example, an n -dimensional representation of a group is available, its characters show if it can be *reduced* to lower-dimensional representations or if it is *irreducible*. This is made possible by the

Theorem: *The sum of the squared characters of an irreducible representation equals the order N of the group.*

It is easily verified that for the representations $\Gamma_1, \dots, \Gamma_4$ of the group C_{2v} , this sum of squares is always $1 + 1 + 1 + 1 = 4$, the number of group elements.

Because of their great importance for finding the representations of the different symmetry types, the characters χ_{ik} of all irreducible representations are tabulated in so-called *character tables* for all molecular point groups (see, e.g., [5.1]). An example of such a character table, here for the group C_{3v} , is given in Table 5.7. For the one-dimensional representations of the group C_{2v} , Table 5.5 is identical to the character table.

It can be seen from these tables that for a given irreducible representation, the character of all symmetry operations belonging to the same class is identical. For example, for the representation Γ_3 , the three reflections σ_v , σ'_v and σ''_v of the group C_{3v} are in the same class and have the character $\chi = 0$, whereas the two rotations C_3 and C_3^2 are in another class with the character $\chi = -1$, and the identity I with character $\chi = 2$ is in its own class.

For each molecular point group, there exists a one-dimensional *totally symmetric* representation Γ_1 of symmetry type A_1 , the character of which is $\chi_{ik} \equiv +1$ ($k = 1, \dots, N$) for all N symmetry operations.

We can express all representations of a symmetry group in the form of a block matrix. The identity operation I is always represented by a unit matrix with a dimension N which equals the order of the corresponding symmetry group. Its character

Tab. 5.7 Character table of the group C_{3v} .

C_{3v}	I	C_3	C_3^2	σ_v	σ'_v	σ''_v
$\Gamma_1 (A_1)$	1	1	1	1	1	1
$\Gamma_2 (A_2)$	1	1	1	-1	-1	-1
$\Gamma_3 (E)$	2	-1	-1	0	0	0

Tab. 5.8 Representation of the direct sum $\Gamma_2 \oplus \Gamma_3$ of the group C_{3v} .

I	C_3	C_3^2	σ_v	σ'_v	σ''_v
$\begin{pmatrix} 1 & 0 & 0 \\ 0 & 1 & 0 \\ 0 & 0 & 1 \end{pmatrix}$	$\begin{pmatrix} 1 & 0 & 0 \\ 0 & -\frac{1}{2} & \frac{\sqrt{3}}{2} \\ 0 & -\frac{\sqrt{3}}{2} & -\frac{1}{2} \end{pmatrix}$	$\begin{pmatrix} 1 & 0 & 0 \\ 0 & -\frac{1}{2} & -\frac{\sqrt{3}}{2} \\ 0 & \frac{\sqrt{3}}{2} & -\frac{1}{2} \end{pmatrix}$	$\begin{pmatrix} -1 & 0 & 0 \\ 0 & -1 & 0 \\ 0 & 0 & 1 \end{pmatrix}$	$\begin{pmatrix} -1 & 0 & 0 \\ 0 & \frac{1}{2} & -\frac{\sqrt{3}}{2} \\ 0 & -\frac{\sqrt{3}}{2} & -\frac{1}{2} \end{pmatrix}$	$\begin{pmatrix} -1 & 0 & 0 \\ 0 & \frac{1}{2} & \frac{\sqrt{3}}{2} \\ 0 & \frac{\sqrt{3}}{2} & -\frac{1}{2} \end{pmatrix}$

$\chi_{ii} = N$, that is, the trace of this unit matrix, gives immediately the dimension N of the representation.

It is easily verified for the example of the group C_{3v} that for each of the three representations A_1 , A_2 , and E , the sum of the squared characters, $\sum_{k=1}^6 \chi_{ik}^2$, summed over all elements in a row in Table 5.7, equals the group order $N = 6$.

5.5.4

Sums, Products, and Reduction of Representations

If a representation Γ_a comprises N matrices A_n of dimension n and a representation Γ_b comprises N matrices B_m of dimension m , the direct sum $\Gamma_d = \Gamma_a \oplus \Gamma_b$ is defined to be the representation

$$D_n = \begin{pmatrix} A_n & 0 \\ 0 & B_n \end{pmatrix} \quad (5.10)$$

of dimension $m + n$. For example, the direct sum $\Gamma_2 \oplus \Gamma_3$ of the group C_{3v} is given by the matrices listed in Table 5.8.

We see that the characters of the direct sum equal the sum of the characters of the individual summands, because the diagonal elements of the individual representations add up to the total trace.

The *direct product* $\Gamma_{ab} = \Gamma_a \otimes \Gamma_b$ of two representations Γ_a and Γ_b with dimensions n and m are the matrices of dimension $n \cdot m$ formed according to the following scheme:

$$\Gamma_a \otimes \Gamma_b = \Gamma_{ab} \quad (5.11)$$

$$\begin{pmatrix} 1 & 2 & 3 \\ 4 & 5 & 6 \\ 7 & 8 & 9 \end{pmatrix} \otimes \begin{pmatrix} a & b & c & d \\ e & f & g & h \\ i & j & k & l \\ m & n & o & p \end{pmatrix} = \begin{pmatrix} 1a & 2a & 3a & | & 1b & 2b & 3b & | & \dots \\ 4a & 5a & 6a & | & 4b & 5b & 6b & | & \dots \\ 7a & 8a & 9a & | & 7b & 8b & 9b & | & \dots \\ \hline 1e & 2e & 3e & | & 1f & 2f & 3f & | & \dots \\ 4e & 5e & 6e & | & 4f & 5f & 6f & | & \dots \\ 7e & 8e & 9e & | & 7f & 8f & 9f & | & \dots \\ \hline \cdot & \cdot & \cdot & | & \cdot & \cdot & \cdot & | & \cdot \\ \cdot & \cdot & \cdot & | & \cdot & \cdot & \cdot & | & \cdot \\ \cdot & \cdot & \cdot & | & \cdot & \cdot & \cdot & | & \cdot \end{pmatrix} \cdot$$

Tab. 5.9 Direct product of the representations Γ_2 and Γ_3 of the group C_{2v} .

C_{2v}	I	C_2	σ_v	σ'_v	
Γ_2	1	1	-1	-1	A_2
Γ_3	1	-1	1	-1	B_1
$\Gamma_2 \otimes \Gamma_3$	1	-1	-1	1	$B_2 = A_2 \otimes B_1$

Tab. 5.10 Multiplication table of the symmetry species of the group C_{2v} .

C_{2v}	A_1	A_2	B_1	B_2
A_1	A_1	A_2	B_1	B_2
A_2	A_2	A_1	B_2	B_1
B_1	B_1	B_2	A_1	A_2
B_2	B_2	B_1	A_2	A_1

It can be shown that *the character of the direct product of two representations equals the product of the characters of these representations* (see, e.g., [5.6]). This can be used to determine the symmetry type of a product of two wavefunctions. This will be elucidated again for the example of the group C_{2v} . We choose one factor to be of symmetry type A_2 , the other of type B_1 . Multiplication of the characters from Table 5.9 shows that the product must be of symmetry type $A_2 \times B_1 = B_2$. This multiplication can be carried out for all combinations of A_1 , A_2 , B_1 , and B_2 (see Table 5.1); this yields the last row in Table 5.9. As an example, Table 5.10 shows the multiplication table for the group C_{2v} , which may be compared with Table 5.1.

If a multidimensional representation of a symmetry group has been found, the next question is if it is reducible, that is, if it can be decomposed into a direct sum of representations of lower dimension. This is the case if a similarity transformation can be found that diagonalizes, or at least block-diagonalizes, all matrices of the representation simultaneously. To solve this problem, the following theorems can be helpful [5.2, 5.7].

- Each reducible representation can be decomposed into a direct sum of m irreducible representations.
- The number m of these reducible representations equals the number of classes in the corresponding point group.
- The sum of the squared dimensions n_i of these m irreducible representations equals the order N of the point group, that is

$$\sum_{i=1}^m n_i^2 = N.$$

- (d) The sum of the squared characters of an arbitrary irreducible representation of a symmetry group equals the group order N ,

$$\sum_{k=1}^N \chi_{ik}^2 = N.$$

- (e) The *scalar product* of the characters of two irreducible representations Γ_a and Γ_b is

$$\sum_{k=1}^N \chi_{ak} \chi_{bk} = 0.$$

We will illustrate these theorems for the group D_{3d} (see Fig. 5.4b). The character table of group D_{3d} is displayed in Table 5.11. Its irreducible representations are

- the four one-dimensional representations with $\chi(I) = 1$,

$$\Gamma_1 = A_{1g}, \quad \Gamma_2 = A_{2g}, \quad \Gamma_4 = A_{1u}, \quad \Gamma_5 = A_{2u},$$

- and the two two-dimensional representations with $\chi(I) = 2$,

$$\Gamma_3 = E_g, \quad \Gamma_6 = E_u.$$

According to theorem c),

$$\sum n_i^2 = 1^2 + 1^2 + 2^2 + 1^2 + 1^2 + 2^2 = 12 = N.$$

The symmetry operations fall into six classes, I (one element), C_3 (two elements), C_2 (three elements), i (one element), S_6 (two elements) and σ_d (three elements).

Consequently, there must be six irreducible representations Γ_1 through Γ_6 . The sum $\sum \chi_{ik}^2$ is, for Γ_6 ,

$$2^2 + 2(-1)^2 + 3 \times 0^2 + (-2)^2 + 2 \times 1^2 + 3 \times 0^2 = 12$$

Note that the summation runs over all group elements, that is over $2 \times C_3$, $3 \times C_2$, $2 \times S_6$, and $3 \times \sigma_d$.

Tab. 5.11 Abbreviated character table of group D_{3d} .

D_{3d}	I	$2C_3$	$3C_2$	i	$2S_6$	$3\sigma_d$	
Γ_1 A_{1g}	1	1	1	1	1	1	
Γ_2 A_{2g}	1	1	-1	1	1	-1	R_z
Γ_3 E_g	2	-1	0	2	-1	0	R_x, R_y
Γ_4 A_{1u}	1	1	1	-1	-1	-1	
Γ_5 A_{2u}	1	1	-1	-1	-1	1	T_z
Γ_6 E_u	2	-1	0	-2	1	0	T_x, T_y

The scalar product is, for $\Gamma_3 \cdot \Gamma_5$,

$$\sum_{k=1}^N \chi_{3k} \chi_{5k} = 2 \times 1 + 2(-1) \times 1 + 3 \times 0(-1) + 2 \times (-1) \\ + 2 \times (-1) \times (-1) + 3 \times 0 \times 1 = 0.$$

For the reduction of a reducible representation Γ_r we use the following

Theorem: In the decomposition of a reducible representation into a direct sum of irreducible representations Γ_i ,

$$\Gamma_r = a_1 \cdot \Gamma_1 \oplus a_2 \cdot \Gamma_2 \oplus \dots \oplus a_m \Gamma_m, \quad (5.12)$$

the j th irreducible representation Γ_j occurs exactly a_j times,

$$a_j = \frac{1}{N} \sum_{k=1}^N \chi_k^{(R)} \times \chi_{jk}^{(i)}, \quad (5.13)$$

where $\chi_k^{(R)}$ is the character of the reducible representation for the k th group element (i.e., the k th symmetry operation), and $\chi_{jk}^{(i)}$ is the character of the j th irreducible representation of the k th symmetry operation.

As an example, we discuss the symmetry of a rotation–vibration level in the electronic ground state of the NH_3 molecule with C_{3v} symmetry (Fig. 5.2).

The wavefunction

$$\Psi = \psi_{\text{el}} \times \psi_{\text{vib}} \times \psi_{\text{rot}} \quad (5.14)$$

is written as a product of electronic, vibrational, and rotational contributions.

The electronic ground state is totally symmetric with symmetry A_1 . For the vibrational state, we assume a superposition of the ν_3 and ν_4 normal modes (see Sect. 6.3), which both have E symmetry. If the rotational angular momentum \mathbf{J} is not oriented along the C_3 symmetry axis (i.e., the projection $K\hbar$ of \mathbf{J} onto the symmetry axis is $\neq 0$), the symmetry axis precesses around the laboratory-fixed angular momentum axis (see Sect. 6.2). The symmetry of such a rotational state is E .

The total wavefunction Eq. (5.14) has then the symmetry type $\Gamma = A_1 \otimes E \otimes E \otimes E$, and its representation has the dimension

$$n = \prod n_i = 1 \times 2 \times 2 \times 2 = 8.$$

How can this product representation be reduced?

From the character table, Table 5.7, which is shown again in Table 5.12 in abbreviated form, we see that the characters of the product representations $E \otimes E$ and $E \otimes E \otimes E$, which must equal the products of the characters of the individual E representations, have the values listed in Table 5.13.

Tab. 5.12 Abbreviated character table of the group C_{3v} .

C_{3v}	I	$2C_3$	$3\sigma_v$
A_1	1	1	1
A_2	1	1	-1
E	2	-1	0

Tab. 5.13 Characters of the direct products of two-dimensional representations of the group C_{3v} .

C_{3v}	I	$2C_3$	$3\sigma_v$
$E \otimes E$	4	+1	0
$E \otimes E \otimes E$	8	-1	0
$E \otimes E \otimes E \otimes A_1$	8	-1	0

To decompose this product representation into a direct sum of irreducible representations, we use Eq. (5.13) to find out how often the three possible irreducible representations A_1, A_2 , and E are contained, for example, in the product representation

$$E \otimes E \otimes E \otimes A_1 = a_1 A_1 + a_2 A_2 + a_3 E, \quad (5.15)$$

that is, we need to find the values of the a_i . With the group order $N = 6$, we obtain from Eq. (5.13),

$$a_1 = \frac{1}{6} (8 \times 1 + 2 \times (-1) \times 1 + 3 \times 0 \times 1) = 1,$$

$$a_2 = \frac{1}{6} (8 \times 1 + 2 \times (-1) \times 1 + 3 \times 0 \times (-1)) = 1,$$

$$a_3 = \frac{1}{6} (8 \times 2 + 2 \times (-1) \times (-1) + 3 \times 0 \times 0) = 3.$$

The direct sum is therefore

$$E \otimes E \otimes E \otimes A_1 = 1 \times A_1 \oplus 1 \times A_2 \oplus 3 \times E.$$

It is easily verified that the sum of the characters of the reduced representation equals the characters of the product representation given before.

6

Rotations and Vibrations of Polyatomic Molecules

As in the discussion of diatomic molecules in Ch. 3, we will now try to understand the vibrational–rotational levels of polyatomic molecules by employing successively refined models. We start with the rigid rotor model and harmonic vibrations of a nonrotating molecule, and we will finally include the interactions between vibrations and rotations, which are more complicated in this case than for diatomic molecules.

The larger number of vibrational modes in polyatomic molecules, which in general lead to three-dimensional motions of the nuclear framework, constitutes a significant complication with respect to the diatomic case, where only one-dimensional vibrations along the internuclear axis were possible. Such vibrations can be described more easily in a reference frame with the origin in the molecule's center of mass and with axes that are fixed to the equilibrium nuclear framework so that it rotates with the molecule. In this so-called *molecule-fixed* reference frame, all nuclei assume constant, time-independent coordinates in their equilibrium positions, that is, the nuclei of the *rigid* (nonvibrating) molecule are *at rest* in the molecule-fixed reference frame.

The Schrödinger equation (2.4) was formulated in the laboratory-fixed reference frame, which is connected to the molecule-fixed system through a suitable coordinate transformation. There are two approaches to arrive at the Schrödinger equation in the molecule-fixed reference frame:

- (a) Starting from the classical Hamiltonian function $H = T + V$ in the laboratory system, the quantum-mechanical Hamiltonian is obtained by introducing canonical momenta and substituting $p \rightarrow -\frac{\hbar}{i} \frac{\partial}{\partial q}$. Then, the coordinate transformation to the molecule-fixed system is performed in the Hamiltonian.
- (b) First, the coordinate transformation is carried out for the classical Hamiltonian function and the transformed function is then converted into the quantum-mechanical Hamiltonian. This approach poses serious problems, however, because the canonical momenta are, in general, complicated expressions. For small vibrational amplitudes, however, the molecule can be treated approximately as a rigid system at the equilibrium configuration, and it is then possible, to construct the correct Hamiltonian [6.1].

We will use the second approach and start with the coordinate transformation for the classical kinetic energy expression to the molecule-fixed reference frame. As the potential energy depends only on *relative* coordinates, its form is unchanged by the coordinate transformation.

6.1

Transformation From the Laboratory System to the Molecule-fixed System

We denote the coordinates of the i th nucleus in the molecule-fixed system by lower-case letters,

$$\mathbf{r}_i = \{x_i, y_i, z_i\},$$

and choose the molecule's center of mass as the origin so that $\mathbf{r}_{\text{c.m.}} = \{0, 0, 0\}$.

The coordinates of the same nucleus in the laboratory system are denoted by upper-case letters,

$$\mathbf{R}_i = \{X_i, Y_i, Z_i\}.$$

The molecule's center of mass $\mathbf{r}_{\text{c.m.}} = \{0, 0, 0\}$ is denoted in the laboratory system by the vector $\mathbf{R}_{\text{c.m.}} = \{X_{\text{c.m.}}, Y_{\text{c.m.}}, Z_{\text{c.m.}}\}$.

For the transformation from one system to the other (Fig. 6.1), we obtain

$$\mathbf{R}_i = \mathbf{R}_{\text{c.m.}} + \mathbf{r}_i. \quad (6.1)$$

If we want to compare the time variation of the position of the i th nucleus measured in the laboratory system, $d\mathbf{R}_i/dt$, and measured in the molecule-fixed system, $d\mathbf{r}_i/dt$, we must take into account that both systems are accelerated with respect to each other: The molecule-fixed system rotates with an angular velocity ω around its center of mass, which in turn moves with a velocity $d\mathbf{R}_{\text{c.m.}}/dt$ with respect to the laboratory system.

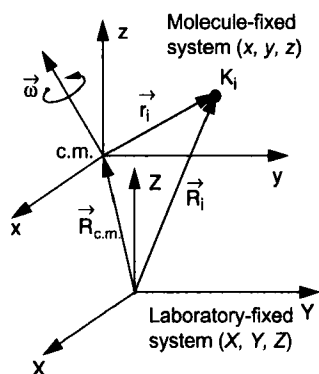


Fig. 6.1 Transformation from the laboratory reference frame to a molecule-fixed reference frame.

Using the unit vectors $\hat{e}_x, \hat{e}_y, \hat{e}_z$, the position vector \mathbf{r} in the molecule-fixed system can be written as

$$\mathbf{r} = x\hat{e}_x + y\hat{e}_y + z\hat{e}_z . \quad (6.2)$$

Differentiation with respect to time yields the time variation of \mathbf{r} ,

$$\frac{d\mathbf{r}}{dt} = \frac{dx}{dt}\hat{e}_x + \frac{dy}{dt}\hat{e}_y + \frac{dz}{dt}\hat{e}_z + x\frac{d\hat{e}_x}{dt} + y\frac{d\hat{e}_y}{dt} + z\frac{d\hat{e}_z}{dt} \quad (6.3)$$

as seen by an observer in the laboratory system, expressed by the coordinates in the molecule-fixed system. As the unit vectors $\hat{e}_x, \hat{e}_y, \hat{e}_z$ of the molecule-fixed system rotate with respect to the laboratory system at an angular velocity $\boldsymbol{\omega}$ around the center of mass, the derivatives

$$\frac{d\hat{e}_x}{dt} = \boldsymbol{\omega} \times \hat{e}_x ; \quad \frac{d\hat{e}_y}{dt} = \boldsymbol{\omega} \times \hat{e}_y ; \quad \frac{d\hat{e}_z}{dt} = \boldsymbol{\omega} \times \hat{e}_z \quad (6.4)$$

indicate the velocities with which the points of the unit vectors move due to the rotation of the system around the axis $\boldsymbol{\omega}$ (the magnitude of their velocities must be $|\boldsymbol{\omega}|$ and the direction must be $\perp \boldsymbol{\omega}$ and $\perp \hat{e}_x$).

By differentiating Eq. (6.1) with respect to time, we obtain for the velocity of the i th nucleus in the laboratory system,

$$\mathbf{V}_i = \dot{\mathbf{R}}_i = \dot{\mathbf{R}}_{\text{c.m.}} + \dot{\mathbf{r}}_i + (\boldsymbol{\omega} \times \mathbf{r}_i) . \quad (6.5)$$

The total kinetic energy T of all N nuclei with masses M_i measured in the laboratory system, but expressed in the molecule-fixed system, is then

$$T = \frac{1}{2} \left(\sum_{i=1}^N M_i V_i^2 \right) = \frac{1}{2} \sum M_i (\dot{\mathbf{R}}_{\text{c.m.}} + \dot{\mathbf{r}}_i + \boldsymbol{\omega} \times \mathbf{r}_i)^2 . \quad (6.6)$$

Evaluation of the terms in parentheses yields, with $\dot{\mathbf{r}}_i = \mathbf{v}_i$,

$$T = \frac{1}{2} \left[\dot{\mathbf{R}}_{\text{c.m.}}^2 \sum M_i + \sum M_i (\boldsymbol{\omega} \times \mathbf{r}_i)^2 + \sum M_i v_i^2 + 2\dot{\mathbf{R}}_{\text{c.m.}} (\boldsymbol{\omega} \times \sum M_i \mathbf{r}_i) + 2\dot{\mathbf{R}}_{\text{c.m.}} \sum M_i \mathbf{v}_i + 2 \sum M_i \mathbf{v}_i (\boldsymbol{\omega} \times \mathbf{r}_i) \right] . \quad (6.6a)$$

The following relations hold:

- (a) $\sum M_i = M$, total mass of the nuclear framework.
- (b) $\mathbf{r}_{\text{c.m.}} = (\sum M_i \mathbf{r}_i) / M = \mathbf{0}$, because for the center of mass in the molecule-fixed system $\mathbf{r}_{\text{c.m.}} = \{0, 0, 0\}$.
- (c) $\sum M_i \mathbf{v}_i = \mathbf{0}$, because the total momentum of all nuclei in the center-of-mass system is always zero.

- (d) If the nuclei are in their equilibrium positions $\mathbf{r}_i = \mathbf{r}_i^0$, the angular momentum of the nuclear framework in the molecule-fixed system must be zero,

$$\sum M_i (\mathbf{r}_i^0 \times \mathbf{v}_i) = 0 \Rightarrow \sum M_i (\mathbf{r}_i \times \mathbf{v}_i) = \sum M_i (\Delta \mathbf{r}_i \times \mathbf{v}_i) \text{ with } \Delta \mathbf{r}_i = \mathbf{r}_i - \mathbf{r}_i^0.$$

- (e) $\mathbf{a} \cdot (\mathbf{b} \times \mathbf{c}) = \mathbf{b} \cdot (\mathbf{c} \times \mathbf{a}) \Rightarrow$

$$\sum M_i \mathbf{v}_i \cdot (\boldsymbol{\omega} \times \mathbf{r}_i) = \boldsymbol{\omega} \cdot \sum M_i (\mathbf{r}_i \times \mathbf{v}_i) = \boldsymbol{\omega} \cdot \sum M_i (\Delta \mathbf{r}_i \times \mathbf{v}_i).$$

Note: Strictly speaking, the molecule-fixed system is only defined for the rigid, nonvibrating molecule, in which all nuclei are at their equilibrium positions \mathbf{r}_i^0 . For example, a molecule executing bending vibrations possesses an angular momentum, even in the molecule-fixed system. This is taken into account by the last term in Eq. (6.6a). For sufficiently small vibrational amplitudes, the nuclear geometry changes only slightly, and the molecule-fixed system (also called the Eckart system) remains defined (for a detailed justification, see [6.2]).

Taking (a)–(e) into account, it follows from Eq. (6.6a) with $\Delta \mathbf{r}_i = \mathbf{r}_i - \mathbf{r}_i^0$ for the kinetic energy,

$$T = \frac{1}{2} M \dot{\mathbf{R}}_{\text{c.m.}}^2 + \frac{1}{2} \sum_i M_i (\boldsymbol{\omega} \times \mathbf{r}_i)^2 + \frac{1}{2} \sum_i M_i v_i^2 + \boldsymbol{\omega} \cdot \sum_i M_i (\Delta \mathbf{r}_i \times \mathbf{v}_i). \quad (6.7)$$

The first term describes the *translational energy* of the molecule, whose center of mass moves with a velocity $\mathbf{V}_{\text{c.m.}} = \dot{\mathbf{R}}_{\text{c.m.}}$. It is responsible for the Doppler shift of spectral lines (see Sect. 4.3.3) and can be eliminated using Doppler-free spectroscopic techniques (see Sect. 12.4).

The second term describes the *rotational energy* of the molecule, the third term the *vibrational energy*. The fourth term is only then different from zero if the nuclei are displaced from their equilibrium position in the rotating molecule so that $\Delta \mathbf{r}_i = \mathbf{r}_i - \mathbf{r}_i^0$ and \mathbf{v}_i are not parallel. It describes the *Coriolis interaction* between vibration and rotation.

If the kinetic energy of the molecule were to be described in the laboratory system, there would be no inertial forces, that is, the Coriolis interaction would be zero. However, the expressions for the rotational and vibrational energies would become significantly more complicated.

Note: The last three terms in Eq. (6.7) describe the respective contributions to the nuclear kinetic energy as measured in the laboratory system, but expressed in the coordinates of the molecule-fixed system. Equation (6.7) is the classical expression for the kinetic energy. For a correct description of the different contributions, it has to be converted into a quantum-mechanical form.

We will now discuss the individual terms successively, starting with the second, that is, with the rotational energy of the rigid rotor.

6.2

Molecular Rotation

The classical treatment of the rigid rotor is usually described in detail in texts on theoretical mechanics [6.3], and we will therefore summarize the results only briefly. The quantum-mechanical treatment of the symmetric and asymmetric top can be found at length in [6.4–6.6]. We start with the classical model.

6.2.1

The Rigid Rotor

For the rotational energy of a rigid rotor we obtain from Eq. (6.7)

$$\begin{aligned}
 T_{\text{rot}} &= \frac{1}{2} \sum M_i (\boldsymbol{\omega} \times \mathbf{r}_i)^2 \\
 &= \frac{1}{2} \sum M_i \left[(\boldsymbol{\omega} \times \mathbf{r}_i)_x^2 + (\boldsymbol{\omega} \times \mathbf{r}_i)_y^2 + (\boldsymbol{\omega} \times \mathbf{r}_i)_z^2 \right] \\
 &= \frac{1}{2} \sum M_i \left[\omega_x^2 (z_i^2 + y_i^2) + \omega_y^2 (x_i^2 + z_i^2) + \omega_z^2 (x_i^2 + y_i^2) \right. \\
 &\quad \left. - \omega_x \omega_y x_i y_i - \omega_x \omega_z x_i z_i - \omega_y \omega_z y_i z_i \right]. \tag{6.8}
 \end{aligned}$$

Introducing the inertia tensor

$$\tilde{I} = \begin{pmatrix} I_{xx} & I_{xy} & I_{xz} \\ I_{yx} & I_{yy} & I_{yz} \\ I_{zx} & I_{zy} & I_{zz} \end{pmatrix}, \tag{6.9}$$

this can be written as

$$T_{\text{rot}} = (\omega_x, \omega_y, \omega_z) \begin{pmatrix} I_{xx} & I_{xy} & I_{xz} \\ I_{yx} & I_{yy} & I_{yz} \\ I_{zx} & I_{zy} & I_{zz} \end{pmatrix} \begin{pmatrix} \omega_x \\ \omega_y \\ \omega_z \end{pmatrix}, \tag{6.10a}$$

or, in abbreviated form, as

$$T_{\text{rot}} = \frac{1}{2} \boldsymbol{\omega} \tilde{I} \boldsymbol{\omega}. \tag{6.10b}$$

The components of the inertia tensor are

$$\begin{aligned}
 I_{xx} &= \sum M_i (y_i^2 + z_i^2) & I_{xy} &= I_{yx} = - \sum M_i x_i y_i \\
 I_{yy} &= \sum M_i (x_i^2 + z_i^2) & I_{xz} &= I_{zx} = - \sum M_i x_i z_i \\
 I_{zz} &= \sum M_i (x_i^2 + y_i^2) & I_{yz} &= I_{zy} = - \sum M_i y_i z_i.
 \end{aligned} \tag{6.11}$$

Thus, Eq. (6.10) becomes, in component notation,

$$T_{\text{rot}} = \frac{1}{2} (I_{xx}\omega_x^2 + I_{yy}\omega_y^2 + I_{zz}\omega_z^2 + I_{xy}\omega_x\omega_y + I_{yz}\omega_y\omega_z + I_{zx}\omega_x\omega_z) . \quad (6.12)$$

If the molecule-fixed reference frame is chosen so that its axes point along the directions of the three principal moments of inertia, the tensor I is diagonal, that is, in this system $I_{xy} = I_{xz} = I_{yz} = 0$. The three principal moments of inertia are obtained as the three solutions of the equation

$$\begin{vmatrix} I_{xx} - I & I_{xy} & I_{xz} \\ I_{yx} & I_{yy} - I & I_{yz} \\ I_{zx} & I_{zy} & I_{zz} - I \end{vmatrix} = 0 \quad (6.13)$$

for the determinant obtained for the principal axes transformation. The three solutions yield the three principal moments of inertia, which are denoted I_A , I_B , and I_C , and ordered so that $I_A \leq I_B \leq I_C$.

The rotational energy of a rigid rotor is, expressed by components in the principal axes system,

$$T_{\text{rot}} = \frac{1}{2} (I_x\omega_x^2 + I_y\omega_y^2 + I_z\omega_z^2) , \quad (6.14)$$

where the principal moments of inertia I_x, I_y, I_z each assume one of the values I_A, I_B , or I_C .

In Eq. (6.14), the angular velocity ω can be replaced by the angular momentum

$$\mathbf{J} = \sum (\mathbf{r}_i \times \mathbf{p}_i) = \sum M_i (\mathbf{r}_i \times (\boldsymbol{\omega} \times \mathbf{r}_i)) \quad (6.15)$$

of the nuclear framework. Using the inertia tensor \tilde{I} , Eq. (6.15) can be written as

$$\mathbf{J} = \tilde{I}\boldsymbol{\omega} , \quad (6.15a)$$

as can be verified by inserting Eq. (6.11). In the principal axes system, Eq. (6.15a) becomes

$$\mathbf{J} = \{I_x\omega_x; I_y\omega_y; I_z\omega_z\} . \quad (6.16)$$

Note: \mathbf{J} and $\boldsymbol{\omega}$ are only parallel if all principal moments of inertia $I_x = I_y = I_z$ are equal (spherical top) or if only one component of $\boldsymbol{\omega}$ is different from zero (rotation around one of the principal axes of inertia). In general, \mathbf{J} and $\boldsymbol{\omega}$ have different directions (Fig. 6.2).

If we express the components of the angular velocity ω in Eq. (6.14) by the corresponding angular momentum components from Eq. (6.16), we obtain for the rotational energy

$$T_{\text{rot}} = \frac{1}{2} \left(\frac{J_x^2}{I_x} + \frac{J_y^2}{I_y} + \frac{J_z^2}{I_z} \right) . \quad (6.17)$$

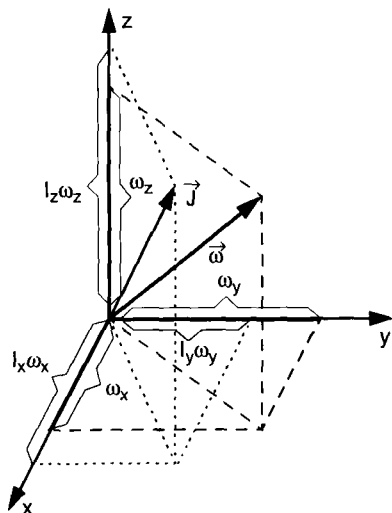


Fig. 6.2 Rotational angular momentum \mathbf{J} and angular velocity $\boldsymbol{\omega}$ for differing moments of inertia I_x and I_y .

As the angular momentum \mathbf{J} and the rotational energy of a rigid rotor are both constant in the absence of external torques, two conservation laws must be satisfied:

$$\frac{J_x^2}{I_x} + \frac{J_y^2}{I_y} + \frac{J_z^2}{I_z} = \text{const.} \quad (\text{energy conservation}) \quad (6.18a)$$

$$J_x^2 + J_y^2 + J_z^2 = \text{const.} \quad (\text{angular momentum conservation}). \quad (6.18b)$$

Note: While the components J_x, J_y, J_z in the laboratory system are constant, this is not in general true for the components J_x, J_y, J_z in the molecule-fixed system. However, for both systems $J^2 = J_x^2 + J_y^2 + J_z^2 = J_x^2 + J_y^2 + J_z^2 = \text{const.}$

In angular momentum space with the coordinates J_x, J_y, J_z , Eq. (6.18b) describes a sphere, Eq. (6.18a) an ellipsoid. As the components of the vector \mathbf{J} must satisfy both equations simultaneously, the point of the vector \mathbf{J} must be located on the intersecting curves between the sphere and the ellipsoid (Fig. 6.3). As the ellipsoid is determined by the principal axes of the molecule and is therefore constant in the *molecule-fixed* system, whereas the angular momentum \mathbf{J} is constant in the *laboratory* system and thus varying in the molecule-fixed system, the molecule's rotation must be such that the point of the laboratory-fixed vector \mathbf{J} always remains on the intersecting curve between sphere and ellipsoid, Eq. (6.18a). This condition leads to a nutation of both the momentary rotation axis $\boldsymbol{\omega}$ and a possible symmetry axis (for the case of a symmetric top) around the laboratory-fixed angular momentum axis (Fig. 6.4), except if $\boldsymbol{\omega}$ happens to point along the figure axis so that $\boldsymbol{\omega}$ and \mathbf{J} coincide. If α is the angle between the figure axis z and \mathbf{J} and β the angle between z and $\boldsymbol{\omega}$, the nutation cones for the figure axis and for $\boldsymbol{\omega}$ have apex angles of α and $\beta - \alpha$, respectively.

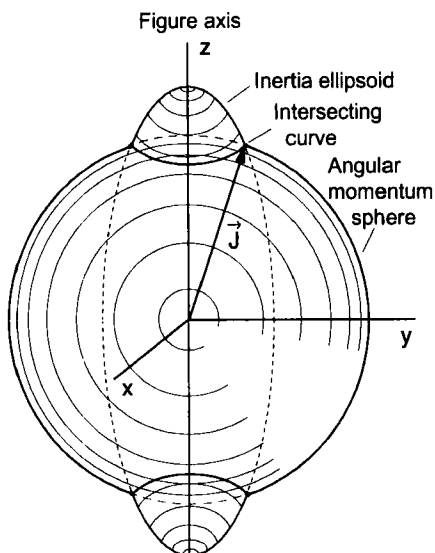


Fig. 6.3 The inertia ellipsoid with the figure axis along the molecule-fixed z direction performs a nutational motion so that the laboratory-fixed angular momentum

vector J stays on the intersection of the inertia ellipsoid Eq. (6.18a) and angular momentum sphere Eq. (6.18b).

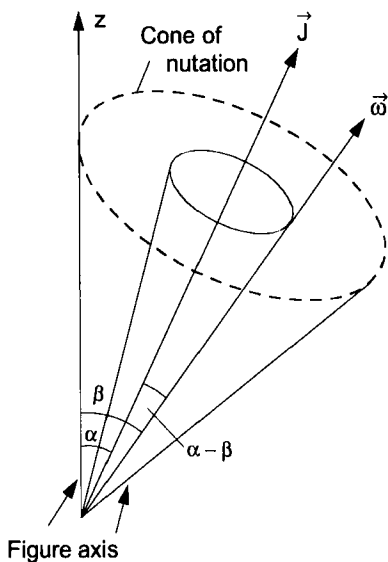


Fig. 6.4 Nutation of figure axis z and current rotation axis ω around the laboratory-fixed angular momentum axis J .

6.2.2

The Symmetric Top

If two of the principal moments of inertia are equal, the molecule possesses a symmetry axis coinciding with the principal inertia axis. The moment of inertia for a rotation around this axis is then in general different from the other two equal moments of inertia. The inertia ellipsoid is then rotationally symmetric with respect to the symmetry axis of the rotor. All molecules with a symmetry axis C_n ($n > 2$) are symmetric tops. If all three moments of inertia are equal, the inertia ellipsoid becomes a sphere, and the rotor is called a spherical top. For the general symmetric top, two cases can be distinguished:

- (a) *The prolate symmetric top: $I_A < I_B = I_C$*

Here, the two *larger* moments of inertia are equal. This corresponds to a rotational ellipsoid which is elongated along the symmetry axis (Fig. 6.5a).

Examples

A cylinder with a diameter D smaller than its height; all linear molecules; the molecule CClH_3 (Fig. 6.5a).

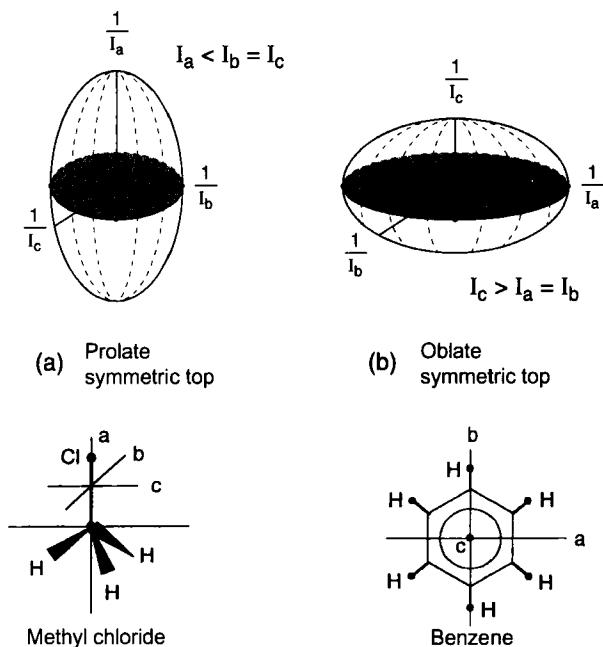


Fig. 6.5 Inertia ellipsoid and example molecules for a) a prolate top and b) an oblate top.

(b) *The oblate symmetric top:* $I_A = I_B < I_C$

Here, the two *smaller* moments of inertia are equal; this corresponds to a flattened inertia ellipsoid.

Examples

A disc rotating around its symmetry axis (Fig. 6.5b); the benzene molecule; all planar molecules.

If, for example, $I_x = I_y$, the rotational energy Eq. (6.17) can be written, using $J^2 = J_x^2 + J_y^2 + J_z^2$, as

$$T_{\text{rot}} = \frac{1}{2} \left(\frac{J^2}{I_x} + \frac{J_z^2}{I_z} - \frac{J_z^2}{I_x} \right). \quad (6.19)$$

The rotational energy of an asymmetric top depends on the magnitude of the angular momentum and its projection J_z onto the symmetry axis of the top.

6.2.3

Quantum-mechanical Treatment of Rotation

To obtain the Hamiltonian H_{rot} for the symmetric top from Eq. (6.18), we replace as usual [6.4] the classical quantities by their operators,

$$p_x \rightarrow \left(\frac{\hbar}{i} \right) \frac{\partial}{\partial x}, \quad \mathbf{p} \rightarrow \left(\frac{\hbar}{i} \right) \nabla, \quad \mathbf{r} \rightarrow \hat{\mathbf{r}}. \quad (6.20)$$

Hence, the angular momentum

$$\mathbf{J} = \sum_i (\mathbf{r}_i \times \mathbf{p}_i) \quad (6.21a)$$

becomes the operator

$$\hat{\mathbf{J}} = \frac{\hbar}{i} \sum_{i=1}^3 (\hat{\mathbf{r}}_i \times \nabla_i). \quad (6.21b)$$

For the symmetric top, both the projection J_Z onto the laboratory-fixed Z axis and the projection J_z onto the symmetry axis of the top (which we choose to be the z axis) are constant (the symmetry axis precesses around the laboratory-fixed \mathbf{J} direction, see Fig. 6.4); therefore J^2 , J_Z and J_z are constants of the motion. This means that in the quantum-mechanical description, the operator \hat{J}^2 commutes with \hat{J}_z and \hat{J}_Z ,

$$[\hat{J}^2, \hat{J}_Z] = 0 \quad \text{and} \quad [\hat{J}^2, \hat{J}_z] = 0. \quad (6.22)$$

Hence, the three operators possess common eigenfunctions, which we denote by $\psi_{J,K,M}$ and which we can determine as follows.

The operator components of the laboratory-fixed angular momentum J can be expressed in spherical coordinates θ (angle against the Z axis) and ϕ (azimuth angle),

$$\hat{J}_X = \frac{\hbar}{i} \sum_i \left[Y \frac{\partial}{\partial Z} - Z \frac{\partial}{\partial Y} \right]_i = \frac{\hbar}{i} \left[-\sin \phi \frac{\partial}{\partial \theta} - \cot \theta \cos \phi \frac{\partial}{\partial \phi} \right] \quad (6.23a)$$

$$\hat{J}_Y = \frac{\hbar}{i} \sum_i \left[Z \frac{\partial}{\partial X} - X \frac{\partial}{\partial Z} \right]_i = \frac{\hbar}{i} \left[-\cos \phi \frac{\partial}{\partial \theta} - \cot \theta \sin \phi \frac{\partial}{\partial \phi} \right] \quad (6.23b)$$

$$\hat{J}_Z = \frac{\hbar}{i} \sum_i \left[X \frac{\partial}{\partial Y} - Y \frac{\partial}{\partial X} \right]_i = \frac{\hbar}{i} \frac{\partial}{\partial \phi} \quad (6.23c)$$

For the square of the operator \hat{J} we obtain with $J^2 = J_X^2 + J_Y^2 + J_Z^2$

$$\hat{J}^2 = -\hbar^2 \left[\frac{1}{\sin \theta} \frac{\partial}{\partial \theta} \left(\sin \theta \frac{\partial}{\partial \theta} \right) + \frac{1}{\sin^2 \theta} \frac{\partial^2}{\partial \phi^2} \right] \quad (6.24)$$

The eigenvalue equations for the three commuting operators are

(a)

$$\hat{J}^2 \psi_{JKM} = J(J+1) \hbar^2 \psi_{JKM} \quad (6.25a)$$

with the spherical harmonics Y_{JM} as solutions [6.4].

(b)

$$\hat{J}_Z \psi_{JKM} = M \hbar \psi_{JKM} \quad (6.25b)$$

where Eq. (6.25b) follows from Eqns. (6.23) and (6.24). $M\hbar$ is the projection of J onto the laboratory-fixed Z axis. If we express J by the coordinates of the molecule-fixed system and use the commutation rules, we obtain for the projection J_z of the angular momentum onto the symmetry axis of the symmetric top,

(c)

$$\hat{J}_z \psi_{JKM} = K \hbar \psi_{JKM} \quad (6.25c)$$

Obviously, K is the quantum number of the angular momentum projection onto the molecule's symmetry axis.

If we insert the corresponding eigenvalues into Eq. (6.19), we obtain for the prolate symmetric top with $I_z = I_a < I_x = I_y = I_b = I_c$,

$$T_{\text{rot}} = E_{J,K} = \frac{\hbar^2}{2} \left[\frac{J(J+1)}{I_b} + K^2 \left(\frac{1}{I_a} - \frac{1}{I_b} \right) \right] \quad (6.26)$$

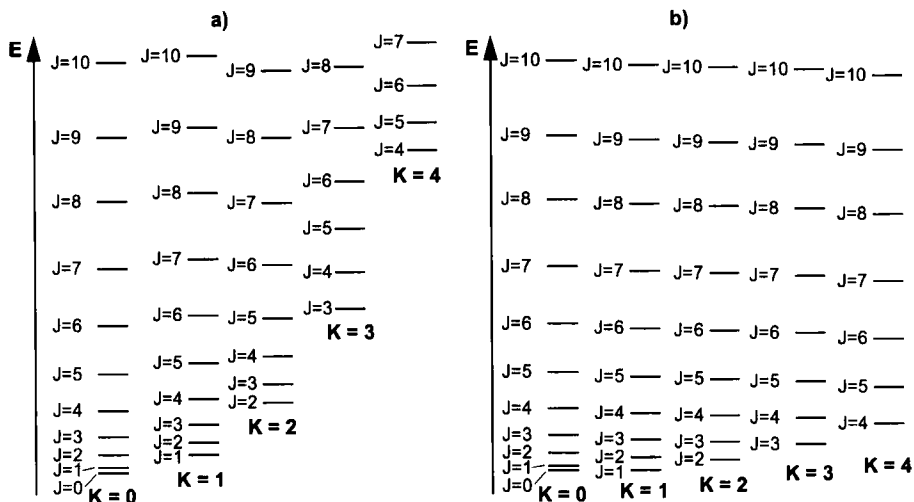


Fig. 6.6 Rotational term diagram for the a) prolate and b) the oblate symmetric top.

With the rotational constants

$$A = \frac{\hbar}{4\pi c I_a}, \quad B = \frac{\hbar}{4\pi c I_b}, \quad C = \frac{\hbar}{4\pi c I_c}, \quad (6.27)$$

we obtain the rotational term values $F_{J,K} = E/hc$, expressed in cm^{-1} ,

$$F_{J,K} = BJ(J+1) + (A-B)K^2 \quad (\text{prolate top}). \quad (6.28)$$

For the oblate symmetric top, we have

$$I_z = I_c > I_x = I_A = I_y = I_b$$

$$E_{J,K} = \frac{\hbar^2}{2} \left[\frac{J(J+1)}{I_b} + K^2 \left(\frac{1}{I_c} - \frac{1}{I_b} \right) \right], \quad (6.29)$$

$$F_{J,K} = BJ(J+1) + (C-B)K^2 \quad (\text{oblate top}). \quad (6.30)$$

Figure 6.6 compares the rotational levels $|J, K\rangle$ of the prolate and the oblate top for different values of K . We see that for the prolate top the energy $E_{J,K}$ increases with K for fixed J , because $(A-B) > 0$, whereas for the oblate top $E_{J,K}$ decreases with increasing K for fixed J because $(C-B) < 0$.

Table 6.1 lists the rotational constants for some linear and nonlinear molecules, illustrating the orders of magnitude of term energies.

6.2.4

Centrifugal Distortion of the Symmetric Top

The centrifugal distortion of a symmetric top is more complicated than in the diatomic case (see Sect. 4.2.2), because it depends both on the magnitude of the angular mo-

Tab. 6.1 Rotational constants of some molecules (all values in gigahertz, $1 \text{ GHz} \doteq 1/30 \text{ cm}^{-1}$).

Linear molecules		Nonlinear molecules			
Isotopomer	B	Molecule	A	B	C
$^1\text{H}^{12}\text{C}^{14}\text{N}$	44.316	$^{12}\text{CH}_2^{35}\text{Cl}$	32.002	3.320	3.065
$^1\text{H}^{13}\text{C}^{14}\text{N}$	43.170	CH_2O	282.106	33.834	34.004
$^2\text{D}^{12}\text{C}^{14}\text{N}$	36.207	ClF_3	13.653	4.612	3.443
$^{12}\text{C}^{79}\text{Br}^{14}\text{N}$	4.120	H_2^{32}S	316.304	276.512	147.536
$^{13}\text{C}^{79}\text{Br}^{14}\text{N}$	4.073	HD^{32}S	290.257	145.218	94.134
$^{12}\text{C}^{81}\text{Br}^{14}\text{N}$	4.096				

mentum and on its direction in the molecule-fixed reference frame, that is, it depends both on the angular momentum quantum number J and on the projection quantum number K . As the centrifugal distortion must be independent of the sense of the molecular rotation (i.e., clockwise or counterclockwise), the expansion of the rotational energy in terms of powers of J and K contains only even powers. A detailed classical calculation [6.5, 6.6] shows that we can write the term values of the nonrigid symmetric top with $A = B \neq C$, in analogy to Eq. (3.18b) for the diatomic case,

$$F(J, K) = BJ(J+1) + (C-B)K^2 - D_J J^2(J+1)^2 - D_{JK} J(J+1)^2 K^2 - D_K K^4 + \dots, \quad (6.31)$$

where three centrifugal constants D_J , D_{JK} and D_K have been introduced, which are much smaller than the rotational constants B and C . Whereas the constants D_J are always positive (the distortion increases the moment of inertia and hence decreases the rotational energy), D_{JK} can be positive or negative, depending on the molecule [6.7, 6.9].

As for diatomic molecules, the centrifugal distortion depends on the force constants of the molecule. Therefore, the experimental determination of D provides information on the molecular potential in the vicinity of the nuclear equilibrium positions.

6.2.5

The Asymmetric Top

In the asymmetric top, all three principal moments of inertia are different, ($I_x \neq I_y \neq I_z \neq I_x$). To determine the energy levels $E_{J,K}$, that is, the eigenvalues of the rotational Hamiltonian Eq. (6.17),

$$\hat{H}_{\text{rot}} = \frac{1}{2} \left(\frac{\hat{J}_x^2}{I_x} + \frac{\hat{J}_y^2}{I_y} + \frac{\hat{J}_z^2}{I_z} \right), \quad (6.32)$$

we can no longer express \hat{J}_x^2 and \hat{J}_y^2 by \hat{J}^2 and \hat{J}_z^2 , as we did in the case of the symmetric top. Hence, we need to determine the eigenfunctions and eigenvalues of \hat{J}_x^2 and \hat{J}_y^2 .

To achieve this, we write the unknown eigenfunctions ψ of \widehat{H}_{rot} as linear combinations of the known eigenfunctions $\psi_n = \psi_n(J, K, M)$ of the symmetric top,

$$\psi = \sum_n c_n \psi_n(J, K, M) \quad (6.33)$$

and insert this ansatz into the Schrödinger equation

$$\widehat{H}_{\text{rot}}\psi = E\psi.$$

After multiplication with $\psi_m^*(J, K, M)$ and integration over all coordinates, we obtain, using the orthogonality of the ψ_n , the equation

$$\sum_n c_n [\langle m | H_{\text{rot}} | n \rangle - E\delta_{nm}] = 0, \quad (6.34)$$

which has nontrivial solutions only if the determinant of coefficients vanishes,

$$|\langle m | H_{\text{rot}} | n \rangle - E\delta_{mn}| = 0. \quad (6.35)$$

To determine the energy eigenvalues from this relation, we must evaluate the matrix elements

$$\langle m | \widehat{H}_{\text{rot}} | n \rangle = \int \psi_m^*(J, K, M) \widehat{H}_{\text{rot}} \psi_n(J, K, M) d\tau$$

of the operator Eq. (6.32) with the eigenfunctions of the symmetric top, that is, the spherical harmonics Y_{JM} . For \widehat{J}^2 and \widehat{J}_z , only the diagonal elements Eq. (6.25) survive, because the functions Y_{JM} are eigenfunctions of \widehat{J}^2 and \widehat{J}_z . However, as \widehat{J}_x and \widehat{J}_y do *not* commute with \widehat{J}^2 and \widehat{J}_z , the functions Y_{JM} can *not* be eigenfunctions of \widehat{J}_x and \widehat{J}_y , that is, the matrix representation of the Hamiltonian Eq. (6.32) is not diagonal in this basis!

From the commutation relations for the angular momentum components in the laboratory-fixed system,

$$J_x J_y - J_y J_x = i\hbar J_z \quad \text{etc.}, \quad (6.36)$$

we obtain the corresponding commutation relations for the components in the molecule-fixed system,

$$\begin{aligned} J_x J_y - J_y J_x &= -i\hbar J_z, \\ J_y J_z - J_z J_y &= -i\hbar J_x, \\ J_z J_x - J_x J_z &= -i\hbar J_y, \end{aligned} \quad (6.37)$$

which differ from the aforementioned relations by the reversed sign [6.4, 6.5]. Using the step operators,

$$J_+ = J_x + iJ_y \quad \text{and} \quad J_- = J_x - iJ_y,$$

we arrive at the matrix elements [6.4],

$$\langle J, K, M | J_x | J, K \pm 1, M \rangle = \frac{i\hbar}{2} [J(J+1) - K(K \pm 1)]^{1/2} \quad (6.38a)$$

$$\langle J, K, M | J_y | J, K \pm 1, M \rangle = \frac{\hbar}{2} [J(J+1) - K(K \pm 1)]^{1/2} \quad (6.38b)$$

Using the product rule for matrix multiplication,

$$\langle J, K, M | J_i^2 | J', K', M' \rangle = \sum_{J'', K'', M''} \langle J, K, M | J_i | J'', K'', M'' \rangle \times \langle J'', K'', M'' | J_i | J', K', M' \rangle, \quad (6.39)$$

we can compute the matrix elements for J_x^2 and J_y^2 from Eq. (6.38). For the diagonal elements, we obtain

$$\langle J, K, M | J_x^2 | J, K, M \rangle = \frac{\hbar^2}{2} [J(J+1) - K^2], \quad (6.40)$$

and for the nonvanishing off-diagonal elements

$$\begin{aligned} \langle J, K, M | J_x^2 | J, K \pm 2, M \rangle &= -\frac{\hbar^4}{4} [J(J+1) - K(K \pm 1)]^{1/2} \\ &\quad \times [J(J+1) - (K \pm 1)(K \pm 2)]^{1/2}, \end{aligned} \quad (6.41)$$

and correspondingly for J_y^2

$$\langle J, K, M | J_y^2 | J, K, M \rangle = \frac{\hbar^2}{2} [J(J+1) - K^2] \quad (6.42)$$

$$\begin{aligned} \langle J, K, M | J_y^2 | J, K \pm 2, M \rangle &= \frac{\hbar^2}{4} [J(J+1) - K(K \pm 1)]^{1/2} \\ &\quad \times [J(J+1) - (K \pm 1)(K \pm 2)]^{1/2}. \end{aligned} \quad (6.43)$$

If we substitute these results into Eq. (6.32), we obtain the nonvanishing matrix elements of the Hamiltonian,

$$\langle J, K | H_{\text{rot}} | J, K \rangle = \frac{\hbar^2}{4} \left[J(J+1) \left(\frac{1}{I_x} + \frac{1}{I_y} \right) + K^2 \left(\frac{2}{I_z} - \frac{1}{I_x} - \frac{1}{I_y} \right) \right] \quad (6.44)$$

$$\begin{aligned} \langle J, K | H_{\text{rot}} | J, K \pm 2 \rangle &= \frac{\hbar^2}{8} [J(J+1) - K(K \pm 1)]^{1/2} \\ &\quad \times [J(J+1) - (K \pm 1)(K \pm 2)]^{1/2} \left(\frac{1}{I_y} - \frac{1}{I_x} \right). \end{aligned} \quad (6.45)$$

This matrix is no longer diagonal! The eigenvalues of H_{rot} and hence the term values of the rotational levels can be found by diagonalizing this matrix.

The coefficients c_n in the expansion Eq. (6.33) can then be determined from Eq. (6.34). The eigenvalues E and eigenfunctions thus obtained are of course only approximate because we can include only a finite number of terms in the expansion Eq. (6.33).

Example

To illustrate the procedure, we will calculate the energy levels of an asymmetric top for $J = 1$. We use $A^* = hcA = \hbar^2(2I_x)$; $B^* = hcB = \hbar^2/(2I_y)$; $C^* = \hbar^2/(2I_z)$. We obtain the diagonal matrix elements $\langle m | H_{\text{rot}} | n \rangle$ from Eq. (6.44) with Eqns. (6.40) and (6.42) and with the rotational constants of Eq. (6.27),

$$\langle J, K | H_{\text{rot}} | J, K \rangle = \frac{A^*}{2} [J(J+1) - K^2] + \frac{B^*}{2} [J(J+1) - K^2] + C^* K^2 \quad (6.46)$$

and the off-diagonal terms from Eq. (6.45). The Hamiltonian matrix is then

$$\langle 1, K | H_{\text{rot}} | 1, K' \rangle = \begin{pmatrix} K \setminus K' & 1 & 0 & -1 \\ 1 & \frac{A^*+B^*}{2} + C & 0 & -\frac{A^*-B^*}{2} \\ 0 & 0 & A^* + B^* & 0 \\ 1 & -\frac{A^*-B^*}{2} & 0 & \frac{A^*+B^*}{2} - C \end{pmatrix}, \quad (6.47a)$$

from which we obtain the secular equation,

$$\begin{vmatrix} \frac{A^*+B^*}{2} + C^* - E & 0 & -\frac{A^*-B^*}{2} \\ 0 & A^* + B^* - E & 0 \\ -\frac{A^*-B^*}{2} & 0 & \frac{A^*+B^*}{2} - C^* - E \end{vmatrix} = 0. \quad (6.47b)$$

This cubic equation has the three solutions

$$E_1 = A^* + B^*; \quad E_2 = B^* + C^*; \quad E_3 = A^* + C^*. \quad (6.48)$$

The expansion Eq. (6.33) in the wavefunctions of the symmetric top converges the more rapidly, the closer the asymmetric top resembles a symmetric top, that is, the less two of the rotational constants differ.

A measure for the asymmetry is the *asymmetry parameter*,

$$\kappa = \frac{2B - A - C}{A - C} \quad (6.49)$$

which for a prolate symmetric top ($B = C$) is $\kappa = -1$ and for an oblate symmetric top ($A = B$) is $\kappa = +1$. The largest asymmetry $\kappa = 0$ results for a top with $B = \frac{1}{2}(A + C)$.

From Eq. (6.32), we obtain the rotational term value,

$$F(J_x, J_y, J_z) = A \langle J_x^2 \rangle + B \langle J_y^2 \rangle + C \langle J_z^2 \rangle . \quad (6.50)$$

If we substitute the asymmetry parameter κ for B , Eq. (6.50) becomes

$$F = \frac{1}{2}(A+C)J(J+1) + \frac{1}{2}(A-C) [\langle J_x^2 \rangle - \langle J_z^2 \rangle + \kappa \langle J_y^2 \rangle] , \quad (6.51)$$

which is frequently summarized in the form

$$F(J, \tau) = \frac{1}{2}(A+C)J(J+1) + \frac{1}{2}(A-C)F_\tau(\kappa) . \quad (6.52)$$

The parameter τ is introduced to enumerate the $2J+1$ energy levels $|J, K\rangle$ belonging to the same total angular momentum J according to their energy; it assumes values from $-J$ to $+J$.

If we denote the projection quantum number for the limiting case of the prolate top ($\kappa = -1$) by K_a and that of the oblate limiting case ($\kappa = +1$) by K_c , the parameter τ becomes

$$\tau = K_a - K_c . \quad (6.53)$$

The function $F_\tau(\kappa) = [\langle J_x^2 \rangle - \langle J_z^2 \rangle + \kappa \langle J_y^2 \rangle]$ can be determined by calculating the expectation values $\langle J_x^2 \rangle$, $\langle J_y^2 \rangle$ and $\langle J_z^2 \rangle$ using the expansion Eq. (6.33) of the asymmetric top wavefunction in the wavefunctions of the symmetric top (see, e.g., [6.1] or [6.4]). Figure 6.7 displays schematically the term values of an asymmetric top as a function of the asymmetry parameter κ .

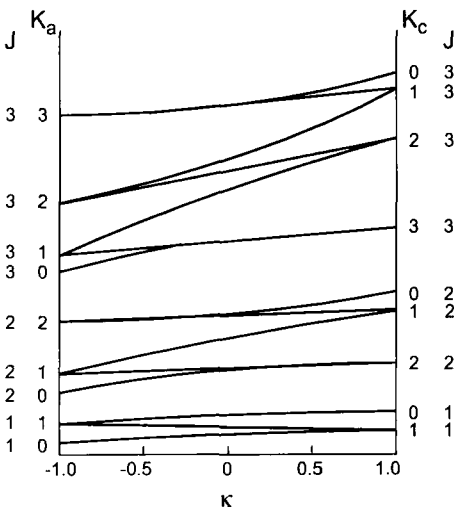


Fig. 6.7 Correlation diagram for the rotational term values of the asymmetric top for the limiting cases of the prolate ($\kappa = -1$) and the oblate ($\kappa = +1$) symmetric top.

Tab. 6.2 Term values of asymmetric top molecules for rotational quantum numbers $J \leq 2$.

J_{K_a, K_c}	J_τ	$F(J_\tau)$
0 ₀₀	0 ₀	0
1 ₀₁	1 ₋₁	$B + C$
1 ₁₀	1 ₁	$A + B$
1 ₁₁	1 ₀	$A + C$
2 ₀₂	2 ₋₂	$2\{A + B + C - [(B - C)^2 + (A - C)(A - B)]^{1/2}\}$
2 ₂₀	2 ₂	$2\{A + B + C + [(B - C)^2 + (A - C)(A - B)]^{1/2}\}$
2 ₂₁	2 ₁	$4A + B + C$
2 ₁₁	2 ₀	$A + 4B + C$
2 ₁₂	2 ₋₁	$A + B + 4C$

If we vary κ continuously from -1 to $+1$ (e.g., by continuously deforming the structure of the nuclear framework from a prolate to an oblate symmetric top), the projection quantum number K is undefined except for the two limiting cases $\kappa = \pm 1$, because the asymmetric top possesses no symmetry axis. In fact, the parameter τ takes on the role of K for distinguishing between the $(2J + 1)$ energy levels for a given J , although τ itself is *not* a quantum number!

The limiting values K_a and K_c are frequently used instead of τ to characterize a rotational level. For example, we write either

$$J_{K_a, K_c} = 3_{1,3} \quad \text{or} \quad J_\tau = 3_{-2}. \quad (6.54)$$

From the correlation diagram in Fig. 6.7, we see that the asymmetry leads to a splitting of all twofold degenerate states (J, K) of the symmetric top for $K \neq 0$ into two components. This asymmetry splitting is largest for states with $K = 1$ in the symmetric limiting case, where

$$\Delta F_{(K=1)} = \frac{1}{2}(B - C)J(J + 1). \quad (6.55)$$

For larger values of K , it converges rapidly towards zero (for more details, see [6.1, 6.8]).

Table 6.2 lists the term values for rotational quantum numbers $J \leq 2$. Similar tables for larger values of J can be found in the literature [6.4].

6.3

Vibrations of Polyatomic Molecules

We will start the discussion with a classical description of molecular vibrations. To simplify the notation, we introduce *mass-weighted* generalized coordinates

$$\begin{aligned} q_1 &= \sqrt{m_1} \Delta x_1 ; & q_2 &= \sqrt{m_1} \Delta y_1 ; & q_3 &= \sqrt{m_1} \Delta z_1 ; \\ q_4 &= \sqrt{m_2} \Delta x_2 ; & q_5 &= \sqrt{m_2} \Delta y_2 ; & \dots , \end{aligned} \quad (6.56)$$

weighting the displacements $\Delta x_i = x_i - x_{i0}$, Δy_i , Δz_i of the nuclei from their equilibrium positions according to the masses of the vibrating nuclei. The third, kinetic-energy, term in Eq. (6.7) can then be written as a quadratic form

$$T = \frac{1}{2} \sum_{i=1}^{3N} \dot{q}_i^2 . \quad (6.57)$$

The Taylor expansion of the potential

$$V = V_0 + \sum_{i=1}^{3N} \left[\frac{\partial V}{\partial q_i} \right]_0 q_i + \frac{1}{2} \sum_{i=1}^{3N} \left[\frac{\partial^2 V}{\partial q_i \partial q_k} \right]_0 q_i q_k + \dots \quad (6.58)$$

starts with the third term if we place the zero point of the energy scale at the minimum potential energy ($V_0 = 0$), because all first derivatives vanish at this point. For sufficiently small displacements q_i , higher terms in Eq. (6.58) can be neglected, and we obtain

$$V = \sum_{i,k=1}^{3N} b_{ik} q_i q_k \quad \text{with} \quad b_{ik} = \frac{1}{2} \left[\frac{\partial^2 V}{\partial q_i \partial q_k} \right] . \quad (6.59)$$

With the Lagrange function $L = T - V$, we obtain the Lagrange equation

$$\frac{d}{dt} \left(\frac{\partial L}{\partial \dot{q}_i} \right) - \frac{\partial L}{\partial q_i} = 0 , \quad (6.60)$$

which corresponds to the Newtonian equation of motion for oscillating masses m_i . With Eqns. (6.57) and (6.59), we obtain from Eq. (6.60)

$$\ddot{q}_i + \sum_{k=1}^{3N} b_{ik} q_k = 0 ; \quad i = 1, \dots, 3N . \quad (6.61a)$$

Equation (6.61a) constitutes a coupled system of differential equations describing the motions of $3N$ coupled oscillators with displacements

$$q_i = A_i \cos(\omega_i t + \varphi_i) . \quad (6.62a)$$

In the general case, the restoring force for the displacement q_i is influenced by the other displacements q_k , because the off-diagonal terms b_{ik} in the potential Eq. (6.59) effect a coupling between the different oscillations. Only for certain initial conditions will all nuclei oscillate with identical frequency ω_n and identical phase φ_n . Such vibrational states are called *normal modes*; they will be discussed in the following section in some detail.

6.3.1

Normal Modes

In vector notation, $\mathbf{q} = \{q_1, \dots, q_{3N}\}$, Eq. (6.61a) simplifies to

$$\ddot{\mathbf{q}} + \tilde{\mathbf{B}}\mathbf{q} = 0, \quad (6.61b)$$

where $\tilde{\mathbf{B}} = (b_{ik})$ is the matrix with components (b_{ik}) . If $\tilde{\mathbf{B}}$ were a special diagonal matrix $\tilde{\mathbf{B}} = \lambda\tilde{\mathbf{E}}$ ($\tilde{\mathbf{E}}$ = unit matrix), Eq. (6.61b) would reduce to a system of $3N$ *decoupled* vibrational equations for the q_i , with solutions

$$q_i = a_i \cos(\sqrt{\lambda}t) \quad i = 1, \dots, 3N, \quad (6.62b)$$

which describe a molecular state in which all nuclei oscillate with the same frequency $\omega = \sqrt{\lambda}$ and pass their equilibrium positions simultaneously. Hence, we need to find a system of vibrational coordinates that makes $\tilde{\mathbf{B}}$ diagonal.

The condition

$$\tilde{\mathbf{B}}\mathbf{q} = \lambda\tilde{\mathbf{E}}\mathbf{q} \quad \Rightarrow \quad (\tilde{\mathbf{B}} - \lambda\tilde{\mathbf{E}})\mathbf{q} = 0 \quad (6.63)$$

is equivalent to a *principal axis transformation*. It has nontrivial solutions exactly if the coefficient determinant satisfies

$$\det(\tilde{\mathbf{B}} - \lambda\tilde{\mathbf{E}}) = 0. \quad (6.64)$$

For each solution λ_n of Eq. (6.64), we obtain from Eq. (6.63) a set of $3N$ vibrational components q_{kn} ($k = 1, \dots, 3N$), which represent the time-dependent displacements of all N nuclei. The q_{kn} can be collected in a vector

$$\mathbf{Q}_n = \mathbf{A}_n \sin(\omega_n t + \varphi_n) \quad \text{with} \quad \omega_n = \sqrt{\lambda_n} \quad (6.65)$$

specifying the simultaneous motion of all nuclei during the n th normal vibration. The magnitude of the vector \mathbf{Q}_n is called the *normal coordinate* Q_n of the normal mode with frequency $\omega_n = \sqrt{\lambda_n}$. Hence, the normal coordinate $Q_n(t)$ gives the mass-weighted displacements of *all nuclei* at time t during the n th normal vibration.

Using normal coordinates, Eq. (6.61b) can be written as a set of $3N$ decoupled equations

$$\ddot{Q}_n + \omega_n^2 Q_n = 0 \quad n = 1, \dots, 3N, \quad (6.66)$$

because now both kinetic and potential energy are quadratic forms,

$$T = \frac{1}{2} \sum_{n=1}^{3N} \dot{Q}_n^2; \quad V = \frac{1}{2} \sum_{n=1}^{3N} \lambda_n \cdot Q_n^2, \quad (6.67)$$

if terms higher than quadratic are neglected in the potential energy. The solutions of Eq. (6.66) are the normal vibrations Eq. (6.65).

In other words, for sufficiently small oscillation amplitudes, where the potential is still harmonic, a molecule executes harmonic oscillations in normal coordinates for which all nuclei possess the same frequency $\omega_i = \sqrt{\lambda_i}$ and the same or the opposite phase φ_i for a given normal vibration i . The total vibrational energy of the molecule equals the sum of the vibrational energies of the individual excited normal vibrations.

Note:

1. As the potential energy V depends only on internal coordinates (distances between nuclei and electrons) but not on translation and rotation of the nuclear framework, some of the $3N$ coefficients b_{ik} in Eq. (6.61a) must vanish. After allowing for three degrees of freedom for each translation and rotation, there remain $(3N - 6)$ degrees of freedom for the vibration of a nonlinear molecule, and $(3N - 5)$ for linear molecules, because these do not rotate around the internuclear axis.¹ Hence, there are $(3N - 6)$ (nonlinear molecules) or $(3N - 5)$ (linear molecules) nonvanishing solutions λ_n for the normal vibrations.

This fact can also be understood with the aid of the following consideration. In the molecule-fixed reference frame (center-of-mass system), the sum of all momenta and angular momenta must be zero for each normal vibration. This yields five (six) auxiliary conditions for linear (nonlinear) molecules. Together with Eq. (6.64) and the requirement for five (six) of the b_{ik} to be zero, this makes sure that six (five) solutions λ_n vanish [6.9].

1) The reason for this is the quantization of angular momentum: rotation around the internuclear axis is possible if the associated angular momentum is $\pm\hbar$ (or a multiple thereof). Due to the extremely small moment of inertia around this axis (which is only due to the electron cloud), this requires a very high angular velocity $\omega = \hbar/I$, which in turn implies a large excitation energy $E = I\omega^2 = \hbar\omega$. Excitation of this rotation can therefore be neglected under normal circumstances.

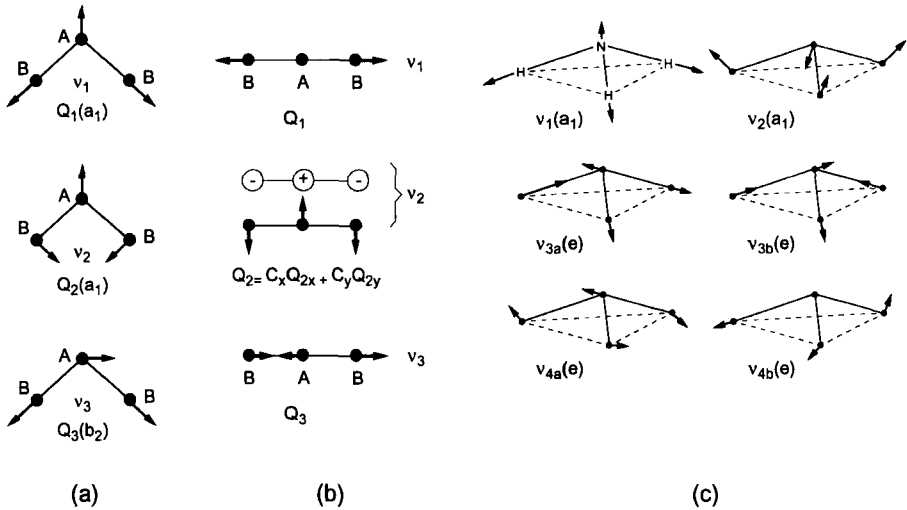


Fig. 6.8 Normal vibrations of some types of molecules: a) non-linear AB_2 molecule; b) linear AB_2 molecule; c) nonplanar AB_3 molecule. In b), the bending vibration ν_2 is twofold degenerate; in c), both ν_3 and ν_4 are twofold degenerate.

2. The homogeneous differential equation (6.61b) determines the nuclear vibrational amplitudes a_i only up to a common constant factor, and therefore the amplitude A_n of the n th normal vibration (which summarizes the vibrational amplitudes of all nuclei during this normal vibration) is also not defined unambiguously by Eq. (6.66). The same is true for the phases φ_n . The only requirement is that all nuclei pass through their equilibrium positions simultaneously and hence the phases of all nuclei be equal for a given normal vibration. Amplitude and phase can be determined from the initial conditions (e.g., $Q(t=0) = Q_0$ and $\dot{Q}(t=0) = \dot{Q}_0$). Frequently, the amplitudes are normalized so that for the individual amplitudes a_{in} of the solution vector $A_n = \{a_{1,n}, \dots, a_{3N,n}\}$

$$\hat{a}_{in} = \frac{a_{in}}{|A_n|} = \frac{a_{in}}{\sqrt{\sum_i |a_{in}|^2}}. \quad (6.68)$$

Figure 6.8 shows the normal vibrations of some types of molecules: non-linear AB_2 (e.g., H_2O , NO_2 or SO_2), linear AB_2 (e.g., CO_2) and nonplanar AB_3 (e.g., NH_3).

6.3.2

Example: Calculation of the Stretching Vibrations of a Linear Molecule AB₂

We will elucidate the calculation of the normal vibrations for the example of a linear triatomic molecule AB₂. For the sake of simplicity, we consider only the one-dimensional stretching vibrations along the molecular axis. For the kinetic and potential energies, we obtain at displacements $\Delta z_i = q_i / \sqrt{m_i}$ (Fig. 6.9)

$$\begin{aligned} 2T &= \dot{q}_1^2 + \dot{q}_2^2 + \dot{q}_3^2 \\ 2V &= k(\Delta z_2 - \Delta z_1)^2 + K(\Delta z_3 - \Delta z_2)^2 \\ &= k \left[\frac{q_1^2}{m_1} + \frac{2q_2^2}{m_2} + \frac{q_3^2}{m_1} - \frac{2q_1 q_2}{\sqrt{m_1 m_2}} - \frac{2q_2 q_3}{\sqrt{m_1 m_2}} \right], \end{aligned} \quad (6.69)$$

where k is the force constant of the restoring force $F_i = -k\Delta z_i$, and we have used $m_1 = m_3$.

Thus, we obtain from Eq. (6.59) for the matrix elements b_{ik}

$$\begin{aligned} b_{11} &= k/m_1, & b_{12} &= b_{21} = -k/\sqrt{m_1 m_2}, & b_{13} &= b_{31} = 0 \\ b_{22} &= 2k/m_2, & b_{23} &= b_{32} = -k/\sqrt{m_1 m_2}, & b_{33} &= k/m_1. \end{aligned} \quad (6.70)$$

The condition Eq. (6.64),

$$\det(b_{ij} - \lambda \delta_{ij}) = 0$$

yields a cubic equation for λ with the solutions

$$\lambda_1 = \frac{k}{m_1}; \quad \lambda_2 = \frac{k(2m_1 + m_2)}{m_1 m_2}; \quad \lambda_3 = 0. \quad (6.71)$$

$\lambda_3 = 0$ corresponds to a translation of the whole molecule along the molecular axis. The mass-weighted vibrational amplitudes q can be obtained from the system of equations Eq. (6.61a), which becomes in this case (because $\ddot{q}_i = -\lambda q_i$),

$$\begin{aligned} b_{11}q_{11} + b_{12}q_{12} + b_{13}q_{13} - \lambda_1 q_{11} &= 0 \\ b_{21}q_{21} + b_{22}q_{22} + b_{23}q_{23} - \lambda_2 q_{21} &= 0 \\ b_{31}q_{31} + b_{32}q_{32} + b_{33}q_{33} - \lambda_3 q_{31} &= 0, \end{aligned} \quad (6.72)$$

where q_{ki} is the mass-weighted vibrational amplitude of the i th nucleus during the normal vibration with frequency $\omega_k = \sqrt{\lambda_k}$.

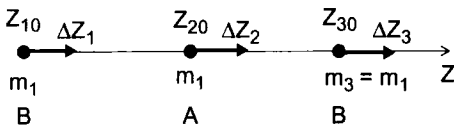


Fig. 6.9 Calculation of the stretching vibrations of a linear AB₂ molecule.

Substituting the values for the b_{ik} yields, for example, for the first normal vibration with $\omega_1 = \sqrt{k/m_1}$:

$$q_{21} = 0; \quad q_{11}/q_{31} = -\sqrt{m_3/m_1} = -1, \quad (6.73)$$

where $q_{i1} = \Delta z_i \sqrt{m_i}$ is the mass-weighted displacement of the nucleus i during the first normal vibration. Hence, the central nucleus is at rest during this vibration, and the two nuclei 1 and 3 with masses $m_1 = m_3$ oscillate in opposite directions with relative amplitudes $\Delta z_1/\Delta z_2 = -1$.

The displacements for the vibrations with frequencies $\sqrt{\lambda_2}$ and $\sqrt{\lambda_3}$ can be calculated analogously.

The absolute values of the q_{ik} can be fixed by defining suitable initial conditions.

Note: Besides the two stretching vibrations with frequencies $\sqrt{\lambda_1}$ and $\sqrt{\lambda_2}$ considered in this example, the molecule can also execute two bending vibrations in the xz plane and the yz plane. These normal vibrations are degenerate, that is, they possess the same energy. This case will be considered in the next section. The total number of normal vibrations is $3N - 5 = 4$.

6.3.3

Degenerate Vibrations

If two or more solutions λ_k are equal, the corresponding normal vibrations with identical frequencies are called *degenerate*. For $\lambda_i = \lambda_k$, not only the normal coordinates Q_i and Q_k are solutions of Eq. (6.66), but also each linear combination

$$Q = c_i Q_i + c_k Q_k, \quad (6.74)$$

that is, there exist infinitely many solutions, all of which can be linearly combined from the two linearly independent solutions Q_i and Q_k . This can be visualized using a simple model.

The k th normal vibration of a molecule corresponds to the harmonic vibration of a molecule in the potential $V = \frac{1}{2} \lambda_k Q_k^2$. For a twofold degenerate vibration with $\lambda_i = \lambda_k = \lambda$, the motion of the particle can be described as being in a *two-dimensional* potential (in normal coordinate space)

$$V = \frac{1}{2} \lambda (Q_i^2 + Q_k^2). \quad (6.75)$$

The generalized trajectory is an ellipse (Fig. 6.10).

$$\begin{aligned} Q_i &= Q_{i0} \cos(\sqrt{\lambda}t + \varphi_i) \\ Q_k &= Q_{k0} \cos(\sqrt{\lambda}t + \varphi_k). \end{aligned} \quad (6.76)$$

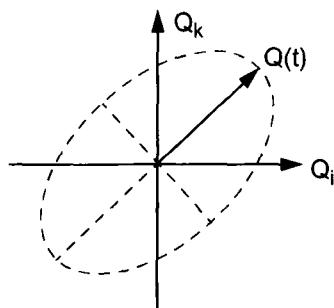


Fig. 6.10 Trajectory of a normal coordinate $Q = c_i Q_i + c_k Q_k$ of a degenerate vibration with $\varphi_i \neq \varphi_k$.

If the two phases φ_i and φ_k of Q_i and Q_k are identical, the resulting trajectory $Q(t)$ is a straight line in the plane of the two normal coordinates Q_i and Q_k .

Figure 6.8 displays the two degenerate bending vibrations of the linear molecule CO_2 in the xz and the yz planes. Each combination of these two vibrations can therefore occur as a possible vibration of the molecule. Figure 6.11a shows such a combined vibration, in which the two bending vibrations have a phase difference of 90° so that the two nuclei B and the nucleus A exert circular motions around the z axis in real space. Note that such a vibration possesses angular momentum $l\hbar$ around the z axis, whereas the rotation of a rigid linear molecule effects only angular momentum components perpendicular to this axis. This vibrational angular momentum leads to a coupling between rotation and vibration (see Sect. 6.3.6), in addition to the coupling mechanisms already discussed for diatomic molecules in Sect. 3.4.

Such degenerate vibrations occur also in nonlinear molecules. For example, the two pairs of normal vibrations ν_3 and ν_4 of the nonplanar AB_3 molecule in Fig. 6.8 are degenerate. A superposition of such degenerate vibrations can lead to a synchronous motion of all nuclei on almost circular trajectories around their equilibrium positions (Fig. 6.11b). The superposition of two normal vibrations of the Na_3 molecule, which

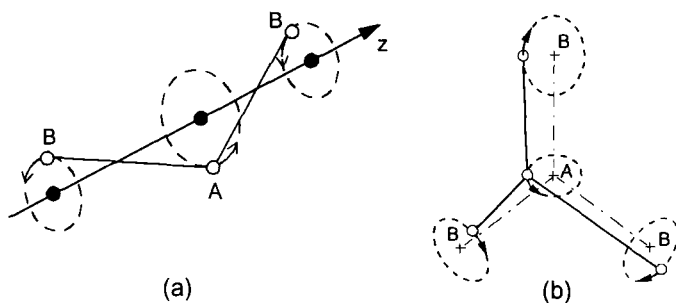


Fig. 6.11 a) Motion of the nuclei upon superposition of two degenerate bending vibrations of an AB_2 molecule. b) Pseudorotation of a planar AB_3 molecule.

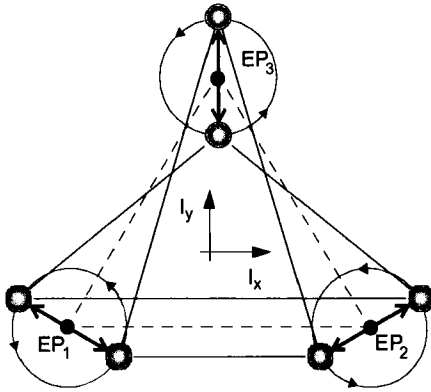


Fig. 6.12 Pseudorotation of the Na_3 molecule as a superposition of two normal vibrations that are degenerate in D_{3h} . The motions of the sodium nuclei are

synchronized, with a 120° phase shift; they rotate along three circles around centers that correspond to the edges of the equilateral triangle.

are degenerate in D_{3h} , is illustrated in Fig. 6.12. For a phase shift of $\varphi_i - \varphi_k = \pi/2$, this superposition leads to a circular motion of the three nuclei around their equilibrium positions, which is also called a *pseudorotation* of the molecule.

6.3.4

Quantum-mechanical Treatment

From the vibrational energy of normal coordinates,

$$E_v = \frac{1}{2} \sum_{i=1}^{3N-6} Q_i^2 + \frac{1}{2} \sum_{i=1}^{3N-6} \lambda_i Q_i^2, \quad (6.77)$$

we obtain the Hamiltonian

$$\hat{H}_v = -\frac{\hbar^2}{2} \sum_{i=1}^{3N-6} \frac{\partial^2}{\partial Q_i^2} + \frac{1}{2} \sum_{i=1}^{3N-6} \lambda_i Q_i^2. \quad (6.78)$$

Note that the nuclear masses are contained in the mass-weighted normal coordinates Q_i .

Due to the decoupling mediated by the normal coordinates, the Schrödinger equation

$$H\psi_v = E\psi_v$$

can be separated, using the product wavefunction

$$\psi_v = \psi_{v_1}(Q_1)\psi_{v_2}(Q_2)\dots\psi_{v_{3N-6}}(Q_{3N-6}), \quad (6.79)$$

into $(3N - 6)$ decoupled equations [$(3N - 5)$ for linear molecules]

$$-\frac{\hbar^2}{2} \frac{\partial^2 \psi_{v_i}(Q_i)}{\partial Q_i^2} + \frac{1}{2} \lambda_i Q_i^2 \psi_{v_i}(Q_i) = E_i \psi_{v_i}(Q_i) \quad i = 1, \dots, 3N - 6. \quad (6.80)$$

The total vibrational energy is then

$$E_v = \sum E_i, \quad (6.81)$$

where the E_i are the eigenvalues of Eq. (6.80), that is, the eigenvalues of the harmonic oscillator (see Sect. 3.3.1),

$$E_i = \hbar \omega_i \left(v_i + \frac{1}{2} \right). \quad (6.82)$$

The eigenfunctions $\psi_{v_i}(Q_i)$ are, in analogy to the vibrational functions of diatomic molecules,

$$\psi_{v_i}(Q_i) = N_{v_i} H_{v_i}(\zeta_i) e^{-\zeta_i^2/2}, \quad (6.83)$$

where N is a normalization factor, H_{v_i} are the Hermite polynomials, and $\zeta_i = Q_i \sqrt{\lambda_i / \hbar^2}$.

Note: For degenerate vibrations with the degree of degeneracy d_i for the i th vibration, the zero-point energy is correspondingly $\hbar \omega_i d_i / 2$. The total energy E_v of all vibrations is therefore

$$E_v = \sum_{i=1}^p h \nu_i (v_i + d_i / 2) \quad (6.84a)$$

where p is the number of normal vibrations with different frequencies. As for the diatomic molecules, we use term values $G = E_{\text{vib}} / hc$ rather than energies, and thus we obtain

$$G(v_1, v_2, \dots, v_p) = \sum_{i=1}^p \tilde{\nu}_i (v_i + d_i / 2), \quad (6.84b)$$

where we have used the vibrational constants $\tilde{\nu}_i = \nu_i / c$ in cm^{-1} instead of the vibrational frequencies ν_i .

It must again be emphasized that the normal coordinate Q_i is no geometrical coordinate of a nucleus but an abbreviation for the vector $q_i = \{q_{i1}, q_{i2}, \dots, q_{i3N}\}$ describing the ensemble of mass-weighted displacements q_{ik} of all nuclei from their equilibrium positions during the normal vibration ν_i . In the space of normal coordinates,

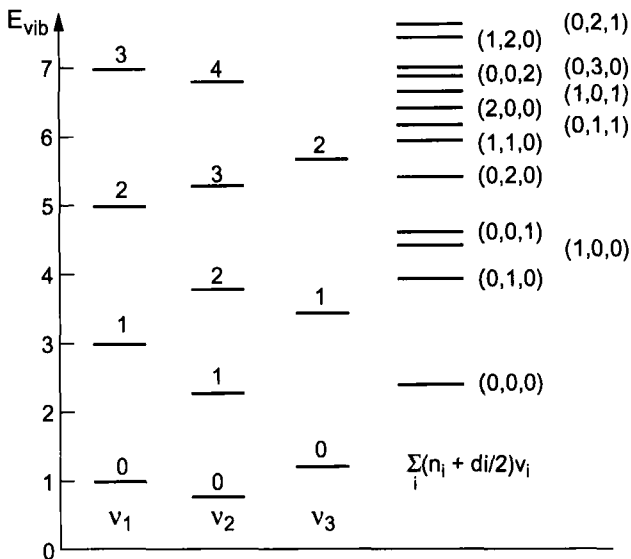


Fig. 6.13 Schematic vibrational term diagram for a triatomic molecule. For the combination modes, the zero-point energies of the combining normal vibrations is taken into account.

each nondegenerate normal vibration of a molecule corresponds to a linear oscillation of a point. In the case of twofold degenerate normal vibrations, this point moves along an ellipse in the subspace spanned by the two normal coordinates belonging to the degenerate vibrations.

Figure 6.13 shows a schematic vibrational term diagram of a triatomic molecule; it illustrates the different possibilities for combining the normal vibrations from Eq. (6.84).

6.3.5

Anharmonic Vibrations

The real potential in which the nuclei oscillate is given by an infinite Taylor expansion

$$\begin{aligned}
 V = V_0 + \sum_{ij} \left(\frac{\partial V}{\partial q_i} \right)_0 q_i + \frac{1}{2} \sum_i \sum_j \left(\frac{\partial^2 V}{\partial q_i \partial q_j} \right)_0 q_i q_j \\
 + \frac{1}{3!} \sum_i \sum_j \sum_k \left(\frac{\partial^3 V}{\partial q_i \partial q_j \partial q_k} \right)_0 q_i q_j q_k + \dots \quad (6.85)
 \end{aligned}$$

The termination of the series after the quadratic term is justified only for small displacements q_i . For larger vibrational amplitudes, as encountered in real molecules for high vibrational excitations, the eigenvalues can be determined using a perturbation calculation, starting from the harmonic potential V (where the first two terms vanish)

and including the higher terms of the Taylor expansion as the perturbation potential V' . Hence, the Hamiltonian becomes

$$\hat{H} = \hat{H}_0 + \hat{H}' \quad \text{with} \quad \hat{H}_0 = \hat{T} + \hat{V} \quad \text{and} \quad \hat{H}' = \hat{V}' .$$

The eigenfunctions ψ_v of the harmonic Hamiltonian in Eq. (6.83) serve as the basis in which the solutions

$$\psi = \sum_k c_k \psi_{v_k} \quad (6.86)$$

of the Schrödinger equation $H\psi = E\psi$ are expanded.

Following the usual procedure in perturbational calculations, we substitute Eq. (6.86) into $H\psi = E\psi$, multiply by $\psi_{v_i}^*$ and integrate. This yields the matrix elements H_{ik} ,

$$H_{ik} = \int \psi_{v_i}^* \hat{H}' \psi_{v_k} \, d\tau , \quad (6.87)$$

of the perturbation operator \hat{H}' computed with the wavefunctions of the harmonic oscillator. The energy eigenvalues E_i of the harmonic oscillator with vibrational quantum numbers (v_1, v_2, v_3) can then be expressed for nondegenerate vibrations as

$$E_i^{\text{anarm}} = E_i^0(v_1, v_2, v_3) + \sum_k \frac{H_{ik}^2}{E_i^0 - E_k^0} , \quad (6.88)$$

where E_i^0 are the *unperturbed* energies in the harmonic approximation. If two vibrational levels are almost degenerate in the harmonic approximation (i.e., $E_i^0 \simeq E_k^0$), the perturbation becomes large and the shifts of the perturbed levels E_i^{anarm} and E_k^{anarm} are particularly large (the two levels *repel each other*). This phenomenon is called *Fermi resonance*; it is discussed in more detail in the general treatment of perturbations in Ch. 9.

As \hat{H}' in Eq. (6.87) is symmetric with respect to all symmetry operations of the molecule, H_{ik} must vanish if ψ_{v_i} and ψ_{v_k} are of different symmetry types. In other words, only vibrational levels of *like symmetry* can interact due to the anharmonicity of the potential.

Hence, the anharmonic potential effects couplings between the different normal vibrations, which means that every normal vibration Q_i influences all other vibrations Q_k of the same symmetry for which $H_{ik} \neq 0$.

The anharmonicity of the potential does not change the symmetry type of a vibrational state $|v\rangle = \sum n_i |v_i\rangle$, because the additional term V' in the potential Eq. (6.85) is totally symmetric, and therefore only harmonic oscillator functions of like symmetry contribute to a normal vibration in the expansion Eq. (6.86). The symmetry of a vibrational state $|v\rangle$ is therefore the same as for the corresponding state for a harmonic potential.

Classically, this phenomenon can be understood as follows. In an anharmonic potential, it is not possible for all nuclei to oscillate at the same frequency along straight lines through their equilibrium positions, because the higher terms in the potential create lateral forces which deflect the trajectories and modify the vibrational frequencies individually for each nucleus. In other words, pure normal vibrations cease to exist.

In the case of anharmonic potentials, the total vibrational energy can not be calculated as a simple sum of energies of the individual normal vibrations, because the couplings change the vibrational energies.

These couplings can be taken into account generically by introducing coupling coefficients x_{ij} into the equation for the term energy,

$$G(v_1, v_2, \dots, v_{3N-6}) = \sum_i \omega_i \left(v_i + \frac{d_i}{2} \right) + \sum_i \sum_j x_{ij} \left(v_i + \frac{d_i}{2} \right) \left(v_j + \frac{d_j}{2} \right) + \text{higher terms} . \quad (6.89)$$

6.3.6

Vibration–Rotation Coupling

In the diatomic case, vibration–rotation interaction could be accounted for by introducing an effective rotational constant B_v [see Eq. (3.33)]. Also, the rotational constants in polyatomic molecules depend on the respective vibrational level, because the nuclear displacements change the moments of inertia. This dependency can be written, in analogy to Eq. (3.44a), as

$$\begin{aligned} A_v &= A_e - \sum_i \alpha_i^A (v_i + d_i/2) ; \\ B_v &= B_e - \sum_i \alpha_i^B (v_i + d_i/2) ; \\ C_v &= C_e - \sum_i \alpha_i^C (v_i + d_i/2) . \end{aligned}$$

In diatomic molecules, the Coriolis force is only for the electron shell of some (minor) relevance, because the nuclear vibration occurs only one-dimensionally along the internuclear axis, and the corresponding Coriolis term in Eq. (6.7) vanishes because of $\Delta \mathbf{r}_i \parallel \mathbf{v}_i$.

In polyatomic molecules with their two- and three-dimensional vibrations, the situation is more complex. Besides the modification of the mean moments of inertia by vibrations (vibration-dependent rotational constants), Coriolis forces mediate a coupling between different normal vibrations in rotating molecules. Furthermore, as we have seen in Sect. 6.3.3, degenerate vibrations can possess an angular momentum $l\hbar$ that interacts with the angular momentum of molecular rotation.

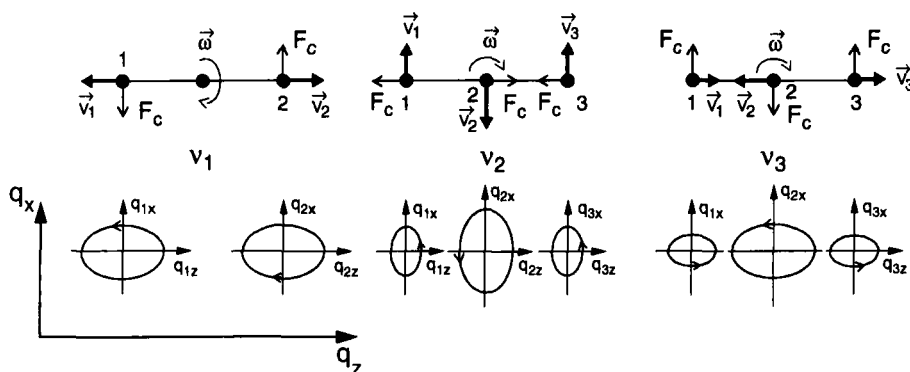


Fig. 6.14 Coriolis coupling between the bending vibration ν_2 and the antisymmetric stretching vibration of a linear triatomic molecule rotating around an axis perpendicular to the plane of the figure.

Such coupling will be treated in this section in an illustrative manner. As we can see from Fig. 6.14, the Coriolis force

$$\mathbf{F}_C = 2m(\boldsymbol{\omega} \times \mathbf{v}) \quad (6.90)$$

for a nucleus oscillating with velocity \mathbf{v} points in a direction perpendicular to \mathbf{v} . It therefore results in a deflection of its otherwise straight trajectory, producing a curved path. Hence, under the influence of the total (restoring plus Coriolis) force, the nuclei do not oscillate through their equilibrium positions in straight lines, as viewed in the rotating reference frame of the molecule, even for small-amplitude normal vibrations, but they move along elliptic paths around their equilibrium positions $q = 0$. Figure 6.14 illustrates the displacements q_x and q_z of the nuclei from their equilibrium positions during one vibrational period for a linear molecule. For nuclei oscillating along z , the Coriolis force results in a displacement along x , and for nuclei with a velocity component v_x , it creates a corresponding displacement along z . This establishes a coupling between different normal vibrations, as can easily be seen.

For example, due to the Coriolis force, the bending vibration ν_2 is excited during the antisymmetric vibration ν_3 and vice versa. In other words, in a rotating molecule, ν_2 and ν_3 are mutually coupled by the Coriolis force, whereas the symmetric vibration ν_1 shows no Coriolis coupling but produces only a (small) change of the rotational constant as in the diatomic case, where we have accounted for this effect by introducing an effective rotational constant Eq. (3.33). Which normal vibrations are coupled by the Coriolis force depends on their symmetry. In contrast to the pure vibrational coupling in the nonrotating molecule, the Coriolis force results in a coupling between vibrational levels of different symmetry (see Ch. 8).

As the rotational constants for the vibrational state (ν_1, ν_2, ν_3) are determined by the expectation value of the moment of inertia formed with the vibrational wavefunctions, the rotational constants depend – exactly as for diatomic molecules – on the vibrational state. Furthermore, they are influenced by Coriolis coupling.

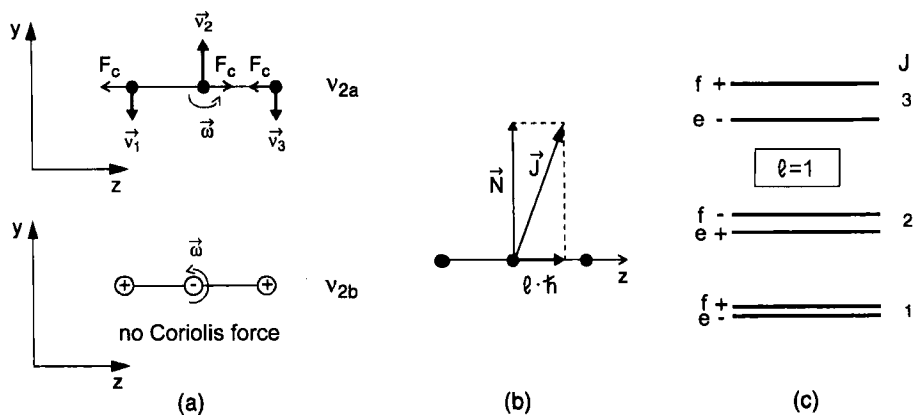


Fig. 6.15 a) Different influences of the Coriolis forces in a rotating molecule on two bending vibrations that are degenerate in the nonrotating molecule. b) Addition of the angular momenta N of molecular rotation and $l\hbar$ of vibration to the total angular momentum J .

c) Removal of the l degeneracy of a bending vibration in a linear triatomic molecule by a rotation of the molecule around an axis perpendicular to the z axis, shown for the vibrational angular momentum quantum number $l = 1$ [4.5].

Vibrational states that are degenerate in the nonrotating molecule need special attention. As illustrated in Fig. 6.15a for the bending vibrations of a linear molecule, such degenerate states split into two levels. The two vibrations, which are degenerate in the absence of rotation, can occur either in the yz plane (top) or in the xz plane (bottom), while the molecule is rotating around the x axis. Now we have to consider two effects:

1. The mean moment of inertia with respect to the rotational axis is slightly smaller for the vibration shown at the top than for the rotation at the bottom. Hence, the rotational energy must also be different.
2. In case (a), there exist Coriolis forces coupling to the antisymmetric stretching vibration, whereas in (b) there are *no* Coriolis forces, because the nuclear displacements are along the rotational axis.

Therefore, the two levels split. In general, however, the energy of the antisymmetric stretching vibration is much larger than that of the bending vibration, and the two interacting levels are far apart. Hence, the coupling is weak, and the splitting is small. There exists, however, a much larger effect: if the two bending vibrations are superimposed with a phase shift, the nuclei exert elliptic motions around the internuclear axis of the linear molecule (Fig. 6.14), and a vibrational angular momentum l along z arises (Sect. 6.3.3), which adds to the rotational angular momentum N perpendicular to the z axis. The resulting total angular momentum J is then no longer perpendicular to the z axis (Fig. 6.15b).

For a linear molecule, the vibrational angular momentum is (except for the contribution from the electron shell) the only contribution to the component of the total angular momentum along the molecular axis. The total angular momentum J is then no longer perpendicular to the internuclear axis. For a given molecular total angular momentum of J , the contribution available for rotational energy of a rotation around an axis perpendicular to the molecular axis is therefore only $B_v [J(J+1) - l^2]$.

If we want to take this vibrational angular momentum into account for the rotation of a vibrating molecule, we must modify the rotational terms in Eq. (3.18b) to give, for a Σ state with $\Lambda = 0$,

$$F(J) = B_v [J(J+1) - l^2] - D_v [J(J+1) - l^2]^2, \quad (6.91)$$

where $J = |l|, |l| + 1, |l| + 2, \dots$ is the total angular momentum quantum number. A rotating linear molecule in a bending vibrational state with vibrational angular momentum $l\hbar$ can therefore possess no rotational levels with $J < |l|$.

According to Eq. (6.91), the term value of a rotation–vibration level depends on l^2 and is therefore independent of the direction of l . Here, Coriolis coupling is not yet included, however. If we introduce it, coupling terms appear in Eq. (6.91), and we obtain, after lengthy calculations,

$$F_{v_i}^{\pm}(J, l^{\pm}) = B_v [J(J+1) - l^2] - D_v [J(J+1) - l^2]^2 \pm \frac{q_i}{4} (v_i + 1) J(J+1), \quad (6.92)$$

where the parameter q_i depends on the strength of the Coriolis-induced coupling between the vibrational states. It decreases with increasing values of l , so that the l splitting of levels with the same $|l|$ caused by the interaction,

$$\Delta F = F^+ - F^- = (q_i/2)(v_i + 1)J(J+1),$$

is significant only for $|l| = 1$, and is usually negligible for $l > 1$.

For example, for a symmetric linear molecule AB_2 we obtain for the bending vibration with $l = 1$,

$$q_{v_2}(l = 1) = \frac{B_c^2}{\omega_e} \left(1 + \frac{\xi_{23} 4\omega_2^2}{\omega_3^2 - \omega_2^2} \right), \quad (6.93)$$

where ω_2 is the frequency of the bending vibration and ω_3 that of the antisymmetric stretching vibration, which couples to the bending vibration (described by the parameter ξ_{23}) through a Coriolis interaction [6.10].

Hence, we obtain for the term values T of a vibration–rotation level,

$$T(v_1, v_2, v_3, J, l) = G(v_1, v_2, v_3) + F_v(J, l), \quad (6.94)$$

where the vibrational term value

$$G(v_1, v_2, v_3) = \sum_i \omega_i (v_i + d_i/2) + \sum_{i,k} x_{ik} (v_i + d_i/2) (v_k + d_k/2) \quad (6.95)$$

is the same as for a nonrotating molecule, whereas in the rotational term value

$$F_v^\pm(J, v) = B_v (J(J+1) - l^2) - D_v [J(J+1) - l^2]^2 \pm \frac{q_v}{4} (v+1)J(J+1), \quad (6.96)$$

the effective rotational constant B_v contains the dependency of the moment of inertia on the vibrational quantum number and thus describes one part of the vibration-rotation coupling. The second term accounts for centrifugal distortion, and the third term describes the influence of the Coriolis interaction on l splitting. The two l components of a rotational level possess opposite parity. In analogy to A doubling, they are denoted by e and f (Fig. 6.15c). A more detailed presentation of these topics can be found in [6.11].

7

Electronic States of Polyatomic Molecules

Whereas the electronic energies of diatomic molecules could be described, within the Born–Oppenheimer approximation, by potential curves $E_{\text{pot}}(R)$ depending only on the internuclear distance R , the corresponding functions for polyatomic molecules are potential surfaces in N -dimensional space. For example, the potential surfaces $E(R_1, R_2, \alpha)$ of triatomic molecules depend on three parameters (two internuclear distances R_i and an angle α).

7.1

Molecular Orbitals

As for diatomic molecules, the wavefunctions of the electronic states are needed to determine $E_{\text{pot}}(R_1, R_2, \dots, \alpha_1, \alpha_2, \dots)$ from the corresponding Schrödinger equation. As discussed in Sect. 2.8, approximate wavefunctions Ψ can be constructed as linear combinations of basis functions ϕ_i (e.g., Gaussian functions or atomic orbitals),

$$\Psi = \sum_i^n c_i \phi_i, \quad (7.1)$$

where the coefficients c_i are optimized using the variational principle so that the expectation value of the energy is minimized. The functions Ψ are called *molecular orbitals*. From n basis functions, n different mutually orthogonal molecular orbitals can be constructed.

We saw in Sect. 2.8 that only basis functions belonging to the same symmetry species contribute to the linear combination.

In the language of group theory (see Ch. 5), this means that only those molecular orbitals Ψ are allowed that constitute a basis of an irreducible representation of the molecular point group.

If atomic orbitals (or, for that matter, any type of atom-centered basis functions) are used as basis functions ϕ_i , we must take into account that each atomic orbital is centered at *its own* atomic nucleus. The molecular orbitals formed from such ba-

sis functions are therefore called *multi-centered*. To describe the linear combination Eq. (7.1) in a common reference frame, we must therefore apply a suitable coordinate transformation.

If we compute the wavefunction Ψ_k of an electronic state $|k\rangle$ for many possible arrangements of the N nuclei, the real (i.e., “correct”) molecular structure is that corresponding to the lowest energy, that is,

$$\frac{\partial E_k^{\text{pot}}}{\partial \mathbf{R}_i} = 0, \quad i = 1, 2, \dots, N. \quad (7.2)$$

The computation of energy surfaces becomes more accurate if we include more symmetry-adapted basis functions. However, this makes the computations more time-consuming [7.1].

There are simpler schemes, which employ only a few basis functions but which try to select them according to their importance for chemical bonding, thereby restricting them to the valence electrons of the atoms involved in bonding.

Although this *valence bond method* yields more qualitative than exact quantitative results because of the small basis set employed, it provides a clear insight into the origin and the character of chemical bonding [7.2]. It is particularly valuable because it gives in many cases simple explanations for the actual molecular geometry. It also allows an estimation of the energetic ordering of the different molecular orbitals built from atomic valence orbitals.

A simple rule of thumb is that the lower the number of radial nodal planes of a wavefunction Ψ , the lower the energy of the corresponding state. The physical explanation for this rule is based on two facts:

1. The lower the number of nodes, the smaller is the second derivative $\partial^2 \psi / \partial r^2$, which in turn is proportional to the kinetic energy.
2. With decreasing number of nodes, $|\psi|^2$ and therefore the electron density between the nuclei increases, giving a larger bond energy.

The symmetry classification of the molecular orbitals depends on the molecular point group and the transformation properties of the orbitals under the symmetry operations of the group. In linear molecules of point group $D_{\infty h}$, the orbitals have *even* parity if the wavefunction is unchanged upon inversion at the center of charge, and they have *odd* parity if they change sign (see also the corresponding discussion in Sect. 2.4.2).

The symmetry of the orbitals with respect to reflection at a plane containing the molecular axis is denoted *positive* (+) if the orbital remains unchanged and *negative* (−) if it changes sign.

For nonlinear molecules, the symmetry operations of the respective point group must be considered. For example, the orbitals of molecules belonging to the group C_{2v} can have the symmetries A_1 , A_2 , B_1 , or B_2 , depending on their behavior under the different symmetry operations of the group. For point groups containing a symmetry axis

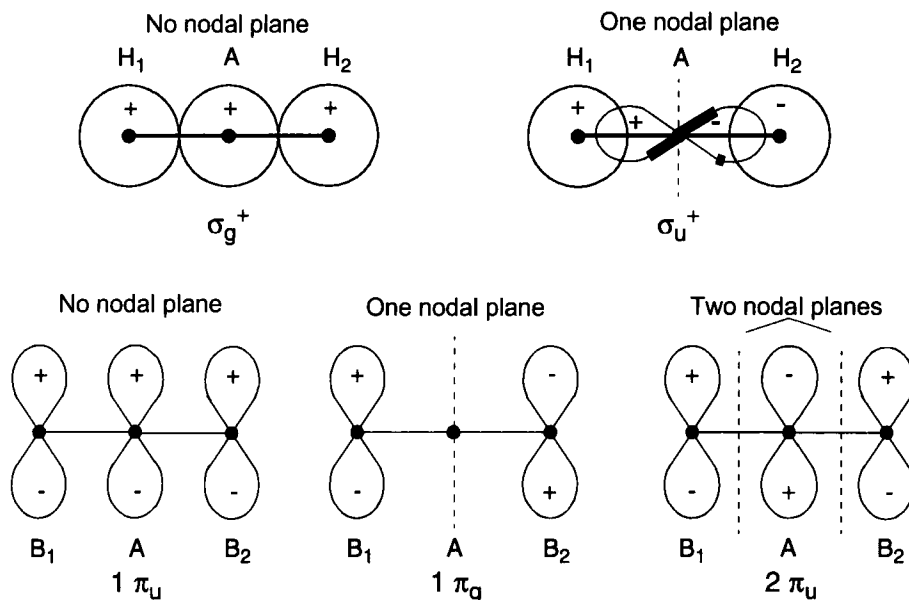


Fig. 7.1 Examples of molecular orbitals. *Top*: σ orbitals of linear AH_2 molecules; *bottom*: π orbitals of linear AB_2 molecules.

C_n with $n > 2$, degenerate orbitals of symmetry type E (or even higher-dimensional irreducible representations) occur, which are transformed into linear combinations of themselves under the symmetry operations of the group (see the character tables in the appendix).

Figure 7.1 illustrates some molecular orbitals schematically. The top row displays the lowest-energy orbitals for linear triatomic molecules AH_2 (where A is an arbitrary atom) resulting from the combinations $\sigma_g^+ = 1s(H_1) + 1s(H_2) + ns(A)$ (no nodal plane) and $\sigma_u^+ = 1s(H_1) - 1s(H_2) + np_z(A)$ (one nodal plane).

At the bottom of Fig. 7.1, some molecular π orbitals for linear AB_2 molecules are displayed. The combination $1\pi_u = p_x(B_1) + p_x(A) + p_x(B_2)$ has no nodal plane between the nuclei and corresponds to the lowest of the three π states. The molecular orbital $1\pi_g = p_x(B_1) - p_x(B_2)$ has one internuclear nodal plane at the position of atom A , whereas the combination $2\pi_u = p_x(B_1) - p_x(A) + p_x(B_2)$ possesses two internuclear nodal planes and thus corresponds to the highest energy of the three π orbitals.

Figure 7.2 shows some molecular orbitals of nonlinear molecules. The top row displays nondegenerate orbitals of molecules belonging to group C_{2v} together with their symmetry designations; the bottom row shows orbitals of molecules belonging to group D_{3h} .

These general principles will now be elucidated for a number of specific examples. Before doing so, however, we will briefly discuss the concept of *hybridization*.

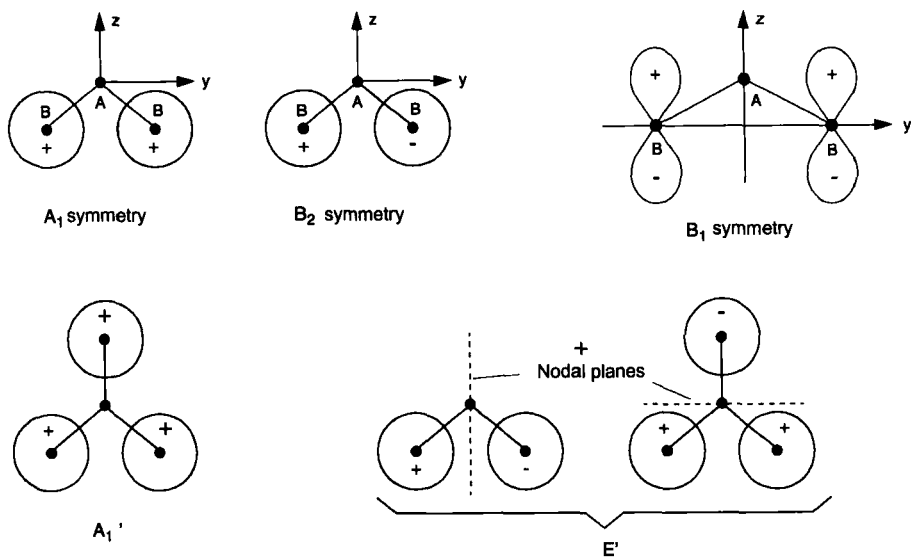


Fig. 7.2 Top: Orbitals of molecules belonging to the group C_{2v} ; bottom: nondegenerate A_1' orbital and degenerate E' orbital of molecules belonging to the group D_{3h} .

7.2

Hybridization

The electron clouds of two atoms involved in bonding are deformed by their interaction. For example, $1s$ orbitals do not remain spherically symmetric. This effect can approximately be taken into account if we construct the corresponding molecular orbitals as linear combinations of s , p , d , ... atomic orbitals. Such functions are also called hybrid functions. If only s and p orbitals are included, the result is called sp hybridization.

This process will be illustrated for the case of the carbon atom (Fig. 7.3). The ground-state carbon atom has an electron configuration $(1s^2)(2s^2)(2p_x)(2p_y)$ with two unpaired electrons in the p_x and p_y orbitals, respectively. As only unpaired electrons can contribute to bonding, this configuration leads to two bonds directed along x and y . If, for example, two hydrogen atoms would bond to the carbon atom, their $1s$ orbitals would experience maximum overlap in the x and y directions, and the resulting bond angle would be 90° .

It may be energetically favorable, however, to include also one of the $2s$ electrons in bonding, in addition to the two $2p$ electrons. This will be true if the energy needed to promote the $2s$ electron to the $2p$ orbital is over-compensated by the gain in bonding energy, and this situation is indeed found in many compounds.

As each of the two p_x and p_y orbitals is already occupied by one electron, only the p_z function is available for hybridization.

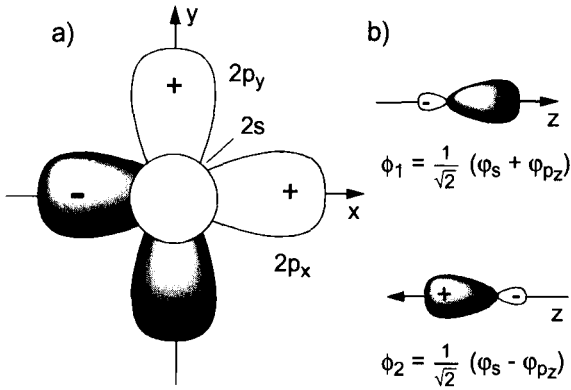


Fig. 7.3 a) Atomic orbitals of the free carbon atom with the directions of the unpaired electrons in the p_x and p_y orbitals. b) The two sp_z hybrid orbitals.

The two possible, mutually orthogonal sp_z hybrid atomic orbitals are then

$$\phi_1(s, p_z) = c_1\phi(s) + c_2\phi(p_z), \quad (7.3)$$

$$\phi_2(s, p_z) = c_3\phi(s) + c_4\phi(p_z).$$

From the normalization condition

$$\int |\phi_i|^2 d\tau = 1; \quad \int \phi_1\phi_2 d\tau = 0, \quad (7.4)$$

we obtain the coefficients by substituting Eq. (7.3) into Eq. (7.4),

$$c_1 = c_2 = c_3 = \frac{1}{\sqrt{2}}; \quad c_4 = -\frac{1}{\sqrt{2}},$$

so that the two hybrid atomic orbitals are

$$\phi_1 = \frac{1}{\sqrt{2}} [\phi(s) + \phi(p_z)], \quad (7.5)$$

$$\phi_2 = \frac{1}{\sqrt{2}} [\phi(s) - \phi(p_z)].$$

If we substitute atomic hydrogen wavefunctions [7.3] for $\phi(s)$ and $\phi(p_z)$, we see that the normalized angular part of the hybrid orbitals is

$$\phi_{1,2}(\vartheta) = \frac{1}{2\sqrt{2\pi}} [1 \pm \sqrt{3} \cos \vartheta], \quad (7.6)$$

where ϑ is the angle towards the z axis. This shows that $|\phi_1|^2$ assumes its maximum value for $\vartheta = 0^\circ$, and $|\phi_2|^2$ for $\vartheta = 180^\circ$ (Fig. 7.3b).

Hence, by the sp hybridization, the carbon atom receives two additional bonds in the $\pm z$ direction, which are described by the hybrid orbitals Eq. (7.5). Together with the p_x and p_y orbitals this yields a total of four available bonds.

In some cases, it is energetically more favorable if the s electron and the two p electrons assume a charge distribution described by a linear combination of an s orbital and two p orbitals. During such an sp^2 hybridization, three atomic hybrid orbitals are created from different linear combinations of $\phi(s)$, $\phi(p_x)$ and $\phi(p_y)$. As in the case of sp hybridization, the three mutually orthogonal hybrid orbitals

$$\begin{aligned}\phi_1(sp^2) &= \frac{1}{\sqrt{3}}\phi(s) + \sqrt{\frac{2}{3}}\phi(p_x), \\ \phi_2(sp^2) &= \frac{1}{\sqrt{3}}\phi(s) - \frac{1}{\sqrt{6}}\phi(p_x) + \frac{1}{\sqrt{2}}\phi(p_y), \\ \phi_3(sp^2) &= \frac{1}{\sqrt{3}}\phi(s) - \frac{1}{\sqrt{6}}\phi(p_x) - \frac{1}{\sqrt{2}}\phi(p_y)\end{aligned}\quad (7.7)$$

are obtained. Their angular parts are

$$\begin{aligned}\phi_1(\varphi) &= \frac{1}{2\sqrt{\pi}} \left(\frac{1}{\sqrt{3}} + \sqrt{2} \cos \varphi \right), \\ \phi_2(\varphi) &= \frac{1}{2\sqrt{\pi}} \left(\frac{1}{\sqrt{3}} - \frac{1}{\sqrt{2}} \cos \varphi + \sqrt{\frac{3}{2}} \sin \varphi \right), \\ \phi_3(\varphi) &= \frac{1}{2\sqrt{\pi}} \left(\frac{1}{\sqrt{3}} - \frac{1}{\sqrt{2}} \cos \varphi - \sqrt{\frac{3}{2}} \sin \varphi \right),\end{aligned}\quad (7.8)$$

where φ is the angle towards the x axis (Fig. 7.4). By substituting into Eq. (7.8), we find that the three functions assume their maximum values at $\varphi = 0^\circ$ (ϕ_1), $\varphi = 120^\circ$ (ϕ_2) and $\varphi = 240^\circ$ or -120° (ϕ_3).

Hence, sp^2 hybrid atomic orbitals allow for three identical bonds, which are directed from the center towards the corners of a planar equilateral triangle.

In some cases, such as the methane molecule CH_4 , which has the shape of a regular tetrahedron, the atomic orbitals of the carbon atom are best described by sp^3 hybrid

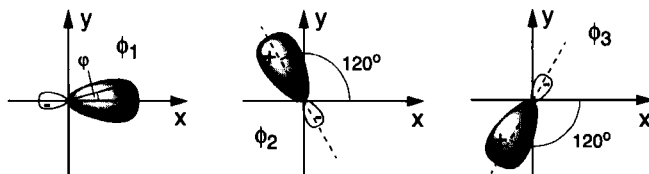


Fig. 7.4 sp^2 hybridization.

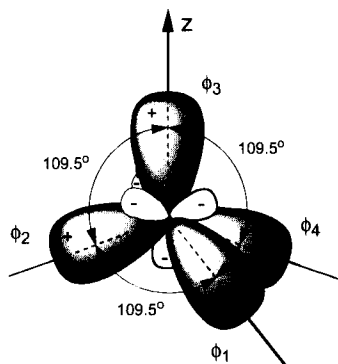


Fig. 7.5 sp^3 hybrid orbitals and their spatial orientation.

functions, which means that the s orbital combines with all three p orbitals. The orthonormal hybrid functions are then

$$\begin{aligned}
 \phi_1 &= \frac{1}{2}\phi(s) + \frac{\sqrt{3}}{2}\phi(p_z), \\
 \phi_2 &= \frac{1}{2}\phi(s) + \sqrt{\frac{2}{3}}\phi(p_x) - \frac{1}{2\sqrt{3}}\phi(p_z), \\
 \phi_3 &= \frac{1}{2}\phi(s) - \frac{1}{\sqrt{6}}\phi(p_x) + \frac{1}{\sqrt{2}}\phi(p_y) - \frac{1}{2\sqrt{3}}\phi(p_z), \\
 \phi_4 &= \frac{1}{2}\phi(s) - \frac{1}{\sqrt{6}}\phi(p_x) - \frac{1}{\sqrt{2}}\phi(p_y) - \frac{1}{2\sqrt{3}}\phi(p_z).
 \end{aligned}
 \tag{7.9}$$

If we substitute the angular parts of these functions into Eq. (7.9), sp^3 hybridization yields the atomic orbitals displayed in Fig. 7.5, which are directed towards the corners of a regular tetrahedron with the carbon atom at its center.

In addition to p orbitals, d orbitals can also contribute to hybridization in heavy atoms. This gives again directed bonds leading to specific molecular geometries. For example, sp^2d hybridization leads to four hybrid orbitals which are located in a plane and enclose angles of 90° . An atom with valence orbitals described by sp^2d hybrid orbitals can therefore form a molecule with square planar geometry with four equal other atoms. Table 7.1 summarizes some examples of atomic hybrid orbitals.

Tab. 7.1 Hybrid orbitals.

Orbital	Geometrical arrangement	Coordination number
sp, dp	linear	2
p^2, sd	bent	2
sp^2, s^2d	trigonal planar (120°)	3
p^3	trigonal pyramidal	3
sp^3	tetrahedral	4
sp^3d	trigonal bipyramidal	5
sp^3d^2	octahedral	6

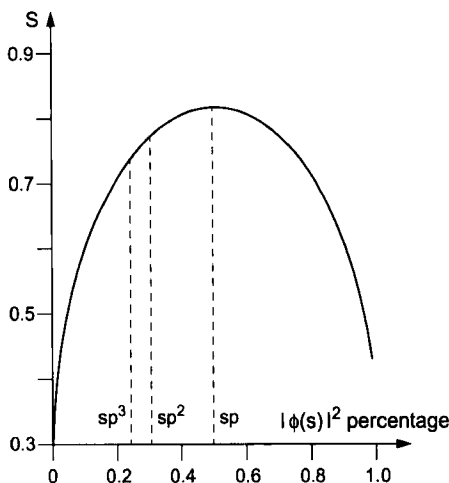


Fig. 7.6 Overlap integral between two hybrid atomic orbitals as a function of the s orbital contribution for a C–C bond at an internuclear distance $R = 4a_0/3$ [7.4].

The reason for the choice of hybrid orbitals is the minimization of the total energy through maximization of the (negative) bonding energy. The latter depends on the value of the overlap integral S between the atomic orbitals involved in bonding.

To maximize S for sp hybridization we use, instead of Eq. (7.5), the more flexible trial function

$$\phi = \frac{1}{\sqrt{1+\lambda^2}} [\phi(s) + \lambda\phi(p)] , \quad (7.10)$$

where λ is an optimization parameter in the range between 0 and 1.

Figure 7.6 shows the overlap integral S between the two atomic hybrid orbitals of a C–C bond as a function of the s contribution

$$\frac{|S(\phi(s))|^2 dt}{|S(\phi)^2| dt} = \frac{1}{1+\lambda^2} .$$

We see that the overlap is largest for sp hybrid orbitals with 50% s contribution. The value of S increases from $S = 0.3$ without hybridization to $S = 0.85$ for the optimum sp hybridization. Hence, the energy necessary for the promotion of the two s electrons to the hybrid orbitals is by far compensated for by the gain in bonding energy, which leads to a lower total energy.

Upon formation of a molecule, the atomic electron clouds are deformed (i.e., rearranged) so that the maximum overlap for all bonds and a minimum total energy is achieved. This requirement determines the ground-state molecular geometry.

All ground-state molecules assume the geometry which minimizes their total energy, that is, the ground-state geometry corresponds to the global minimum of the potential energy surface.

7.3

Triatomic Molecules

Many of the principal aspects involved in the formation of optimum molecular orbitals are already evident in triatomic molecules. The potential energy surface of a nonlinear molecule ABC depends on the three parameters R_1 (AB), R_2 (BC) and $\alpha = \angle ABC$. In linear triatomic molecules, which belong to the same point groups $C_{\infty h}$ or $D_{\infty h}$ as the diatomic molecules, $E(R_1, R_2)$ depends on the two internuclear distances. Their potential surface shows a potential energy valley for $\alpha = 180^\circ$.

The construction of molecular orbitals will now be illustrated for some molecules.

7.3.1

The BeH₂ Molecule

The beryllium dihydride molecule BeH₂ is linear; it belongs to group $D_{\infty h}$. The electron configuration of Be is $1s^2 2s^2$, and there are in addition three unoccupied 2p orbitals, which are only slightly higher in energy than the 2s orbitals. The 1s electrons are located close to the beryllium nucleus and do not significantly contribute to the bonding with the hydrogen atoms.

We choose the z axis as the internuclear axis; the $2p_x$ and $2p_y$ orbitals are then orthogonal to the two hydrogen 1s orbitals (Fig. 7.7) and do not contribute to bonding (the overlap integral is zero!).

From the remaining four atomic orbitals (two 1s orbitals from the two hydrogen atoms and 2s and $2p_z$ of the beryllium atom) we can construct four molecular orbitals as linear combinations,

$$\psi_1(\sigma_1) = c_1\phi_1(\text{H}_{1s}) + c_2\phi_2(\text{Be}_{2s}) + c_3\phi_3(\text{H}_{1s}).$$

For symmetry reasons, $c_1 = c_3$, which we normalize to be 1. The orbital ψ_1 is then, in a self-explaining shorthand notation,

$$\Psi_1 = s_1 + \lambda_1 s + s_2, \quad \oplus \quad \oplus \quad \oplus \quad (7.11)$$

where $\lambda_1 s$ is the relative contribution of the beryllium 2s orbital. This molecular orbital has σ symmetry.

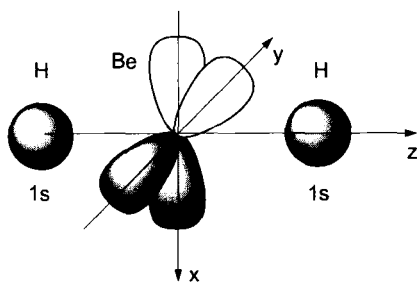


Fig. 7.7 Nonbonding molecular orbitals in the BeH₂ molecule.

The next higher molecular orbital possesses a nodal plane at the beryllium atom, and is written

$$\Psi_2 = s_1 + \lambda_2 p_z - s_2 \quad \oplus \quad \oplus \quad \begin{array}{c} \vdots \\ \text{nodal plane} \\ \vdots \end{array} \quad \ominus \quad \ominus \quad (7.12)$$

Ψ_2 is also a σ orbital.

The third molecular orbital has two nodal planes and is written

$$\Psi_3 = s_1 - \lambda_3 s + s_2 . \quad \oplus \quad \begin{array}{c} \vdots \\ \vdots \end{array} \quad \ominus \quad \begin{array}{c} \vdots \\ \vdots \end{array} \quad \oplus \quad (7.13)$$

Calculation of the corresponding energies shows that Ψ_3 is antibonding, that is, the energy $\langle \psi_3 | \hat{H} | \psi_3 \rangle$ is higher than the energies of the atomic orbitals from which it is built. It is actually even higher than that of the π atomic orbitals constructed from the p_x and p_y of the beryllium atom and the $1s$ atomic orbitals of the hydrogen atoms.

Finally, the molecular orbital with the highest energy has three nodal planes,

$$\Psi_4 = -s_1 + \lambda_4 p_z + s_2 . \quad \ominus \quad \begin{array}{c} \vdots \\ \vdots \end{array} \quad \oplus \quad \begin{array}{c} \vdots \\ \vdots \end{array} \quad \ominus \quad \begin{array}{c} \vdots \\ \vdots \end{array} \quad \oplus \quad (7.14)$$

As each molecular orbital can be occupied by two electrons (with opposite spins), the four valence electrons from beryllium and hydrogen fill the orbitals $\Psi_1(\sigma_1)$ and $\Psi_2(\sigma_2)$, creating two bonds in the H–Be–H molecule. The two Be $1s$ core electrons are not included (note that we also did not include their orbitals!).

Figure 7.8 shows the corresponding energy diagram, and Fig. 7.9 illustrates the spatial electron density distribution in the ground-state BeH_2 molecule by the density of printed dots.

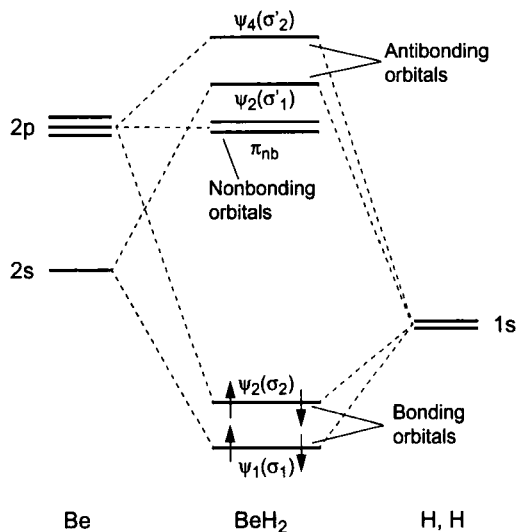


Fig. 7.8 Orbital energies of the BeH_2 molecule as compared with the atomic energies.

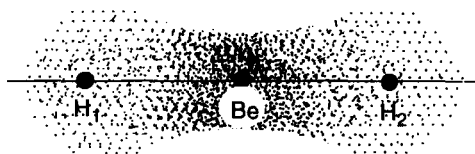


Fig. 7.9 Electron density distribution in the electronic ${}^1\Sigma_g$ ground state of the BeH_2 molecule.

7.3.2

The H_2O Molecule

In the following, the H_2O molecule will be discussed in some detail as an example for general bent AH_2 molecules ($A =$ arbitrary atom). It is also useful to demonstrate the symmetry properties of atomic and molecular orbitals. The bent molecules AH_2 belong to the point group C_{2v} , which contains the symmetry species A_1 , A_2 , B_1 , and B_2 (see Sect. 5.5).

For the construction of molecular orbitals, two $1s$ orbitals from the hydrogen atoms and the four occupied $2s$ and $2p$ orbitals of the oxygen atom (with configuration $1s^2 2s^2 2p^4$) are available. We place the molecule in the xy plane; the $2p_z$ atomic orbital has therefore zero overlap with the hydrogen $1s$ orbitals (Fig. 7.10).

In a first approximation, we neglect the contribution from the oxygen $2s$ electrons. Thus, we consider only the oxygen $2p_x$ and $2p_y$ orbitals, which overlap with the hydrogen $1s$ orbitals, leading to chemical bonding.

In this approximation, we obtain for the two molecular orbitals

$$\begin{aligned}\Psi_1 &= \phi(1s) + \lambda\phi(2p_x), \\ \Psi_2 &= \phi(1s) + \lambda\phi(2p_y),\end{aligned}\tag{7.15}$$

which assume their maximum values along x and y , respectively. Therefore, we are led to expect a bent structure with a bond angle of $\alpha = 90^\circ$ for the H_2O molecule. The experimental value is $\alpha = 105^\circ$. This small, yet significant difference has two reasons:

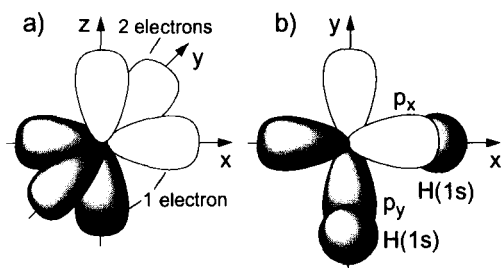


Fig. 7.10 a) The three $2p$ orbitals of the oxygen atom. b) Bonding between the hydrogen $1s$ orbitals and the oxygen $2p_x$, $2p_y$ orbitals.

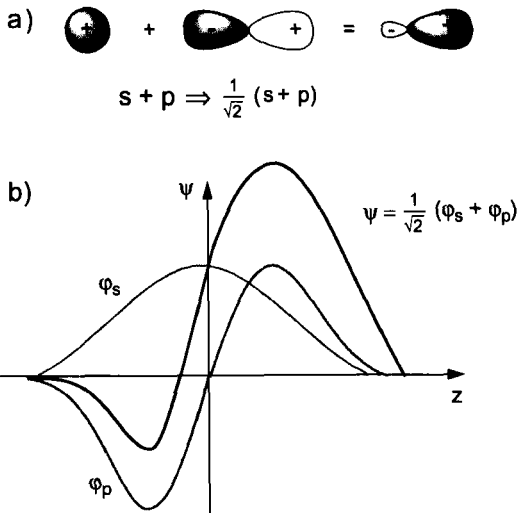


Fig. 7.11 a) Oxygen hybrid orbitals. b) Shift of the charge distribution of the hybrid orbital with respect to the $2s$ orbital.

1. The interaction between the hydrogen and oxygen atoms leads to a charge transfer from the hydrogen atoms to the oxygen atom, creating a small negative charge on the oxygen atom and small positive charges on the hydrogen atoms, as reflected by the molecular dipole moment of the H_2O molecule. In consequence, there arises a Coulomb repulsion between the hydrogen atoms. However, this effect leads only to a small increase in the angle α .
2. The major effect is hybridization of the oxygen atom. The charge transfer mentioned above leads to a deformation of the electron cloud at the oxygen atoms, distorting the $2s$ orbital, which can now be written as a linear combination

$$\phi = c_1\phi(2s) + c_2\phi(2p) . \quad (7.16)$$

This distortion of the electron cloud leads to a shift of the center of charge (Fig. 7.11) and thus to a larger overlap of the oxygen hybrid orbital with the $1s$ orbitals of the hydrogen atoms.

The bonds constructed from those hybrid orbitals do not form a 90° angle, but give indeed, upon exact calculation of all polarization and exchange effects (which have been included here only approximately), the experimentally determined bond angle (Fig. 7.12).

It is common in molecular physics to denote the symmetry species of orbitals by lower-case letters and those of the molecular states constructed from them by upper-case letters. For example, the electron configuration of the ground-state H_2O molecule is $(2a_1)^2 (1b_2)^2 (3a_1)^2 (1b_1)^2$. The molecular ground state derived from it is denoted X^1A_1 .

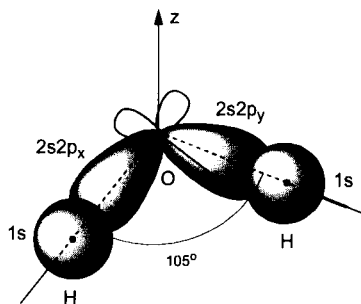


Fig. 7.12 Bonding in the H_2O molecule using hybrid atomic orbitals.

We will now determine the symmetry properties of the atomic orbitals, from which the molecular orbitals of H_2O are constructed. To do this, we choose a coordinate system (x', y', z') adapted to the C_{2v} molecular symmetry by placing the molecular symmetry axis along x' and the plane of the molecule into the $x'y'$ plane (Fig. 7.13). The p orbitals are therefore transformed according to

$$p_{x'} = \frac{1}{\sqrt{2}}(p_x + p_y); \quad p_{y'} = \frac{1}{\sqrt{2}}(p_x - p_y).$$

From Fig. 7.14 we see that $2s$ and $2p_{x'}$ transform into themselves and thus belong to symmetry species a_1 , whereas $2p_{y'}$ changes sign upon rotation around the x' axis and thus has b_2 symmetry, whereas $2p_z$ changes sign upon reflection at the plane of the molecule and therefore has b_1 symmetry.

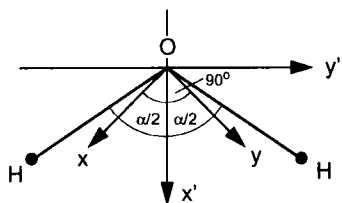


Fig. 7.13 Geometrical arrangement for the discussion of symmetry properties of atomic and molecular orbitals.

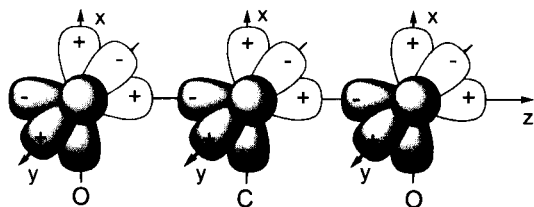


Fig. 7.14 The twelve atomic orbitals in the CO_2 molecule.

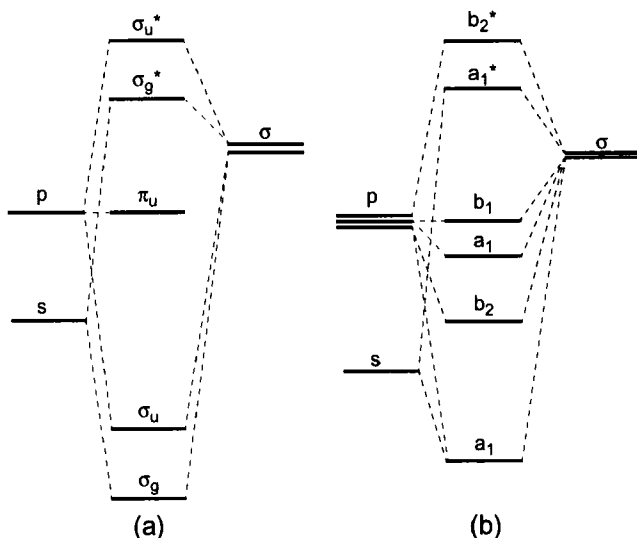


Fig. 7.15 Energy level diagram of the molecular orbitals in AH₂ molecules for a) linear and b) nonlinear structures.

To construct molecular orbitals with a_1 symmetry, we can therefore combine the oxygen hybrid orbital $c_1\varphi(2s) + c_2\varphi(2p_x)$ with the sum $\varphi_+(1s) = \varphi_1(1s) + \varphi_2(1s)$ of the two hydrogen 1s orbitals to form the linear combination $c_1\varphi(2s) + c_2\varphi(2p_x) + c_3\varphi_+(1s)$, because these orbitals all have a_1 symmetry and therefore their sum must also have a_1 symmetry.

sp^3 hybridization makes $2p_y$ and $2p_z$ also bonding molecular orbitals with b_1 and b_2 symmetry, respectively (Fig. 7.15b). As there are a total of eight valence electrons involved in bonding (the 1s core electrons of the oxygen atom contribute virtually nothing and are neglected), the four lowest molecular orbitals are occupied by two electrons each (with antiparallel spins). This yields three bonding molecular orbitals with symmetries a_1 , b_2 , and a_1 , and one weakly antibonding orbital with symmetry b_1 that are occupied in the ground state of H₂O.

7.3.3

The CO₂ Molecule

In this example, we can build molecular orbitals from twelve valence orbitals of the participating atoms, namely the 2s, 2p_x, 2p_y, and 2p_z atomic orbitals of each of the three atoms (Fig. 7.14). From these twelve atomic orbitals, twelve orthogonal molecular orbitals can be constructed as linear combinations of atomic orbitals of like symmetry. These molecular orbitals are ordered according to their energies, and are then filled successively, according to the Pauli principle, with two electrons each. As there are only 16 valence electrons in CO₂, (four from the carbon atom and six from each

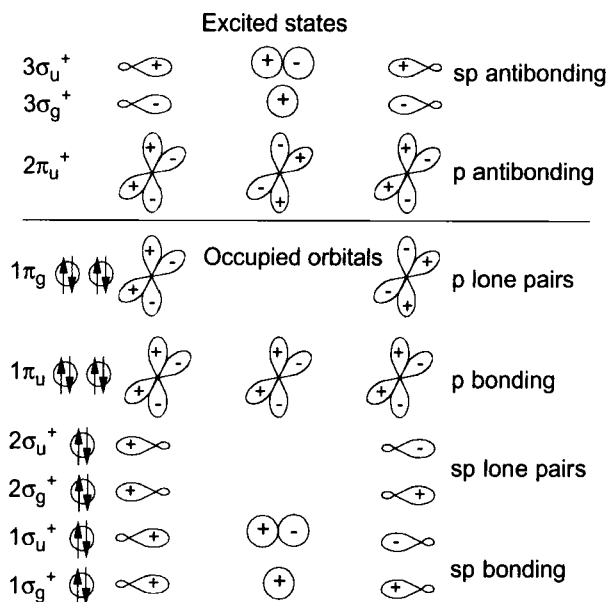


Fig. 7.16 Schematic representation of the molecular orbitals of CO_2 .

oxygen atom), only the eight lowest molecular orbitals are occupied in the ground state of the CO_2 molecule. Excited states arise if one electron is excited from an occupied (in the ground state) orbital into a higher, unoccupied molecular orbital. The highest occupied molecular orbital is often abbreviated HOMO, the lowest unoccupied molecular LUMO.

The symmetry group of CO_2 is $D_{\infty h}$. The only atomic orbitals of σ_g^+ symmetry are the three $2s$ orbitals of the carbon atom and the two oxygen atoms and the two $2p_z$ orbitals of the oxygen atoms.

As discussed in Sect. 7.2, the overlap between the atomic orbitals of the different atoms involved in bonding can be optimized (i.e., maximized) by the formation of hybrid atomic orbitals. As can be seen from Figs. 7.11a and 7.14, sp hybridization provides the largest overlap and therefore the largest contribution to bonding, and thus we expect a linear structure. For such a linear molecule we place, following the usual conventions, the internuclear axis along z . The symmetry species are ordered according to the projections Λ of the electronic angular momentum onto the molecular axis (z axis) and according to their parity (see Sect. 2.4). Then hybrid atomic orbitals are constructed from $2s$ and $2p_z$, which both have Σ symmetry with $\Lambda = 0$, and from p_x and p_y , which lead to π orbitals with $\Lambda = 1$.

Figure 7.16 shows a schematic representation of the occupied and some unoccupied molecular orbitals with their symmetries. The electron configuration of CO_2 is therefore

$$(1\sigma_g)^2(1\sigma_u)^2(2\sigma_g)^2(2\sigma_u)^2(1\pi_u)^4(1\pi_g)^4.$$

Apart from the bonding orbitals $1\sigma_g$, $1\sigma_u$ and $1\pi_u$, there are *nonbonding* molecular orbitals that are not involved in chemical bonding and which are therefore called *lone pairs*, and furthermore *antibonding* orbitals that lead to a destabilization of the molecule if they are occupied. The total bonding energy is the sum of all positive, negative and vanishing contributions of all these molecular orbitals.

7.4

AB₂ Molecules and Walsh Diagrams

The bond angle in triatomic molecules AB₂ (where A and B denote arbitrary atoms) can be determined approximately by calculating the dependence of the orbital energies on the bond angle for all occupied molecular orbitals. This is shown in Fig. 7.17a for the triatomic hydrides AH₂ and in Fig. 7.17b for the more general case of AB₂ molecules (which differ from the former by the availability of p orbitals at the B atoms). At the right, the orbital symmetries for a linear structure (point group $D_{\infty h}$) are indicated, at the left those for a bent structure (point group C_{2v}), where in both cases the molecule is arranged following the convention introduced by Mulliken. This means that in the linear case the z axis coincides with the internuclear axis, but in the bent case it coincides with the molecular symmetry axis. Hence, in going from left to right in the correlation diagram, the y and z axis are exchanged! (This is of course only relevant for the symmetry labels of the orbitals, not for their energies!)

From Walsh diagrams [7.5], the bond angles of triatomic molecules can be estimated by determining the point along the horizontal (bond angle) coordinate for which the sum of the energies of all occupied molecular orbitals assumes a minimum. We will elucidate this point for a number of examples.

(a) The H₂O molecule has the electron configuration

$$(2a_1)^2(1b_2)^2(3a_1)^2(1b_1)^2,$$

where orbitals of like symmetry are enumerated in order of increasing energy. (The $(1a_1)$ orbital has been omitted from the list because it does not contribute to bonding.) The two orbitals $(2a_1)$ and $(1b_2)$ assume, according to Fig. 7.17a, their minimum energies at $\alpha = 180^\circ$, the $(3a_1)$ orbital at $\alpha = 90^\circ$, and the energy of the $(1b_1)$ orbital does not depend on α . The total energy assumes its minimum value at $\alpha \approx 105^\circ$.

If an electron is excited from the $(1b_1)$ orbital into higher orbitals, we see from the diagram that the energies of those orbitals depends only weakly on α , and we expect therefore the structure of the molecule to change only slightly upon such an excitation. Indeed, the bond angle in the excited $C(B_1)$ state, in which an electron is excited into the 3p state, is found to be $\alpha = 106.9^\circ$, only slightly enlarged compared to the ground state.

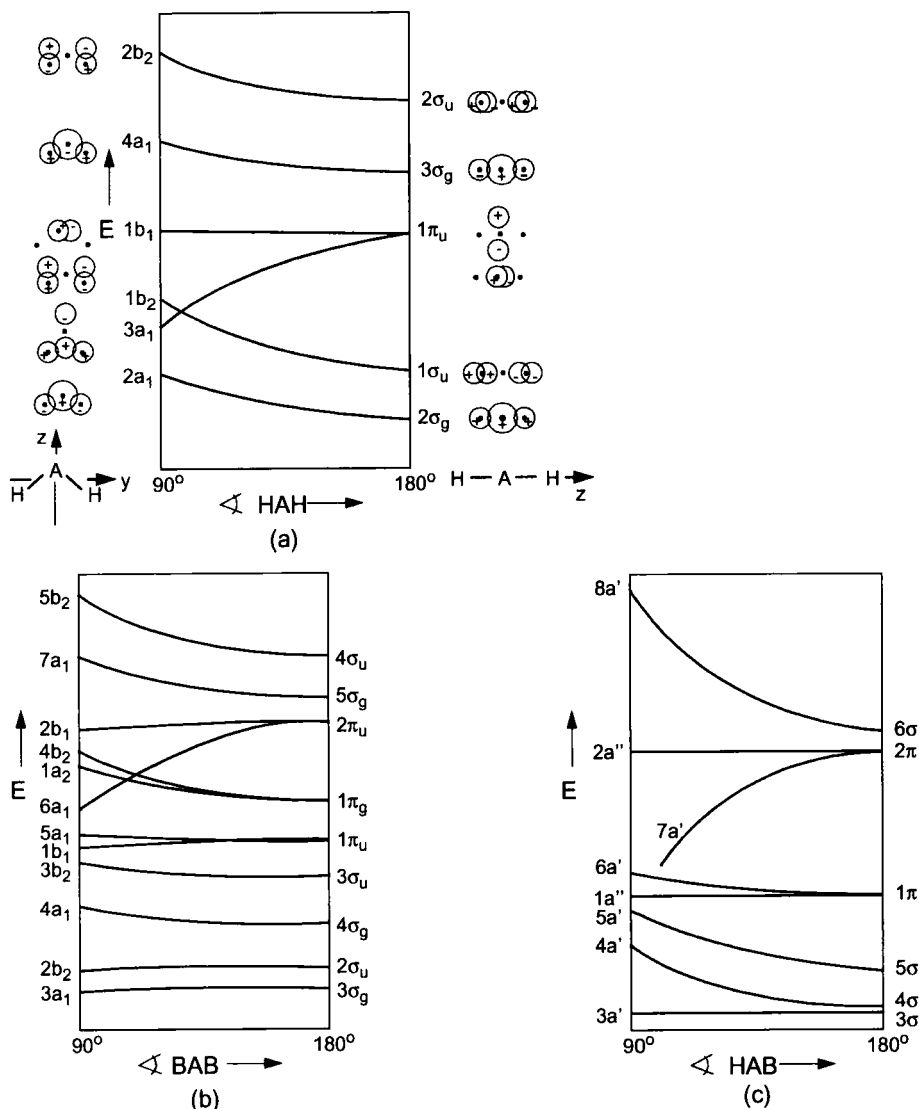


Fig. 7.17 Walsh diagrams for a) AH₂ molecules, b) AB₂ molecules, and c) HAB molecules.

(b) The boron dihydride molecule BH₂ has a ground-state electron configuration ... $(2a_1)^2(1b_2)^2(3a_1)^1$ and a bond angle $\alpha = 131^\circ$, because the influence of the $3a_1$ electron is stronger than that of the four electrons in $(2a_1)$ and $(1b_2)$.

(c) The CO₂ molecule has 16 valence electrons leading to an electron configuration ... $(2\sigma_u)^2(1\pi_u)^4(1\pi_g)^4$ for its $X^1\Sigma_g^+$ ground state. From Fig. 7.17b we see that the total energy assumes a minimum for $\alpha = 180^\circ$, because the strong dependence of the π_g orbitals on the bond angle exerts the largest influence.

Tab. 7.2 Occupancy of molecular orbitals in the ground and first excited states of some triatomic molecules.

Molecule	Z_v	Orbital occupancy	State	\angle BAB
C_3	12	$(3\sigma_g)^2(2\sigma_u)^2(4\sigma_g)^2(1\pi_u)^2(3\sigma_u)^2$	$X^1\Sigma_g^+$	180°
		$(3\sigma_g)^2(2\sigma_u)^2(4\sigma_g)^2(1\pi_u)^2(3\sigma_u)^1(1\pi_g)^1$	$A^1\Pi_u$	180°
CNC	13	$(3\sigma_g)^2(2\sigma_u)^2(4\sigma_g)^2(1\pi_u)^4(3\sigma_u)^2(1\pi_g)^1$	$X^2\Pi_g$	180°
		$(3\sigma_g)^2(2\sigma_u)^2(4\sigma_g)^2(1\pi_u)^4(3\sigma_u)^1(1\pi_g)^2$	${}^4\Sigma_u, A^2\Delta_u, B^2\Sigma_u$	180°
BO_2	15	$(3\sigma_g)^2(2\sigma_u)^2(4\sigma_g)^2(3\sigma_u)^2(1\pi_u)^4(1\pi_g)^3$	$X^2\Pi_g$	180°
		$(1\pi_u)^3(1\pi_g)^4$	$A^2\Pi_u$	
NO_2	17	$(3\sigma_g)^2(2\sigma_u)^2(4\sigma_g)^2(3\sigma_u)^2(4b_2)^2(6a_1)^1$	X^2A_1	134°
AlH_2	17	$(3\sigma_g)^2(2\sigma_u)^2(4\sigma_g)^2(3\sigma_u)^2(2a_1)^2(1b_2)^2(3a_1)^1$	X^2A_1	130°
		$(3\sigma_g)^2(2\sigma_u)^2(4\sigma_g)^2(3\sigma_u)^2(2a_1)^2(1b_2)^2(1b_1)^1$ $\cong (2\sigma_g)^2(1\sigma_u)^2(1\pi_u)^1$	$A^2\Pi_u$	180°
O_3	18	$(3\sigma_g)^2(2\sigma_u)^2(4\sigma_g)^2(3\sigma_u)^2(4b_2)^2(1a_2)^2(6a_1)^2$	\tilde{X}^1A_1	116.8°
		$(6a_1)^1(2b_1)^1$	\tilde{A}^1B_1	

Figure 7.17c shows the Walsh diagram for asymmetric molecules HAB such as HCO, HCN or HNO. Table 7.2 lists the electron configurations (i.e., the occupancy of the molecular orbitals forming the electron cloud) and the resulting ground states and first excited states for a number of AB_2 and A_3 molecules, allowing an estimation of the bond angles of these molecules from Fig. 7.17.

7.5

Molecules With More Than Three Atoms

The procedure to construct molecular orbitals from basis functions (atomic orbitals) of like symmetry can be applied analogously to molecules with more than three atoms. However, for molecules with double bonds, in which π electrons play an important role, new phenomena occur, which will be treated in Sect. 7.6.

Again, the procedure will be illustrated for a few examples.

7.5.1

The NH_3 Molecule

The electron configuration of the nitrogen atom is $(1s)^2(2s)^2(2p_x)(2p_y)(2p_z)$. Neglecting hybridization, the three unpaired electrons in the p orbitals allow three bonds

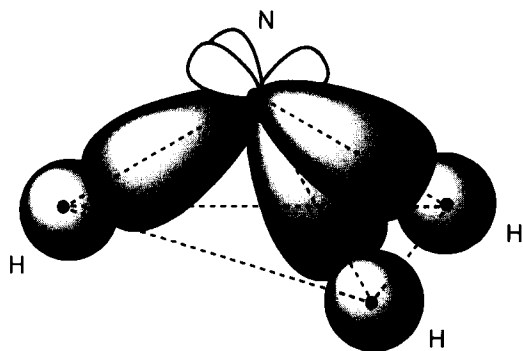


Fig. 7.18 Hybrid valence orbitals of the NH_3 molecule.

to the hydrogen $1s$ orbitals enclosing angles of 90° . The molecule possesses a three-fold symmetry axis C_3 ; its symmetry group is C_{3v} . For a planar structure, bond angles of 120° were to be expected, indicating sp^2 hybridization. As the real NH_3 molecule is pyramidal rather than planar, the actual bond angles must be smaller. It turns out that sp^3 hybridization of the nitrogen atom provides optimum overlap with the hydrogen $1s$ orbitals, resulting in bond angles of 107.3° (Fig. 7.18). The structure of the ammonia molecule resembles a trigonal pyramid with the nitrogen atom at the apex. The asymmetric charge distribution in the molecular orbitals creates an electric dipole moment P_{es} of magnitude $5 \times 10^{-30} \text{ Cm}$ ($\hat{=} 1.5 \text{ D}$), pointing from the nitrogen atom along the symmetry axis to the center of the triangle consisting of the three hydrogen atoms.

The molecular potential energy as a function of the height h of the nitrogen atom above the plane of the three hydrogen atoms assumes a maximum for $h = 0$ and two minima for $h = \pm h_0$ (Fig. 7.19). In the ground state, the nitrogen atom can therefore be above or below the plane $h = 0$. The two equivalent mirror-image conformations are indistinguishable, therefore both must be included in the calculation of vibrational wavefunctions and energies. Hence, the vibrational wavefunctions are written as sym-

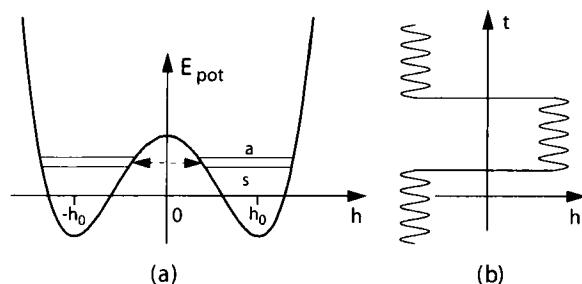


Fig. 7.19 Double-minimum potential $E_{\text{pot}}(h)$ for the NH_3 ground state with symmetric and antisymmetric vibrational states.

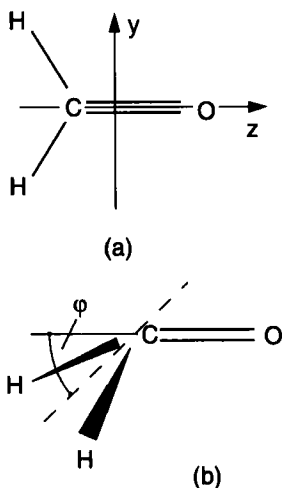


Fig. 7.20 The formaldehyde molecule a) in the ground state and b) in an excited state.

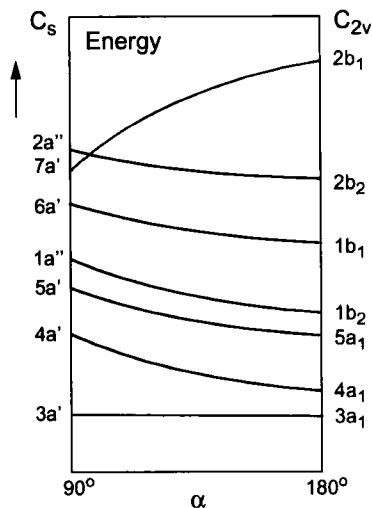


Fig. 7.21 Walsh diagram and molecular orbitals for the ground state of H_2CO .

metric and antisymmetric linear combinations

$$\Psi_{\text{sym}} = N_1(\Phi_1 + \Phi_2); \quad \Psi_{\text{asym}} = N_2(\Phi_1 - \Phi_2), \quad (7.17)$$

where the Φ_i are the vibrational wavefunctions for the left-hand and right-hand region of the potential below the barrier, respectively, and the N_i are normalization constants. In the vicinity of the minima, the potential can be described by a parabola so that the Φ_i are harmonic-oscillator functions. The energy eigenvalues of Ψ_{sym} and Ψ_{asym} are slightly different (inversion splitting).

In a semiclassical model (Fig. 7.19b), the nitrogen atom with vibrational period T_1 oscillates for some time above the plane $h = 0$ around its equilibrium position $h = +h_0$, before tunneling, after an average time T_2 , through the potential barrier and oscillating around $h = -h_0$. Its vibrational energy is then $E_{\text{vib}} = h\nu_{\text{vib}} = h/T_1$, and the inversion splitting is given by $\Delta E = h/T_2$, where $T_1 \ll T_2$ holds.

7.5.2

Formaldehyde

As an example for a molecule with a planar structure (point group C_{2v}) in the ground state (all atoms lie in the xz plane) and a pyramidal structure in the first excited state ${}^1\tilde{A}$, we will consider the formaldehyde molecule H_2CO (Fig. 7.20). In the excited state, the two hydrogen atoms lie above and below the yz plane and define together with the carbon atom a plane intersecting the yz plane at an angle $\varphi = 38^\circ$. The molecular symmetry in this state is C_s . The lowest molecular orbitals are $3A_1$, $4A_1$, $5A_1$, and $1B_2$, which all describe σ bonds (Fig. 7.21). The remaining four of the twelve valence

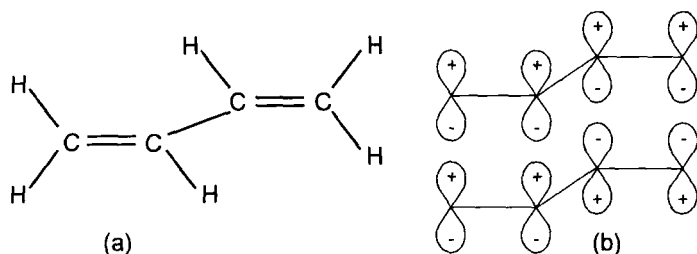


Fig. 7.22 The butadiene molecule. a) Structure formula, and b) schematic representation of the two lowest π orbitals.

electrons occupy the next-higher orbitals $1B_1$ and $2B_2$. The $1B_1$ molecular orbital is a π orbital contributing mainly to the bonding between carbon and oxygen, whereas the $2B_1$ orbital, which is built from two p_y atomic orbitals, is antibonding. Upon optical excitation to the \tilde{A} state, one electron is promoted from the nonbonding $2B_2$ molecular orbital into the antibonding $2B_1$ molecular orbital ($\pi^* \leftarrow n$ transition).

The potential energy of the \tilde{A} state as a function of the displacement during the ν_4 vibration possesses two minima, similar to what we learned for the ammonia molecule. Again, the two hydrogen atoms can tunnel through the barrier, similarly to the nitrogen atom in NH_3 . However, in this case the tunneling frequency is much larger because the mass of the hydrogen atoms is much smaller and the height of the barrier is smaller than for ammonia.

7.6

π -Electron Systems

In the preceding examples, we have discussed *localized* bonds in molecules, that is, the electron density of the valence electrons was concentrated in a closely confined region between the bonded atoms.

There is a significant class of molecules, however, in which *delocalized* electrons play an important role. An example is the butadiene molecule (Fig. 7.22), where single and double bonds between the carbon atoms alternate.

The electrical polarizability along the chain of carbon atoms in such molecules is much larger than in molecules with localized bonds, which is a first indication that delocalized electrons with a high mobility are present. It turns out that these electrons are from overlapping p orbitals, forming π bonds [7.6].

7.6.1

Butadiene

The *trans* isomer of the butadiene molecule $\text{CH}_2=\text{CH}-\text{CH}=\text{CH}_2$ is planar. The length of the central C–C bond is 148 pm, which is significantly longer than the C=C

double bonds. Apart from the σ orbitals, there are four π orbitals, which are linear combinations of the four carbon 2p orbitals and which are perpendicular to the plane of the carbon atoms (Fig. 7.22b). The relative contributions of the four p orbitals in the four molecular orbitals

$$\Psi_{\pi} = \sum_{n=1}^4 c_n \phi_n(\text{p}) \quad (7.18)$$

can be determined using the variational principle (see Sect. 2.5.1), which requires solution of the determinant equation

$$|H_{mn} - ES_{mn}| = 0. \quad (7.19)$$

To facilitate the calculations, we make the following assumptions:

- (a) All integrals H_{mm} are equal to a parameter α .
- (b) Integrals H_{mn} with $n \neq m$ are nonvanishing only for adjacent atoms, and they are equal to a second parameter $\beta < 0$.
- (c) All overlap integrals S_{mn} with $m \neq n$ are zero, and $S_{mm} = 1$.

These assumptions are the basis of the so-called *Hückel method*. This yields the energies

$$\begin{aligned} E_1 &= \alpha + 1.62\beta, & E_2 &= \alpha + 0.62\beta, \\ E_3 &= \alpha - 0.62\beta, & E_4 &= \alpha - 1.62\beta, \end{aligned} \quad (\beta < 0!) \quad (7.20)$$

for the molecular orbitals

$$\begin{aligned} \Psi_{\pi_1} &= 0.37\phi_1 + 0.60\phi_2 + 0.60\phi_3 + 0.37\phi_4, \\ \Psi_{\pi_2} &= 0.60\phi_1 + 0.37\phi_2 - 0.37\phi_3 - 0.60\phi_4, \\ \Psi_{\pi_3} &= 0.60\phi_1 - 0.37\phi_2 - 0.37\phi_3 + 0.60\phi_4, \\ \Psi_{\pi_4} &= 0.37\phi_1 - 0.60\phi_2 + 0.60\phi_3 - 0.37\phi_4. \end{aligned} \quad (7.21)$$

This shows that the largest contributions for the lowest molecular orbital π_1 stems from carbon atoms two and three.

Figure 7.23 shows a graphical representation of these four orbitals. It emphasizes that the orbital π_1 is completely delocalized, which means that the electrons in this orbital are distributed uniformly over the complete chain of carbon atoms.

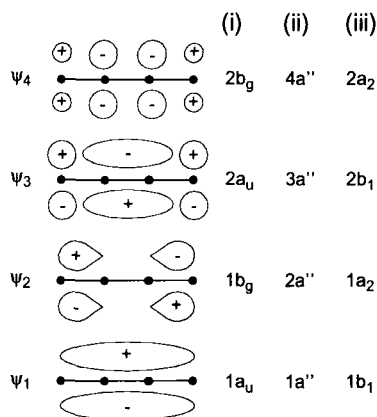


Fig. 7.23 Schematic representation of the four π molecular orbitals in the butadiene molecule.

7.6.2

Benzene

The explanation of the benzene structure was an important milestone in the history of molecular orbital theory, which had been postulated by Kekulé as early as 1865.

It became clear from many experiments, particularly from spectroscopic investigations, that C_6H_6 has to be a planar molecule in which the carbon atoms form a six-membered ring. The carbon bonds enclose therefore angles of 120° , which indicates sp^2 hybridization, as was discussed in Sect. 7.2. Hence, there are localized C–C and C–H σ bonds, each of which contains one valence electron from the carbon atom (Fig. 7.24a). This makes a total of three valence electrons from each carbon atom, which are used to form the σ bonds originating from it. One p_z electron per carbon atom, or six in total, are not involved in hybridization and are available for additional bonds (Fig. 7.24b).

There are, however, two indistinguishable ways, displayed schematically in Fig. 7.24c and d, to form three π bonds in a six-membered ring from the six available p_z orbitals. As in the butadiene case, we must therefore construct linear combinations

$$\Psi = \sum_{i=1}^6 c_i \phi_i, \quad (7.22)$$

where the ϕ_i are the p_z orbitals of the six carbon atoms.

The crucial point is now that the wavefunctions Ψ are not confined to a single carbon atom or a pair of bonded carbon atoms, but extend over the complete ring of carbon atoms. These delocalized electrons contribute significantly to the stability of this planar arrangement because their density is distributed symmetrically with respect to the molecular plane.

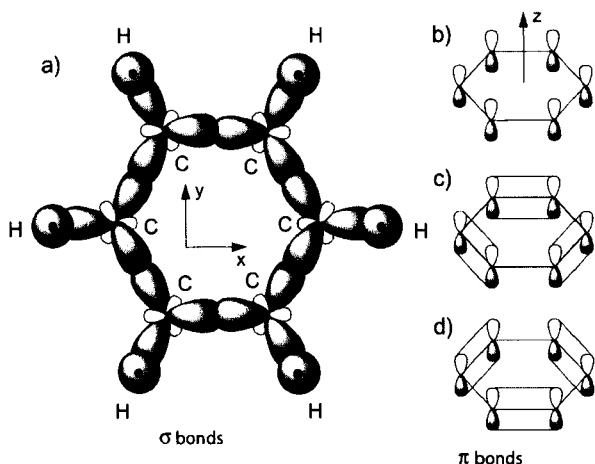


Fig. 7.24 Bonding in the benzene molecule. a) σ bonds, b) p_z orbitals, c), d) different alternatives for π bonding around the ring system.

A very simple model, the so-called Hückel model suggested by Hückel, treats the delocalized π electrons, which are distributed over the whole ring system, as electrons in a square-well potential of width L , where L corresponds to the circumference of the benzene hexagon. The de Broglie wavelength λ of these electrons must satisfy the condition $n\lambda = L$. Their kinetic energy is, using $\lambda = h/p$,

$$E_{\text{kin}} = \frac{p^2}{2m_e} = \frac{h^2}{2m_e\lambda^2} = \frac{n^2 h^2}{2m_e L^2}. \quad (7.23)$$

If the potential energy at the bottom of the potential well is chosen to be $E_{\text{pot}} = 0$, we obtain for the energies of the levels $|n\rangle$

$$E_n = \frac{n^2 h^2}{2m_e L^2},$$

with E_1 denoting the ground state.

The interaction of one of the π electrons with the other electrons is indirectly taken into account by choosing an effective potential, similar to the Hartree method in atoms, where the depth of the potential can be adjusted in order to match the experimental observations. The Hückel method is therefore a one-electron approximation for many-electron molecules.

Upon excitation of π electrons (e.g., by photon absorption), higher-energy states with $n > 1$ can be occupied.

For benzene with a C-C distance of 140 pm, $L = 6 \times 140 \text{ pm} = 840 \text{ pm}$, and we obtain for the energy difference for the transition $n = 1 \rightarrow n + 1 = 2$,

$$\Delta E = \frac{h^2(2n+1)}{2m_e L^2}.$$

Inserting the numerical values yields $\Delta E = 1 \times 10^{-18} \text{ J} = 6.5 \text{ eV}$.

This corresponds to a wavelength of $\lambda \approx 200 \text{ nm}$, in fair agreement with the experimental value of $\lambda \approx 220 \text{ nm}$, considering the crude model employed. The difference is due to the fact that we neglected the interactions between the electrons.

Additional information on the electronic states of larger molecules can be found in [7.8–7.10].

8

Spectra of Polyatomic Molecules

Owing to the larger number of degrees of freedom, the energy level diagrams of polyatomic molecules are far more complicated than those of diatomic molecules, where only one vibrational mode and a simple rotational structure exist.

Consequently, the number of possible transitions between different energy levels is also much larger, and the spectra are complex. In many cases, several lines or even whole bands overlap, and only the application of high-resolution, Doppler-free techniques has enabled spectroscopists to resolve the rotational structure of electronic transitions for larger molecules such as benzene or naphthalene (see Sect. 12.4).

The spectral region and the structure of the spectra depend, as in the case of diatomic molecules (see Ch. 4), on the upper and lower levels of the transition. If only the rotational quantum numbers change during the transition, pure rotational spectra in the microwave region are obtained; if the vibrational quantum numbers also change, this results in vibration–rotation spectra in the infrared; if the transition is between different electronic states, electronic spectra in the visible and UV region are observed.

In any case, only such electric dipole transitions between states $|m\rangle$ and $|k\rangle$ are possible for which at least one component of the transition dipole matrix element

$$(D_{mk})_p = \int \Psi_m^* p \Psi_k dt, \quad p = x, y, z$$

is nonvanishing. This condition is only satisfied if the integrand is totally symmetric under the symmetry operations of the molecular point group (see Sect. 8.2.2).

Apart from these electric dipole transitions, much weaker magnetic dipole transitions or (even weaker) electric quadrupole transitions can also occur.

8.1

Pure Rotational Spectra

The structure of rotational spectra depends on the structure of the molecule under consideration and on possible centrifugal distortions during its rotation. Pure rotational transitions are only possible for molecules with a permanent electric dipole moment (see Sect. 4.2.1). This will be elucidated in the following for different types of molecules.

8.1.1

Linear Molecules

The spectra of linear polyatomic molecules are similar to those of diatomic molecules. The molecule rotates only around an axis perpendicular to the internuclear axis, and hence there is only one rotational constant B_v as in the diatomic case. The wavenumbers of the rotational lines due to transitions from a level with rotational quantum number J to the level $(J + 1)$ in the same vibrational state are, in analogy to Eq. (3.18),

$$\bar{\nu} = F(J + 1) - F(J) = 2B_v(J + 1) - 4D_v(J + 1)^3. \quad (8.1)$$

As an example, Fig. 8.1 shows the pure rotational spectrum of the linear N_2O molecule. From the distances of the lines, the moment of inertia can be determined, which shows that N_2O is asymmetric, N–N–O, and that it must therefore possess a permanent electric dipole moment, in contrast to the symmetric linear CO_2 (O=C=O).

As linear molecules consisting of N atoms possess $(3N - 5)$ vibrational degrees of freedom, the rotational constant

$$B_v = B_e - \sum_{i=1}^{3N-5} \alpha_i \left(v_i + \frac{d_i}{2} \right) \quad (8.2)$$

and the centrifugal constant

$$D_v = D_e + \sum_{i=1}^{3N-5} \beta_i \left(v_i + \frac{d_i}{2} \right) \quad (8.3)$$

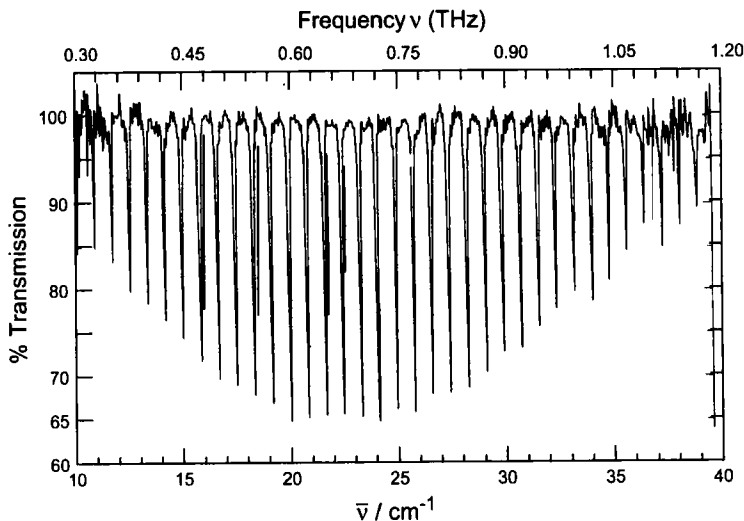


Fig. 8.1 Rotational spectrum (microwave spectrum) of the linear molecule N_2O [8.1].

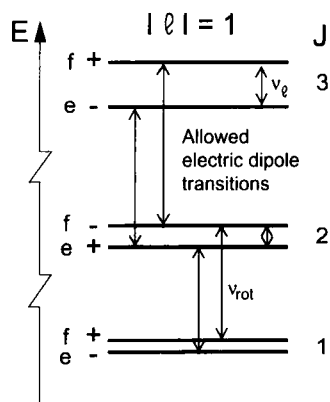


Fig. 8.2 l -splitting of the rotational levels of a linear molecule for degenerate bending vibrations with vibrational angular momentum $|l| = 1 \hbar$, and allowed transitions between the components.

[cf. Eq. (3.44)] will in general depend on all $(3N - 5)$ vibrational quantum numbers v_i (the degree of degeneracy is $d_i = 2$ for bending vibrations and $d_i = 1$ for all other modes).

As the superposition of two degenerate bending vibrations (Fig. 6.11a) leads to a rotation of the nuclei around the internuclear axis, the linear molecule assumes in this case a vibrational angular momentum $l\hbar$ along z , and the Coriolis interaction between rotation and vibration leads to an l -splitting of the otherwise degenerate levels into two l components of opposite parity. They are denoted e and f components (Fig. 8.2), respectively (see Sect. 6.3.6). According to Eq. (6.92) and Fig. 8.2, the wavenumber of the allowed dipole transitions between the adjacent rotational levels is then

$$\begin{aligned} \tilde{\nu}_{\text{rot}} &= F_{v_i}^+(J+1, l^+) - F_{v_i}^-(J, l^+) \\ &= 2B_v(J+1) - 4D_v[(J+1)^3 - l^2(J+1)] + \frac{q_i}{2}(v_i+1)(J+1), \end{aligned} \quad (8.4)$$

and between the split l components of the same rotational level,

$$\tilde{\nu}_l = F_{v_i}^+(J, l^+) - F_{v_i}^-(J, l^-) = \frac{q_i}{2}(v_i+1)J(J+1). \quad (8.5)$$

The selection rules for electric dipole transitions are

$$\begin{aligned} e \leftrightarrow e; \quad f \leftrightarrow f; \quad e \leftrightarrow f \quad \text{for } \Delta J = \pm 1, \\ e \leftrightarrow f; \quad e \leftrightarrow e; \quad f \leftrightarrow f \quad \text{for } \Delta J = 0. \end{aligned} \quad (8.6)$$

Whereas the frequencies ν_{rot} of the rotational transitions Eq. (8.4) lie in the microwave (i.e., gigahertz) region, the ν_l transitions between the l components of the same rotational level are usually found in the radiofrequency range.

8.1.2

Symmetric Top Molecules

The dipole moment μ_L ($L = X, Y, Z$) in the laboratory-fixed system (X, Y, Z)

$$\mu_L = \mu_x \phi_{L_x} + \mu_y \phi_{L_y} + \mu_z \phi_{L_z} \quad (8.7a)$$

can be expressed by the components μ_i in the molecule-fixed system using the direction cosine elements ϕ_{L_i} ($i = x, y, z$).

In symmetric top molecules, μ must be directed along the symmetry axis z (i.e., $\mu_x = \mu_y = 0$). The square of the transition dipole matrix element

$$|D_{ik}|^2 = |\langle J, k | \mu | J', k' \rangle|^2$$

yields then [8.2] the only nonvanishing elements

$$|\langle J, K | \mu | J + 1, K \rangle|^2 = \mu^2 \frac{(J + 1)^2 - K^2}{(J + 1)(2J + 1)}, \quad (8.7b)$$

$$|\langle J, K | \mu | J, K \rangle|^2 = \mu^2 \frac{K^2}{J(J + 1)}, \quad (8.7c)$$

$$|\langle J, K | \mu | J - 1, K \rangle|^2 = \mu^2 \frac{J^2 - K^2}{J(2J + 1)}, \quad (8.7d)$$

where $\mu = |\mu| = \mu_z$. The selection rules for pure rotational transitions are

$$\Delta J = \pm 1, \quad \Delta K = 0. \quad (8.7e)$$

If we substitute the expressions Eqns. (6.28) and (6.30) for the energy levels of the prolate and oblate symmetric top, respectively, we obtain for the wavenumbers of the rotational transitions

$$\begin{aligned} \tilde{\nu} &= F_v(J + 1, K) - F_v(J, K) \\ &= 2(B_v - D_{JK}K^2)(J + 1) - 4D_J(J + 1)^3. \end{aligned} \quad (8.8)$$

Note: Equation (8.8) contains none of the rotational constants A_v , C_v or D_k . As a consequence, these constants cannot be determined from a measurement of the pure rotational spectrum of symmetric top molecules!

According to the selection rules Eq. (8.7), there is for a given level (J, K) one absorption transition to a higher level ($J + 1, K$) and, for $J > 0$, one emission transition to the lower level ($J - 1, K$). The wavenumbers of transitions with different K but

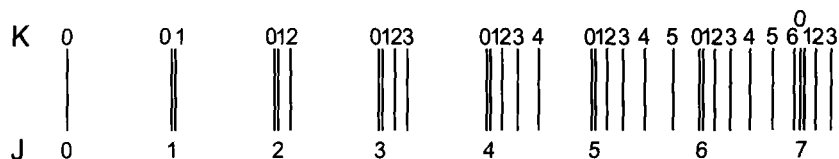


Fig. 8.3 Schematic representation of the rotational spectrum of a symmetric top molecule [8.4].

equal J in Eq. (8.8) differ only marginally because $D_{JK} \ll B_v$. As the projection quantum number K is in the range $0 < K < J$, each rotational transition contains a substructure of $J + 1$ different K components (Fig. 8.3).

The intensities of the corresponding absorption lines are proportional to the population $N(J, K)$ of the absorbing level (see Sect. 8.1.4) and to $|D_{ik}|^2$.

8.1.3

Asymmetric Top Molecules

We saw in Sect. 6.2.5 that the energy levels of an asymmetric top molecule cannot be given in closed form but must be expanded in a power series. For each value of the rotational quantum number J , there are $(2J + 1)$ different energy levels, which are enumerated either by a subscript τ running from $-J$ to $+J$ or by the projection quantum numbers K_a, K_c , which are defined in the limiting cases of the prolate or oblate symmetrical top. Hence, a rotational level is denoted by either J_τ or by J_{K_a, K_c} . The relation between both labeling schemes is given by $\tau = K_a - K_c$. The values of K_a and K_c are in the range from 0 to J with the additional conditions $K_a + K_c = J$ or $(J + 1)$, depending on the parity of the specific state.

The wavenumber of a transition between two rotational levels is given by

$$\tilde{\nu} = F(J + 1, K'_a, K'_c) - F(J, K''_a, K''_c). \quad (8.9)$$

Whether such a transition actually occurs is determined by the selection rules, which are more complicated for asymmetric tops than for symmetric tops, where the rule was simply $\Delta K = 0$. They depend on the orientation of the permanent dipole moment and on the parity of the states involved (specifically, the question is if K_a and K_c are even or odd). If the dipole moment is oriented along the a axis (smallest moment of inertia I_a), the transitions are called A -type transitions, and analogously for the b (medium moment of inertia) and c (largest moment of inertia) axes. If the dipole moment is oriented arbitrarily within the molecule, the same arguments hold for its components along a, b or c .

The selection rules for pure rotational transitions in asymmetric top molecules are summarized in Table 8.1 in terms of parity (e or o), the rotational quantum number J and the projection quantum numbers K_a and K_c . We see that for a transition to be allowed, the parity of either K_a or K_c must change. In contrast to the selection rules for

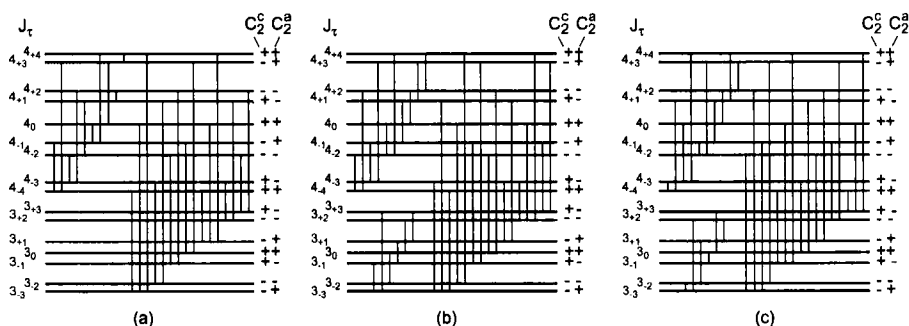
Tab. 8.1 Selection rules for pure rotational transitions of an asymmetric top molecule.

Orientation of dipole moment	Selection rules		
	Symmetries upon rotation around a, c	$K'_a, K'_c \leftrightarrow K''_a, K''_c$	$\Delta J, \Delta K_a, \Delta K_c$
a axis	$++ \leftrightarrow -+$	$ee \leftrightarrow eo$	and: $\Delta J = 0, \pm 1$ $\Delta K_a = 0, \pm 1, \pm 2, \dots$ $\Delta K_c = 0, \pm 1, \pm 2, \dots$ depending on parity.
	$-- \leftrightarrow +-$	$oe \leftrightarrow oo$	
b axis	$++ \leftrightarrow --$	$ee \leftrightarrow oo$	
	$+ - \leftrightarrow - +$	$oe \leftrightarrow eo$	
c axis	$++ \leftrightarrow +-$	$ee \leftrightarrow oe$	
	$-+ \leftrightarrow --$	$eo \leftrightarrow oo$	

the symmetric top discussed before, not only transitions with ΔK_a or $\Delta K_c = 0, \pm 1$ are allowed in asymmetric tops, but depending on the parity of the K_a and K_c levels, also transitions with $\Delta K_a, \Delta K_c = \pm 1, \pm 3, \dots$ or $\pm 2, \pm 4, \dots$, respectively, are now allowed. The intensities of the corresponding lines in the spectrum are weak, however, and decrease even further the more the molecular geometry approaches that of a symmetric top.

If the molecule is an almost symmetric prolate top, the selection rule is $\Delta K_a = 0, \pm 1$; for an almost symmetric oblate top, it is $\Delta K_c = 0, \pm 1$.

The selection rules can also be expressed by the symmetry behavior of the rotational wavefunction upon rotation by 180° around a C_2 axis along a, b or c . If the wavefunction is unchanged under this operation, its symmetry is denoted (+), if it changes sign, it is denoted (-). Usually, only the behavior upon rotation around C_2^a and C_2^c is indicated; the behavior upon rotation around the b axis is then fixed. The symmetry of a rotational level J_{K_a, K_c} or J_τ can then be denoted by $(++)$, $(+-)$, etc. (Fig. 8.4).

**Fig. 8.4** Dipole-allowed rotational transitions of an asymmetric top molecule if the dipole moment is oriented along a) the a axis, b) the b axis and c) the c axis [8.4].

8.1.4

Intensities of Rotational Transitions

If an electromagnetic wave with incident intensity I_0 passes through an absorbing medium with absorption coefficient $\alpha(\nu)$, the transmitted intensity I_{trans} after a path of length L is

$$I_{\text{trans}}(\nu) = I_0(\nu) e^{-\alpha(\nu)L}. \quad (8.10)$$

For $\alpha L \ll 1$, the net absorption is

$$\Delta I(\nu) = I_{\text{abs}}(\nu) - I_{\text{trans}}(\nu) \approx I_0(\nu)\alpha(\nu)L. \quad (8.11)$$

Using the Einstein coefficients B_{ik} , the net absorption is obtained as the difference between absorption and stimulated emission,

$$\Delta I(\nu) = [N_i B_{ik} - N_k B_{ki}] \varrho(\nu) h\nu L, \quad (8.12)$$

where $\varrho(\nu) = I(\nu)/c$ is the spectral energy density.

Integrating over the line profile $\alpha(\nu)$ with full width at half maximum $\Delta\nu$, we obtain the total absorption from this transition. To perform the integration, we must replace the quantity $\varrho(\nu)$ in Eq. (8.12) by

$$\varrho = \int \varrho(\nu) d\nu; \quad I = \int I(\nu) d\nu \approx I(\nu_0)\Delta\nu.$$

In thermal equilibrium at a temperature T , the ratio of the population densities follows the Boltzmann relation,

$$\frac{N_k}{N_i} = \frac{g_k}{g_i} e^{-\Delta E/k_B T} \quad \text{with} \quad \Delta E = E_k - E_i = h\nu. \quad (8.13)$$

Using the relations $g_i B_{ik} = g_k B_{ki}$, we obtain for Eq. (8.12),

$$\Delta I = \frac{I_0}{c} h\nu L B_{ik} N_i \left[1 - e^{-\Delta E/k_B T} \right]. \quad (8.14)$$

For transitions in the microwave region, $h\nu = \Delta E \ll k_B T$ so that Eq. (8.14) becomes

$$\Delta I = I_0 L N_i B_{ik} \frac{(\Delta E)^2}{c k_B T} \implies \alpha = N_i B_{ik} \frac{(\Delta E)^2}{c k_B T}. \quad (8.15)$$

This shows that the net absorption is proportional to the density N_i of absorbing molecules and to the ratio $(\Delta E)^2/k_B T = (h\nu)^2/k_B T$.

The population density N_i in the absorbing level $|i\rangle$ and the total density of molecules N are related by the Boltzmann relation,

$$N_i = g_i \left(\frac{N}{Z} \right) e^{-E_i/k_B T} \approx g_i \left(\frac{N}{Z} \right) (1 - E_i/k_B T), \quad (8.16)$$

where

$$Z = \sum_n g_n e^{-E_n/k_B T} \quad (8.17)$$

is the partition function, which runs over all molecular states E_n and which serves as a normalization factor ensuring $\sum N_n = N$.

If we use also the relation

$$B_{ik} = \frac{2\pi^2}{2\varepsilon_0 h^2} |D_{ik}|^2 \quad (8.18)$$

between the Einstein coefficient B_{ik} and the transition matrix element D_{ik} , we finally arrive at the relation valid for $(E_k - E_i) \ll k_B T$,

$$\Delta I = I_0 L g_i \frac{N}{Z} \frac{2\pi^2 \nu^2}{3\varepsilon_0 c k_B T} |D_{ik}|^2. \quad (8.19)$$

The transition dipole matrix element D_{ik} depends on the molecular structure. For linear molecules, the dipole moment points along the molecular axis, whereas it is oriented along the symmetry axis for nonlinear symmetric top molecules.

If we calculate the sum over all possible values of M , that is, over the $(2J + 1)$ possible orientations of J , we obtain for a transition with $\Delta J = +1$ and $\Delta K = 0$ in symmetric tops

$$|D_{ik}|^2 = \mu^2 \frac{(J+1)^2 - K^2}{(J+1)(2J+1)}. \quad (8.20)$$

The intensities of the rotational absorption lines for transitions $(J+1, K) \leftarrow (J, K)$ are therefore

$$\Delta I(J, K) = \mu^2 I_0 g_i \frac{N}{Z} L \frac{2\pi^2 \nu^2}{3\varepsilon_0} \frac{(J+1)^2 - K^2}{(J+1)(2J+1)}, \quad (8.21)$$

where the statistical weight of the absorbing level is the product $g_i = g_{JK} \times g_{ns}$ of the weights $g_{JK} = 2(2J + 1)$ of the rotational level $|J, K\rangle$ and g_{ns} of the nuclear spins.

This will be examined more closely in the following.

8.1.5

Symmetry Properties of Rotational Levels

The symmetry properties of rotational levels and their statistical weights depend on the molecular point group, the quantum numbers J and K , the vibrational and electronic states, and the nuclear spins. Within the Born–Oppenheimer approximation, the total wavefunction can be written as a product of electronic, vibrational, rotational, and nuclear spin wavefunctions,

$$\Psi = \psi_{el} \psi_{vib} \psi_{rot} \psi_{ns}. \quad (8.22)$$

Hence, its symmetry depends on the individual symmetries of these four factors.

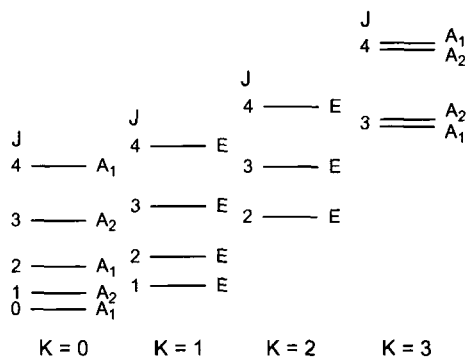


Fig. 8.5 Symmetry types of rotational levels for molecules belonging to point group D_{3h} .

For rotational transitions within the same electronic and vibrational state we only need to take into account the symmetries of ψ_{rot} and ψ_{ns} , because the square moduli $|\psi_{e1}|^2$ and $|\psi_{\text{vib}}|^2$ in the matrix element D_{ik} are always totally symmetric.

The symmetry species of ψ_{rot} correspond to those of the molecule's rotational group. The rotational group is, for example, C_3 for molecules belonging to group C_{3v} (such as ammonia, NH_3) or D_3 for molecules belonging to D_{3h} (such as ethane, C_2H_6). The point group C_3 comprises the symmetry species A and E , whereas in D_3 , there are A_1 , A_2 and E (see the character tables in the appendix).

The rotational wavefunctions expressed in the laboratory-fixed system can be written as the product

$$\psi_{\text{rot}} = \Theta_{JKM}(\theta) e^{iM\kappa} e^{\pm iK\varphi} \quad (8.23)$$

of the Legendre polynomial $\Theta(\theta)$ and two exponentials. They depend on the Euler angles θ , κ and φ between the axes of the molecule-fixed and those of the laboratory-fixed system, where φ is the rotational angle around the symmetry axis. A rotation by an angle $\varphi = 2\pi/3$ leaves ψ_{rot} unchanged if $K = 3m$ ($m = 0, 1, 2, 3, \dots$). Hence, the rotational levels with $K = 3m$ belong to symmetry species A for C_{3v} molecules, whereas for all other levels, ψ_{rot} neither changes sign nor is it left unchanged upon this operation, but is transformed into a linear combination of two functions and belongs thus to symmetry species E (see Sect. 5.5.2).

For molecules belonging to point group D_{3h} , the rotational levels with $K = 0$ have symmetry A_1 for even rotational quantum numbers J and A_2 for odd J . For $K = 3m \neq 0$ there is one K component with symmetry A_1 and one with A_2 symmetry. For $K = 3m \pm 1$, the symmetry type of the rotational wavefunction is E (Fig. 8.5).

In a similar manner, the symmetries of rotational levels can be determined for other point groups using the corresponding character tables (see, e.g., [8.3]). The symmetry type of rotational levels is important for the determination of statistical weights, as will be discussed in the following section.

8.1.6

Statistical Weights and Nuclear Spin Statistics

The rotational angular momentum of a molecule can assume $(2J + 1)$ orientations in space, which are all degenerate in the absence of an external field. Hence, the statistical weight $g(J, K)$ of a rotational level (J, K) is $g(J, K = 0) = 2J + 1$ for $K = 0$. For $K \neq 0$ there are two K components with a very small splitting that cannot be resolved in most cases. The statistical weight of these levels is therefore $2(2J + 1)$.

Again, as for diatomic molecules, the symmetry of the nuclear spin wavefunction is an important factor in determining the populations of rotational levels and hence the intensities of the rotational lines. The total wavefunction Ψ must be symmetric with respect to the exchange of two identical *bosonic* nuclei (integer nuclear spin) and antisymmetric with respect to the exchange of two identical *fermionic* nuclei (half-integer nuclear spin).

The symmetry operations of a molecule may interchange more than two identical nuclei. The number of possible permutations depends on the molecular point group and on the symmetry properties of the wavefunction ψ . As this number determines the statistical weight of the nuclear spin functions, the intensities of rotational lines and the intensity alternation for transitions between symmetric or antisymmetric rotational levels depend also on the number of identical nuclei in the molecule, on the vibrational level, and on the symmetry group of the molecule. For example, a molecule with a C_n symmetry axis must possess at least n identical nuclei that are interchanged upon rotation by an angle $2\pi m/n$. This will now be detailed for a number of examples.

In the case of a C_3 symmetry axis, a rotation by an angle $\varphi = 120^\circ$ is equivalent to an exchange of two pairs of nuclei. As Fig. 8.6 shows, such a rotation passes nucleus 1 into 2, 2 into 3, and 3 into 1. This situation is equivalent to two pair interchanges $2 \leftrightarrow 1$ and $3 \leftrightarrow 1$. Hence, such a rotation is always connected with a symmetric nuclear spin function, irrespective of the fermionic or bosonic nature of the nuclei.

Next, we consider a nonplanar molecule AB_3 of point group C_{3v} , in which the B nuclei have nuclear spin $I = 0$, that is, they are bosons. In this case, there exists only a symmetric nuclear spin function. As the total wavefunction must be symmetric, only rotational levels with $K = 3m$ are possible for symmetric functions ψ_{el} and ψ_{vib} . Therefore, no lines starting from levels with $K = 3m \pm 1$ occur in the rotational spectrum.

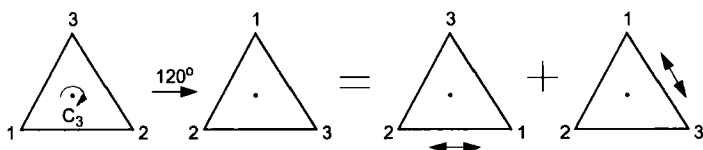


Fig. 8.6 Equivalence of a rotation by 120° around a C_3 axis and a double pair interchange of identical nuclei.

Nuclei	I	II	III	IV	V	VI	VII	VIII
1	↑	↑	↑	↓	↑	↓	↓	↓
2	↑	↑	↓	↑	↓	↓	↑	↓
3	↑	↓	↑	↑	↓	↑	↓	↓

Fig. 8.7 The eight possible orientation of nuclear spins $1/2$ in molecules with a C_3 symmetry axis.

For a planar molecule, rotations around the C_2 axes are also possible that interchange only one pair of identical nuclei. If the nuclei are bosons, the nuclear spin wavefunction is left unchanged by this operation, and therefore only A_1 levels are possible in Fig. 8.5, whereas for fermionic nuclei, only A_2 rotational levels are allowed.

For nuclei with nuclear spin $I \neq 0$, the number of possible nuclear spin functions depends on the value of I .

In the nonplanar molecule NH_3 , there are three hydrogen atoms with nuclear spin $I = 1/2$. A rotation of the molecule around its C_3 axis by an angle $\pi/3$ or $2\pi/3$ interchanges two pairs of hydrogen nuclei. There are eight nuclear spin wavefunctions, which are listed in Fig. 8.7. The combinations I and VIII are obviously symmetric. However, linear combinations $\psi_{\text{ns}}(\text{II}) + \psi_{\text{ns}}(\text{III}) + \psi_{\text{ns}}(\text{IV})$ and $\psi_{\text{ns}}(\text{V}) + \psi_{\text{ns}}(\text{VI}) + \psi_{\text{ns}}(\text{VII})$ are also symmetric (symmetry type A_1) under a rotation by 120° . The four remaining nuclear spin functions (which are also linear combinations of II–VII) are linearly independent of the functions discussed until now. They can be combined into two pairs of linear combinations, which upon rotation by 120° are transformed into linear combinations of each other; that is, they have symmetry type E .

As the product $\psi_{\text{rot}}\psi_{\text{ns}}$ must have symmetry A_2 , no rotational levels with symmetry A_1 occur for $K = 0$. For $K > 0$, the rotational levels with symmetry A_2 ($A_2 \times A_1 = A_2$) have statistical weight four (because there are four nuclear spin functions with symmetry A_1), whereas the rotational levels with symmetry E , belonging to the nuclear spin functions with E symmetry ($E \times E = A_1 + A_2 + E$), have statistical weight two, because there are two nuclear spin functions with E symmetry. The statistical weights alternate like 1:1:2:1:1:2 for $K = 1, 2, 3, 4, 5, 6, \dots$

For nuclear spins $I > 1/2$, there are more nuclear spin functions, among them also some with symmetry A_2 , which is the reason why now all rotational levels can occur irrespective of their J values. The statistical weights for molecules with a C_3 axis are, for three identical spin- I nuclei,

$$g_{\text{ns}} = (2I + 1)(4I^2 + 4I + 3)/3 \quad \text{for } K = 3m, \quad (8.24a)$$

$$g_{\text{ns}} = (2I + 1)(4I^2 + 4I)/3 \quad \text{for } K = 3m \pm 1. \quad (8.24b)$$

For molecules belonging to other point groups, the statistical weights can be determined analogously. Often, this requires a tedious analysis of the possible nuclear spin functions and their symmetry. A more detailed account with many examples can be found in [8.3].

8.1.7

Line Profiles of Absorption Lines

The spontaneous lifetimes of rotational levels in the electronic ground state are long enough so that the natural linewidths of the absorption lines are too small to be resolved experimentally. Doppler widths are also small in the microwave region, because the frequencies are small compared to those of optical transitions, and they are in general negligible compared with pressure broadening. The line profile of the absorption coefficient $\alpha(\nu)$ is therefore a Lorentz profile,

$$\alpha(\nu) = \alpha(\nu_0) \frac{(\Delta\nu/2)^2}{(\nu - \nu_0)^2 + (\Delta\nu/2)^2}, \quad (8.25)$$

where $\alpha(\nu_0)$ is the maximum absorption at the mean frequency $\nu(0)$ and $\Delta\nu$ is the full width at half maximum. The area below the absorption profile $\alpha(\nu)$ is a measure for the total absorption due to this rotational transition. It is also called line strength S . Integration of Eq. (8.25) yields

$$S = \int \alpha(\nu) d\nu = \Delta\nu \alpha(\nu_0) \pi/2 \quad \Rightarrow \quad \alpha(\nu_0) = \frac{2S}{\pi \Delta\nu}. \quad (8.26)$$

For the absorption at the line maximum of a rotational transition $|i\rangle \rightarrow |k\rangle$, we obtain from Eq. (8.19)

$$\alpha(\nu_0) = g(J, K) g_{\text{ns}} \frac{N}{Z} \frac{4\pi\nu_0^2}{3\varepsilon_0 k_B T \Delta\nu} |D_{ik}|^2. \quad (8.27)$$

Hence, the absorption coefficient at the line maximum is proportional to the square ν_0^2 of the transition frequency and inversely proportional to the line width and the temperature.

8.2

Vibration–Rotation Transitions

In the harmonic approximation, the term value of an arbitrary vibrational state can be written as the sum of the term values of the excited normal vibrations with degrees of degeneracy d_i ,

$$G(v_k) = \sum \omega_i \left(v_i + \frac{d_i}{2} \right). \quad (8.28)$$

Tab. 8.2 Wavenumbers (cm^{-1}) of normal modes for some triatomic molecules.

Molecule	ν_1	ν_2	ν_3
CO ₂	1383.3	667.3	2284.5
CS ₂	658.0	396	1535.4
HCN	2096.7	713.5	3311.5
H ₂ O	3657.1	1594.8	3755.8
D ₂ O	2668.1	1178.4	2787.7
H ₂ S	2614.4	1182.6	2628.5
NO ₂	1319.8	749.7	1616.9
SO ₂	1151.7	517.8	1362.0

Hence, in the harmonic approximation, the molecule can be considered a superposition of harmonic oscillators, each of which experiences vibrational transitions by absorption or emission of radiation that can be treated exactly as those of a diatomic molecule (see Sect. 4.2.4).

Table 8.2 lists the wavenumbers of normal modes for a number of molecules.

Due to the anharmonicity of the molecular potential, the vibrational term values in real molecules are not equidistant but move closer if the vibrational energy increases. Furthermore, the anharmonic potential mediates a coupling between different normal vibrations, thereby shifting their term values, which are no longer a simple sum of the term values of normal modes but include additional coupling terms (see Sect. 6.3.5). The wavefunctions of higher vibrational levels are then linear combinations of vibrational functions of the individual coupling states. This renders possible transitions to levels which would be forbidden in the absence of this coupling. This is one of the reasons why the density of levels increases rapidly with increasing energy, and correspondingly the spectrum becomes more complex.

8.2.1

Selection Rules and Intensities of Vibrational Transitions

The symmetries of the vibrational wavefunctions decide between which vibrational levels transitions can occur. If we expand the nuclear dipole moment

$$\mu_{\text{nuc}}(q) = \mu_{\text{nuc}}(0) + \left(\frac{d\mu_{\text{nuc}}}{dq} \right)_0 q + \dots \quad (8.29)$$

in a Taylor series in powers of the displacements q from the equilibrium positions $q = 0$ of a normal mode and substitute it into the matrix element

$$\begin{aligned} D_{mk} &= \int \Psi_m^{\text{vib}} \mu_{\text{nuc}}(q) \Psi_k^{\text{vib}} \\ &= \mu_{\text{nuc}}(0) \int \Psi_m^{\text{vib}} \Psi_k^{\text{vib}} dq + \frac{d}{dq} (\mu_{\text{nuc}})_0 \int \Psi_m^{\text{vib}} q \Psi_k^{\text{vib}} dq, \end{aligned} \quad (8.30)$$

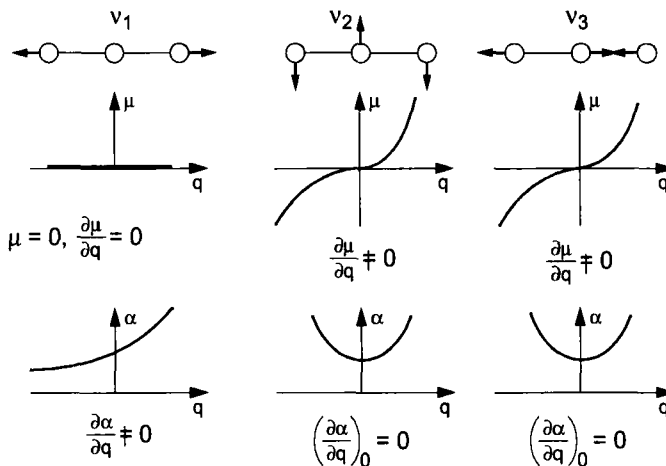


Fig. 8.8 Dipole moment μ_{nuc} and polarizability α as a function of the normal coordinate q in CO_2 .

the first term vanishes, in complete analogy to the situation in diatomic molecules, because the vibrational wavefunctions are orthogonal. Hence, the second term in Eq. (8.30) is the matrix element for transitions between the vibrational levels $|m\rangle$ and $|k\rangle$. It is nonzero only if both factors $[d(\mu_{\text{nuc}})/dq]_0$ and the integral are nonzero.

This means that only normal vibrations during which the molecular dipole moment changes contribute to the infrared absorption; they are thus called *infrared active*. In asymmetric molecules such as HCN, all normal modes change either the magnitude or the direction of the dipole moment and are thus infrared active. Only in symmetric molecules such as CO_2 can normal modes exist for which the dipole moment does not change; they are called *infrared inactive*. For example, the symmetric stretching vibration ν_1 in CO_2 is infrared inactive, because the dipole moment remains zero throughout this vibration, whereas the bending vibration ν_2 and the antisymmetric stretching vibration are infrared active (Fig. 8.8). However, there are also symmetric molecules (such as H_2O) in which all normal vibrations are infrared active because the dipole moment μ_{nuc} changes during all of them.

For nondegenerate vibrational levels, the second integral in Eq. (8.30) is nonzero only if the integrand is totally symmetric. In the language of group theory (see Sect. 5.5.4), this means that for transitions between nondegenerate vibrational levels ψ_m and ψ_k the following relation for the respective symmetry species Γ must hold:

$$\Gamma(\psi_m)\Gamma(q)\Gamma(\psi_k) = A, \quad (8.31)$$

where A is the totally symmetric representation for an arbitrary point group.

If at least one of the vibrational levels is degenerate, the product Eq. (8.31) can be written as a sum of irreducible representations, and the condition $D_{mk} \neq 0$ reduces to the requirement that upon reduction of the product Eq. (8.31) to a sum (see Sect. 5.5.4) at least one of the summands is the totally symmetric representation A .

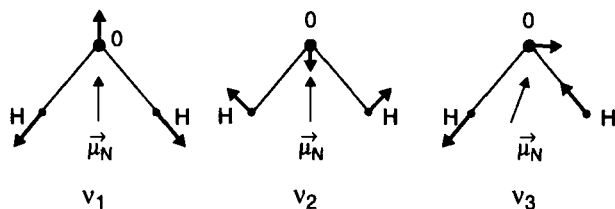


Fig. 8.9 Changing magnitude of the dipole moment during the symmetric vibrations ν_1 and ν_2 and changing direction of μ_{nuc} during the antisymmetric stretching vibration ν_3 .

If we consider absorption transitions starting from the vibrational ground state, their vibrational wavefunctions will always be totally symmetric, that is, their symmetry type is A . For the integrand to be totally symmetric, the product $\Gamma(q)\Gamma(\kappa_k)$ must then also be of symmetry A . Hence, all vibrational levels satisfying this symmetry condition can be reached through electric dipole transitions.

The product $d(\mu_{\text{nuc}})/dq|_{q_0} \times q$ has the same symmetry properties as q because the first factor is simply a number, that is, a scalar. The vibrational amplitude $q = (q_x, q_y, q_z)$ is a vector transforming like a translation vector under the symmetry operations of the group, and we can therefore gather the symmetry species of the components of μ_{nuc} directly from the character table of the respective symmetry group.

As an example, we will consider molecules of point group C_{2v} . A quick glance at the character table shows that for the z component of q , having A_1 symmetry, all vibrational levels with A_1 symmetry can be reached from the ground state, whereas for the x component with B_1 symmetry, only levels with symmetry B_1 can be reached, because the group multiplication table (Table 5.1) shows that $B_1 \times B_1 = A_1$.

Analogously, the y component of q enables transitions into states with symmetry B_2 . The totally symmetric stretching vibration ν_1 and the bending vibration ν_2 (both of symmetry A_1) can therefore only be excited from the ground state if q possesses a component along z , whereas the antisymmetric stretching vibration ν_3 can be excited if q possesses a component along y .

Another example is the bent H_2O molecule, in which the dipole moment is oriented along the C_2 axis (Fig. 8.9), which we choose to coincide with the z axis, and μ_{nuc} changes during all normal vibrations so that all are infrared active. For the normal vibrations ν_1 and ν_2 (both with symmetry A_1) only the magnitude of μ_{nuc} changes, but for the antisymmetric stretching vibration ν_3 , the direction of μ_{nuc} changes, too (Fig. 8.9).

The linear molecule CO_2 belongs to the point group $D_{\infty h}$. The symmetric stretching vibration ν_1 , in which the two oxygen atoms oscillate symmetrically with respect to the center of inversion, has symmetry Σ_g^+ as evident from the character table, because the vibration remains unchanged under all symmetry operations.

The antisymmetric stretching vibration ν_3 (Fig. 6.8b) has Σ_u^+ symmetry. For transitions of ν_1 , $d(\mu_{\text{nuc}})/dt = 0$ and there is thus no absorption in the infrared. The upper

level in ν_3 transitions has Σ_u^+ symmetry. As the displacement q has also Σ_u^+ symmetry for ν_3 , the integrand of the second term in Eq. (8.30) is totally symmetric, and the transition is infrared active.

The doubly degenerate bending vibration ν_2 has E symmetry. The vector q points along x or y . Hence, the integrand has symmetry

$$\Sigma_g^+ \otimes E_{1u} \otimes E_{1u} = \Sigma_g^+ \otimes \Pi_u \otimes \Pi_u = \Sigma_g^+ \otimes (\Sigma_g^+ + \Sigma_g^- + \Delta_g)$$

and contains the totally symmetric representation. The ν_2 vibration is therefore infrared active.

If for a transition $|k\rangle \leftarrow |0\rangle$ starting from the vibrational ground state $|0\rangle$ the upper vibrational level is degenerate, the condition $\Gamma(\mu_{\text{nuc}})\Gamma(\psi_0)\Gamma(\psi_k) \ni A_1$ still must be satisfied for the transition to be infrared active.

As an example, we consider the NH_3 molecule, belonging to point group C_{3v} . The two normal vibrations ν_{3a} and ν_{3b} in Fig. 6.8c are degenerate, and their wavefunctions are linear combinations of symmetry type E . From the C_{3v} character table we see that the x and y components of μ_{nuc} have also E symmetry. The product $E \times E = A_1 + A_2 + E$ contains the totally symmetric representation A_1 , and therefore the matrix elements for the transitions from the vibrational ground state to the ν_3 levels are allowed for the x and y components of μ_{nuc} .

We see from these examples that group theory is a powerful tool for deciding whether a transition is allowed or forbidden. However, symmetry arguments provide no information on the intensity of an allowed transition, which is given by the product [see Eqns. (8.19) and (8.27)]

$$\Delta I(m \leftrightarrow k) \propto I_0 N_m L \left(\frac{d\mu_{\text{nuc}}}{dq} \right)_{q_e} \left| \int \psi_m^* q \psi_k dq \right|^2 \quad (8.32)$$

of population density $N_m = g_m N / Z$ in the absorbing vibrational state ν_m (where ν_m represents the ensemble of all vibrational quantum numbers of the absorbing level), the statistical weight g_m , the dipole moment change $d\mu_{\text{nuc}}/dq$, and the square of the transition matrix element D_{mk} . In other words, it depends on the electron configuration of the specific molecule and not only on its symmetry group.

8.2.2

Fundamental Transitions

In Sect. 6.3 we saw that except for very large vibrational excitations, the energy of the upper vibrational level can be written as a linear combination of the energies of the contributing normal vibrations Eq. (6.81). The nuclei oscillate synchronously around their equilibrium positions, but for degenerate vibrational modes not necessarily in

phase. As the vibrational frequencies depend on the masses of the vibrating nuclei and on the force constants of the restoring forces $F = -\text{grad} E_{\text{pot}}$, which in turn are determined by the change in potential energy upon displacement from the equilibrium position, these vibrational frequencies are characteristic for each specific type of molecule. For transitions from the vibrational ground state into excited vibrational states, they appear as absorption frequencies in the spectrum. The line positions provide spectroscopists with unique information on the molecules contained in a sample. The corresponding spectral region is therefore often called the *fingerprinth region* of the spectrum (Table 8.2). Vibrational transitions from the ground into an excited state are enumerated according to their symmetry, and the transitions are arranged in order of decreasing frequencies within a symmetry class. The ordering of the different symmetry species follows the scheme introduced by Mullikan and completed by Herzberg [8.4].

For example, in a molecule with C_{2v} symmetry, the two totally symmetric a_1 vibrations are designated ν_1 and ν_2 , the antisymmetric stretching vibration of b_2 symmetry is ν_3 . Hence, the three vibrations of the H_2O molecule are ν_1 (a_1 stretching vibration, 3657 cm^{-1}), ν_2 (a_1 bending vibration, 1595 cm^{-1}) and ν_3 (b_2 antisymmetric stretching vibration, 3756 cm^{-1}).

Apart from the normal vibrational modes, in which more or less all atoms in the molecule participate, so-called *local vibrational modes* occur frequently, arising from the vibration of a specific group of atoms within the molecule rather than the complete molecule. For example, if a lightweight atom A is connected to a heavy atom B which in turn is bonded weakly to the rest of molecule, then the frequency ν_{loc} of the local vibration between A and B is almost independent of the remainder of the molecule. The heavy atom B acts in this case like a wall against which A vibrates. An example for such local modes is the O–H vibrational frequency, which does not differ significantly in the two molecules CH_3OH (methanol) and $\text{CH}_3\text{CH}_2\text{OH}$ (ethyl alcohol).

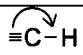
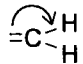
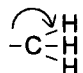
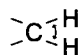
The absorption frequencies of such local vibrational modes are therefore characteristic for specific groups of atoms within the molecule. Table 8.3 lists some examples for the wavenumbers of local vibrations of typical groups of atoms in molecules.

8.2.3

Overtone and Combination Bands

For harmonic potentials, the selection rule for transitions between vibrational levels is simply $\Delta v = 1$ for each normal vibration, as in the case of diatomic molecules. The anharmonicity of the potential, which is more pronounced in polyatomic than in diatomic molecules, enables transitions with $\Delta v = 2, 3, 4, \dots$ to occur in the infrared spectrum. The intensities of these so-called *overtone transitions* decreases rapidly with increasing Δv , however.

Tab. 8.3 Characteristic vibrational wavenumbers for stretching and bending vibrations for some groups of atoms in molecules [8.5].

Stretching vibrations		Bending vibrations	
Group	$\tilde{\nu} / \text{cm}^{-1}$	Group	$\tilde{\nu} / \text{cm}^{-1}$
$\equiv\text{C}-\text{H}$	3300		700
$\text{C}=\text{C}\begin{matrix} \text{H} \\ \diagup \\ \text{H} \end{matrix}$	3020		1100
$\text{O}=\text{C}\begin{matrix} \text{H} \\ \diagup \\ \text{H} \end{matrix}$	2800		1000
$\geq\text{C}-\text{H}$	2960	$\text{C}\equiv\text{C}-\text{C}$	300
$-\text{C}\equiv\text{C}-$	2050		1450
$\geq\text{C}=\text{C}\leq$	1650		
$\geq\text{C}=\text{O}$	1700		

In addition, so-called combination transitions can appear in the spectrum, in which the quantum numbers of two or more normal modes change simultaneously (Fig. 8.10).

There are essentially two reasons for the appearance of overtone transitions.

1. The anharmonicity of the potential, which effects the appearance of overtones in the frequency spectrum of the anharmonic oscillator (Fourier analysis of the anharmonic vibration).
2. In such anharmonic potentials, the dependence of the dipole moment on the nuclear coordinates is no longer linear, but Eq. (8.29) contains higher-order terms $d^n \mu_{\text{nuc}} / dq^n$ with $n > 1$, and these can lead to overtone frequencies.

The symmetry selection rules for overtone transitions starting from the vibrational ground state are the same as for fundamental transitions.

Thus, an overtone transition is infrared active if at least one component of the transition dipole moment belongs to the same symmetry species as the vibrational function of the upper level. Table 8.4 shows the symmetry types of some excited vibrational states for a linear and a bent triatomic molecule. From this list it is immediately evident which of the overtone transitions are infrared active and which are Raman active (see Sect. 8.4).

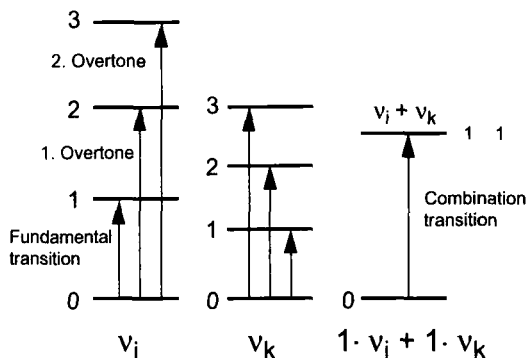


Fig. 8.10 Term diagram for fundamental, overtone and combination transitions.

To describe an overtone or combination transition in a shorthand notation, the transition $\nu_n(v'') \rightarrow \nu_n(v')$ from v'' to v' vibrational quanta in the n th normal vibration ν_n is abbreviated by

$$n_{v''}^{v'} = (0, 0, \dots, \nu_n^{v''}, 0) \rightarrow (0, 0, \dots, \nu_n^{v'}, 0).$$

Analogously, a combination transition $\nu_n(v_n'') + \nu_m(v_m'')$ to $\nu_n(v_n') + \nu_m(v_m')$ is written

$$n_{v_n''}^{v_n'} m_{v_m''}^{v_m'} = (0, 0, \dots, \nu_n^{v_n''}, 0, \nu_m^{v_m''}, 0) \rightarrow (0, 0, \dots, \nu_n^{v_n'}, 0, \nu_m^{v_m'}, 0).$$

Hence, the transition $(0, 0, 0) \rightarrow (0, 2, 0)$ is abbreviated 2_0^2 , and the transition $(0, 0, 1) \rightarrow (1, 0, 2)$ becomes $1_0^1 3_1^2$.

Measurement of overtone transitions provides important information on the anharmonicity of the potential and the coupling between different vibrations, which lead to a shift in the vibrational energies. In Sect. 6.3.5, the influence of the anharmonic potential on the coupling between different vibrational levels has been discussed. The coupling becomes particularly large if the levels are closely spaced. Again, a strict symmetry selection rule governs the coupling: *only levels of like symmetry can interact!*

Tab. 8.4 Symmetry types of excited vibrational states in linear and bent triatomic XY_2 molecules.

ν_1	ν_2	ν_3	bent XY_2 (C_{2v})	linear XY_2 ($D_{\infty h}$)
0	0	0	A_1	Σ_g^+
0	1	0	A_1	Π_u
1	0	0	A_1	Σ_g^+
0	0	1	B_2	Σ_u^+
1	0	2	A_1	Σ_g^+
1	3	0	A_1	Π_u, Φ_u

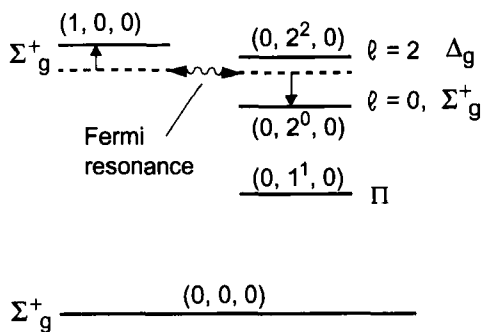


Fig. 8.11 Fermi resonance between the vibrational levels $(0, 2^0, 0)$ and $(1, 0, 0)$ of like symmetry in the CO₂ molecule. The dotted lines show the positions of the unperturbed levels, which repel each other due to the Fermi resonance.

Often, a fundamental transition of one normal vibration and an overtone transition of another normal vibration lead to excited levels of equal symmetries and almost equal energies. In such cases, the interaction between the levels is particularly strong and leads to large frequency shifts for both interacting levels (*Fermi resonance*). For example, the two vibrational levels $(0, 2, 0)$ at 1285.5 cm^{-1} and $(1, 0, 0)$ at 1388 cm^{-1} of the CO₂ molecule have the same symmetry and are, neglecting the perturbation, energetically very close (Fig. 8.11). The interaction shifts the lower level to lower wavenumbers and the higher level to higher wavenumbers (see also Sect. 9.1.3).

For high vibrational excitation, the density of levels becomes larger, and an excited level can interact with several other levels of like symmetry. Such mutually coupled levels are called a *Fermi polyad*.

In some molecules, two fundamental transitions of normal vibrations with different symmetries have almost identical energies. Although they cannot interact directly, overtone vibrations of both modes can possess the same symmetry and can interact with each other. This was first recognized by Darling and Dennison, and this interaction is therefore called Darling–Dennison resonance. For example, the two overtone vibrations $2\nu_1$ and $2\nu_3$ in the H₂O molecule both have a_1 symmetry (although ν_3 has b_2 symmetry), because for $2\nu_3$, $b_2 \times b_2 = a_1$, and they lie closely adjacent at 7201 cm^{-1} and 7445 cm^{-1} , respectively.

At sufficiently high vibrational excitation, a molecule may dissociate. In normal vibrations, all atoms of the molecule participate in the vibration. To dissociate a molecule, however, sufficient energy must be concentrated in the bond between the prospective fragments. If we compare the experimentally determined bond dissociation energies with the total vibrational energy in a molecule, we see that for very high vibrational excitation, the energy cannot be distributed evenly among all atoms in a normal-mode model but must be concentrated in those bonds that finally break. To explain this phenomenon, the model of localized vibrational modes has been introduced (see Sect. 8.2.2).

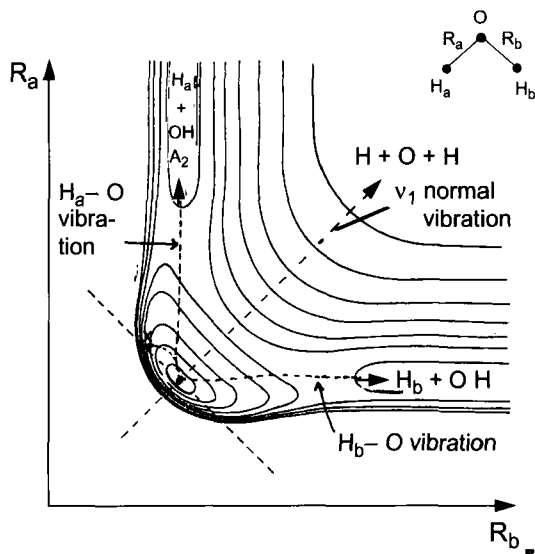


Fig. 8.12 Contour line representation of the H_2O potential energy surface illustrating the dissociation upon excitation of local vibrational modes.

In this model the H_2O molecule is treated, for example, as consisting of two anharmonic diatomic oscillators, each consisting of a hydrogen atom vibrating against the much heavier oxygen atom. The restoring force is the O–H bond. The two oscillators are weakly coupled by the heavy oxygen atom. The coupling mediates a periodic shift of the vibrational energy from one oscillator to the other. If the energy concentrated in one oscillator is large enough to break the O–H bond, the molecule dissociates into $\text{OH} + \text{H}$.

In the potential energy diagram of Fig. 8.12, this means that the dissociation proceeds over the lowest possible energy barrier.

8.2.4

Rotational Structure of Vibrational Bands

Exactly as in diatomic molecules, vibrational transitions in polyatomic molecules consist of many rotational lines originating from all occupied rotational levels (J, K) for symmetric top rotors or ($J, K_a K_c$) for asymmetric top molecules in the lower vibrational level and obeying the selection rules $\Delta J = 0, \pm 1$, $\Delta K = 0, \pm 1, \pm 2, \dots$ and the symmetry selection rules discussed in Sect. 8.2.2.

In linear molecules, vibrational transitions $\Sigma \rightarrow \Sigma$ contain only rotational lines with $\Delta J = \pm 1$ (Fig. 8.13), whereas in transitions $\Sigma \leftrightarrow \Pi$ rotational lines with $\Delta J = 0$ can also occur, because here the vibrational angular momentum ensures angular momentum conservation (of the complete system of photon plus molecule) during absorption.

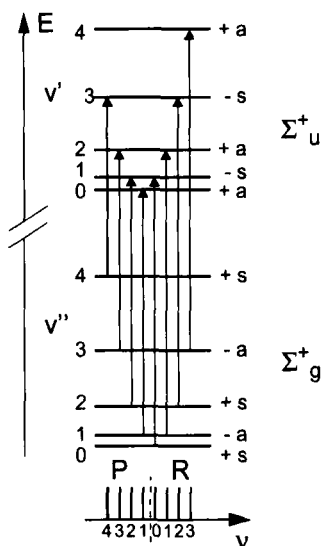


Fig. 8.13 Rotational structure of a vibrational band in a $\Sigma_g \leftrightarrow \Sigma_u$ vibrational transition of a linear molecule.

For symmetric top molecules, both parallel ($\Delta K = 0$) and perpendicular ($\Delta K = \pm 1$) vibrational bands contain P, Q and R branches, except for transitions from $K = 0 \rightarrow K = 0$, where the Q branch with $\Delta J = 0$ is missing. Hence, each vibrational band consists of two or three K subbands. The wavenumbers of the rotational lines are given by the differences of the rotational term values Eq. (6.28) and the vibrational term values Eq. (6.84b). For example, for perpendicular bands with $\Delta K = \pm 1$,

$$\begin{aligned} \nu(\Delta K = \pm 1) &= \nu_0 + F'_{v'}(J', K \pm 1) - F''_{v''}(J'', K) \\ &= \nu_0 + B'_v J'(J' + 1) - B''_v J''(J'' + 1) + (A' - B') \\ &\quad \pm 2(A' - B')K + [(A' - A'') - (B' - B'')]K^2, \end{aligned} \quad (8.33)$$

where ν_0 denotes the band origin.

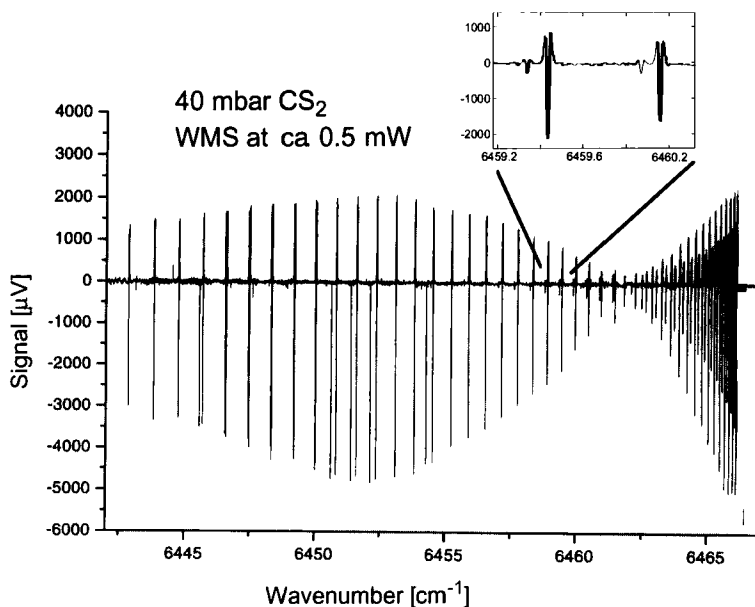
In transitions to vibrational levels with E symmetry (twofold degenerate), all rotational levels with $K > 0$ are split into two components because of the Coriolis interaction in the rotating molecule (see Sect. 6.3.6) and hence all rotational transitions are also split into two components (l doubling). We therefore obtain from Eq. (6.96) for the wavenumbers in place of Eq. (8.33),

$$\begin{aligned} \nu(\Delta K = \pm 1) &= \nu_0 + B'_v [J'(J' + 1) - l^2] \\ &\quad - B''_v J''(J'' + 1) \pm (q'_v/4)(v' + 1)J'(J' + 1) \\ &\quad + (A' - B') \pm 2(A' - B')K + [(A' - A'') - (B' - B'')]K^2. \end{aligned} \quad (8.34)$$

Tab. 8.5 Selection rules in vibration–rotation transitions of asymmetric top molecules.

Transition	Selection rules for asymmetric tops		Band type in symmetric tops	
	$K'_a, K'_c \leftrightarrow K''_a, K''_c$	$\Delta K, \Delta J$	prolate	oblate
Type A	$ee \leftrightarrow eo$ $eo \leftrightarrow oo$	$\Delta K_a = 0, \pm 2, \pm 4$ $\Delta K_c = 1, \pm 3, \dots$ $\Delta J = 0, \pm 1$	\parallel $\Delta K_a = 0$	\perp $\Delta K_c = \pm 1$
Type B	$ee \leftrightarrow oo$ $oe \leftrightarrow eo$	$\Delta K_a = \pm 1, \pm 3, \dots$ $\Delta K_c = \pm 1, \pm 3, \dots$ $\Delta J = 0, \pm 1$	\perp $\Delta K_a = \pm 1$	\perp $\Delta K_c = \pm 1$
Type C	$ee \leftrightarrow oe$ $eo \leftrightarrow oo$	$\Delta K_a = \pm 1, \pm 3, \dots$ $\Delta K_c = 0, \pm 2, \dots$ $\Delta J = 0, \pm 1$	\perp $\Delta K_a = \pm 1$	\parallel $\Delta K_c = 0$

For asymmetric top molecules, the symmetry selection rules for the quantum numbers J , K_a and K_c in vibration–rotation transitions are the same as for pure rotational transitions, see Table 8.1. They depend on the orientation of the dipole moment in the molecule. Table 8.5 shows the relations between the A , B and C transitions and the parallel and perpendicular transitions in the limiting cases of the prolate and oblate symmetric top, respectively. Figure 8.14 shows, as an example for an overtone vibration–rotation spectrum, a section from the high-resolution overtone spectrum of the band $(22^0_3) \leftarrow (000)$ of the CS_2 molecule.

**Fig. 8.14** Section from the high-resolution spectrum of the overtone band $(22^0_3) \leftarrow (000)$ of the CS_2 molecule [8.6].

8.3

Electronic Transitions

An electronic transition consists of a band system, that is, of a manifold of vibrational bands, each consisting of many rotational lines, originating from the occupied vibration-rotation levels (v'', J'', K'') in the lower electronic state and ending in the levels (v', J', K') in the upper electronic state. The intensities of the individual lines depend on the corresponding matrix element, which is determined, in complete analogy to the case of diatomic molecules, solely by the first term in Eq. (4.25) representing the electronic contribution to the dipole moment, because the second term vanishes, within the Born-Oppenheimer approximation, on account of the orthogonality of the electronic wavefunction.

In polyatomic molecules with N atoms, the integration over $d\tau_{\text{nuc}}$ comprises all $3N$ nuclear coordinates.

The electronic dipole matrix element

$$D_{\text{el}} = \int \psi_{\text{el}}'^* \mu_{\text{el}} \psi_{\text{el}}'' d\tau_{\text{el}} \quad (8.35)$$

in general depends on the nuclear configuration, and it changes during a molecular vibration from its value $D_{\text{el}}(q_e)$ at the equilibrium configuration q_e to the value

$$D_{\text{el}}(q) = D_{\text{el}}(q_e) + \sum_k \left(\frac{\partial D_{\text{el}}}{\partial Q_k} \right)_0 Q_k + \dots \quad (8.36)$$

at a displacement $Q_k = q_k - q_{k,e}$ of the k th normal vibration, where q is a shorthand notation for all nuclear coordinates. If we substitute the Taylor series expansion Eq. (8.36) into the matrix element

$$D_{\text{el,vib}} = \int \psi_{\text{el}}'^* \chi_m'^*(v') \mu_{\text{el}} \psi_{\text{el}}'' \chi_k''(v'') d\tau_{\text{el}} d\tau_{\text{nuc}}, \quad (8.37)$$

where $\chi = \psi_{\text{vib}} \psi_{\text{rot}}$ are the nuclear wavefunctions, we obtain in analogy to the vibrational transitions in Sect. 8.2,

$$D_{\text{el,vib}} = D_{\text{el}}(q_e) \int \psi_{\text{vib}}'^* \psi_{\text{vib}}'' d\tau_{\text{nuc}} + \sum_k \left(\frac{\partial D_{\text{el}}}{\partial Q_k} \right)_0 \int \Psi_v'^* Q_k \Psi_v'' d\tau_{\text{nuc}} + \dots \quad (8.38)$$

This is the same result as in Sect. 8.2, only with the nuclear dipole moment μ_{nuc} replaced by the electronic dipole moment μ_{el} . For allowed electronic transitions, $D_{\text{el}}(q_e) \neq 0$, and the first term in Eq. (8.38) usually provides the largest contribution to $D_{\text{el,vib}}$. For forbidden electronic transitions (i.e., transitions for which the product $\psi_{\text{el}}'^* \mu_{\text{el}} \psi_{\text{el}}''$ does not contain the totally symmetric representation), $D_{\text{el}}(q_e) = 0$, and the second term (the sum) in Eq. (8.38) provides the only contribution to the transition probability.

As the different vibrational levels can possess different symmetries and the transition probability depends on these symmetries, it is helpful to split the sum in Eq. (8.38)

into one partial sum over totally symmetric vibrations and a second partial sum over the other vibrations,

$$\sum_k = \sum_s \left(\frac{\partial D_{el}}{\partial Q_s} \right)_0 \int \Psi_v'^* Q_s \Psi_v'' d\tau_{nuc} + \sum_a \left(\frac{\partial D_{el}}{\partial Q_a} \right)_0 \int \Psi_v'^* Q_a \Psi_v'' d\tau_{nuc} . \quad (8.39)$$

For forbidden electronic transitions, not only $D_{el}(q_e) = 0$, but also the first term in Eq. (8.39) is zero, because here the integrand does not contain the totally symmetric representation. In this case, the second sum in Eq. (8.39) is solely responsible for the transition probability. This means that the transition is only made possible by the dependence of the electronic transition dipole moment on the nuclear coordinates.

In the quantum-mechanical description, this fact enters as a coupling between electronic and vibrational states of like symmetry. Such a coupling constitutes a violation of the Born–Oppenheimer approximation, because the wavefunction $\Psi_{el,vib}$ can now no longer be written as a product $\psi_{el}\psi_{vib}$. Such coupled states are a mixture of electronic and vibrational contributions, and they are thus called *vibronic states* $|\Psi_{el,vib}\rangle$. Their symmetry types can always be written as products, however, even if the BO approximation ceases to be valid.

An electronic transition $|\Psi'_{el,vib}\rangle \rightarrow |\Psi''_{el,vib}\rangle$ is allowed only if the product of the symmetry species obeys the relation

$$\Gamma(\Psi'_{el,vib}) \times \Gamma(\Psi''_{el,vib}) = \Gamma(\psi'_{el}) \times \Gamma(\psi'_{vib}) \times \Gamma(\psi''_{el}) \times \Gamma(\psi''_{vib}) \in \Gamma(T_x), \Gamma(T_y) \text{ or } \Gamma(T_z) , \quad (8.40)$$

that is, if it corresponds to a translation T_x , T_y or T_z , because the dipole moment is a vector $\mu = (\mu_x, \mu_y, \mu_z)$, and the product of the representations $\Gamma(T_i) \times \Gamma(\mu_i)$ ($i = x, y, z$) has symmetry A .

To elucidate these considerations, we give two examples illustrated by Fig. 8.15.

In the SO_2 molecule (point group C_{2v}), the transition ① from the electronic ground state A_1 into the excited state A_2 is forbidden (Fig. 8.15a), because none of the components of the dipole moment has A_2 symmetry. The transition ② from the vibrational

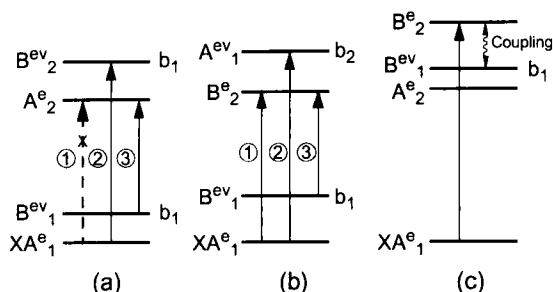


Fig. 8.15 Electronic transitions enabled by coupling of electronic and vibrational wavefunctions.

ground state with a_1 symmetry in the A_1 state into a vibrational level v' with b_1 symmetry in the electronic A_2 state is allowed, however, if the coupling between electronic and vibrational wavefunction is sufficiently strong. In this case the wavefunction $\Psi_{\text{el,vib}}$ has symmetry B_2 , and the matrix element has A_1 symmetry for μ_y . The transition probability is then determined by the second sum in Eq. (8.39). Similarly, the transition ③ from an excited b_1 vibrational level in the electronic ground state into an a_1 vibrational level in the A_2 state is also allowed. Such a transition is also called a *hot band*, because the population of the absorbing excited vibrational level b_1 increases with the temperature T , and therefore the intensity of this band increases with T .

Another example (Fig. 8.15b) is an electronic transition $A_1 \rightarrow B_2$, which is allowed for the y component of the dipole moment (with symmetry b_2) if the upper vibrational level has symmetry a_1 . Transitions into vibrational levels with b_2 symmetry are also allowed, however, for the z component of the dipole moment.

A coupling between two electronic states can also lead to a mixing of wavefunctions and can allow additional transitions. For example, in Fig. 8.15c an electronic state with B_2 symmetry couples with a vibronic state $A_2^{\text{el}} \times b_1^{\text{vib}} = B_2^{\text{el,vib}}$ and thus enables the otherwise forbidden transition from the A_1 state into the A_2^{el} state for the y component of the dipole moment.

For the rotational structure of a band, the same selection rules as for vibration-rotation transitions apply. However, the rotational constants in the two electronic states differ in general more strongly than in two vibrational levels of the same electronic state so that the relative positions of the lines within a band can differ markedly for these two cases.

8.4

Fluorescence and Raman Spectra

An absorption spectrum consists of all allowed transitions originating from thermally occupied lower levels into all possible upper levels. The multitude of lines thus obtained depends on the number of occupied lower levels, that is, on the temperature. Lowering the temperature can simplify an absorption spectrum significantly (see Sect. 12.4.7).

In contrast, an emission spectrum can only be observed if energetically excited levels are occupied, for example, through electron impact in gas discharges, optical excitation, or at very high temperatures (e.g., in stellar atmospheres). In many cases it is possible experimentally to excite only a few or, ideally, even only a single upper level selectively. In such a case, the emission spectrum (also called *fluorescence spectrum*) becomes relatively simple. It consists of all allowed emission transitions from this single level into lower levels (Fig. 8.16a).

To illustrate the difference, Fig. 8.17 shows the Doppler-limited absorption spectrum of NO_2 at a temperature of 300 K compared with the fluorescence spectrum of a single, selectively excited vibration-rotation level in the electronically excited 2B_2

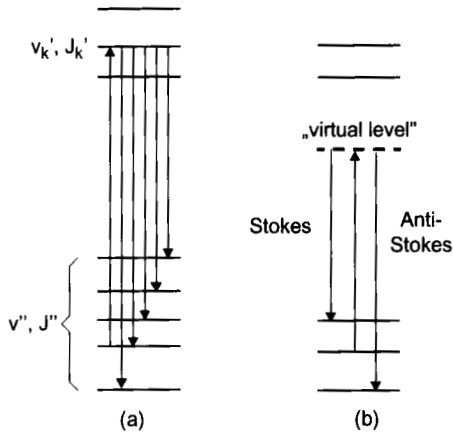


Fig. 8.16 Term diagram a) for fluorescence transitions from a selectively excited level in the upper electronic state and b) for Raman transitions which are

shifted to lower wavenumbers (Stokes lines) or to higher wavenumbers (anti-Stokes lines) against the nonresonant excitation line.

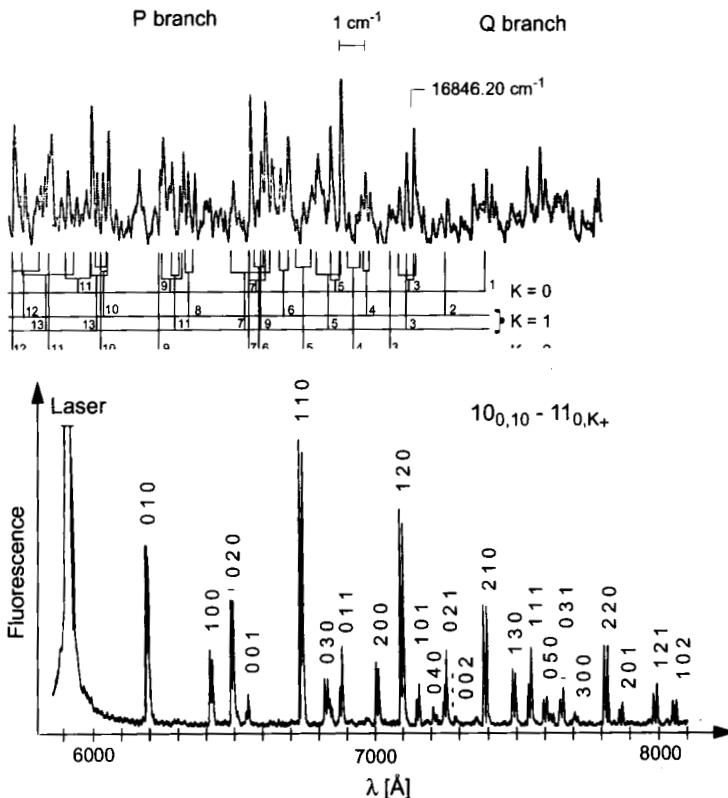


Fig. 8.17 Comparison of a high-resolution absorption spectrum of NO_2 and a laser-excited fluorescence spectrum.

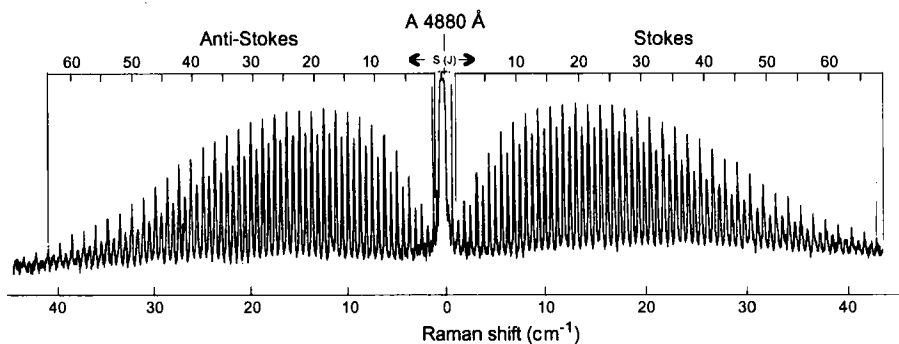


Fig. 8.18 Example of a rotational Raman spectrum for the linear molecule C_2N_2 upon excitation with an argon laser at $\lambda = 488 \text{ nm}$, showing Raman lines shifted by the energy differences $F(J+2) - F(J)$ with respect to the exciting line [8.7].

state. Whereas the line density in the absorption spectrum is so large that even at high resolution lines still overlap, all lines can easily be resolved in the fluorescence spectrum, which consists of all allowed vibrational bands. The reason for this difference is that because of the selection rule for the rotational quantum number J only transitions with $\Delta J = 0, \pm 1$ occur in the latter, so that each band consists of three lines only, a P, a Q, and an R branch (in the fluorescence spectrum, the Q lines are not visible because they are much weaker than P and R lines).

Whereas for optically excited fluorescence spectra, the exciting radiation must be in resonance with a molecular transition, this is not necessary for Raman spectra (Fig. 8.16b). Here, the *difference* between the wavenumbers of the exciting radiation and the Raman lines corresponds to the term values of the vibration–rotation levels in the electronic ground state. Apart from this principal difference, Raman spectra resemble fluorescence spectra very closely. The Raman lines are much weaker than fluorescence lines, however. Only in the resonant Raman effect can line intensities comparable to those of fluorescence spectra be achieved. Yet, there is one significant difference: spontaneous fluorescence transitions appear after a delay which corresponds to the lifetime of the excited level, whereas Raman radiation is due to inelastic scattering of the incident photons and appears essentially without delay.

The treatment of the Raman effect for polyatomic molecules is completely analogous to the case of diatomic molecules (see Sect. 4.4.2). However, because of the large number of vibration–rotation levels, the Raman spectrum of polyatomic molecules is in general more complex and contains more lines than in diatomic molecules. Figure 8.18 shows the rotational Raman spectrum of the C_2N_2 molecule, excited by the 488 nm line of an argon laser. The intensity alternation between even and odd rotational quantum numbers due to nuclear spin statistics (see Sect. 8.1.6) can be seen very clearly.

The positions of Raman lines can be calculated using a classical model. The incident light wave $\mathbf{E} = E_0 \cos \omega t$ induces a dipole moment

$$\boldsymbol{\mu}_{\text{ind}} = \tilde{\alpha} \mathbf{E} \quad (8.41a)$$

in the molecule, where $\tilde{\alpha}$ is the polarizability of the molecule, which in polyatomic molecules must be represented by a tensor of rank two, because the displacement of charges within the molecule depends on the direction of \mathbf{E} in the molecule-fixed reference frame. In component notation, Eq. (8.41a) becomes

$$\begin{aligned} \mu_x &= \alpha_{xx} E_x + \alpha_{xy} E_y + \alpha_{xz} E_z, \\ \mu_y &= \alpha_{yx} E_x + \alpha_{yy} E_y + \alpha_{yz} E_z, \\ \mu_z &= \alpha_{zx} E_x + \alpha_{zy} E_y + \alpha_{zz} E_z. \end{aligned} \quad (8.41b)$$

The polarizability depends in general on the displacements $q - q_e$ of the nuclei in the molecule. If we expand the polarizability $\tilde{\alpha}(q)$ at an arbitrary nuclear configuration in a Taylor series around the equilibrium position $q = q_e$, we obtain, in complete analogy to the expansion of the dipole moment,

$$\tilde{\alpha}_{ij}(q) = \tilde{\alpha}_{ij}(0) + \sum_{n=1}^{Q_N} \left(\frac{\partial \alpha_{ij}}{\partial q_n} \right)_0 Q_n + \dots, \quad (8.42)$$

where $Q_N = 3N - 6$ (or $3N - 5$ for linear molecules) is the number of normal vibrations $Q_n = Q_{n0} \cos(\omega_n t)$ of a molecule with N atoms. If we substitute Eq. (8.42) into Eq. (8.41a), we obtain

$$\boldsymbol{\mu}_{\text{ind}} = \tilde{\alpha}_{ij}(0) E_0 \cos(\omega t) + \frac{1}{2} \sum_{n=1}^{Q_N} \left(\frac{\partial \alpha_{ij}}{\partial q_n} \right)_0 Q_{n0} E_0 \times [\cos(\omega - \omega_n)t + \cos(\omega + \omega_n)t]. \quad (8.43)$$

The first term describes elastic Rayleigh scattering, the second inelastic Stokes Raman scattering, and the third anti-Stokes scattering. According to this argumentation, there should be a Stokes band for each normal vibration during which the molecular polarizability changes, and if the excitation starts from an excited vibrational level, an anti-Stokes band should also occur. Taking the anharmonicity of the potential into account, the vibrations q_n comprise overtone and combination bands in addition to the fundamental frequencies ω_n , which appear in the spectrum as additional lines.

As Fig. 8.8 shows, infrared and Raman spectra provide complementary information. For example, for the CO_2 molecule, the frequency of the ν_1 vibration can only be obtained from the Raman spectrum, because here $\partial \mu / \partial q_1 = 0$ but $\partial \alpha / \partial q_1 \neq 0$, whereas the opposite is true for ν_2 and ν_3 . In many molecules there are vibrations, however, which are both Raman and infrared active.

The intensities of Raman lines, which depend on the components of the polarizability tensor, can only be calculated using quantum theory. As the tensor is symmetric,

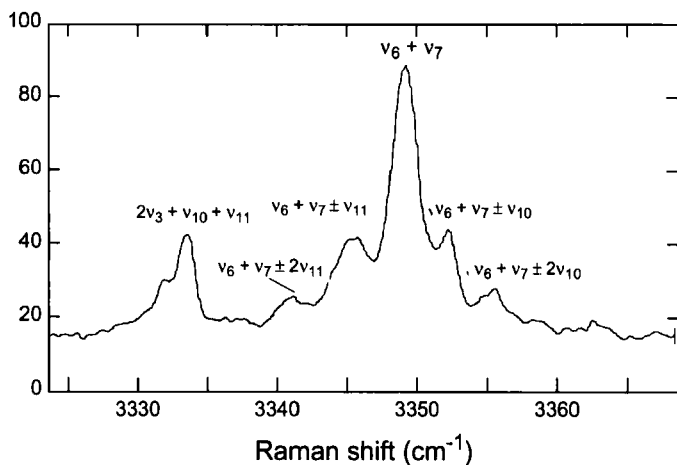


Fig. 8.19 Stokes Raman spectrum of the overtone vibrations in allene (C_3H_4) [8.8].

there are six unique components α_{ik} . A Raman transition is allowed if at least one of the six matrix elements

$$D_{mn}^{\text{Raman}} = \int \psi_m^* \alpha_{ik} \psi_n \, d\tau \quad i, k = x, y, z$$

is nonzero. The wavefunctions ψ_m and ψ_n are the vibrational wavefunctions of the initial and final levels of the Raman transition. Matrix elements with $m = n$ describe elastic Rayleigh scattering. As for electrical dipole transitions, the matrix elements for Raman transitions must contain the totally symmetric representation of the molecular point group.

For the rotational quantum number, similar selection rules apply. As Raman scattering is a two-photon process, the rotational quantum number can change by two. The condition $\Delta J = 0, \pm 1, \pm 2$ must be satisfied, with the additional constraint that $(J' + J'') \geq 2$. The angular momenta of the incident and scattered photons can be oriented parallel or antiparallel. If bending vibrations are excited, vibrational angular momentum also contributes to the balance of angular momentum.

Using lasers, even overtone vibrations can be detected in Raman spectra (Fig. 8.19), although their transition probabilities are smaller than for fundamental transitions by several orders of magnitude.

Raman spectroscopy, with its recent modification CARS (coherent anti-Stokes Raman spectroscopy, see Sect. 12.4.11), has provided pivotal contributions to the explanation of vibrational–rotational structures in the electronic ground states of polyatomic molecules [8.9, 8.10].

9

**Breakdown of the Born–Oppenheimer Approximation,
Perturbations in Molecular Spectra**

Measured molecular spectra often show deviations from what would be expected on the basis of our previous considerations. Certain lines in these spectra are said to be “perturbed” if their positions and intensities differ from the expected values. Also, the measured lifetimes of excited states are often shorter or longer than expected from transition probabilities determined from experimentally observed integrated absorption cross-sections. If the lifetimes are shorter, there must be deactivation channels other than spontaneous decay, called *radiationless transitions*. If the lifetimes are longer, there must be mechanisms that reduce the probability of radiative transitions.

All these perturbations are caused by couplings between the occupied excited level and two or more other levels. This chapter will deal with the most important types of perturbations.

9.1

What is a Perturbation?

We saw in Sect. 3.6.2 that the states of diatomic molecules can be expressed in the form of a rapidly converging polynomial in the vibrational and rotational quantum numbers v and J , where the coefficients are the *molecular constants*. This Dunham expansion describes the molecular structure in a given electronic state by a set of constants without making reference to a specific molecular model. With the aid of these molecular constants the majority of the different molecular term energies can be calculated, but they fail to provide physical insight in the reasons for specific deviations.

One of the assumptions in the Dunham expansion is that for each electronic state, a unique potential energy $E_{\text{pot}}(R)$ can be specified as a function of the nuclear arrangement, which determines the vibrational and rotational levels of this state. In other words, the validity of the Born–Oppenheimer approximation is assumed, in which the total wavefunction can be written as a product of electronic, vibrational, and rotational contributions (see Sect. 2.1). This means also that the total energy of a state is the sum of electronic, vibrational, and rotational energies.

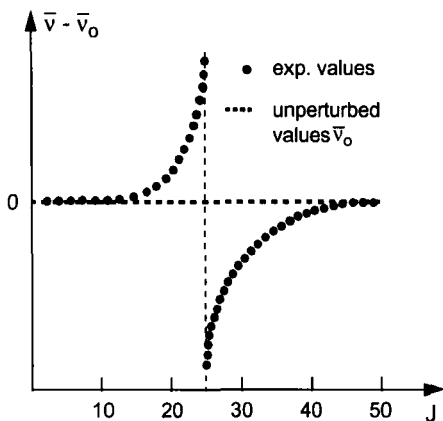


Fig. 9.1 Perturbation of rotational levels in the $4^1\Delta_g$ state of the Li_2 molecule.

If the experimentally determined energies of states and thus the line positions or transition intensities deviate more or less pronouncedly from the values calculated as described above (Fig. 9.1), perturbations are manifest. They are the result of couplings between the electronic wavefunction and the nuclear wavefunction, or between different electronic states, and they are particularly strong if two potential curves approach each other closely or even intersect. Such couplings entail a breakdown of the Born–Oppenheimer approximation, because as a consequence, the total wavefunction can no longer be written as a product $\psi_{el}\psi_{vib}\psi_{rot}$. This is especially important in electronically excited states, because here the spacings between different states are particularly small and the number of possible couplings is particularly large.

Another reason of deviations from the BO approximation are couplings between the electronic orbital angular momentum and the electron spins (*spin–orbit coupling*), mixing singlet and triplet states, or the nuclear spins, creating a hyperfine structure in the spectra. These spin-induced couplings can only be exactly described by relativistic calculations because they are not included in the nonrelativistic Schrödinger equation. However, they can be taken into account qualitatively by a vector model.

Two states do not necessarily interact with each other, because there are certain selection rules which must be satisfied, quite similar to the situation for absorption or emission transitions.

1. The total angular momentum of the molecule must be the same in both coupled states.
2. In molecules with a center of inversion, only states with like parity can interact, that is, $g \leftrightarrow u$, $g \leftrightarrow g$, $u \leftrightarrow u$.
3. In homonuclear diatomic and symmetric linear polyatomic molecules, both states must have the same symmetry, that is, $+\leftrightarrow -$, $+\leftrightarrow +$, $-\leftrightarrow -$.

These three selection rules are strictly obeyed.

If the projection quantum number Λ of the electronic orbital angular momentum in linear molecules is well defined (see below), the two interacting states must not differ by more than $\Delta\Lambda = 0$ or ± 1 .

Perturbations with $\Delta\Lambda = 0$ are called *homogeneous*, those with $\Delta\Lambda = \pm 1$ *heterogeneous*. Heterogeneous perturbations can occur only in rotating molecules or in linear molecules with vibrational angular momentum, because the total angular momentum can be conserved only if the change in Λ is compensated by a corresponding change in the rotational or vibrational angular momentum. In these heterogeneous perturbations, the coupling is mediated by Coriolis forces.

The extent of the perturbations depends on the coupling matrix element and on the overlap of the vibrational wavefunctions of the two coupling states. Hence, they are particularly large for nuclear arrangements where the potential curves of the interacting states intersect, because there the overlap of the vibrational functions of the two electronic states assumes a maximum.

In polyatomic molecules there are many more possible couplings than in diatomic molecules because of the much larger number of electronic, vibrational, and rotational states. For example, different energetically close vibrational levels in the same or in different electronic states can interact. Therefore, perturbations are much more prevalent in polyatomic molecules than in diatomic molecules. The application of group theory to their description proves highly advantageous, because the symmetry selection rules can be expressed in terms of the symmetry species of the participating states (see Ch. 5). If the symmetry of a state is expressed as a product $\Gamma_{\text{el,vib}} = \Gamma_{\text{el}} \times \Gamma_{\text{vib}}$ of the symmetry species of vibrational and electronic states, this product must be equal in both interacting states, even if the two factors may be different.

For example, in a C_{2v} molecule, only vibrations of symmetry $\Gamma_{\text{vib}} = a_1$ or b_2 occur. For possible perturbations by electronic states of symmetry Γ_{el} , the selection rule $A_1 \leftrightarrow B_2$ or $A_2 \leftrightarrow B_1$ for the electronic transition must be satisfied, because only then is there at least one normal vibration for which the total symmetry $\Gamma_{\text{el,vib}} = A_1 \times b_2 = B_2 \times a_1$ is the same for both interacting states [2.10, 9.1].

9.1.1

Quantitative Treatment of Perturbations

In the following, we will discuss perturbations in the spectra of di- and polyatomic molecules for a number of examples, and we will learn about some ways to eliminate them. The usual procedure to treat perturbations is to split the total Hamiltonian

$$\hat{H} = \hat{H}_0 + \hat{H}'$$

in an unperturbed part \hat{H}_0 and a perturbation part \hat{H}' (cf. Sect. 2.1.2). The exact choice of the splitting depends on the model chosen for the unperturbed system. In general, the BO approximation is used for the unperturbed system, that is, the eigenfunctions

of \widehat{H}_0 are the product functions Eq. (2.16)

$$\Psi_{ni}^{(0)} = \Phi_n^{\text{el}}(\mathbf{r}) \chi_{ni}(\mathbf{R}) \quad \text{with} \quad \chi = \psi_{\text{vib}} \psi_{\text{rot}} \quad (9.1)$$

of the BO approximation, where the Φ_{el} are the electronic wavefunctions of the rigid molecule, and the matrix $\langle \Psi_n^{(0)} | \widehat{H}_0 | \Psi_k^{(0)} \rangle$ is diagonal.

The Hamiltonian is the sum

$$\widehat{H} = \widehat{H}_{\text{el}} + \widehat{T}_{\text{vib}} + \widehat{T}_{\text{rot}} = \widehat{H}_0 + \widehat{H}' \quad (9.2)$$

of electronic, vibrational and rotational contributions. Which of these contributions are included in \widehat{H}_0 and which in \widehat{H}' depends on the specific problem (see below).

If we substitute into the Schrödinger equation

$$\widehat{H}\Psi_i = E_i\Psi_i \quad (9.3)$$

the linear combination

$$\Psi_i = \sum_{j=1}^n c_{ij} \Psi_j^{(0)} \quad (9.4)$$

for the wavefunction Ψ_i of a perturbed level $|i\rangle$, where the $\Psi_j^{(0)}$ are the unperturbed eigenfunctions of the interacting states, that is, the solutions of the equation $\widehat{H}\psi_j^{(0)} = E_j^{(0)}\psi_j^{(0)}$, we obtain

$$\sum_{j=1}^n c_{ij} (\widehat{H}_0 + \widehat{H}' - E_i) \Psi_j^{(0)} = 0. \quad (9.5)$$

Multiplication by $\Psi_k^{(0)}$ from the left and integration yields, because of the orthogonality of the functions $\Psi_j^{(0)}$,

$$\sum c_{ij} [(E_j^0 - E_i)\delta_{jk} + H'_{kj}] = 0, \quad (9.6)$$

where E_j^0 is the energy of the unperturbed state $|\Psi_j^{(0)}\rangle$, and

$$H_{kj} = \langle \Psi_k^{(0)} | \widehat{H}' | \Psi_j^{(0)} \rangle \quad (9.7)$$

is the perturbation matrix element describing the interaction energy between the states $|k\rangle$ and $|j\rangle$. The homogeneous Eq. (9.5) has a nontrivial solution for the coefficients c_{ij} only if the determinant

$$|(E_j^0 - E_i)\delta_{jk} + H_{kj}| = 0 \quad \text{for} \quad i, j = 1, 2, \dots, n \quad (9.8)$$

vanishes. The solutions of this equation yield the energies E_j of the perturbed states, which depend on the energies of the unperturbed states, on the spacing $E_j^0 - E_k^0$, and on the magnitude of the interaction elements H_{kj} .

The integrals

$$H_{kj} = \langle \Psi_k^{(0)} | \hat{H} | \Psi_j^{(0)} \rangle \quad (9.9)$$

can be arranged in the form of a matrix and are therefore called *matrix elements*. While the diagonal elements

$$H_{kk} = \langle \Psi_k^{(0)} | \hat{H} | \Psi_k^{(0)} \rangle = E_k^0 \quad (9.10)$$

give the energies of the unperturbed states, the off-diagonal elements describe the interaction energy between the states $|j\rangle$ and $|k\rangle$, which depends on the exact nature of the mutual coupling. The coupling is zero for H_0 , and is therefore described by the perturbation operator H' , because

$$H_{kj} = \langle \Psi_k^{(0)} | \hat{H}_0 + \hat{H}' | \Psi_j^{(0)} \rangle = E_k^0 \delta_{kj} + \langle \Psi_k^{(0)} | \hat{H}' | \Psi_j^{(0)} \rangle (1 - \delta_{kj}). \quad (9.11)$$

Diagonalization of the matrix H_{kj} yields the condition Eq. (9.8) for the energies of the perturbed levels.

The partitioning into \hat{H}_0 and \hat{H}' is to some degree arbitrary; it depends on the choice for the basis functions Ψ_0 . In general, it is useful to choose the unperturbed Hamiltonian so that it already contains the major part of the interaction. Of course, the final result of a perturbational calculation does not depend on the chosen basis, but the effort involved in arriving at this result can be significantly reduced by a suitable choice of basis functions.

9.1.2

Adiabatic and Diabatic Basis

The Schrödinger equation (2.6) for a molecule with a rigid nuclear framework,

$$\hat{H}_{\text{el}} \Phi_j = E_j^0 \Phi_j,$$

yields electronic wavefunctions, which lead, for the electronic part $\hat{H}_0 = \hat{H}_{\text{el}}$ of the Hamiltonian, to diagonal elements of the matrix Eq. (9.9), while the off-diagonal elements are zero. The adiabatic potential curves are then given by

$$E_j^0(R) = \langle \Phi_j | \hat{H}_{\text{el}} | \Phi_j \rangle. \quad (9.12)$$

The deviations from the adiabatic approximation are mediated by the contributions $\hat{H}' = \hat{T}_{\text{kin}} = \hat{T}_{\text{vib}} + \hat{T}_{\text{rot}}$ in the complete Hamiltonian. This means that the perturbation is caused by the kinetic energy of the vibrating or rotating molecule.

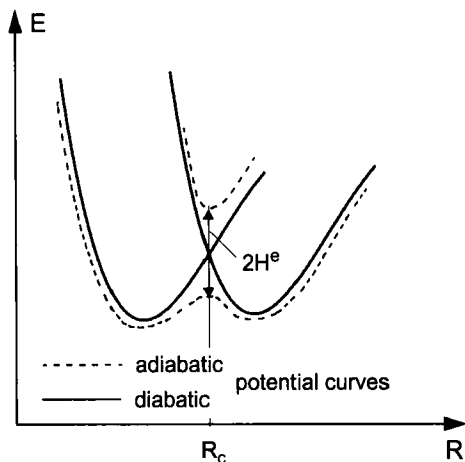


Fig. 9.2 Diabatic, crossing potential curves and adiabatic potential curve with avoided crossing.

The off-diagonal elements of the perturbation operator $\hat{H}' = \hat{T}_{\text{kin}}(R)$ describe non-adiabatic perturbations, which means that different electronic states are coupled, and the motions of the nuclei are no longer restricted to one potential curve (or potential surface in polyatomic molecules), see Sect. 2.2. The off-diagonal elements of \hat{T}_{rot} describe perturbations originating from the rotation of the molecule, which are zero in the nonrotating molecule.

If we want to describe quantitatively the perturbations arising from terms neglected in the BO approximation, we can start from two different BO representations. If we begin with noncrossing adiabatic molecular potentials (adiabatic representation), the matrix

$$\langle \Phi_j | \hat{H}_{\text{el}} | \Phi_k \rangle = E_j^0(R) \delta_{jk} \quad (9.13)$$

becomes diagonal, and the operator $\hat{T}_{\text{kin}} + \hat{T}_{\text{rot}}$ is responsible for the perturbations. However, the corresponding potential curves are often complicated and may possess, for example a double minimum. If this is to be avoided, we can use diabatic potential curves, which can intersect (Fig. 9.2). They are obtained by using approximate electronic wavefunctions $\Phi_{\text{el}}^{\text{app}}$ in place of the exact wavefunctions. Then

$$\langle \Phi_j^{\text{app}} | \hat{H}_{\text{el}} | \Phi_k^{\text{app}} \rangle \neq 0 \quad \text{for } j \neq k, \quad (9.14)$$

and off-diagonal elements of \hat{H}_{el} arise, which describe electrostatic perturbations. Which of the two models is preferable depends on the relative influence of the different couplings.

9.1.3

Perturbations Between Two Levels

The quantitative description of perturbation and the procedure to remove it will be illustrated for the case of two interacting levels. The energy matrix for the coupling states in the basis of the unperturbed wavefunctions $\Psi_1^{(0)}$ and $\Psi_2^{(0)}$ is

$$\begin{pmatrix} H_{11} & H_{12} \\ H_{21} & H_{22} \end{pmatrix} = \begin{pmatrix} E_1^0 & H_{12} \\ H_{21} & E_2^0 \end{pmatrix} \quad \text{with} \quad H_{12} = H_{21}, \quad (9.15)$$

where the diagonal elements describe the energies of the unperturbed levels and the off-diagonal elements the interaction energy. To obtain the energies of the perturbed levels, this matrix must be diagonalized. This yields, according to Eq. (9.8),

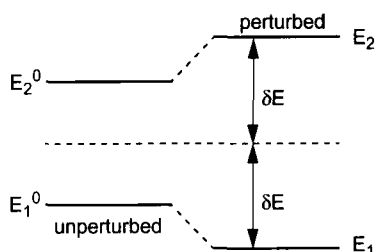
$$E_{1,2} = \frac{E_1^0 + E_2^0}{2} \pm \sqrt{\left(\frac{E_1^0 - E_2^0}{2}\right)^2 + H_{12}^2} \quad (9.16a)$$

for the energies E_1 and E_2 of the perturbed levels (that is, for the measured lines in the spectrum). We see that the energies of the perturbed levels are shifted symmetrically, and their spacing increases with increasing coupling strength (Fig. 9.3). To determine the shifts quantitatively, the expression for the perturbation operator \hat{H}' and the unperturbed wavefunctions must be known, from which the off-diagonal elements $H_{12} = H_{21}$ can then be calculated.

Solving the two equations for the energies E_1^0 and E_2^0 of the unperturbed levels yields the equations

$$E_{1,2}^0 = \frac{E_1 + E_2}{2} \pm \sqrt{\left(\frac{E_1 - E_2}{2}\right)^2 - H_{12}^2}, \quad (9.16b)$$

in analogy to Eq. (9.16a). If H_{12} is known, the energies E_1^0 and E_2^0 of the unperturbed levels (i.e., the energies that would be observed if no perturbation existed) can be calculated from the measured energies $E_{1,2}$ of the perturbed levels.



$$\delta E = \left[\left(\frac{E_1^0 - E_2^0}{2} \right)^2 + (H_{12})^2 \right]^{1/2}$$

Fig. 9.3 Mutual repulsion of two interacting levels.

9.2

Hund's Coupling Cases

The extent of the perturbations depends on the type of the perturbation. In many cases, perturbations can be classified according to the strength of the different couplings between the angular momenta involved. The resulting different coupling schemes are also important for the selection rules for perturbations, in addition to the symmetries of the states involved.

To order the different possible couplings according to their strength and to facilitate the choice of suitable basis functions, Hund discussed several coupling schemes for linear molecules with the aid of a vector model [9.2]. In a quantum-mechanical discussion, the different coupling cases are characterized by a corresponding choice of basis functions and the distinction between “good” (i.e., well-defined) and “bad” (i.e., not properly defined) quantum numbers.

In *Hund's coupling case a*) (Fig. 9.4a), the interaction between the electron spin S and the magnetic field arising from the precession of the electronic angular momentum L around the internuclear axis of the linear molecule is larger than the direct coupling between L and S . In the vector model, the vectors L and S precess independently around the internuclear axis, which is chosen to coincide with the z axis.

Well-defined quantum numbers are the projection quantum numbers Λ and Σ and their sum $\Omega = \Lambda + \Sigma$ (see Sect. 2.4.2). The total angular momentum J is combined from the rotational angular momentum R perpendicular to the molecular axis and the projections Λ and Σ ,

$$\begin{aligned} \mathbf{J} &= \mathbf{R} + (\Lambda + \Sigma)\hat{z} \\ &= \mathbf{R} + \Omega\hat{z} \quad \text{with} \quad \Omega = \Lambda + \Sigma \quad \text{and} \quad \hat{z} = \text{unit vector}. \end{aligned} \quad (9.17)$$

The set of all good quantum numbers is $(n, J, S, \Lambda, \Sigma, \Omega)$, where n describes the collection of all other quantum numbers of the electronic and vibrational state and indicates, for example, also the energetic enumeration of the electronic state.

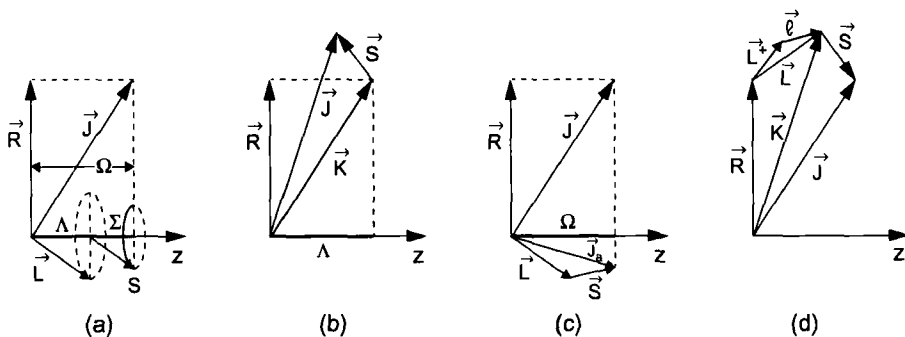


Fig. 9.4 Vector model for Hund's coupling cases.

The basis functions are, in abbreviated notation, $|nJS\Omega\Lambda\Sigma\rangle$; the undisturbed Hamiltonian is chosen to be $\hat{H}_0 = \hat{H}_{el} + \hat{B}J^2$.

In *Hund's case b*), the coupling of the electronic orbital angular momentum L with the molecular axis is stronger than the coupling with S (Fig. 9.4b). This condition is satisfied for molecules with small spin-orbit coupling. Therefore the projection $\Lambda\hat{z}$ of L and the vector R combine to an angular momentum K , which finally couples with S to yield the total angular momentum J . Therefore, the vector sums

$$K = \Lambda\hat{z} + R \quad \text{and} \quad J = K + S \quad (9.18)$$

are well-defined. As the unperturbed Hamiltonian we choose now

$$\hat{H}_0 = \hat{H}_{el} + \hat{B}K^2. \quad (9.19)$$

In *Hund's case c*), the spin-orbit coupling is stronger than the coupling of L with the molecular axis (Fig. 9.4c). This situation is found in molecules with heavy atoms, that is, large nuclear charges Ze . Here, L and S couple to the total electronic angular momentum $J_{el} = L + S$ with the projection $\Omega\hbar$ onto the molecular axis. When this is combined with the molecule's rotational angular momentum R , the total angular momentum becomes

$$J = \Omega\hbar\hat{z} + R; \quad L \cdot S \gg L \cdot A, \quad (9.20)$$

where A is a vector along the molecular axis \hat{z} . The unperturbed part of the Hamiltonian is chosen to be

$$H_0 = H_{el} + H_{so} + BJ^2, \quad (9.21)$$

and the basis functions are $|nJ\Omega\rangle$.

The projection quantum numbers Λ and Σ are not defined in Hund's case c), that is, they cease to be good quantum numbers.

Finally, there is an additional, but rarer, case d) (Fig. 9.4d), which is encountered, for example, in molecular Rydberg states. Here, the coupling of the electronic angular momentum l of the Rydberg electron with the molecular axis is weaker than with the rotational axis R . Therefore, the angular momenta l of the Rydberg electron and L^+ of the ionic electron shell couple to $L = l + L^+$, and L couples with the rotational angular momentum R to $K = L + R$. The projection of K onto the rotational axis is denoted N , that of $K - l = L^+ + R$ is denoted N^+ . The electron spin S couples to K to produce the total angular momentum $J = K + S$. Here, $L \cdot A \gg L \cdot S$ and $S \cdot K \gg S \cdot A$.

The unperturbed Hamiltonian is chosen to be

$$\hat{H}_0 = \hat{H}_{el} + \hat{B}N^{+2} - \hat{B}(J^+l^- + J^-l^+), \quad (9.22)$$

where $J^\pm = J_x \pm iJ_y$ and $l^\pm = l_x \pm il_y$. The basis functions are $|nJSNN^+\rangle$.

9.3

Discussion of Different Types of Perturbations

The different possible couplings between molecular states are described by the corresponding perturbation operators \hat{H}' . The choice of a suitable basis depends on the type of perturbation.

In the following, we will discuss the following perturbations:

1. electrostatic interactions;
2. spin–orbit coupling;
3. rotational perturbations;
4. vibronic coupling;
5. Renner–Teller effect;
6. Jahn–Teller effect;
7. predissociation;
8. autoionization;
9. radiationless transitions.

While the mechanisms 1–3 and 7–9 occur both in diatomic and polyatomic molecules, processes 4–6 are only possible in polyatomic molecules.

We will now discuss the different types of perturbations in some detail. We start with perturbations in diatomic molecules before turning to the more complicated case of polyatomic molecules. Obviously, only levels with the same total angular momentum J can interact, because the total angular momentum must be conserved in the absence of external forces.

The Hamiltonian

$$H = H_{\text{el,vib}} + H_{\text{rot}}$$

is partitioned into a part $H_{\text{el,vib}}$ acting on the electronic and vibrational functions, and a rotational part H_{rot} depending on the total angular momentum, which contains also coordinates appearing in $H_{\text{el,vib}}$. The operator $H_{\text{el,vib}}$ describes the nonrotating molecule, whereas $H = H_{\text{el,vib}} + H_{\text{rot}}$ describes the rotating molecule. H can be partitioned into an operator H_0 of the unperturbed system and a perturbational part H' (see next section).

9.3.1

Electrostatic Interaction

Electrostatic interactions can only occur between electronic states of the same symmetry and multiplicity, that is, with the same set of quantum numbers Λ , Σ and S (Fig. 9.5). The description of this perturbation depends on the choice of basis functions.

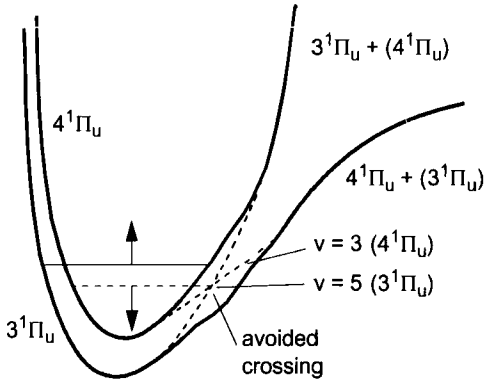


Fig. 9.5 Electrostatic interaction between the electronic states $3^1\Pi_u$ and $4^1\Pi_u$ of Li_2 , leading to a deformation of the potential curve due to an avoided crossing and thus also to shifts of vibrational levels in both states.

If we choose the *adiabatic electronic basis functions* from the BO approximation, which are the solutions of the Schrödinger equation (2.6),

$$H_{\text{el}}\Phi_j^{\text{el}} = E_j^0\Phi_j^{\text{el}},$$

for a rigid (i.e., nonvibrating) molecule, we can partition the Hamiltonian \hat{H} according to

$$\hat{H} = \hat{H}_0 + \hat{H}' \quad \text{with} \quad \hat{H}_0 = \hat{H}_{\text{el}} \quad \text{and} \quad \hat{H}' = \hat{T}_{\text{kin}} = \hat{H}_{\text{vib}} + \hat{H}_{\text{rot}}.$$

The diagonal elements of the matrix $\langle \Phi_j^{\text{el}} | \hat{H} | \Phi_k^{\text{el}} \rangle$,

$$\langle \Phi_j^{\text{el}} | \hat{H}_0 | \Phi_j^{\text{el}} \rangle = E_j(R) \quad (9.23)$$

describe the adiabatic potential curves $E_j(R)$ for the state $|j\rangle$ (see Sect. 2.2). The coupling between different electronic states is given by the perturbation operator \hat{T}_{kin} , that is, the off-diagonal elements

$$\langle \Phi_j^{\text{el}} | \hat{H} | \Phi_k^{\text{el}} \rangle = \langle \Phi_j^{\text{el}} | \hat{T}_{\text{kin}} | \Phi_k^{\text{el}} \rangle \quad \text{for} \quad j \neq k \quad (9.24)$$

describe the interaction energy between different electronic states caused by the motions of the nuclei. Inclusion of these perturbational terms has the pictorial consequence that the potential curves of the states are deformed. For example, it may then not be possible to approximate it by a Morse potential, and it may even possess a double minimum. The deformation is particularly pronounced for all values R_c of the internuclear distances where potential curves approach each other closely. Here, both potential curves are deformed so that curves of states with the same symmetry do not cross; this situation is called *avoided crossing* (Fig. 9.2).

To avoid these complicated potential curves, we can choose *diabatic basis functions*. They do not obey Eq. (9.15) exactly, but minimize the perturbation term caused by \hat{T}_{kin} . In a diabatic basis Φ^{d} , the coupling between two states is described by \hat{H}_{el} , whereas in an adiabatic basis Φ^{a} , it is described by \hat{T}_{kin} . Thus, in a diabatic basis Φ^{d} , the interaction term for $j \neq k$,

$$\langle n_1, \Lambda, \Sigma, S | \hat{H} | n_2, \Lambda, \Sigma, S \rangle = \langle \Phi_j | \hat{H}_{\text{el}} | \Phi_k \rangle + \langle \Phi_j | \hat{T}_{\text{kin}} | \Phi_k \rangle, \quad (9.25)$$

contains only the first term in Eq. (9.25) because the second term is small, whereas in an adiabatic basis Φ^{a} , it contains only the second term because the first term is zero.

The experimental values for the energies of the perturbed levels can then be obtained in both models by diagonalizing the matrix

$$\begin{pmatrix} H_{jj} & H_{jk} \\ H_{jk} & H_{kk} \end{pmatrix} \quad \text{with} \quad H_{jk} = \langle n_j, \Lambda, \Sigma, S | \hat{H} | n_k, \Lambda, \Sigma, S \rangle. \quad (9.26)$$

In the case of a diabatic basis, the potential curves $E_{\text{pot}}(R)$ may cross; in an adiabatic basis an avoided crossing results. In the vicinity of the avoided crossing, the character of the electronic wavefunction changes strongly with the internuclear distance R . The reason is that it is constructed as a linear combination of the electronic wavefunctions of the two interacting states. In the vicinity of the avoided crossing, the relative contributions of the two functions in the linear combination vary particularly quickly, because here the two potential curves approach each other very closely.

The interaction between two vibrational states v_1 and v_2 in two different electronic states is described, in a diabatic basis, by

$$\begin{aligned} H_{1,v_1,2,v_2}^{\text{d}} &= \langle \Phi_1^{\text{d}} \chi_1^{\text{d}} | \hat{H}_{\text{el}} | \Phi_2^{\text{d}} \chi_2^{\text{d}} \rangle = H_{\text{el}} \langle v_1^{\text{d}} | v_2^{\text{d}} \rangle \\ \text{with } H_{\text{el}} &= \langle \Phi_1^{\text{d}} | \hat{H}_{\text{el}} | \Phi_2^{\text{d}} \rangle \quad \text{and} \quad \langle v_1^{\text{d}} | v_2^{\text{d}} \rangle = \int \chi_{v_1}^*(R) \chi_{v_2}(R) \, dR. \end{aligned} \quad (9.27)$$

The electronic part H^{el} of the matrix element is often assumed to be independent of R . If we want to include the weak dependence, we can use the R centroid approximation (see Sect. 4.2.6), employing

$$H^{\text{el}}(R_{\text{c}}) = \frac{\langle v_1 | H^{\text{el}} | v_2 \rangle}{\langle v_1 | v_2 \rangle} \quad \text{at the internuclear distance} \quad R_{\text{c}} = \frac{\langle v_1 | R | v_2 \rangle}{\langle v_1 | v_2 \rangle} \quad (9.28)$$

as the optimum mean value. In an adiabatic basis, this interaction is described by

$$H_{1,v_1,2,v_2}^{\text{a}} = \langle \Phi_1^{\text{a}} \chi_1 | \hat{T}_{\text{kin}} | \Phi_2^{\text{a}} \chi_2^{\text{a}} \rangle \quad \text{because} \quad \langle \Phi_1^{\text{a}} | H_{\text{el}} | \Phi_2^{\text{a}} \rangle = 0. \quad (9.29)$$

The perturbed adiabatic potential curves are obtained by diagonalizing the matrix

$$\begin{pmatrix} H_{1,v_1,1,v_1} & H_{1,v_1,2,v_2} \\ H_{2,v_2,1,v_1} & H_{2,v_2,2,v_2} \end{pmatrix} \quad (9.30)$$

for fixed values of R distributed as evenly as possible over the range of relevant values.

If diabatic basis functions are used, the off-diagonal elements Eq. (9.21) are the diabatic coupling elements. Diagonalization of the matrix Eq. (9.30) yields the conditional equation

$$\begin{vmatrix} E_1^d(R) - E & H_{12}^d(R) \\ H_{12}^d(R) & E_2^d - E \end{vmatrix} = 0 \quad (9.31)$$

for the perturbed diabatic potential curves $E^d(R)$, where the matrix elements are integrals over electronic coordinates for fixed nuclear distances R_i .

9.3.2

Spin–Orbit Coupling

The Hamiltonian for the coupling between the spin s_i of the i th electron and its orbital angular momentum l_i with respect to the nucleus k with the effective nuclear charge Z_{eff} for diatomic molecules is given, completely analogous to the situation in atoms, by

$$\hat{H}^{s,l} = \sum_i \hat{a}_i l_i s_i \quad \text{with} \quad a_i l_i = \sum_{k=1}^2 \frac{\alpha^2 Z_k^{\text{eff}}}{2 r_{ik}^2} l_{ik} , \quad (9.32)$$

where $\alpha = 1/137$ is the fine-structure constant and r_{ik} is the distance between electron i and nucleus k . Here, it is appropriate to recollect that we can express the electronic coordinates, which usually refer to different nuclei, in a unified reference frame so that they all refer to a common origin by applying an appropriate coordinate transformation [9.3].

Spin–orbit coupling not only mediates an interaction between states with different values of Λ and Σ , but also leads to a splitting of the term energies of a state $n\Lambda S$ in fine-structure components with equal values of Λ , but differing in the spin projection quantum number Σ and hence also in Ω .

If the couplings between the different angular momenta l_i of the electrons and between their spins s_i are stronger than the interaction between l_i and s_i [L – S coupling; Hund’s case a)], the spin–orbit interaction within a state with equal quantum numbers Λ , which leads to a fine-structure splitting in components with different values $\Omega = \Lambda + \Sigma$, can be written in simplified form,

$$\hat{H}^{S,L} = \Lambda L S \quad \text{with} \quad L = \sum l_i \quad \text{and} \quad S = \sum s_i . \quad (9.33)$$

Usually, basis functions for Hund’s coupling case a) are chosen, because in this case Λ and Σ are good quantum numbers.

The diagonal elements

$$\langle \Lambda, \Sigma, S, \Omega, v | \hat{H}^{LS} | \Lambda, \Sigma, S, \Omega, v \rangle = \Lambda \Lambda \Sigma \quad (9.34)$$

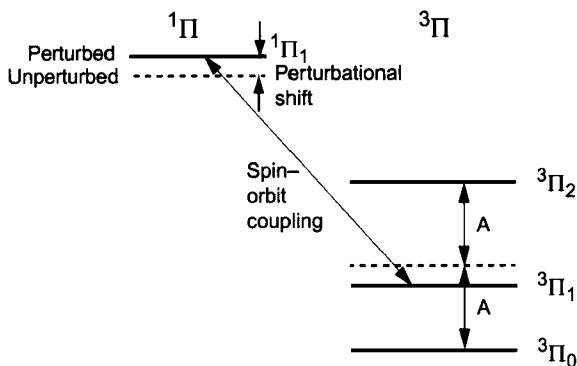


Fig. 9.6 Spin–orbit coupling between a ${}^1\Pi$ and a ${}^3\Pi_1$ state with the selection rule $\Delta\Lambda = 0$; $\Delta S = 1$; $\Delta\Sigma = \Delta\Omega = 0$.

give the energies of these components. From Eq. (9.34), we see that the fine-structure components of a multiplet have constant spacing $A\Lambda$ as long as spin–orbit coupling, Eq. (9.33), is the only interaction (Fig. 2.18). Frequently, additional higher-order couplings ($s_j l_j$ or $s_i s_j$) occur so that the spacings of the multiplet components become different.

The selection rules for the nonvanishing matrix elements

$$\langle n_i, \Lambda_i, S_i, \Omega_i, v_i | \hat{H}^{s,l} | n_j, \Lambda_j, S_j, \Omega_j, v_j \rangle \quad (9.35)$$

of the spin–orbit coupling are

$$\begin{aligned} \Delta J &= 0; \quad \Delta S = 0, \pm 1; \quad \Delta\Omega = 0; \\ \Rightarrow \Delta\Lambda &= \Delta\Sigma = 0 \quad \text{or} \quad \Delta\Lambda = -\Delta\Sigma = \pm 1. \end{aligned} \quad (9.36)$$

Generally, only rotational levels with the same total angular momentum quantum number J can interact through spin–orbit interaction (Fig. 9.6). If the two interacting states belong to the same electron configuration (see Sect. 2.7.1), $\Delta\Lambda = \Delta\Sigma = 0$ holds; if the two states differ by one spin orbital, the rule is $\Delta\Lambda = -\Delta\Sigma = \pm 1$. For homonuclear molecules, the selection rules $g \leftrightarrow u$ is also obeyed.

Apart from the interaction Eq. (9.35), a (usually much weaker) coupling between the spin s_i of the i th electron and the orbital angular momentum l_j of another electron can occur. This mechanism can enable couplings between states, which would normally be forbidden according to the selections rules for the one-electron operator.

The spin–orbit coupling between two different states also leads to a shift of specific fine-structure components. As this coupling is determined by the selection rule $\Delta\Omega = 0$, only components with the same Ω can interact. This is illustrated in Fig. 9.6 for the example of spin–orbit coupling between a ${}^1\Pi$ and a ${}^3\Pi$ state. Here, only the component with $\Omega = 1$ is influenced, the two remaining components remain unchanged.

In *linear polyatomic* molecules, the situation is completely analogous to that in diatomic molecules. For strong spin-orbit coupling in linear molecules, Hund's coupling case c) applies, that is, the quantum numbers Λ and Σ are not defined any more but only their sum Ω . In nonlinear molecules, no precession of the orbital angular momentum is possible because the potential is not cylindrically symmetric. Therefore, spin-orbit coupling is in general small. In this case, the diagonal terms Eq. (9.34) give, for weak spin-orbit coupling, the fine-structure splitting of the rotational levels in the respective vibrational state, which is small compared with the spacing of the rotational levels.

The total wavefunction can be written, for this case, as a product

$$\Psi = \Psi(R, r)\chi(s) \quad (9.37)$$

of spatial wavefunction and spin function (see Sect. 2.8.1).

9.3.3

Rotational Perturbations

All perturbations connected with the coupling of angular momenta, such as the spin-orbit coupling discussed in the preceding section, can be derived from the Hamiltonian for angular momenta. The rotational Hamiltonian for a diatomic molecule aligned along the z axis with the rotational angular momentum \mathbf{R} perpendicular to $\hat{\mathbf{z}}$ is

$$H_{\text{rot}} = B(R_x^2 + R_y^2) = B[(J_x - L_x - S_x)^2 + (J_y - L_y - S_y)^2], \quad (9.38)$$

because the total angular momentum is $\mathbf{J} = \mathbf{L} + \mathbf{S} + \mathbf{R}$.

Equation (9.38) can be recast to yield

$$H_{\text{rot}} = B(J^2 - J_z^2) + B(L^2 - L_z^2) + B(S^2 - S_z^2) \\ + B(L_+ S_- + L_- S_+) - B(J_+ L_- + J_- L_+) - B(J_+ S_- + J_- S_+), \quad (9.39)$$

where $J_{\pm} = J_x \pm iJ_y$, $L_{\pm} = L_x \pm iL_y$, and $S_{\pm} = S_x \pm iS_y$ [9.4].

The first three terms in Eq. (9.39) give the energies of the unperturbed rotational levels. The first term can be rewritten as

$$H_{\text{rot}}^0 = B[J(J+1) - \Omega^2], \quad (9.40)$$

which is equivalent to the rotational term values from Eq. (3.21), if the centrifugal distortion and the electron spin are neglected.

The next two terms,

$$B(L^2 - L_z^2) + B(S^2 - S_z^2) = B(L^2 + S^2) - B(\Lambda^2 + \Sigma^2) \quad (9.41)$$

are usually included in the energy of the electronic state $|n, \Lambda, \Sigma, \Omega\rangle$ because they do not depend on the specific vibration-rotation levels.

The second line in Eq. (9.39) characterizes the perturbations between the levels. The first term describes spin–orbit coupling, which leads to a homogeneous perturbation between two electronic states with $\Delta\Omega = 0$ (see preceding section).

The second term describes the interaction between the rotational levels of two electronic states differing in Λ , which leads to Λ doubling of the rotational levels. This is a heterogeneous perturbation with $\Delta\Omega = \pm 1$, which occurs only in rotating molecules.

Due to the rotation of the molecule, Λ ceases to be a good quantum number, because the rotation couples states with $\Delta\Lambda = \pm 1$. Therefore, the rotational levels of both interacting states are slightly shifted. This effect can be expressed by an effective rotational constant

$$B_v^{\text{eff}} = B_v + \delta_v. \quad (9.42)$$

In electronic states with $\Lambda > 0$, the rotational levels, which would be twofold degenerate in the absence of this interaction, are now split into two components. The two Λ components (denoted c and d in the literature) have different symmetries. Thus, the interaction with the coupling state affects only one of the two components because of the symmetry selection rule. This component is shifted, the other remains unperturbed. The splitting (Λ doubling) can be described by

$$\Delta\nu = q_v J(J+1) \quad (9.43)$$

with the Λ doubling constant

$$q_v = B_v^c - B_v^d. \quad (9.44)$$

If the interacting states have the same angular momentum quantum number l for the valence electron for $R \rightarrow \infty$ (e.g., the two states $A^1\Sigma_u$ and $B^1\Pi_u$ of the alkali metal dimers, which both dissociate to the same atomic p state), q_v can be expressed by the rotational constant B_v of the Π state and the energy difference $\Delta\tilde{\nu}$ between Σ and Π state,

$$q_v = \frac{2B_v^2 l(l+1)}{\Delta\tilde{\nu}(\Pi - \Sigma)}. \quad (9.45)$$

The constant q_v is in general small compared with B , so that Λ doubling is a small yet appreciable effect, particularly for large rotational quantum numbers.

In multiplet states, Λ splitting is different for the distinct fine-structure components. For example, it is almost independent of J for the Π_0 component, similar to that in a $^1\Pi$ state for the $^3\Pi_1$ component, and small but proportional to $J^2(J+1)^2$ for the $^3\Pi_2$ component (Fig. 9.7).

The third term in the second line of Eq. (9.39) describes spin–rotation coupling, in which the electron spin can assume different orientations in the magnetic field originating from the rotation of the nuclear framework, leading to slightly different energies. Again, this is a heterogeneous perturbation with $\Delta\Lambda = 0$; $\Delta\Sigma = \Delta\Omega = \pm 1$.

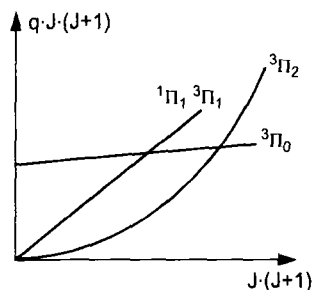


Fig. 9.7 J -dependence of A doubling for the states $^1\Pi$, $^3\Pi_0$, $^3\Pi_1$, and $^3\Pi_2$.

The term values of the components of a rotational level with quantum number $J = N + S$ split by a spin-rotation interaction are, for example, for a spin $S = 1/2$,

$$F_1(N) = B_v N(N+1) + \frac{1}{2} \gamma N, \quad (9.46)$$

$$F_2(N) = B_v N(N+1) - \frac{1}{2} \gamma(N+1).$$

The constant γ is called *spin-rotation coupling constant*. The splitting of the term is usually very small and can only be observed with high spectral resolution. In $^3\Sigma$ states, an additional magnetic interaction arises between the spin moments of the two unpaired electrons, so that the term values

$$F_1(N) = B_v N(N+1) + (2N+3)B_v + \gamma(N+1) - \lambda - [(2N+3)^2 B_v^2 + \lambda^2 - 2\lambda B_v]^{1/2},$$

$$F_2(N) = B_v N(N+1),$$

$$F_3(N) = B_v N(N+1) - (2N+1)B_v - \gamma N - \lambda + [(2N-1)^2 B_v^2 + \lambda^2 - 2\lambda B_v]^{1/2} \quad (9.47)$$

contain additional terms with the spin-spin coupling constant λ . If the (usually very small) splittings are measured for several rotational levels (i.e., for different values of N) in the same vibrational state, the constants B_v , λ and γ can be determined [9.4].

9.3.4

Vibronic Coupling

At sufficiently low vibrational energies, the vibrations of polyatomic molecules can be described as a superposition of normal vibrations (see Ch. 6). In normal vibrations, all nuclei in the molecule move synchronously, that is, they all pass through their equilibrium positions at the same time. The different normal vibrations are independent; they maintain their identity, and the atoms store their vibrational energy in a mode

consisting of a linear combination of all excited normal vibrations until it is released by means of radiation or through collisions with other molecules. The total vibrational energy is the sum of the normal vibrational energies. The potential in which the vibration occurs is approximately harmonic.

Upon higher vibrational excitation, anharmonicities in the potential become noticeable, leading to couplings between the normal vibrations [see Eq. (6.89)]. If these couplings are sufficiently strong, the normal vibrations lose their identity. The vibrational energy is quickly transferred from the originally excited mode onto other vibrational modes. It is finally distributed randomly about all energetically accessible modes, a process called *internal vibrational redistribution* (IVR). Its description depends on the density of vibrational states around the excitation energy and on the overlap of the vibrational wavefunctions of the interacting levels [9.5].

IVR processes usually occur on a picosecond timescale. For example, if an energetically high-lying vibrational level of a dissociation coordinate is selectively excited, the energy can be redistributed so quickly that the dissociation is avoided although the energy pumped into the excited mode would have been sufficient to cause dissociation. The wavefunction of the perturbed primary excited state $|k\rangle$ can be written as a linear combination

$$\Psi_k = a_k \Phi_k + \sum a_{i\Phi} \Phi_i \quad \text{with} \quad a_k^2 + \sum a_{i\Phi}^2 = 1$$

of all N coupling eigenstates of the N vibrational modes. If the perturbing states $|i\rangle$ are not accessible by absorption transitions from the ground state (dark states), the intensity

$$I \propto |a_k|^2$$

of the absorption line is determined solely by the “light” state although the population probability is distributed among all coupled states. The intensity is therefore lower than for an unperturbed state because $a_k < 1$. The oscillator strength of the absorption transition is said to be “diluted” by the coupling to the dark states. The lifetime of the excited state is increased because it mixes with states of very long lifetime.

In larger molecules, the following simplified model is used to discuss IVR. The primary excited level in an excited electronic state couples with several high vibrational levels of a lower electronic state with a higher level density than that in the excited electronic state (Fig. 9.8). Three cases can be distinguished [9.6]:

1. The region of small level density, where the mean spacing between the vibrational levels is large compared with the widths of the levels. In this case, the levels can influence each other through their interaction, but for a narrow-band excitation with continuous lasers, the absorption lines are resolved, and stationary excited levels are observed for each selectively excited transition into the coupling levels.

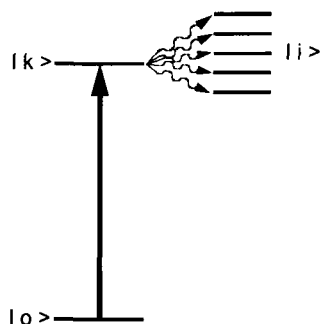


Fig. 9.8 Vibronic coupling and IVR processes.

2. In the transition region of medium level densities, the mean spacing between the perturbing vibrational levels is comparable to the linewidths of the absorption transitions. Now, not all lines can be resolved even for excitation by a narrow-band laser, and some levels are excited simultaneously. In the case of an excitation by a pulsed laser, all levels accessible within the bandwidth of the laser are excited coherently, and the superimposed fluorescence of these levels displays quantum beats due to the interference between the emissions from the different levels.
3. If the level density is large compared with the excitation linewidth, a multitude of levels are excited simultaneously. The absorption spectrum appears quasi-continuous even when viewed in high resolution.

The IVR process can also occur for highly excited vibrational states in the electronic ground state, provided the level density is large enough. It can be observed by Doppler-free overtone spectroscopy (see Ch. 12).

Vibronic coupling is controlled by the selection rules listed in Sect. 9.1. For example, within the same electronic state, only vibrational states of like symmetry can interact. Hence, in a triatomic molecule with symmetry C_{2v} in which only vibrations with symmetry a_1 or b_2 occur, the vibrational levels $2\nu_1$ and $4\nu_2$ can interact if their energies do not differ too much, but also the vibrational levels $2\nu_1$ and $2\nu_3$ can interact because both have a_1 symmetry. Vibrational levels from different electronic states can interact if the vibronic symmetry $\Gamma_{el,vib} = \Gamma_{el} \times \Gamma_{vib}$ of both states is equal.

9.3.5

Renner–Teller Coupling

In linear molecules, a special type of vibronic coupling occurs. If the electronic state is degenerate in the linear configuration, it can be split into two potential curves $E^+(\varphi)$ and $E^-(\varphi)$ during a bending vibration, where φ is the bond angle (Fig. 9.9). Such degenerate electronic states with cylindrical symmetry possess an electronic angular

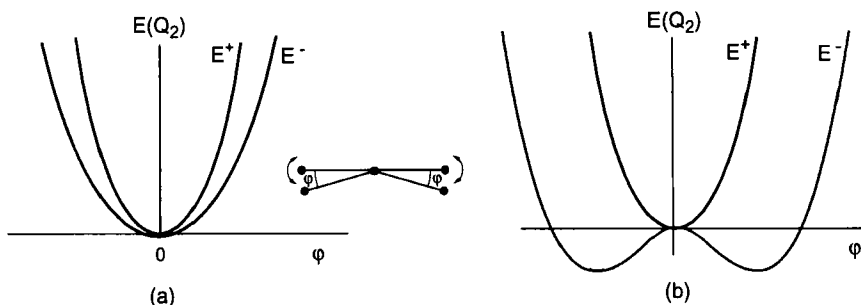


Fig. 9.9 Possible splittings of the potential curves in the Renner–Teller effect a) for $\alpha < 2a$ and b) for $\alpha > 2a$.

momentum along the molecular axis due to the precession of the electrons around this axis. If the unperturbed potential is described by the quartic function

$$E^0(\varphi) = a\varphi^2 + b\varphi^4, \quad (9.48)$$

and the difference of the two Renner–Teller components by

$$E^+(\varphi) - E^-(\varphi) = \alpha\varphi^2 + \beta\varphi^4, \quad (9.49)$$

the lower potential curve possesses a maximum at $\phi = 0$ and two minima at

$$\phi_{\min} = \pm \sqrt{\frac{1}{2} \frac{2-a}{b-\beta}},$$

provided $\alpha > a$ and $\beta < b$ or $\alpha < a$ and $\beta > b$ (Fig. 9.9). Hence, the electronic energy is modified by the bending vibration.

The coupling between the electronic orbital motion and the nuclear motion influences the vibronic levels in both potential curves. The rotational constant changes also due to the coupling. The resulting shifts of the levels depend on the size of the potential splitting as quantified by the Renner parameter $\varepsilon = \alpha/2a$ and on the vibrational angular momentum of the bending vibration.

The Renner–Teller effect constitutes a special case of vibronic coupling in which vibrational levels are influenced by the electronic motion [9.7]. Thus, the Born–Oppenheimer approximation collapses, and the levels resulting from the coupling of electronic and nuclear motion are called *vibronic levels*.

For a linear molecule in a Σ , Π , or Δ state, the electronic orbital angular momentum is characterized by the quantum numbers $\Lambda = 0, 1$ or 2 . If a bending vibration is excited, an additional vibrational angular momentum with the projection quantum number $l = 0, 1, 2, \dots$ arises.

The resulting vibronic angular momentum around the molecular axis is then Kh with the quantum number

$$K = |\pm\Lambda \pm l|.$$

The quantum number K corresponds to the rotational quantum number K_a in a bent triatomic, almost prolate, symmetric top molecule. The levels with $K = 0, 1, 2, \dots$ are labeled Σ, Π, Δ , etc. states.

For $K = 0$, the vibrational term values for the case of Fig. 9.9a are

$$G(v_2) = \omega_2(1 \pm \varepsilon)^{1/2}(v_2 + 1). \quad (9.50)$$

For $K \neq 0$ and $v_2 = K - 1$, they can be described by

$$G(v_2, K) = \omega_2 \left[v_2 + 1 - \frac{1}{8} \varepsilon^2 K(K + 1) \right], \quad (9.51)$$

where ω_2 is the vibrational constant of the bending vibration. The Renner–Teller coupling can also be considered a Coriolis interaction between the electronic angular momentum and the vibrational angular momentum, which is proportional to the product $K\Lambda$ of the projections of electronic and vibrational angular momentum onto the molecular axis of the linear molecule.

The Renner–Teller coupling splits each vibrational level into several sublevels. For example, in an electronic Π state with $\Lambda = \pm 1$, a bending vibrational level with $v_2 = 1, l = \pm 1$ is split into four levels with the quantum numbers $K = | + 1 + 1 | = 2$, $K = | - 1 - 1 | = 2$, $K = | 1 - 1 | = 0$ and $K = | - 1 + 1 | = 0$, where the first two levels are degenerate. The symmetry type of the vibronic levels can be obtained by multiplications of the electronic and vibrational symmetry types. For the above example, the symmetry of the electronic Π state is $\Gamma_{\text{el}} = \Pi_u$ and that of the vibrational state is also $\Gamma_{\text{vib}} = \Pi_u$, so that the vibronic symmetry

$$\Gamma_{\text{el,vib}} = \Pi_u \times \Pi_u = \Sigma_g^+ + \Sigma_g^- + \Delta_g. \quad (9.52)$$

The two Σ states correspond to the levels with $K = 0$, whereas the degenerate Δ state corresponds to the levels with $K = 2$ (Fig. 9.10).

9.3.6

Jahn–Teller Effect

If a nonlinear molecule possesses degenerate electronic states of symmetry type E or T , each vibration leading to a lower molecular symmetry effects a splitting of the potential surface into two branches. In other words, the degenerate state is not stable, and the lowest-energy equilibrium structure corresponds to the lower symmetry. This spontaneous symmetry breaking is called the Jahn–Teller effect [9.8] after the discoverers. It is the analog of the Renner–Teller effect occurring in linear molecules. As discussed there, the Jahn–Teller effect is also mediated by the coupling between vibrations and electronic motions, and is thus another example for the breakdown of the Born–Oppenheimer approximation. We will discuss the Jahn–Teller effect for the example of the Li_3 molecule.

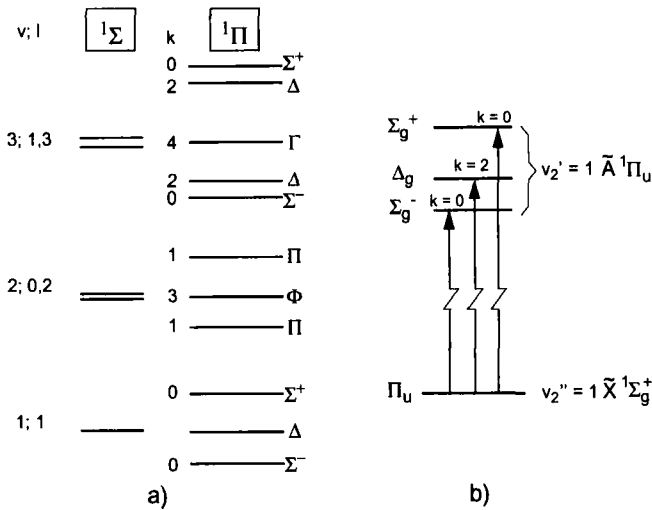


Fig. 9.10 a) Splitting of the vibronic states in an electronic Π state compared with the l splitting in a ${}^1\Sigma$ state. b) Qualitative splitting of an electronic transition $A^1\Pi_u \leftarrow X^1\Sigma_g^+$.

For symmetry reasons, we would expect the structure of Li_3 to be an equilateral triangle, belonging to the point group D_{3h} . In this structure, the electronic ground state and also some of the excited states are twofold degenerate with symmetry type E . Due to the Jahn–Teller effect, a linear combination of ν_2 and ν_3 vibrations (bending vibration and antisymmetric stretching vibration, the frequencies of which are degenerate in the D_{3h} configuration) brings the molecule into an isosceles C_{2v} structure. Figure 9.11 illustrates the two branches of the potential $E^\pm(Q_2, Q_3)$ as a function of the two normal coordinates $Q_2 = Q_x + iQ_y$, $Q_3 = Q_x - iQ_y$ of the vibrations ν_2 and ν_3 in a three-dimensional representation for the approximation of the linear Jahn–Teller effect. The two surfaces are axially symmetric around the axis $Q_2 = Q_3 = 0$.

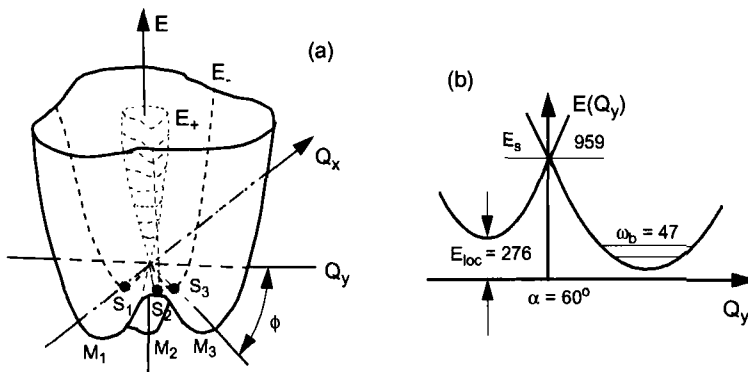


Fig. 9.11 a) Three-dimensional representation of the two Jahn–Teller potential surfaces for the quadratic Jahn–Teller effect. b) Slice through the lower potential

surface of the Li_3 molecule as a function of the apex angle showing the minimum, saddle point, and conical intersection.

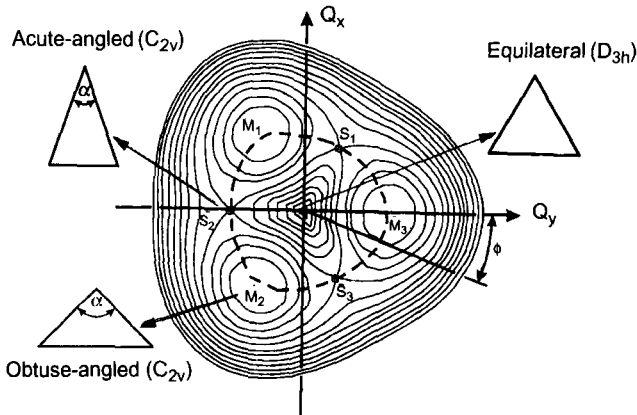


Fig. 9.12 Contour line diagram of the lower potential surface for the quadratic Jahn–Teller effect in Li_3 [9.9].

If higher terms are included in the expansion of the potential in normal coordinates (quadratic Jahn–Teller effect), three minima and three saddle points appear in the trough of the lower potential in Fig. 9.11, belonging to structures with $\alpha < 60^\circ$ and $\alpha > 60^\circ$. Figure 9.12 shows a contour line diagram of the lower Jahn–Teller potential surface, and Fig. 9.11b displays a slice through this surface.

For sufficiently low vibrational energy, the molecule will remain in the lowest-energy structure. If its vibrational excitation increases, however, it can start tunneling through the potential barriers and alter its structures periodically from $\alpha < 60^\circ$ to $\alpha > 60^\circ$. In the representation of Fig. 9.12, the molecule moves along the dotted trajectory. This tunneling leads, as in the analogous case for the ammonia molecule (see Sect. 7.5.1), to a splitting of the energy levels that increases sharply with increasing vibrational excitation (Fig. 9.13b).

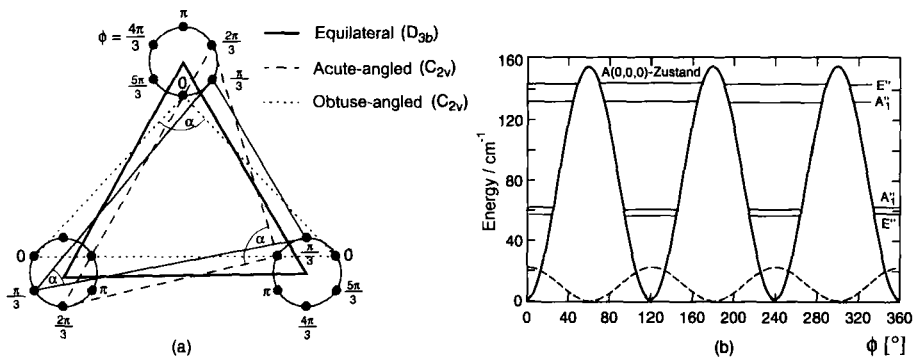


Fig. 9.13 a) Pseudorotation and b) tunnel splitting as a function of the vibrational energy in the Jahn–Teller-active vibrational modes $\nu_2 + \nu_3$.

This periodical motion is also called *pseudorotation* because it can be represented by a synchronous rotation of all three nuclei around the corners of the equilateral triangle of the degenerate nonstable configuration (Fig. 9.13a). If the vibrational energy exceeds the barrier height, free pseudorotation occurs. The time-averaged equilibrium structure of the molecule is then indeed the equilateral triangle. In measurements that take longer than one pseudorotation period, the molecule displays a D_{3h} geometry.

Pseudorotation is an example for molecular dynamics that changes the molecular geometry to a large extent, in contrast to low-amplitude vibrations, during which the geometry does not differ significantly from the equilibrium structure.

9.3.7

Predissociation

A level below the dissociation limit of an electronic state, which is excited by photon absorption, can dissociate by coupling to continuous energy states above the dissociation threshold of another electronic state. The rate of dissociation depends then on the strength of the coupling. Two cases can be distinguished:

- (a) predissociation by rotation (Fig. 9.14a), and
- (b) predissociation of a bound state by coupling to a repulsive electronic state (Fig. 9.14b).

In case a), the potential curve of a rotating diatomic molecule displays a potential barrier (see Ch. 3). States below the barrier but above the dissociation limit penetrate the barrier by tunneling processes and can thus dissociate. The decay rate depends exponentially on the width of the barrier and the difference between barrier height and molecular energy, and it varies by many orders of magnitude in the energy range between the dissociation threshold and the barrier height. The phenomenon shows up as a broadening of the corresponding spectral lines.

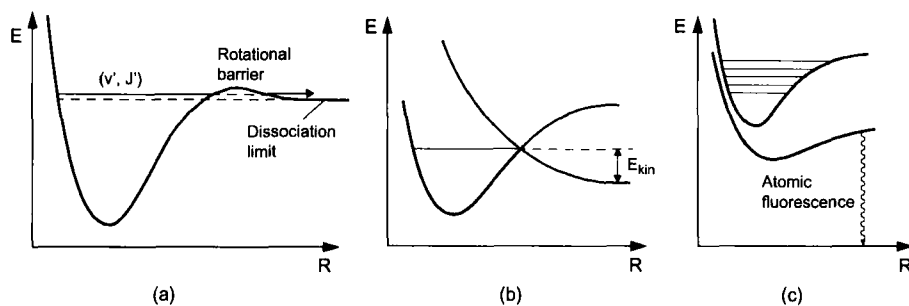


Fig. 9.14 Predissociation. a) Tunneling through a rotational barrier, b) crossing of the outer branch of the potential surface with a repulsive potential curve of

another electronic state, and c) interaction of two electronic states in the inner branches of their potential curves.

The rate of predissociation for case b) depends on the overlap of the vibrational wavefunctions of the two coupling states, where the wavefunction of the dissociating nuclei in the repulsive state can be expressed by an Airy function. The overlap assumes a maximum at those positions where the potential curves intersect. In the vicinity of these intersections, sharp maxima of the predissociation rate are observed. However, the overlap can also occur in the inner regions of the potential curves where both repulsive potential curves approach each other. Usually, there is no intersection in this region, but the energetic spacing between both curves does not vary much over a wide range of energies (Fig. 9.14c). In this case, no sharp maximum of the line broadening by predissociation is found, but the linewidths increase slowly with increasing energy until the dissociation limit of the excited state is reached and direct dissociation commences.

Predissociation can be detected either by the broadening of absorption lines or by the decrease in lifetime of the excited state [9.10]. If one is interested in the atomic states formed by the dissociation, the atomic fluorescence after the decay can be measured, provided that excited atomic states are produced (Fig. 9.14c) [9.11].

The interaction between two states is often mediated by spin-orbit coupling. This means, for example, that an excited $^1\Sigma$ state can predissociate through spin-orbit coupling with a $^3\Pi$ state if the energy of the excited level is above the dissociation limit of the lower triplet state. As the projection Ωh of the electronic total angular momentum must be conserved ($\Delta\Omega = 0$), however, only the component $^3\Pi_1$ with $\Omega = 1$ can contribute to predissociation.

9.3.8

Autoionization

If a bound molecular state of a neutral molecule lies above states of the molecular ion, it can couple with the latter, thus producing an ionic state. This process is called *autoionization*.

Whereas an atomic state can only autoionize if at least two electrons are excited and the sum of their excitation energies is larger than the ionization threshold, the excitation of a single electron can be sufficient to enable autoionization in molecules, provided the sum of electronic excitation energy and vibrational or rotational kinetic energy exceeds the ionization energy. This situation occurs, for example, if an electron is excited into a Rydberg state of the neutral molecule (Fig. 9.15). As the Rydberg electron has its largest probability density far apart from the cloud of the remaining electrons, it contributes virtually nothing to bonding, that is, the potential curves of all Rydberg states proceed parallel, only shifted with respect to each other by the differences of the excitation energies of the Rydberg electron in the respective Rydberg states with principal quantum number n . If the vibrational energy in the ion is smaller than in the neutral molecule, a portion of the vibrational energy of the Rydberg state can be transferred to the electron during autoionization. The transferred amount of

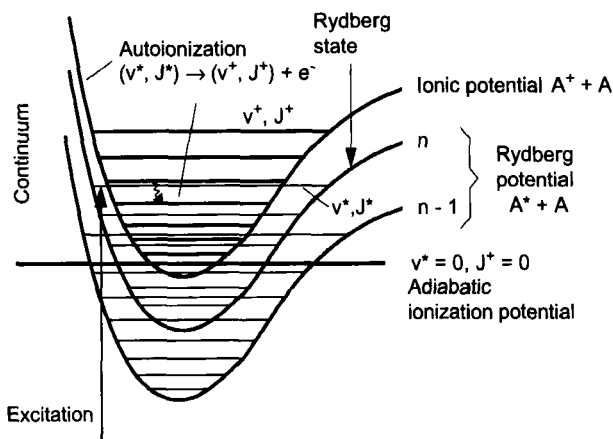


Fig. 9.15 Autoionization of molecular Rydberg states [9.12].

vibrational energy ΔE_{vib} must be equal to or larger than the energy difference

$$\Delta E = E_{\text{IP}} - \frac{E_{\text{Ry}}}{(n - \delta)^2} \quad (9.53)$$

between the Rydberg state and the ionization energy, where δ is the quantum defect taking into account the deviation of the Rydberg electron's real potential from the Coulomb potential.

For large principal quantum numbers n , a change in the vibrational quantum number of $\Delta v = v^* - v^+ = 1$ is sufficient, whereas for lower Rydberg states, larger differences in the vibrational energies are necessary. For very large principal quantum numbers n , autoionization can take place by transfer of only rotational energy, that is, the rotational quantum number J is smaller in the ion than in the neutral molecule. As the total angular momentum is conserved, the Rydberg electron must receive angular momentum during the ionization.

The coupling between the neutral state $|v^*\rangle$ and the ionic state $|v^+\rangle$ with almost identical potential curves depends, as for all perturbations discussed in the preceding sections, on the overlap of the vibrational wavefunctions. As the coupling constitutes a breakdown of the Born–Oppenheimer approximation and is much weaker than the electrostatic coupling between the electrons, the autoionization rate is in general much smaller in molecules than in atoms, which can only autoionize through an energy transfer between the two excited electrons. Whereas typical lifetimes of autoionizing atomic states are in the range 10^{-13} – 10^{-10} s, they are 10^{-10} – 10^{-6} s for molecules [9.13].

The line profile of absorption transitions into autoionizing states is asymmetric and is called a *Fano profile*. It emerges from the interference between two undistinguishable transitions: excitation of the Rydberg state followed by autoionization on the one hand, and direct photoionization into a continuum state at the same energy on the other

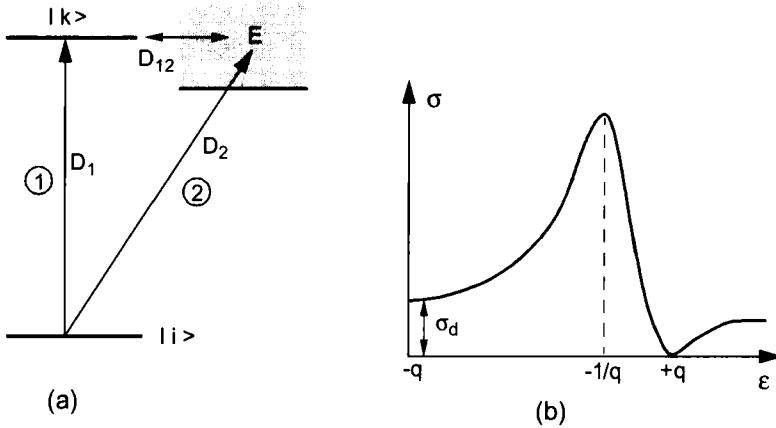


Fig. 9.16 a) Two indistinguishable possibilities to arrive at a state E above the ionization threshold through absorption of a photon. b) Fano profile.

hand (Fig. 9.16). The total probability W_{ik} for an excitation of the coupled system Rydberg state–continuous state from the discrete bound level $|i\rangle$ equals the square of the sum of both excitation amplitudes. It can be described by the absorption cross-section

$$\sigma_{\text{abs}} \propto W_{ik} = |D_1 + D_2|^2 \quad \text{with} \quad D_1 = \langle k|D|i\rangle \quad \text{and} \quad D_2 = \langle E|D|i\rangle. \quad (9.54)$$

If the excitation energy is varied continuously, its phase hardly changes upon excitation into continuum states, but changes drastically upon excitation of the Rydberg state, because then the excitation is resonant.

This phase shift changes the excitation probability and leads to the typical Fano profile shown in Fig. 9.16b for the absorption cross-section,

$$\sigma_{\text{abs}} = \sigma_d + \sigma_1 \frac{(q + \varepsilon)^2}{1 + \varepsilon^2}, \quad (9.55)$$

where σ_d is the absorption cross-section for transitions into continuum states that do not interact with the Rydberg state Ry, and σ_1 is that for transitions into the continuum coupling to Ry, and

$$\varepsilon = \frac{(E - E_r)}{\Gamma} \quad (9.56)$$

is the distance to the resonance energy in units of the full width at half maximum Γ of the line profile of the transition to the Rydberg state. The dimensionless Fano parameter

$$q = \frac{D_1^2}{(D_2 D_{12})} \quad (9.57)$$

is the ratio of the transition probability D_1^2 into the Rydberg state and the product of the

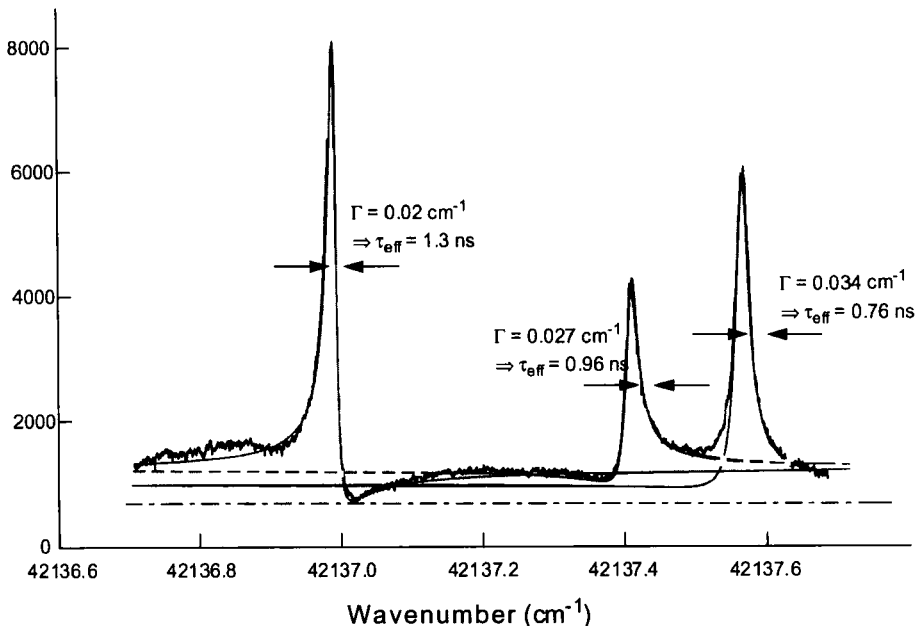


Fig. 9.17 Measured Fano profiles of absorption lines in Doppler-free spectroscopic investigations of Rydberg states of Li_2 [9.14].

transition amplitude D_2 into the continuum and the coupling coefficient D_{12} between Rydberg state and continuum.

For $\varepsilon = -q$, the Fano profile approaches the background, $\sigma(\varepsilon = -q) = \sigma_d$. The maximum of the absorption profile $\sigma_{\text{abs}}^{\text{max}} = \sigma_d + \sigma_i(q^2 + 1)$ is at $\varepsilon = -1/q$. At $\varepsilon = q$, a minimum is observed.

From a measurement of the linewidth Γ of the Fano profile, the lifetime of the autoionizing state can be determined, and from the parameter q the strength of the coupling to the continuum.

Figure 9.17 shows measured Fano profiles observed upon excitation of autoionizing Rydberg states of the Li_2 molecule [9.14]. It can be seen that the autoionization-limited lifetimes of about 10^{-9} s are significantly shorter than the radiative lifetimes, which are in the microsecond range. Hence, the decay of these Rydberg states occurs almost exclusively by autoionization.

9.4 Radiationless Transitions

An excited level cannot only decay by emission of radiation but also by a number of nonradiative processes such as predissociation, autoionization, or energy transfer to higher vibrational levels in lower electronic states with the same total energy as the originally excited level. In this process, the electronic energy is partially converted to

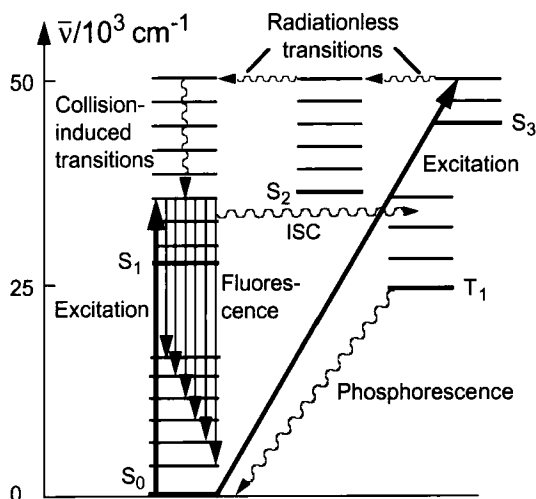


Fig. 9.18 Schematic representation of radiationless transitions.

vibrational energy. Particularly this last process is called *radiationless transition* in the literature. It occurs most frequently in polyatomic molecules, and its probability increases sharply with increasing density of vibrational states. Another cause of radiationless transitions is collisional energy transfer, where part of the excitation energy is converted into translational energy of the collision partner or into thermal energy of the other colliding molecule.

The coupling between initial and final state determining the probability of the process can be mediated by spin-orbit interaction, vibronic coupling, the Renner-Teller effect in linear molecules, or electrostatic interaction.

Such radiationless transitions will be illustrated in the following for a number of examples.

In larger aromatic molecules such as dyes, fluorescence is observed to originate exclusively from the S_1 state after several singlet states S_1 , S_2 , S_3 , etc., have been excited. Thus, a very fast radiationless process must exist that transfers the excitation energy so quickly into highly excited vibrational levels of S_1 that the much slower radiative decay paths are quenched. (Fig. 9.18).

The effective lifetime of these excited states,

$$\tau_{\text{eff}} = \frac{1}{k_{\text{rad}} + k_{\text{nonrad}}}, \quad (9.58)$$

is given by the reciprocal sum of radiative and nonradiative decay rates k_{rad} and k_{nonrad} , respectively. The quantum yield of the excited state,

$$\Phi_q = \frac{k_{\text{rad}}}{k_{\text{rad}} + k_{\text{nonrad}}}, \quad (9.59)$$

describes the relative proportion of the radiative decay to the total deactivation rate.

The quantities Φ_q and τ_{eff} can be determined experimentally, so that the radiative lifetime and the radiationless decay rate can be calculated according to

$$\tau_{\text{rad}} = \frac{1}{k_{\text{rad}}} = \frac{\tau_{\text{eff}}}{\Phi_q}; \quad k_{\text{rad}} = \frac{\Phi_q}{\tau_{\text{eff}}}; \quad k_{\text{nonrad}} = \frac{1 - \Phi_q}{\tau_{\text{eff}}}. \quad (9.60)$$

Such radiationless transitions between different singlet states are also called *internal conversion* (IC) [9.15].

The S_1 state itself is energetically far apart from the ground state so that its radiationless deactivation is far less probable. However, it can interact with, and finally be transferred to, the first excited triplet state, a process called *intersystem crossing* (ISC). The triplet state can then return to the S_0 ground state by emission of photons, albeit with much longer lifetime. This weak fluorescence from the normally forbidden T_1 – S_0 transition is called *phosphorescence*.

It turns out that the probability of radiationless transitions S_1 – S_0 increases with increasing vibrational energy in the S_1 state, despite the large difference $E(S_1) - E(S_0)$. The reason behind this fact is that both the density of states and the overlap between the vibrational wavefunctions of the interacting states increase sharply with increasing vibrational energy. The rate k_{nonrad} of radiationless transitions can be written as a product

$$k_{\text{nonrad}} = \left| \langle \Phi_i^{\text{el}} | H' | \Phi_k^{\text{el}} \rangle \langle \chi_i | \chi_k \rangle \right|^2 \rho(E), \quad (9.61)$$

where $\langle \Phi_i^{\text{el}} | H' | \Phi_k^{\text{el}} \rangle$ is the electronic part of the matrix element for the coupling between the two electronic states, H' is the perturbation operator describing the coupling, $\langle \chi_i | \chi_k \rangle$ is the overlap integral of the vibrational wavefunctions, the square of which is the Franck–Condon factor, and $\rho(E)$ is the density of states in the final state at the energy E [9.16].

Higher vibrational states in the S_1 state have a shorter effective lifetime because of their higher probability of radiationless transitions. Therefore, the absorption lines of transitions into these states are broadened.

The time response of such radiationless transitions can be studied in some simple systems. A good example is the van der Waals molecule I_2A consisting of a iodine molecule I_2 and a rare-gas atom A (see Ch. 10). The weak van der Waals bond gives rise to low vibrational frequencies for the vibration of the rare-gas atom against the molecule I_2 . If an internal vibration of the I_2 molecule of much higher energy than the van der Waals vibration is excited, the van der Waals bond can be excited, through the coupling with the I_2 vibration, into such a high vibrational level that it breaks and the molecule dissociates (Fig. 9.19).

This process can be best observed if a vibrational level ($v'J'$) of I_2 in the excited electronic state of the I_2A complex is excited that can return to the electronic ground state by fluorescence. The energies of the levels in the I_2A molecule are slightly shifted with respect to those in the I_2 molecule so that it is easy to distinguish if

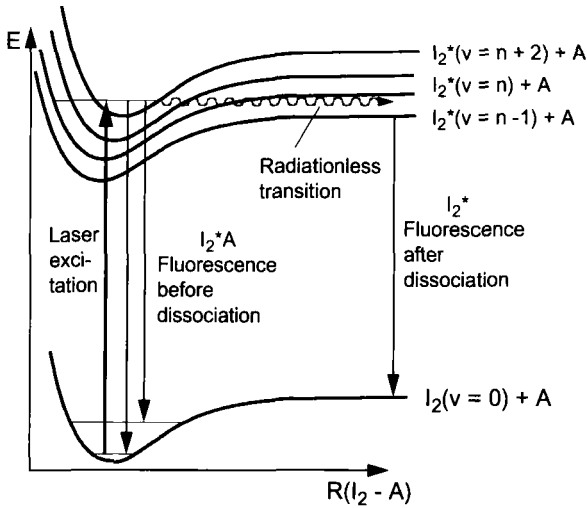


Fig. 9.19 Vibronic coupling with predissociation in the van der Waals molecule I_2Ar .

the I_2A complex or an I_2 molecule is excited. The radiationless transition through coupling with the van der Waals bond is much faster than the decay by spontaneous emission from the excited level, that is, the fluorescence is primarily emitted by the I_2 molecule after dissociation of the I_2A complex [9.17].

From the linewidth of the excitation line of the I_2A complex, the lifetime of the excited level can be determined, which is mainly determined by the fast dissociation. Measuring the I_2 fluorescence wavelengths from the excited final state ($v' - \Delta v', J' - \Delta J'$) of the dissociated I_2A complex gives unambiguous information on the upper emitting level, so that the energy transfer inside the van der Waals molecule can be calculated.

10

Molecules in External Fields

In an external magnetic field, molecules with magnetic moments experience splittings and shifts of their energy levels due to the Zeeman effect, the measurement of which can give information on the origins of the magnetic moments and the angular momenta associated with them. Magnetic moments can arise from the spin of unpaired electrons, from electronic orbital angular momenta, or from nuclear spins. Molecular rotation can also create a magnetic moment, which is small, however, compared with the permanent moments of the molecule at rest. The magnitude of the resulting moment depends on the coupling of the different angular momenta in the molecule, which in turn is influenced by the coupling between different states (see Ch. 9). Thus, measuring the magnetic moments opens additional ways for the investigation of the perturbations treated in Ch. 9.

Analogously, molecules with permanent or induced electric moments experience splittings and shifts of their energy levels in electric fields due to the Stark effect, providing information on their electron distribution and the electric polarizability of their electron cloud.

These magnetic and electric properties of molecules are exploited in numerous diagnostic techniques. Important examples are electron spin resonance (ESR) spectroscopy, nuclear magnetic resonance tomography, which is of profound importance in medicine, and laser magnetic resonance or Stark spectroscopy (see Ch. 12).

In this chapter, we will consider the electric and magnetic properties of molecules and learn what information the Zeeman or Stark effects can provide.

The magnetic moments μ_m are specified in A m^2 , and their magnitudes are often compared with that of the Bohr magneton $\mu_B = 9.27 \times 10^{-24} \text{A m}^2$.

The electric moments μ_{el} are specified in As m . Frequently, the unit Debye with $1 \text{D} = 3.34 \times 10^{-30} \text{As m}$ is used.

Examples

The NO molecule has, in its ${}^2\Pi_{3/2}$ ground state, a permanent magnetic moment $\mu_m = 1.7 \times 10^{-23} \text{A m}^2 = 1.83\mu_B$ and an electric dipole moment $\mu_{el} = 0.153 \text{D}$. The electric dipole moment of the HCl molecule is $\mu_{el} = 3.70 \times 10^{-30} \text{As m} = 1.108 \text{D}$, whereas its magnetic dipole moment in the ${}^1\Sigma$ ground state is very small: $\mu_m = g_J J \mu_N \approx 0.46 J \mu_N$, where $\mu_N = 5.05 \times 10^{-27} \text{A m}^2$ is the nuclear magneton.

10.1

Diamagnetic and Paramagnetic Molecules

Molecules with permanent magnetic moments are called *paramagnetic*.

Most ground-state homonuclear diatomic molecules, however, possess neither a magnetic spin moment, because the electron spins compensate pairwise for an even number of electrons, nor a magnetic orbital moment, because the ground states are usually Σ states with $L = 0$ (see Sect. 2.4.2). Exceptions are molecules with an electron spin $S \neq 0$ (such as O_2 or all radicals with an unpaired electron) or heteronuclear molecules with $L \neq 0$ or $S \neq 0$ (such as NO).

In nonlinear polyatomic molecules, the electron shell cannot possess orbital angular momentum, and the total electron spin in the ground state is usually also zero. Such molecules without a permanent magnetic moment are called *diamagnetic*.

In an external magnetic field, however, diamagnetic molecules acquire an *induced magnetic moment*

$$\mu_m^{\text{ind}} = -\beta B, \quad (10.1)$$

which depends on the external magnetic field B and the *magnetic polarizability* β and which is oriented opposite to the external field.

Table 10.1 lists the magnetic polarizabilities β for some molecules. This shows, for example, that the magnetic moment induced in the H_2 molecule in an external field $B = 1 \text{ T}$ is smaller than the Bohr magneton $\mu_B = 9.3 \times 10^{-24} \text{ A m}^2$ by six orders of magnitude. Thus, the induced magnetic moments are very small compared with the permanent moments of paramagnetic molecules.

The magnetic polarizability β is anisotropic in all molecules that are not spherically symmetric. Hence, the induced moment depends on the direction of the external field with respect to a specific axis within the molecule [10.1]. For example, in diatomic molecules β_{\parallel} parallel to the molecular axis differs from β_{\perp} perpendicular to the axis. The largest induced moments are obtained if the external magnetic field is perpendicular to the axis of maximum electron mobility within the molecule, because the induced magnetic moment arises from a current perpendicular to the magnetic field. For example, in a molecule such as benzene, in which the electrons can move freely

Tab. 10.1 Magnetic susceptibility χ and magnetic polarizability β for some diamagnetic molecules and permanent magnetic moments for some paramagnetic molecules.

	Diamagnetic molecules		Paramagnetic molecules		
	$\chi \times 10^6$	$\beta / (\text{A m}^4 / \text{Vs})$		$\mu_m / (\text{A m}^2)$	$\chi \times 10^6$
H_2	-0.002	-2.4×10^{-30}	NO	1.7×10^{-23}	0.78
H_2O	-9.0	-4.5×10^{-27}	O_2	2.58×10^{-23}	1.8
NaCl	-13.9	-6.9×10^{-27}			

along the ring of carbon atoms due to the π bonding, the maximum induced magnetic moment is obtained with the external field perpendicular to the molecular plane.

All molecules with unpaired electrons or with a nonvanishing electronic orbital moment possess a permanent magnetic moment and are therefore paramagnetic.

In a sample of freely moving paramagnetic molecules, the molecules are randomly oriented. In the absence of external fields, the directions of the magnetic moments are therefore distributed statistically due to thermal motion. If an external field exists, the molecules are partially oriented, and the degree of orientation increases with increasing field strength, but decreases with increasing temperature. If the magnetic energy

$$W_m = -\mu_m \cdot B \quad (10.2)$$

is large compared with the thermal energy kT , an almost complete orientation in the external field is achieved. The macroscopic magnetization M of N molecules per unit volume in an external field $B = B_z$ along z is given by the vector sum of all magnetic moments,

$$M = \sum \mu_m = N\mu_m^* = N\eta\mu_m, \quad (10.3)$$

where μ_m^* is the effective fraction of the magnetic moments contributing to the magnetization, and

$$\eta = \frac{\mu_m^*}{\mu_m} = \frac{1}{3} \frac{|\mu_m| |B|}{kT} \quad (10.4)$$

is the degree of orientation, which is given by the ratio of the potential energy of the dipoles in the field B to the thermal energy kT . (As the directions of the dipoles are randomly oriented in space in the absence of an external field, on average only 1/3 of the N molecules contribute to the maximum potential energy $|\mu_m B|$.)

If we substitute Eq. (10.4) into Eq. (10.3), we obtain

$$M = N \frac{\mu_m^2}{3kT} B = \frac{\chi}{\mu_0} B \quad (10.5)$$

with the magnetic constant $\mu_0 = 4\pi \times 10^{-7}$ Vs/(Am) and the dimensionless magnetic susceptibility

$$\chi = \frac{1}{3} \frac{N\mu_m^2}{kT}. \quad (10.6)$$

10.2

Zeeman Effect in Linear Molecules

The magnetic moment of a linear paramagnetic molecule in a state with electronic orbital angular momentum L and electron spin S depends on the coupling of the angular momenta, that is, on the corresponding Hund's case (see Sect. 9.2).

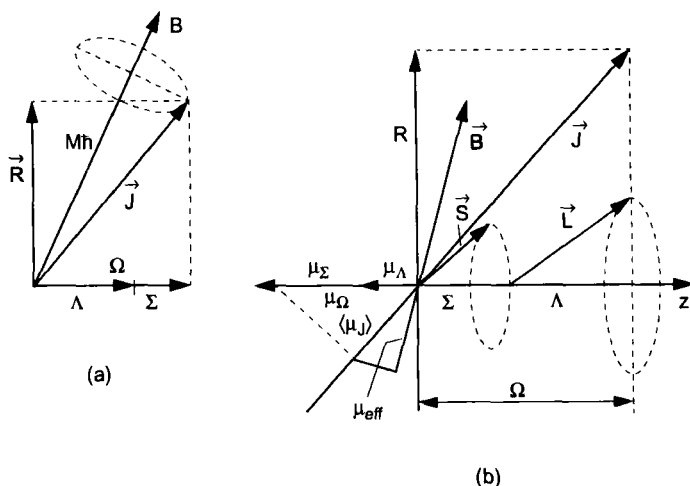


Fig. 10.1 a) Coupling of angular momenta and b) coupling of magnetic moments with an external magnetic field in Hund's coupling case a).

In coupling case a), L and S precess around the molecular axis with projections (in the molecule-fixed reference frame) Λ and Σ (cf. page 300). The corresponding magnetic moment along the molecular axis is then

$$\mu_\Omega = (\Lambda + 2\Sigma)\mu_B, \quad (10.7)$$

where we have taken into account that the gyromagnetic ratio is twice as large for the spin than for the orbital angular momentum.

Examples

In a $^1\Pi$ state, $\mu_m = 1\mu_B$. In a $^3\Sigma$ state, $\mu_m = 2\mu_B$, in a $^2\Pi_{3/2}$ state $\mu_m = 2\mu_B$, but in a $^2\Pi_{1/2}$ state, in which M_L and M_S have opposite signs, $\mu_m = 0$.

If the molecule rotates, the molecular axis precesses around the angular-momentum axis \vec{J} , which is stationary in the laboratory-fixed system in the absence of an external field, so that only the time-averaged magnetic moment

$$\langle \mu_J \rangle = \mu_\Omega \cos(\angle z, \vec{J}) = (\Lambda + 2\Sigma)\mu_B \frac{\Lambda + \Sigma}{\sqrt{J(J+1)}} \quad (10.8)$$

along \vec{J} survives. In an external magnetic field, μ_J is no longer stationary but precesses around the direction of the field \vec{B} (Fig. 10.1). Now, the time-averaged component

$$\mu_{\text{eff}} = \langle \mu_J \rangle \cos(\angle \vec{J}, \vec{B}) = \frac{(\Lambda + 2\Sigma)(\Lambda + \Sigma)M}{J(J+1)} \mu_B \quad (10.9)$$

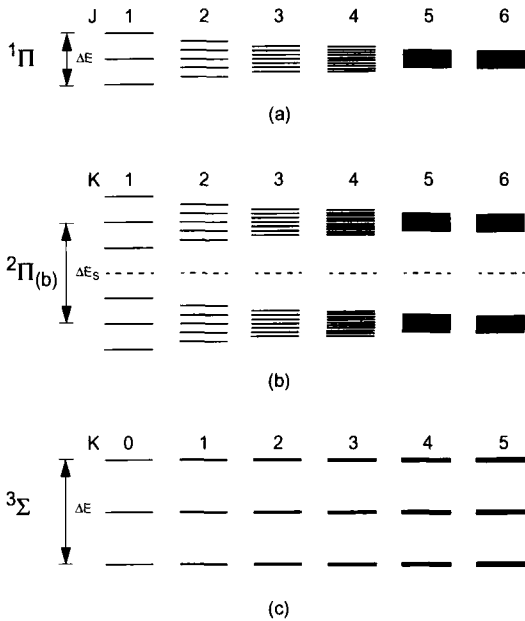


Fig. 10.2 Zeeman splitting of rotational levels. a) For a 1Π state [Hund's case (a)], b) for a 2Π state [Hund's case (b)], c) for a 3Σ state [10.2].

remains as the effective magnetic moment of a rotating molecule in an external magnetic field, where $M\hbar$ is the projection of \mathbf{J} onto the direction of the field \mathbf{B} . Note the strong dependency of the effective magnetic moment on J !

The energy of a Zeeman level is then

$$E(J, B) = E_0 + \mu_{\text{eff}} \cdot \mathbf{B}, \quad (10.10)$$

where E_0 is the energy for $B = 0$. With increasing rotational quantum number J , the Zeeman splitting of the rotational levels decreases rapidly. The total splitting

$$\begin{aligned} \Delta E &= E(B, M = J) - E(B, M = -J) \\ &= 2 \frac{(A + 2\Sigma)(A + \Sigma)}{J + 1} B \end{aligned} \quad (10.11)$$

decreases as $(J + 1)^{-1}$ (Fig. 10.2a).

In Hund's coupling case (b), the electronic orbital angular momentum \mathbf{L} couples to the molecular axis, but the electron spin \mathbf{S} couples to the rotation axis (Fig. 10.3). The time-averaged projection of the magnetic moment onto the direction of the total angular momentum is then composed of the contributions

$$\mu_L = A\mu_B \quad \text{and} \quad \mu_S = 2[S(S + 1)]^{1/2} \mu_B. \quad (10.12)$$

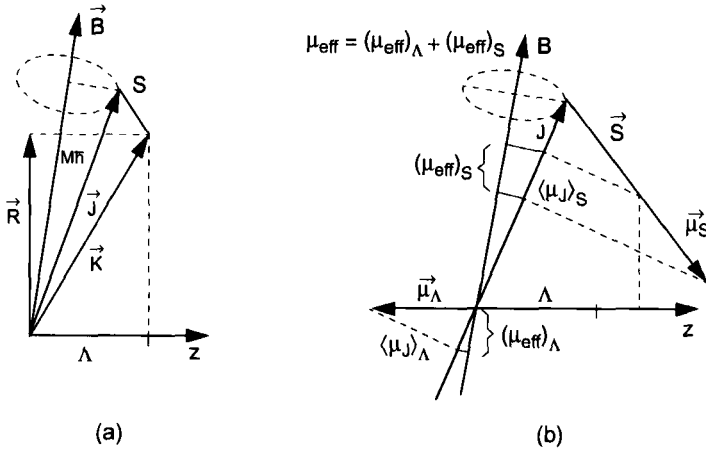


Fig. 10.3 Coupling of a) angular momenta and b) magnetic moments in Hund's coupling case (b).

The projection onto the direction of J is then

$$\langle \mu_J \rangle = \Lambda \mu_B \cos(z, K) \cos(K, J) + 2\sqrt{S(S+1)} \mu_B \cos(S, J). \quad (10.13)$$

In the external magnetic field, J precesses around the direction of B , and thus we obtain for the time-averaged effective magnetic moment

$$\mu_{\text{eff}} = \left[\frac{\Lambda^2 \cos(K, J)}{\sqrt{K(K+1)}} + 2\sqrt{S(S+1)} \cos(S, J) \right] \frac{M}{\sqrt{J(J+1)}} \mu_B, \quad (10.14)$$

where we have used $\cos(z, K) = \Lambda/[K(K+1)]^{1/2}$ and $\cos(J, B) = M/[J(J+1)]^{1/2}$.

The $2S+1$ possible orientations of the spin with respect to K entail $2S+1$ different values of $\cos(S, J)$. Hence, we obtain $2S+1$ groups of Zeeman components, each of which contains $(2J+1)$ equidistant Zeeman levels with energies

$$E = E_0 + \mu_{\text{eff}} B,$$

the spacing of which decreases rapidly with increasing J (Fig. 10.2b).

For large values of K , the first term in Eq. (10.14) is small compared with the second term so that the total splitting

$$\begin{aligned} \Delta E &= \mu_{\text{eff}}(M) - \mu_{\text{eff}}(-M) \approx 2[S(S+1)]^{1/2} \frac{2J+1}{\sqrt{J(J+1)}} \mu_B B \\ &\approx 4[S(S+1)]^{1/2} \mu_B B \end{aligned}$$

is essentially determined by S and is independent of J (Fig. 10.2b).

If the magnetic field is strong enough so that the coupling of μ with the magnetic field is stronger than the mutual coupling of the magnetic moments (i.e., that the

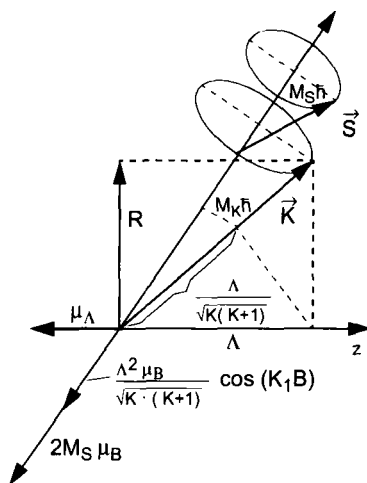


Fig. 10.4 Independent precession of K and S in the Paschen-Back effect.

Zeeman splitting becomes larger than the multiplet splitting), S and K couple independently with B (Paschen-Back effect) and

$$\mu_{\text{eff}} = \frac{\Lambda^2 \mu_B}{\sqrt{K(K+1)}} \cos(K, B) + 2\sqrt{S(S+1)} \mu_B \cos(S, B). \quad (10.15)$$

With $\cos(K, B) = M_K / \sqrt{K(K+1)}$ and $\cos(S, B) = M_S / \sqrt{S(S+1)}$, Eq. (10.15) becomes

$$\mu_{\text{eff}} = \frac{\Lambda^2 M_K}{K(K+1)} \mu_B + 2M_S \mu_B. \quad (10.16)$$

The first term corresponds to Eq. (10.9) for $\Sigma = 0$ and $J = K$. The contribution from the first term decreases rapidly with increasing quantum number K , until the splitting into spin components dominates. For Σ states with $\Lambda = 0$, the first term vanishes. As the coupling of S with J is weaker than the coupling of S with B even for small field strengths, the Paschen-Back effect occurs for relatively weak external fields (Fig. 10.4). This is the case, for example, for the $^3\Sigma$ state (Fig. 10.2c), where the molecular rotation creates only a small splitting of the three spin components with a spacing independent of J .

In an electronic transition from a lower level with Zeeman splitting to an excited level without magnetic moment (e.g., $^1\Sigma \leftarrow ^1\Pi$), the splitting of the lines essentially corresponds to that of the lower level. The selection rules are $\Delta M = 0, \pm 1$. The polarization of the lines can contain components parallel or perpendicular to the magnetic field. As the transition moment is perpendicular to the molecular axis for Q transitions, but along the molecular axis for P and R transitions, the polarization for

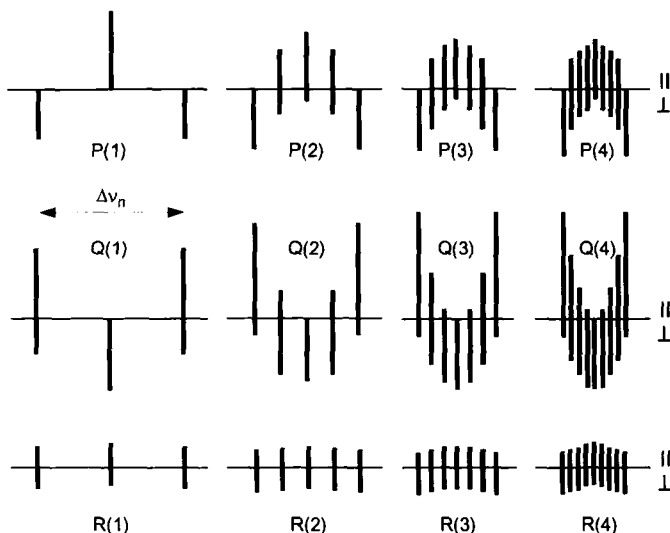


Fig. 10.5 Zeeman splittings of the lowest rotational lines from a ${}^1\Sigma \leftarrow {}^1\Pi$ transition with indication of the corresponding polarization. The portion above the horizontal line corresponds to parallel, the portion below the line corresponds to perpendicular polarization with respect to the magnetic field [10.2].

transitions with different ΔJ is also different (Fig. 10.5). If both states display different Zeeman splittings, the frequency difference of the transitions with $\Delta M = 0, \pm 1$ can be used to determine the individual splittings (Fig. 10.6).

Diamagnetic nonrotating molecules possess no permanent magnetic moment. However, molecular rotation can create a minute magnetic moment

$$\mu_J \propto \mu_N J \quad (10.17a)$$

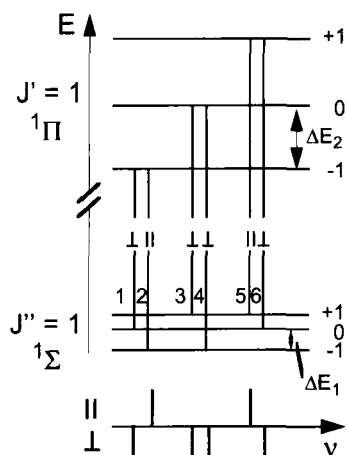
even in ${}^1\Sigma$ states, where $\mu_N = (e/2m_p)\hbar$ is the nuclear magneton. The nuclear magneton is smaller than the Bohr magneton of the electron shell by a factor $(m_e/m_p) = 1/1836$ [10.3].

The origin of this moment can be visualized as follows.

If, in a homonuclear diatomic molecule with rotational angular momentum J , only the nuclei with charges Ze , mass numbers A , zero nuclear spins, and internuclear distance R were to rotate at a frequency ν , a magnetic moment $\mu_m = \mu_J$ would follow from classical electrodynamics,

$$\mu_J = IF = 2Zev\pi \left(\frac{R}{2}\right)^2, \quad (10.17b)$$

where $I = 2Zev$ is the electric current due to the circular motion of the charged nuclei moving periodically with frequency ν on a circle with area $F = \pi(R/2)^2$. As the classical angular momentum of the two nuclei with reduced mass $m_1 m_2 / (m_1 + m_2) =$



$$\nu_2 - \nu_1 = \Delta E_1; \quad \nu_4 - \nu_2 = \Delta E_2$$

Fig. 10.6 Absorption transitions between two levels with different Zeeman splittings, here the Q (1) line of a ${}^1\Pi \leftarrow {}^1\Sigma$ transition.

$\frac{1}{2}m_{\text{nuc}}$ is $|\mathbf{J}| = \frac{1}{2}m_{\text{nuc}}Rv = \frac{1}{2}m_{\text{nuc}}R^2\omega = \pi m_{\text{nuc}}R^2\nu$, giving $\nu = |\mathbf{J}| / (\pi m_{\text{nuc}}R^2)$, we obtain by inserting ν into Eq. (10.17b)

$$\boldsymbol{\mu}_J = \frac{Ze}{2m_{\text{nuc}}}\mathbf{J}. \quad (10.17c)$$

With the nuclear magneton $\mu_N = \frac{e}{2m_p}\hbar$ (m_p = proton mass), we finally obtain for the nuclear contribution to the magnetic moment of the rotating molecule

$$(\boldsymbol{\mu}_J)_{\text{nuc}} = \frac{Z}{A}\mu_N\mathbf{J}/\hbar, \quad (10.17d)$$

with the mass number $A \approx m_{\text{nuc}}/m_p$.

As the negatively charged electron shell is rotating together with the nuclear framework, an opposite electric current arises. However, the electronic charge is distributed over a range of distances so that this opposing electric current can only partially compensate for the current due to the rotating nuclei, and a contribution to the magnetic moment proportional to J survives.

The energy of the Zeeman components is then

$$E(B) = E_0 - (\boldsymbol{\mu}_J)_{\text{eff}} \cdot \mathbf{B} = E_0 - g_J\mu_N M_J B, \quad (10.18)$$

where E_0 denotes the energy for $B = 0$, M_J is the quantum number of the projection of J onto the field direction ranging from $M = -J$ to $M = +J$, and g_J is a measure of the compensation. Hence, each level splits into $2J + 1$ equidistant Zeeman components.

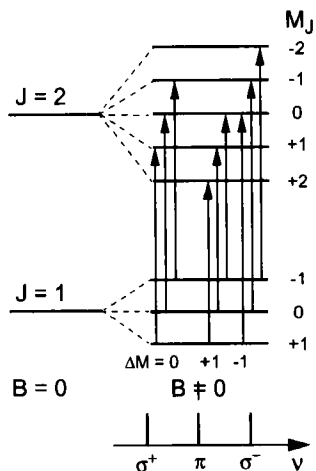


Fig. 10.7 Zeeman splitting for a diamagnetic molecule in a $^1\Sigma$ state without hyperfine structure.

The spacing $\Delta E = g_J \mu_N B$ between two adjacent Zeeman components does not depend on J (Fig. 10.7).

Microwave transitions between the Zeeman components of two adjacent rotational levels must satisfy the selection rules $\Delta J = 1$; $\Delta M = 0$ (linear polarized wave with the E vector parallel to the magnetic field B) or $\Delta J = 1$; $\Delta M = \pm 1$ (circularly polarized transitions).

In nonrotating diamagnetic molecules (e.g., in solids) only the induced magnetic moments $\mu_{\text{ind}} = \tilde{\beta} B$ are left. It is important to note that the magnetic polarizability $\tilde{\beta}$ is, in general, anisotropic, that is, $\tilde{\beta}$ is a tensor. The induced magnetic moment therefore depends on the molecule's orientation in the magnetic field. As the magnetic moments induced by practicable magnetic fields are very small compared to the permanent moments of paramagnetic molecules, they are only relevant in solids, where the density of molecules is large.

If the atomic nuclei also possess spins and hence magnetic moments, a *hyperfine structure* arises due to the interaction between the nuclear and the electronic magnetic moments. For molecules with a nonzero resulting electron spin, the *Fermi contact interaction* between electron and nuclear spin gives the major contribution, provided the electron density at the nuclei is nonzero. The interaction energy for a nuclear spin I_k of the k th nucleus and an electron spin s_i of the i th electron is

$$E_{\text{hf}} = A_c \sum_k \sum_i I_k s_i \delta(\mathbf{r}_i - \mathbf{r}_k) . \quad (10.19)$$

The constant

$$A_c = \frac{8\pi}{3} g_e \mu_B g_{\text{nuc}} \mu_N \quad (10.20)$$

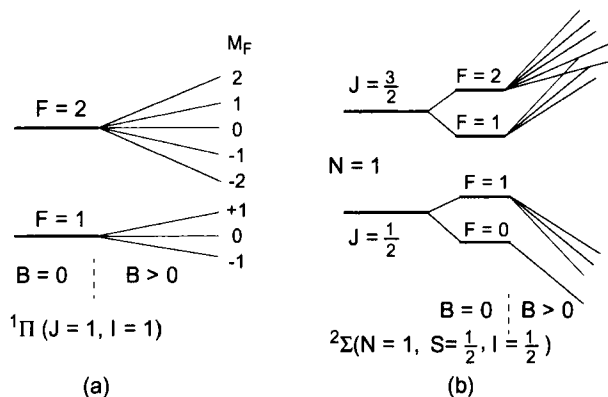


Fig. 10.8 Zeeman splitting of hyperfine components if the Zeeman splitting is a) small compared to the hyperfine splitting, and b) larger than the hyperfine splitting.

is called the *Fermi contact constant*. If we introduce the total spins

$$S = \sum s_i \quad \text{and} \quad I = \sum I_k \quad \text{and} \quad G = S + I,$$

the hyperfine interaction for an isotropic electron spin density can be written, using $I \cdot S = (1/2)(G^2 - I^2 - S^2)$, as

$$E_{\text{hf}} = \frac{A_c}{2} [G(G + 1) - I(I + 1) - S(S + 1)]. \quad (10.21)$$

In an external magnetic field, the hyperfine components are split. The exact structure of the splitting depends on whether the hyperfine splitting is larger or smaller than the Zeeman splitting. For sufficiently weak magnetic fields, it is large compared with the Zeeman splitting, and the coupling of the internal angular momenta remains intact. If we introduce the total angular momentum

$$F = G + R = S + I + R$$

as vectorial sum of electron spin S , nuclear spin I , and rotational angular momentum R , each hyperfine level splits into $(2F + 1)$ equidistant Zeeman components (Fig. 10.8a).

For stronger magnetic fields, the coupling between nuclear and electron spins becomes weaker than the coupling of both with the magnetic field. In this case, electron spin and nuclear spin couple independently with the magnetic field. As the magnetic moment of the electron spin is larger than that of the nuclear spins by three orders of magnitude, the Zeeman splitting is first into $2S + 1$ components M_s of the electron spin, and each of these components displays a substructure of $2I + 1$ components (Fig. 10.8b).

In the transient regime between these two limiting cases, the structure of the Zeeman levels is more complicated.

10.3 Spin–Orbit Coupling and External Magnetic Fields

While a singlet state of a nonlinear molecule is not influenced by an external magnetic field B (except for potential minute nuclear spin effects), the terms of a triplet state are split and experience a Zeeman shift proportional to B due to the interaction of the electron spin moment with the magnetic field. If two rotational levels with the same J in a singlet and a triplet state with an energy separation ΔE interact due to spin–orbit coupling, the magnetic field influences the energetic spacing $\Delta E(B)$ between these two levels (Fig. 10.9) and hence the strength of the perturbation, that is, the degree of mixing of the states.

This will be illustrated for the CS_2 molecule. Here, an optical excitation occurs from the $^1\Sigma$ ground state of the linear molecule into a rotational level of the bent 1B_2 excited state (Fig. 10.10). This state interacts through spin–orbit coupling with a 3B_2 state. In the absence of an external magnetic field ($B = 0$), only the singlet state is excited because the transition from the $^1\Sigma$ ground state into the triplet state is forbidden. With increasing magnetic field strength, the coupling between the two states also increases, that is, the triplet state acquires an increasing contribution from the singlet state, which increases the transition probability. Figure 10.11 shows that the intensity of the split Zeeman components in the triplet state increases with increasing B and that these components are shifted towards the singlet transition. Simultaneously, the singlet state acquires an admixture of triplet eigenfunctions and thus also a Zeeman splitting [10.6].

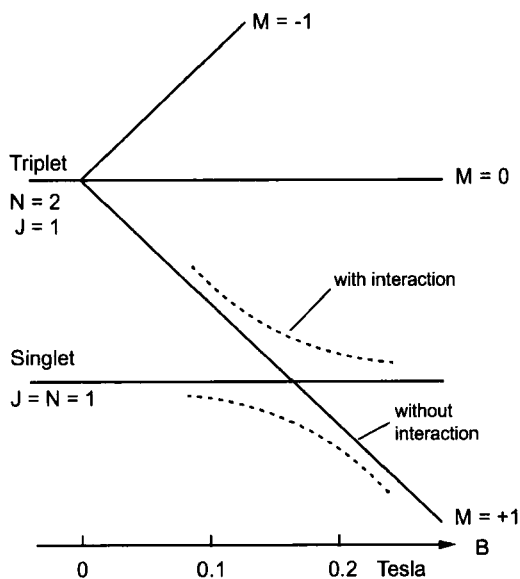


Fig. 10.9 Zeeman splitting of two rotational levels in a singlet and a triplet state interacting through spin–orbit coupling.

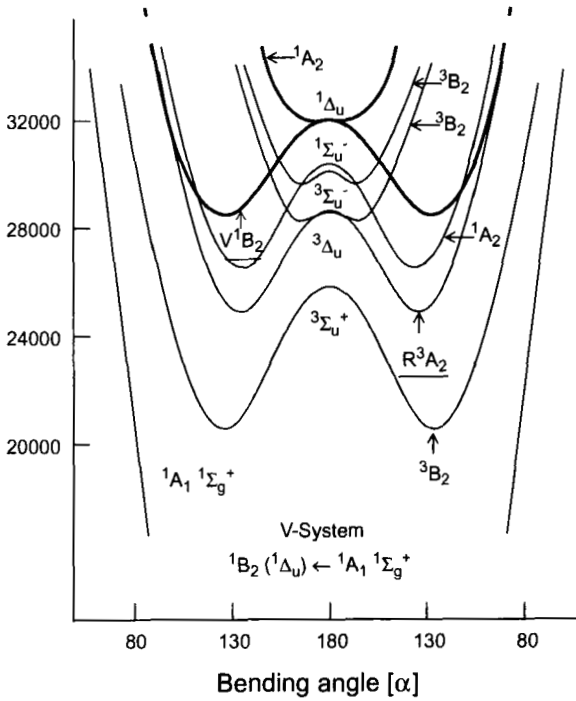


Fig. 10.10 Section from the potential curve diagram of the CS₂ molecule.

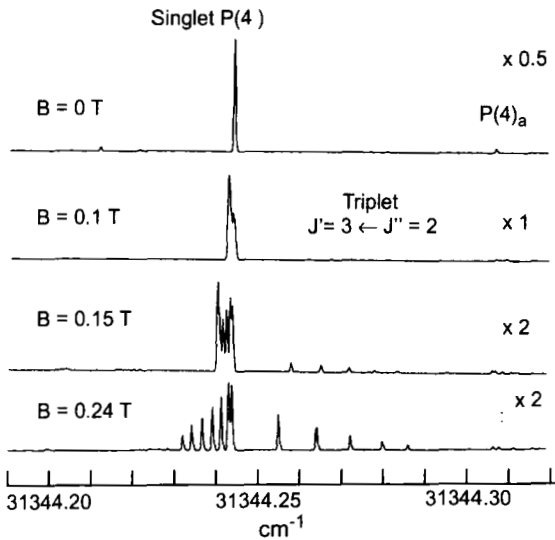


Fig. 10.11 Zeeman splitting of absorption lines of CS₂ leading from the ground state to rotational levels of the $1B_2$ and $3B_2$ states interacting through spin–orbit coupling for different strengths of the external magnetic field [10.4].

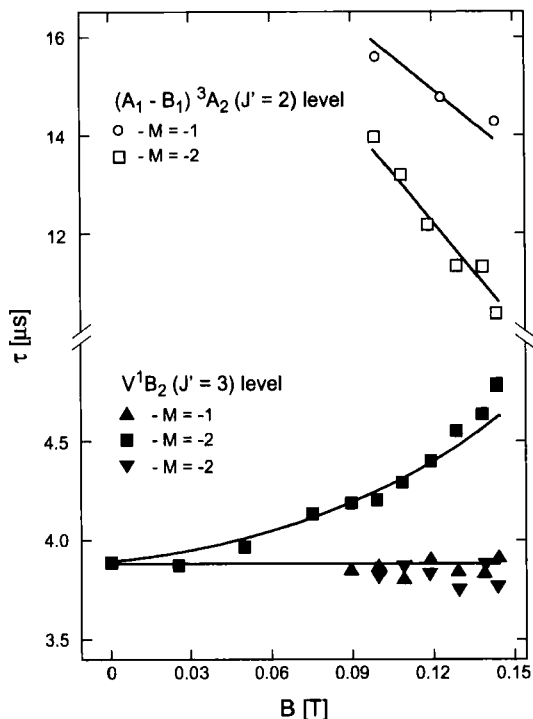


Fig. 10.12 Lifetimes of singlet and triplet levels as a functions of the magnetic field strength [10.5].

From the field-dependent splittings and shifts of the two Zeeman structures, the magnetic moment of the triplet state and the strength of the spin-orbit coupling can be deduced.

Above an excitation energy E_c , the maximum of the potential curve $E_{\text{pot}}(\alpha)$ of the 1B_2 (${}^1\Delta_u$) state in Fig. 10.10, located at a linear structure with $\alpha = 180^\circ$ (in this linear arrangement, the state is ${}^1\Delta_u$ with $\Lambda = 2$), is exceeded. During bending vibrations across the potential barrier, an electronic orbital moment can then arise, which is quenched in the bent conformation. This effect leads to an increase of the total magnetic moment and hence to a larger Zeeman splitting as confirmed by experiments.

As the spontaneous lifetime of the triplet state is much larger than that of the singlet state, any mixing between the states extends the lifetime of the singlet state and shortens the lifetime of the triplet state. The magnetic field increases the coupling between both states and thus an increase of the magnetic field strength will lead to a shorter lifetime τ of the triplet state and a larger lifetime of the singlet state (Fig. 10.12). Measurement of the dependency $\tau(B)$ allows a highly accurate determination of the mixing coefficients of the wavefunctions of the coupled states.

This shows that the measurements of the Zeeman splitting can provide detailed information on the excited molecule, its potential surface, and the coupling between different states.

10.4

Molecules in Electric Fields: The Stark Effect

Molecules possess an *electric dipole moment* if the centers of charge for the positive charges of the nuclear framework and the negative charges of the electron shell do not coincide. Table 10.2 lists the dipole moments of some polar molecules. Analogously to molecules with magnetic moments in magnetic fields, molecules with electric dipole moments experience splittings and shifts of their levels in electric fields. [10.7].

Molecules with a center of inversion or with more than one C_n axis with $n > 2$ (see Sect. 5.1) cannot possess an electric dipole moment for symmetry reasons; they are called *nonpolar*. This is the case for all homonuclear diatomic molecules such as H_2 , N_2 , O_2 , but also for CH_4 or CCl_4 .

In an external electric field \mathcal{E} , both in polar and nonpolar molecules induced moments

$$\mu_{\text{ind}}^{\text{el}} = -\alpha\mathcal{E} \quad (10.22)$$

emerge. The electric polarizability α is a measure for the ease with which the negatively charged electron cloud can be shifted with respect to the positively charged nuclear framework. In polar molecules, the total dipole moment is the vector sum of the permanent and the induced moment. Like the magnetic polarizability β , the electric α is also a tensor, because the induced moment depends on the orientation of the electric field \mathcal{E} with respect to the molecular axis. For example, the polarizability of CO along the molecular axis is three times as large as that perpendicular to it.

The energy of an electric dipole in an electric field is

$$E = -\mu^{\text{el}}\mathcal{E}, \quad (10.23)$$

which means that for induced dipole moments, the energy

$$E = \alpha|\mathcal{E}|^2 \quad (10.24)$$

in the electric field increases as \mathcal{E}^2 .

Tab. 10.2 Permanent electric dipole moments of some molecules^a.

Diatomic molecules		Polyatomic molecules	
Molecule	$\mu_{\text{el}}/10^{-30}$ Asm	Molecule	$\mu_{\text{el}}/10^{-30}$ Asm
CO	0.37	C_6H_6	0.0
BF	1.67	N_2O	0.54
HF	6.00	NO_2	1.05
AgCl	19.0	H_2S	3.24
NaCl	30.0	H_2O	6.18
BaS	35.4	$C_2H_2O_2$	16.01

^a1 Debye (D) = 3.336×10^{-30} Asm.

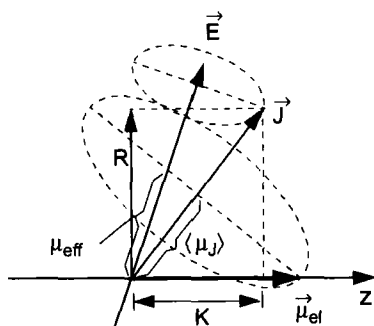


Fig. 10.13 Derivation of the effective electric dipole moment in an external electric field.

In polar molecules with axial symmetry, the permanent dipole moment must be oriented along the molecular axis. During a rotation of the molecule, all components perpendicular to the rotation axis are averaged to zero, and averaged over time only the component

$$\langle \mu_J^{el} \rangle = |\mu| \cos(\mathbf{J}, z) = \frac{\mu K}{\sqrt{J(J+1)}}$$

along the rotational axis \mathbf{J} survives, where K is the component of \mathbf{J} along the molecular axis (Fig. 10.13).

In an electric field, \mathbf{J} precesses around the direction of the field, so that only the component

$$\mu_{\text{eff}}^{el} = \langle \mu_J^{el} \rangle \cos(\mathbf{J}, \mathbf{E}) = \frac{KM}{J(J+1)} \mu^{el} \quad (10.25)$$

survives. According to Eq. (10.23), the *first-order Stark shift*, that is, the shift of the energy of a level due to the electric field, is then given by

$$\Delta E^{(1)} = -\frac{KM\mathcal{E}\mu^{el}}{J(J+1)}. \quad (10.26)$$

For a linear molecule in a $^1\Sigma$ state (i.e., $L = 0$ and $S = 0$), the total angular momentum is perpendicular to the molecular symmetry axis, that is, the projection quantum number is $K = 0$ and therefore $E^{(1)} = 0$. Hence, these states show no first-order Stark effect!

However, there is also a second-order effect, as can easily be understood. The energy of a dipole in an electric field depends on its orientation. If it is aligned with the electric field, its energy is, according to Eq. (10.23), lower by an amount $2\mu\mathcal{E}$ than if it is opposed to it. Thus, the molecule will not rotate uniformly around an axis perpendicular to the dipole moment, but will rather spend a larger fraction of its time in the energetically favorable orientation where it rotates slower. This fraction is given

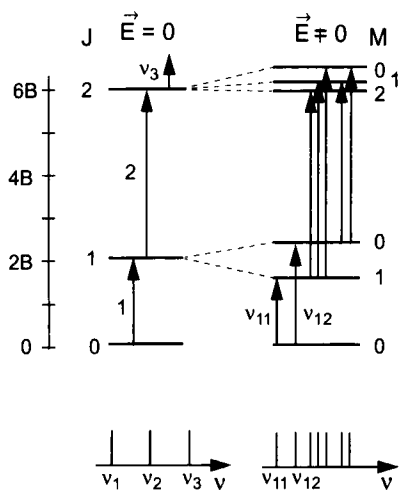


Fig. 10.14 Second-order Stark splitting of rotational levels in states with $K = 0$.

by the ratio

$$R \propto \frac{\mu \cdot \mathcal{E}}{E_{\text{rot}}} \quad (10.27)$$

of electrostatic energy and rotational energy $E_{\text{rot}} = hcBJ(J+1)$. For molecules with a permanent dipole moment, the shifts of the molecular energy levels in the field can be calculated as

$$\Delta E^{(2)} \propto \frac{|\mu \mathcal{E}|^2}{hcBJ(J+1)}. \quad (10.28)$$

The shift is proportional to the square of the electric field strength and to the square of the dipole moment (second-order Stark effect) and is always positive. Thus, the Stark shift depends only on the magnitude of the projection quantum number M , not on its sign (Fig. 10.14).

A quantum-mechanical treatment using a second-order perturbational calculation [10.1] yields, instead of Eq. (10.28),

$$E_{JM}^{(2)} = E_0 + \frac{\mu^2 \mathcal{E}^2}{2hcB_v} \frac{J(J+1) - 3M^2}{J(J+1)(2J-1)(2J+3)}. \quad (10.29)$$

Each rotational level with rotational quantum number J is split into $(J+1)$ Stark components because M runs from $-J$ to $+J$ and M^2 can assume $J+1$ different values.

For molecular states with $K \neq 0$ (e.g., linear molecules with electronic angular momentum L , where $K = \Lambda$, or bent symmetric top molecules), the first-order Stark effect occurs. Of course, the rotation is in these cases also influenced by the electric field, so that there is in addition also a second-order Stark effect.

Hence, all molecular states with $K \neq 0$ show both first- and second-order Stark effects, and the second-order effect is in general smaller than the first-order effect. The quantum-mechanical calculation, which will not be given here, yields for the energy of a Stark component (J, K, M) of a symmetric top molecule [10.1]

$$E(\mathcal{E}) = E_0 - \frac{\mu K M_J \mathcal{E}}{J(J+1)} + \frac{\mu^2 \mathcal{E}^2}{2hB} \left[\frac{(J^2 - K^2)(J^2 - M_J^2)}{J^3(2J-1)(2J+1)} - \frac{[(J+1)^2 - K^2][(J+1)^2 - M_J^2]}{(J+1)^3(2J+1)(2J+3)} \right], \quad (10.30)$$

where E_0 is the energy for $\mathcal{E} = 0$, the second term describes the first-order Stark effect and the third term describes the second-order Stark effect.

In asymmetric top molecules, the K -degeneracy is removed (see Sect. 6.2.3). Hence, they show only a second-order Stark effect. However, the calculation of the energies of their Stark components is not possible in closed form, but must be done numerically.

11

Van der Waals Molecules and Clusters

In recent years, the investigation of weakly bound systems, in which van der Waals interactions rather than covalent chemical bonds cause cohesion, has progressed rapidly. Such van der Waals bonds are dominant, for example, in compounds between atoms with completely filled electron shells, because here no valence electrons are available for an ordinary chemical bond. Examples of such van der Waals molecules (Fig. 11.1) are rare-gas dimers such as He_2 , Ne_2 , Ar_2 , Kr_2 or Xe_2 , halide–rare-gas compounds such as XeCl or ArF , metal atom–rare-gas atom compounds such as NaAr , or compounds of dipolar molecules with rare-gas atoms such as Ar-CO or Ar-HF . There are also larger van der Waals molecules such as ammonia dimers, $(\text{NH}_3)_2$, benzene dimers, $(\text{C}_6\text{H}_6)_2$, or compounds of organic molecules with rare-gas atoms such as $(\text{C}_6\text{H}_6)\text{Ar}$.

As discussed in Sect. 3.7.2, the van der Waals bond arises from the interaction between two induced dipole moments in neutral atoms or groups (Fig. 3.21). In other words, it is a dispersion interaction, which is much weaker than chemical bonds and also weaker than hydrogen bonds. A van der Waals bond is characterized by a potential curve with a shallow minimum which can accommodate only a few vibrational levels (Fig. 11.2). The restoring forces are weak, and the vibrational energy is small.

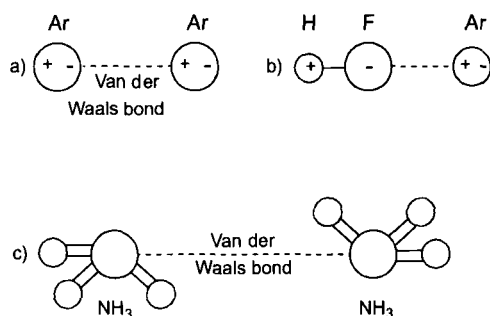


Fig. 11.1 Examples of van der Waals molecules. a) Ar_2 , b) HF-Ar , c) $(\text{NH}_3)_2$.

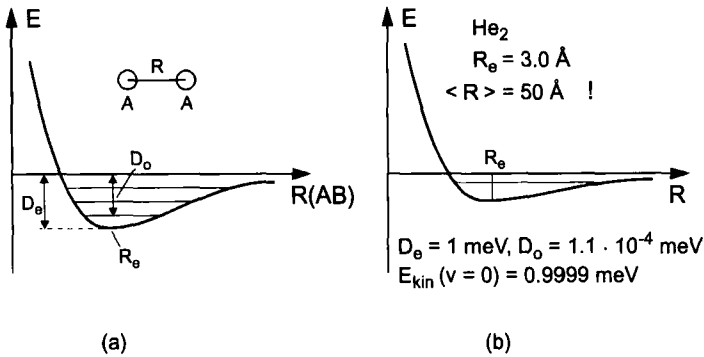


Fig. 11.2 a) Typical potential of a van der Waals bond with only a few vibrational levels; b) potential curve of the He_2 molecule.

The bond can easily be broken by sufficient vibrational excitation, and many van der Waals molecules are therefore only stable at sufficiently low temperatures. For example, the depth of the potential minimum for the He_2 molecule is only about 1 meV. The lowest vibrational level $v = 0$ lies at $E_{\text{vib}}(v = 0) = 0.9999$ meV, so that an additional energy of only 10^{-7} eV can already lead to dissociation [11.1].

In larger van der Waals molecules, the vibrational excitation of a strongly bound part of the molecule can be transferred to the van der Waals bond by vibrational coupling, leading to dissociation of the molecule. An example is the van der Waals molecule I_2He (Fig. 11.3), where an excitation of the $v = 1$ vibrational level of the I_2 vibration leads to dissociation by coupling with the van der Waals bond [11.3]. The investigation of van der Waals molecules and their dissociation channels thus provides insight into the strengths of the couplings between the different vibrational modes in polyatomic molecules.

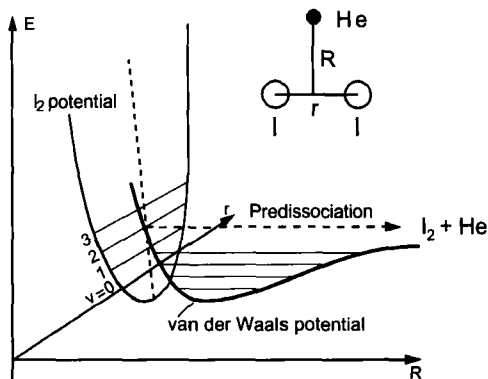


Fig. 11.3 Predissociation of a van der Waals molecule $\text{M}-\text{A}$ by vibrational excitation of M for the example of the I_2He complex.

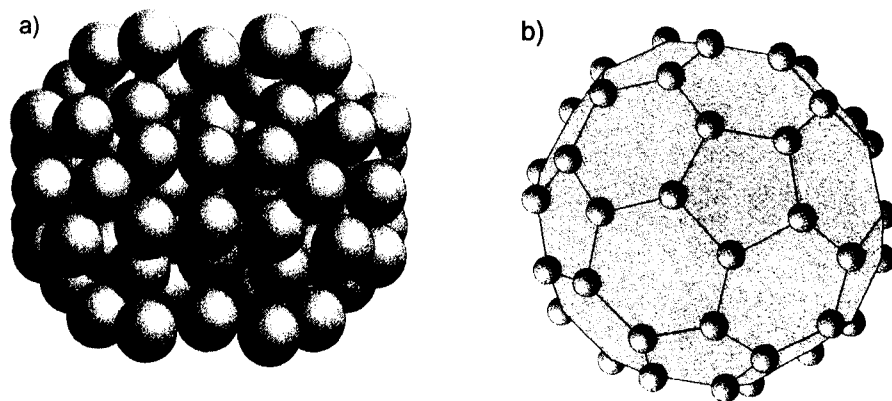


Fig. 11.4 a) Rare-gas cluster Ar₁₀₅; b) fullerene C₆₀.

Certain types of clusters are in some ways related to van der Waals molecules. They are more or less strongly bound systems, depending on the type of cluster, consisting of N atoms or molecules, where the number N can be as low as three or as high as several thousand. The weakly bound van der Waals clusters consist of rare-gas atoms or, in general, of atoms with closed electron shells (Fig. 11.4a), whereas metal clusters consisting of metal atoms are more strongly bound. Silicon or carbon clusters such as C₆₀ (Fig. 11.4b) are particularly stable due to the strong covalent bonding between the atoms.

Clusters are intermediate between individual isolated molecules or van der Waals complexes and liquid droplets or solid microparticles. It is therefore highly interesting to investigate how their properties such as bond energies, melting temperature, ionization potential, or the geometrical arrangement of the atoms approach with increasing N the corresponding bulk properties of liquid or solid bodies.

The number of publications on clusters has increased enormously in recent years [11.3–11.7] because a number of experimental techniques for the generation and investigation of clusters have been developed, and the accuracy of theoretical methods for numerical calculation of cluster properties has been improved significantly. Nowadays, cluster physics is a firmly established branch of molecular physics.

11.1

Van der Waals Molecules

To give us an idea of bond energies in van der Waals molecules, Table 11.1 lists some examples and compares them to the CO molecule with its strong covalent chemical bond. We see from the table that the bond energies in van der Waals molecules are lower than in ordinary molecules by about two orders of magnitude. Correspondingly, the distances R between atoms or groups bonded by van der Waals forces are significantly larger.

Tab. 11.1 Comparison of bond energies for van der Waals bonding, hydrogen bonding, and covalent bonding.

Molecule	Bond type	D_e / cm^{-1}	D_e / eV	$R_e / \text{Å}$
He ₂	van der Waals	7.6	9×10^{-4}	3.0
Ne ₂	van der Waals	30	3.6×10^{-3}	3.1
ArCO	van der Waals	110	1.4×10^{-2}	3.3
(NH ₃) ₂	van der Waals & hydrogen bond	1000	0.12	3.4
(H ₂ O) ₂	hydrogen bond	1900	0.24	3.0
CO	covalent	90500	11.2	1.1

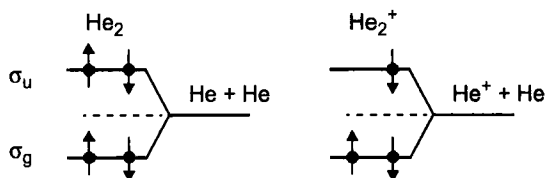
The weakest bond is found for the He₂ molecule with a depth of the potential minimum of only $-D_e = -1 \text{ meV}$, just enough to accommodate the ground-state vibrational level with a zero-point energy of 0.9999 meV . Thus, its bond energy is only $D_0 = 1.1 \times 10^{-7} \text{ eV}$, and the mean distance between the two helium atoms [11.1] is $\langle R \rangle = 50 \text{ Å}$!

In the molecular orbital diagram (Fig. 11.5), the four electrons of He₂ can be distributed over the two σ_g and σ_u orbitals, which means that the bonding effect of the two σ_g electrons is almost compensated by the two σ_u electrons. If, however, a σ_u electron is removed by excitation or ionization, the bonding contribution of the σ_g electrons prevails. Therefore, the bond energy of He₂⁺ of 2.5 eV is larger than that of neutral He₂ by more than three orders of magnitude.

Hence, van der Waals molecules can have larger bond energies in excited electronic states than in the ground state. For example, Fig. 11.6 shows the potential curve of the NaKr molecule, which has a bond energy of $70 \text{ cm}^{-1} = 8.8 \text{ meV}$ in the $^2\Sigma$ ground state, but of $790 \text{ cm}^{-1} = 99 \text{ meV}$ in the excited $^2\Pi_{1/2}$ state [11.8].

If a rare-gas atom is bound to a diatomic molecule by van der Waals interactions (Fig. 11.7), the van der Waals potential depends on the distances R and r and the angle θ against the molecular axis.

The van der Waals molecule CO–Ar has been studied particularly thoroughly [11.9]. Here, the coupling between Ar and CO is several orders of magnitude weaker than that between C and O. Hence, the lines in the infrared absorption spectrum are shifted only slightly with respect to those of the free CO molecule. From the lines

**Fig. 11.5** Molecular orbital diagram of He₂ and He₂⁺.

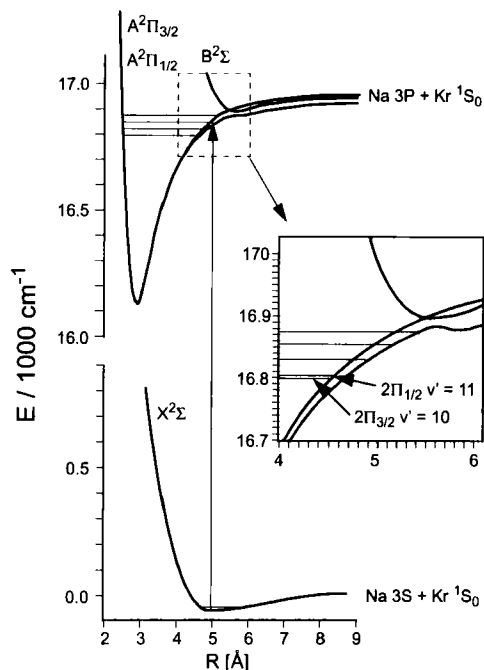


Fig. 11.6 Adiabatic potential curves for the $^2\Sigma$ ground and the $A^2\Pi$ excited state of the NaKr van der Waals molecule [11.8].

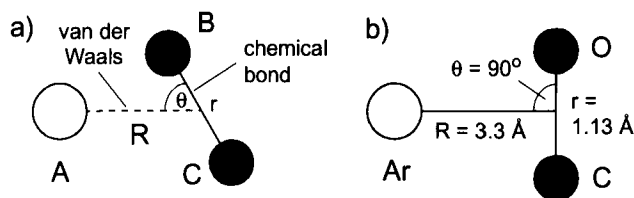


Fig. 11.7 a) Schematic representation of a van der Waals complex consisting of an atom and a diatomic molecule. b) CO-Ar in the vibrational ground state.

of many rotational transitions, the rotational and vibrational constants of the CO-Ar molecule can be determined, and hence its potential surface (Fig. 11.8) and its structure (Fig. 11.7) can be obtained. In the vibrational ground state, the minimum of the potential curve is at $R(\text{CO-Ar}) = 3.3 \text{ \AA}$ and an angle $\theta = 90^\circ$. The depth of the potential minimum is $D_e = 130 \text{ cm}^{-1}$. The CO-Ar bond energy is therefore $D_0 = D_e - E_{\text{vib}}(v = 0)$, that is, it equals the depth of the potential minimum minus the zero-point vibrational energy. There is a second minimum for a linear structure that can only be reached in vibrationally excited states, because it is separated from the global minimum at 90° by a potential barrier.

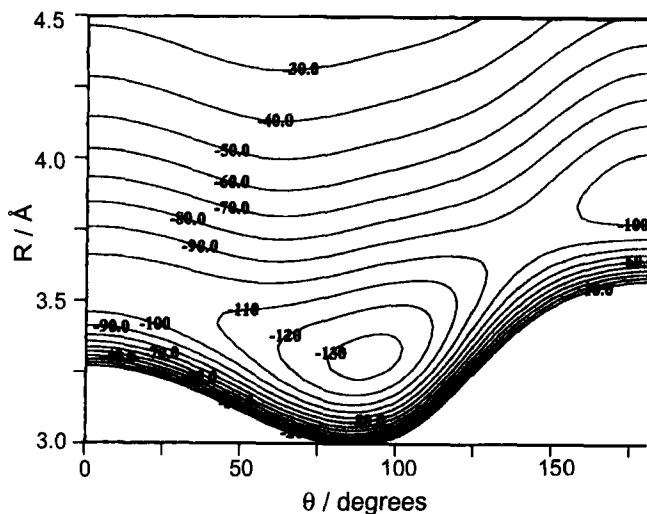


Fig. 11.8 Contour line diagram of the potential surface of CO-Ar in the vibrational ground state in cm^{-1} [11.9].

If the vibrational level $v = 1$ of CO is excited, its energy is far beyond the dissociation energy of the van der Waals bond. Hence, this state predissociates by coupling with the van der Waals vibrational mode, in which CO oscillates against Ar (Fig. 11.7). From the measured narrow linewidth it can be deduced that this coupling is very weak for CO-Ar so that sharp lines are obtained despite the predissociation. If the spectral resolution is sufficiently high, the radiationless lifetime of the excited level can be determined, and the coupling strength between the C=O and the van der Waals vibration can be deduced. In Fig. 11.9, measured linewidths are plotted against the depth of the potential minimum for some van der Waals complexes. We see that the coupling between the *intramolecular* vibration and the *intermolecular* van der Waals vibration becomes stronger as the depth of the potential minimum increases [11.10].

Because of the weak bond, van der Waals molecules often exhibit nonrigid structures, that is, they can alter their nuclear framework periodically by passing over shallow potential barriers or by tunneling through them. There exist several isomers with slightly different ground-state energies corresponding to the diverse minima on the potential surface. For example, in the NH_3 dimer vibrational excitation can induce a mutual rotation of the two NH_3 units around the axis of the van der Waals bond.

As the potential of the van der Waals bond is very shallow, the restoring forces acting against a change in the bond length are very small. Hence, vibrational amplitudes are large and vibrational frequencies are small. Because of the large mean internuclear distance, the moments of inertia are large, and rotational constants are correspondingly small. Hence, a high spectral resolution and low temperatures are

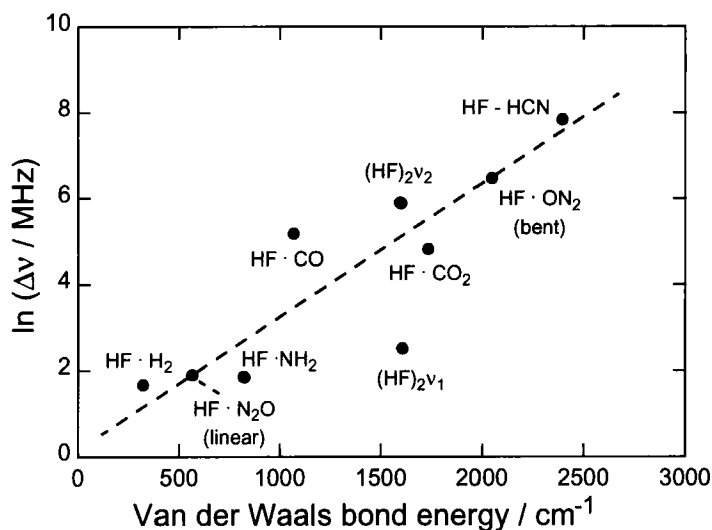


Fig. 11.9 Measured linewidths of absorption transitions into pre-dissociating levels of some van der Waals complexes as a function of the depth of the potential minimum of the van der Waals bond [11.10].

needed to resolve the closely spaced rotational lines and to populate only a few levels.

The question as to whether the $(\text{O}_2)_2$ (oxygen dimer) molecule possesses a linear, bent, or rectangular structure remained a matter of debate for a long time. Only recently, rotationally resolved spectra showed that the rectangular structure in Fig. 11.10a) has the largest binding energy [11.11]. Upon vibrational excitation, the dimer can be transformed into another structure. In contrast, the $(\text{OCS})_2$ molecule possesses a trapezoidal structure with D_{2h} symmetry, in which the two linear OCS molecules are oriented antiparallel and are shifted with respect to each other (Fig. 11.10b).

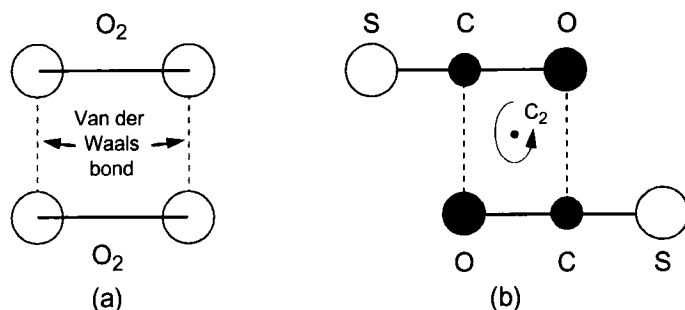


Fig. 11.10 a) Structure of the $(\text{O}_2)_2$ molecule in the ground state and b) structure of the $(\text{OCS})_2$ molecule.

11.2 Clusters

If we want to know how and why the properties of clusters approach the characteristic properties of liquid droplets or microcrystals with increasing number N of constituents (atoms or molecules), and for which size of N this transition occurs, we must start by elucidating the differences between clusters and (solid or liquid) bulk matter.

As some cluster properties are caused by surface effects, we will first determine the important parameter N_s/N , the fraction of surface atoms in a cluster. For sufficiently large N , the cluster can be considered a sphere of radius R consisting of N spherical atoms with radius r . With these assumptions, we obtain for a close packing $R \approx 0.9\sqrt[3]{N}$ with the volume filling factor $f_v = N(4\pi/3)r^3 / (4\pi/3)R^3 = Nr^3/R^3 = 0.9^3 = 0.74$,

$$Nr^3 = 0.74R^3 \quad \Rightarrow \quad N = 0.74 \left(\frac{R}{r} \right)^3. \quad (11.1)$$

For the surface S of the cluster, which is assumed to be spherical, containing N_s atoms with cross-sections πr^2 , we obtain with the coverage factor $f_s = N_s(\pi r^2) / (\pi R^2) \approx 0.78$,

$$N_s \pi r^2 = 0.78 \times 4\pi R^2 \quad \Rightarrow \quad N_s = 4 \times 0.78 \left(\frac{R}{r} \right)^2. \quad (11.2)$$

Division of Eq. (11.2) by Eq. (11.1) yields

$$\frac{N_s}{N} \approx 4 \left(\frac{r}{R} \right) \propto N^{-1/3}, \quad (11.3)$$

because $N \propto R^3$. Whereas for small clusters, the number N_s of surface atoms constitutes a large fraction of all N atoms, the ratio N_s/N decreases for larger clusters proportional to $N^{-1/3}$ (Table 11.2).

Above a critical cluster size N_c , a fixed structure for the cluster is established, and at sufficiently low temperatures the cluster cannot change its general structure if new atoms are added.

Tab. 11.2 Ratio N_s/N and radius R of a spherical cluster of identical atoms with radius $r = 2.2 \text{ \AA}$.

N	$R / \text{\AA}$	N_s / N
10	—	1
10^2	10.3	0.8
10^3	22	0.4
10^4	48	0.23
10^5	100	0.08
10^{10}	4800	2.3×10^{-3}
10^{20}	10^7	10^{-6}

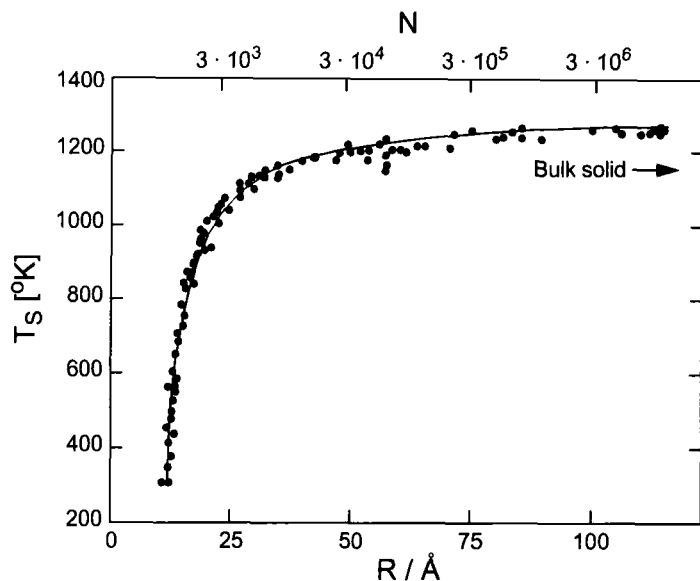


Fig. 11.11 Melting temperatures of gold clusters $(\text{Au})_N$ as a function of N [11.12].

If the temperature rises, clusters can also exhibit phase transitions from the solid to the liquid state. However, the *melting temperature* depends on cluster size, and approaches its bulk value only for very large clusters (Fig. 11.11). This effect is also connected with the ratio N_s/N , because the surface tension and hence the intrinsic pressure of the cluster decrease with decreasing N_s/N (i.e., increasing cluster radius R).

Clusters can be categorized in several ways. First, they can be classified as *atomic* or *molecular* clusters according to the type of their constituents. A second attribute is their size, that is, the number N of atoms or molecules in the cluster. The following scheme may serve as an approximate categorization:

- (a) microclusters with $N = 2$ to ≈ 10 –13. Here, all atoms are surface atoms, and the properties of these clusters can frequently be described by molecular models, particularly for nonmetallic clusters;
- (b) small clusters with $N = 10$ –13 up to about $N = 100$. Here, many isomers exist and molecular models are not adequate;
- (c) large clusters with $N = 100$ up to $N = 1000$. Here, a beginning transition to bulk properties can already be observed for some cluster properties;
- (d) small droplets or microcrystals with $N > 10^3$. Many, but not all properties of liquids or solids are already distinct.

Using the type of bonding within the cluster as a characteristic, clusters can be categorized as

- (a) metal clusters with metallic bonding, such as alkali metal clusters, mercury clusters or gold clusters;
- (b) van der Waals clusters such as rare-gas clusters;
- (c) clusters with hydrogen bonding such as water or ammonia clusters, which form a special subgroup of molecular clusters;
- (d) molecular clusters such as $(\text{SiO})_N$ or $(\text{CO})_N$;
- (e) clusters with covalent bonds such as $(\text{Si})_N$ or C_N .

However, such a categorization is not always unambiguous. Frequently, a transition from one bonding type to another is encountered for a specific type of cluster. For example, Hg_N clusters display van der Waals bonding for small values of N , but show a gradual transition to metallic bonding for larger N .

The dependence of the melting temperature (Fig. 11.11) and the progression of the liquid–solid phase transition on cluster size is an interesting and much investigated question. For some clusters, a transition from the solid to the liquid phase can be observed at a fixed temperature for increasing N .

In the following, we will discuss some types of clusters in more detail.

11.2.1

Alkali Metal Clusters

Alkali metal clusters can be considered prototypes of metallic clusters with one valence electron per cluster atom. With increasing cluster size, the bonding changes from covalent to metallic, where the valence electrons cannot be allocated to specific atoms but resemble an *electron gas* confined to the cluster volume. In the so-called *Jellium model* [11.7], this volume is filled uniformly with the positive charges of the nuclei and the negative charges of the electrons. This leads to the problem, well-known in quantum mechanics, of optimizing the arrangement of fermions in a three-dimensional, spherically symmetric potential well. There are discrete energy levels, which according to the Pauli principle can be occupied by a certain maximum number of electrons. This number depends, as in the case of the hydrogen atom, on the principal quantum number n and the allowed angular momentum states of the electrons. If we order the electrons according to their energies, a shell structure analogous to that in atoms is obtained. States with the same n but different values of the angular momentum quantum number l have very similar energies. All electrons in such states with identical n form a shell.

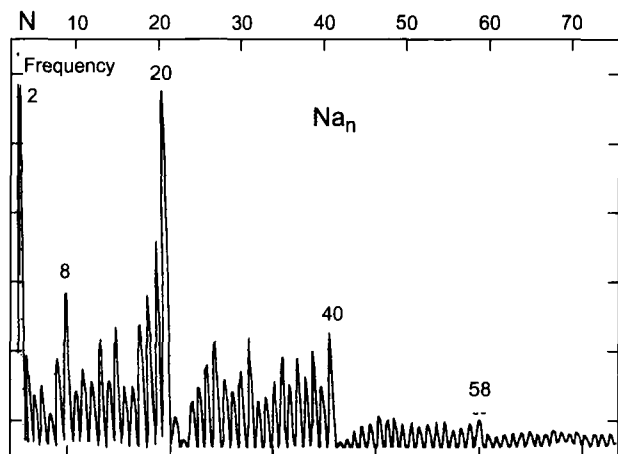


Fig. 11.12 Frequency distribution of $(\text{Na})_N$ clusters, measured as $(\text{Na})_N^+$ distribution in a mass spectrometer after electron impact ionization.

The observed abundance distribution of Na_N clusters as a function of N (Fig. 11.12) displays maxima at $N = 2, 8, 20, 40, 58, \dots$. These numbers correspond to the electron occupation numbers of the levels in a three-dimensional, slightly anharmonic potential (Fig. 11.13). According to this model, the stability of metallic clusters is determined less by the geometrical arrangement of the atoms and more by the arrangement of the electrons, clusters with completely filled shells being the most stable.

The measured dissociation and ionization energies of alkali metal clusters (Fig. 11.14) show the same shell structure. For large N , the ionization energies approach the electronic work function for solid sodium.

The small alkali metal clusters Li_3 and Na_3 have been investigated very thoroughly [11.13], and the rotational structure and even the hyperfine structure could be resolved using Doppler-free spectroscopy (see Sect. 12.4.7). From symmetry arguments, an equilateral triangle with D_{3h} symmetry would be expected for the structures of these trimers. It turns out, however, that the electronic state for this configuration would be degenerate. Therefore, the Jahn–Teller effect (see Sect. 9.3.6) has the consequence that each vibration of lower symmetry (such as the antisymmetric stretching vibration or the bending vibration) leads to a splitting of the electronic potential surface into two potential sheets, where the lower surface possesses a minimum at a bond angle of about 70° with a lower energy than the D_{3h} configuration [11.14]. Figure 9.12 shows a contour line diagram for the ground state of Li_3 as a function of the displacements Q_x and Q_y from the D_{3h} configuration ($Q_x = Q_y = 0$), and Fig. 9.11 displays a cut through such a diagram. To first approximation, the potential surfaces can be obtained from these curves by rotating them around the z axis. The intersection of the curves corresponds to the conical intersection of the potential surfaces (D_{3h} symmetry at $Q_x = Q_y = 0$) at which the degeneracy occurs.

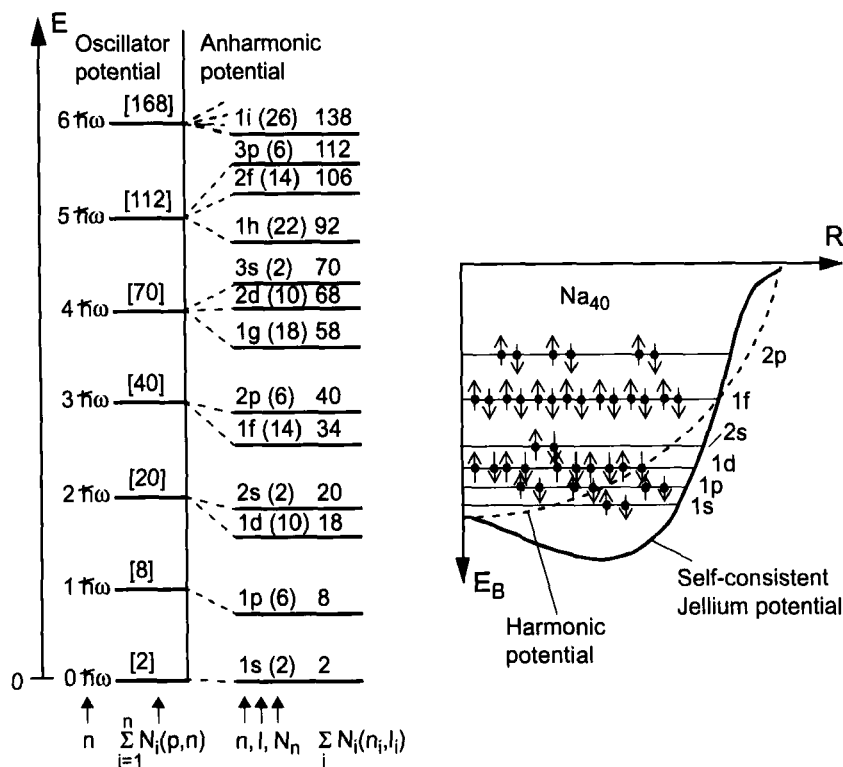


Fig. 11.13 Energy levels and their electronic occupation numbers in a harmonic and a slightly anharmonic three-dimensional potential well as determined by self-consistent iteration based on the Jellium model.

The combinations $Q_x \pm iQ_y$ of the vibrations ν_2 and ν_3 lead to a periodic motion of the nuclei along the dotted curve in Fig. 9.11, called pseudorotation because it can be represented by a synchronous rotation of all three nuclei around the three corners of the equilateral triangle of the D_{3h} configuration (see Fig. 6.12). During this motion, the structure of the Na_3 molecule changes periodically from an obtuse-angled to an acute-angled triangle [11.16]. The potential surface exhibits minima at these two configurations, which are separated by a potential barrier. Even if the kinetic energy of the vibrational motion is lower than the barrier height, the system can still tunnel through the barrier. The frequency of the pseudorotation in the vibrational ground state of Na_3 is very small (about 1 MHz), but it increases rapidly with increasing vibrational energy and it exceeds the spacing of the molecule's rotational lines when the barrier height is reached. In Li_3 , the barrier height is smaller, but the vibrational energy is larger because of the smaller masses, so that the pseudorotation frequency is much larger than the molecule's rotational frequency even in the vibrational ground state [11.17].

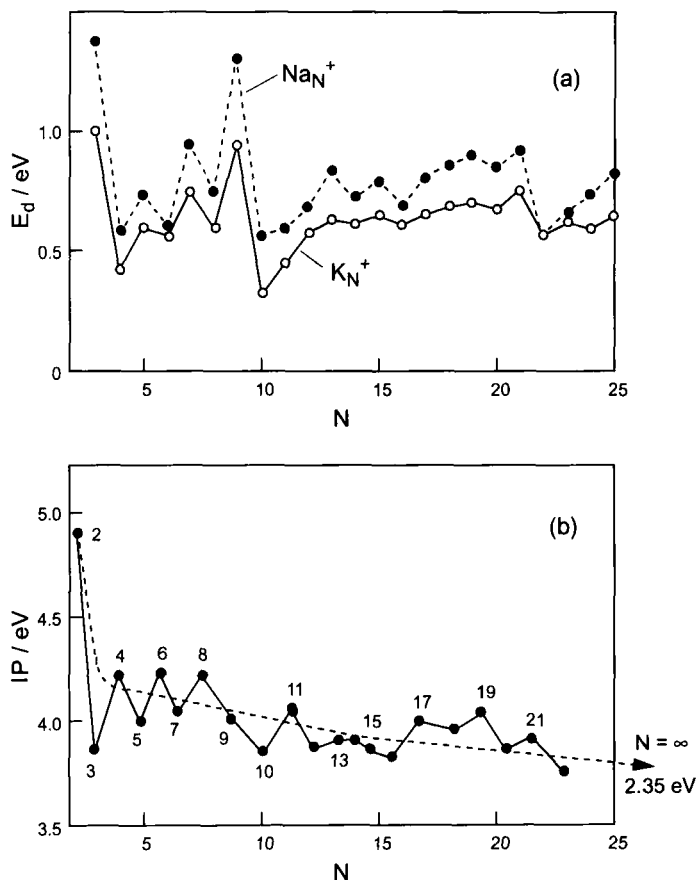


Fig. 11.14 a) Dissociation energies $D_c(N)$ of $(Na)_N$ and K_N clusters. b) Ionization energies of $(Na)_N$ clusters [11.15].

This example shows that even the small alkali metal clusters do not necessarily exhibit fixed structures, but that the large-amplitude vibrations can alter their geometries – despite the relatively large bond strength of the metallic bonds as compared to van der Waals bonds. This is in sharp contrast to the situation in stable molecules, where the vibrations occur around equilibrium positions, and the vibrational amplitudes are small compared with internuclear distances.

11.2.2

Rare-gas Clusters

Rare-gas clusters are typical representatives of van der Waals clusters (Fig. 11.4a). Due to their small bond energies, they are only stable at low temperatures. The structures of solid rare-gas crystals are determined by the close packing of the face-centered

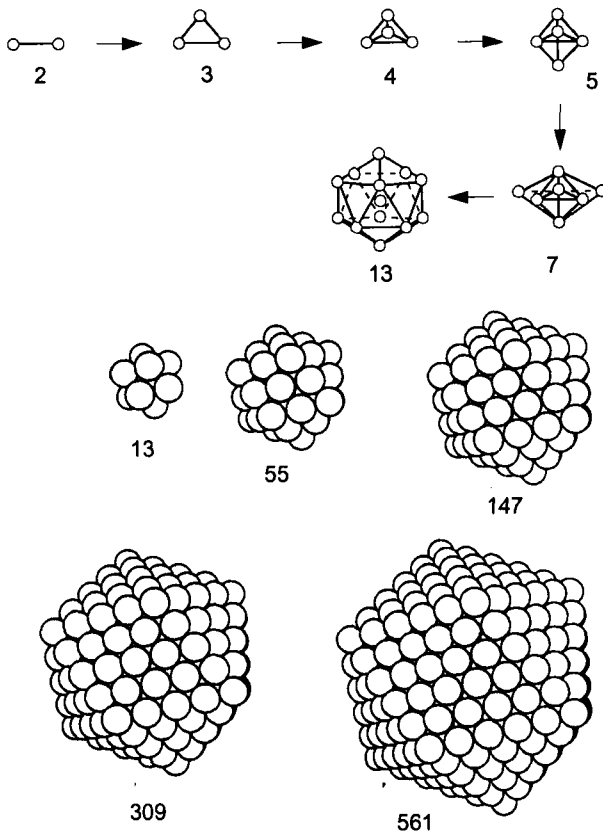


Fig. 11.15 Structure of rare-gas clusters as a function of N . The bond energy for the icosahedral structure possesses maxima for the magic numbers $N_m = 13, 55, 147, 309, \dots$ [11.18].

cubic structure. Electron diffraction studies have revealed, however, that small clusters with $N < 1000$ prefer a regular icosahedral structure, which is energetically more favorable. This structure possesses a fivefold symmetry axis, which cannot occur in solids, and it leads to a spherical organization of the clusters with a shell structure. The clusters are most stable for certain *magic numbers* N_m , for which a complete shell is filled. For xenon clusters (Fig. 11.15), the numbers $N_m = 13, 55, 147, 309, \dots$ are magic. The mass distribution of xenon cluster ions shown in Fig. 11.16 displays pronounced maxima at these magic numbers.

In contrast to metal clusters, it is not the occupation of the electronic levels but the geometric arrangements of the atoms in shells that determines the stability of the clusters. This result is comprehensible because the ionization energy of the rare-gas atoms is very high, and thus the electrons remain at their respective nuclei and do not form an electron gas as in metal clusters. At sufficiently low temperatures, larger ^4He clusters exhibit superfluidity [11.20].

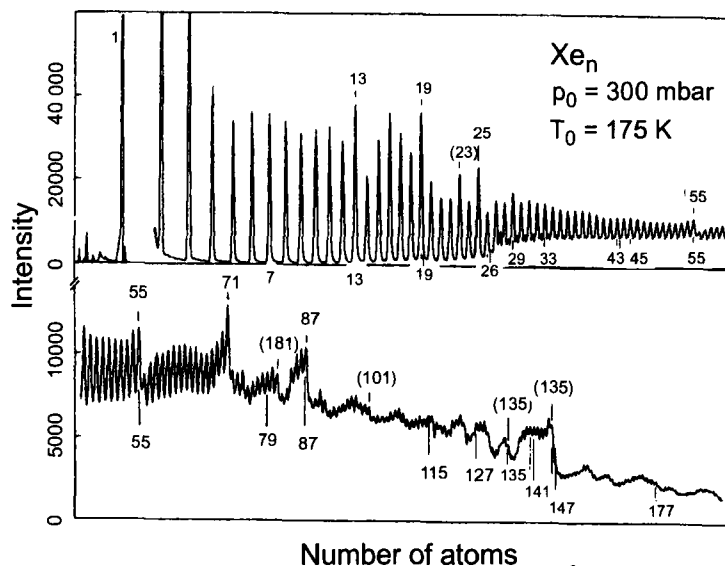


Fig. 11.16 Intensity distribution in the mass spectrum of $(\text{Xe})_N^+$ cluster ions [11.19].

11.2.3

Water Clusters

The investigation of water clusters $(\text{H}_2\text{O})_N$ is particularly interesting because it contributes to our understanding of the formation and evaporation of water droplets in the atmosphere and because it can help to elucidate the anomalous absorption and scattering of sunlight by water droplets. Highly accurate *ab initio* calculations for small water clusters arrived at the structures shown in Fig. 11.17, which agree well with experimental results. For N in the range of three to five, the clusters form a planar framework with only the hydrogen atoms protruding from the plane (Fig. 11.17b). It turns out that the stability of the clusters is secured mainly by hydrogen bonds between the individual water molecules. The potential surface exhibits many minima at different structures, which are separated by small potential barriers through which the system can easily tunnel. For example, the hydrogen atoms can tunnel through the molecular plane during their vibrations and can thus form different isomers. Therefore, the water clusters have no fixed structures but show dynamical behavior even at low temperatures, corresponding to frequent structural transformations (or isomerizations). If the tunneling time is shorter than the average measurement time, a time-averaged planar structure is observed.

Detailed investigations of such cluster structures as a function of N can help to verify model potentials and open up new paths to an improved understanding of the structure of liquid water.

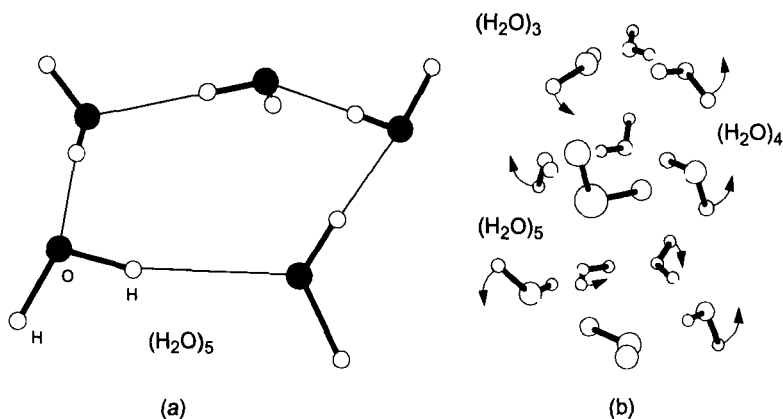


Fig. 11.17 Structure of small $(\text{H}_2\text{O})_N$ clusters with hydrogen bonds for $N = 3, 4$ and 5 . The hydrogen atoms can tunnel through the molecular plane and form different isomers [11.21].

For example, we can see from Raman spectra recorded with high spectral and spatial resolution that the relative fraction of water monomers, dimers, and multimers varies strongly between the surface and the bulk of liquid water. This is the reason, for example, for the large surface tension of water.

11.2.4

Covalently Bonded Clusters

The building blocks of covalently bonded clusters are the tetravalent group-IV elements carbon, silicon and germanium. Whereas in macroscopic crystals, the covalent bonding determines the crystal structure, where each of the four bonds is directed towards the adjacent atom and is occupied by two electrons with opposite spins, the surface atoms in a cluster have a pronounced effect on the arrangement of the atoms, because they have free valences protruding out of the cluster surface that are not connected to neighboring atoms (dangling bonds). These *free valences* can attract new atoms while the cluster grows. The location of these new atoms at the cluster surface determines its structure, which can change each time new atoms are added to the growing cluster. If we start building a cluster from a tetrahedron with $N = 4$, we arrive at a trigonal bipyramid for $N = 7$, and at an icosahedron for $N = 13$ (Fig. 11.18). If we start from an octahedral cluster with $N = 6$, the next complete shell occurs for $N = 14$.

Carbon clusters C_N form linear structures for $N < 6$, whereas for $N > 6$ ring structures are energetically favored. The discovery of very stable carbon clusters for $N = 60$ and $N = 70$ with soccerball-like cage structures (Fig. 11.4b) has found worldwide interest. Here, the carbon atoms form five- and six-membered rings that are all located at the surface of the cage, the inside remaining void. For the discovery and character-

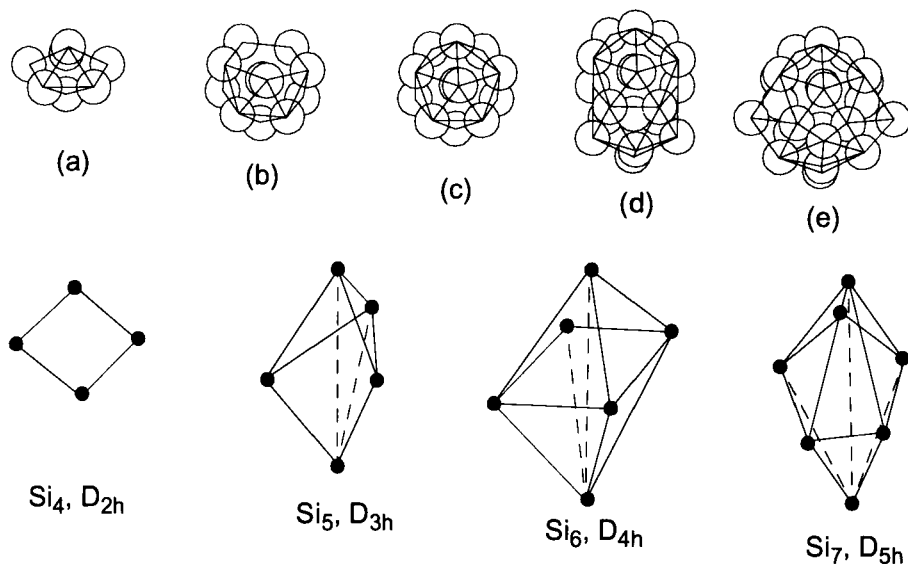


Fig. 11.18 Top row: The pentagonal structures of Ge clusters, a) pentagonal bipyramid for $N = 7$; b) for $N = 12$, additional atoms are attached symmetrically around the fivefold symmetry axis of a); c) icosahedron for $N = 13$; d) dou-

ble icosahedron for $N = 19$; e) cluster with D_{5h} symmetry and partially filled second shell for $N = 24$. Bottom row: Structures and symmetries of small silicon clusters [11.22].

ization of C_{60} . R. Curl, H. W. Kroto and W. Smalley were awarded the 1996 Nobel prize for chemistry [11.23]. These carbon clusters are also called *fullerenes* after the American architect and engineer *Richard Buckminster Fuller* (1895–1983) because they resemble his famous geodesic domes.

Related carbon clusters C_N with structures resembling tiny tubes have also been discovered [11.24]. These large carbon clusters may serve as microtraps for smaller atoms or molecules, which is one of the reasons why they have produced such an overwhelming interest [11.4].

11.3

Generation of Clusters

There are several procedures to produce clusters. A frequently employed method uses cold molecular beams (see Ch. 12). If rare-gas atoms effuse from a container with a large rare-gas partial pressure into vacuum through a nozzle, a rapid adiabatic cooling occurs so that the random kinetic energy of the atoms in the beam is almost completely converted to directed kinetic energy $\frac{1}{2}mu^2$ of atoms with mass m and beam velocity u . During this process, the relative velocities of the atoms become very small, that is, all atoms in the beam proceed with almost identical velocities following the

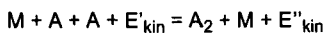
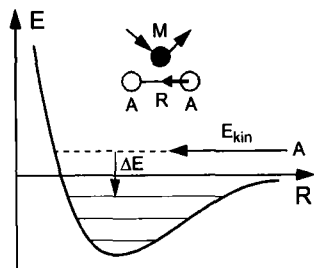


Fig. 11.19 Formation of a molecule upon collision between two atoms with relative energy E_{kin} , which must be discarded with the aid of a third collision partner.

expansion. This allows the formation of dimers, provided the small kinetic energy of the relative motion is carried away by a third collision partner (Fig. 11.19). The dimer thus formed can then combine with another atom, forming a trimer, etc. This process can be continued as long as the collision frequency is sufficiently large, that is, as long as the pressure in the beam is large enough. Therefore, the cluster formation rate can be optimized by a suitable choice of pressure and nozzle diameter.

To generate metal clusters, an amount of the metal is introduced into the container in addition to the rare gas and the contained is heated, so that the effusing beam consists of rare-gas atoms with a certain percentage of metal atoms. The rare-gas atoms act as collision partners, carrying away the relative kinetic energy upon a collision of two metal atoms. With this method metal clusters with atom numbers from $N = 2$ up to several thousand can be generated. The clusters are characterized by mass spectrometry after laser or electron-impact ionization [11.25].

Another method is based on the use of a supersaturated metal vapor in a rare-gas atmosphere. If the temperature of such a mixture is lowered, condensation occurs, and clusters with a size distribution depending on the particular experimental conditions are generated [11.26]. For the generation of clusters consisting of elements with high evaporation temperatures, a solid sample of the element is irradiated by an intense laser beam, evaporating atoms from the sample, which are then mixed with a rare gas at low pressure. The mixture of rare gas and evaporated atoms is then expanded through a nozzle into vacuum, which causes it to cool adiabatically. Again, condensation occurs, leading to clusters A_N with a size distribution depending on the experimental conditions (pressure, temperature, and nozzle characteristics) [11.27].

12

Experimental Techniques in Molecular Physics

In recent years, a number of experimental techniques for the investigation of molecules have been newly developed, and existing techniques have been improved and extended by new methods or instruments. This includes Fourier spectroscopy, laser spectroscopy with high spectral and temporal resolution, spectroscopy with synchrotron radiation, electron spin resonance spectroscopy, electron and ion spectroscopy, and the combination of different techniques such as the combination of mass spectrometry and molecular beam techniques with laser-spectroscopic methods. The application of these methods to the study of molecules has significantly enhanced our understanding of their structure and dynamics.

These techniques can be grouped into three principal categories:

1. *Spectroscopic techniques*

a) Radiation spectroscopy

In these methods, the absorption or emission of electromagnetic radiation by molecules in the different spectral regions is studied. Measurement of the frequencies of absorption or emission lines gives information on the energies of molecular states (see Chapters 4 and 8). The line intensities are a measure of the transition probabilities, and their measurement can be used to test calculated wavefunctions of the states between which the transitions occur. From the linewidths, the lifetimes of the involved states can be determined. The splitting of the lines in external fields gives information on electric or magnetic moments of the molecule and hence on the coupling of the different angular momenta (see Ch. 10).

b) Particle spectroscopy

Energy and momentum of the electrons produced by the ionization of molecules can be measured using electron spectrometers. They give information on the energy states of inner-shell electrons of the atoms in the molecule, on correlation effects between the electrons in these shells, on molecular Rydberg states, and on the ionic energy levels.

2. *Measurement of integral and differential scattering cross-sections in collisions between atoms or molecules*

Such measurements enable the determination of interaction potentials between the collision partners. In combination with laser-spectroscopic techniques, individual states of the collision partners can be selected, so that the dependence of the interaction energy on the internal states of the collision partners can be determined. Measurement of inelastic and reactive collision processes allows the study of energy transfer processes and can give detailed information on the primary processes in chemical reactions.

3. *Measurements of macroscopic phenomena depending on molecular properties*

Examples for this class are transport phenomena such as diffusion (mass transport), thermal conduction (energy transport) and viscosity (momentum transport) in molecular gases, which depend on the interactions between the molecules.

Another example are the relations between thermodynamic quantities (pressure p , volume V , and temperature T) in an isolated macroscopic amount of an atomic or molecular gas, which depend on the type of particles in the gas and their intermolecular potentials.

While categories 1) and 2) measure interactions between individual atoms or molecules, that is, they are microscopic probes, the experiments of category 3) give average values over large numbers of molecules.

Different methods often complement each other, providing different information on the molecules studied. For example, scattering measurements at thermal energies give information on the long-range part of the interaction potential between the collision partners (see Sect. 3.7), whereas the energies of the bound molecular levels obtained from spectroscopic methods allow the determination of the potential for small internuclear distances (see Sect. 3.6).

In this last chapter of the book, we will briefly present the most important of these experimental techniques, and we will elucidate how the knowledge outlined in the previous chapters has been gained in an active interplay between theory and experiment.

12.1

Microwave Spectroscopy

Using microwave spectroscopy, molecular transitions with wavelengths λ between 0.03 cm and 1 m (corresponding to the wavenumber range $30 \text{ cm}^{-1} > \tilde{\nu} > 0.01 \text{ cm}^{-1}$ or the frequency range $10^{12} \text{ Hz} > \nu > 5 \times 10^8 \text{ Hz}$) can be investigated. In this spectral region, molecular rotational transitions $|J'\rangle \leftarrow |J''\rangle$ with wavenumbers

$$\tilde{\nu} = 2B_v(J'' + 1) + \dots \quad \text{with} \quad J' = J'' \pm 1 \quad (12.1)$$

or transitions between hyperfine levels or closely spaced vibration-rotation levels of different interacting electronic states can be observed.

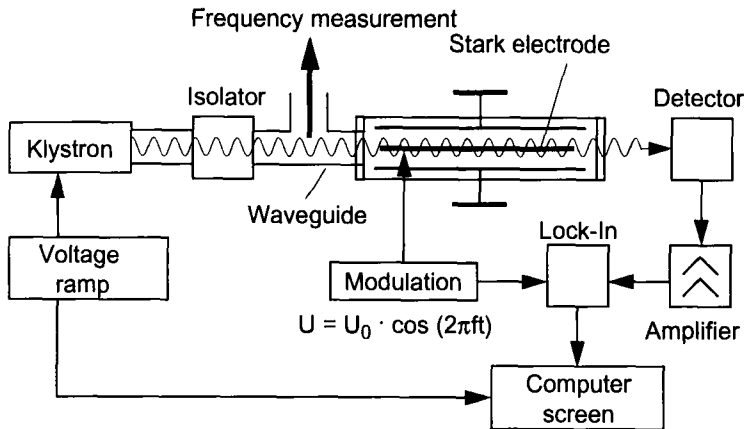


Fig. 12.1 Schematic representation of the experimental setup in microwave absorption spectroscopy.

Examples

The rotational transition $J' = 1 \leftarrow J'' = J = 0$ in the ground state of CO with $B_e = 1.93 \text{ cm}^{-1}$ occurs at $\tilde{\nu} = 3.8 \text{ cm}^{-1}$ or $\nu = 114 \text{ GHz}$; the lowest transition $J' = 3/2 \leftarrow J = 1/2$ in the $^2\Sigma$ ground state of BeH with $B_e = 10.308 \text{ cm}^{-1}$ occurs at $\tilde{\nu} = 30.924 \text{ cm}^{-1}$ or $\nu = 927 \text{ GHz}$, and the next-higher transition $J' = 5/2 \leftarrow J = 3/2$ at $\nu = 1.5 \text{ THz}$; in the PbS molecule, the frequency of the $J' = 1 \leftarrow J = 0$ transition is only $\nu = 6.36 \text{ GHz}$ due to the small rotational constant $B_e = 0.106 \text{ cm}^{-1}$.

Figure 12.1 shows the experimental setup for the measurement of microwave absorption in a molecular gas. Microwaves with a continuously (within a given range) tunable frequency are generated in a klystron or carcinotron and are transmitted through the molecular sample with the aid of metallic waveguides of suitable dimensions. The transmitted intensity I_{trans} is measured by a detector (bolometer or semiconductor detector) and compared to the incident intensity I_0 .

As discussed in Sect. 8.1, the thermal populations of the lower and upper levels of a microwave transition are almost equal at room temperature, and the rate of absorption is therefore only slightly larger than that of stimulated emission (Fig. 12.2), so that the net absorption coefficient

$$\alpha(\nu) = \left[N_1 - \left(\frac{g_1}{g_2} \right) N_2 \right] \sigma(\nu) \approx N_1 \left(\frac{\Delta E}{kT} \right) \sigma(\nu) \quad (12.2)$$

is in general very small due to the small population difference and the small absorption cross-section. It is therefore crucial to achieve long absorption paths and to develop

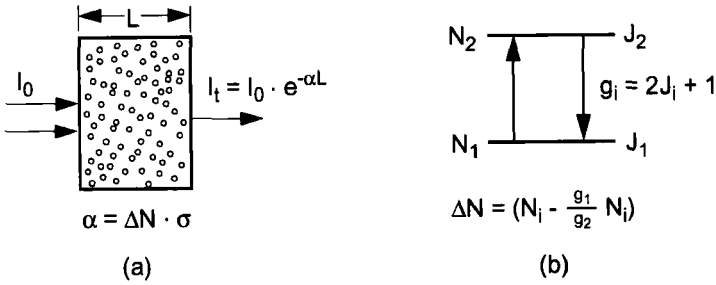


Fig. 12.2 Absorption of an electromagnetic wave. a) Transmitted intensity; b) level diagram.

methods to measure the difference

$$\Delta I = I_0 - I_{\text{trans}} = I_0 (1 - e^{-\alpha L}) \approx I_0 \alpha L \approx I_0 L N_1 \left(\frac{\Delta E}{kT} \right) \sigma, \quad (12.3)$$

which is generally small for $\Delta E \ll kT$ even for long absorption paths L , and it is often smaller than the fluctuations in I_0 .

A frequently used method for improving the sensitivity is based on frequency modulation

$$\nu = \nu_m (1 + a \cos(2\pi f t)) \quad (12.4)$$

of the microwave frequency ν , which means that the incident intensity

$$I(t) = A \cos^2 [2\pi \nu_m (1 + a \cos(2\pi f t)) t] \quad (12.5)$$

is modulated with a frequency f around the mean microwave frequency ν_m . The maximum frequency deviation $a\nu$ is in general chosen to be small compared with the linewidths of the absorption lines. The microwave frequency is measured using fast frequency counters or, for high frequencies, by superposition with a wave of known frequency so that the frequency difference of both is in a range suitable for frequency counters. To achieve the highest possible frequency stability, oscillators and electronic control circuits are used to keep the frequency at a target value and to compare it with a frequency standard, so that absolute frequencies may be determined.

If the modulated microwave frequency is tuned continuously over the range of an absorption line, the absorption coefficient $\alpha(\nu)$ and hence the measured transmitted intensity is also modulated correspondingly (Fig. 12.3).

If we expand I_{trans} in a Taylor series around the mean frequency ν_m , we obtain

$$I_{\text{trans}}(\nu) = I_{\text{trans}}(\nu_m) + \sum_n \frac{\alpha^n}{n!} \left(\frac{d^n I_{\text{trans}}}{d\nu^n} \right)_{\nu_m} \nu_m^n \cos^n(2\pi f t). \quad (12.6)$$

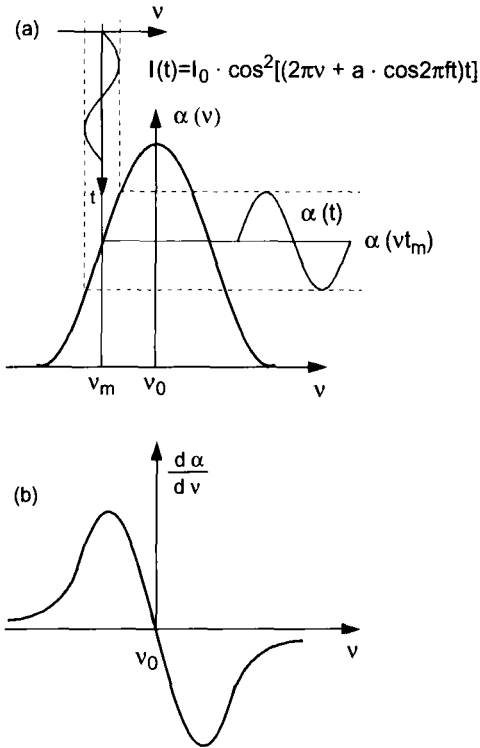


Fig. 12.3 Absorption of a frequency-modulated wave.

A phase-sensitive detector (lock-in) which detects only the signal at the frequency f , measures the difference

$$\Delta I_{\text{trans}}(\nu) = I_{\text{trans}}(\nu) - I_{\text{trans}}(\nu_m) = \alpha\nu_m \left(\frac{dI_{\text{trans}}}{d\nu} \right)_{\nu_m} \cos(2\pi f t), \quad (12.7)$$

which is proportional to the first derivative $(dI_{\text{trans}}/d\nu)$ at the frequency ν_m . With Eq. (12.3), this is also proportional to the first derivative of the absorption coefficient $\alpha(\nu)$, which is zero for the center frequency ν_m of a line.

This detection technique offers the advantage that only intensity variations at the frequency f are recorded as disturbing background noise, whereas all other frequency contributions to the noise are suppressed. The modulation frequency f is chosen so that the disturbing noise in this frequency range is minimized.

Instead of modulating the microwave frequency, the molecule's absorption frequency ν_m can also be modulated. This can be achieved, for example, by placing the molecules in a modulated electric field created by a metallic plate at a potential $U = U_0 \cos(2\pi f t)$ at the center of the absorption cell and two grounded walls of the cell (Fig. 12.1). The absorption frequencies are then shifted due to Stark shifts of the molecular energy levels. Due to the Stark shift (see Sect. 10.4), the absorption

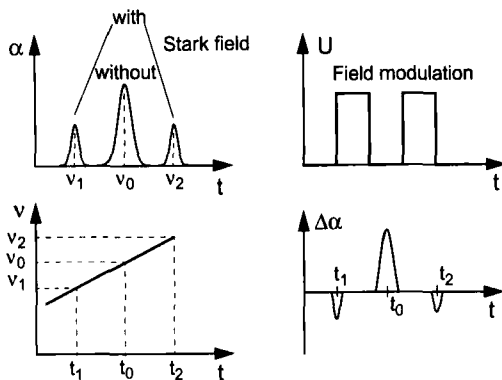


Fig. 12.4 Explanation of the observed signals during Stark modulation.

lines are periodically shifted and split. The splitting into Stark components allows an identification of the rotational quantum number J , thus facilitating the identification of the absorption spectrum (Fig. 12.4). To achieve sufficiently large Stark shifts, voltages of up to 20 kV are used. More detailed accounts of experimental methods in microwave spectroscopy and their importance in molecular physics can be found in [6.5, 12.1–12.3].

12.2

Infrared and Fourier Spectroscopy

Infrared spectroscopy comprises the spectral range $0.75 \mu\text{m} < \lambda < 100 \mu\text{m}$, in which the vibration–rotation transitions in molecules occur (see Sect. 8.2). Absorption spectra in this frequency range can be measured in two principal ways:

- (a) A monochromatic radiation source with tunable wavelength can be used (e.g., a semiconductor or difference-frequency laser or optical parametric oscillators), and the transmitted intensity is measured as a function of the wavelength λ . In this case, the situation is analogous to microwave spectroscopy.
- (b) A broadband radiation source (such as a Nernst glower or a high-pressure mercury lamp) can be used that emits a continuous thermal radiation with an intensity maximum depending on the temperature of the source; for example, for $T = 2000 \text{ K}$ the maximum is at $\lambda = 1.5 \text{ mm}$. In this case, a monochromator is needed to disperse the radiation.

In case a), the spectral resolution depends on the linewidth of the radiation source. If this is smaller than the width of the absorption lines, the latter determines the spectral resolution.

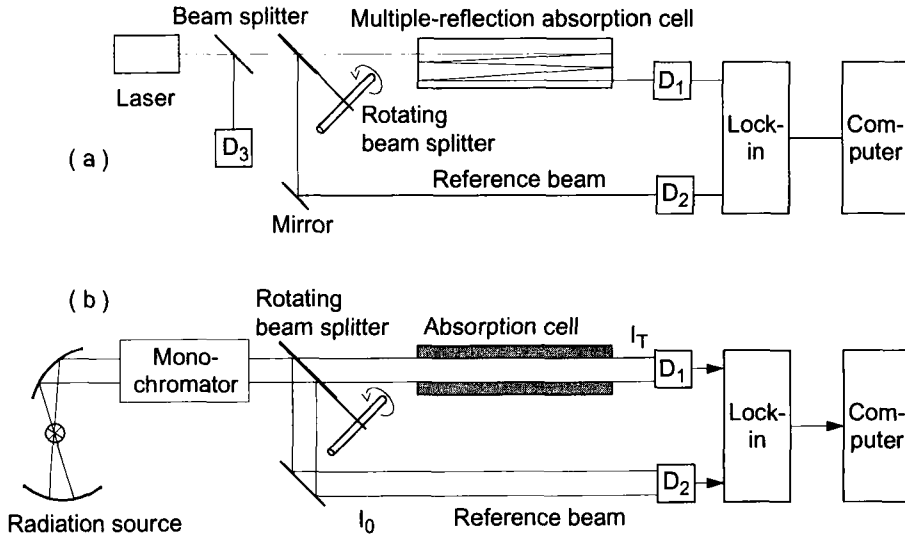


Fig. 12.5 Comparison of absorption spectroscopy with a) a tunable laser and b) a thermal radiation source.

In case b), the spectral resolution is usually limited by the resolution of the monochromator. Only if interferometers are used (e.g., in Fourier spectroscopy) can the linewidths of the absorption lines be resolved.

Figure 12.5 compares the experimental setups for cases a) and b). In case a) with a tunable monochromatic radiation source, no monochromator is needed. The highly collimated laser beam allows the use of multiple-reflection absorption cells, thus enlarging the absorption path. If a rotating beam splitter is used in front of the absorption cell that splits the laser beam into a probe beam passing through the absorption cell and a reference beam, the difference of the two signals measured with a lock-in detector at the chopping frequency f is

$$\frac{I_0 - I_{\text{trans}}}{I_0} = 1 - e^{-\alpha L} \approx \alpha L, \quad (12.8)$$

which allows the determination of the absorption coefficient $\alpha(\nu)$, largely eliminating variations in the radiation source. If the linewidth of the laser is smaller than the spectral width of the absorption lines, their line profiles can be measured.

Figure 12.5b shows a schematic representation of a typical infrared spectrometer for case b). Again, a beam splitter is employed, which consists of a segmented mirror that reflects alternately the reference beam and the probe beam onto the detectors D_1 or D_2 so that the difference $I_0 - I_{\text{trans}}$ can be measured by a lock-in detector tuned to the beam splitter frequency f .

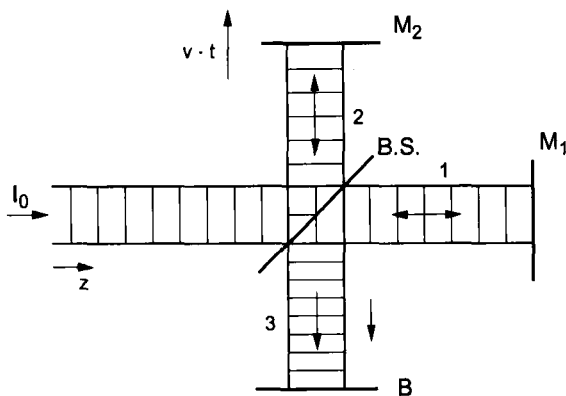


Fig. 12.6 Principle of a Michelson interferometer.

The signals are analyzed with the aid of a computer, and the spectra are then either printed or stored electronically for further processing.

A new technique which is increasingly displacing conventional infrared spectroscopy is Fourier-transform spectroscopy [12.4, 12.5]. In addition to a higher spectral resolution, it offers a number of other advantages over classical absorption spectroscopy that will be discussed below. The measured signals are the Fourier transform of the spectrum, and therefore a computer is needed for the reconstruction (backtransformation of the Fourier transform) of the spectra, and this factor determined the cost of a Fourier spectrum in the early days. Since fast and cheap PCs with built-in Fourier-transform capabilities are readily available nowadays, this price has dropped drastically, and today virtually all infrared spectroscopy laboratories use Fourier-transform spectrometers.

A Fourier spectrometer is based on a two-beam interference in a modified Michelson interferometer (Fig. 12.6). The radiation incident from a spectrally continuous radiation source is split into two partial beams by a beam splitter BS, which pass onto the mirrors M_1 and M_2 . There, they are reflected and are superimposed at the beam splitter. At plane B, the observed intensity depends on the path difference Δs of the two partial beams. If the mirror M_2 is moved continuously in one direction with a velocity v , the path difference $\Delta s = \Delta s_0 + 2vt$ changes constantly, and hence the observed intensity changes also. If the time $t = 0$ is chosen so that $\Delta s_0(0) = 0$, the path difference $\Delta s = 2vt$ is a linear function of time.

The principle will be elucidated for the measurement of a monochromatic incident wave with intensity $I = I_0 \cos(\omega t - kz)$ (Fig. 12.7a). If the two interfering partial waves have amplitudes A_1 and $A_2 = A_1$ (where $A_1^2 + A_2^2 = I_0$), the intensity at the detector, averaged over one wave period, is

$$I_d = [A_1 \cos(\omega t + \varphi_1) + A_2 \cos(\omega t + \varphi_2)]^2$$

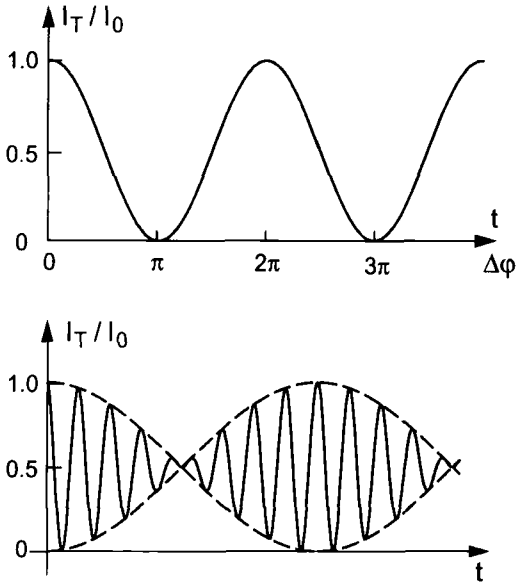


Fig. 12.7 Interferogram of a) a monochromatic wave and b) a wave with two frequencies.

Since the detector cannot follow the rapid oscillations at the frequency ω , its output signal is the time average of the intensity,

$$\langle I_d \rangle = \frac{1}{2} I_0 [1 + \cos(\varphi_1 - \varphi_2)] \quad \text{with} \quad \varphi_1 - \varphi_2 = 2\pi \Delta s / \lambda. \quad (12.9a)$$

As the path difference $\Delta s = 2vt$ increases proportionally with time and

$$2\pi \frac{\Delta s}{\lambda} = 2 \left(\frac{v}{c} \right) \omega t, \quad (12.9b)$$

the signal

$$S(t) \propto \langle I_d(t) \rangle = \frac{I_0}{2} \left[1 + \cos \left(\frac{v}{c} \omega t \right) \right] \quad (12.9c)$$

at the detector is a periodic function of time with frequency $\Omega = 2(v/c)\omega$. Hence, the frequency ω of the incident wave is transformed into the much smaller frequency $\Omega = 2(v/c)\omega$ which can be measured electronically.

Example

$$v = 5 \text{ cm/s}; \quad \omega = 10^{14} \text{ s}^{-1} \Rightarrow \Omega = 33.2 \times 10^3 \text{ s}^{-1}.$$

If two partial waves with the frequencies ω_1 and ω_2 are passed through the Michelson interferometer, the detector receives the superimposed intensity

$$\begin{aligned}
 I_d &= A_1^2 [\cos(\omega_1 t + \varphi_1) + \cos(\omega_1 t + \varphi_2)]^2 \\
 &\quad + A_2^2 [\cos(\omega_2 t + \varphi_3) + \cos(\omega_2 t + \varphi_4)]^2 \\
 &= I_{01} [\cos^2(\omega_1 t + \varphi_1) + \cos^2(\omega_1 t + \varphi_2) \\
 &\quad + \cos(2\omega_1 t + \varphi_1 + \varphi_2) + \cos(\varphi_1 - \varphi_2)] \\
 &\quad + I_{02} [\cos^2(\omega_2 t + \varphi_3) + \cos^2(\omega_2 t + \varphi_4) \\
 &\quad + \cos(2\omega_2 t + \varphi_3 + \varphi_4) + \cos(\varphi_3 - \varphi_4)]. \quad (12.10)
 \end{aligned}$$

The detector averages over the fast oscillations with frequencies ω_1 and ω_2 , so that the average intensity as a function of time during the motion of the mirror M_2 becomes

$$\langle I_d \rangle = \frac{1}{2} I_{10} \left[1 + \cos \left(\frac{2\omega_1 vt}{c} \right) \right] + \frac{1}{2} I_{20} \left[1 + \cos \left(\frac{2\omega_2 vt}{c} \right) \right].$$

With $I_{10} = I_{20} = I_0$ and $\Omega = \omega v/c$, we obtain

$$\langle I_d \rangle = I_0 \left[1 + \cos \left(\frac{\Omega_1 - \Omega_2}{2} t \right) \times \cos \left(\frac{\Omega_1 + \Omega_2}{2} t \right) \right]. \quad (12.11)$$

This is a beat signal with the mean frequency $\Omega_m = \frac{1}{2}(v/c)(\omega_1 + \omega_2)$ and the beat frequency $\Omega_b = \frac{1}{2}(v/c)(\omega_1 - \omega_2)$ (Fig. 12.7b). From this beat signal, the two frequencies of the incident wave

$$\omega_1 = \frac{c}{v} (\Omega_m + \Omega_b) \quad \text{and} \quad \omega_2 = \frac{c}{v} (\Omega_m - \Omega_b) \quad (12.12)$$

can be determined, provided that the mirror shift is large enough so that at least one complete beat period can be measured.

In either case, the measured signal $S(t)$ is the Fourier transform of the incident intensity $I(\omega)$, because with $\Delta s = \delta = 2vt$,

$$S(t) \propto S(\delta) = \int_{-\infty}^{+\infty} I(\omega) \cos(\delta\omega/c) d\omega. \quad (12.13)$$

If the incident wave comprises only one frequency ω_0 , $I(\omega) = I_0 \cos \omega_0 t$ and we obtain Eq. (12.9a) for $I(t)$. If the incident wave contains many different frequencies, the superposition intensity $I(t)$ at the detector is more complicated. However, Eq. (12.13) still holds. Solving for $I(\omega)$ yields

$$I(\omega) = \int_{-\infty}^{+\infty} S(\delta) \cos \left[2\omega \left(\frac{v}{c} \right) t \right] d\delta. \quad (12.14)$$

Thus, the Fourier transform of the measured time function $S(\delta) \propto I(t)$ yields the spectrum of the incident intensity $I(\omega)$.

If spectrally continuous radiation is passed through the absorption cell, the transmitted intensity lacks contributions at the absorptions frequencies. The transmitted intensity can then be written as

$$I_{\text{trans}} = I_0 - I_{\text{abs}}(\omega),$$

where we assume that the spectrum I_0 of the radiation source is constant over the spectral range of the absorption lines. As the Fourier transform of a constant is again a constant, the same arguments apply to $I_{\text{abs}}(\omega)$ as for an emission spectrum $I_{\text{em}}(\omega)$.

The integration limits for the mathematical Fourier transformation are $t = -\infty$ and $+\infty$, respectively. In experiments, however, a measurement is only performed over a limited time span T . To take this into account, we can introduce a time slot function $g(t)$ into the Fourier transformation, so that the integral Eq. (12.14) becomes

$$I(\omega) = \int_{-\infty}^{+\infty} g(t) S(\delta) \cos \left[2\omega \left(\frac{v}{c} \right) t \right] d\delta, \quad (12.15)$$

where $g(t) = 1$ for $0 > t > T$ and zero otherwise. However, such a rectangular time slot function leads to side maxima during Fourier transformation of the measured spectrum that can overlap adjacent lines, in analogy to the diffraction of light at a rectangular slit. To avoid these annoying artifacts, an apodization function is introduced. The time slot function $g(t)$ is then not a rectangular function, but follows a Gaussian profile

$$g(t) = e^{-(t-t_0)^2/\Delta t^2}. \quad (12.16)$$

For the cosine Fourier transform the zero point of time, for which the path difference $\Delta s = 0$, must be known precisely. This can be achieved by simultaneously recording the interferogram of a broadband radiation source (Fig. 12.8). Because of its large spectral bandwidth, the coherence length of such a source is very small, and a narrow interference structure is obtained for $\Delta s = 0$ only. To obtain a continuous path-time function $\Delta s(t)$ with equidistant time markers, the interferogram of a constant-frequency He-Ne laser is recorded simultaneously, which has the form shown in Fig. 12.7a. The path difference between two maxima is exactly $\Delta s = \lambda/2$, so that precise time markers for the Fourier transformation are available.

The advantages of Fourier spectroscopy can be summarized as follows:

- (a) The complete spectral range transmitted through the spectrometer and recorded by the detector is measured simultaneously, whereas in classical and laser infrared spectroscopy only a narrow frequency interval $\Delta\nu$ is measured at a time, where $\Delta\nu$ corresponds to the laser linewidth or the monochromator resolution. The total spectral range $\nu_1 - \nu_2$ is scanned in $Z = (\nu_1 - \nu_2)/\Delta\nu$ steps. Hence

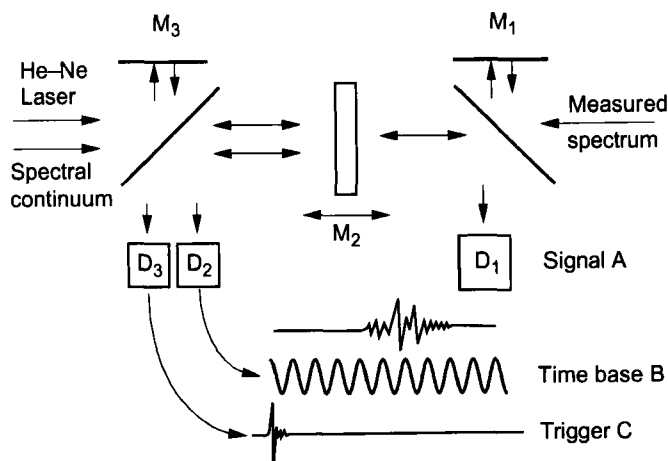


Fig. 12.8 Schematic setup of a Fourier spectrometer.

for a given total measurement time, the measuring time available for each spectral interval in Fourier spectroscopy is Z times that of classical spectroscopy. This leads to an enhancement in the signal-to-noise ratio by a factor of $Z^{1/2}$.

- (b) The spectral resolution $\Delta\nu$ can be adjusted by choosing the maximum path difference Δs , that is, the distance through which the moving mirror moves. Both quantities are related by $\Delta\nu = c / (2\pi\Delta s)$.

Example

For a maximum path difference $\Delta s = 0.3$ m, a resolution of $\Delta\nu = 150$ MHz is obtained. At a frequency of $\nu = 10^{14}$ Hz, this corresponds to a relative resolution of $\nu/\Delta\nu = 6.3 \times 10^5$. For $\Delta s = 2$ m, $\nu/\Delta\nu = 4.2 \times 10^6$. For a frequency $\nu = 10^{14} \text{ s}^{-1}$, $\Rightarrow \Delta\nu = 240$ MHz. This already reaches the Doppler width at $\nu = 10^{14} \text{ s}^{-1} \hat{=} \lambda = 3 \mu\text{m}$.

As an example, Fig. 12.9 shows the Fourier spectrum of an overtone vibrational transition in the chloroform molecule.

12.3

Classical Spectroscopy in the Visible and Ultraviolet

Most electronic transitions in molecules occur in the visible or ultraviolet region of the electromagnetic spectrum. Spectroscopy in these wavelength regions thus provides information on excited electronic states. In combination with techniques that allow high

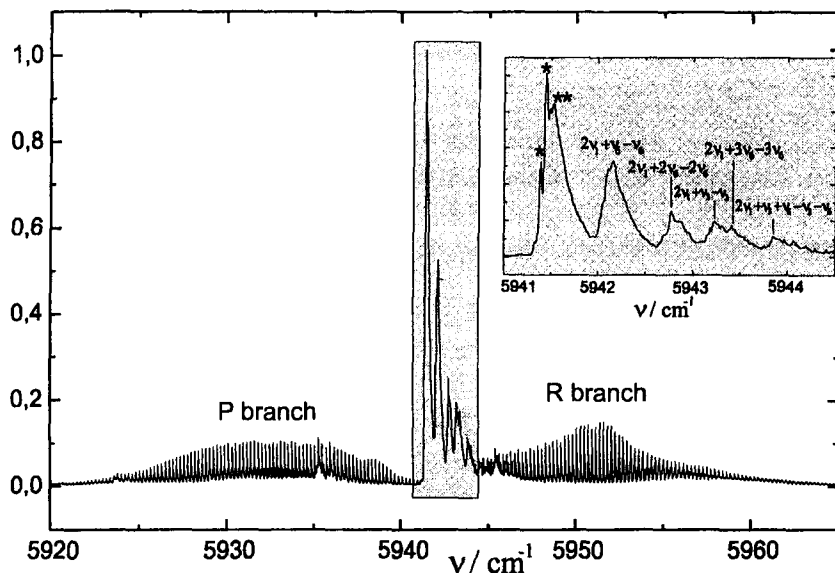


Fig. 12.9 Section from the Fourier spectrum of the overtone transition $2\nu_1$ of CHCl_3 [12.6].

temporal resolution, spectroscopic methods can be used to study the dynamics of excited states, that is, relaxation processes in excited states or energy transfer processes after optical excitation. Further applications of such experiments are in photochemistry, which studies the initiation of chemical processes by absorption of photons.

This section gives an overview of equipment and methods of classical molecular spectroscopy in this spectral region. Detailed accounts of special topics can be found in the referenced literature.

For a long time, high-pressure gas-discharge lamps or tungsten lamps were used as continuous radiation sources, that is, thermal emitters at $T = 1200\text{--}2000\text{ K}$. For time-resolved measurements, pulsed flashlights or sparc discharges were employed as sources of short pulses of radiation. New synchrotron radiation sources provide intense radiation pulses with high repetition rates, covering a spectrum from the near infrared to the vacuum ultraviolet or x-ray region. However, the overwhelming majority of spectroscopic experiments is nowadays conducted using different types of lasers (see next section).

The radiation emitted by broadband radiation sources must be spectrally dispersed. Usually, this is achieved by prism or grating spectrographs (Fig. 12.10). Two spectral lines are considered resolved if their wavelength separation is equal to or larger than their full width at half maximum (Fig. 12.11). The minimum linewidth that can be achieved is determined either by the resolution of the equipment used or by the inherent linewidth of the absorption lines as given by the Doppler width or pressure broadening (see Sect. 4.3).

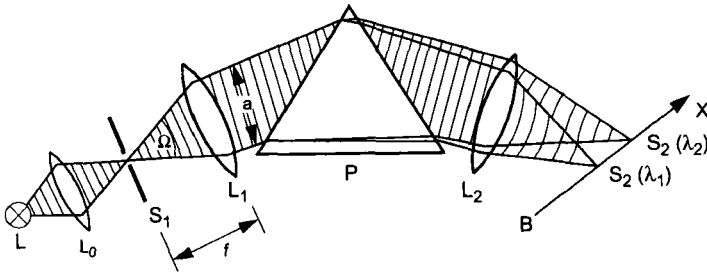


Fig. 12.10 Prism spectrograph.

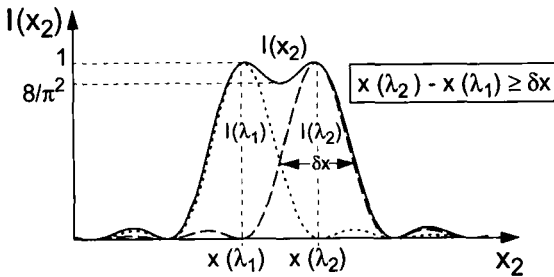


Fig. 12.11 Resolution of two spectral lines.

The spectral resolution

$$\left| \frac{\lambda}{\Delta\lambda} \right| = \left| \frac{\nu}{\Delta\nu} \right| \tag{12.17}$$

of a spectrometer can be derived as follows.

We consider a radiation comprising two spectral lines with wavelengths λ and $\lambda + \Delta\lambda$ passing through the spectrometer. It is diffracted in the monochromator by angles of θ and $\theta + \Delta\theta$, respectively (Fig. 12.12). If the parallel beam of rays is focused onto the plane of observation by the lens L_2 or a concave mirror with focal length f_2 , the lateral distance of the images $S(\lambda)$ of the two spectral lines becomes

$$\Delta x_2 = f_2 \frac{d\theta}{d\lambda} \Delta\lambda = \frac{dx}{d\lambda} \Delta\lambda. \tag{12.18}$$

For a width δx_1 of the entrance slit and focal lengths f_1 and f_2 of the collimation lens and the image lens L_2 , respectively, the width of the slit image in the plane of observation is

$$\delta x_2 = \left(\frac{f_2}{f_1} \right) \delta x_1. \tag{12.19}$$

In this case, the spectral resolution becomes, with $\Delta x_2 \geq \delta x_2$,

$$\frac{\lambda}{\Delta\lambda} = \frac{\lambda}{\Delta x_2} \frac{dx}{d\lambda} \leq \frac{f_1}{f_2} \frac{\lambda}{\delta x_1} \frac{dx}{d\lambda}. \tag{12.20}$$

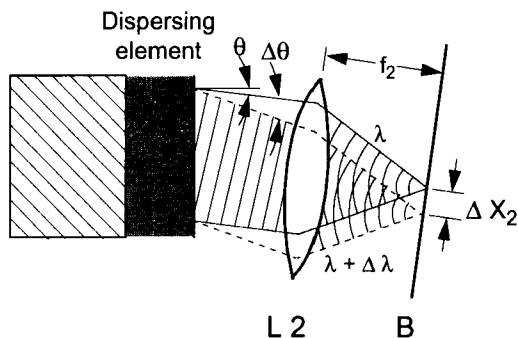


Fig. 12.12 Angular dispersion of a spectrometer.

Hence, the spectral resolution can in principle be increased by increasing the dispersion $dx/d\lambda$ and by reducing the width δx_1 of the entrance slit. However, the latter is only feasible up to a limit imposed by diffraction. Even for an infinitely narrow slit, the slit image will be a diffraction pattern with a full width of the central diffraction maximum of

$$\delta x_2 = \frac{2f_2\lambda}{a} \quad (12.21)$$

(Fig. 12.13) caused by diffraction at the boundaries of the optical path in the spectrometer, where a is the size of the limiting aperture (e.g., the width of the prism or grating). Two spectral lines are considered resolved if the central diffraction maximum of the first line is located at the first diffraction minimum of the second. Their distance in the plane of observation is then

$$\Delta x_2 = \frac{f_2\lambda}{a}. \quad (12.22)$$

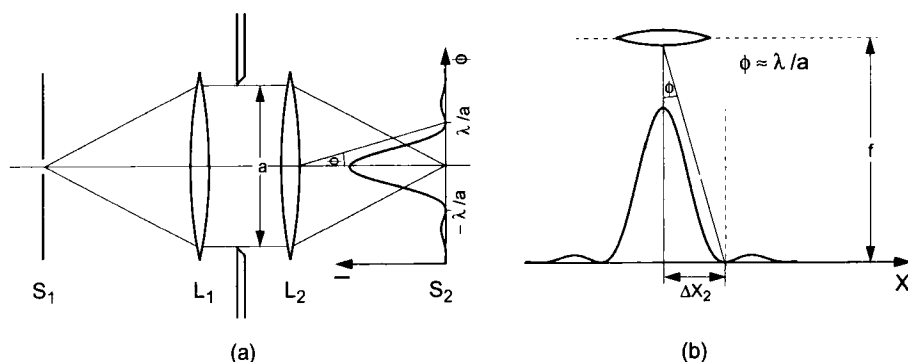


Fig. 12.13 Diffraction structure of the image of a narrow entrance slit caused by diffraction at the limiting aperture of width a in the spectrometer.

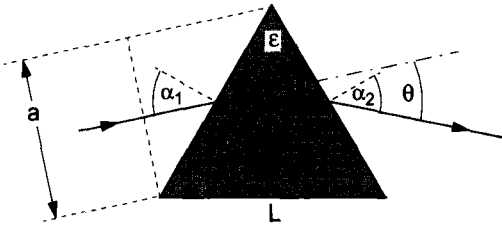


Fig. 12.14 Symmetric optical path upon refraction at the faces of the prism.

The entrance slit must have a finite width, because otherwise no radiation could enter. The optimum slit width δx_1 with respect to spectral resolution and transmitted power is obtained if the width δx_2 of the slit image equals the distance Δx_2 . The minimum distance of the slit images is then $(2f_2)\lambda/a$. This gives for the optimum slit width $\delta x_1^{\text{opt}} = (f_1/f_2)\Delta x_2 = f_1\lambda/a$.

The upper limit for the spectral resolution is then

$$\frac{\lambda}{\Delta\lambda} \leq \frac{a}{2f_2} \frac{dx}{d\lambda} = \frac{a}{2} \frac{d\theta}{d\lambda} \quad (12.23)$$

In a prism spectrograph with a 60° -prism of edge width L , the angular dispersion is, for a symmetric optical path (Fig. 12.14),

$$\frac{d\theta}{d\lambda} = \frac{1}{\sqrt{1 - (n/2)^2}} \frac{dn}{d\lambda}, \quad (12.24)$$

and the spectral resolution is therefore, according to Eq. (12.20) with $n = 1.5$,

$$\frac{\lambda}{\Delta\lambda} \leq \frac{a/2}{\sqrt{1 - (n/2)^2}} \frac{dn}{d\lambda} \approx 0.76a \frac{dn}{d\lambda}. \quad (12.25)$$

The spectral dispersion $dn/d\lambda$ depends on the material of the prism and the wavelength λ .

For a sufficiently narrow entrance slit, the spectral resolution of a prism spectrograph is determined by the dimensions of the prism and the dispersion of the prism material.

Example

For a 60° -prism made of synthetic quartz with $L = 10$ cm, $a = L/\sqrt{3}$. For $\lambda = 300$ nm, the refractive index is $n = 1.52$ and $dn/d\lambda = 1400 \text{ cm}^{-1}$. Hence, the spectral resolution is $\lambda/\Delta\lambda = 6200$. Here, two spectral lines can be resolved if they have a minimum distance of $\Delta\lambda = 0.05$ nm at $\lambda = 300$ nm.

For a grating spectrograph, the angular dispersion can be derived from the grating equation

$$d(\sin\alpha + \sin\beta) = m\lambda; \quad m = 1, 2, 3, \dots \quad (12.26)$$

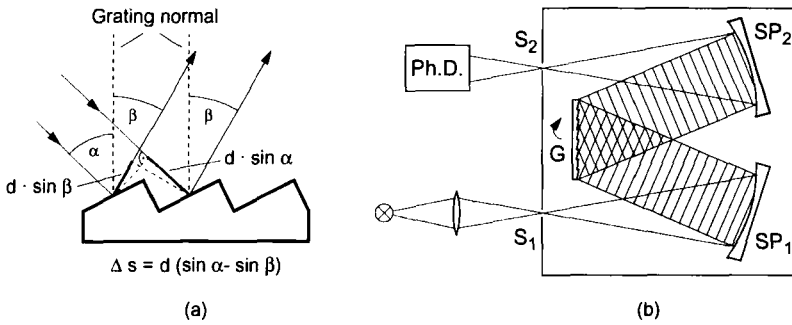


Fig. 12.15 Interference at a diffraction grating. a) Derivation of the grating equation; b) grating spectrograph.

(Fig. 12.15), where d is the distance between two grooves in the grating, α is the incident angle, and β is the diffraction angle. The angular dispersion is then

$$\frac{d\beta}{d\lambda} = \frac{1}{d\lambda/d\beta} = \frac{m}{d \cos \beta} = \frac{1}{\lambda} \frac{\sin \alpha + \sin \beta}{\cos \beta}. \quad (12.27)$$

The angular full half width $\delta\beta$ between the two minima at both sides of the central diffraction maximum of the image of the entrance slit is determined by the number N of interfering partial beams, that is, by the number of illuminated grooves in the grating. More precisely,

$$\delta\beta = \frac{\lambda}{Nd} = \frac{\lambda}{D}. \quad (12.28)$$

Hence, the width of the central diffraction maximum is the same as for diffraction at a slit of width $D = Nd$.

For the spectral resolution, this gives

$$\frac{\lambda}{\Delta\lambda} \leq \frac{Nd(\sin \alpha + \sin \beta)}{\lambda} = mN. \quad (12.29)$$

The spectral resolution equals the product of diffraction order m and number N of illuminated grating grooves.

Examples

$N = 10^5$, $m = 1$, $\Rightarrow \lambda/\Delta\lambda = 10^5$. At a wavelength of 500 nm, two spectral lines can be resolved if their spacing is at least $\Delta\lambda = 0.005$ nm. In reality, however, the finite width of the slit must be taken into account. With $\alpha = \beta = 30^\circ$, we obtain from Eq. (12.27) the angular dispersion $d\beta/d\lambda = 2.3 \times 10^{-3}$ rad/nm. For a focal length of 1 m, this gives a linear dispersion of 2.3 mm/nm. For a slit of width 0.02 mm, the width of the slit image corresponds to a spectral interval of $\Delta\lambda = 0.01$ nm, so that the realistic resolution is about 0.015 nm.

This example shows that the resolution of grating spectrographs is much larger than that of prism spectrographs [12.7].

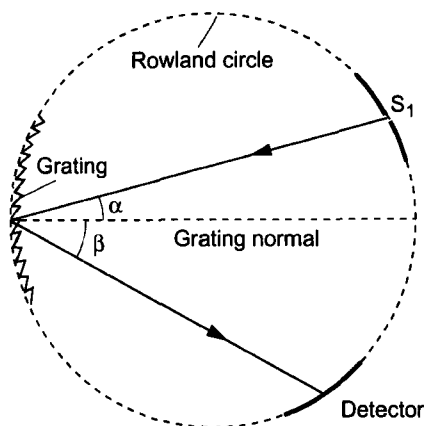


Fig. 12.16 Rowland spectrograph with curved grating for the spectral analysis of VUV radiation.

The experimental setup for classical absorption spectroscopy of molecular gases in the visible or ultraviolet region does not differ significantly from the one shown in Fig. 12.5. To achieve the highest possible spectral resolution, large grating spectrographs have been constructed with focal lengths of up to 10 m in some laboratories. Here, the spectrometer is located in its own, separate room, in which grating and mirrors are mounted on concrete blocks, and the spectra are recorded on a long curved photoplate. The curvature is chosen so that the photoplate remains in the focal plane of the imaging mirror over a large spectral region. The recorded spectra are then analyzed using a microdensitometer.

The reflectivity of metallic surfaces decreases in the vacuum UV (VUV) region, and it is therefore convenient to replace the planar grating and the two spherical mirrors by a curved imaging grating (Rowland grating) that images S_1 onto the detector, thus combining dispersion and imaging. Figure 12.16 displays a typical setup for the absorption spectroscopy of molecular gases in the VUV using a Rowland grating. If the curvature is properly chosen, the grating and the entrance and exit slits are located on a circle (Rowland circle). The complete spectrometer must be evacuated, because otherwise the VUV radiation would be absorbed by the air [12.8].

A particularly intense source of radiation is synchrotron radiation. The high-energy electrons orbiting in a circular path in the synchrotron emit *bremsstrahlung*, which is located essentially in the electrons' orbital plane and which is emitted along the tangent to the electron orbit (Fig. 12.17). The radiation is linearly polarized for radiation in the orbital plane, and circularly polarized for radiation outside the orbital plane (Fig. 12.17b). Its spectral distribution depends on the electron energy and the curvature of their path (Fig. 12.18); it ranges from the x-ray to the visible region of the spectrum. Electron storage rings have been built (e.g., BESSY in Berlin, Germany) for the sole purpose of providing synchrotron radiation. These *dedicated sources* employ

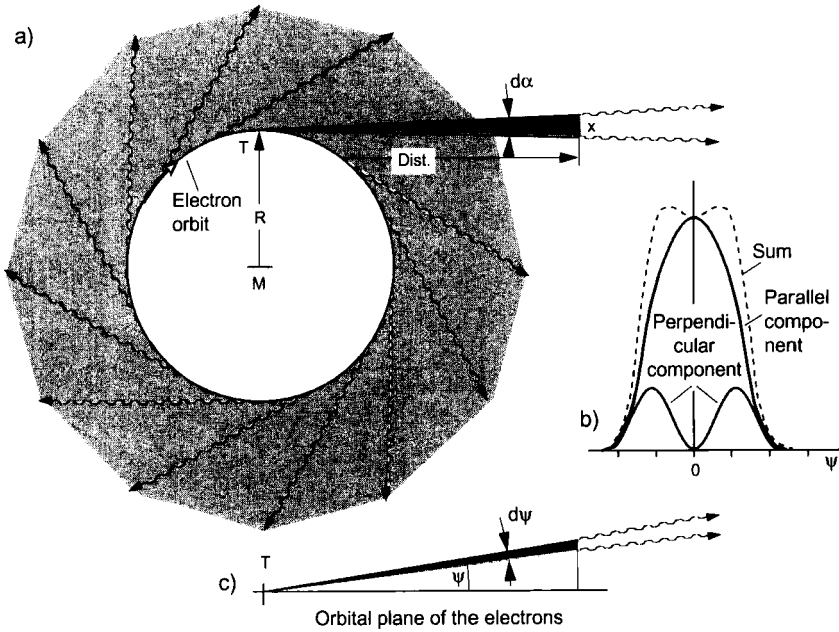


Fig. 12.17 Synchrotron radiation. a) Direction of radiation in the plane of the orbiting electrons; b) intensity distribution of the different polarizations as a function of the out-of-plane angle ψ ; c) definition of the out-of-plane angle ψ .

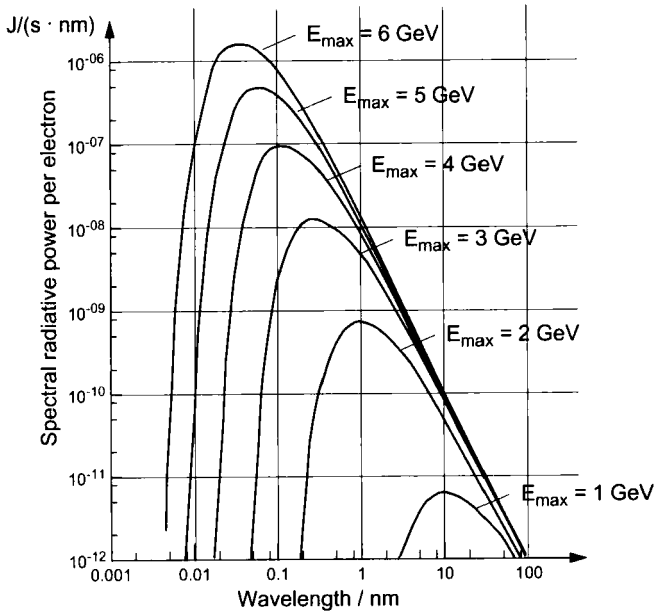


Fig. 12.18 Spectral distribution of synchrotron radiation for different electron energies at a radius of curvature of 31.7 m [12.8].

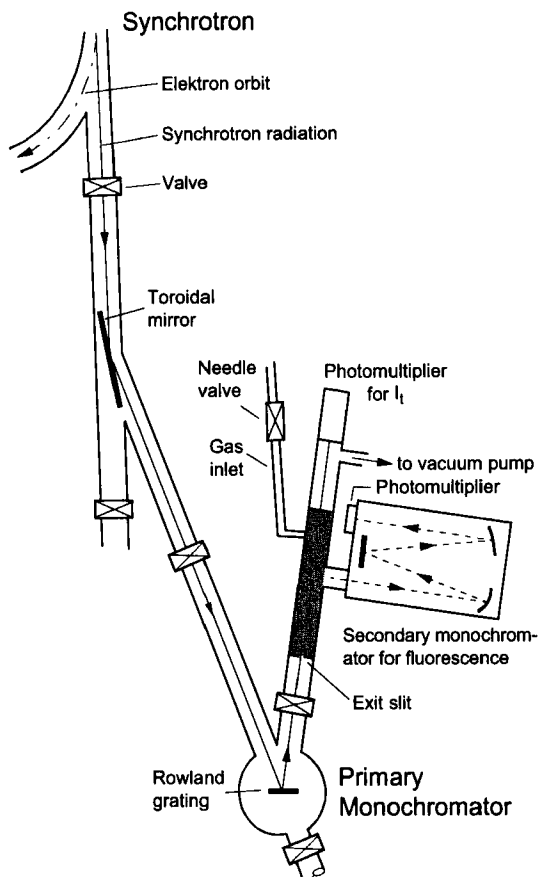


Fig. 12.19 Experimental setup for vacuum UV spectroscopy with spectrally dispersed synchrotron radiation.

magnetic devices located around the electron orbit, which deflect and thus accelerate the electrons periodically (*undulators* and *wigglers*). This increases the intensity of synchrotron radiation by about two orders of magnitude [12.9]. The radiation emerging through tangential exit tubes is collimated by a toroidal mirror and is focused onto the entrance slit of the Rowland spectrograph (Fig. 12.19). The absorption cell is located behind the spectrograph, and the transmitted intensity is measured by UV-sensitive detectors (e.g., by an open photomultiplier, in which the radiation ejects photoelectrons from a first metallic dynode, which are then accelerated onto further dynodes by an electric field, in each step creating about four to eight secondary electrons per incident electron).

Either the attenuation of the transmitted radiation by the absorbing molecules (absorption spectrum) or the fluorescence emitted by the absorbing molecules (excitation spectrum) can then be monitored.

Recently, other intense VUV radiation sources have been realized that utilize the radiation from extremely hot microplasmas, which can be generated with the aid of focused radiation from pulsed lasers. This method has the advantages that the space requirements for the equipment is vastly reduced (the whole equipment fits into an average laser laboratory) and the much lower price. Its disadvantage is the lower repetition rate.

12.4 Laser Spectroscopy

The introduction of lasers to spectroscopy has spawned a revolution in molecular physics. The much higher spectral intensity as compared to classical radiation sources, the narrow linewidths of single-mode lasers, the good beam collimation, and particularly the availability of ultrashort pulses of light have enabled a vast number of new techniques that surpass experimental limitations of classical spectroscopy with respect to detection sensitivity and spectral and temporal resolution. In this section, the most important of these techniques will be discussed [12.10].

12.4.1 Laser Absorption Spectroscopy

Figure 12.5 shows a comparison of absorption spectroscopy with lasers and with continuous radiation sources.

Apart from the good collimation of laser beams, which enables long absorption paths in multiple-reflection cells, the narrow linewidth of tunable single-mode lasers is particularly relevant for the possible increase in sensitivity. This can be rationalized as follows.

If $\Delta\omega_{\text{abs}}$ is the width of an absorption line and $\Delta\omega$ the spectral resolution of the equipment, which in the case of laser spectroscopy is determined by the linewidth $\Delta\omega_{\text{laser}}$ of the laser, the measured relative absorption is

$$\frac{I_0 - I_{\text{trans}}}{I_0} = \frac{L \int_{\omega_0 - \Delta\omega_{\text{abs}}/2}^{\omega_0 + \Delta\omega_{\text{abs}}/2} I_0(\omega) \alpha(\omega) d\omega}{\int_{\omega_0 - \Delta\omega/2}^{\omega_0 + \Delta\omega/2} I_0(\omega) d\omega} \approx \begin{cases} \alpha(\omega_0)L & \text{for } \Delta\omega \ll \Delta\omega_{\text{abs}} \\ \bar{\alpha}L \frac{\Delta\omega_{\text{abs}}}{\Delta\omega} & \text{for } \Delta\omega > \Delta\omega_{\text{abs}} \end{cases} \quad (12.30)$$

where $\bar{\alpha}$ is the absorption coefficient averaged over the interval $\Delta\omega$. This shows that for identical absorption paths, the relative absorption for $\Delta\omega > \Delta\omega_{\text{abs}}$ is smaller than for $\Delta\omega < \Delta\omega_{\text{abs}}$ by a factor of $\Delta\omega_{\text{abs}}/\Delta\omega$.

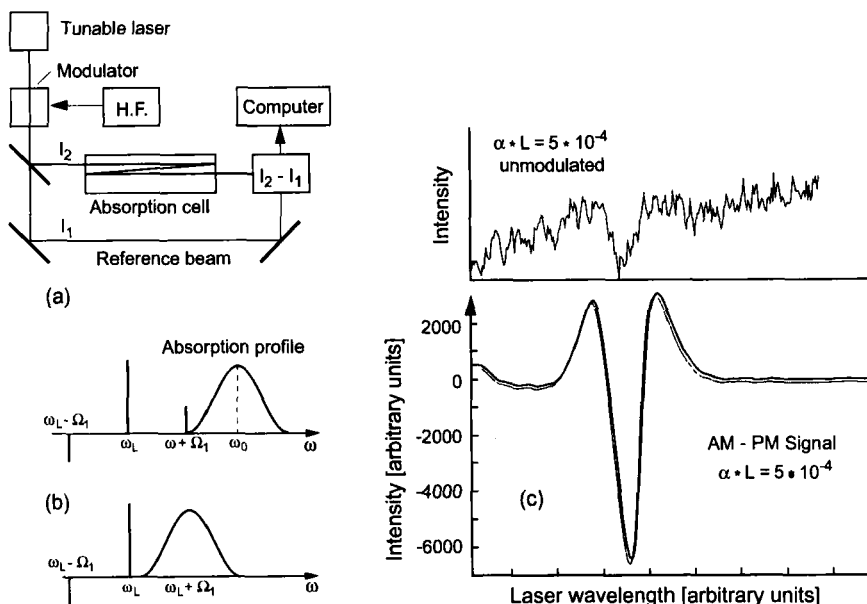


Fig. 12.20 Laser absorption spectroscopy with frequency-modulated radiation. a) Experimental setup; b) principle of modulation spectroscopy; c) ro-

tational line of the overtone transition $(1, 2, 1) \leftarrow (0, 0, 0)$ in the H_2O molecule measured with and without modulation.

Example

If the smallest measurable absorption is $\alpha L = 10^{-5}$ and the absorption path is 1 m, an absorption coefficient $\alpha = 10^{-7} \text{ cm}^{-1}$ is detectable for $\Delta\omega \ll \Delta\omega_{\text{abs}}$, whereas for $\Delta\omega = 50\Delta\omega_{\text{abs}}$, the limit is $\alpha = 5 \times 10^{-6} \text{ cm}^{-1}$.

As in microwave spectroscopy, the sensitivity can be increased by modulation techniques. As examples, we will consider two such methods. In the first, a laser beam is passed through a Pockels cell that is connected with a high-frequency electrical voltage, which modulates the refractive index of the crystal periodically (Fig. 12.20a). Hence, the transmitted laser wave experiences a phase modulation that in turn leads to a frequency modulation, because frequency is the time derivative of the phase.

This phase modulation leads to side bands in the frequency spectrum of the transmitted laser wave (Fig. 12.20b). The first two sidebands at $\omega_{\text{laser}} \pm 2\pi f$ have equal amplitudes but opposite signs, whereas for amplitude modulation, they have the same sign. If the transmitted intensity is measured using a phase-sensitive detector tuned to the modulation frequency f , no signal is detected at the lock-in output unless at least one of the sidebands is absorbed by the molecules in the absorption cell, because the phases of both sidebands shifted by 180° with respect to each other, and the detector receives two equal signals of opposite phase. All variations in the laser intensity are eliminated from the detected signal by this difference detection. However, if one of the sidebands coincides with an absorption line while tuning the laser

frequency ω , this sideband is weakened, and the balance is disturbed. Hence, the detector notices a signal. A detailed calculation shows that this signal $S(\omega)$ has approximately the form of the second derivative $d^2\alpha/d\omega^2$ of the absorption coefficient [12.11].

The best signal is obtained if the modulation frequency equals the linewidth of the absorption lines. For sufficiently low pressure, this is determined by the Doppler width, and which assumes values of about 1 GHz in the visible and near infrared spectral region. Such high frequencies cannot be processed by the lock-in detector without special precautions. Therefore, the amplitude of the high-frequency voltage controlling the Pockels cell is modulated with a lower frequency (two-tone modulation), and the signal is detected at this lower frequency. Another method employs a frequency mixer at the outlet of the fast detector, in which the signal frequency is superimposed with a reference frequency, and the difference frequency is detected at the output of the mixer.

Figure 12.20c illustrates how the signal-to-noise ratio can be improved by about two orders of magnitude. It shows a rotational line in the overtone vibrational transition $(1,2,1) \leftarrow (0,0,0)$ of the H_2O molecule, recorded with and without modulation. Using this method, relative absorptions as low as $\alpha L = 10^{-6}$ can be detected [12.12].

In the second method, the wavelength of the laser is modulated by mounting one of the mirrors of the laser cavity on a piezoelectric crystal, so that it can be moved periodically by applying an alternating voltage to the piezoelectric crystal, thus modulating the length of the laser cavity. Figure 12.21 illustrates the effect of this modulation

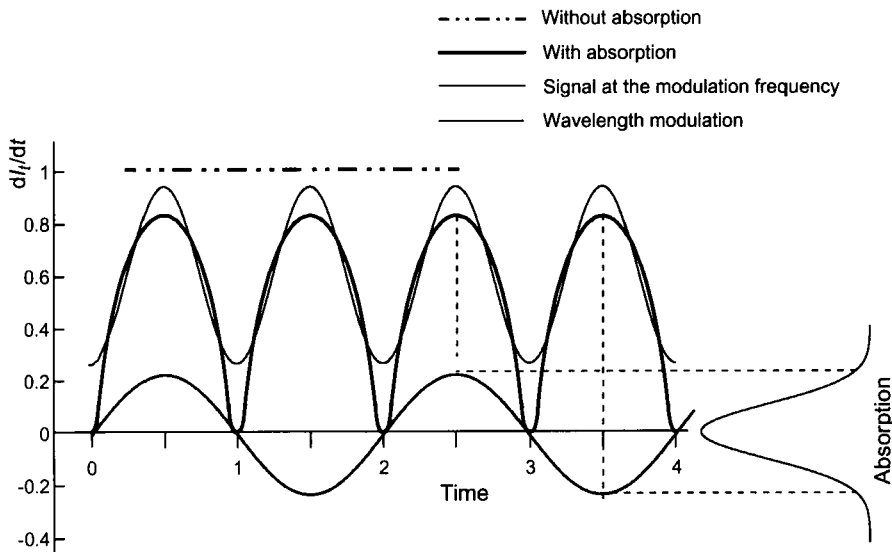


Fig. 12.21 Principle of wavelength modulation.

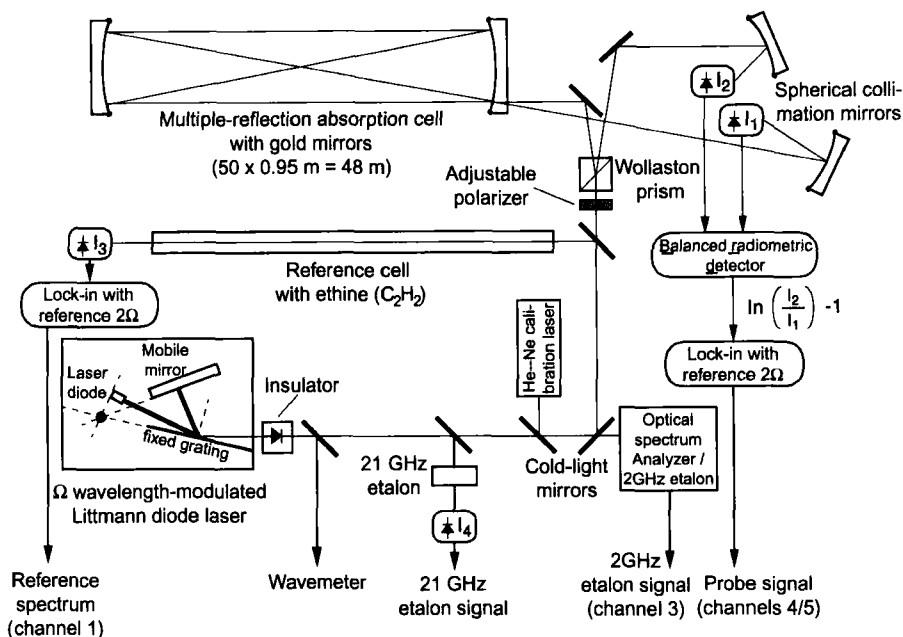


Fig. 12.22 Complete experimental setup for modulation spectroscopy [12.13].

on the signal form for the case where the laser frequency coincides with the peak of the absorption line. The form of the signal depends on the modulation range. The largest signal amplitude is obtained if the modulation is approximately equal to the linewidth. This method offers the advantage that no Pockels cell and no high modulation frequencies are needed. However, the drawback is that the modulation frequency is restricted to maximum values of about 100 Hz due to the mass of the moving mirror.

The sensitivity of the absorption measurement can be further enhanced by using a multiple-reflection cell and by recording the difference $I_t - I_r$ of the intensities of a reference beam and the probe beam that has passed through the absorption cell. The ratio $(I_t - I_r)/I_0$ can be detected by a ratio recorder, which further reduces the influence of fluctuations of the laser intensity. The complete experimental setup shown in Fig. 12.22 reveals that additional partial beams of the laser are usually employed for calibration purposes. They are first passed through an absorption cell containing a reference gas for wavelength calibration and then through thermally stable Fabry-Pérot interferometers, which create evenly-spaced frequency marks that can be used to correct for nonuniform frequency tuning of the laser. As an example for an actual measurement performed using this setup, Fig. 12.23 shows a section from the overtone spectrum of gaseous ozone in the spectral region around 6500 cm^{-1} where the absorption coefficient is very small.

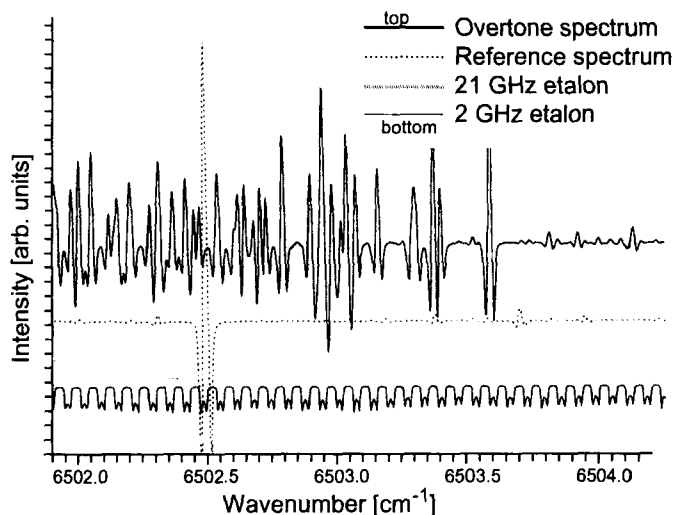


Fig. 12.23 Section from the overtone spectrum of the O_3 molecule, recorded using wavelength modulation [12.14].

12.4.2

Intracavity Laser Spectroscopy

If the absorbing sample is placed inside the laser cavity, the resulting laser intensity is reduced due to the losses introduced by the sample. In a tunable single-mode laser with a two-mirror cavity with reflectivities $R_1 = 1$ and $R_2 < 1$, each laser photon passes, on average, $1/(1 - R_2)$ times through the cavity so that the total path $L_{\text{eff}} = L/(1 - R_2)$ through the absorption cell of length L is increased by a factor of $(1 - R_2)^{-1}$. For $R_2 = 0.99$, this factor is already 100. The change in laser intensity brought about by the absorption losses is particularly large if the laser is operated closely above the laser threshold. While tuning the laser, large changes in the output power are then observed whenever the laser wavelength coincides with an absorption line. Either the change of the laser power or the fluorescence emitted by the molecules in the absorption cell can be recorded (Fig. 12.24).

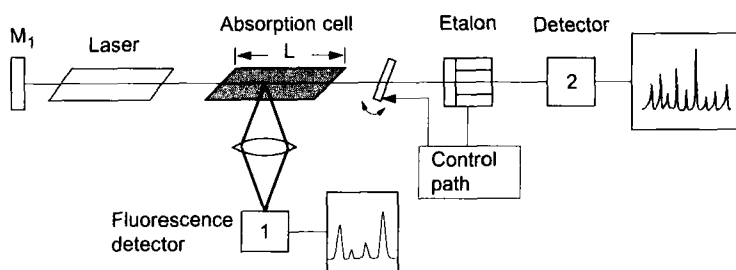


Fig. 12.24 Intracavity laser spectroscopy.

The sensitivity can be increased even further if a multi-mode laser is used, and the broadband output radiation is passed through a monochromator and is then detected spectrally resolved. The enhanced sensitivity is caused by couplings between the laser modes brought about by the active, homogeneously broadened laser medium due to a saturation of the amplification by stimulated emission. Each laser mode reduces the amplification not only for its own frequency but also for adjacent modes. If a specific mode is weakened by the absorbing medium, this results in a decreased reduction of the amplification factor in the active medium. Hence, adjacent modes benefit and are amplified, thus reducing the amplification for the weakened mode. In effect, the absorbed mode is weakened even further and can be suppressed completely. The recorded laser spectrum thus shows a marked decrease in laser intensity at the wavelength of the absorption, even for very weak absorptions. Hence, a very high sensitivity for the detection of weak absorptions is achieved. This is often expressed by an effective absorption path L_{eff} , which can amount to several hundred kilometers [12.15].

12.4.3

Absorption Measurements Using the Resonator Decay Time

In recent years, a very sensitive method has been developed in which the absorbing sample is placed in an external high-quality resonator, similar to laser-cavity spectroscopy. Now, however, a pulsed laser is used, and the absorption is measured using the decay time of the radiation energy stored in the resonator (Fig. 12.25).

At the end of a laser pulse introduced into the resonator, the power circulating in the empty resonator and partly transmitted through the output mirror decays exponentially,

$$P(t) = P_0 e^{-t/\tau_1} \quad (12.31)$$

with the decay time

$$\tau_1 = \frac{-2L}{c \ln(R^2)} \approx \frac{T_r}{2(1-R)}, \quad (12.32)$$

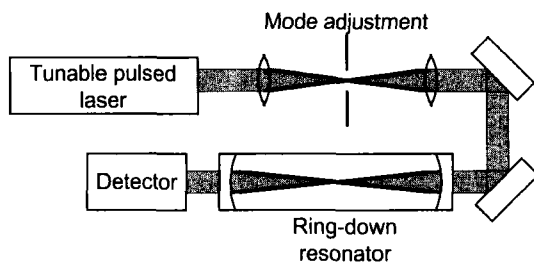


Fig. 12.25 Absorption measurement using the decay time of a resonator.

where $T_r = 2L/c$ is the time of circulation in the resonator of mirror distance L and $R \approx 1$ is the reflectivity of the two resonator mirrors.

If the extraction mirror with absorption A and reflectivity R has the transmittivity $T = 1 - R - A$, the detector registers the time-resolved signal $S(t) = TP(t)$.

If a sample of absorbing molecules is introduced into the resonator, the additional losses cause the decay time to decrease to

$$\tau_2 = \frac{T_r}{2(1 - R + \alpha L)}. \quad (12.33)$$

From Eqns. (12.32) and (12.33), we obtain

$$\alpha L = (1 - R) \frac{\tau_1 - \tau_2}{\tau_2}. \quad (12.34)$$

Hence, we can infer the absorption coefficient $\alpha = \sigma N_i$ from the difference $\tau_1 - \tau_2$ of the measured decay times, and, knowing the density N_i of molecules in the absorbing state $|i\rangle$, also the absorption cross-section σ [12.16].

Example

$R = 0.99$, $L = 1 \text{ m} \Rightarrow T_r = 2L/c = 6.7 \times 10^{-9} \text{ s} \Rightarrow \tau_1 = 3.3 \times 10^{-6} \text{ s} = 3.3 \mu\text{s}$.

With $\alpha L = 5 \times 10^{-4}$, it follows that $\tau_2 = 2.23 \times 10^{-6} \text{ s} \Rightarrow (\tau_1 - \tau_2)/\tau_2 = 0.48$.

Hence, the relative change of decay times is 48%.

12.4.4

Photoacoustic Spectroscopy

If, in addition to the absorbing molecules, a rare gas is introduced into the cavity as a collision partner, the molecules excited by absorption of laser photons can release their excitation energy by collisions with the rare-gas atoms and transform it into translation energy of the collision partners. This process increases the temperature of the gas and, for constant density, its pressure. If the exciting laser radiation is interrupted periodically (Fig. 12.26), periodic pressure changes are observed in the absorption cell.

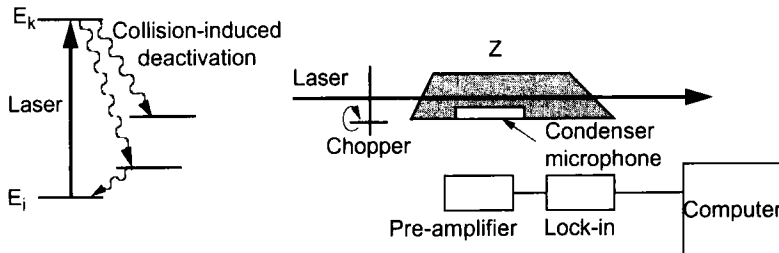


Fig. 12.26 Photoacoustic spectroscopy.

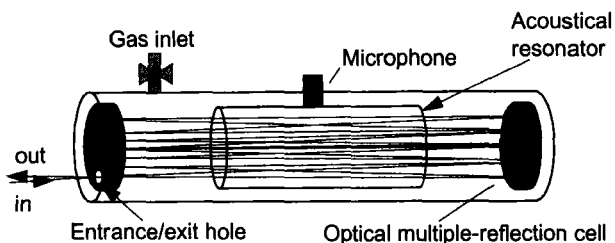


Fig. 12.27 Acoustic resonator without end windows inside an optical multiple-reflection cell.

By a suitable choice of the interrupt frequency (it should match one of the acoustic resonance frequencies of the cell), resonant standing acoustic waves can be excited in the absorption cell, which can then be detected using a sensitive microphone. The standing acoustic waves are selected so that the microphone is located at a point of maximum pressure oscillation. If the laser wavelength is varied continuously through the absorption spectrum of the sample, each absorption line yields an acoustic signal. The method is called photoacoustic spectroscopy because the absorbed photons are detected as an acoustic signal.

The sensitivity of the method can be further enhanced by placing the acoustic resonator inside an optical resonator or a multiple-reflection cell (Fig. 12.27). Using this technique, absorption coefficients $\alpha < 10^{-9} \text{ cm}^{-1}$ can be measured [12.17].

12.4.5

Laser-magnetic Resonance Spectroscopy

We discussed in the case of microwave spectroscopy that instead of tuning the frequency of the radiation source to the molecular absorption lines, the absorption lines of the molecules can also be shifted by an applied magnetic or electric field (Fig. 12.28a) and can thus be tuned over the frequency of a fixed-frequency source. The same procedure is of course possible in laser spectroscopy. This offers the advantage, particularly in the infrared region, that well-established powerful molecular lasers such as the CO or CO₂ laser can be used, which emit several hundred lines, of which one desired line can be selected using a diffraction grating inside the laser cavity.

As the Zeeman shifts of molecules in $^1\Sigma$ states are very small (see Sect. 10.2), this method is primarily applied to the spectroscopy of radicals, where the spin of the unpaired electron creates a large magnetic moment [12.18].

Again, different techniques discussed before can be combined. For example, the molecular sample can be placed inside the laser cavity, or the magnetic field strength can be modulated. Two examples are illustrated in Fig. 12.28. In Fig. 12.28b, the sample is placed inside the laser cavity, and the laser medium is separated from the absorbing sample by a transparent thin foil. The magnet is then tuned, and the laser

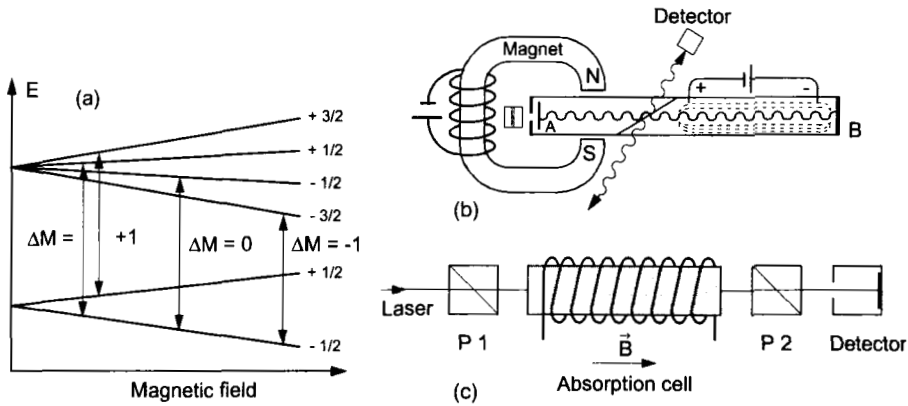


Fig. 12.28 Laser-magnetic resonance spectroscopy. a) Term diagram; b) sample in the laser cavity; c) Faraday effect in a longitudinal magnetic field.

radiation reflected at the separating foil is measured. Another technique utilizes the rotation of the plane of polarization of light in a longitudinal magnetic field (Faraday effect). The detector is placed behind a polarization analyzer and records only transitions with polarizations influenced by the magnetic field (Fig. 12.28c).

12.4.6

Laser-induced Fluorescence

Until now, we have presented techniques in which either the laser frequency was tuned across the absorption lines or the absorption lines were tuned over the laser wavelength. In laser-induced fluorescence, the laser is adjusted to the center of an absorption transition (ν_k, J_k) \leftarrow (ν_i, J_i) and then kept constant. The fluorescence emitted by the molecules in the defined state (ν_k, J_k) is measured either in total or spectrally resolved (Fig. 12.29). If only a single level has been excited selectively, the resulting fluorescence spectrum is relatively simple and easy to analyze. The fluorescing tran-

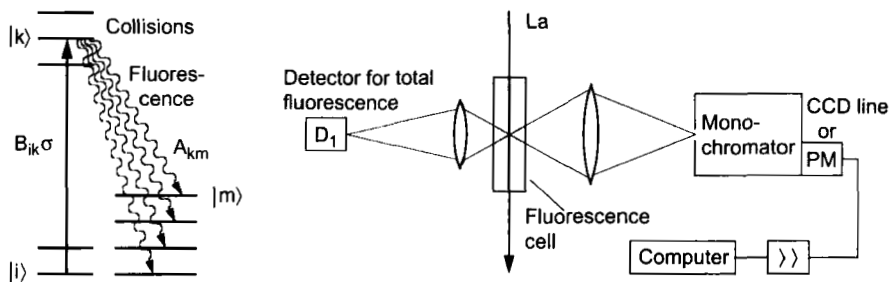


Fig. 12.29 Laser-induced fluorescence.

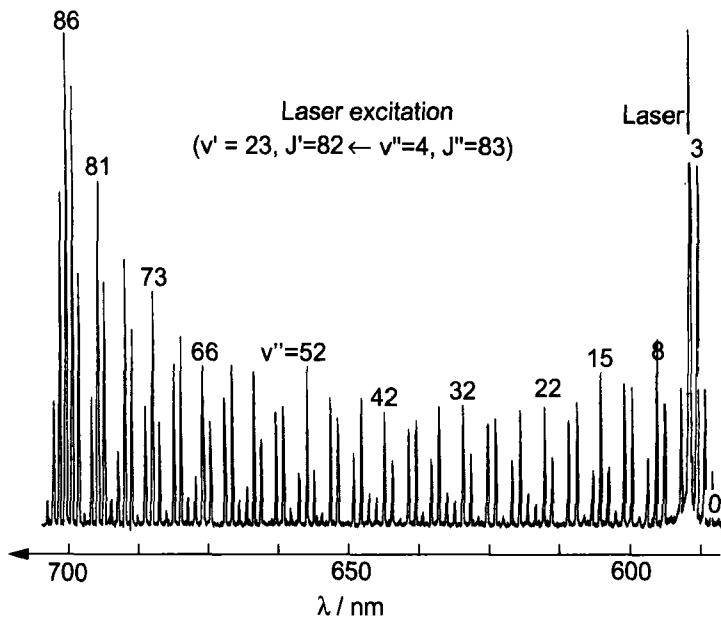


Fig. 12.30 Laser-induced fluorescence spectrum of the Cs_2 molecule after excitation with a dye laser at $\lambda = 591.7 \text{ nm}$. Each of the vibrational bands consists of two rotational lines, which are not resolved in this example [12.19].

sitions occur to all vibrational–rotational levels in a lower electronic state for which the transition is allowed. In diatomic molecules, there are at most three rotational lines with $\Delta J = 0, \pm 1$ per vibrational transition. In $\Sigma\text{--}\Sigma$ transitions, only P and R lines with $\Delta J = \pm 1$ are allowed. Measurement of the wavelengths of these transitions yields the term values of the vibration–rotation levels in the lower electronic state relative to the absorbing initial state. The relative intensities of the fluorescence bands give the Franck–Condon factors. As an illustration, Fig. 12.30 shows the fluorescence spectrum of the Cs_2 molecule excited into the $D^1\Sigma(v' = 23, J' = 82)$ state by a single-mode dye laser.

Laser-induced fluorescence is a highly sensitive method, as the following numerical example illustrates.

For N_i absorbing molecules per unit volume in the absorbing state $|i\rangle$ and a flux of n_{laser} laser photons at the absorption frequency per unit time and unit area,

$$n_{\text{abs}} = N_i n_{\text{laser}} \sigma_{ik} \Delta x \quad (12.35)$$

photons are absorbed per unit time on a path Δx , where σ_{ik} is the absorption cross-section for the transition $|k\rangle \leftarrow |i\rangle$. The number of fluorescence photons emitted per unit time is then

$$n_{\text{fl}} = N_k A_k = n_{\text{abs}} \eta_k, \quad (12.36)$$

where A_k is the Einstein coefficient of spontaneous emission and $\eta_k = A_k / (A_k + R_k)$ is the quantum yield of the upper level, which can possibly also be deactivated by other radiationless processes R_k .

Of these fluorescence photons, only a fraction δ can be gathered by lenses or mirrors and imaged onto the cathode of a photomultiplier. If that has a quantum efficiency η_{ph} , we obtain

$$n_{\text{pe}} = n_{\text{fl}} \delta \eta_{\text{ph}} = N_i n_{\text{laser}} \sigma_{ik} \Delta x \eta_k \eta_{\text{ph}} \delta \quad (12.37)$$

photoelectrons per unit time. Modern cooled photomultipliers have a quantum yield $\eta_{\text{ph}} = 0.2$ and a dark current of less than ten electrons per second. Hence, for a flux of just one hundred photoelectrons per second, the signal-to-noise ratio is already $S/R > 10$. To achieve this, according to Eq. (12.36) at least 10^3 laser photons must be absorbed per second for a fluorescence collection probability $\delta = 0.1$ and a quantum yield $\eta_k \approx 1$ of the excited molecular state. A laser power of 300 mW corresponds to a photon flux of $n_{\text{laser}} = 10^{18}$ photons per second at a wavelength of $\lambda = 500$ nm. An absorption of 10^3 photons per second thus corresponds to a relative absorption $(I_0 - I_{\text{trans}}) / I_0 = 10^{-15}$. This means an increase in sensitivity by a factor of $10^8 - 10^{10}$ as compared to the classical absorption method!

12.4.7

Laser Spectroscopy in Molecular Beams

The combination of molecular beam techniques and laser spectroscopy has brought about a wealth of interesting methods for high-resolution molecular spectroscopy. One important aspect is the decrease of the Doppler width in collimated molecular beams. Here, the molecules effuse from a reservoir through a narrow hole A into vacuum (Fig. 12.31). Molecules can only pass through the aperture B at a distance d downstream of A if their velocity component v_x satisfies

$$v_x \leq v_z \tan \vartheta = v_z b / (2d), \quad (12.38)$$

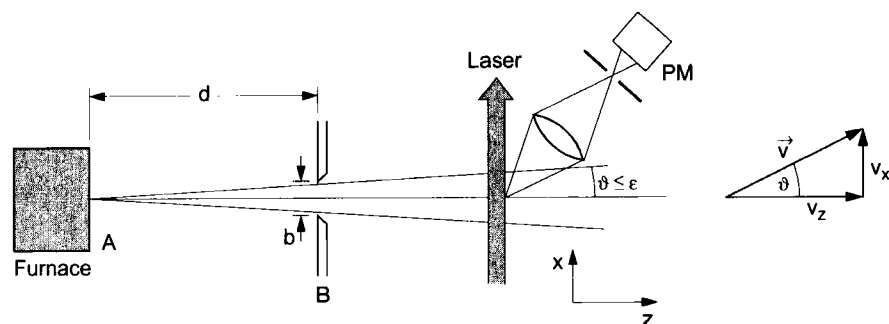


Fig. 12.31 Laser spectroscopy in a collimated molecular beam.

where we chose the z axis to be the beam direction. If a laser beam passes through the molecular beam in the x direction, the molecules have only small velocity components along the direction of the laser beam, and thus the Doppler width of the absorption lines is reduced by a factor of $\tan \vartheta \ll 1$ as compared to absorption in a gas cell.

Example

With the values $b = 1$ mm and $d = 100$ mm, we obtain $\tan \vartheta = 5 \times 10^{-3}$, that is, the Doppler width at $\lambda = 500$ nm is reduced from its typical value of 1 GHz to 5 MHz. Consequently, the spectral resolution is improved by the same factor.

A second aspect important for spectroscopy in molecular beams is the cooling of molecules in supersonic beams. If a gas at pressure p_0 in the reservoir expands through the nozzle A into vacuum, it is cooled adiabatically, because the expansion is so fast that virtually no heat exchange with the surrounding can occur. The energy $E = E_{\text{kin}} + E_{\text{pot}}$ of the gas in the reservoir at temperature T_0 is transformed into directed flow energy $1/2 mu^2$ of the gas molecules moving with the mean velocity u in the z direction. Whereas the internal energy of the gas decreases, its enthalpy is conserved. Hence,

$$\frac{f}{2} kT_0 + p_0 V = \frac{1}{2} mu^2 + (E_{\text{tr}} + E_{\text{rot}} + E_{\text{vib}}), \quad (12.39)$$

where f denotes the number of degrees of freedom of the molecules. The first term on the right-hand side of Eq. (12.39) is the kinetic energy of the molecules flowing with mean velocity u in the z direction. The first term in parentheses on the right-hand side describes the relative kinetic energy of the molecules in a system moving with velocity u . This term is small compared with $1/2 mu^2$. In other words: the *translational temperature* of the molecules, measured in a coordinate system moving with the drift velocity u , is very small [12.20]. This means that the internal temperature T at the expanded flowing gas is small ($T \ll T_0$). The gas has cooled down.

The cooling can be visualized using a simple molecular picture (Fig. 12.32). The fast molecules collide with the slower molecules ahead of them. Thus, central elastic collisions will lead to an exchange of kinetic energies and a narrowing of the velocity distribution until the relative velocities are small enough so that no further collisions occur. In contrast, noncentral collisions will deflect both collision partners from the beam direction so that they will not be able to pass through the aperture B. As there are also inelastic collisions, during which the molecular vibrational–rotational energy is transformed into translational energy, the internal degrees of freedom will also cool down. The larger the pressure p_0 in the reservoir, the more pronounced is the cooling. Therefore, the molecular gas in the reservoir is mixed with a rare gas, which serves as an inert collision partner, helping to dissipate the internal energy of the molecules.

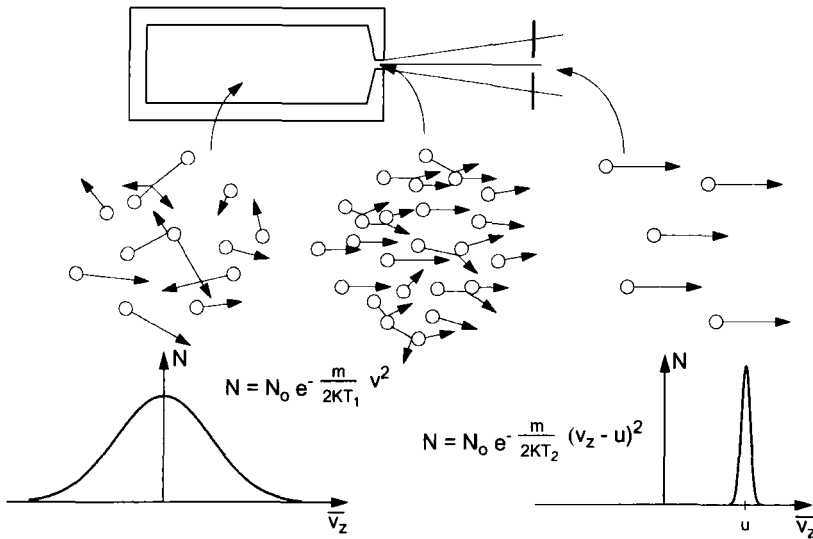


Fig. 12.32 Decrease of relative velocities during the adiabatic expansion of an ultrasonic beam [12.20].

As the collision cross-sections for the rotation–translation energy transfer are smaller than the elastic collision cross-sections, and those of the vibration–translation transfer are even smaller, there exists no thermodynamic equilibrium between the different degrees of freedom during the adiabatic expansion. The system is therefore described by a set of temperatures $T_{tr} < T_{rot} < T_{vib}$. Typical values, as observed, for example, during the expansion of sodium vapor in argon at a total pressure p_0 of 3 bar in the reservoir through a $50\ \mu\text{m}$ nozzle, are $T_{tr} = 1\text{--}5\ \text{K}$, $T_{rot} = 10\ \text{K}$, and $T_{vib} = 50\ \text{K}$. By optimizing pressure and nozzle diameter, much lower temperatures can be achieved, however. For example, in a helium supersonic beam with $p_0 = 100\ \text{bar}$, translational temperatures as low as $30\ \text{mK}$ were observed.

The reason why cooling is so important in molecular spectroscopy is the fact that the molecular level population is now concentrated in the lowest vibration–rotation levels. As only transitions from thermally populated levels occur in absorption spectra, the spectrum is thus greatly simplified, and the number of lines is significantly reduced. Overlap between hot bands is virtually eliminated, because higher vibrational or rotational levels are not occupied. The additional decrease of the Doppler width makes it often possible to resolve the rotational structure of a transition even for large molecules, whereas the lines overlap completely at room temperature. As an example, Fig. 12.33 compares a section from the spectrum of the NO_2 molecule recorded in a cell at room temperature, where the rotational structure cannot be resolved, with the indicated section from the upper spectrum recorded in a cooled molecular beam, where in addition to the rotational structure also the hyperfine structure of the rotational lines caused by the nuclear spin $I = 1$ of nitrogen can be resolved.

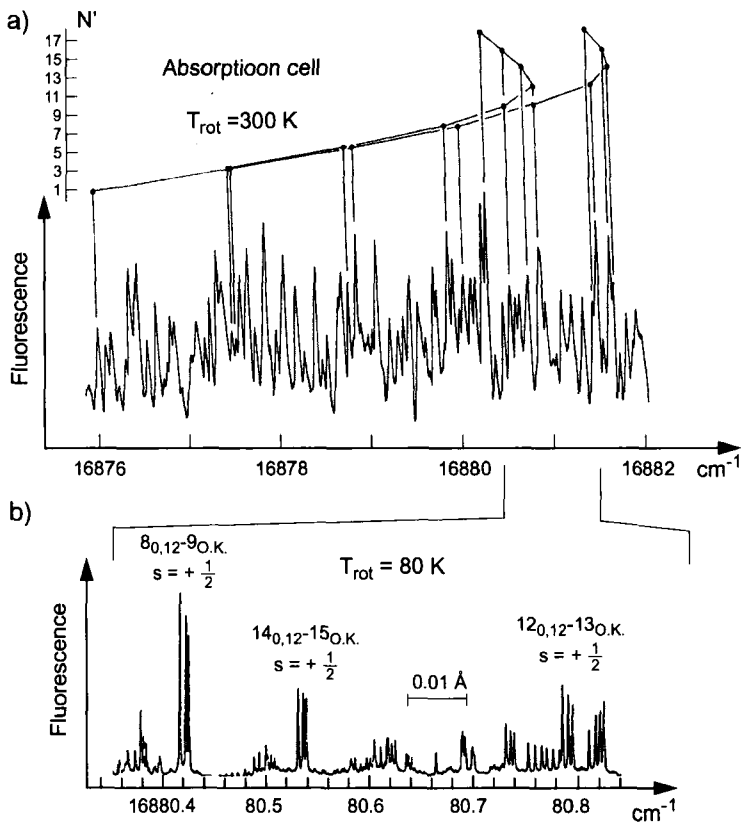


Fig. 12.33 Section from the spectrum of NO_2 a) in a cell at $T = 300$ K and b) partial section (as indicated) recorded in a collimated molecular beam at $T_{\text{rot}} = 50$ K [12.21].

As a further example, we will discuss *optothermal spectroscopy* in cold molecular beams, which is a good example for a highly sensitive detection technique for the excitation of long-lived molecular states in molecular beams [12.22]. Its principle is illustrated in Fig. 12.34. The collimated molecular beam is crossed perpendicularly by a laser beam. Mirrors or reversing prisms enable multiple passes through the molecular beam, thus enlarging the total absorption path. Even better, the intersection can be placed in the center of a high-quality resonator, where the laser intensity can be enhanced by a factor of 100 to 500.

The excited molecules impinge onto a cooled bolometer containing a doped semiconductor element. Here they stick to the cold surface and release their excitation energy, provided their lifetime is larger than the time of flight to the bolometer. The energy transferred to the bolometer kept at $T = 1.5$ K leads to a small increase in temperature ΔT and thus to a decrease $\Delta R = (dR/dT)\Delta T$ of the electrical resistance R . If a small current I (of about 1 mA) is passed through the bolometer, the excitation

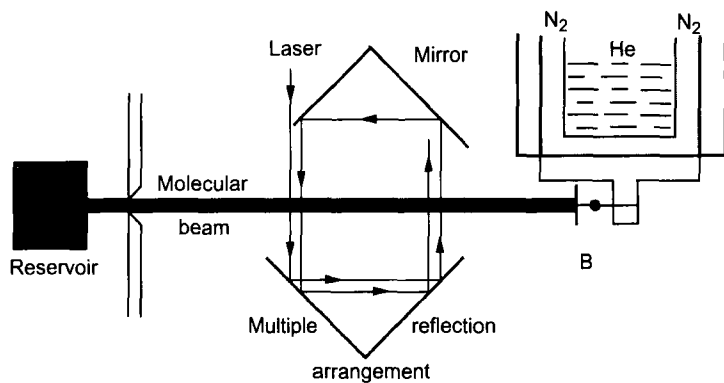


Fig. 12.34 Optothermal spectroscopy in a molecular beam.

of the molecules by a periodically interrupted laser shows up as a periodic voltage change $\Delta U = I\Delta R$ across the resistance R of the bolometer with the interrupt frequency, which is measured by a lock-in detector behind a cooled pre-amplifier. If the laser wavelength is tuned over the spectral range of interest, an optothermal spectrum is obtained, because the optical energy is converted to a temperature increase.

The sensitivity of the method depends on the heat capacity H , the heat conductivity G , and the quantity dR/dT . For an absorbed power P_0 and a chopping frequency Ω , the temperature amplitude is

$$\Delta T = \frac{P_0 G}{\sqrt{G^2 + (\Omega H)^2}}.$$

For $T = 1.5$ K and a suitably chosen bolometer material, detection limits as low as 10^{-14} W incident power can be realized.

A major advantage of this technique, in addition to its high sensitivity, is the decrease in Doppler width caused by the collimation of the molecular beam. For comparison, Fig. 12.35 shows the same section from the overtone spectrum of C_2H_4 at $1.6\mu\text{m}$ [12.23] recorded using Fourier spectroscopy, optoacoustic spectroscopy (both in a cell), and optothermal spectroscopy in a molecular beam. Clearly, not only the resolution is enhanced, but the signal-to-noise ratio is also much better.

12.4.8

Doppler-free Nonlinear Laser Spectroscopy

Even for molecular gases in a cell, the Doppler width of the absorption lines can be reduced using special techniques of nonlinear spectroscopy. Here, the selection of a narrow range of velocity components is achieved not by geometrical apertures but through a nonlinear interaction of the molecules with two laser beams.

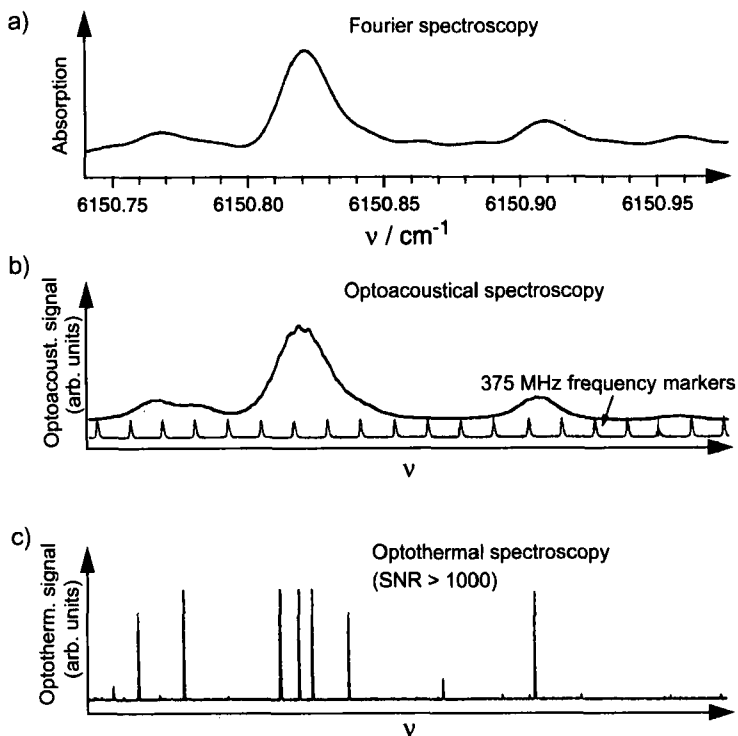


Fig. 12.35 Comparison of the same section from the C_2H_4 spectrum recorded by a) Fourier spectroscopy, b) optoacoustical spectroscopy in a cell at room temperature, and c) optothermal spectroscopy in a collimated molecular beam [12.6].

If the laser intensity I becomes so large that the depletion of the absorbing state $|i\rangle$ is stronger than its re-population by relaxation processes, its population number N_i decreases from its unsaturated value $N_i(0)$ to

$$N_i(I) = N_i(0) - aI. \quad (12.40)$$

The rate of absorption for the transition $|k\rangle \leftarrow |i\rangle$ is then, using the Einstein coefficient B_{ik} and the relation $I = \rho c$ (see Sect. 4.1),

$$-\frac{dN_i}{dt} = +\frac{dN_k}{dt} = N_i(I)\rho B_{ik} = (N_i(0)I - aI^2) B_{ik}/c. \quad (12.41)$$

Hence, it depends nonlinearly on the laser intensity I . This fact can be demonstrated experimentally if the fluorescence from the upper state is measured as a function of the exciting intensity I_{laser} (Fig. 12.36). The fluorescence intensity is no longer a linear function of the laser intensity (dashed line) but deviates from a straight line for higher values of I_{laser} .

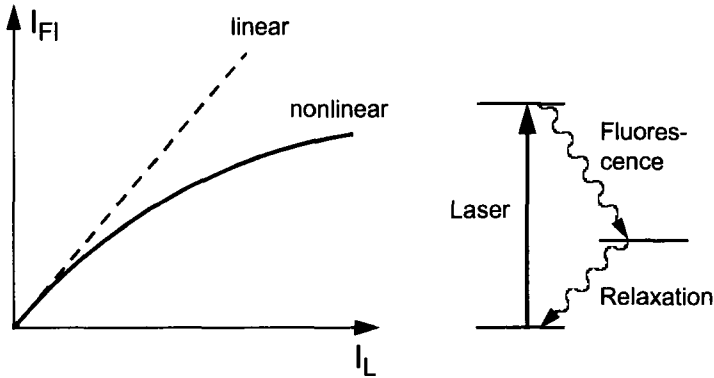


Fig. 12.36 Nonlinear absorption as demonstrated by the fluorescence intensity $I_{\text{fl}}(I_{\text{laser}})$ as a function of the laser intensity I_{laser} .

Now we consider a monochromatic laser beam passing along the z direction through a cell containing absorbing molecules with a Doppler-broadened absorption profile. Molecules with velocity components v_z experience a Doppler shift $\Delta\omega = \omega - \omega_0 = kv_z$ of the central absorption frequency ω_0 , where $k = 2\pi/\lambda = \omega/c$ is the wavenumber of the transition. They can therefore absorb the laser beam only if the laser frequency is within the homogeneous width J around the shifted frequency, that is $\omega_{\text{laser}} = \omega_0 + v_z k \pm J$. Of all the molecules in state $|i\rangle$, only those with a velocity component

$$v_z = \frac{(\omega_{\text{laser}} - \omega_0)}{k} \pm \frac{\gamma}{k}, \quad (12.42)$$

that is, within the homogeneous linewidth γ around the absorption frequency ω_0 , can absorb the laser photons. For sufficiently small pressure inside the cell, the homogeneous linewidth corresponds to the natural linewidth, which is about two orders of magnitude smaller than the Doppler width in the visible region. This means that only about 1% of all molecules in the state $|i\rangle$ contribute to the absorption. The saturation of the transition $|i\rangle \rightarrow |k\rangle$ by the monochromatic laser causes a hole in the population distribution $N_i(v_z)$ at the laser frequency ω_{laser} , or, correspondingly, at the velocity component v_z of Eq. (12.42). The width of this hole is determined by the homogeneous width and is given, in terms of velocity, by

$$\delta v_z = 2\gamma/k \quad (12.43)$$

(Fig. 12.37). This hole can only be detected, however, by passing a second *probe* laser beam in the opposite direction through the cell. The absorption of this laser shows a local minimum at the frequency of the first *pump* laser.

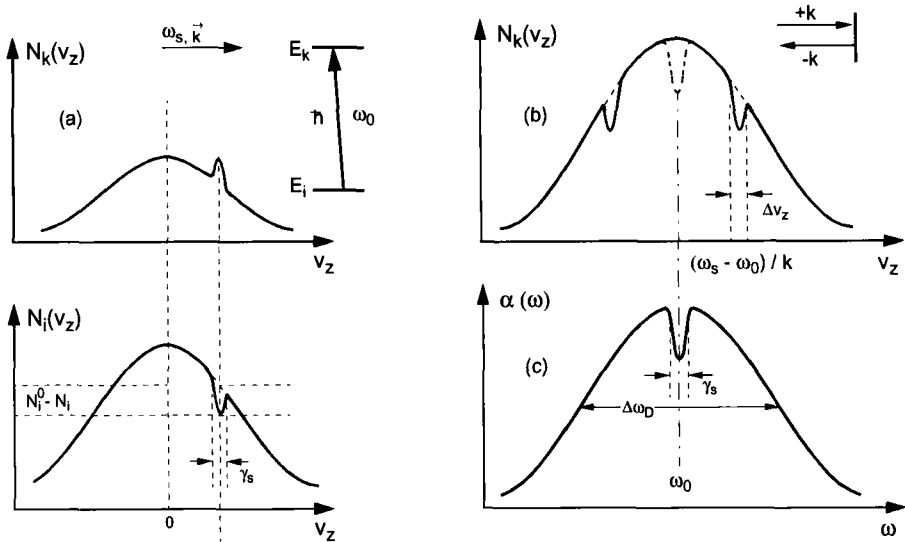


Fig. 12.37 a) Saturation hole in the population distribution $N_i(v_z)$ of the absorbing molecules, and corresponding population peak at $N_k(v_z)$. b) Saturation holes located symmetrically to $v_z = 0$ in the interaction with a standing light wave. c) Lamb dip in the Doppler-broadened absorption profile $\alpha(\omega)$.

This effect is exploited in *saturation spectroscopy*, where the laser beam is split into a strong pump beam and a weaker probe beam (Fig. 12.38). If $\omega_{\text{laser}} \neq \omega_0$, the two beams are absorbed by different groups of molecules due to the opposite Doppler shifts (Fig. 12.37b), that is, by molecules with the velocity components

$$v_{z1} = + \frac{(\omega_{\text{laser}} - \omega_0 \pm \gamma)}{k} \quad \text{and} \quad v_{z2} = - \frac{(\omega_{\text{laser}} - \omega_0 \pm \gamma)}{k}. \quad (12.44)$$

If $\omega_{\text{laser}} = \omega_0$, the two groups coincide, and both laser beams are absorbed by the same molecules in the velocity interval $v_z = 0 \pm \gamma/k$.

As the intensity $I = I_1 + I_2$ is larger for these molecules, the saturation increases, and hence the population density $N_i(v_z = 0)$ decreases, which shows up as a dip in the middle of the Doppler-broadened absorption profile $\alpha(\omega)$, called *Lamb dip* after Willis Lamb, who was the first to give a theoretical explanation for its occurrence (Fig. 12.37c).

The Lamb dip can either be detected by the reduced absorption of the probe beam or by the reduced fluorescence induced by it.

If there are two transitions with overlapping Doppler profiles in the molecule (Fig. 12.38b), the much narrower Lamb dips can still be resolved. If the pump beam is periodically interrupted, a lock-in detector can measure the difference of the unsaturated and the saturated spectra so that the Doppler background is eliminated (Fig. 12.38b bottom).

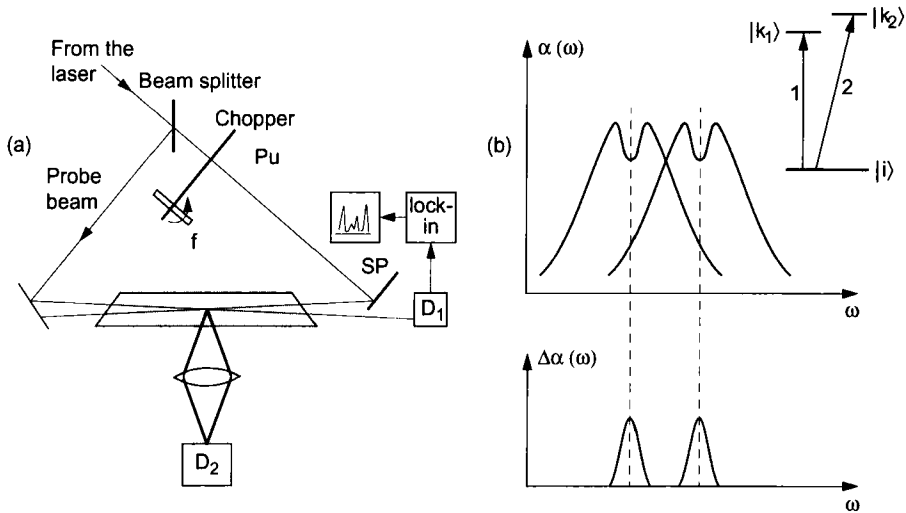


Fig. 12.38 a) Experimental setup for saturation spectroscopy; b) schematic representation of the resolution of two closely adjacent transitions.

If the absorption cell is placed inside the laser cavity and the wavelength is tuned, the laser intensity shows a pronounced peak at the location of the Lamb dip because there the absorption and thus the laser losses are smaller. As an example, Fig. 12.39a) shows the saturation spectrum of a rotational line in the electronic transition ${}^3\Pi_{0u} \leftarrow X\,{}^1\Sigma_g$ of the iodine molecule I_2 , where the 15 hyperfine components are visible, which cannot be resolved in Doppler-limited spectroscopy.

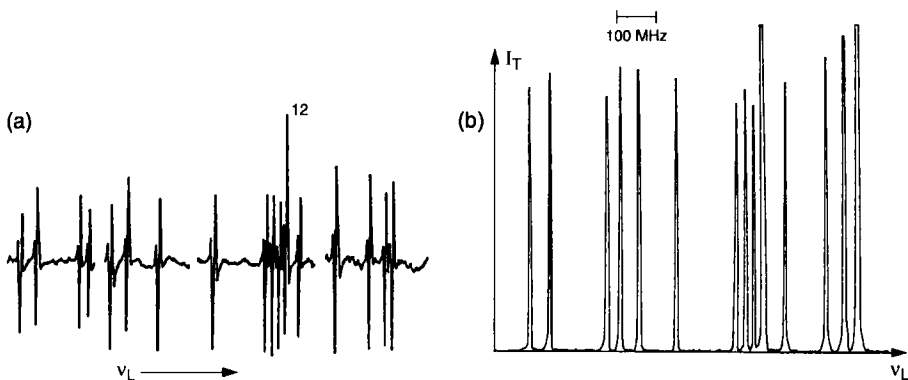


Fig. 12.39 Spectrally resolved hyperfine components of the rotational line ($v' = 58, J' = 99 \leftarrow v'' = 1, J'' = 98$) in the transition ${}^3\Pi_{0u} \leftarrow X\,{}^1\Sigma_g$ in the iodine molecule I_2 recorded by a) saturation spectroscopy and b) polarization spectroscopy.

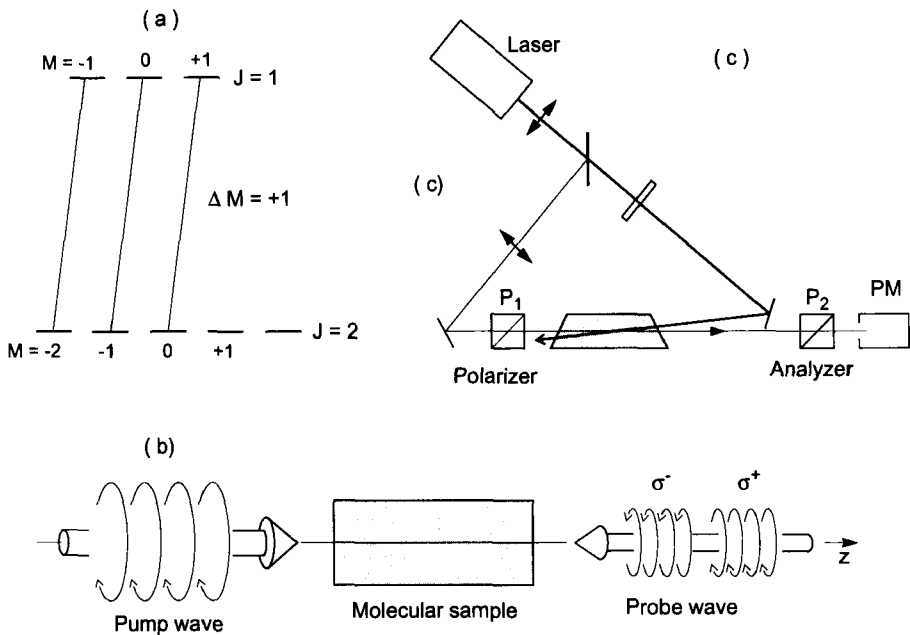


Fig. 12.40 Principle of polarization spectroscopy.

A still more sensitive technique of Doppler-free spectroscopy is *polarization spectroscopy*, the principle of which is illustrated in Fig. 12.40.

As in saturation spectroscopy, the laser beam is split into a pump and a probe beam. The probe beam is linearly polarized by the polarizer P_1 , passes through the absorption cell and then through a second polarizer P_2 with an orientation perpendicular to that of P_1 . The intensity of the transmitted beam is thus reduced by the quenching power of the two crossed polarizers (about 10^{-5} – 10^{-7} , depending on the quality of the polarizer crystals). The transmitted intensity is measured by the photomultiplier PM.

The pump wave is circularly polarized by a $\lambda/4$ plate and passes through the absorption cell in the opposite direction to the probe wave. It can induce transitions with $\Delta M = \pm 1$, where M is the projection of the rotational angular momentum J onto the direction of the pump wave. As Fig. 12.40a shows, optical pumping modifies the otherwise even population distribution of the M levels; the molecules become oriented. Their angular momenta J are no longer distributed randomly, but prefer to align with the direction of the pump wave (for σ^+ polarization) or opposed to it (for σ^- polarization). If the laser frequency ω_{laser} is tuned to the mean frequency of a molecular absorption line, both pump and probe beams can be absorbed by the same molecules. As these are oriented, they cause a rotation of the plane of polarization of the linearly polarized probe wave so that the intensity transmitted through P_2 increases. This is analogous to the Faraday effect, where the orientation of the molecules is achieved by an external magnetic field. Here, the orientation is selectively caused by the pump wave, that is, it applies only to molecules that can absorb the pump wave.

The detected signal $S(\omega_{\text{laser}})$ is Doppler free, exactly as in saturation spectroscopy. However, the sensitivity of polarization spectroscopy is much higher, because in this case the background in the absence of the pump wave is virtually zero on account of the crossed polarizers, so that the background noise (caused essentially by variations in laser intensity) is almost completely eliminated. In contrast, in saturation spectroscopy, the change in transmitted intensity I_{trans} of the probe laser brought about by the pump wave is small compared with I_{trans} , and the detected signal is therefore only slightly larger than the background. For comparison, Fig. 12.39b shows the polarization spectrum of the I_2 molecule for the same rotational line as in the saturation spectrum in Fig. 12.39a.

12.4.9

Multi-photon Spectroscopy

The large intensity of lasers enabled for the first time the experimental verification [12.24] of multi-photon absorption in molecules (see Sect. 4.4), which had been predicted and treated theoretically by Maria Göppert-Mayer [12.25]. Until now, most experiments have been performed using pulsed lasers, because they provide a large peak power, and hence multi-photon transitions can be observed despite their small transition probabilities without the need to focus the laser beam.

Much larger absorption cross-sections are observed if at least one of the photons is in resonance with a molecular transition. A two-photon absorption in which both photons are resonant corresponds to a stepwise excitation of two one-photon transitions.

The detection of multi-photon absorption can be achieved using the fluorescence from the excited states or, if states beyond the ionization threshold are populated, by detecting the ions or photoelectrons. Again, the ion yield assumes a maximum in the case of resonance. The method of *resonant multi-photon ionization* (REMPI) has proven valuable for the excitation of high-lying Rydberg states (that can afterwards be ionized by an electric field) or for the investigation of the states of molecular ions (Fig. 12.41). When combined with photoelectron spectroscopy, REMPI can provide very detailed information on these states.

With narrow-band continuous lasers, Doppler-free two-photon spectroscopy can be realized if the two absorbed photons pass through the absorption cell in opposite directions. If the molecule moves with a velocity component v_z , the Doppler shift for both absorbed photons is opposed, and both shifts cancel. If the two-photon transition occurs from state $|i\rangle$ to state $|f\rangle$,

$$E_f - E_i = \hbar(\omega_{\text{laser}} + kv_z) + \hbar(\omega_{\text{laser}} - kv_z) = 2\hbar\omega_{\text{laser}}, \quad (12.45)$$

so that the velocity of the molecules cancels. This means that all molecules in state $|i\rangle$ contribute to two-photon absorption, irrespective of their velocity – in sharp contrast to saturation spectroscopy, where only molecules from a narrow velocity interval around $v_z = 0$ contribute to the signal. This effect partially compensates for the much

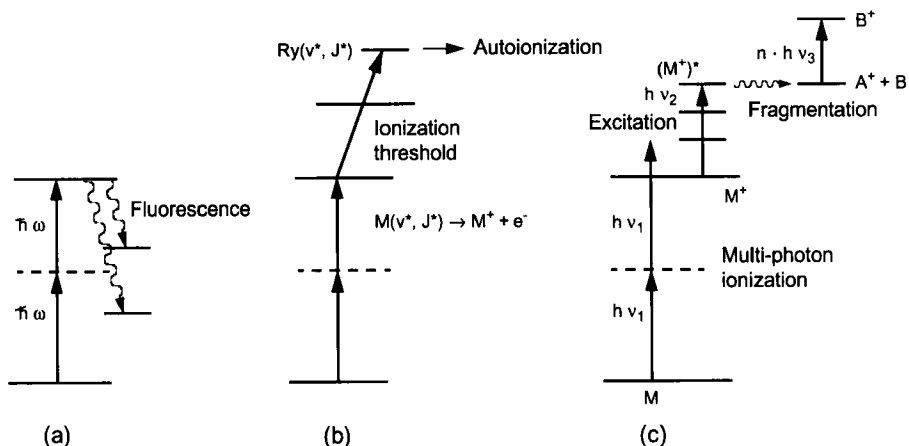


Fig. 12.41 Multi-photon spectroscopy. a) Detection using laser-induced fluorescence, b) detection using ionization, and c) multi-photon excitation with ionization and ion fragmentation.

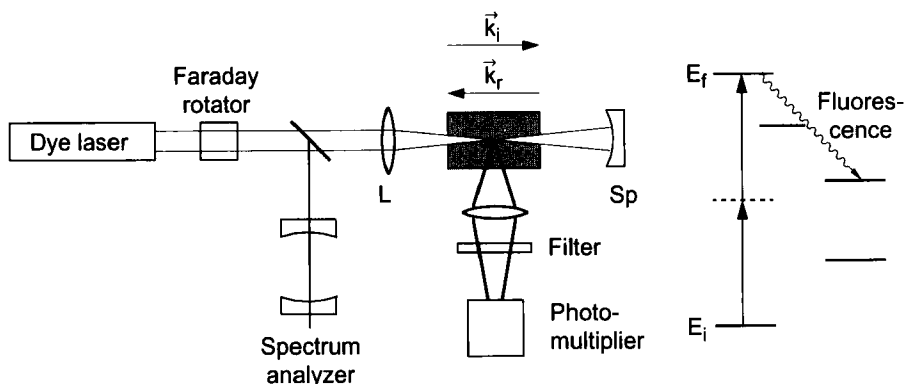


Fig. 12.42 Experimental setup for Doppler-free two-photon spectroscopy.

smaller transition probabilities of two-photon transitions as compared to those of one-photon absorption. Figure 12.42 shows an experimental setup for the measurement of Doppler-free two-photon absorption, and Fig. 12.43 displays a spectrum of naphthalene obtained using this method in which the rotational structure can be resolved.

12.4.10

Double Resonance Techniques

Despite the high spectral resolution, not all lines can usually be completely resolved in spectra with closely spaced lines. Furthermore, the analysis of spectra, especially of disturbed spectra, is often difficult or even impossible. In these cases, a method can be

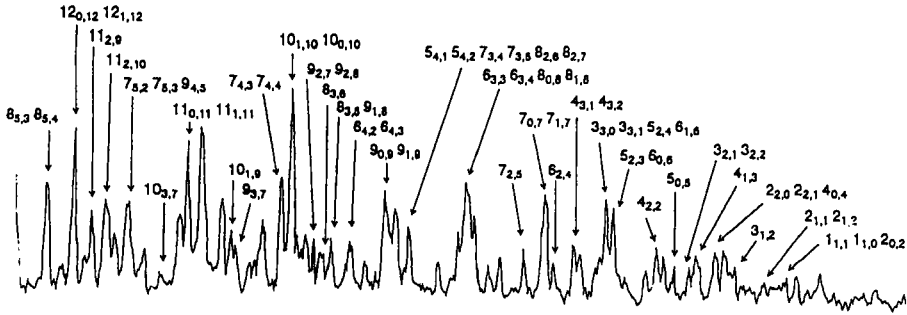


Fig. 12.43 Section from the Doppler-free rotationally resolved two-photon spectrum of naphthalene [12.26].

used in which the molecules interact with two electromagnetic waves simultaneously, and two transitions sharing a common level are in resonance (Fig. 12.44). In this *double resonance*, either the lower level (V-type double resonance) or the upper level (Λ -type) can be common to both transitions, or a stepwise excitation with a common intermediate level can occur. The two waves can be from completely different spectral regions. For example, there is optical–radiofrequency, optical–microwave, optical–optical, or infrared–ultraviolet double resonance.

Such a double resonance can simplify a spectrum considerably, as will be illustrated for the example of optical–optical double resonance. If the pump wave is kept on a transition $|1\rangle \rightarrow |2\rangle$, the population N_1 will decrease due to saturation, whereas N_2 will increase. If the intensity of the pump laser is periodically interrupted, the population densities N_1 and N_2 are also modulated with opposed phases: if the laser is off, N_1 increases and N_2 decreases. If the probe wave is tuned through the spectrum, its absorption is modulated by the interrupt frequency exactly if its wavelength matches a transition from one of the levels $|1\rangle$ or $|2\rangle$. If this absorption (either as transmitted intensity or as induced fluorescence) is detected by a lock-in detector at the interrupt frequency, only lines appear in the spectrum belonging to transitions from one of the two modulated levels. The crucial point is that only a single level is marked, so that the absorption spectrum of the probe wave does not contain the multitude of transitions from all thermally populated levels but only the transitions starting from the marked level.

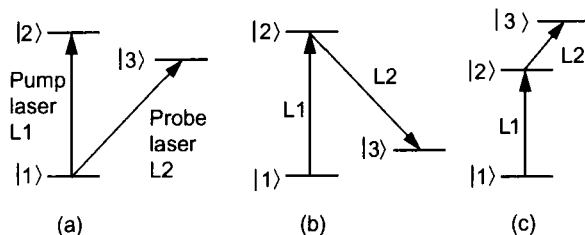


Fig. 12.44 Different double-resonance schemes. a) V-type; b) Λ -type; c) stepwise excitation.

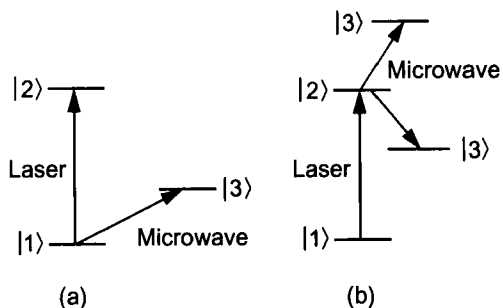


Fig. 12.45 Infrared–microwave double resonance. a) General scheme with common lower level; b) microwave spectroscopy in excited states after infrared excitation.

As a second example, we will consider infrared–microwave double resonance. In Sect. 12.1 we saw that one of the reasons for the weak absorption of a microwave by a molecular gas at room temperature is the almost identical population of the upper and lower levels of the microwave transition $|1\rangle \rightarrow |3\rangle$. If we use an infrared laser to pump a transition $|1\rangle \rightarrow |2\rangle$ sharing the lower level $|1\rangle$ with the microwave transition and to excite molecules into the higher vibrational level $|2\rangle$ (Fig. 12.45a), the population density N_1 is drastically reduced while $|3\rangle$ is unaffected so that in the microwave transition, stimulated emission now dominates absorption markedly. If the infrared laser is switched on, a larger microwave signal is therefore detected with a different sign as compared to the situation when the infrared laser is switched off.

Optical pumping with a laser populates specific levels in excited states selectively, and double-resonance techniques can thus be used to realize microwave spectroscopy in excited states which are not populated thermally (Fig. 12.45b).

Λ -type double resonance, in which the second laser stimulates emission from the upper level $|2\rangle$ populated by the pump laser to lower levels $|3\rangle$, allows the investigation of highly excited vibrational levels in the electronic ground state. If these levels are slightly lower than the dissociation limit, couplings between different electronic states dissociating into the same atomic states can be investigated. As an example, Fig. 12.46 shows a section from the Λ -type double-resonance spectrum of the Cs_2 molecule, in which the pump laser excites a vibrational level $v' = 50$ in the $D^1\Sigma$ state, and transitions into vibrational levels with $v'' > 130$ in the $X^1\Sigma_g$ state are reached by emission induced by the second tunable laser [12.27]. At large internuclear distances, this state interacts with the $^3\Sigma_u$ state through nuclear spin–electron spin coupling, because the difference between these states is smaller than the hyperfine splitting in the atomic states into which the molecule dissociates. For these coupled states, there are three slightly different dissociation energies, depending on the atomic hyperfine components into which the molecular states dissociate. The mixing of singlet and triplet states yields four components in stimulated emission (Fig. 12.46b) instead of one single rotational line that would appear without this coupling.

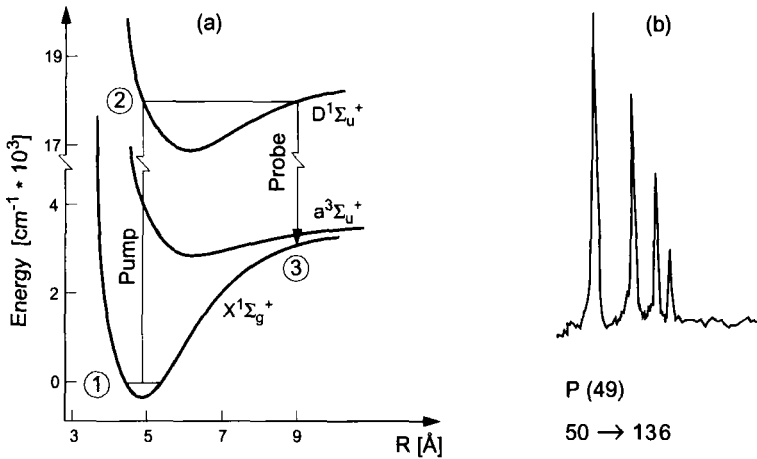


Fig. 12.46 Components of the rotational transition in the Cs_2 molecule obtained by stimulated emission. a) Term diagram; b) measured spectrum [12.27].

Another interesting effect in A -type double resonance is that the linewidth is reduced below the natural linewidth of one of the transitions if the two laser beams proceed collinearly. It can be shown [12.28] that in this case the linewidth of the double-resonance signal is given by the sum of the widths of the two lower levels and is independent of the upper level. If the lower levels are vibration-rotation levels in the electronic ground state, their lifetime is long compared to that of the upper level, so that extremely sharp lines appear in the double-resonance spectrum.

The stepwise excitation allows the investigation of high-lying molecular states with lasers in the visible range. For example, molecular Rydberg states $R(n, v, J)$ can be investigated in detail, where the energy depends on the vibrational state v and the rotational state J as well as on the principal quantum number n (Fig. 12.47). Measurement

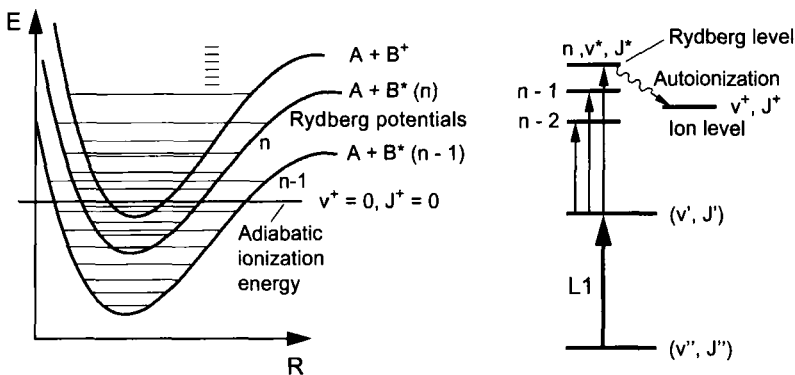


Fig. 12.47 Measurement of molecular Rydberg states. a) Level diagram; b) section from the Rydberg spectrum of the

Ag_2 molecule, in which the series converging to the different vibrational levels are indicated.

of Rydberg series with $v = 0$ for many principal quantum numbers n permits a very precise extrapolation to the ionization limit at $n = \infty$. Using this procedure, precise ionization energies have been determined for a number of molecules. As the Rydberg series converge, for $v > 0$, towards excited vibrational levels of the molecular ion, measuring several Rydberg series with different values of v gives information on the vibrational levels of the ion.

12.4.11

Coherent Anti-Stokes Raman Spectroscopy

Coherent anti-Stokes Raman spectroscopy (CARS) utilizes two lasers with frequencies $\omega_1 = \omega_L$ and $\omega_2 = \omega_S$ that differ by the frequency ω_v of a Raman-active vibrational mode. The induced Raman effect populates the vibrational level $|v\rangle$, so that the laser wave ω_1 can stimulate another Raman process starting from level v , which leads to an emission of the anti-Stokes wave (Fig. 12.48), bringing the molecule back to its ground state. The anti-Stokes wave is emitted in a well-defined direction determined by conservation of momentum, $2\vec{k}_1 = \vec{k}_2 + \vec{k}_a$ (Fig. 12.48b). This nonlinear CARS process is also called *four-wave mixing* because four different waves are involved.

The advantage of the CARS technique as compared to spontaneous Raman scattering lies in the much larger intensity of the coherent anti-Stokes radiation and its good spatial collimation, which allows large distances between the sample and the detector so that any disturbing spontaneous background radiation can be eliminated.

Both continuous and pulsed lasers can be used as pump lasers. Pulsed lasers offer the advantage of higher peak power and thus a better signal-to-noise ratio. Therefore, CARS using pulsed lasers is employed, for example, for the detection of minute molecular concentrations in combustion processes, where the large distance to the detector makes it possible to suppress the continuous thermal radiation of the hot flame by geometrical apertures.

The advantage of narrow-band continuous lasers is their higher spectral resolution. For example, they allow one to record rotationally resolved CARS spectra even for larger molecules.

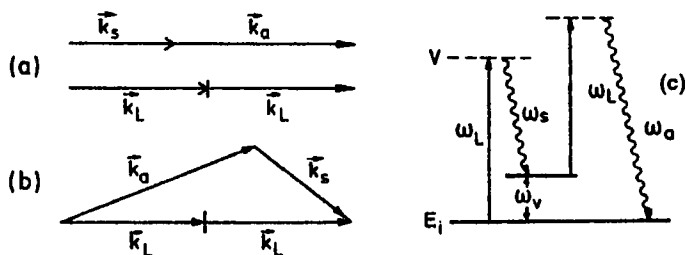


Fig. 12.48 The CARS process. Conservation of momentum for a) collinear and b) noncollinear incident beams; c) term diagram.

There are many experimental versions of this interesting spectroscopic method such as resonant CARS or box CARS. More detailed accounts can be found in the specialized literature [12.29, 12.30].

12.4.12

Time-resolved Laser Spectroscopy

While stationary spectroscopy can determine the *structure* of molecules, time-resolved spectroscopy can provide information on *dynamic* processes in molecules such as the lifetimes of excited states, intramolecular energy transfer processes, or the energy transfer during molecular collisions. Many of these processes occur on short timescales ranging from microseconds to femtoseconds. Here, laser spectroscopy has opened a wealth of new possibilities by supplying ultrashort laser pulses. This will be elucidated in the following for a number of examples. More detailed accounts can be found in the specialized literature [12.31–12.33].

Lifetime Measurements

If a molecular level $|k\rangle$ is excited by absorption of a photon or by electron impact at time $t = 0$, its population density decays exponentially according to

$$N_k(t) = N_k(0) e^{-(t/\tau)}. \quad (12.46)$$

After a mean lifetime τ , $N(\tau) = N(0)/e$. This can be verified either by time-resolved measurement of the fluorescence intensity

$$I(t) = A_k N_k(t), \quad (12.47)$$

where A_k is the Einstein coefficient of spontaneous emission (see Sect. 4.1), or by monitoring the decay of the absorption for transitions from the state $|k\rangle$ into higher states.

Nowadays, pulsed or mode-coupled lasers are predominantly used as exciting radiation sources. The decaying fluorescence can either be measured by a fast detector, and the decay curve can directly be visualized on an oscillograph, or the signal from the detector can be sent to a multichannel analyzer, which measures the signal for predefined time slots t_n to $t_n + \Delta t$ and integrates over the time interval Δt (Fig. 12.49a).

For small fluorescence intensities, a time-resolved single-photon coincidence method has proven successful that will be described in the following.

The molecules are excited by short pulses from a mode-coupled laser with a constant repetition rate f and a pulse energy which is small enough so that the detection probability for a fluorescence photon excited by a single pulse is much smaller than unity. Hence, a maximum of one fluorescence photon is emitted per excitation pulse. The exciting laser pulse starts a linearly increasing voltage ramp $U(t) = at$, which is later stopped by the fluorescence photon at a voltage at_n that is proportional

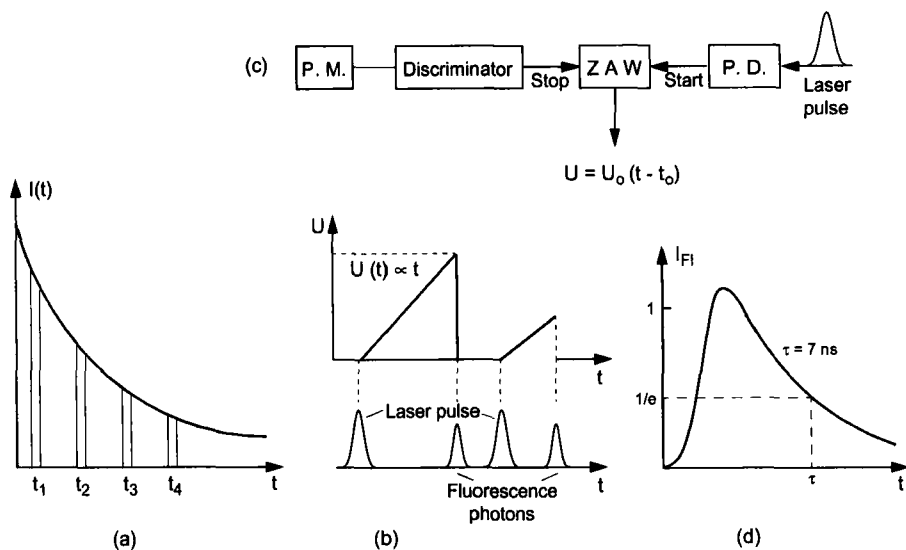


Fig. 12.49 Lifetime measurement a) using time slots, b) with single-photon measurement in delayed coincidence, and c) decay curve of the excited level ($J' = 27, v' = 6$) in the ${}^1\Pi$ state of Na_2 .

to the delay time t_n of the photon (Fig. 12.50b). The voltages $U(t_n)$ are measured for many excitation pulses and stored in a multichannel analyzer or in a computer, and the signals caused by single fluorescence photons measured in the time interval $t_n + \Delta t$ are added up. The probability W_n that a photon has a delay time t_n is proportional to the fluorescence intensity $I(0)e^{-t/\tau}$. Hence, the frequency distribution $N(t_n)$ of the measured fluorescence photons yields the time response, from which the mean lifetime τ can be determined. Figure 12.49c illustrates the experimental setup schematically, and Fig. 12.49d shows a typical decay curve measured with such a setup.

The two methods discussed until now can be used for decay as short as about 100 ps. For shorter times, the time resolution of the electronic devices used in detection is inadequate. For a time resolution as low as one picosecond, the streak camera can be used (Fig. 12.50). In principle, this is a combination of photodetector and a fast oscillograph. The photon pulse considered hits the photocathode of the streak camera and ejects photoelectrons. These pass through a plate capacitor to which a fast voltage ramp is applied. The electrons are therefore deflected more or less strongly, depending on the time at which they pass the capacitor, and the abscissa on the oscillograph becomes a time axis. If the photon pulse is passed through a spectrograph before entering the streak camera, so that the different wavelengths are dispersed in the y direction, the screen of the oscillograph displays the decay curves $I(\lambda, t)$ for the different wavelengths.

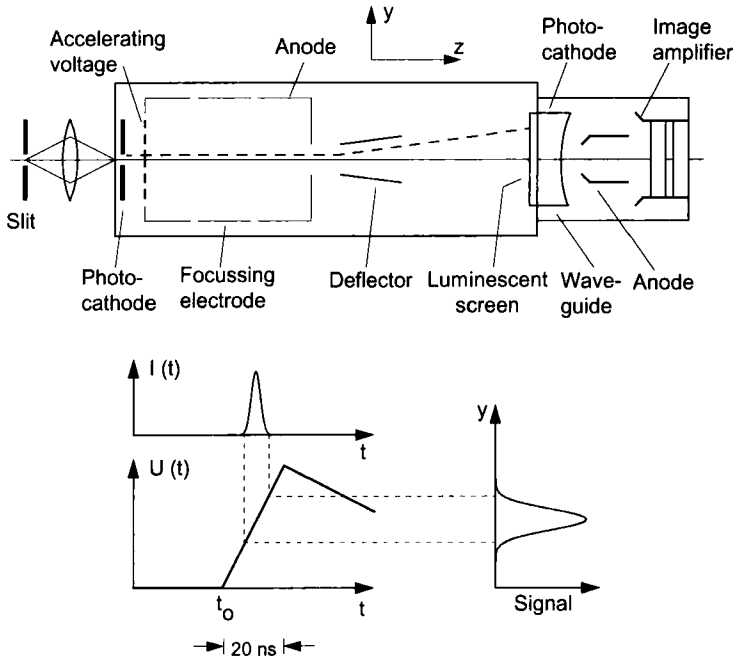


Fig. 12.50 Principle of a streak camera and connection between the time profile $I(t)$ of the incident laser pulse and the signal $S(y)$ at the output.

Correlation Methods

In the femtosecond range, the streak camera also fails. There are correlation methods, however, which can provide a sufficient time resolution. The shortest laser pulses yet realized are below 4 fs. From these femtosecond pulses in the visible region, harmonics in the visible UV or even in the x-ray region can be created by frequency doubling, with pulse widths below one femtosecond, that is, in the attosecond range ($1 \text{ as} = 10^{-18} \text{ s}$), so that a temporal resolution of less than one femtosecond is possible [12.34].

To measure such ultrashort laser pulses reliably, a setup as shown in Fig. 12.51 is used. A beam splitter splits the laser pulse into two parts, of which one runs through a fixed and the other one through a variable path length. If both partial beams are superimposed afterwards, their time delay τ with respect to each other is variable. The total intensity is then $I(t) = I_1(t) + I_2(t + \tau)$. If the time constant T of the detector is large compared with the duration of a laser pulse, the detector will effectively integrate over $I(t)$ and measure the total incident energy, which is independent of τ as long as $\tau < T$. Therefore, it provides no information on the time profile of the laser pulse at the optical frequency ω .

However, if the recombined laser beam passes through an optically nonlinear crystal in which an optical harmonic at frequency 2ω is generated, the intensity in the

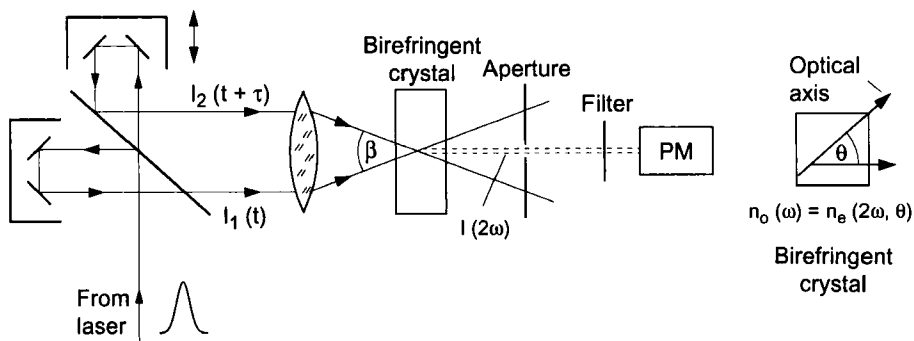


Fig. 12.51 Measurement of the time profile of a femtosecond pulse using the correlation method. a) Schematic setup; b) orientation of the birefringent crystal (potassium dihydrogen phosphate) for phase matching.

harmonic is

$$\begin{aligned}
 I(2\omega) &\propto (I(\omega))^2 = (I_1(t) + I_2(t + \tau))^2 \\
 &= I_1^2 + I_2^2 + 2I_1(t)I_2(t + \tau).
 \end{aligned}
 \tag{12.48}$$

While the first two terms on the right-hand side are independent of the time delay τ , the time profile of the last term depends on τ , corresponding to the convolution of the identical pulse profiles $I_1(t)$ and $I_2(t + \tau)$. If the detector signal is recorded as a function of the time delay τ , the original pulse profile can be obtained by deconvolution. Hence, the time measurement is reduced to a distance measurement $\Delta s = c\tau$. Usually, the back-reflection prism that controls the delay distance is moved by a high-precision micrometer screw powered by a stepping motor [12.32].

Pump-Probe Technique

Fast molecular processes can be investigated using the pump-probe technique. Here, one part of the laser beam is transmitted through the molecular sample, where photons are absorbed from the pulse and some molecules are lifted into excited states. The time evolution of these excited states is then monitored using a probe pulse passing through the sample after a variable time delay. For this purpose, either the fluorescence induced by the probe pulse is measured or the ions or electrons created upon ionization of the excited state by one- or multi-photon transitions. Either way, decay curves are obtained, as in the case of the lifetime measurements, from which the decay of the excited state can be reconstructed.

In many cases, excitation leads to a dissociation of the molecule or (for multi-photon excitation) the molecular ion. The fragments can then be identified using a mass spectrometer. If the signal for a specific fragment mass is measured as a function of the time delay of the probe pulse, the different decay channels of the excited molecular state and their relative probabilities can be determined. The fragmentation

of $\text{Fe}(\text{CO})_5$ may be mentioned as an example [12.35]. Starting from the initially excited state, the system proceeds “downhill” on the potential surface until it reaches a conical intersection with the potential surface of another molecular state. This means that a fraction of the electronic energy is transformed into molecular vibrational energy. During this process, the molecule is ionized by the delayed probe pulse. The observed fragmentation pattern depends on the position on the potential surface at which the ionization occurs, that is, on the time delay of the probe pulse.

12.4.13

Femtochemistry

For many years, photochemists have been dreaming of ways to influence chemical reactions by exciting molecules through the absorption of photons, or even to control them in this manner. With the advent of lasers as light sources, these aims seemed to be close. If a specific molecular bond (i.e., a local vibrational mode) leading to the dissociation of the molecules into the desired targets could be excited selectively, the reaction could be influenced by an appropriate choice of the wavelength of the exciting laser. At first, however, many attempts in this direction remained unsuccessful – for a simple reason.

In order to influence chemical reactions significantly, high-lying vibrational levels in the electronic ground state or in excited electronic states must be populated by the exciting radiation source. Due to the anharmonicities at higher energies and the increasing density of states, however, these levels usually exhibit strong couplings with other levels. These cause the initially selective population of one or a few levels, in which the excitation energy is concentrated, to spread about many levels before the desired reaction starts. The selective excitation therefore simply results in thermal activation by an increase in temperature, accelerating all possible reactions with an activation barrier.

Hence, the excitation must occur so fast that the reaction begins *before* the energy is dissipated between many degrees of freedom. As this redistribution takes place on a picosecond scale, femtosecond pulses must be employed. Photochemistry using femtosecond lasers has also been termed *femtochemistry* [12.36, 12.37].

With the aid of the pump–probe technique, fast molecular reactions can be monitored in real-time. An example is the dissociation of a molecule after excitation with a femtosecond laser (Fig. 12.52). The probe pulse stimulates transitions between the potential curves of the molecule, which is dissociating with the velocity $v(R)$ at the internuclear distance $R = \int v dt$. For each time delay τ , there is a wavelength λ of the probe pulse matching the energy difference $E_2(R) - E_1(R) = hc/\lambda$. The pump laser stimulates fluorescence in the states of $\text{BC}(R = \infty)$ into which the molecule dissociates, which can be measured as a function of the time delay τ . From this measurement, the velocity $v(R)$ of the dissociating fragments and hence the difference of the slopes of the two potential curves can be determined.

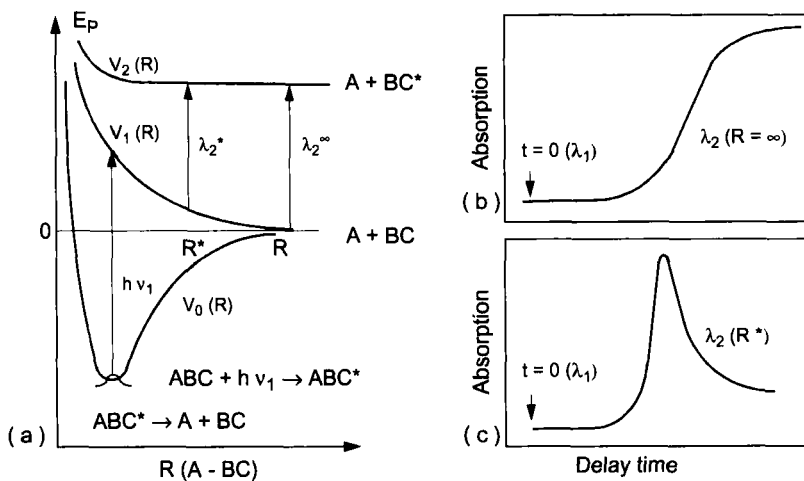


Fig. 12.52 Direct observation of a molecular dissociation using the pump-probe technique [12.36].

An interesting standard example for the use of femtosecond lasers to control chemical reactions is the excitation of Na_2 molecules (Fig. 12.53).

A femtosecond laser pulse with a pulse width of Δt excites molecules from their $v'' = 0$ vibrational level in the electronic ground state $X^1\Sigma_g$ into a coherent superposition of several vibrational states in the excited $^1\Sigma_u$ state because of its broad frequency spectrum $\Delta\nu = h/\Delta t$. This superposition forms a wavepacket oscillating with the mean vibrational period between the turning points. The second probe pulse delayed by a time τ can excite the molecule even further. Depending on the position $R(t)$ of the wavepacket on the potential curve of the $^1\Sigma_u$ state, either states of the molecular ion Na_2^+ or the dissociation continuum of the fragmentation channel $\text{Na}^+ + \text{Na}(3s)$ can be reached by the probe laser. If the ratio $\text{Na}_2^+/\text{Na}^+$ is measured as a function of the delay time, the oscillating curve shown in Fig. 12.53b is obtained, reflecting the periodic motion of the wavepacket in the $^1\Sigma_u$ state. By choosing a suitable time delay, the yield of atomic or molecular ions can be controlled.

12.4.14

Coherent Control

Apart from the time delay between pump and probe pulse, the phase distribution in the excitation pulse can also be used to control the phase of the molecular wavefunction in the excited state. In polyatomic molecules, this phase determines the temporal distribution of the wavefunction on the excited potential surface and therefore the decay channels admissible within a time interval between τ and $\tau + \Delta t$ after the excitation. This method of controlling the excited molecule by the phase distribution $\varphi(\lambda)$ in the excitation pulse is called *coherent control*; its principle is illustrated in Fig. 12.54.

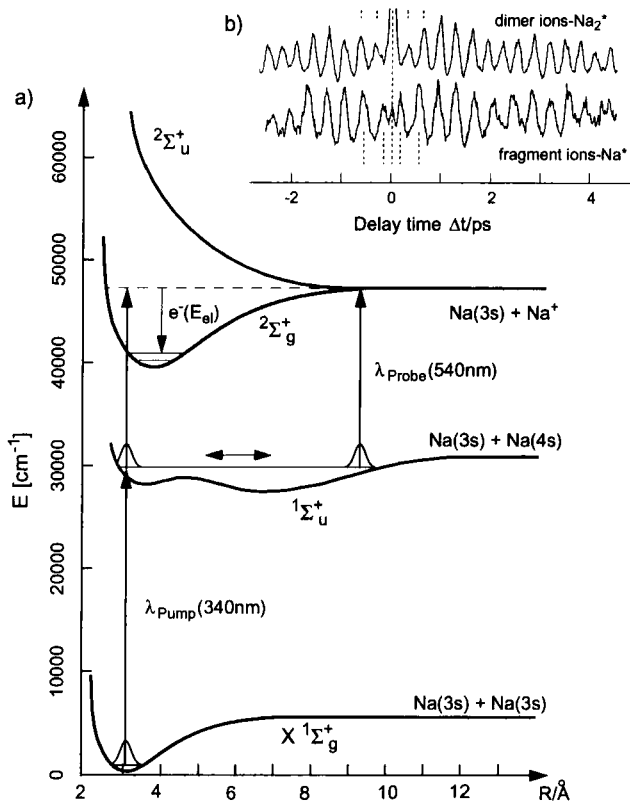


Fig. 12.53 Application of the pump–probe technique to the ionization of the Na_2 molecule. a) Term diagram; b) ion signals $N(\text{Na}_2^+)$ and $N(\text{Na}^+)$ as a function of the time delay τ [12.38].

The individual spectral components of the femtosecond pulse of spectral width $\Delta\lambda$ are separated spatially by an optical grating and pass through a liquid-crystal mask consisting of many pixels which are electrically isolated from each other. If a voltage is applied to this mask, its refractive index changes, and hence the phase of the corresponding spectral component of the transmitted wave also changes.

A second grating recombines the spectral components spatially. The phase differences between the individual components influence the time profile of the total pulse. It turns out that the dissociation channels through which the molecule can decay depend on this time profile. Although the connection is not yet understood in detail, a learning algorithm can be used to modify the pulse shape so that the desired products of the decay are formed preferentially (Fig. 12.55). This can be demonstrated for a number of examples such as medium-sized [12.40] and even very large biological molecules [12.41]. To arrive at a detailed understanding of these processes, very demanding calculations have to be performed that can determine the potential surfaces and the time-dependent wavefunctions (the wavepacket) of the excited nonstationary states and their time evolution.

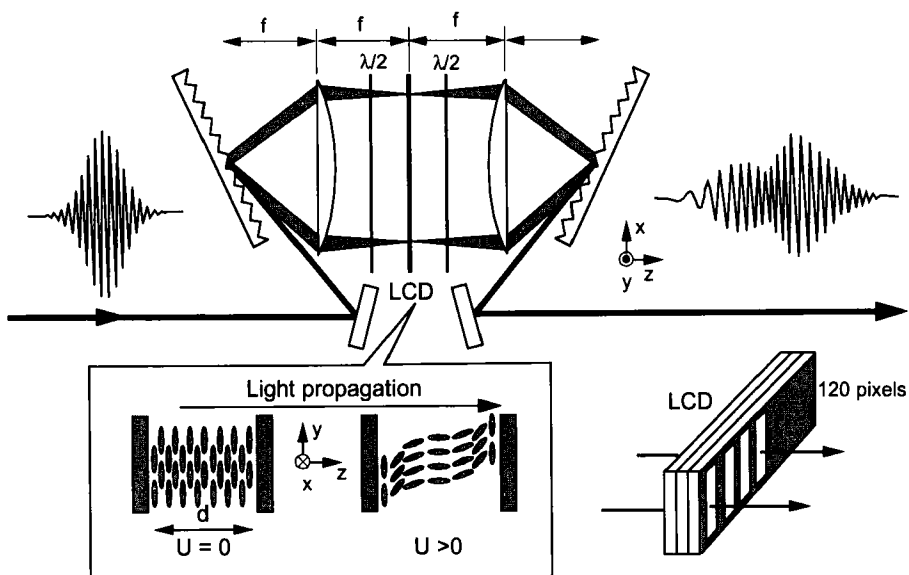


Fig. 12.54 Setup for the optimization of femtosecond pulses [12.39].

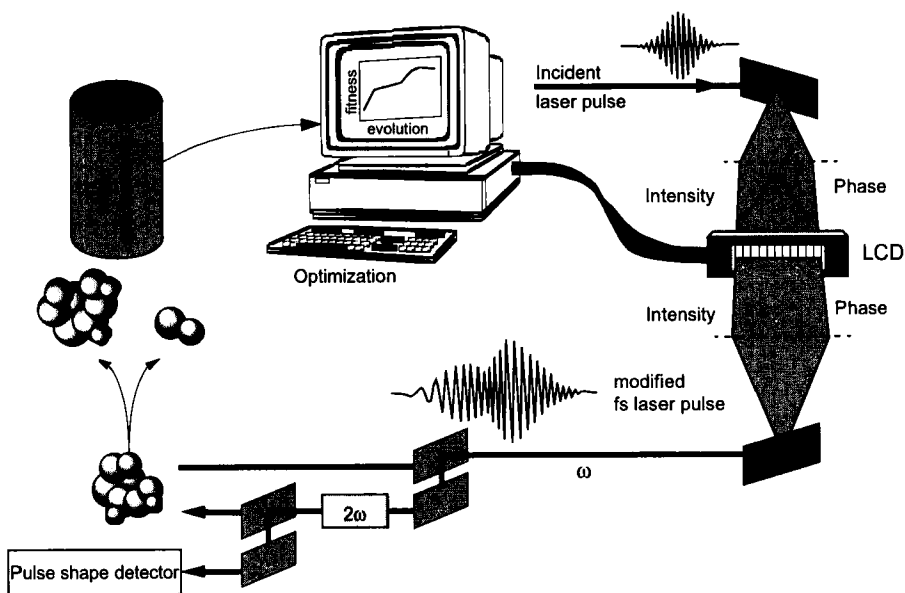


Fig. 12.55 Learning algorithm for the optimization for coherent control of chemical reactions [12.39].

12.5 Photoelectron Spectroscopy

Photoelectron spectroscopy and its recent variations have been developed into highly useful tools of molecular spectroscopy. Its principle is very simple: a light source with wavelength λ ionizes molecules, and the kinetic energy E_{el} of the ejected photoelectrons is measured using an energy analyzer. If the electron is emitted from a state with ionization energy E_{I} , conservation of energy requires that

$$E_{\text{el}} = h\nu - E_{\text{I}} \quad \text{with} \quad \nu = c/\lambda. \quad (12.49)$$

Hence, from the measured electron energy E_{el} , the energy of the molecular orbital from which it was ejected can be determined. As ionization energies of most molecules are in the 10 eV range, the photon energy must exceed this value, that is, the wavelength must be shorter than about 120 nm. Frequently, helium discharge lamps are used, and the helium line at $\lambda = 58.4$ nm ($E = 21.2$ eV) in the vacuum ultraviolet region is used to ionize the molecules. The method is thus also called ultraviolet photoelectron spectroscopy (UPS). Excitation of the helium resonance line can be effected by means of a gas discharge or by microwave discharges. Using large currents in the gas discharge, a sufficient number of helium ions can be excited into higher states to make even the He^+ resonance line at $\lambda = 30.4$ nm ($E = 40.8$ eV) intense enough to be useful as a radiation source with higher photon energy.

In recent years, however, VUV lasers have been employed more frequently because of their higher intensity. Often, the ionization limit of a molecule is reached via multi-photon transitions, where the photons for the stepwise excitation of the molecule can be from the same or from different lasers. This method is used particularly for the generation of low-energy photoelectrons, which allow the determination of the energy levels in molecular ions (see below).

Photoelectron spectroscopy of inner electron shells is of particular interest because for these low-energy orbitals, the correlation energy due to the mutual electron-electron interaction has a crucial influence on the orbital's total energy. Thus, the correlation energy may be determined by comparing the measured term energies with calculations in which the correlation was neglected. For inner-shell spectroscopy, photon sources in the x-ray region are necessary; the technique is therefore called x-ray photoelectron spectroscopy (XPS). The characteristic lines of x-ray tubes can be used as radiation sources. Nowadays, however, synchrotron radiation is usually employed, which is spectrally dispersed by a primary monochromator (see Sect. 12.3).

Many of the insights on molecular orbitals discussed in Ch. 7 are based on results of photoelectron spectroscopy. It offers an additional and complementary source of information as compared to absorption and emission spectroscopy, and it is therefore applied in many molecular physics laboratories [12.42, 12.43].

12.5.1

Experimental Setups

Figure 12.56 shows schematically an experimental setup for photoelectron spectroscopy. The radiation source is imaged into the sample volume by an elliptical mirror. The ejected photoelectrons are extracted by a small electric field and their energies are analyzed before they reach the detector. As energy analyzers, different designs are used. One of them employs a planar capacitor with a distance d between the plates (Fig. 12.57a), where the electrons enter the capacitor through an entrance slit at an angle α with respect to the capacitor plates, follow a parabolic path in the homogeneous electric field, and, for an energy

$$E_{\text{el}} = \frac{DeU}{2d \sin 2\alpha}, \quad (12.50)$$

reach the exit at a distance D from the entrance. A second design is based on a cylindrical capacitor, which offers the advantage that it focuses the electrons (Fig. 12.57b), thus providing larger transmitted intensities. It consists of two cylinder segments with an aperture angle of 127° ($\pi/\sqrt{2}$). For a voltage U between the capacitor plates, this arrangement focuses all electrons with an energy

$$E_{\text{el}} = \frac{eU}{2 \ln(R_2/R_1)} \quad (12.51)$$

emitted from a point-like source into a solid angle accepted by the capacitor onto the exit slit. The detector thus recognizes only electrons with this energy, which can be selected by varying the capacitor voltage.

Instead of cylindric capacitors, spherical capacitors (spherical surfaces with radii R_1 and R_2) are frequently employed, because they accept a larger solid angle of the incident electron beam and therefore enable a larger signal at the detector. The transmitted electrons have an energy

$$E_{\text{el}} = \frac{eUR_1R_2}{R_1^2 - R_2^2}. \quad (12.52)$$

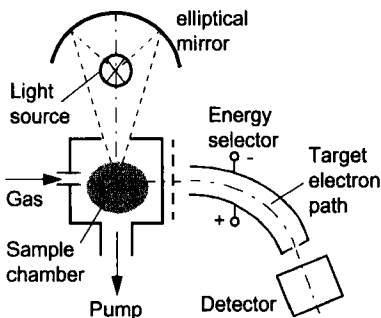


Fig. 12.56 Schematic setup for photoelectron spectroscopy.

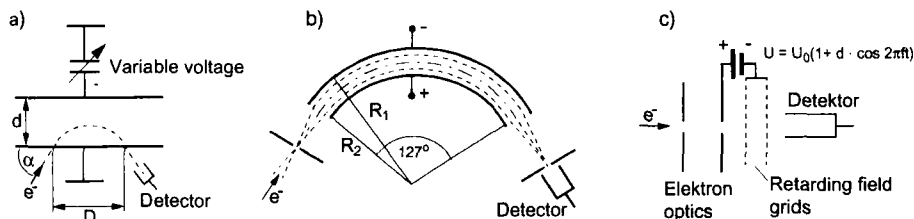


Fig. 12.57 Possible realization of the energy selection of photoelectrons. a) Planar capacitor; b) cylindric capacitor; c) opposed-field method.

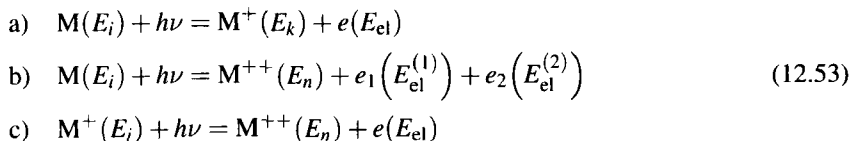
In place of electrostatic capacitors, a retarding-field method is also frequently used. Here, the photoelectrons pass through a retarding electric field and can only reach the detector if their energy exceeds a limiting energy E_{lim} (Fig. 12.57c). The retarding field is realized by means of a planar conducting wire mesh at a potential $-U$. If the photoelectron source is at a potential $U = 0$, the threshold energy becomes $E_{\text{lim}} = eU$. If the voltage $U = U_0(1 + a \cos(2\pi ft))$ is modulated with a frequency f around a mean value U_0 , a lock-in detector at the frequency f will detect only electrons from the energy interval $\Delta E_{e1} = 2aeU_0$ around the energy eU_0 .

The energy resolution of a photoelectron spectrometer depends on the spectral width of the radiation source, the energy resolution of the energy selector, and possibly also on the kinetic energy of the molecules, because their velocity implies an energy shift of the photoelectrons on account of the Doppler effect. When the helium resonance line is used, the spectral width of the radiation is very narrow so that the remaining limitations on the energy resolution are effective. Today, electron spectrometers with an energy resolution better than 5 meV can be constructed. To make this possible, however, all external magnetic fields such as the Earth's magnetic field must be shielded very carefully, because these would cause a deflection particularly of slow electrons, thus leading to a selection of electrons with the wrong energy.

12.5.2

Photoionization Processes

Upon ionization of a molecule M by absorption of photons, the following processes can occur:



In case a), a molecule M in the ground state E_i is ionized by the photon, and a molecular ion in the state E_k (which can be its ground state or an excited state) is generated. The photoelectron with kinetic energy E_{e1} is detected. If it is a valence electron, it has

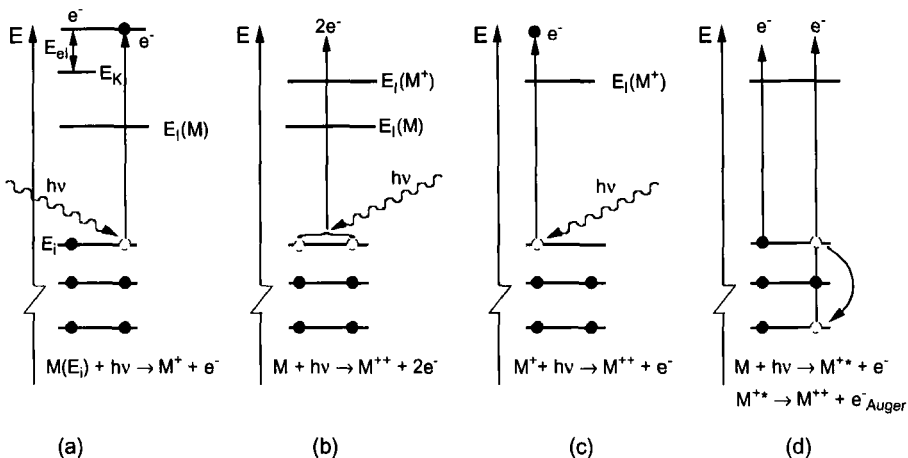


Fig. 12.58 Occupation of molecular orbitals for the different photoionization processes. a) Ionization of a valence electron; b) double ionization; c) sub-

sequent ionization of a molecular ion; d) inner-shell ionization with subsequent Auger-electron emission.

been ejected from the highest occupied molecular orbital (HOMO). If E_k is the ionic ground state, the difference

$$\Delta E = h\nu - E_{el}$$

corresponds to the ionization energy of the molecule. However, smaller electron energies are also observed in the spectrum, which occur if the ion is left in an excited state.

For sufficiently large photon energies, double ionization may occur (process b). With high-intensity lasers, stepwise ionization by absorption of two or more photons is also possible. The ions generated by process a) are further ionized by the absorption of a second photon. The probability of this process increases with increasing photon density. It is therefore particularly relevant for photoelectron spectroscopy with high-power lasers. Figure 12.58 shows schematically the occupation of the molecular orbitals in the different processes.

12.5.3

ZEKE Spectroscopy

In recent years, a variation of photoelectron spectroscopy has been developed in which only photoelectrons with very small energies $E_{el} \approx 0$ are detected during laser ionization of molecules in a collimated molecular beam, and which is therefore called zero kinetic energy (ZEKE) spectroscopy [12.44, 12.45].

If the wavelength of the ionizing laser is continuously tuned, these (ZEKE) electrons are generated when the ground-state level or excited vibrational levels in the electronic ground state of the molecular ion M^+ are reached by the exciting photon.

The photoelectrons are extracted from the generation area (crossing volume of molecular beam and laser beam) by an electric field, which is switched on only after a time Δt , which ensures that all fast electrons have already left the area. Hence, the photoionization channel leading to a definite state of the molecular ion is selectively detected, and no energy selector for the electrons is needed. When narrow-band lasers are used, the energy resolution is much better than in conventional photoelectron spectroscopy, and it is limited only by the molecular velocity distribution in the beam.

Example

Electrons with an energy of 0.1 meV have a velocity of $v = 5.8 \times 10^3$ m/s. Hence, they leave the area of ionization with a typical size of 1 mm^3 within about 200 ns. Choosing a time delay of $1 \mu\text{s}$ after ionization with a laser pulse with a width of 10 ns, all electrons with energies $E_{\text{el}} > 10^{-5}$ eV have left the ionization area and are therefore not detected.

ZEKE spectroscopy offers not only the advantage of higher energy resolution, which allows the resolution of vibrational and sometimes even rotational levels of the molecular ions, but also a much higher detection probability. This is due to the fact that the photoelectrons, which have statistically distributed velocities, are all captured by the electric field due to their small kinetic energy, and are thus all collected on the detector.

As an example, Fig. 12.59 shows the ZEKE spectrum of NO, which demonstrates the achievable energy resolution.

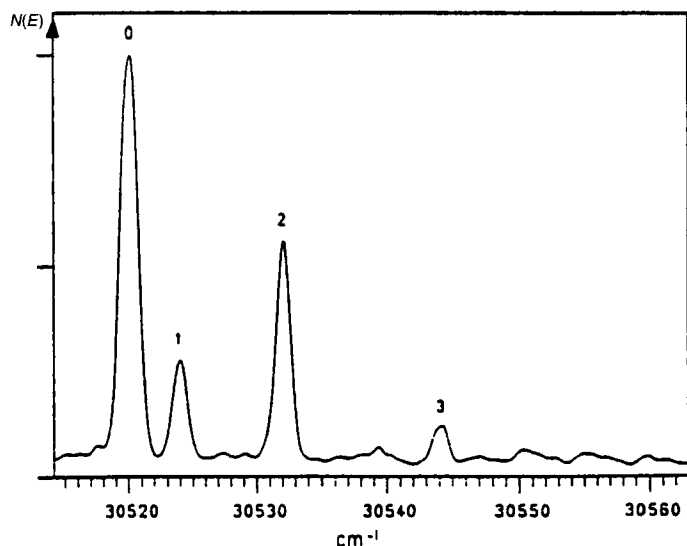


Fig. 12.59 ZEKE spectrum of NO. The abscissa gives the wavenumber of the ionizing laser; the peaks correspond to excitations from different rotational levels $J = 0 \dots 3$ of the ground state ($1 \text{ meV} \cong 8.07 \text{ cm}^{-1}$) [12.46].

Unfortunately, the collecting electric field can also field-ionize electrons from very high long-lived Rydberg states of the neutral molecule, thus giving erroneously a smaller ionization energy. These field electrons must therefore be separated from the true photoelectrons. One possible way to achieve this is to apply a weak extraction field at a time t_1 after ionization, which is then increased at a time t_2 . The electron signal displays then a step at t_2 , which indicates the additional amount of electrons from field ionization of Rydberg states.

12.5.4

Angular Distribution of Photoelectrons

Conservation of angular momentum requires that the total angular momentum on both sides of Eq. (12.53) be equal. The angular momentum of the ionizing photon is zero for linearly polarized light, and $\pm 1\hbar$ for circularly polarized light. The photoelectrons may also possess angular momentum, which determines their angular distribution. At very small electron energies, such as those occurring in ZEKE spectroscopy, the angular momentum of the photoelectrons is zero, and their angular distribution is isotropic. In general, however, the photoelectrons may possess an angular momentum $0, 1\hbar, 2\hbar, 3\hbar, \dots$. The electronic wavefunction is then a superposition of s, p, d, ... contributions. As the angular momentum quantum number l is well defined for highly excited electrons (e.g., in Rydberg states) even in molecules, the selection rule $\Delta l = \pm 1$ for the angular momentum quantum number l is satisfied for electric dipole transitions from the Rydberg level to a vibration-rotation level of the ion by absorption of a photon. If the transition starts from an s state, the final state must then be a p state, and the photoelectron must be a p electron due to conservation of angular momentum. Its angular distribution is given by the spherical harmonic Y_{10} , and the intensity distribution of the photoelectrons as a function of the angle Θ between the line of incidence of the photon and the line of observation of the photoelectron is given by

$$I(\Theta) \propto Y_{10}^2 = \frac{3}{4\pi} \cos^2 \Theta. \quad (12.54)$$

In general, the angular distribution of photoelectrons with arbitrary angular momentum can be described, for unpolarized light, by the expression [12.47]

$$I(\Theta) = \frac{\sigma}{4\pi} \left[1 + \frac{\beta}{2} \left(\frac{3}{2} \sin^2 \Theta - 1 \right) \right]. \quad (12.55)$$

The photoionization cross-section σ and the anisotropy parameter β depend on the initial and final states of the photon-induced transition in the molecule and on the polarization of the photon. It summarizes the influence of the different angular momenta of the photoelectrons on the angular distribution. From the measured anisotropy, information on the molecular states involved in photoionization can be gained. Mea-

surement of the angular distribution of photoelectrons in addition to their energies gives important clues on the molecular states from which the electron was ejected.

We see from Eq. (12.55) that for a “magic” angle of observation of $\Theta = 54.7^\circ$, the angular distribution becomes isotropic because $\sin^2 54.7^\circ = 2/3$.

12.5.5

X-ray Photoelectron Spectroscopy (XPS)

Inner-shell electrons are usually localized at “their” atom in the molecule. However, the interaction with the remaining electrons in the molecule leads to shifts of the energies of inner-shell molecular levels as compared to the corresponding levels in the free atoms. These shifts (also called “chemical shifts”) are in general very small, but they can nevertheless be determined accurately using XPS. As an example, Fig. 12.60 shows the XPS spectrum of the transitions from the $1s$ levels of the four carbon atoms that are located in different environments in the ethyl trifluoroacetate (trifluoroacetic acid ethyl ester) molecule, and which therefore experience slightly different shifts. The aluminum K_α line was used as the excitation line.

To calculate these shifts, the potential at the location of the electron in the initial state must be determined, which depends on the interaction of this electron with all the charges around it. If r_{ik} is the distance between the electron e_i under consideration and the charge q_k , its potential energy is

$$E_{\text{pot}}^{(i)} = - \sum_{k=1}^p \frac{q_k e}{4\pi\epsilon_0 r_{ik}} = - \left(\sum_k \frac{q_k e}{4\pi\epsilon_0 r_{ik}} \right)_A - \left(\sum_j \frac{q_j e}{4\pi\epsilon_0 r_{ij}} \right)_N \quad (12.56a)$$

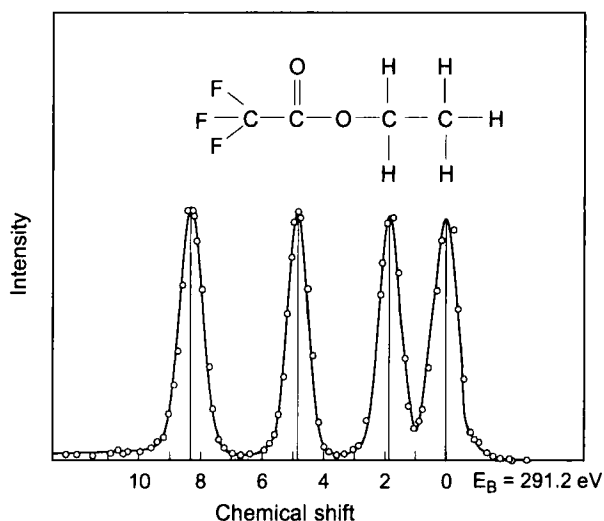


Fig. 12.60 XPS spectrum for transitions from the $1s$ level of the carbon atom [12.48].

The energy depends not only on the electron distribution in the “own” atom (first sum), but also on the charge distribution in the neighboring atoms (second sum). If an electron is removed from an inner shell of atom A by photoabsorption, the electron distribution in atom A changes, and due to the interaction with the neighboring atoms N, their charge distribution changes also, so that the potential energy in the final state is

$$E_{\text{pot}}^{(f)} = - \left(\sum_{k=1}^{p-1} \frac{q_k e}{4\pi\epsilon_0 r_{ik}^*} \right)_{A^+} - \left(\sum_j \frac{q_j e}{4\pi\epsilon_0 r_{ij}^*} \right)_N \quad (12.56b)$$

The chemical shift is then

$$\Delta E = \frac{e}{4\pi\epsilon_0} \left(\sum_j \frac{q_j}{r_{ij}^*} - \sum_j \frac{q_j}{r_{ij}} \right), \quad (12.56c)$$

where r_{ij}^* denotes the distances to the adjacent charges modified by the photoabsorption process.

If the XPS photoionization process leaves a hole in an inner shell, an electron from a higher shell can make a transition into this hole, transferring its surplus energy to another valence electron, which can then leave the molecule (Auger process, Fig. 12.58d). In this case, the photoelectron spectrum shows, in addition to the normal line at an energy

$$E_{\text{el}} = h\nu - E_B(1s), \quad (12.57)$$

a second line from the Auger electron from the state $|n\rangle$ with the energy

$$E_{\text{Aug}} = E_B(1s) - E_B(n), \quad (12.58)$$

so that additional information on the energies of the states $|n\rangle$ can be obtained.

12.6

Mass Spectroscopy

Mass spectroscopy monitors the fragmentation of a molecule into charged fragments after excitation into a dissociative state by electron impact or photon absorption. In combination with laser spectroscopy, much fundamental knowledge on highly excited states of neutral molecules or molecular ions has been gained in recent years.

Furthermore, mass spectrometers can be utilized in the spectroscopy of gaseous mixtures (e.g., in cluster beams) to record selectively the spectra of the individual components or to determine isotope shifts in mixtures of different isotopomers of a molecule. This can be useful in determining the vibrational and rotational quantum number of an excited level, because the isotope shift depends on both quantum numbers (see Sect. 3.5.4).

A mass spectrometer comprises an ion source, an arrangement to separate the ions spatially or temporally, and a detector. In the following, we will briefly present the three most important types of spectrometers.

12.6.1

Magnetic Mass Spectrometers

A magnetic field transverse to the direction of motion of ions with mass m , charge q and velocity v exerts the Lorentz force $\mathbf{F} = q(\mathbf{v} \times \mathbf{B})$ and hence deflects the ions according to their momentum mv . If the homogeneous magnetic field is restricted to a circular sector with an apex angle 2φ , ions emerging from a slit S_1 are focused on the slit S_2 (Fig. 12.61b). This can be rationalized as follows. We consider one half of the sector field with the apex angle φ . Ions entering the magnetic field in a parallel beam of width b perpendicularly to the field boundary (y axis) are deflected by the magnetic field onto circular paths with a radius

$$R = \frac{mv}{qB}, \quad (12.59)$$

because the centripetal force mv^2/R is equal to the Lorentz force mvB . After leaving the field, they continue on a straight path. If the magnetic field strength is properly chosen, the center of the circular arc for the center beam S is the center M_0 of the sector, and the ions are deflected by the sector angle φ . The center M_1 of the arc for ions on the path 1 is then shifted by $b/2$ with respect to M_0 . These ions cover a larger distance in the magnetic field and are therefore deflected by the larger angle $\varphi + \alpha$

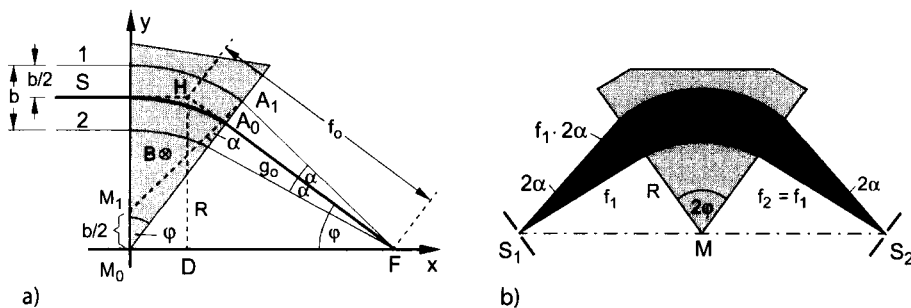


Fig. 12.61 Principle of a mass spectrometer with magnetic sector field.

from point A_0 . With $\overline{M_0A_0} = R$, we obtain from the law of sines for the triangle $M_1A_1M_0$

$$M_0A_1 = R \frac{\sin(\varphi + \alpha)}{\sin \varphi} . \quad (12.61)$$

Thus,

$$\overline{A_0A_1} = R \left(\frac{\sin(\varphi + \alpha)}{\sin \varphi} - 1 \right) .$$

For sufficiently small angles α , $\cos \alpha \approx 1$ and $\sin \alpha \approx \tan \alpha$, so that

$$g_0 = \frac{\overline{A_0A_1}}{\sin \alpha} = R \cotan \varphi . \quad (12.62)$$

We define the focal length of the cylindrical magnetic lens to equal the distance $f_0 = \overline{HF}$, and we obtain from $\overline{HD} = R$ and $\overline{HF} = R / \sin \varphi$,

$$f_0 = \frac{R}{\sin \varphi} . \quad (12.63)$$

Now we add the second half of the sector field, so that we arrive, for symmetry reasons, at the representation in Fig. 12.61b.

In front of the slit S_1 , an acceleration voltage U is applied, which supplies the ions with a kinetic energy

$$\left(\frac{m}{2} \right) v^2 = qU ,$$

that is, with a velocity $v = (2qU/m)^{1/2}$, so that the focal width becomes, using $R = mv/(qB)$,

$$f_0 = \frac{mv}{aB \sin \varphi} = \frac{1}{B \sin \varphi} \sqrt{\frac{2mU}{q}} . \quad (12.64)$$

If the magnetic field strength B is changed, ions with a different mass are focused on the exit slit according to Eq. (12.64) [12.49]. Thus, ions with specific masses can be selectively transmitted by changing the magnetic field strength B .

12.6.2

Quadrupole Mass Spectrometers

In a quadrupole mass spectrometer consisting of four parallel, electrically conducting round rods at a distance $2r_0$ (Fig. 12.62), the ions are selected using *electrical* fields. The ions traveling along the y direction experience a hyperbolic electric potential

$$\Phi(x, z) = \frac{\Phi_0}{2r_0^2} (x^2 - z^2) , \quad (12.65)$$

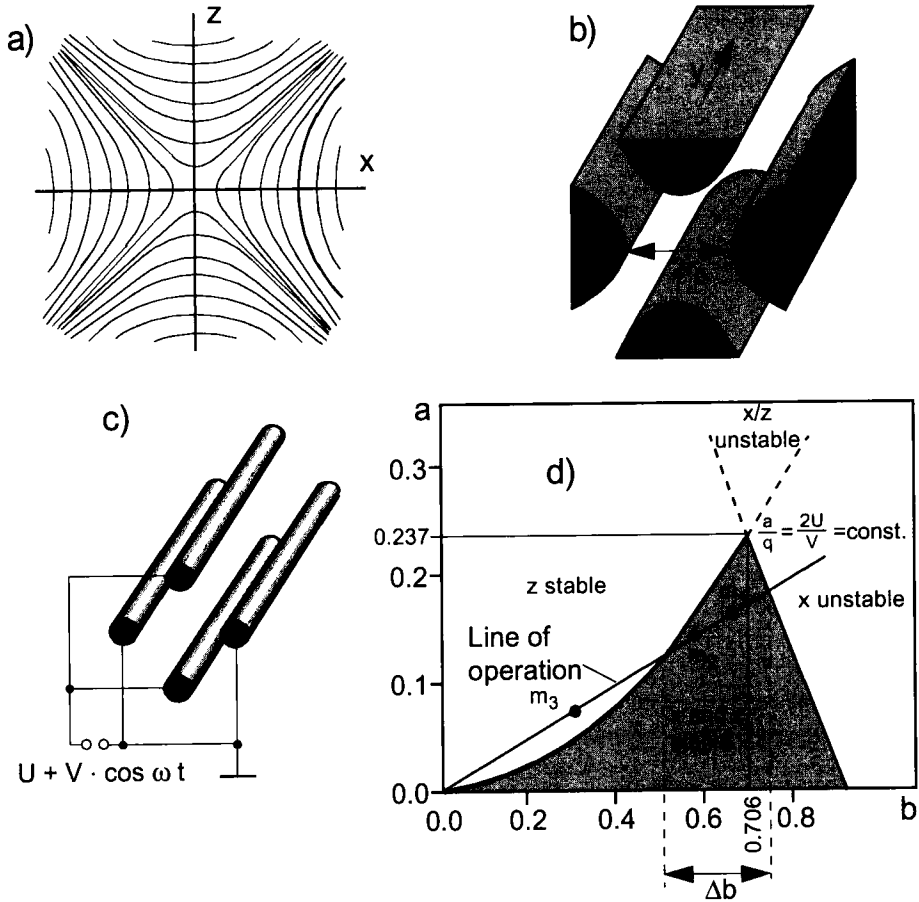


Fig. 12.62 Quadrupole mass spectrometer. a) Hyperbolic potential $\Phi(x, z)$; b) optimum arrangement of electrodes; c) real arrangement with four rods; d) stability diagram.

with $\Phi_0 = U + V \cos \omega t$, which is a superposition of a static potential U and a high-frequency contribution $V \cos \omega t$. While the y component of the ion velocity is constant, the x and z components oscillate with frequency ω . The equations of motion for these directions are

$$\begin{aligned} \ddot{x} + \frac{q}{mr_0^2}(U + V \cos \omega t)x &= 0, \\ \ddot{z} - \frac{q}{mr_0^2}(U + V \cos \omega t)z &= 0. \end{aligned} \tag{12.66}$$

These differential equations have stable solutions only for specific ranges of the parameters

$$a = \frac{4qU}{mr_0^2\omega^2} \quad \text{and} \quad b = \frac{2qV}{mr_0^2\omega^2}. \quad (12.67)$$

Within these ranges, the vibrational amplitudes along x and z remain finite, whereas they tend to infinity for other values of the parameters. Depending on the choice of the potentials U and V , ions with specific masses can reach the detector behind the quadrupole rods, while ions with different masses oscillate so strongly that they hit the rods and are lost. As shown in Fig. 12.62d, the mass range of the transmitted ions can be adjusted to be narrow or broad by choosing suitable values for the parameters a and b . That is the main reason why the quadrupole mass spectrometer, developed by W. Paul in 1953, is a highly versatile instrument with adjustable mass resolution, which is also much more compact and lightweight than magnetic spectrometers [12.49, 12.50].

12.6.3

Time-of-flight Mass Spectrometers

In a time-of-flight mass spectrometer, the mass-dependent time of flight of ions with the same energy $(m/2)v^2$ is exploited to separate the ions in time. The principle is illustrated in Fig. 12.63. At time $t = 0$, ions with mass m and charge q are generated in a confined region of space (e.g., the crossing volume of laser and molecular beam) by pulsed ionization (e.g., using a pulsed laser). A voltage U accelerates them to a velocity $v = (2qU/m)^{1/2}$, and they pass through a field-free distance L with constant velocity, before they are registered by an ion detector (channeltron or channel-plate amplifier).

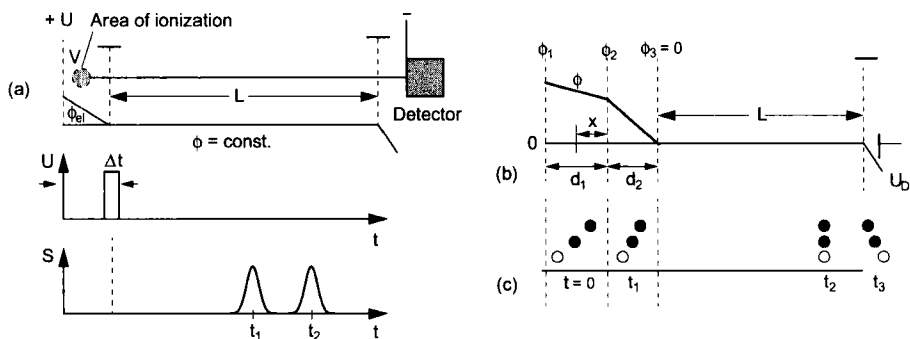


Fig. 12.63 Time-of-flight mass spectrometer. a) Principle; b) potential characteristics of the McLaren type; c) Time-focusing of ions that are generated simultaneously at different locations in the ionization area.

Ions generated at different locations in the ionization area, and hence at different potentials, possess different velocities, and the time of flight for ions of the same mass is distributed around a mean value. To improve the time resolution and thus also the mass resolution, McLaren and coworkers suggested a modified field distribution (Fig. 12.63b), in which the ions are accelerated in two stages [12.51]. The two electric fields are adjusted (depending on the length of the field-free propagation distance) so that all ions of equal mass arrive at the detector simultaneously, irrespective of the location where they were generated.

The mass resolution of a time-of-flight spectrometer can be improved further if the ions are reflected by an opposing electric field at the end of their propagation path. Fast ions penetrate farther into the opposing field and must therefore cover a larger distance. Such a reflectron can achieve a mass resolution of several thousand [12.52].

More information on the combination of lasers and mass spectrometry can be found in [12.53].

12.7

Radiofrequency Spectroscopy

In 1929, Rabi [12.54] developed an experimental technique which allows very precise measurements of fine and hyperfine splittings in molecules with magnetic or electric dipole moments, of the magnitudes of these moments and the corresponding Zeeman or Stark splittings. The technique is illustrated in Fig. 12.64a. The molecules effuse from their reservoir (for substances with a low vapor pressure, a heated furnace may be used) through a small hole or a nozzle into vacuum. They are then collimated by an aperture and deflected in an inhomogeneous magnetic field A according to their

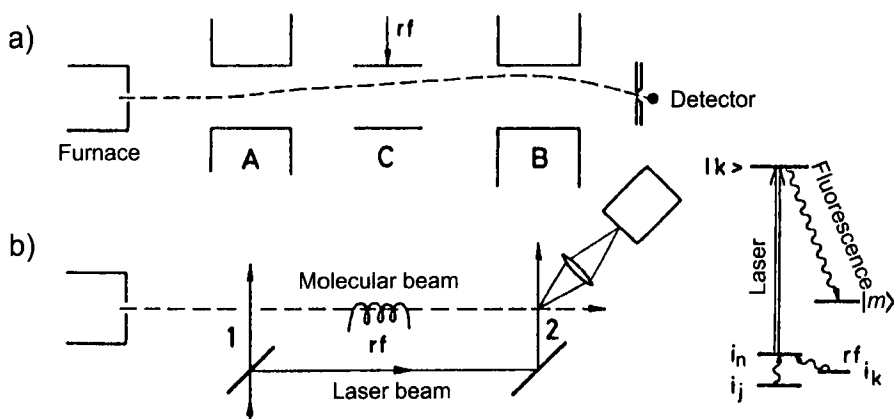


Fig. 12.64 Principle of radiofrequency spectroscopy. a) Rabi method with deflecting magnets A and B; b) modern laser variant.

magnetic moment. The force acting on the molecules is $F = -\mu \cdot \text{grad } B$. Finally, they are deflected in a second magnetic field B of the same magnitude, but opposed to A , and reach the detector behind an aperture.

At C , between the two static magnetic fields, the molecules are irradiated with a variable radiofrequency field. If the frequency corresponds to an allowed transition between two levels $|i_k\rangle$ and $|i_n\rangle$ of the molecule, the populations of both levels are changed. If the molecular dipole moment is different in both states, the deflection in field B changes, and the molecule cannot reach the detector.

The decrease in the detector signal is measured as a function of the radiofrequency. The maximum decrease occurs at the resonance frequency f_0 . Usually, both levels belong to the electronic ground state of the molecule, so that their lifetimes are long. Hence, the signals exhibit very narrow linewidths, which are often limited by the molecular passage time through the radiofrequency field. The time-of-flight linewidth can be reduced by using a larger passage time through the radiofrequency field or by a method developed by N. Ramsey, in which the radiofrequency is applied simultaneously to two widely separated areas [12.55]. This method of separated fields results in very narrow linewidths, and the resonance frequencies can be measured very accurately.

If the two magnetic fields A and B are replaced by electric fields, electric dipole moments and their dependence on the molecular state can be measured [12.56].

The accuracy of the measurements is essentially limited by the signal-to-noise ratio achieved. As the energy difference between the two levels is very small ($\Delta E = hf \ll k_B T$), both levels are almost equally populated at room temperature. The net absorption of the radiofrequency and thus the change of the level populations is therefore very small, and consequently the same holds for the change of the magnetic moments. By using a cooled supersonic beam (see Sect. 12.4.7), the temperature can be reduced to a few kelvin, and the population difference can be correspondingly increased.

Much more effective, however, is a laser variation of the Rabi method. Here, the two magnets A and B are replaced by two partial beams of a laser, crossing the molecular beam perpendicularly (Fig. 12.64b). If the laser wavelength is tuned to an optical transition $|i_n\rangle \rightarrow |k\rangle$ of the molecule, the transition can be saturated even for small laser powers, that is, the population of $|i_n\rangle$ is then much smaller than the thermal population, in favorable cases it can become virtually zero. This increases the transition rate on the radiofrequency transition $|i_k\rangle \rightarrow |i_n\rangle$ drastically. The states of the molecules arriving at the second intersection B can then be measured through the absorption of the second laser beam via laser-induced fluorescence at position B [12.57].

This technique offers not only a much higher sensitivity but has the additional advantage that radiofrequency transitions in molecules without magnetic or electric moments can be measured.

A large number of molecules have been investigated using this technique [12.58]. Specifically, vibrational transitions of the weak van der Waals bond in van der Waals molecules or rotational transitions of large van der Waals complexes can be measured,

which have very small rotational constants due to the large mass of the complex and the large bond length, so that the transitions are in the radiofrequency or microwave regions [12.59].

If the laser excites states with a lifetime which is longer than the time of flight from the point of excitation to the second crossing point B, radiofrequency transitions in these excited states can be measured. The method can also be termed an *optical-radiofrequency double resonance spectroscopy*, because the resonant interaction of the molecule with the laser and the radiofrequency field is exploited.

12.8 Nuclear Magnetic Resonance Spectroscopy

Nuclear magnetic resonance (NMR) spectroscopy has evolved into a powerful tool for the elucidation of the structures of large molecules containing nuclei with nuclear spins. Its principle is very simple.

The sample of interest is placed in a magnetic field B , in which the nuclear spins I will be oriented relative to the direction of the magnetic field so that their projections onto this direction are $M_I \hbar$, where the magnetic projection quantum number M_I can take all $2I + 1$ integer or half-integer values from $-I$ to $+I$. Hence, the hyperfine levels split into Zeeman components with energies

$$E(M, B) = -\mu_{\text{nuc}} \cdot B = -\frac{g_I \mu_N}{\hbar} I \cdot B = -g_I \mu_N M_I B = -\gamma \hbar M_I B,$$

where g_I is the Landé factor of the respective nucleus, $\mu_N = 5.05 \times 10^{-27} \text{ A m}^2$ is the nuclear magneton, and $\gamma = \mu_{\text{nuc}} / I = g_I \mu_N / \hbar$ is the gyromagnetic ratio.

The nuclear spin quantum number of the proton is $I = 1/2$, and there are two Zeeman levels with $M_I = \pm 1/2$ (Fig. 12.65). If the sample is irradiated with radiation

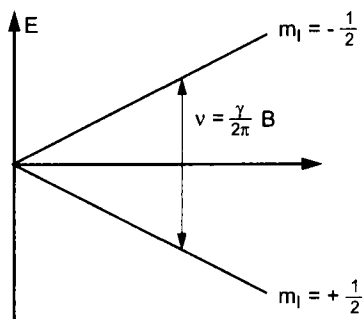


Fig. 12.65 Zeeman splitting of proton spins $I = 1/2$ in a magnetic field B .

of the frequency

$$\nu_{\text{rf}} = \left(\frac{\gamma}{2\pi} \right) B,$$

the proton spin can be flipped, that is, a transition is stimulated to the second Zeeman level.

Example

For a hydrogen nucleus, $I = 1/2$, $\mu_{\text{nuc}} = 2.79\mu_{\text{N}}$, and therefore $\gamma = 1.55 \times 10^8 \text{ m}^2 \text{ V}^{-1} \text{ s}^{-2}$. For a magnetic field strength of $1 \text{ T} = 1 \text{ Vs m}^{-2} = 10^4 \text{ G}$, a frequency $\nu_{\text{rf}} = 24.7 \text{ MHz}$ results.

The crucial point, however, is that the magnetic field B at the location of a nuclear spin is not simply given by the external magnetic field B_0 , but that the surrounding atoms and nuclei with their permanent or induced magnetic moments provide also a (albeit small) contribution. Therefore, the splitting of the Zeeman levels and thus the radiofrequency ν_{rf} depends on the location of a nucleus in the molecule. For a molecule containing several protons in different atomic environments, there is not just one transition but there are several components with frequency spacings that reflect the difference of the effective magnetic fields at the location of the nucleus under consideration due to the neighboring atoms. As these additional magnetic fields depend on the magnetic moments of the atoms (including nuclei) and their respective distances from the nucleus under consideration, this magnitude of the resulting shifts can be used to determine the distances of the surrounding atoms, provided the magnetic moments are already known. This contributes significant information to the determination of the molecular structure.

The resonance frequency of a proton i that experiences a shielding or amplification $\sigma_i B_0$ of the external magnetic field B_0 due to the neighboring magnetic moments is given by

$$\nu_i = \left(\frac{\gamma B_0}{2\pi} \right) (1 - \sigma_i),$$

where the shielding constant σ_i can assume positive as well as negative values (positive values denote shielding of the external field by the surrounding atoms, negative values amplification). If the surrounding atoms are diamagnetic, they possess only an induced dipole moment in the external field, which is opposed to the external field and thus reduces the field at the location of the nucleus under consideration. As the induced moment is proportional to the field strength, the frequency shift will also be proportional to the external field. The shielding constant σ is then positive. If the surrounding atoms possess permanent magnetic moments, the dipoles are oriented along the direction of the external field and amplify the magnetic field. If the field is strong enough to achieve complete alignment, the positive shift becomes independent of the external field.

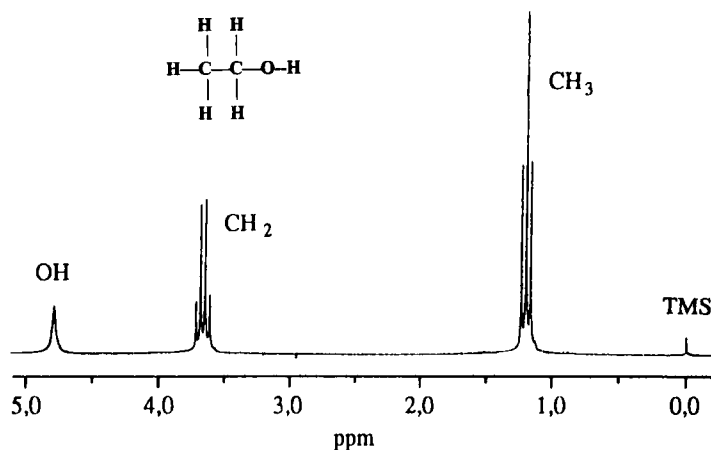


Fig. 12.66 NMR spectrum of the protons in the ethanol molecule, showing the multiplet structure due to the interaction between the nuclear spins [12.63].

If the nuclei of the surrounding atoms possess nuclear spins and thus nuclear magnetic moments, there arises an additional interaction between the nuclear moments, leading to a fine structure of the resonance lines.

As an example, Fig. 12.66 shows the NMR spectrum of the protons in the ethanol molecule $\text{CH}_3\text{CH}_2\text{OH}$. It consists of a triplet from the three protons of the CH_3 group, a quartet from the CH_2 group, and a single line from the OH proton. The abscissa shows that the frequency shifts between the multiplets are in the ppm range (ppm = parts per million = 10^{-6}). The fine-structure splitting due to the interaction between the nuclear spins is even smaller, and can only be resolved with high-resolution spectrometers. At a resonance frequency of 100 MHz (for $B_0 = 4 \text{ T}$), the chemical shifts amount to a few hundred hertz, and the spacings of the fine structure are only a few hertz. The magnetic field B_0 must therefore be held constant to less than 10^{-6} . This can be achieved by using special stabilization techniques; for example, by simultaneously measuring the resonance frequency of a reference substance and stabilizing the magnetic field at the middle of this resonance. As a reference substance, tetramethyl silane $(\text{CH}_3)_4\text{Si}$ (TMS) is commonly employed, and the shifts of the resonance lines are then measured with respect to the TMS resonance (Fig. 12.66).

Figure 12.67 illustrates the principle. The sample is placed in the stable static magnetic field B_0 , which is commonly generated by cooled electromagnets with iron cores or by superconducting coils. The radiofrequency is then transmitted onto the sample by a coil, and a second coil receives the signal from the sample.

To perform the measurement, either the radiofrequency can be tuned through all resonances, or the magnetic field can be varied at a fixed radiofrequency. For this purpose, auxiliary coils are employed which permit small yet precise changes of B .

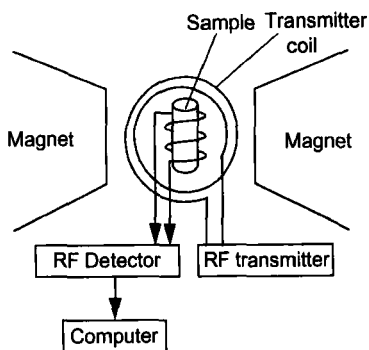


Fig. 12.67 Schematic setup of an NMR apparatus.

The chemical shifts of the proton resonance and also for the nuclear spin interaction possess typical values for specific atomic groups containing hydrogen atoms (e.g., CH_3 , CHCl_3 , OH , C_6H_6), so that one can deduce from its measured chemical shift the chemical group in which a specific hydrogen atom resides.

Apart from protons, other nuclei with magnetic moments, that is, with $I \neq 0$, can also be used as probes. Common examples include the isotopes ^{13}C , ^{14}N , ^{15}N or ^{31}P . Measuring the chemical shifts of these special nuclei facilitates the structure determination of more complicated molecules, in particular large biomolecules such as proteins [12.60, 12.61].

12.9

Electron Spin Resonance

Electron spin resonance (ESR) spectroscopy is a useful tool for the investigation of molecular states with an electron spin $S \neq 0$. Most molecules have $S = 0$ in their ground state, but radicals (molecules with one or more unpaired electrons) have also a resulting electron spin in the ground state. In ESR spectroscopy, the resonance frequencies for transitions between Zeeman levels is measured, in complete analogy to NMR spectroscopy. However, in this case the Zeeman splitting is not determined by the nuclear magneton but by the Bohr magneton, which is larger by a factor of 1836. Hence, comparable magnetic fields yield now transition frequencies in the microwave region at a few GHz [12.62, 12.63]. Again, the hyperfine structure in molecules with nuclear spins, which is caused mainly by the interaction between electronic and nuclear spins, leads to a multiplet splitting of the transitions between two Zeeman levels M_S of the electron spin (Fig. 12.68). The energy of such a component is, for a radical with electron spin S and two nuclear spins I_1 and I_2 ,

$$E = E_0 - \mu_s \cdot B - \mu_{\text{nuc}} \cdot B + a_1 S \cdot I_1 + S \cdot I_2 ,$$

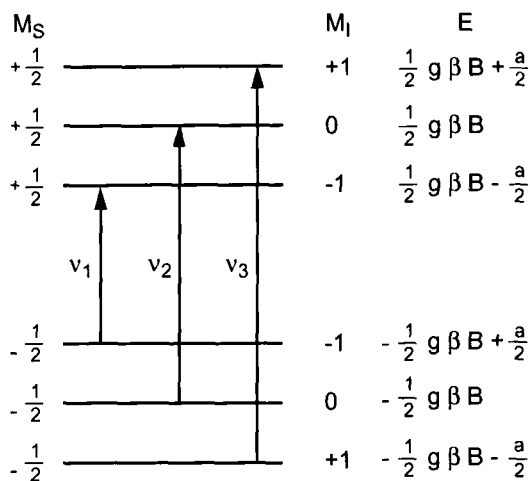


Fig. 12.68 Transitions between the hyperfine components of the two Zeeman levels of the electron spin $S = 1/2$.

where E_0 is the energy of the level without magnetic interaction. The second term can usually be neglected because $\mu_{\text{nuc}} \ll \mu_s$. Figure 12.68 shows the transitions between the hyperfine components of the two Zeeman levels of the electron spin for the case of a radical with just one nuclear spin $I = 1$.

In a radical with several nuclear spins, the ESR spectrum looks more complicated. For example, for two protons, the spectrum contains four lines (Fig. 12.69a): the electron-spin transition is split into two components by the interaction with the nuclear spin of a proton. Each of these components is then split a second time by the interaction with the second proton.

If there are two equivalent protons (i.e., two protons at equivalent positions in the radical which cause identical shifts), two components coincide, and the intensity of the corresponding line in the spectrum is doubled (Fig. 12.69b). The same argumentation holds for more than two equivalent nuclear spins (Fig. 12.69c).

The intensities and shifts of the different components are used in ESR spectroscopy to derive the spatial distribution of the unpaired electron (i.e., its wavefunction) in the molecule. As an example, the investigation of the Na_3 radical in a cold rare-gas matrix [12.64] is considered. From the measured ESR spectrum, it could be shown that the unpaired electron is not distributed evenly over all three sodium atoms but that the probability density is significantly reduced for one of them.

Another area where ESR is commonly employed is the investigation of triplet states in excited hydrocarbons. Again, the spatial distribution of the electrons in these states can be determined and hence the shape of the delocalized orbitals.

Until now we have considered only stationary NMR or ESR spectroscopy. However, as discussed in the case of laser spectroscopy (Sect. 12.4), the transition between the Zeeman components can be excited by a short electromagnetic pulse, and the time

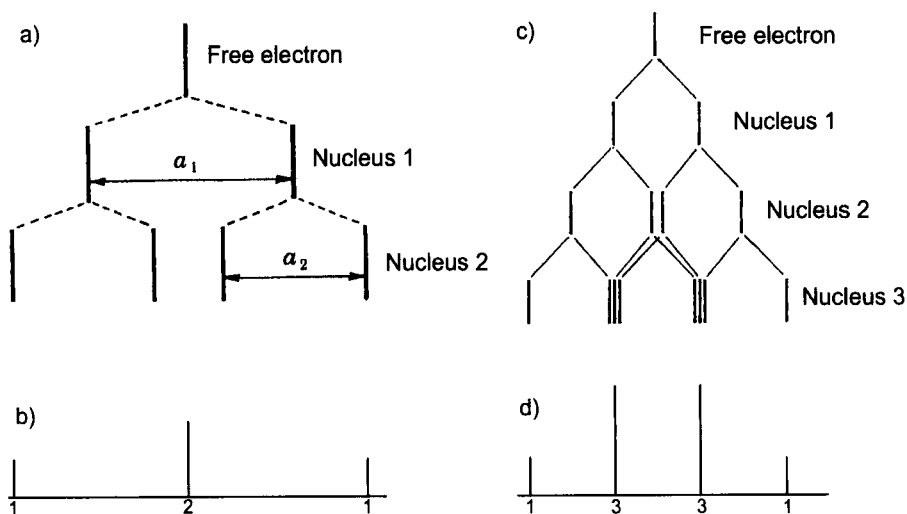


Fig. 12.69 ESR spectrum for the case of several equivalent nuclear spins. a) Two proton spins; b) two equivalent proton spins; c) three equivalent proton spins.

evolution of the population of one Zeeman level can be monitored by delayed probe pulses while it decays by spin relaxation. This results in very detailed information on the interaction of the nuclear or electron spin with its environment. In fact, NMR tomography, used in medical diagnostics, is based on the measurement of these relaxation times rather than of frequency shifts [12.65].

More detailed accounts can be found in the specialized literature [12.66].

12.10

Conclusion

We have restricted our presentation of experimental methods used in molecular physics mainly to spectroscopic techniques, because they constitute the primary source of information for the elucidation of molecular structure and dynamics. For space constraints, the whole field of molecular collision processes received less attention than it would have deserved. However, there are many worthwhile textbooks on this topic, to which the reader is referred [12.67].

Also, the investigation of chemical reactions has only briefly been touched upon, although the elucidation of the elementary processes in such reactions represents a direct application of molecular physics to a field of great importance for chemistry [12.68].

The transfer of insight from molecular physics to biophysical questions [12.69, 12.70] is of special importance; however, this is beyond the scope of this book. For

example, the puzzle as to which types of interactions effect the unfolding of DNA strands is yet unsolved. X-ray structure analysis of crystallized biomolecules, which led to the discovery of the DNA structure 50 years ago, could also not be treated here, because it would have required some knowledge about molecular solids.

However, the foundations of molecular physics discussed in this book will hopefully enable the reader to progress to these advanced topics.

Appendix: Character Tables of Some Point Groups

C_{2v}	E	C_2	$\sigma_v(xz)$	$\sigma'_v(yz)$		
A_1	1	1	1	1	z	$x^2; y^2; z^2$
A_2	1	1	-1	-1	R_z	xy
B_1	1	-1	1	-1	$x; R_y$	xz
B_2	1	-1	-1	1	$y; R_x$	yz

C_{3v}	E	$2C_3$	$3\sigma_v$		
A_1	1	1	1	z	$x^2 + y^2; z^2$
A_2	1	1	-1	R_z	
E	2	-1	0	$(x, y); (R_x, R_y)$	$(x^2 - y^2, xy); (xz, yz)$

C_{2h}	E	C_2	i	σ_h		
A_g	1	1	1	1	R_z	$x^2; y^2; z^2; xy$
B_g	1	-1	1	-1	$R_x; R_y$	$xz; yz$
A_u	1	1	-1	-1	z	
B_u	1	-1	-1	1	x, y	

C_{3h}	E	C_3	C_3^2	σ_h	S_3	S_3^5		$\varepsilon = \exp(2\pi i/3)$
A'	1	1	1	1	1	1	R_z	$x^2 + y^2; z^2$
E'	$\left\{ \begin{array}{cccccc} 1 & \varepsilon & \varepsilon^* & 1 & \varepsilon & \varepsilon^* \\ 1 & \varepsilon^* & \varepsilon & 1 & \varepsilon^* & \varepsilon \end{array} \right\}$						(x, y)	$(x^2 - y^2, xy)$
A''	1	1	1	-1	-1	-1	z	
E''	$\left\{ \begin{array}{cccccc} 1 & \varepsilon & \varepsilon^* & -1 & -\varepsilon & -\varepsilon^* \\ 1 & \varepsilon^* & \varepsilon & -1 & -\varepsilon^* & -\varepsilon \end{array} \right\}$						(R_x, R_y)	(xz, yz)

D_{2d}	E	$2S_4$	C_2	$2C'_2$	$2\sigma_d$		
A_1	1	1	1	1	1	R_z	$x^2 + y^2; z^2$
A_2	1	1	1	-1	-1		
B_1	1	-1	1	1	-1	z	$x^2 - y^2$
B_2	1	-1	1	-1	1		xy
E	2	0	-2	0	0	$(x, y); (R_x, R_y)$	(xz, yz)

D_{6d}	E	$2S_{12}$	$2C_6$	$2S_4$	$2C_3$	$2S^5_{12}$	C_2	$6C'_2$	$6\sigma_d$		
A_1	1	1	1	1	1	1	1	1	1	R_z	$x^2 + y^2; z^2$
A_2	1	1	1	1	1	1	1	-1	-1		
B_1	1	-1	1	-1	1	-1	1	1	-1	z	$(x^2 - y^2, xy)$
B_2	1	-1	1	-1	1	-1	1	-1	1		
E_1	2	$\sqrt{3}$	1	0	-1	$-\sqrt{3}$	-2	0	0	(x, y)	
E_2	2	1	-1	-2	-1	1	2	0	0		
E_3	2	0	-2	0	2	0	-2	0	0		
E_4	2	-1	-1	2	-1	-1	2	0	0		
E_5	2	$-\sqrt{3}$	1	0	-1	$\sqrt{3}$	-2	0	0	(R_x, R_y)	(xz, yz)

S_4	E	S_4	C_2	S^3_4		
A	1	1	1	1	R_z	$x^2 + y^2; z^2$
B	1	-1	1	-1		z
E	$\left\{ \begin{array}{l} 1 \\ 1 \end{array} \right.$	$\left\{ \begin{array}{l} i \\ -i \end{array} \right.$	$\left\{ \begin{array}{l} -1 \\ -1 \end{array} \right.$	$\left\{ \begin{array}{l} -i \\ i \end{array} \right.$	$(x, y); (R_x, R_y)$	(xz, yz)

O_h	E	$8C_3$	$6C_2$	$6C_4$	$3C_2$	i	$6S_4$	$8S_6$	$3\sigma_h$	$6\sigma_d$		
A_{1g}	1	1	1	1	1	1	1	1	1	1	(R_x, R_y, R_z)	$x^2 + y^2 + z^2$
A_{2g}	1	1	-1	-1	1	1	-1	1	1	-1		
E_g	2	-1	0	0	2	2	0	-1	2	0		$(2z^2 - x^2 - y^2, x^2 - y^2)$
T_{1g}	3	0	-1	1	-1	3	1	0	-1	-1		(xy, xz, yz)
T_{2g}	3	0	1	-1	-1	3	-1	0	-1	1		
A_{1u}	1	1	1	1	1	-1	-1	-1	-1	-1		
A_{2u}	1	1	-1	-1	1	-1	1	-1	-1	1		
E_u	2	-1	0	0	2	-2	0	1	-2	0		
T_{1u}	3	0	-1	1	-1	-3	-1	0	1	1	(x, y, z)	
T_{2u}	3	0	1	-1	-1	-3	1	0	1	-1		

Bibliography

Molecular Physics Textbooks

1. G. Herzberg, *Molecular Spectra and Molecular Structure*, Vols. 1–3. Van Nostrand; New York 1964–1966.
2. J. M. Hollas, *Modern Spectroscopy*, 2nd ed. John Wiley & Sons; Chichester 1992.
3. H. Haken, H. Ch. Wolf, *Molecular Physics and Elements of Quantum Chemistry: Introduction to Experiments and Theory*. Springer; Berlin, Heidelberg, New York 2003.
4. P. W. Atkins, *Atkins' Molecules*, 2nd ed. Cambridge University Press; Cambridge 2003.
5. J. I. Steinfeld, *Molecules and Radiation. An Introduction to Modern Molecular Spectroscopy*, 2nd ed. Dover Publications; 2005.
6. J. D. Graybeal, *Molecular Spectroscopy*, 2nd ed. McGraw-Hill; New York 1993.
7. J. L. McHale, *Molecular Spectroscopy*. Prentice Hall; Upper Saddle River 1999.
8. J. M. Brown, *Molecular Spectroscopy*. Oxford University Press; Oxford 1998.
9. S. Svanberg, *Atomic and Molecular Spectroscopy*, 4th ed. Springer; Heidelberg 2004.
10. C. N. Banwell, E. M. McCash, *Fundamentals of Molecular Spectroscopy*, 4th ed. McGraw-Hill; New York 1995.
11. J. de Paula, P. W. Atkins, *Physical Chemistry*, 7th ed. W. H. Freeman; New York 2001.
12. P. W. Atkins, R. S. Friedman, *Molecular Quantum Mechanics*, 4th ed. Oxford University Press; Oxford 2005.

Chapter 1

- 1.1. J. R. Partington, *A Short History of Chemistry*, 3rd ed. Dover Publications; 1989.
- 1.2. W. H. Brock, *The Norton History of Chemistry*. W. H. Norton and Co.; 1993.
- 1.3. R. McCormach, L. Pyenson (eds.), *Historical Studies in the Physical Science*. John Hopkins University Press Ltd.; London 1970–2003.
- 1.4. B. Jaffe, *Crucibles: The Story of Chemistry*, 4th ed. Dover Publications; 1977. A. J. Ihde, *The Development of Modern Chemistry*. Dover Publications; 1984. J. Henry, *The Scientific Revolution and the Origin of Modern Science*, 2nd ed. Palgrave Macmillan; 2002.
- 1.5. R. J. E. Clausius, “Über die Art der Bewegung, welche wir Wärme nennen”, *Ann. Phys. (Leipzig)* **100**, 353 (1857). R. L. Liboff, *Kinetic Theory*. Springer; Berlin, Heidelberg, New York 2003. See also physics textbooks.
- 1.6. C. N. Banwell, E. M. McCash, *Fundamentals of Molecular Spectroscopy*, 4th ed. McGraw-Hill; New York 1995.
- 1.7. D. Brewster, “Observations on the Lines of the Solar Spectrum and on those produced by the Earth’s Atmosphere, and by Action of Nitrous Acid Gas”, *Trans. Roy. Soc. (Edinburgh)* **12**, 519 (1834).
- 1.8. G. R. Kirchhoff, R. W. Bunsen, *Chemische Analyse durch Spektralbeobachtungen. Ostwalds Klassiker No. 72*, Leipzig 1895. H. Schimank, “Robert Wilhelm Bunsen”, *Phys. Bl.* **5**, 489 (1949).
- 1.9. G. W. Stroke, “Ruling, Testing and Use of Optical Gratings for High Resolution Spectroscopy”, in *Progress in Optics*, Vol. II, p. 1–72. North Holland Publishing Company; Amsterdam 1963.
- 1.10. J. Mehra, A. Rechenberg, *The Historical Development of Quantum Theory*, Vols. 1–5. Springer; Berlin, Heidelberg 1982. P. O. Löwin (ed.), *Quantum Theory of Atoms, Molecules and Solids. A Tribute to C. J. Slater*. Academic Press; New York 1966.
- 1.11. E. Schrödinger, “Quantisierung als Eigenwertproblem”, *Ann. Phys. (Leipzig)* **79**, 489 (1926). W. Heisenberg, “Zur Quantentheorie der Linienstruktur und der anomalen Zeeman-Effekte”, *Z. Phys.* **8**, 273 (1922).
- 1.12. P. M. Morse, “Diatomic Molecules According to Wave Mechanics: Vibrational Levels”, *Phys. Rev.* **34**, 57 (1929).
- 1.13. E. B. Wilson, *Introduction to Quantum Mechanics*. McGraw-Hill; New York 1935. F. Lütgemeier, “Zur Quantentheorie des drei- und mehratomigen Moleküls”, *Z. Phys.* **38**, 251 (1926).

- 1.14. P. W. Atkins, R. S. Friedman, *Molecular Quantum Mechanics*, 4th ed. Oxford University Press; Oxford 2005.
- 1.15. A. Szabo, N. S. Ostlund, *Modern Quantum Chemistry: Introduction to Advanced Electron Structure Theory*. Dover Publications; 1996.
- 1.16. R. M. J. Cotterill, *Biophysics: An Introduction*. John Wiley & Sons; New York 2002.
- 1.17. M. Daune, D. BLow, *Molecular Biophysics: Structures in Motion*. Oxford University Press; Oxford 1999.
- 1.18. M. V. Diuden, I. Gutman, J. Lorentz, *Molecular Topology*. Nova Science Publications; 2001.
- 1.19. A. T. Balaban (ed.), *From Chemical Topology to Three-dimensional Geometry*. Plenum Press; New York 1997.
- 1.20. J. P. Maier, "Mass Spectrometry and Spectroscopy of Ions and Radicals", in *Encyclopedia of Spectroscopy and Spectrometry*. Academic Press; New York 1999.
- 1.21. M. Havenith, *Infrared Spectroscopy of Molecular Clusters. Springer Tracts in Modern Physics*, Vol. 176. Springer; Berlin, Heidelberg 2002.
- 1.22. H. Haberland (ed.) *Clusters of Atoms and Molecules*. Springer; Berlin, Heidelberg 1994.

Chapter 2

- 2.1. C. J. H. Schutte, *The Wavemechanics of Atoms, Molecules and Ions*. Arnold; London 1968.
- 2.2. A. Messiah, *Quantum Mechanics*. Dover Publications; 2000.
- 2.3. D. J. Griffiths, *Introduction to Quantum Mechanics*, 2nd ed. Prentice Hall; 204.
- 2.4. R. McWeeny, *Methods of Molecular Quantum Mechanics*, 2nd ed. Academic Press; New York 1992.
- 2.5. C. Cohen-Tannoudji, J. Dupont-Roc, G. Grynberg, *Atom-Photon Interactions*. John Wiley & Sons; New York 1992.
- 2.6. M. Born, R. Oppenheimer, "Zur Quantentheorie der Molekeln", *Ann. Phys. (Leipzig)* **84**, 457 (1927)
- 2.7. M. Born, K. Huang, *Dynamical Theory of Crystal Lattices*, p. 166ff. Clarendon Press; Oxford 1968.

- 2.8. P. R. Bunker, "On the Breakdown of the Born–Oppenheimer Approximation for a Diatomic Molecule", *J. Mol. Spectrosc.* **42**, 478 (1972).
- 2.9. R. G. Wooley, B. T. Sutcliffe, "Molecular Structure and the Born–Oppenheimer Approximation", *Chem. Phys. Lett.* **45**, 393 (1977). W. Kolos, L. Wolniewicz, "Nonadiabatic Theory for Diatomic Molecules and its Application to the Hydrogen Molecule", *Rev. Mod. Phys.* **35**, 473 (1963). References to papers on adiabatic and nonadiabatic theoretical treatments can be found in W. Kutzelnigg, *Mol. Phys.* **90**, 909 (1997).
- 2.10. H. Lefebvre-Brion, R. W. Field, *The Spectra and Dynamics of Diatomic Molecules*, 2nd ed. Academic Press; New York 2004.
- 2.11. G. Herzberg, *Molecular Spectra and Molecular Structure*, Vol. 1. Van Nostrand; New York 1964.
- 2.12. M. Kotani, K. Ohno, K. Kayama, "Quantum Mechanics of Electronic Structure of Simple Molecules", in *Handbuch der Physik* Vol. XXXVII/2. Springer; Berlin, Heidelberg 1961.
- 2.13. R. N. Zare, *Angular Momentum: Understanding Spatial Effects in Chemistry and Physics*. John Wiley & Sons; New York 1988.
- 2.14. G. W. King, *Spectroscopy and Molecular Structure*. Holt, Reinhart and Winston; New York 1964.
- 2.15. I. Schmidt-Mink, W. Müller, W. Meyer, *Chem. Phys.* **92**, 263 (1985). W. Spies, PhD Thesis, University of Kaiserslautern, 1990.
- 2.16. W. Kutzelnigg, J. D. Morgan III, "Hund's rules", *Z. Phys. D* **36**, 197 (1996). W. Kauzmann, *Quantum Chemistry*. Academic Press; New York 1957.
- 2.17. A. G. Gaydon, *Dissociation Energies and Spectra of Diatomic Molecules*. Chapman and Hall; London 1968.
- 2.18. J. Simmons, *An Introduction to Theoretical Chemistry*. Cambridge University Press, Cambridge 2003.
- 2.19. W. Kutzelnigg, *Einführung in die Theoretische Chemie*, Vols. 1&2, 3rd ed. Wiley-VCH; Weinheim 2003.
- 2.20. A. C. Hurley, *Introduction to the Electron Theory of Small Molecules*. Academic Press; London 1976.
- 2.21. P. Jensen, *Computational Molecular Spectroscopy*. Wiley-VCH; Weinheim 2000.
- 2.22. K. Ruedenberg, *Rev. Mod. Phys.* **34**, 326 (1962). G. H. F. Dierksen, S. Wilson (eds.), *Methods in Computational Molecular Physics*, in *Nato Science Series C*. Kluwer Academic Publishers; 1983.

- 2.23. M. J. Feinberg, K. Ruedenberg, *J. Chem. Phys.* **59**, 1495 (1971).
- 2.24. W. J. Hehre, L. Radom, P. v. R. Schleyer, J. A. Pople, *Ab-initio Molecular Orbital Theory*. Wiley-Interscience; New York 1986.
- 2.25. W. Heitler, F. London, "Wechselwirkung neutraler Atome und homöopolare Bindung nach der Quantenmechanik", *Z. Phys.* **44**, 455 (1927).
- 2.26. H. M. James, A. S. Coolidge, "The ground state of the Hydrogen Molecule", *J. Chem. Phys.* **1**, 825 (1933).
- 2.27. C. C. J. Roothan, "Self-Consistent Field Theory for Open Shells of Electronic Systems", *Rev. Mod. Phys.* **32**, 179 (1960). W. Kolos, L. Wolniewicz, *Rev. Mod. Phys.* **35**, 473 (1963).
- 2.28. W. Kolos, L. Wolniewicz, "Potential-Energy Curves for the $X^1\Sigma_g^+$, $b^3\Sigma_u^+$ and $C^1\Pi_u$ States of the Hydrogen Molecule", *J. Chem. Phys.* **43**, 2429 (1965).
- 2.29. D. R. Yarkony, *Modern Electronic Structure Theory*. World Scientific; Singapore 1995.
- 2.30. H. F. Schaefer, *Quantum Chemistry: The Development of Ab-initio Methods in Molecular Electronic Structure Theory*. Dover Publications; 2004.
- 2.31. D. R. Hartree, *The Calculation of Atomic Structures*. Wiley-Interscience; New York 1957.
- 2.32. C. Froese-Fischer, *The Hartree-Fock Method for Atoms*. John Wiley & Sons; New York 1977.
- 2.33. W. Kutzelnigg, in *Localization and Delocalization in Quantum Chemistry*, O. Chalvet *et al.* (eds.). D. Reidel; Dordrecht 1975.
- 2.34. A. C. Hurley, *Electron Correlation in Small Molecules*. Academic Press; New York 1976.
- 2.35. W. Kutzelnigg, P. v. Herigonte, "Electron Correlation at the Dawn of the 21st Century", *Adv. Quantum Chem.* **36**, 185 (1999).
- 2.36. K. P. Lawley, *Ab-initio Methods in Quantum Chemistry*, Parts I&II. John Wiley & Sons; New York 1987.

Chapter 3

- 3.1. H. Haken, H. C. Wolf, *The Physics of Atoms and Quanta: Introduction to Experiments and Theory*. Springer; Berlin, Heidelberg, New York 1996.

- 3.2. J. W. Flemming, J. Chamberlain, *Infrared Phys.* **14**, 277 (1974).
- 3.3. P. M. Morse, "Diatomic Molecules According to the Wave Mechanics: Vibrational Levels", *Phys. Rev.* **34**, 57 (1929).
- 3.4. E. M. Greenawalt, A. S. Dickison, "On the Use of Morse Eigenfunctions for the Variational Calculations of Bound States of Diatomic Molecules", *J. Mol. Spectrosc.* **30**, 427 (1969).
- 3.5. W. Demtröder, M. McClintock, R. N. Zare, "Spectroscopy of NA_2 Using Laser-induced Fluorescence", *J. Chem. Phys.* **51**, 5495 (1969).
- 3.6. S. Flügge, *Practical Quantum Mechanics*. Springer; Heidelberg 1984.
- 3.7. D. Truhlar, "Oscillators with Quartic Anharmonicity. Approximate Energy Levels", *J. Mol. Spectrosc.* **30**, 427 (1969).
- 3.8. C. L. Pekeris, "The Rotation-Vibration Coupling in Diatomic Molecules", *Phys. Rev.* **45**, 98 (1934). H. H. Nielsen, "The Vibration-Rotation Energies of Molecules", *Rev. Mod. Phys.* **23**, 90 (1951). *Encyclop. Phys.* **37**, 173 (1959). D. L. Albritton, A. L. Schmeltekopf, R. N. Zare, "An Introduction to the least-squares fitting of spectroscopic data", in *Molecular Spectroscopy, Modern Research*, K. N. Rao (ed.), p. 1. Academic Press; New York 1976
- 3.9. J. L. Dunham, "The Energy Levels of a Rotating Vibrator", *Phys. Rev.* **41**, 721 (1932).
- 3.10. W. C. Stwalley, "Mass-reduced Quantum Numbers, Application to the Isotopic Mercury Hydrides", *J. Chem. Phys.* **63**, 3062 (1975). A. D. Buckingham, W. Urland, "Isotope Effects on Molecular Properties", *Chem. Rev.* **75**, 113 (1975).
- 3.11. J. A. Coxon, "The Calculation of Potential Energy Curves of Diatomic Molecules: Application to Halogen Molecules", *J. Quant. Spectrosc. Rad. Transf.* **11**, 443 (1971).
- 3.12. M. Defranceschi, J. Delhalle, *Numerical Determination of the Electronic Structure of Atoms, Diatomics and Polyatomic Molecules*, in *NATO ASI Series C*. Kluwer Academic Publishers; 1989.
- 3.13. a) G. Wentzel, "Eine Verallgemeinerung der Quantenbedingungen für die Zwecke der Wellenmechanik", *Z. Phys.* **38**, 518 (1926). b) H. A. Kramers, "Wellenmechanik und halbzahlige Quantisierung", *Z. Phys.* **39**, 828 (1926). c) L. Brioullin, *J. de Physique* **7**, 353 (1926).
- 3.14. E. Merzbacher, *Quantum Mechanics*. John Wiley & Sons; New York 1970.
- 3.15. C. H. Townes, A. L. Schawlow, *Microwave Spectroscopy*. Dover Publications; New York 1975.

- 3.16. J. Finlan, G. Simons, "Capabilities and Limitations of an Analytical Potential Expansion for Diatomic Molecules", *J. Mol. Spectrosc.* **57**, 1 (1975).
- 3.17. A. J. Thakkar, "A New Generalized Expansion for the Potential Energy Curves of Diatomic Molecules", *J. Chem. Phys.* **62**, 1693 (1975).
- 3.18. R. Rydberg, "Graphische Darstellung einiger bandenspektroskopischer Ergebnisse", *Z. Phys.* **73**, 376 (1931).
- 3.19. O. Klein, "Zur Berechnung von Potentialkurven für zweiatomige Moleküle mit Hilfe von Spektraltermen", *Z. Phys.* **76**, 226 (1932).
- 3.20. A. L. G. Rees, "The Calculation of Potential Energy Curves from Band Spectroscopic Data", *Proc. Roy. Soc. (London)* **59**, 998 (1947).
- 3.21. See, for example, textbooks on mathematics.
- 3.22. A. S. Dickinson, "A New Method for Evaluating Rydberg-Klein-Rees Integrals", *J. Mol. Spectrosc.* **44**, 183 (1972).
- 3.23. H. Fleming, K. N. Rao, "A Simple Numerical Evaluation of the RKR Integrals", *J. Mol. Spectrosc.* **44**, 189 (1972).
- 3.24. D. L. Albritton, W. J. Harrop, A. L. Schmeltekopf, R. N. Zare, "Calculation of Centrifugal Distortion Constants for Diatomic Molecules from RKR-Potentials", *J. Mol. Spectrosc.* **46**, 67 (1973).
- 3.25. W. M. Kosman, J. Hinze, "Inverse Perturbation Analysis: Improving the Accuracy of Potential Energy Curves", *J. Mol. Spectrosc.* **56**, 93 (1975).
- 3.26. C. R. Vidal, H. Scheingraber, "Determination of Diatomic Molecular Constants Using an Inverted Perturbation Approach", *J. Mol. Spectrosc.* **65**, 46 (1977).
- 3.27. M. M. Hessel, C. R. Vidal, "The $B^1\Pi_u-X^1\Sigma_g^+$ Band System of the $^7\text{Li}_2$ Molecules", *J. Chem. Phys.* **70**, 4439 (1979).
- 3.28. M. Raab, G. Höning, W. Demtröder, C. R. Vidal, "High-Resolution Laser Spectroscopy of Cs_2 : II. Doppler-free Polarization Spectroscopy of the $C^1\Pi_u \leftarrow X^1\Sigma^+$ System", *J. Chem. Phys.* **76**, 4370 (1982).
- 3.29. Modified Fig. 6 in [3.26].
- 3.30. J. O. Hirschfelder (ed.), *Intermolecular Forces*. John Wiley & Sons; New York 1967.
- 3.31. J. Goodishman, *Diatomic Interaction Potential Theory*, Vols. I&II. Academic Press; New York 1973.

- 3.32. J. O. Hirschfelder, C. F. Curtis, R. B. Byrd, *Molecular Theory of Gases and Liquids*. John Wiley & Sons; New York 1954.

Chapter 4

- 4.1. a) C. Cohen-Tannoudji, B. Diu, F. Laloe, *Quantum Mechanics*, Vol. II. Wiley International; New York 1977. b) C. Cohen-Tannoudji, J. Dupout-Roche, G. Grynberg, *Atom-Photon Interactions*. John Wiley & Sons; New York 1992.
- 4.2. B. H. Bransden, C. J. Joachain, *Quantum Mechanics*, 2nd ed. Prentice Hall; New York 2000.
- 4.3. J. D. Jackson, *Classical Electrodynamics*, 3rd ed. John Wiley & Sons; New York 1998.
- 4.4. H. Kato, "Energy Levels and Line Intensities of Diatomic Molecules", *Bull. Chem. Soc. Japan* **66**, 3203 (1993).
- 4.5. J. M. Hollas, *High-Resolution Spectroscopy*, 2nd ed. John Wiley & Sons; Chichester 1998.
- 4.6. a) E. V. Condon, "Nuclear motions associated with electronic transitions in diatomic molecules", *Phys. Rev.* **32**, 858 (1928). b) S. E. Schwarz, "The Franck-Condon Principle and the Duration of Electronic Transitions", *J. Chem. Educ.* **50**, 608 (1973).
- 4.7. H. Weickenmeier, U. Diemer, M. Wabl, M. Raab, W. Demtröder, W. Müller, "Accurate Ground-state Potential of Cs₂ up to the Dissociation Limit", *J. Chem. Phys.* **82**, 5345 (1985).
- 4.8. J. Tellinghuisen, "*E* → *B* Structured Continuum in I₂", *Phys. Rev. Lett.* **34**, 1137 (1975).
- 4.9. D. Eisel, D. Zevgolis, W. Demtröder, "Sub-Doppler Laser Spectroscopy of the NaK Molecule", *J. Chem. Phys.* **71**, 2005 (1979).
- 4.10. V. Weisskopf, "Zur Theorie der Kopplungsbreite und der Stoßdämpfung", *Z. Phys.* **75**, 287 (1932).
- 4.11. I. I. Sobelman, L. A. Vainstein, E. A. Yukov, *Excitation of Atoms and Broadening of Spectral Lines*, 2nd ed. Springer; Heidelberg, Berlin, New York 1995.
- 4.12. M. Göppert-Mayer, "Über Elementarakte mit zwei Quantensprüngen", *Ann. Phys. (Leipzig)* **9**, 273 (1931).

- 4.13. W. Kaiser, C. G. Garret, "Two-Photon Excitation in LLCA $F_2:Eu^{2+}$ ", *Phys. Rev. Lett.* **7**, 229 (1961).
- 4.14. P. Bräunlich, "Multiphoton Spectroscopy", in *Progress in Atomic Spectroscopy*, W. Hanle, H. Kleinpoppen (eds.). Plenum Press; New York 1978.
- 4.15. S. H. Lin, A. A. Villneys (eds.), *Advances in Multiphoton Processes and Spectroscopy*; Proceedings of biannual conferences. World Scientific; Singapore 1985–2004.
- 4.16. B. Schrader, *Infrared and Raman Spectroscopy*. Wiley VCH; Weinheim 1993.

Chapter 5

- 5.1. J. M. Hollas, *Symmetry in Molecules*. Chapman and Hall; 1972.
- 5.2. R. L. Carter, *Molecular Symmetry and Group Theory*. John Wiley & Sons; New York 1997.
- 5.3. A. Vincent, *Molecular Symmetry and Group Theory: A Programmed Introduction to Chemical Applications*, 2nd ed. John Wiley & Sons; New York 2001.
- 5.4. J. S. Ogden, *Introduction to Molecular Symmetry*. Oxford University Press; Oxford 2002.
- 5.5. D. S. Schonland, *Molecular Symmetry*. Van Nostrand Reinhold; London 1971.
- 5.6. P. R. Bunker, *Molecular Symmetry and Spectroscopy*. NRC Research Press; Ottawa 1998.
- 5.7. S. Sternberg, *Group Theory and Physics*. Cambridge University Press; Cambridge 1995.

Chapter 6

- 6.1. H. C. Allen, P. C. Cross, *Molecular Vib-Rotors*. Wiley-Interscience; New York 1963.
- 6.2. B. T. Sutcliffe, "The Eckart Hamiltonian for Molecules. A Critical Exposition", in R. G. Woolley (ed.) *Quantum Dynamics of Molecules*. Plenum Press; New York 1980.
- 6.3. H. Goldstein, C. Poole, J. L. Safko, *Classical Mechanics*, 3rd ed. Addison-Wesley; New York 2002.

- 6.4. W. Gordy, R. L. Cook, *Microwave Molecular Spectroscopy*. Interscience Publishers; New York 1970.
- 6.5. H. W. Kroto, *Molecular Rotation Spectra*. John Wiley & Sons; London 1992.
- 6.6. J. E. Wollrab, *Rotational Spectra and Molecular Structure*. Academic Press; New York 1979.
- 6.7. G. O. Sorensen, *A New Approach to the Hamiltonian of Nonrigid Molecules*, in *Topics in Current Chemistry* Vol. 82. Springer; Heidelberg 1979.
- 6.8. J. Pesonen, L. Halonen, "Recent Advances in the Theory of Vibration–Rotation Hamiltonians", *Adv. Chem. Phys.* **125**, 269 (2003).
- 6.9. E. B. Wilson, Jr., J. C. Decius, P. L. Cross, *Molecular Vibrations*. McGraw-Hill; New York 1954.
- 6.10. L. A. Woodward, *Introduction to the Theory of Molecular Vibrations and Vibrational Spectroscopy*. Oxford University Press; Oxford 1972.
- 6.11. G. Duxburry, *Infrared Vibration–Rotation Spectroscopy*. John Wiley & Sons; New York 2000.

Chapter 7

- 7.1. J. A. Pople, *Approximate Molecular Orbital Theory*. McGraw-Hill; New York 1976.
- 7.2. J. K. Burdett, *Chemical Bonds, A Dialog*. John Wiley & Sons; Chichester 1997.
- 7.3. See a textbook on atomic physics, e.g., [3.1].
- 7.4. N. A. March, J. F. Mucci, *Chemical Physics of Free Molecules*. Plenum Press; New York 1993.
- 7.5. A. D. Walsh, *J. Am. Chem. Soc.*, 2260 (1953).
- 7.6. A. Rauk, *Orbital Interaction Theory of Organic Chemistry*, 2nd ed. Wiley-Interscience; New York 2000. W. T. Borden, *Modern Molecular Orbital Theory for Organic Chemists*. Prentice Hall; New York 1975.
- 7.7. K. Kates, *Hückel Molecular Orbital Theory*. Academic Press; New York 1978.
- 7.8. J. M. Hollas, *High-Resolution Spectroscopy*, 2nd ed. John Wiley & Sons; Chichester 1998.

- 7.9. G. Herzberg, *Molecular Spectra and Molecular Structure*, Vol. III: *Electronic Spectra and Electronic Structure of Polyatomic Molecules*. Van Nostrand Reinhold; New York 1966.
- 7.10. S. Wilson (ed.), *Handbook of Molecular Physics and Quantum Chemistry*. John Wiley & Sons; New York 2003.

Chapter 8

- 8.1. G. W. Chantry, *Modern Aspects of Microwave Spectroscopy*. Academic Press; New York 1979.
- 8.2. W. Gordy, R. L. Cook, *Microwave Molecular Spectra*, 3rd ed. John Wiley & Sons; New York 1984.
- 8.3. P. Bunker, *Molecular Symmetry and Spectroscopy*, 2nd ed. NRC Research Press; Ottawa 1998.
- 8.4. G. Herzberg, *Molecular Spectra and Molecular Structure*, Vol. II: *Infrared and Raman Spectra*. Van Nostrand Reinhold; 1950. R. S. Mulliken, "Report on Notation for Spectra of Diatomic Molecules", *Phys. Rev.* **36**, 611 (1930).
- 8.5. J. M. Hollas, *Modern Spectroscopy*, 3rd ed. John Wiley & Sons; New York 1998.
- 8.6. H. Wenz, *Laserabsorptionsspektroskopie im nahen Infrarot mit höchster Empfindlichkeit*, Ph. D. Thesis. Department of Physics, University of Kaiserslautern 2001.
- 8.7. A. Weber, "High-resolution rotational raman spectra of gases", Chapter 3 in R. J. H. Clark, R. E. Hester (eds.), *Advances in Infrared and Raman Spectroscopy*, Vol. 9. Heyden; London 1982.
- 8.8. W. Knippers, K. van Helvoort, S. Stolte, "The Allene Raman Spectrum from 250 to 6200 cm^{-1} Stokes Shift", *Chem. Phys.* **105**, 27 (1986).
- 8.9. B. Schrader, *Infrared and Raman Spectroscopy*. Wiley-VCH; Weinheim 1993.
- 8.10. M. J. Pelletier (ed.), *Analytical Applications of Raman Spectroscopy*, Academic Press; New York 1994.

Chapter 9

- 9.1. H. Lefebvre, R. W. Field, *Perturbations in the Spectra of Diatomic Molecules*. Academic Press; New York 1986.

- 9.2. C. H. Townes, A. L. Schawlow, *Microwave Spectroscopy*, p. 177ff. Dover Publications; New York 1975.
- 9.3. W. G. Richards, *Spin–Orbit Coupling in Molecules*. Oxford Science Publications/Clarendon Press; Oxford 1981.
- 9.4. J. T. Hougen, *The Calculation of Rotational Energy Levels and Rotational Line Intensities in Diatomic Molecules*. National Bureau of Standards Monographs Vol. 115 Washington 1970.
- 9.5. G. Fischer, H. Fischer, *Vibronic Coupling Theoretical Chemistry, A Series of Monographs*, Vol. 9. Academic Press; New York 1997.
- 9.6. M. Bixon, J. Jortner, “Intramolecular Radiationless Transitions”, *J. Chem. Phys.* **48**, 715 (1968).
- 9.7. C. Jungen, A. J. Merer, “The Renner–Teller Effect”, in K. N. Rao (ed.), *Spectroscopy, Modern Research*, Vol. II. Academic Press; New York 1976.
- 9.8. I. B. Bersurker, “Modern Aspects of the Jahn–Teller Effect: Theory and Application to Molecular Problems”, *Chem. Rev.* **101**, 1067 (2001).
- 9.9. M. Keil, H. G. Krämer, A. Kudell, M. A. Baig, J. Zhu, W. Demtröder, W. Meyer, “Rovibrational Structures of the Pseudorotating Trimer $^{21}\text{Li}_3$ ”, *J. Chem. Phys.* **113**, 7414 (2000).
- 9.10. A. G. Gaydon, *Dissociation Energies*. Chapman and Hall; London 1968.
- 9.11. S. Kasahara, Y. Hasui, K. Otsuka, M. Baba, W. Demtröder, H. Kato, “High-Resolution Laser Spectroscopy of the $\text{Cs}_2 C^1\Pi_u$ -State: Perturbation and Predissociation”, *J. Chem. Phys.* **106**, 4869 (1997).
- 9.12. D. Eisel, Ph. D. Thesis. Department of Physics, University of Kaiserslautern 1983. M. Schwarz, R. Duchowicz, W. Demtröder, C. Jungen, “Autoionizing Rydberg States of Li_2 : Analysis of Electronic–Rotational Interactions”, *J. Chem. Phys.* **89**, 5460 (1988).
- 9.13. A. Temkin (ed.), *Autoionization: Recent Developments*. Plenum Press; New York 1985.
- 9.14. M. A. Baig, F. Bylicki, M. Keil, J. Zhu, W. Demtröder, “The different line shapes in Doppler-free spectroscopy of molecular Rydberg transitions. Spectral Line Shapes 11”, *AIP Conf. Proc.* Vol. 559, p. 275. New York 2001.
- 9.15. C.H. Greene, “Interaction between Electronic and Vibrational Motions”, *Comm. At. Mol. Phys.* **23**, 209 (1989). H. Köppel, W. Domcke, L. S. Cederbaum, “Multi-mode Molecular Dynamics beyond the B. O. Approximation”, *Adv. Chem. Phys.* **57**, 59 (1984).

- 9.16. D. J. Nesbitt, R. W. Field, "Vibrational Energy Flow in Highly Excited Molecules: Role of Intermolecular Vibrational Redistribution", *J. Phys. Chem.* **100**, 12735 (1996). M. Quack, "Spectra and Dynamics of Coupled Vibrations in Polyatomic Molecules", *Annu. Rev. Phys. Chem.* **41**, 839 (1990).
- 9.17. K. E. Johnson, L. Wharton, D. H. Levy, "The photodissociation lifetime of the Van der Waals molecule I_2He ", *J. Chem. Phys.* **69**, 2719 (1978).

Chapter 10

- 10.1. W. Weltner, *Magnetic Atoms and Molecules*. Dover Publications; New York 1983.
- 10.2. G. Herzberg, *Molecular Spectra and Molecular Structure*, Vol. I. Van Nostrand Reinhold; New York 1950.
- 10.3. S. D. Rosner, T. D. Gaily, R. A. Holt, "Measurement of the zero-field hyperfine structure of a single vibration-rotation level of Na_2 by a laserfluorescence molecular beam resonance", *Phys. Rev. Lett.* **35**, 785 (1975).
- 10.4. A. Habib, R. Görden, G. Brasen, R. Lange, W. Demtröder, "Sub-Doppler Laser Spectroscopy of the 1B_2 ($^1\Delta_u$)-State of CS_2 ", *J. Chem. Phys.* **101**, 2752 (1994).
- 10.5. T. Weyh, W. Demtröder, "Lifetime Measurements of Selectively Excited Rovibrational Levels of the V 1B_2 -State of CS_2 ", *J. Chem. Phys.* **104**, 6938 (1996).
- 10.6. A. Habib, Ph. D. Thesis. Department of Physics, University of Kaiserslautern 1995. A. Habib, R. Lange, G. Brasen, W. Demtröder, "Sub-Doppler Zeeman Spectroscopy of the Cs_2 Molecule", *Ber. Bunsenges. Phys. Chem.* **99**, 265 (1995).
- 10.7. N. Ryde, *Atoms and Molecules in Electric Fields*. Almqvist & Wiksel; Stockholm 1976.

Chapter 11

- 11.1. R. E. Grisente, W. Schöllkopf, J. P. Toennies, G. C. Hegerfeldt, T. Köhler, M. Stoll, "Determination of the Bond Length and Binding Energy of the Helium Dimer", *Phys. Rev. Lett.* **85**, 2284 (2000). J. P. Toennies, "Die faszinierenden Quanteneigenschaften von Helium und ihre Anwendungen", *Phys. J.* **1**, 49 (2002).
- 11.2. N. Halberstadt, K. C. Janda (eds.), *Dynamics of Polyatomic Van der Waals Complexes*, p. 517ff. Plenum Press; New York 1990.

- 11.3. H. Haberland (ed.), *Clusters of Atoms and Molecules*. Springer; Berlin, Heidelberg 1994.
- 11.4. R. L. Johnston, *Atomic and Molecular Clusters*. Taylor and Francis; 2002.
- 11.5. J. Jellinek (ed.), *Theory of Atomic and Molecular Clusters with a Look at Experiments*. Springer; Berlin, Heidelberg 1999.
- 11.6. S. Sugano, Y. Nishina, S. Ohnishi, *Microclusters*. Springer; Berlin, Heidelberg 1998. G. Benedek, T. P. Martin, G. Pacchioni (eds.), *Elemental and Molecular Clusters*. Springer; Berlin, Heidelberg 1988.
- 11.7. W. A. de Heer, "The Physics of Simple Metal Clusters", *Rev. Mod. Phys.* **65**, 611 (1993).
- 11.8. E. Zanger, V. Schmatloch, D. Zimmermann, "Laserspectroscopic Investigations of the Van der Waals Molecule NaKr⁸⁴", *J. Chem. Phys.* **88**, 5396 (1988).
- 11.9. M. Havenith, *Infrared Spectroscopy of Molecular Clusters*. Springer; Berlin, Heidelberg 2002.
- 11.10. D. J. Nesbitt, "High-Resolution Infrared Spectroscopy of Weakly Bound Molecular Complexes", *Chem. Rev.* **88**, 843 (1988). J. M. Hutson, "Intermolecular Forces and the Spectroscopy of Van der Waals Molecules", *Annu. Rev. Phys. Chem.* **41**, 123 (1990).
- 11.11. L. Biennier *et al.*, "Structure and Rovibrational Analysis of the [O₂(¹Δ_g)]₂ ← [O₂(³Σ_g)]₂ Transition of the O₂-Dimer", *J. Chem. Phys.* **112**, 6309 (2000).
- 11.12. Ph. Buffat, J. P. Borel, "Size effect on the melting temperature of gold clusters", *Phys. Rev. A* **13**, 2287 (1976).
- 11.13. W. Meyer, M. Keil, A. Kudell, M. A. Baig, J. Zhu, W. Demtröder, "The Hyperfine Structure in the Electronic A²E' ← X²E' System of the Pseudorotating Lithium Trimer", *J. Chem. Phys.* **115**, 2590 (2001).
- 11.14. H. A. Eckel, J. M. Gress, J. Biele, W. Demtröder, "Sub-Doppler Optical Double-Resonance Spectroscopy and Rotational Analysis of Na₃", *J. Chem. Phys.* **98**, 135 (1993).
- 11.15. C. Brechignac *et al.*, "Alkali-metal clusters as prototypes of metal clusters", *J. Chem. Soc. Faraday Trans.* **86**, 2525 (1990).
- 11.16. H. von Busch, Vas Dev, H.-A. Eckel, S. Kasahara, J. Wang, W. Demtröder, "Unambiguous proof for Berry's Phase in the Sodium Trimer", *Phys. Rev. Lett.* **81**, 4584 (1998).

- 11.17. M. Keil, H.-G. Krämer, A. Kudell, M. A. Baig, J. Zhu, W. Demtröder, "Rovibrational Structures of the Pseudorotating Lithium Trimer $^{21}\text{Li}_3$ ", *J. Chem. Phys.* **133**, 7414 (2000).
- 11.18. M. R. Hoare, *Adv. Chem. Phys.* **40**, 49 (1979).
- 11.19. O. Echt, K. Sattler, E. Recknagel, "Magic Numbers for Sphere Packings: Experimental Verification in Free Xenon Clusters", *Phys. Rev. Lett.* **47**, 1121 (1981).
- 11.20. M. Hartmann, F. Mielke, J. P. Toennies, A. E. Vilesov, G. Benedek, "Direct Spectroscopic Observations of Elementary Excitations in Superfluid He Droplets", *Phys. Rev. Lett.* **76**, 4560 (1996).
- 11.21. K. Liu, J. D. Cruzan, R.-J. Saykally, "Water Clusters", *Science* **271**, 929 (1996).
- 11.22. J. C. Phillips, "Chemical bonding, kinetics and the approach to equilibrium structure of simple metallic, molecular and network microclusters", *Chem. Rev.* **86**, 619 (1988).
- 11.23. H. W. Kroto, J. R. Heath, S. C. O'Brian, R. F. Curland, R. E. Smalley, " C_{60} : Buckminster Fullerene", *Nature* **318**, 162 (1985).
- 11.24. E. E. B. Campbell, "Carbon Clusters", in H. Haberland (ed.), *Clusters of Atoms and Molecules*. Springer; Berlin, Heidelberg 1994.
- 11.25. O. F. Hagen, "Condensation in free jets", *Z. Phys. D* **4**, 291 (1987).
- 11.26. K. Sattler, "Clusters of atoms", *Phys. Scripta* **T13**, 93 (1986).
- 11.27. J. B. Hopkins, P. R. Langridge-Smith, M. D. Morse, R. E. Smalley, "Supersonic Metal Cluster Beams of Refractory Metals: Spectral Investigation of Ultracold Mo_2 ", *J. Chem. Phys.* **78**, 1627 (1983).

Chapter 12

- 12.1. D. J. E. Ingram, *Radio- and Microwave Spectroscopy*. Butterworth; 1976.
- 12.2. A. L. Schawlow, C. H. Townes, *Microwave Spectroscopy*. Dover Publications; New York 1975.
- 12.3. R. Varma, L. W. Hrubesh, *Chemical Analysis by Microwave Rotational Spectroscopy*. John Wiley & Sons; New York 1979.
- 12.4. P. Griffiths, J. A. de Haseth, *Fourier-Transform Infrared Spectroscopy*. John Wiley & Sons; New York 1986.

- 12.5. J. Kauppinen, J. Partanen, *Fourier Transforms in Spectroscopy*. Wiley-VCH; Weinheim 2001.
- 12.6. Th. Platz, Ph. D. Thesis. Department of Physics, University of Kaiserslautern 1998.
- 12.7. E. Popov, E. G. Loewen, *Diffraction Gratings and Applications*. Marcel Dekker; New York 1997.
- 12.8. C. Kunz, *Synchrotron Radiation: Techniques and Applications*. Springer; Berlin, Heidelberg 1979.
- 12.9. D. M. Mills (ed.), *Third-generation Hard X-ray Synchrotron Radiation Sources*. Wiley-Interscience; New York 2002.
- 12.10. W. Demtröder, *Laser Spectroscopy*, 3rd ed. Springer; Berlin, Heidelberg 2003.
- 12.11. D. G. Cameron, D. J. Moffat, "A generalized approach to derivative spectroscopy", *Appl. Spectrosc.* **41**, 539 (1987). P. C. D. Hobbs, "Ultrasensitive Laser Measurements Without Tears", *Appl. Opt.* **36**, 903 (1997).
- 12.12. R. Grosskloß, P. Kersten, W. Demtröder, "Sensitive amplitude and phase modulated absorption spectroscopy with a continuously tunable diode laser", *Appl. Phys. B* **58**, 137 (1994).
- 12.13. H. Wenz, Ph. D. Thesis. Department of Physics, University of Kaiserslautern 2001.
- 12.14. H. Wenz, W. Demtröder, J. M. Flaud, "Highly sensitive absorption spectroscopy of the ozone molecule around 1.5 μm ", *J. Mol. Spectrosc.* **209**, 267 (2001).
- 12.15. A. Campargue, F. Stoeckel, M. Chenevier, "High sensitivity intercavity laser spectroscopy: Applications to the study of overtone transitions in the visible range", *Spectrochim. Acta Rev.* **13**, 69 (1990).
- 12.16. P. Zalicki, R. N. Zare, "Cavity ringdown spectroscopy for quantitative absorption measurements", *J. Chem. Phys.* **102**, 2708 (1995). J. J. Scherer, J. B. Paul, C. P. Collier, A. O'Keefe, R. J. Saykally, "Cavity ringdown laser absorption spectroscopy: History, development and application to pulsed molecular beams", *Chem. Rev.* **97**, 25 (1997).
- 12.17. V. Z. Gusev, A. A. Karabutov, *Laser Optoacoustics*. Springer; Berlin, Heidelberg 1997. A. C. Tam, "Photo-acoustic spectroscopy and other applications", in D. S. Kliger (ed.), *Ultrasensitive Laser Spectroscopy*, p. 1–108. Academic Press; New York 1983.

- 12.18. K. M. Evenson, R. J. Saykally, D. A. Jennings, R. E. Curl, J. M. Brown, "Far infrared laser magnetic resonance", Chap. 5 in C. B. Moore (ed.), *Chemical and Biochemical Applications of Lasers*. Academic Press; New York 1980. W. Urban, W. Herrmann, "Zeeman modulation spectroscopy with spin-flip Raman laser", *Appl. Phys.* **17**, 325 (1978).
- 12.19. H. Weickenmeier, Ph. D. Thesis. Department of Physics, University of Kaiserslautern 1983. H. Weickenmeier, V. Diemer, M. Wahl, M. Raab, W. Demtröder, W. Müller, "Accurate Ground-state Potential of Cs₂ up to the Dissociation Limit", *J. Chem. Phys.* **82**, 5354 (1985).
- 12.20. W. Demtröder, H. J. Foth, "Molekülspektroskopie in kalten Düsenstrahlen", *Phys. Bl.* **43**, 7 (1987).
- 12.21. H. J. Foth, H. J. Vedder, W. Demtröder, "Sub-Doppler laser spectroscopy of NO₂ in the $\lambda = 292\text{--}5$ nm region", *J. Mol. Spectrosc.* **121**, 167 (1987).
- 12.22. G. Scoles, *Atomic and Molecular Beam Methods* Vol. I&II. Oxford University Press; Oxford 1992.
- 12.23. Th. Platz, W. Demtröder "Sub-Doppler optothermal overtone spectroscopy of ethylene and dichloroethylene", *Chem. Phys. Lett.* **294**, 397 (1998).
- 12.24. W. Kaiser, C. G. Garret, "Two-photon excitation in LLCA F₂:Eu²⁺", *Phys. Rev. Lett.* **11**, 414 (1963).
- 12.25. M. Göppert-Mayer, "Über Elementarakte mit zwei Quantensprüngen". *Ann. Phys. (Leipzig)* **9**, 273 (1931).
- 12.26. M. H. Kabir *et al.*, "Doppler-free high resolution laser spectroscopies of the naphthalen molecule", *Chem. Phys.* **283**, 237 (2002).
- 12.27. H. Weickenmeier, V. Diemer, W. Demtröder, M. Broyer, "Hyperfine interaction between the singlet and triplet ground states of Cs₂", *Chem. Phys. Lett.* **124**, 470 (1986).
- 12.28. V. S. Letokhov, V. P. Chebotayev, *Nonlinear Laser Spectroscopy, Series in Optical Science*, Vol. 4. Springer; Berlin, Heidelberg 1977.
- 12.29. G. Marowski, V. V. Smirnov (eds.), *Coherent Raman Spectroscopy, Proceedings Phys.* Vol. 63. Springer; Berlin, Heidelberg 1992.
- 12.30. W. Kiefer, "Nonlinear Raman Spectroscopy", p. 1609 in *Encyclopedia of Spectroscopy and Spectrometry*. Academic Press; New York 2000. J. J. Laserna (ed.), *Modern Techniques in Raman Spectroscopy*. John Wiley & Sons; New York 1996.

- 12.31. P. Hannaford, *Femtosecond Laser Spectroscopy*. Springer; Berlin, Heidelberg 2004.
- 12.32. J. C. Diels, W. Rudolph, *Ultrashort Laser Pulse Phenomena*. Academic Press; San Diego 1996.
- 12.33. C. Rulliere (ed.), *Femtosecond Laser Pulses*, 2nd ed. Springer; Berlin, Heidelberg 2004.
- 12.34. T. Brabec, F. Krausz, "Intense few cycle laser fields: Frontiers of nonlinear optics", *Rev. Mod. Phys.* **77**, 545 (2000).
- 12.35. S. A. Trushin, W. Fuss, K. L. Kompa, W. E. Schmid, "Femtosecond Dynamics of Fe(CO)₅ photodissociation at 267 nm studied by transient ionization", *J. Phys. Chem. A* **104**, 1997 (2000).
- 12.36. A. H. Zewail, *Femtochemistry*. World Scientific; Singapore 1994.
- 12.37. J. Manz, L. Wöste (eds.), *Femtosecond Chemistry*, Vol. I&II. VCH; Weinheim 1995.
- 12.38. T. Baumert, M. Grosser, R. Thalweiser, G. Gerber, "Femtosecond time-resolved molecular multiphoton ionisation: The Na₂ system", *Phys. Rev. Lett.* **67**, 3753 (1991).
- 12.39. T. Brixner, N. H. Damrauer, G. Gerber, *Femtosecond Quantum Control*, p. 1–56 in Vol. 46 of *Advances in Atomic, Molecular and Optical Physics*. Academic Press; New York 2001.
- 12.40. T. Brixner, G. Gerber, "Quantum Control of Gas Phase and Liquid Phase Femtochemistry", *Chem. Phys. Phys. Chem.* **4**, 418 (2003).
- 12.41. W. Wohlleben, T. Buckup, J. L. Herek, R. J. Cogdell, M. Motzkus, "Multichannel carotenoid deactivation in photosynthetic light harvesting", *Biophys. J.* (July 2003).
- 12.42. D. W. Turner, *Molecular Photoelectron Spectroscopy*. John Wiley & Sons; New York 1970.
- 12.43. J. F. Moulder, *Handbook of X-Ray Photoelectron Spectroscopy*. Physical Electronics Publications; 1995. A. M. Ellis, *Electronic and Photoelectron Spectroscopy*. Cambridge University Press; Cambridge 2005.
- 12.44. K. Müller-Dethlefs, E. W. Schlag, "High-resolution ZEKE photoelectron spectroscopy of molecular systems", *Annu. Rev. Phys. Chem.* **42**, 109 (1991).
- 12.45. E. W. Schlag, *ZEKE Spectroscopy*. Cambridge University Press; Cambridge 1998.

- 12.46. M. Sander, L. A. Chewter, K. Müller-Dethlefs, E. W. Schlag, "High-resolution zero-kinetic-energy photoelectron spectroscopy of nitric oxide", *Phys. Rev. A* **36**, 4543 (1987).
- 12.47. St. Hüfner, *Photoelectron Spectroscopy*, 3rd ed. Springer; Berlin, Heidelberg 2003.
- 12.48. V. Gelius, E. Basiliev, S. Svenson, T. Bergmark, K. Siegbahn, *J. Electron. Spectrosc.* **2**, 405 (1974).
- 12.49. E. de Hoffmann, V. Stroobant, *Mass Spectrometry: Principles and Applications*. John Wiley & Sons; New York 2001. J. H. Gross, *Mass Spectrometry: A Textbook*. Springer; Berlin, Heidelberg 2004.
- 12.50. W. Paul, "Elektromagnetische Käfige für geladene und neutrale Teilchen", *Phys. Bl.* **46**, 227 (1990).
- 12.51. W. C. Wiley, I. H. McLaren, "Time-of-flight mass spectrometer with improved resolution", *Rev. Sci. Instr.* **26**, 1150 (1955).
- 12.52. E. W. Schlag (ed.), *Time-of-flight mass spectrometry and its applications*. Elsevier; Amsterdam 1994.
- 12.53. D. M. Lubmann, *Lasers and Mass Spectrometry*. Oxford University Press; Oxford 1990.
- 12.54. I. I. Rabi, "Zur Methode der Ablenkung von Molekularstrahlen", *Z. Phys.* **54**, 190 (1929).
- 12.55. N. F. Ramsey, *Molecular Beams*, 2nd ed. Clarendon Press; Oxford 1989.
- 12.56. J. C. Zorn, T. C. English, "Molecular beam electric resonance spectroscopy", *Adv. Atom. Mol. Phys.* **9**, 243 (1973).
- 12.57. K. Bergmann, "State selection via optical methods", in G. Scoles (ed.), *Atomic and Molecular Beam Methods*. Oxford University Press; Oxford 1988.
- 12.58. N. F. Ramsey, *Spectroscopy with Coherent Radiation*. World Scientific; Singapore 1997.
- 12.59. D. D. Nelson, G. T. Fraser, K. I. Peterson, K. Zhao, W. Klemperer, "The microwave spectrum of K=O states of Ar-NH₃", *J. Chem. Phys.* **85**, 5512 (1986). J. Demaison, *Molecular Constants mostly from Microwave, Molecular Beam and Sub-Doppler Laser Spectroscopy*, Vol. 24 of *Molecules and Radicals*. Springer; Berlin, Heidelberg 1999.
- 12.60. J. Sanders, B. K. Hunter, *Modern NMR spectroscopy – A Guide for Chemists*. Oxford University Press; Oxford 2002.

- 12.61. B. Cowan, *nuclear Magnetic Resonance and Relaxation*. Cambridge University Press; Cambridge 1997. J. H. Nelson, *Nuclear Magnetic Resonance Spectroscopy*. Prentice Hall; 2002. T. L. James, *nuclear Magnetic Resonance of Biological Macromolecules*. Academic Press; New York 2005. E. D. Becker, *High Resolution NMR: Theory and Chemical Applications*. Academic Press; New York 1980.
- 12.62. C. P. Poole, *Electron Spin resonance: A Comprehensive Treatise on Experimental Techniques*, 2nd ed. Dover Publications; 1997. A. Carrington, A. D. McLachlan, *Introduction to Magnetic Resonance*. Chapman and Hall; London 1979.
- 12.63. W. Gordy, *Theory and Applications of Electron Spin Resonance*. John Wiley & Sons; New York 1980.
- 12.64. D. M. Lindsay, D. R. Herschbach, A. L. Kwiram, "Spin population in alkali trimer molecules", *Mol. Phys.* **39**, 529 (1980).
- 12.65. A. Oppelt, *Imaging Systems for Medical Diagnostics. Fundamentals, Technical Solutions and Applications*. Wiley-VCH; Weinheim 2005. P. G. Murriss, *Nuclear Magnetic Resonance Imaging in Medicine and Biology*. Clarendon Press; Oxford 1986.
- 12.66. F. Gerson, W. Huber, *Electron Spin Resonance for Organic Radicals*. Wiley-VCH; Weinheim 2001.
- 12.67. E. W. McDaniel, *Atomic Collisions*. John Wiley & Sons; Chichester 1989. N. Andersen, K. Bartschat, *Polarization, Alignment and Orientation in Atomic Collisions*. Springer; Berlin, Heidelberg 2001.
- 12.68. R. D. Levine, *Molecular Reaction Dynamics*. Cambridge University Press; Cambridge 2005.
- 12.69. R. Glaser, *Biophysics*. Springer; Berlin, Heidelberg 2001.
- 12.70. R. M. J. Cotterill, *Biophysics: An Introduction*. John Wiley & Sons; New York 2002.

Index

a

A-type transition 267
ab initio calculations 76
ab initio methods 72
AB₂ molecule 252
absorption 122
 linearly polarized radiation 134
 nonlinear 397
absorption coefficient 124, 274, 367
absorption path, effective 386
absorption profile, Doppler-free 164
absorption spectroscopy 363, 367
absorption spectrum 289
 continuous 148
action integral 103
adiabatic basis 297
adiabatic basis function 303
Airy function 151
alchemy 2
alkali metal clusters 352
allene 188
angle of observation, magic 421
angular dispersion 375
angular distribution 420
angular momentum 212
 coupling scheme 41
 projection 213
angular momentum component 208
angular momentum coupling 42
anharmonicity 132
anti-Stokes component 166

anti-Stokes scattering 291
anti-Stokes spectrum 168
apodization function 371
associative law 179
asymmetry parameter 218
atomic configuration 43
atomic hypothesis 2
atomic orbital 53, 249
atomic state, combination 43
atomic weight 3
attosecond range 409
aufbau principle 45
Auger process 422
autoionization 317
avoided crossing 304

b

band 147
band edge 146
band strength 139
band system 5
basis function 51, 75
beat signal 370
BeH₂ molecule 245
benzene 259
bolometer 394
bond energy 346
bonding 249
Born–Oppenheimer approximation 10
boron trifluoride 189
boson 172

bracket notation 65
butadiene 191, 257

c

C_{60} 359
carbon cluster 358
CARS 292
center of inversion 178
center-of-mass frame 79
centrifugal constant 84, 264
centrifugal distortion 82, 214
centrifugal energy 81
channeltron 426
character 194
 of direct products 202
 scalar product 200
 sum of squared 197
character table 194, 437–439
 abbreviated 202
class 180
classification 184, 191
cluster 9, 343, 350
 generation 359
 molecular 351
CO–Ar 346, 348
CO₂ molecule 250
 molecular orbitals 251
coincidence, delayed 408
collision
 elastic 159
 inelastic 159
 phase-disturbing 161
collision pair 158
collision process, molecular 434
collisional broadening 158
combination band 279
combination transition 280
combination vibration 281
commutative law 180
configuration interaction 75
conical intersection 314
contour line diagram 283, 315

control of chemical reactions 412
control, coherent 412
coordinate transformation 203
coordinates, generalized mass-weighted 221
Coriolis coupling 233
Coriolis force 232, 233
Coriolis interaction 206
correlation 47
correlation diagram 48, 49, 219, 252
correlation energy 74
correlation method 409, 410
Coulomb integral H_{AA} 55, 58
coupling 231
 magnetic moments 328
coupling coefficient 232
coupling of angular momenta 41
coupling of electronic and vibrational states 287
CS₂ molecule 6
cube 190
cylindric capacitor 417

d

Dalton 2
dark state 310
Darling–Dennison resonance 282
Debye 339
decay time 386
degree of orientation 327
diabatic basis 297
diabatic basis function 304
diabatic coupling element 305
dichlorobenzene 186
dichlorodifluoroethane 189
difference potential 143
 Mulliken 141
diffraction structure 375
diffusion 362
dipole
 electric field 116
 oscillating 125

- dipole approximation 127, 129
 - dipole matrix element 263
 - dipole moment 166, 276
 - induced 115
 - Dirac notation 52
 - direct product 199
 - direct sum 202
 - dissociation energy 91, 355
 - distribution, spectral 379
 - Doppler broadening 154
 - Doppler shift 155
 - Doppler width 156
 - double resonance
 - infrared–microwave 404
 - infrared–ultraviolet 403
 - Λ -type 403, 405
 - optical–microwave 403
 - optical–optical 403
 - optical–radiofrequency 403
 - techniques 402
 - V-type 403
 - double-minimum potential 255
 - Dunham coefficient 99
 - Dunham expansion 97, 99, 104, 293
 - dynamics, molecular 8
- e**
- eigenfunction 296
 - eigenvalue equation 213
 - Einstein coefficient 122
 - absorption 122
 - relations 123
 - spontaneous emission 123
 - stimulated emission 122
 - electric dipole moment 339
 - effective 340
 - permanent 339
 - electric moment μ_{el} 325
 - electron configuration 42, 45, 46, 248, 252, 254
 - electron density distribution 247
 - electron distribution, contraction 61
 - electron rotation 84
 - electron spin resonance 432
 - electron, delocalized 257
 - electronic dipole matrix element 286
 - electronic transition 286
 - electrostatic interaction 302
 - emission
 - spontaneous 122, 123
 - stimulated 122, 405
 - emission spectrum 288
 - energy
 - expectation value 52
 - magnetic 327
 - energy analyzer 416
 - energy eigenvalue 88
 - energy level diagram 250
 - energy transfer processes 407
 - ethene 188
 - ethyne 188
 - exchange integral 55, 58
 - excimer 148
 - excitation, stepwise 403
 - expansion, adiabatic 393
- f**
- Fano profile 318, 320
 - Faraday effect 389
 - femtochemistry 411
 - Fermi contact constant 335
 - Fermi polyad 282
 - Fermi resonance 231, 282
 - fermion 172
 - fine-structure component 50
 - fine-structure constant 305
 - fine-structure splitting 431
 - fine-structure term 41
 - fingerprint region 279
 - fluorescence radiant power 124
 - fluorescence spectrum 288, 289
 - fluorescence, laser-induced 389
 - formaldehyde 256
 - Fortrat diagram 137, 138, 146

- four-wave mixing 406
 Fourier transform 370
 Franck–Condon factor 139, 140, 144
 Franck–Condon principle 139
 quantum-mechanical formulation 142
 frequency distribution 353
 frequency modulation 364, 382
 full width at half maximum 151
 fullerene 345, 359
 fundamental transition 278
- g**
- Gaussian function 75, 76
 cartesian 76
 Gaussian profile 156
 glyoxal 187
 grating equation 377
 grating spectrograph 373, 377
 ground-state geometry 244
 group
 Abelian 180
 commutative 180
 cyclic 180
 multiplicative 179
 noncommutative 183
 group of atoms in molecules 280
 group theory 175, 179
- h**
- H₂ molecule 66
 approximation methods 72
 H₂⁺ molecule
 bond energy 62
 exact treatment 29
 LCAO treatment 56
 potential curve 62
 H₂O molecule 247, 252
 Hamiltonian 228
 Hamiltonian matrix 218
 Hartree approximation 65
 flow diagram 74
 Hartree–Fock approximation 73
- Hartree–Fock method 65
 He₂ molecule 346
 heat, specific 3
 Heisenberg’s uncertainty principle 60
 Heitler–London approximation 68, 69
 Hermite polynomials 88
 HF-CI method 76
 HOMO 418
 Hönl–London factor 139, 140, 148
 hot band 288
 Hückel method 258
 Hückel model 260
 Hund’s coupling cases 300
 case a) 300
 case b) 301
 case c) 301
 case d) 301
 Hund’s rule 47
 hybrid function 240
 hybrid orbital 243, 248
 hybridization 240
 hydrogen bond 357
 hydrogen peroxide 185
 hyperfine component, Zeeman splitting 335
 hyperfine structure 294, 334
- i**
- identity operation 197
 induction 117
 induction contribution 114
 inertia ellipsoid 211
 inertia tensor 207
 infrared active 276, 280
 infrared inactive 276
 infrared spectrometer 367
 infrared spectroscopy 366
 intensity of rotational transitions 269
 intensity profile 156
 interaction potential 116
 interferogram 369
 internal conversion 322

- intersystem crossing 322
 - inversion splitting 256
 - inverted perturbation approach 109
 - ionic character 68
 - ionization energy 355
 - isotopic shifts 100
 - iteration method 111
 - IVR processes 311
- j**
- Jahn–Teller effect 313
 - quadratic 315
 - Jahn–Teller potential surface 314
 - Jellium model 352, 354
- k**
- Kratzer relation 98
- l**
- Lagrange equation 221
 - Lamb dip 398
 - Λ doubling 308, 309
 - laser absorption spectroscopy 382
 - laser spectroscopy 381
 - Doppler-free 395
 - time-resolved 407
 - law of constant proportions 2
 - LCAO approximation 53
 - LCAO function 53
 - learning algorithm 413, 414
 - Lennard-Jones potential 118
 - lifetime 338, 407
 - light, unpolarized 136
 - line
 - polarization 331
 - profile 151, 161, 274
 - linear molecule 264
 - linewidth 323, 349
 - natural 152
 - local vibrational mode 279
 - lock-in 365
 - lone pair 252
 - l splitting 235
- m**
- magic angle 421
 - magnetic energy 327
 - magnetic moment μ_m 325
 - mass resolution 427
 - mass spectrometer
 - magnetic 423
 - quadrupole 424
 - time-of-flight 426
 - mass spectroscopy 422
 - matrix element 125, 126, 138, 217
 - Born–Oppenheimer approximation 128
 - melting temperature 351, 352
 - metal cluster 352
 - methane 190
 - Michelson interferometer 368
 - microcluster 351
 - modulation techniques 382
 - molecular beams 391
 - molecular configuration 76
 - molecular constants 99, 293
 - molecular orbital 45, 53, 65, 75, 237, 247, 259
 - multi-centered 238
 - nonbonding 245
 - molecular orbital approximation 66
 - molecular radical 9
 - molecular rotation 207
 - molecular spectra 4
 - molecular symmetry 11, 175
 - molecular vibration 86
 - molecules
 - diamagnetic 326
 - many-electron 63
 - paramagnetic 326, 327
 - rigid 10
 - triatomic 245
 - Zeeman splitting in diamagnetic 334
 - Morse potential 92
 - Mulliken difference potential 141

- multi-photon absorption 164
- multi-photon spectroscopy 401, 402
- multiple-reflection cell 384, 388
- multiplet component 306
- multiplication table 182
- multipole expansion 113
- multipole interaction 113
- n**
- Na_3 radical 433
- natural linewidth 154
- NH_3 molecule 254
- nitrogen molecule N_2 173
- NMR 429
- NMR spectrum 431
- nodal plane 238, 246
- noncrossing rule 49
- normal coordinate 222
- normal mode 192, 222
- normal vibration 275, 276
- nuclear magneton 332
- nuclear mass, reduced 79
- nuclear resonance 429
- nuclear spin quantum number 429
- nuclear spin statistics 171, 173, 272
- nuclei with magnetic moments 432
- nutaton cone 209
- o**
- $(\text{O}_2)_2$ molecule 349
- O_3 molecule 385
- $(\text{OCS})_2$ molecule 349
- octahedron 190
- one-electron approximation 46
- one-electron state 45
- operator 212
- orbital
 - energy 246
 - parity 238
- order 180
- orientational quantum number 170
- ortho boric acid 187
- ortho hydrogen 172
- oscillation, damped 152
- oscillator
 - anharmonic 91
 - classical damped 152
 - harmonic 87, 88
- overlap integral 55, 58, 244
- overtone band 132, 279
- overtone spectrum 385
- oxygen molecule O_2 173
- p**
- para hydrogen 172
- particle spectroscopy 361
- partition function 170, 270
- Paschen–Back effect 331
- Pauli principle 64
- perturbation 9, 293, 299
 - heterogeneous 295
 - homogeneous 295
- perturbation operator 302, 303
- perturbation potential 231
- phosphorescence 322
- photoelectron spectrum 422
- photoionization
 - cross-section 420
 - process 417
- photon scattering, inelastic 165
- π -electron system 257
- π light 135
- π orbital, molecular 239
- Planck law 123
- point group 181, 184, 185
- polarizability 166, 276, 291
 - electric 339
 - magnetic 326
- polarizability tensor 291
- polarization of lines 331
- polarization of transitions 332
- polarization spectroscopy 400
- polarization state
 - π light 135
 - σ^+ light 135
 - σ^- light 135

- population density 170, 269
 population, thermal 170
 potential
 effective 73
 quartic 93
 potential barrier 316
 potential curve 47, 57, 112, 118
 crossing 298
 diabatic 298
 potential surface 348
 predissociation 316, 344
 pressure broadening 160
 principal axes transformation 208, 222
 principal moment of inertia 208
 prism spectrograph 374
 process, photochemical 8
 projection quantum number Ω 41
 protons, equivalent 433
 pseudorotation 227, 316
 frequency 354
 pump-probe technique 410
- q**
- quantum chemistry 76
 quantum defect 318
 quantum yield 321
- r**
- R* centroid 142
 *n*th order 140
R centroid approximation 139, 142, 304
 radial function 80
 radiation characteristic 125
 radiation field, thermal 123
 radiation sources, continuous 373
 radiation spectroscopy 361
 radiationless transition 320, 321
 Raman effect 290
 Raman scattering 166
 resonant 165
 Raman spectra 167, 288
 Raman transition 165
- rare-gas cluster 345, 355
 Rayleigh scattering 166, 291
 reference frame
 laboratory-fixed 203
 molecule-fixed 203, 206
 reflection 182
 reflectron 427
 relative velocity, mean 159
 Renner-Teller coupling 311
 Renner-Teller effect 312
 representation 192-194
 n-dimensional 195
 irreducible 196
 of group C_{3v} 195
 one-dimensional 195
 product 198
 reducible 196, 199
 reduction 198, 201
 sum 198
 resolution 374
 spectral 376, 377
 resolution of spectral lines 374
 resonance integral H_{AB} 55
 resonance spectroscopy, laser-magnetic 388
 resonator, acoustic 388
 restoring force 225
 retarding-field method 417
 Ritz principle 51
 RKR method 105
 rotary-reflection axes 177
 rotation 81
 quantum-mechanical treatment 212
 rotational constant 82, 90, 214, 264
 mean 96
 rotational energy 84, 206, 207
 mean 96
 rotational group 271
 rotational level
 Zeeman splitting 329
 rotational level, Zeeman splitting 329
 rotational period 90

- rotational perturbation 307
- rotational quantum number J 81
- rotational Raman spectrum 290
- rotational Raman transition 168
- rotational spectrum 5, 83, 263
- rotational structure 145, 283
- rotational term diagram 214
- rotational term value 86, 214
- rotational transition 133
- rotational wavefunction 271
- rotor
 - rigid 81, 207
 - vibrating 96
- Rowland circle 378
- Rowland grating 378
- Rowland spectrograph 378
- Rydberg electron 318
- Rydberg state 317
 - molecular 405
- S**
- saturation hole 398
- saturation spectroscopy 399
- scattering cross-section 362
- Schönflies notation 184
- sector field, magnetic 423
- secular equation 53, 218
- selection rule 135
 - asymmetric top 268
 - electric dipole transitions 265
 - pure rotational transitions 266
 - rotational quantum number J 145
 - vibration-rotation transitions 285
 - vibrational transitions 275
- selection rules 294
- self-pressure broadening 160
- separation ansatz 80
- setup, experimental 380
- shell structure 352
- shielding constant 430
- shift 158
 - chemical 431
- σ^+ light 135
- σ^- light 135
- single-particle approximation 63
- Slater determinant 64
- Slater function 75, 76
- sp_z hybrid atomic orbital 241
- sp^2 hybridization 242
- sp^2d hybridization 243
- sp^3 hybridization 243
- spatial function 75
- spectral analysis 4
- spectrometer, Fourier 372
- spectroscopy 372
 - ESR 432
 - Fourier 366
 - intracavity laser 385
 - microwave 362
 - optothermal 394
 - photoacoustic 387
 - photoelectron 415
 - vacuum UV 380
 - ZEKE 418
- spherical harmonics $Y(\theta, \phi)$ 80
- spin function 75
- spin quantum number S 43
- spin relaxation 434
- spin state 44
- spin-orbit coupling 50, 294, 305, 336
- spin-rotation coupling 308
- spin-rotation coupling constant 309
- stability diagram 425
- Stark effect 339
 - second-order 341
- Stark modulation 366
- Stark shift, first-order 340
- Stark splitting 341
- state
 - excited 251
 - virtual 165
- statistical weight 270, 272
- step operator 216
- Stokes Raman scattering 291

- Stokes Raman spectrum 169
 Stokes spectrum 168
 streak camera 408, 409
 stretching vibration 225
 structure determination 430
 structure, bent 247
 subgroup 180
 surface atom 350
 susceptibility, magnetic 327
 symmetry axis 176
 symmetry element 175, 176
 symmetry operation 175, 181
 symmetry plane 176, 177
 symmetry property 43, 270
 even 44
 odd 44
 symmetry selection rules 295
 symmetry type 192, 295
 synchrotron radiation 379, 380
- t**
- Taylor expansion 230
 of potential 221
 theory of gases, kinetic 3
 thermal conduction 362
 time function 371
 time slot function 371
 top
 asymmetric 215, 267
 oblate symmetric 212
 prolate symmetric 211
 symmetric 85, 211, 266
 term values of asymmetric 220
 topological structure 9
 total angular momentum J 86
 total wavefunction 65
 transition
 electronic 138, 144
 multiphoton 161
 polarization 332
 radiationless 9
 transition point, classical 141
 transition probability 122, 130, 134,
 287
 collision-induced 160
 translation vector 194
 translational energy 206
 translational temperature 392
 transport phenomena 362
 trifluoro benzene 189
 tunneling process 316
 turning point, classical 107
 two-center integral 67, 70
 two-photon absorption 161
 Doppler-free 402
 two-photon resonance 165
 two-photon spectroscopy 163, 402
- u**
- uncertainty relation 154
 united atom 45
 UPS 415
- v**
- valence orbital, hybrid 255
 van der Waals bond 322, 343
 van der Waals cluster 352
 van der Waals interaction 116
 van der Waals molecule 9, 322, 343
 variational method 52
 velocity distribution, Maxwellian 155
 velocity, most probable 155
 vibration
 anharmonic 230
 degenerate 226
 localized 11
 normal modes 11
 of polyatomic molecules 221
 vibration–rotation interaction 95
 vibration–rotation Raman spectrum 168
 vibration–rotation spectrum 5, 129
 vibration–rotation transition 128, 136
 vibrational amplitude 224
 mass-weighted 225

vibrational angular momentum 234,
265
vibrational band 5, 136, 138, 145
vibrational constant ω_e 90
vibrational energy 206
vibrational period 90
vibrational term diagram 230
vibrational transition 131
vibrational wavefunction 89
vibronic coupling 309, 323
vibronic state 287
Voigt profile 157

W

Walsh diagram 252, 256
water clusters 357
water isotopomer 185
wavelength modulation 383
weight, statistical 170, 173
WKB approximation 101

X

x-ray structure analysis 435
XPS 415, 421

Z

Zeeman components 429
Zeeman effect 327
Zeeman splitting
 diamagnetic molecules 334
 of hyperfine components 335
 of rotational levels 329
Zeeman splitting of rotational levels 329
zero-point energy 88, 229